UNIVERSITY OF CALGARY

Rock physics and seismic methods for characterizing the heterogeneity of oil sands reservoirs in the Western Canadian Sedimentary Basin

by

Yong Xu

A THESIS

SUBMITTED TO THE FACULTY OF GRADUATE STUDIES

IN PARTIAL FULFILMENT OF THE REQUIREMENTS FOR THE

DEGREE OF DOCTOR OF PHILOSOPHY

DEPARTMENT OF GEOSCIENCE

CALGARY, ALBERTA

JANUARY, 2012

UNIVERSITY OF CALGARY

FACULTY OF GRADUATE STUDIES

The undersigned certify that they have read, and recommend to the Faculty of Graduate Studies for acceptance, a thesis entitled "Rock physics and seismic methods for characterizing the heterogeneity of oil sands reservoirs in the Western Canadian Sedimentary Basin" submitted by Yong Xu in partial fulfilment of the requirements of the degree of Doctor of Philosophy.

Supervisor, Dr. Laurence R. Lines, Department of Geoscience

Dr. John C. Bancroft, Department of Geoscience

Dr. Gary Margrave, Department of Geoscience

Dr. Harvey Yarranton, Department of Chemical and Petroleum Engineering

---

External Examiner Dr. Michael Enachescu, Department of Earth Sciences, Memorial University of Newfoundland

---

Date

Abstract

This thesis develops seismic prediction of the heavy oil reservoir heterogeneities in the Western Canadian Sedimentary Basin (WCSB). The thesis starts with studies on rock physics of the oil sands reservoirs in Athabasca to find the qualitative and quantitative relationships between the lithology and seismically derivable elastic parameters, which determines the feasibility of seismic applications. With an understanding of rock physics, the thesis makes seismic method developments to derive lithology sensitive elastic parameters for the qualitative and quantitative prediction of reservoir heterogeneity.

The amplitude variation with offset (AVO) inversion is a well-established method to derive elastic parameters from the seismic data. But the AVO inversion is ill-posed if it derives three elastic parameters. To overcome the ill-posedness, a Bayesian constraint is naturally chosen by the industry. The thesis shows that the Bayesian estimator contains two terms – the data term and prior term. While the data term is the solution used in most industrial practices of the AVO inversion, the complete estimate makes more sense with the help of the prior term. The practical implementation of the Bayesian AVO inversion improves the effectiveness of reliably deriving lithology-sensitive density, demonstrated in two case studies in the Athabasca oil sands. The AVO inversion provides attributes for the statistical and qualitative interpretation.

It is the requirement of the quantitative reservoir characterization to convert seismic data into log-like elastic properties. An inversion scheme is designed and tested by a realistic oil sands point bar model. Three band-limited parameters from the AVO inversion are jointly inverted into absolute values by incorporating many constraints including the lateral local geology and rock physics. Seismic geometrical attributes are used to build reliable models for inversion and reservoir geometry mapping.

For reliable reservoir characterizations, the seismic amplitudes should be recovered and preserved properly in data processing. The data fidelity for the extraction of elastic parameters is improved by the post-processing conditioning. Data examples show the amplitude recovery and AVO friendly processing. Developments are made on the offset-dependent tuning and NMO stretching correction and the reduction of impact on AVO by the irregularity of 3D surveys.

Acknowledgements

I would like to thank Dr. Larry Lines, my dissertation supervisor, for his guidance and many useful suggestions. My interests in heavy oils and CHORUS (Consortium for Heavy Oil Research by University Scientists), founded by Larry, are the main reasons why I chose to do a PhD degree under Larry's supervision. Larry's vast knowledge on geophysics and keen and intuitive understanding of geophysics have helped me throughout my studies.

Dr. John Bancroft was the supervisor of my M.Sc. program which brought me from China to Canada 15 years ago. John is a member of my PhD supervisory committee. I thank John for his teaching and guidance during both programs.

My M.Sc. program was completed in CREWES project, Department of Geoscience at University of Calgary, where I built a knowledge base and skills for a career in the petroleum industry. I thank CREWES faculty, Drs. Gary Margrave (member of supervisory committee of my PhD program), Rob Stewart and Ed Krebes, and staff for their teaching, guidance, and support.

I was employed by Integra Geoservices Inc, Corelab Reservoir Technology Division, Paradigm Geophysical, and Arcis Corporation in the past. Many people helped me with their experience, knowledge, and friendship. Among them are Jon Downton and Satinder Chopra. When Jon worked for his PhD degree, he shared with me his thoughts and literature. From his thesis and discussion, I was inspired and started some studies on Bayesian inversion which becomes a major part of my thesis. It was a pleasant time working in the reservoir group in Arcis with Satinder Chopra, an energetic and hard-working person. Satinder is well-known in the local and international communities of geoscientists. I benefited much from his comprehensive knowledge, keen understanding of technology, excellent skills of writing and presentation, and friendship.

Special thanks to Arcis Corporation for providing seismic data used by many examples in this thesis and to an anonymous company for providing a 2D seismic dataset in the Athabasca oil sands. The FOCUS processing system from Paradigm Geophysical and the Hampson-Russell software packages were used to generate many displays in this thesis.

I am indebted to Larry Lines and Joan Embleton for proofreading this thesis.

I thank Drs Larry Lines, John Bancroft, Gary Margrave, Harvey Yarranton, and Michael Enachescu for reading this thesis and being in the committee of thesis defence.

I am grateful for the financial resources from Arcis Corporation (during first year of the program) and Imperial Oil Ltd (during the rest of the program).

To my wife, children, and parents

Table of Contents

List of Tables

List of Figures and Illustrations

List of Symbols, Abbreviations, and Nomenclature

Symbol	*Definition*
Vp (or α)	Compressional wave (P wave) velocity
Vs (or β)	Shear wave (S wave) velocity
ρ (rho)	Bulk density
Ip	P impedance
Is	S impedance
Vp/Vs ratio (or Vp/Vs)	P wave and S wave velocity ratio
σ	Poisson's ratio
λ(lambda)	Incompressibility
μ(mu)	Shear modulus or rigidity
λ/μ (lambda/mu)	Incompressibility and rigidity ratio
$\lambda\rho$(lambda*rho)	Product of incompressibility and density
$\mu\rho$(mu*rho)	Product of shear modulus and density
$\overline{\mathbf{m}}$ (or μ)	Mean of model parameter vector
$\Sigma_{\mathbf{m}}$	Covariance of model parameters
$\hat{\mathbf{m}}$	Estimator of model parameter vector
$\Sigma_{\hat{\mathbf{m}}}$	Covariance of model parameter estimator
$\sigma_1, \sigma_2, \sigma_3$	Variances
ANN	Artificial Neural Network
API	America Petroleum Institute unit for radioactivity logging
API	America Petroleum Institute gravity
AVO/AVA	Amplitude Variation with Offset/Angle
CMP	Common Mid-Point
CDP	Common Depth Point
DC	Direct Current
GR	Gamma Ray
IHS	Inclined Heterolithic Stratification
LMR	Lambda-Mu-Rho
MAP	Maximum *a posteriori*
NMO	Normal Move-Out
PDF	Probability density function
PNN	Probability Neural Network
PP	P wave incidence and P wave reflection
PS	P wave incidence and S wave reflection
PSTM	Pre-stack Time Migration
QDA	Quadratic Discrimant Analysis
RMS	Root of Mean Squares
SAGD	Steam Assisted Gravity Drainage
S/N	Signal-to-Noise
Vshale	Shale Volume
WCSB	Western Canadian Sedimentary Basin

CHAPTER 1: INTRODUCTION

Oil sands reserves have recently been considered to be a significant part of the world's oil reserves, as higher oil prices and new technology enable them to be profitably extracted and upgraded to usable products. Many countries in the world have large deposits of oil sands, including the United States, Russia, and various countries in the Middle East. However, the world's largest heavy oil deposits occur in two countries: Canada and Venezuela, each of which has oil sand reserves probably on the order of 3.5-4 trillion barrels of oil in place (bbl OOIP) (Dusseault, 2001). Since growth of oil sands production has exceeded declines in conventional crude oil production, Canada has become the largest supplier of oil and refined products to the United States, ahead of Saudi Arabia and Mexico – exporting 1.938 million barrels per day in 2010, according to U.S. Energy Information Administration (EIA). Most of the oil sands of Canada are located in three major deposits in northern Alberta. These are the Athabasca-Wabiskaw oil sands of north northeastern Alberta, the Cold Lake deposits of east northeastern Alberta, and the Peace River deposits of northwestern Alberta. They cover over 140,000 square kilometers and hold proven reserves of 1.75 trillion barrels of bitumen in place. About 10% of this, or 173 billion barrels, is estimated by the government of Alberta to be recoverable at current prices using current technology, which amounts to 97% of Canadian oil reserves and 75% of total North American petroleum reserves (Government of Alberta website). The Alberta oil sand deposits contain at least 85% of the world's reserves of natural bitumen (representing 40% of the combined crude bitumen and extra-heavy crude oil reserves in the world), but are the only bitumen deposits concentrated enough to be economically recoverable for conversion to synthetic crude oil at current prices. The largest bitumen deposit, containing about 80% of the Alberta total, and the only one suitable for surface mining, is the Athabasca Oil Sands along the Athabasca River. The mineable area (as defined by the Alberta government) includes 37 townships covering about 3,400 square kilometers near Fort McMurray. The smaller Cold Lake deposits are important because

some of the oil is fluid enough to be extracted by conventional methods. All three Alberta areas are suitable for production using in-situ methods such as the cyclic steam stimulation (CSS) and steam assisted gravity drainage (SAGD).

Figure 1.1 shows the locations of the three major oil sands areas in western Canada. The study in this thesis focuses on the Athabasca oil sands because of the significance of understanding reservoir heterogeneities for the heavy oil production.

Figure 1.1 Canadian oil sands distribution (source: Wikipedia).

In the Athabasca oil sands area, bitumen is predominately contained within the Lower Cretaceous McMurray Formation, which is a part of the Mannville Group (Figure 1.2). The McMurray Formation can be up to 100m thick in the east and less than 10m thick in the west as it thins towards the Grosmont High (Figure 1.3), and has an average pay thickness of 35m. In general, the McMurray Formation was deposited in a north-south trending ridge and valley system formed by fluvial processes, but with subsequent facies change to a marine depositional environment during a sea-level rise.

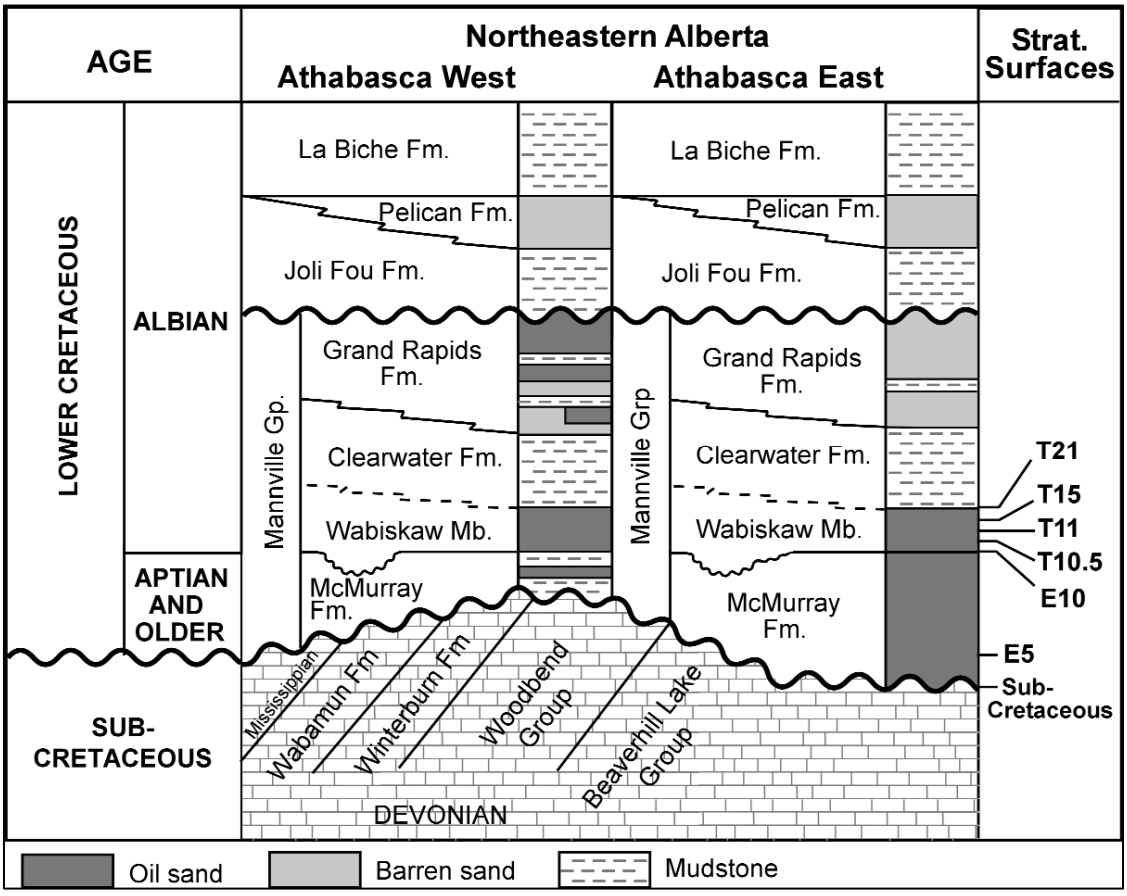

Figure 1.2 Stratigraphy of the Lower Cretaceous in Athabasca oil sands area (Source: Wynne et al 1994).

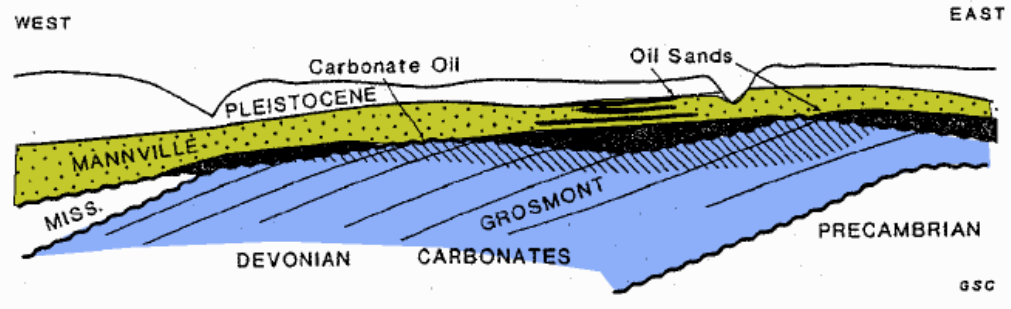

Schematic section showing oil trapped in sands and carbonates (from Proctor et al., 1983). Reproduced with the permission of the Minister of Public Works and government Services Canada, 2004, and Courtesy of Natural Resources Canada, Geological Survey of Canada.

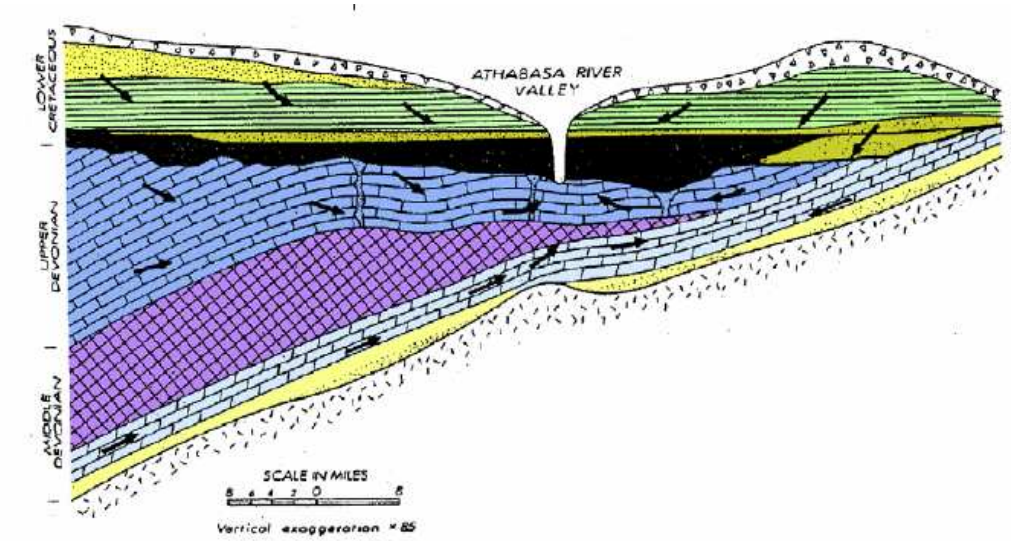

Schematic diagram of regional groundwater flow and salt collapse (from Page, 1974). Reproduced with the permission of the Canadian Society of Petroleum Geologists.

Figure 1.3 Geological cross-sections, Northern Alberta (Source: Stanton, 2004).

There is an informal division of the McMurray Formation which is helpful in understanding the overall geological setting:

Lower McMurray – medium to coarse grained sands, predominantly composed of quartz and feldspar; some eroded cross-bedding, but generally massive; a fluvial environment, with some braided channel systems.

Middle McMurray – sands and silts interpreted to be a tidally influenced point bar and estuarine depositional environment.

Upper McMurray – variable, but generally interpreted to be shallow, low-energy marine shoreface deposit with some small deltaic complexes.

The McMurray Formation is overlain by the Wabiskaw Member (the part of the Clearwater Formation of the Mannville Group)

1.1 RESERVOIR HETEROGENEITY

The McMurray Formation in Athabasca can be quite complex, given that the incursion of estuarine/marine sediments over ridge and valley fluvial sediments generated numerous erosional surfaces. In a regional sense, this geological setting is well-established, but locally predicting the facies type and extents can be very difficult. Deterministic local predictions of the oil-bearing sand units can be subjective, especially if the drillhole/well spacing is too far apart to be able to reliably pick key geological information. It is likely that there would be considerable uncertainties even with closely spaced data.

The complex reservoir stratigraphy and architecture are inherited from dynamic depositional processes that range from fluvial to shallow marine. The main bitumen hosting zones are thought to have been deposited in estuarine settings of the Middle McMurray Formation. It has been suggested that the sequence consists of multiple estuaries overlapping in space and time (Wightman and Pemberton, 1997), and that each estuary comprises several hierarchical levels of heterogeneity. Fluvial, estuarine and shallow marine lithofacies assemblages (i.e. lower, middle and upper McMurray Formation, respectively) are able to be mapped between exploration wells. However, due to significant heterogeneities, correlating individual estuarine facies is difficult, even with closely spaced wells (100-150 meters apart). Heterogeneity is due to a complex interfingering of estuarine architectural elements such as point bars, abandoned channels and tidal flats.

Steam Assisted Gravity Drainage (SAGD) is a commonly used in-situ production technology in the Athabasca oil sands area. The design of SAGD and process of production of bitumen in an ideal homogeneous reservoir are illustrated in Figure 1.4. In the SAGD process, two parallel horizontal oil wells are drilled in the formation, one about 4 to 6 meters above the other. The upper well injects steam, possibly mixed with solvents, and the lower one collects the heated crude oil or bitumen that flows out of the formation, along with any water from the condensation of injected steam. The basis of the process is that the injected steam forms a "steam chamber" that grows vertically and horizontally in the formation. The heat from the steam reduces the viscosity of the heavy crude oil or bitumen which allows it to flow down into the lower wellbore. The steam and gases rise because of their low density compared to the heavy crude oil below, ensuring that steam is not produced at the lower production well. Spatially extensive thick shale plugs become vertical steam barriers and often fail SAGD operation. Successful SAGD wells require good quality reservoirs without thick shale streaks and with enough thick sands (minimum 12 meters, according to Walsh (2005)). When the reservoir heterogeneity is high (with thick shale plugs or many thin shale barriers), the SAGD production is not efficient. The impact of reservoir heterogeneity on the in-situ production is illustrated by the irregular stream chamber development along SAGD wells (Figure 1.5) (Yeung, 2007).

The heterogeneity of reservoirs (shale-prone zones in sands) reduces the efficiency of the in-situ production. Therefore, the reservoir heterogeneity should be understood before the SAGD project starts. The effects due to in-situ productions seem apparent enough to be observed by seismic methods. However, the reliable mapping of lithofacies prior to deploying a SAGD is more difficult but critical to a successful production.

Seismic data has a long history of applications in the characterization of conventional reservoirs with the help of rock physics and petrophysics. It has recent applications on characterizing the heavy oil heterogeneity in the Western Canadian Sedimentary Basin (WCSB). The objective of this thesis is to develop and improve seismic methods for

reliably mapping the heterogeneity in heavy oil reservoirs. As an important part of the reservoir characterization, rock properties are studied prior to seismic applications.

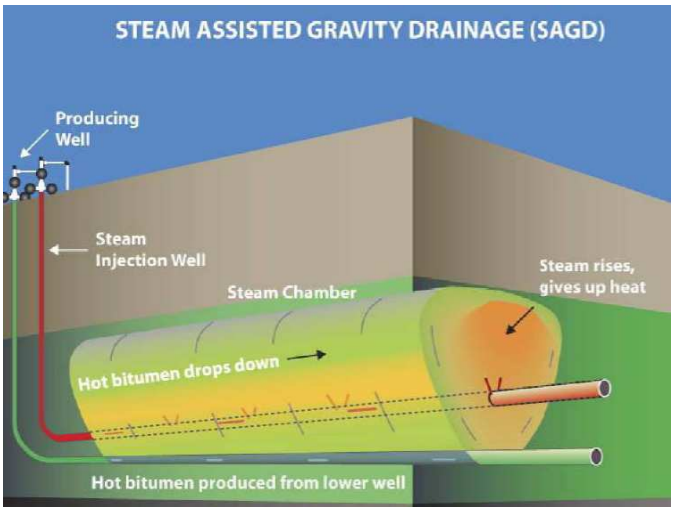

Figure 1.4 Illustration of SAGD and process of streaming injection, steam chamber forming, and production of bitumen. The illustration uses an ideal homogeneous reservoir (Source: Encana/Cenovus webpage).

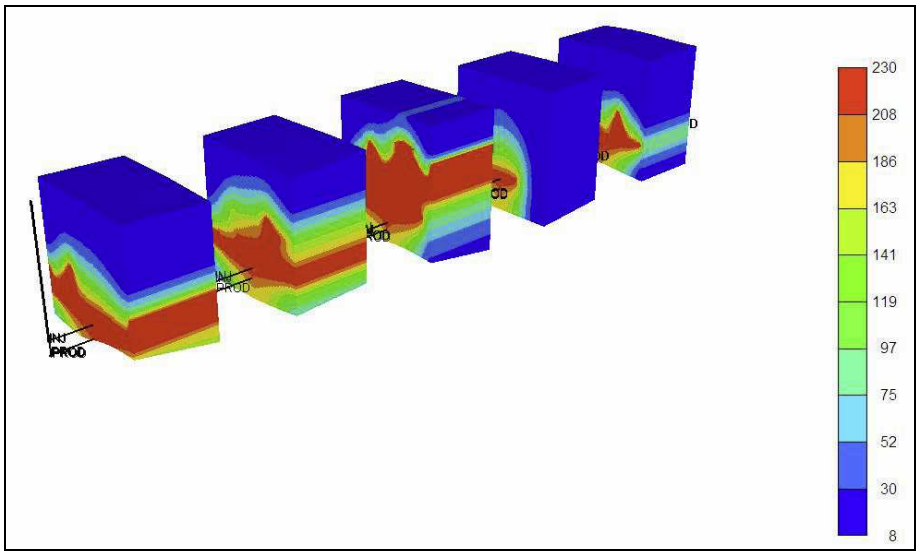

Figure 1.5 Cross section steam chamber along SAGD wells (colors for temperature) (Source: Yeung 2007).

1.2 ROCK PROPERTIES

Rock properties are the foundation for applying the seismic method in reservoir characterizations. The rock property studies for heavy oils in the past have focused on understanding the impact of in-situ production on bitumen and rocks (Han 2008; Kato, 2008; Mochinaga, et al, 2006). The Biot-Gassmann equations are used to model thermal production (Dumitrescu, 2010, Kato, 2008). Viscoelasticity of heavy oils is an important characteristic of oil sands reservoirs (Lines et al, 2008; Vasheghani et al, 2010). Rock physics studies for the lithofacies discrimination have found that the bulk density (Andersen et al, 2005 Gray et al, 2006; Dumitrescu et al, 2005, Xu and Chopra, 2008), Lame's parameters (Bellman, 2008) and the P and S velocity ratio (Vp/Vs ratio) (Dumitrescu and Lines, 2009) are among the parameters useful for distinguishing sand from shale in heavy oil reservoir formations. Since the lithofacies prediction by using seismic methods is the focus of this thesis, the main objective of the rock property study is to understand the relationship between the lithology and seismically derivable elastic parameters.

1.3 SEISMIC METHODS

Due to the limit of the minimum well spacing, it is necessary to use seismic data to understand the reservoir heterogeneity between boreholes. The vertical resolution of the seismic data, which is 5-10 meters in the oilsands area, is lower than that of the well log data, which is usually less than one foot. But seismic data is good at characterizing the geometry of subsurface between wells. In the oilsands area, 2D seismic acquisitions usually aim at a spatial resolution of a few meters. The geometry of point bars can be clearly identified by 3D seismic amplitudes (Fustic et al, 2007; Labrecque, 2010). The seismic data are not only used in the development of oil sands reservoirs requiring in-situ production but also enables mapping the reservoir thickness and integrity of the Devonian, which can be a water issue for open-pit mining of bitumen in the shallow reservoirs --sinkholes from karstification in the Devonian.

Typically, seismic data helps in understanding structures and stratigraphy. Since the McMurray Formation overlies on the top of the Devonian unconformity, accurate mapping of the topography of the Devonian unconformity is critical for mining and in-situ production of oil sands. The industry has been using 2D/3D seismic data to identify the tops of the McMurray and Devonian formations. Sequence stratigraphic and depositional facies framework is done with the help of seismic stack data (Nardin et al 2007). Seismic data are incorporated into the reservoir characterizations of heavy oils (Fustic et al, 2007) and help to understand the structure between wells. Wells have been drilled in very dense grids, but the fluvial/estuarine facies in the McMurray Formation is highly heterogeneous, which makes it impossible to predict the lithology 100 meter or less away from wells. It is necessary to evaluate the feasibility of seismic applications to map reservoir heterogeneity, lithofacies and bitumen saturation. Hopefully seismic data enables us to reduce the uncertainty of structural and lithological prediction between well controls.

Applications of seismic data in prediction of oil sands reservoir lithological heterogeneities have been found in the last decade. The applications can be classified into two categories: the statistical and deterministic approaches. It is certainly more useful if two approaches are combined. Most attributes extracted from seismic data are insensitive to lithofacies changes and some attributes derived from seismic data contain great uncertainties despite the fact that they are sensitive to reservoir heterogeneities. In the statistical approach, many attributes are correlated with well controls through a learning process to extract the linear or nonlinear correlation between the attributes and reservoir properties which can map the reservoir heterogeneity (Tonn, 2002; Anderson et al, 2005; Dumitrescu and Lines, 2008 and 2009). On the other hand, the reservoir types and lithofacies classifications are completed by the deterministic approaches using the AVO inversion and Lambda-Mu-Rho^{TM} (LMR^{TM} – a trade mark of EnCana) technology (Gray and Anderson, 2001; Xu and Chopra, 2008; Bellman 2008; Bellman and Connelly, 2010). The objectives of this thesis are to develop and improve seismic methods in order to

reliably map the heterogeneity in heavy oil reservoirs, and these methods include AVO inversion and quantitative prediction of reservoir properties from seismic data.

1.4 CHAPTERS IN THE THESIS

1.4.1 Rock properties of the heavy oils in the WCSB – Chapter 2

Rock physics of reservoirs plays an important role in the seismic reservoir characterization. The change of reservoir properties causes the variation of rock physics, and therefore generates the seismic anomalies. Rock physics bridges the seismic data, reservoir properties, and geology of reservoir formations. Since the main objective of this thesis is the characterization of reservoir heterogeneities by the application of seismic data, a good understanding of the sensitivity of rock physics parameters behind seismic data to reservoir heterogeneity is necessary. Chapter 2 studies the lithology sensitivity of elastic physical parameters and evaluates the feasibility of seismic applications to derive the lithology-sensitive parameters. Well logs and core data are used in the evaluation. The analysis is done statistically and as quantitatively as possible. In addition, this chapter has a brief discussion on the separation between water and bitumen in the reservoir formations.

1.4.2 Application of AVO in heavy oil reservoir characterization – Chapter 3

The major objective of the AVO application in heavy oil reservoir characterization is the lithology prediction. Prediction of fluids is an equally important objective. The AVO anomalies caused by the lithofacies variation are not as strong as the typical gas saturation in clastic reservoirs. The AVO analysis in heavy oils for the lithology heterogeneity prediction needs to extract lithology sensitive parameters (bulk density in oil sands) from the wide angle pre-stack seismic data. The techniques developed in Chapter 3 include the Bayesian AVO inversion, frequency domain realization, lateral correlation constraints, and other practical treatments for more reliable oil sands reservoir solutions. Two real data examples from the oil sands areas show the effectiveness and reliability of improved AVO inversion. The real data examples also show the

conventional AVO analysis is able to help predict the lithology heterogeneity in the oil sands reservoirs.

1.4.3 Quantitative prediction of the reservoir heterogeneity in oil sands – Chapter 4

The AVO inversion provides bandlimited elastic parameters. However, to quantify the reservoir properties, full bandwidth elastic parameters are needed. Chapter 4 makes developments on the joint inversion of AVO attributes to generate full bandwidth elastic parameters. The process includes the initial model building, seismic geometrical attributes, lateral and rock physics constraints. A realistic reservoir model is built to include a point bar in the McMurray Formation and the modeled AVO dataset is generated to test the inversion algorithm.

1.4.4 Seismic data processing and conditioning for reservoir characterization – Chapter 5

The reliability of seismic reservoir characterization is closely related to the fidelity of seismic amplitudes. Chapter 5 discusses basic flows to preserve the amplitude integrity in the seismic data processing and the techniques to condition the prestack data for the purpose of extracting elastic parameters. Real data examples illustrate the effectiveness of key steps in recovering amplitude losses and removing effects affecting the AVO fidelities in the AVO friendly processing flow. Data conditioning is important for the AVO analysis to meet the basic assumption of the AVO theory. This chapter demonstrates the developments and practices for conditioning data, including the offset-dependent tuning and NMO stretching, residual NMO correction, amplitude preservation quality control and fix, and correction of effects due to the irregularity of 3D surveys and the PSTM binning of 3D data.

1.5 SUMMARY OF ORIGINAL CONTRIBUTIONS

The original contributions in this thesis are summarized as follows:

1. Rock properties from various oil fields in oil sands are compared for lithology prediction. Many elastic parameters are evaluated for lithology separation. It is found that the reservoir depth in oilsands should be considered for choosing parameters to predict lithology.
2. Rock properties of water and bitumen saturated sands are compared showing possibility to distinguish bitumen and water saturated sands. The study of rock elastic properties shows that it is possible to distinguish highly bitumen-saturated sand from highly water-saturated sand using high quality seismic data.
3. Evaluate the possibility of using bandlimited rock properties for lithology prediction. The evaluation on density logs shows that the bandlimited density still show good correlation with lithology, but the correlation becomes poor if the low cut frequency in the data is higher than 20 Hz.
4. In the AVO inversion, an initial model is included and the initial model is built in a data-driven way in the thesis. The function of the rock property covariance matrix is evaluated, and it is found that the solution of the AVO inversion is sensitive to the correlation coefficient of rock properties in the covariance matrix. The implementation of the AVO inversion is in the frequency domain, which is advantageous to cope with offset-dependent tuning and constraints. The AVO inversion is also constrained by lateral continuity in the data.
5. Application of the AVO inversion on two seismic datasets from Athabasca oil sands areas shows that the density reflectivity (and relative density) can be reliably obtained from prestack seismic data and the bandlimited density can be used to identify high quality reservoirs in oil sands.
6. Joint PP and PS AVO inversion is formulated and it is suggested to implement the inversion in the frequency domain to cope with the different bandwidths of PP and PS data. Bayesian constraints are used in the joint PP and PS inversion, showing more reliable output.

7. The output of the AVO inversion, P, S, and density reflectivities, is chosen as the input of post-stack joint inversion to generate full bandwidth elastic parameters from seismic data. Cascading the AVO inversion and post-stack joint inversion separate the ill-posedness and non-uniqueness in two inversion processes makes computation cost-efficient and outputs useful intermediate results.
8. Geometrical attributes are studied to understand their feasibility to predict reservoir heterogeneity in the oil sands.
9. Rock property prediction by probability neural network (PNN) is used in building the initial model for the post-stack P, S, and density joint inversion. The uncertainty of PNN prediction will be studied in the future, and so that the prediction and uncertainty of PNN will be included in a Bayesian post-stack joint inversion.
10. To correct the NMO stretching and offset-dependent tuning effects, decon-like approaches or spectral balancing is usually used in the industry. It is shown in the thesis that the missing high frequency components at far offset could not be recovered from the data at far offset alone. An approach using the frequency domain AVO inversion is introduced to correct the NMO stretching and offset dependent tuning effects, which results in high-fidelity prestack seismic data.
11. Issues of AVO analysis related to 3D data sets are studies. Adaptively superbinning data for more balanced offset-fold distribution is designed and affirmed by real data test.

This page is left blank intentionally.

CHAPTER 2: ROCK PROPERTIES OF HEAVY OILS IN THE WCSB

This chapter investigates the relationship between rock properties and reservoir properties, mainly lithology, in the heavy oil reservoirs in the WCSB. The study includes an analysis of the sensitivity of elastic parameters to the lithology, a discussion on the separation of water and bitumen in the reservoir formations, and an evaluation of the feasibility of seismic applications. The understanding of the inter-relationships between rock physical parameters and reservoir properties, such as lithofacies, porosity, and pore fluid is an essential part of the seismic reservoir characterizations in the later chapters.

2.1 INTRODUCTION

Rock properties play an important role in the seismic reservoir characterization. In a seismic reservoir characterization project, rock properties and reservoir properties are studied for multiple purposes:

1. The change in reservoir properties (such as facies, porosity, saturation, fluid types etc.) causes a change in the physical parameters of the reservoir rocks (such as impedance, density, and Poisson's ratio). Rock property study helps to understand the relationship between the rock physical parameters and reservoir properties.
2. Seismic reservoir characterization uses attributes derived from the seismic data to infer the reservoir properties where there are no well controls. From the rock physical and petrophysical data, we can find the seismically derivable rock physical parameters sensitive to reservoir properties.
3. In a rock property study, one can conduct necessary statistical analyses for the prediction of reservoir properties. The statistics of rock properties is important for the linear or non-linear classification, prediction, and inversion of reservoir properties and types. Statistical distribution (the probability density functions (PDF)) of rock physical parameters for each reservoir classes can be derived from the rock property measurements.

4. Rock physical relationships can be used to model unavailable elastic parameters, to modify reservoir types, and to replace reservoir fluids to understand the feasibility of seismic applications. The synthetic data can also be used to quality-control the real seismic data by comparing the amplitude variation with offset on the synthetic data and real data.

2.1.1 Data and method

There is a large rock property literature (Han et al, 1986; Mavko et al, 1997; Castagna, 1985, 1993; Wang, 2001). These published studies provide methodologies and applications of rock properties in reservoir characterization, as well as useful constants and fundamental principles of rock properties and reservoir properties for oil and gas exploration and production. Also included in the published literature are studies on the rock physics and petrophysics for the heavy oil reservoirs in the WCSB (Bianco et al, 2008; Das and Batzle, 2008; Evans and Hua, 2008; Gray, 2011; Han et al, 2008; Kato et al, 2008; Lines et al, 2010; Mochinaga et al, 2006; Nakayama et al, 2006; Vasheghani et al, 2010). Many results and conclusions in those studies can be used on the heavy oil reservoir characterization in the WCSB. Some of the results are referenced in this chapter.

The principles and relationships of rock properties, such as mudrock lines (Castagna, 1985), are usually meaningful in general in the seismic application. But a local study of rock properties is usually necessary for a creditable reservoir characterization project because of the complexity and statistical nature of rock physics and many regional factors impacting rock physics, such as pressure, temperature, burial depth, and saturation. The rock property study in heavy oil reservoir formations in this thesis also shows that a given physical parameter has variable sensitivities to the reservoir properties, such as facies, for different heavy oil regions even though the reservoirs are all in the same formation, such as the McMurray Formation in the Athabasca oil sands area.

2.1.1.1 Data

The rock property study in this thesis mainly uses well logs, including gamma ray, density, sonic, shear sonic, resistivity, neutron porosity, and calliper. The well logs are from six heavy oil regions in Athabasca and Peace River in the WCSB. The reservoir formations in Athabasca include the McMurray, Wabiskaw, and Grand Rapids formations; the reservoir formation in Peace River is the Bluesky Formation. This study focuses on the McMurray Formation in Athabasca, which is known to be heterogeneous and it is necessary to characterize this heterogeneity. In the Athabasca area, the shear sonic is logged in many wells drilled for oil sands in the last decade; most of the wells in other areas in the study only have gamma ray, density, and sonic logs, and no shear sonic logs. Results of facies analysis based on core data are available for two areas in the Athabasca heavy oils.

2.1.1.2 Method

In the rock property study and AVO analysis, crossplots are well known and commonly used. Two (or three) parameters are cross-plotted to identify anomalies and understand the separation between different groups of rocks, facies, and fluid types. Crossplots are usually good for the visualization and qualitative purpose. Many rock physical parameters are cross-plotted against the lithology in this study.

The gamma ray log (abbreviated as GR) is a record of a formation's radioactivity. The radiation emanates from naturally-occurring uranium, thorium, and potassium. Most rocks are radioactive to some degree. However, amongst the sediments, shales have by far the strongest radiation. Although it is insufficient to equate gamma ray emission with shale occurrence, the gamma ray log is still principally used quantitatively to derive shale volume by petrophysicists for the most sedimentary formations. In the oilsands reservoir formations, the typical lithofacies include cross-bedded sand (the least shale, the top quality reservoir sand)), sandy point bar (sand with some shale), muddy point bar (very shaley sand), and abandoned channel (shale dominated). This classification of lithology is basically determined by the shale volume. Since the gamma ray log is usually used to

quantitatively derive shale volume, it is used to indicate lithology in this study. A gamma ray log curve is usually a good indicator of clay contents or shale volumes. Shale and clay are undistinguished by most petrophysicists. Because of the inclined heterolithic stratification (IHS) in the point bar systems formed in a fluvial-estuarine depositional environment in the Athabasca oil sands reservoirs, shale is a key factor impacting on the quality of reservoirs and the efficiency of in-situ thermal production. It is acceptable to understand relationships between the rock property and lithology by using the gamma ray logs. Gamma ray values have good correlations with grain sizes and facies in the deltaic and fluvial environments where deposition is largely controlled by the flowing current energy (Rider, 2002) while the correlation between gamma ray values and marine or shore facies is weak.

For the reservoir engineers, the facies analysis is more practical than gamma ray logs, as the facies are not only related to lithologies but also indicative of the lateral characteristics of reservoirs. Here facies analysis is referred to the determination of facies based on drilling core samples. The facies data used in the study is well-correlated with gamma ray values in spite of some deviations which are possibly due to the resolution difference in the logging and core analysis. A detailed analysis for these deviations, which could not be made in this thesis, should compare the logs and core samples or core photos. However, the gamma ray logs are not good at indicating the shorefaces in the upper McMurray Formation, which mix the sand and shale.

Twelve elastic parameters are cross-plotted against gamma ray values (unit: API). To be more quantitative, the correlation coefficients between physical parameters and gamma ray values are calculated and used to evaluate the sensitivity of physical parameters to lithology variations. A strong correlation would indicate a strong sensitivity to lithology.

Various pairs of elastic parameters are also cross-plotted and samples are color-coded by gamma ray values. As a qualitative approach, these cross-plots help to look for pairs of parameters good at separating and classifying lithologies.

The mean value and standard deviation of each physical parameter are calculated for the sand and shale in the reservoir with the assumption of a normal distribution. These means and deviations are also used to evaluate the sensitivity of physical parameters to lithology. The assumption mono-modal normal distribution is generally valid for each lithofacies. It is less rigorous to define non-detailed facies classification such as sand versus shale using mono-distribution, but this is left as future work when enough detailed facies data are available.

The probability density function (PDF) of each lithology (facies) is defined in this rock property study. PDFs are used to project the seismically derived physical parameters to facies classes. The means and covariance of elastic parameters for the sand and shale are used to conduct a quadratic discriminant analysis (QDA) to quantify the separation of sand and shale in the multi-parameter space.

One of the purposes in studying rock properties is to apply their relationships in the seismic reservoir characterization. The band-limited nature of seismic data often limits the appreciation. The final part of this chapter evaluates the effect of the limited bandwidth of elastic parameters on their sensitivity to lithology.

2.1.2 The seismically derivable rock physical parameters

2.1.2.1 Compressional wave and shear wave velocities (V_p and V_s)

The V_p-V_s relations are keys to the determination of lithology from seismic or sonic log data as well as for the direct seismic identification of pore fluids using, for example, the AVO analysis. Castagna et al. (1993) provide an excellent review on this subject. V_p and V_s are commonly measured in the lab and in the field. Reflections of the seismic waves at the normal incidence are determined by the impedance contrasts. Sometimes, a relationship between I_p (P impedance) and I_s (S impedance) is used to identify the anomaly caused by hydrocarbon saturation (Gidlow et al 1992; Fatti et al 1994).

The P impedance, S impedance, and density can be regarded as a set of basic rock physical parameters that can be solved from seismic data, although different people can define a different set of basic parameters based on their understanding of the AVO theory and their practice of AVO analysis. The conventional surface seismic data records the P wave reflections from the P impedance contrasts. Therefore the P impedance can be determined more reliably from the surface seismic data than the other two parameters. The S impedance and density contribute to the amplitude variation on the non-normal incidence reflection, and theoretically they can be determined from the offset-dependent seismic data. The commonly-used AVO inversion can obtain the S impedance contrasts in addition to the P impedance contrasts. As is generally perceived, density is difficult to obtain from the AVO inversion reliably. However, as it is shown in the next chapter, density can be determined from the surface seismic data with a reasonably good reliability with improvements to the AVO inversion and favourable reservoir properties.

In the multi-component surface seismic data by using the P wave sources, the radial component records the converted wave data (PS data) which is the S wave converted from the P wave at the underground medium interfaces. It seems that the S impedance could be derived from the converted wave with a high reliability. But the energy partitioned to the converted S wave at the reflection interface is usually less than to the reflected P wave for the small to medium incident angles – this can be understood by comparing the angle dependent reflectivities of PP and PS (Aki and Richards, 1980). The converted wave seismic data processing is challenging because of the difficulties to determine the shear wave statics and enhance the resolution for the converted wave. So the S impedance solved from the converted wave contains much greater errors than the P impedance obtained from the conventional seismic data or the vertical component of the multi-component data. The reliability of elastic properties can be increased by jointly using the PP and PS data (Margrave et al, 2001; Larsen, 1999).

2.1.2.2 Lame's parameters

Lame's parameters are basic elastic parameters and they are advantageous for gas saturation detection (Goodway et al, 1997): replacing the water or oil in the reservoir with gas does not affect the rock shear modulus (rigidity) – mu (μ), but dramatically changes the rock incompressibility – lambda (λ). Although the *lambda* and *mu* can be obtained from the AVO inversion (Gray et al, 1999), the products of the lambda and density (ρ, *rho*) or mu and density (lambda*rho -- λρ or mu*rho -- μρ) are popularly used by the AVO analysts since the lambda*rho (λρ) and mu*rho (μρ) can be transformed from the P and S impedances; secondly, it seems that the two-parameter linear AVO equation expressed by the P and S impedance contrasts (Gidlow et al, 1992) is more accurate than those expressed by other pairs of contrasts of elastic parameters, such as lambda and mu. The relationships between Vp, Vs, Ip, Is, λ, μ, ρ, λρ, and μρ are as follows.

$$\mathbf{Vp}^2 = \frac{\lambda + 2\mu}{\rho}, \tag{2.1}$$

$$\mathbf{Vs}^2 = \frac{\mu}{\rho}, \tag{2.2}$$

$$\lambda\rho = \mathbf{Ip}^2 - 2\mathbf{Is}^2, \tag{2.3}$$

and

$$\mu\rho = \mathbf{Is}^2. \tag{2.4}$$

Bellman (2008) shows the advantage of combining the lambda*rho and mu*rho in the separation of lithology in the McMurray Formation for the Long Lake oil sands project, Athabasca, and Bellman et al (2010) show the similar observations for the heavy oils in the Grand Rapids Formation, Athabasca.

The study in this chapter shows that lambda*rho is a more favourable parameter than lambda itself for the lithology separation in the heavy oil reservoirs in the WCSB because lambda and rho influence each other constructively or at least they do not cancel each other's sensitivity to the reservoir properties (sometimes, the Vp and density varies oppositely, which cancels the sensitivity of P impedance to lithology changes).

2.1.2.3 Ratios

Other rock physical parameters for the indication of lithology and reservoir fluids include the ratios of elastic parameters: Vp/Vs ratio (or Vs/Vp ratio), Poisson's ratio (σ), and lambda/mu ratio (λ/μ). These three ratios are related to each other as follows.

$$\left(\frac{\mathbf{Vs}}{\mathbf{Vp}}\right)^2 = \frac{1-2\sigma}{2(1-\sigma)}, \tag{2.5}$$

$$\lambda/\mu = \left(\frac{\mathbf{Vp}}{\mathbf{Vs}}\right)^2 - 2, \tag{2.6}$$

and

$$\sigma = \frac{1-2(\mathbf{Vs}/\mathbf{Vp})^2}{2-2(\mathbf{Vs}/\mathbf{Vp})^2}. \tag{2.7}$$

These three ratios have slight differences in their sensitivity to reservoir properties: the Vp/Vs ratio is a little more sensitive to gas saturation in unconsolidated sand reservoirs. Studies have found that the Vp/Vs ratio is favourable in characterizing the heavy oil reservoirs in the WCSB (Dumitrescu and Lines, 2009).

2.1.2.4 Bulk density

Bulk density is an appealing parameter for the lithology separation and it is a focus in this thesis to derive the reliable density information from seismic data. Gray et al (2004) show a high correlation between gamma ray logs and bulk density logs within the McMurray Formation using a number of wells from the Long Lake oil sands lease in Athabasca, Alberta. The correlation coefficient between the gamma ray and density values is seen as 0.83 in their study. As a part of the rock property study, work is also done to understand the ability of density to indicate the lithology in various heavy oil reservoirs in the WCSB: the McMurray, Grand Rapids, and Wabiskaw Formations in Athabasca, and Bluesky Formation in Peace River. The density information extracted from the AVO is usually considered unreliable due to the ill-posed nature of the AVO inversion. The feasibility of obtaining density from seismic data will be evaluated in Section 2.5. Chapter 3 will show that density can be extracted from the seismic data with a reasonably

good reliability with special improvements on the AVO inversion and the good quality wide angle seismic data.

2.1.3 Sections in Chapter 2

Section 2.2 evaluates the sensitivity of a number of rock physical parameters and their combinations to the lithology of heavy oil reservoirs using well logs from different regions in the WCSB heavy oils and evaluates the influence of the limited bandwidth on the sensitivity of physical parameters to lithology. Section 2.3 discusses the possibility of separation between water and bitumen in the heavy oil reservoirs. Section 2.4 studies the facies and their statistical features on rock physical parameters. Section 2.5 analyzes the feasibility of AVO to predict the reservoir lithology heterogeneity. Section 2.6 draws conclusions.

2.2 ROCK PHYSICAL PROPERTIES OF HEAVY OIL RESERVOIRS IN THE WCSB

2.2.1 Crossplots of elastic parameters

Twelve rock physical parameters are cross-plotted versus gamma ray values (Table 2.1). The correlation coefficient between every parameter and gamma ray values is calculated using the following equation,

$$\text{corr}= \frac{\sum_{i=1}^{n}(x_i-\mu_x)(y_i-\mu_y)}{\sqrt{\sum_{i=1}^{n}(x_i-\mu_x)^2\sum_{i=1}^{n}(y_i-\mu_y)^2}} \quad . \tag{2.8}$$

where n is the number of samples, x_i and y_i the individual measurements of the elastic parameter and gamma ray value and μ_x and μ_y are the mean values of the elastic parameter and gamma ray values.

The relative change of the parameter for sand and shale is estimated as well. The cross-plots, correlation coefficients and relative changes of the parameters for the sand and shale help to understand the sensitivity of individual parameters to lithology. Some combinations of rock physical parameters are able to separate lithology better than the

individual ones. Table 2.2 shows the pairs of rock physical parameters used in the crossplots. Crossplots are made for every pair in Table 2.2 and samples in the crossplots are color-coded by gamma ray values. The sensitivity of every pair of parameters is quantified by the correlation coefficient and the relative change of parameters between sand and shale. The large correlation coefficient and relative change indicate a better sensitivity to lithology. In the regions without the shear sonic, only the P sonic, P impedance, density and gamma ray values are used for the crossplots (Table 2.3). Since the study focuses on the seismic methods for the heavy oil reservoir heterogeneity, elastic parameters in the cross-plotting are mainly seismically derivable. When crossplotting each pair of parameters in Table 2.2 and Table 2.3, the left parameter is used as the horizontal axis and the right parameter as the vertical axis, while the gamma ray value is used for the color index.

Table 2.1 Twelve elastic parameters for the cross plotting against gamma ray (GR)

GR ~ Vp	GR ~ Vs	GR ~ Vp/Vs
GR ~ ρ	GR ~ Ip	GR ~ Is
GR ~ λ	GR ~ μ	GR ~ λ/μ
GR ~ $\lambda\rho$	GR ~ $\mu\rho$	GR ~ σ

Table 2.2 Combinations of 12 elastic parameters for cross-plots

Vp ~ Vs	Vp ~ Vp/Vs	Vs ~ Vp/Vs
Vp ~ σ	Vp ~ σ	Vp/Vs ~ σ
Vp ~ ρ	Vp ~ ρ	Vp/Vs ~ ρ
Ip ~ Is	Ip ~ ρ	Is ~ ρ
λ ~ μ	λ ~ λ/μ	μ ~ λ/μ
$\lambda\rho$ ~ $\mu\rho$	$\lambda\rho$ ~ λ/μ	$\mu\rho$ ~ λ/μ

Table 2.3 Cross-plots for data without shear wave sonic log

GR ~ Vp	GR ~ ρ	GR ~ Ip
Vp ~ ρ	Ip ~ ρ	

The well logs used in the crossplots are from five different regions in the Athabasca oil sands and one region in the Peace River area. Figure 2.1 show the stratigraphic nomenclature of the WCSB, and columns for the Athabasca oil sands area and Peace River Plains are highlighted by the red boxes. The stratigraphy of the Lower Cretaceous in Athabasca is shown in Figure 2.2 for more details. The McMurray Formation of the Athabasca Oil Sands lies on an angular unconformity that truncates the Devonian strata. In the area of Fort McMurray, the Devonian strata comprise primarily of limestone and calcareous shale of the Waterways Formation in the east and younger carbonate rocks of the Woodbend Group in the west. In general, the McMurray Formation accumulated in incised valleys that were formed by fluvial processes and subsequently transgressed by marginal-marine environments during an early Cretaceous sea-level rise. Thus, the McMurray displays a continuum of sedimentary environments, from fluvial in the lower parts, to estuarine in the middle, and to marine shoreface near the top. This lends a tripartite aspect to the stratigraphy that forms the basis for the subdivision of the McMurray Formation. The Lower, Middle, and Upper McMurray have some consistent lithological expressions. The Lower McMurray is generally medium- to coarse-grained, massive-appearing to crudely cross-bedded. These beds are most commonly interpreted as having a fluvial nature. The Middle McMurray deposits are dominated by inclined heterolithic stratification (IHS) that is interpreted to represent the deposition on tidally influenced point bars. Notably, the Middle McMurray contains a brackish-water trace fossil assemblage and is thereby interpreted as representing a fossil estuary. The Upper McMurray deposits are variable, but generally contain a comparatively open marine signal. These strata are normally interpreted as shallow, low-energy shoreface deposits and small deltaic complexes (Gingras and Rokosh 2004).

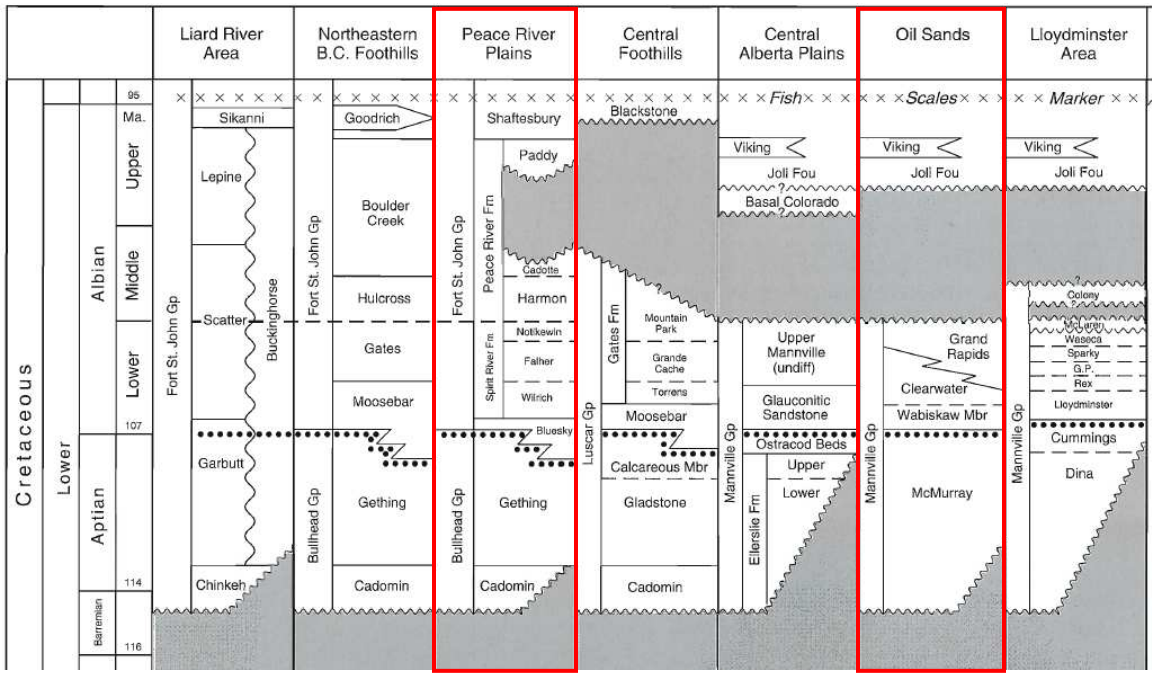

Figure 2.1 Stratigraphic nomenclatures for the Mannville Group and equivalent strata in the WCSB (Adapted from CSPG digital atlas no. 19, by Hayes et al).

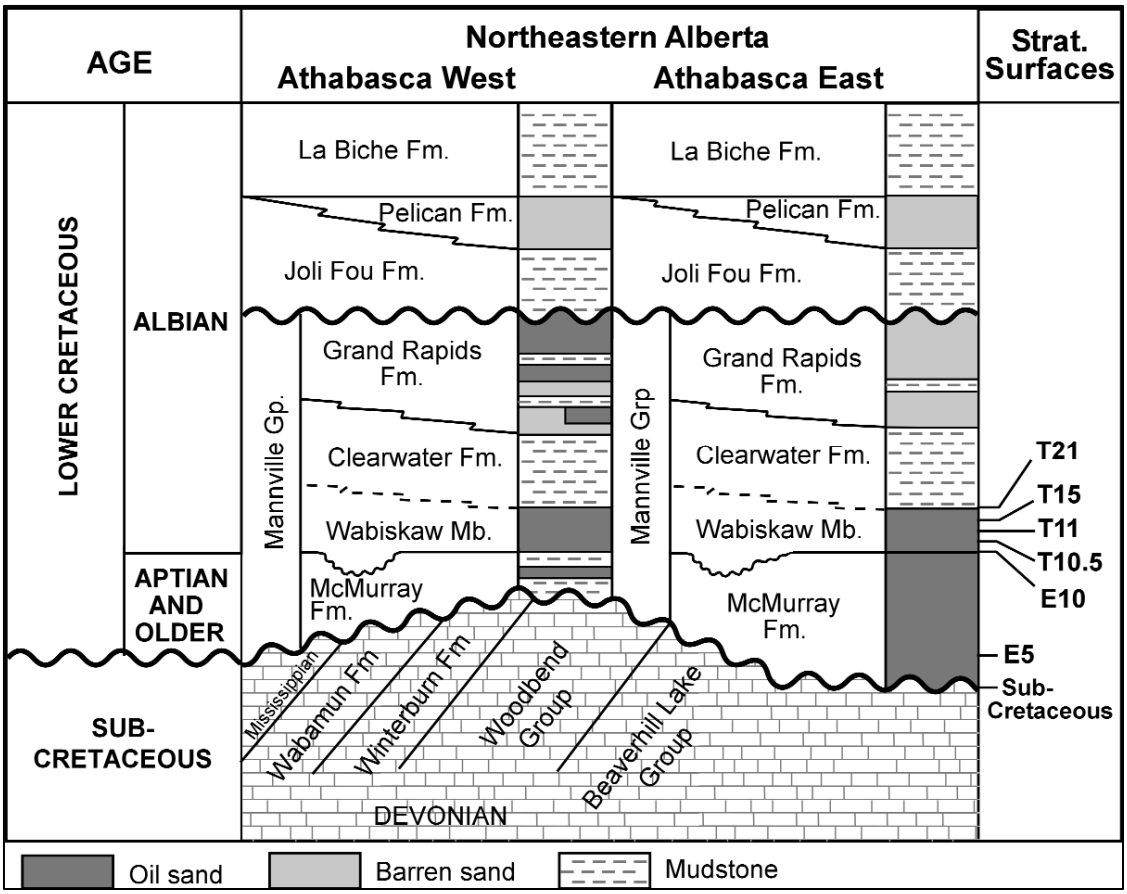

Figure 2.2 Stratigraphy of the Lower Cretaceous in Athabasca oil sands area (Source: Wynne et al 1994).

Figure 2.3 is the township map for the WCSB showing the regions in the study. A brief review of the geology of each region is in the following.

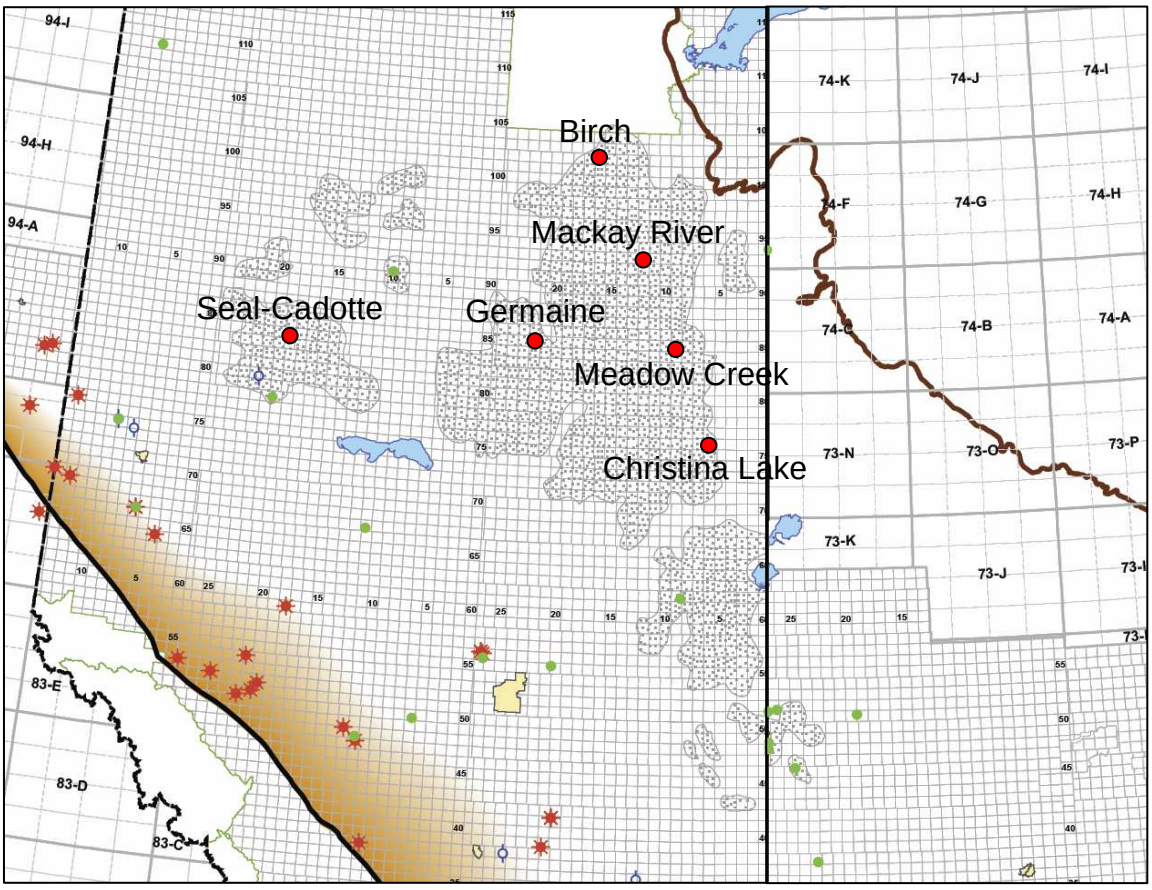

Figure 2.3 Township map marking oil sands areas and regions studied for rock properties by red dots.

2.2.1.1 McMurray Formation – Christina Lake

Christina Lake is located along the northern part of the Primrose Ridge and interpreted to be more marine-influenced compared to Foster Creek. Channels associated with the McMurray system were forced to converge through this relatively narrow opening, resulting in the enhanced stacking of channel deposits. The SAGD exploitable oil sands deposits range from 20 to 60 m in thickness due to the stacking of several channels (Strobl, et al, 2004; Cody et al, 2001). The McMurray Formation is about 330m deep. Five wells with a full suite of logs are used in the study.

2.2.1.2 McMurray Formation – Meadow Creek

In the Meadow Creek area, the Devonian Beaverhill Lake limestones are unconformably overlain by the Cretaceous formations. The base of the Lower Cretaceous McMurray Formation occurs at the measured depths ranging from 450-525meters. The McMurray Formation siliciclastic sediments are overlain by the Wabiskaw Member sandstones and shales of the Clearwater Formation. The McMurray Formation was deposited in a fluvial to estuarine system. Non-eroded portions of the continental Lower McMurray mudstones and sandstones are preserved in paleotopographic lows incised in the Devonian surface. The areal extent of the lower McMurray deposits are constrained laterally, while the middle McMurray is deposited on the flanks of these paleotopographic lows and is not constrained laterally.

2.2.1.3 McMurray Formation – MacKay River

In the Mackay asset area, the McMurray Formation consists of middle and upper members, which are overlain by the Wabiskaw Member of the Clearwater Formation. The lower member of the McMurray Formation was never deposited in the tributary valley. This is because of the limited accommodation space in these thinner and structurally elevated tributary valleys when compared with the main trunk valley. Where preserved in the main valley, the lower member of the McMurray Formation was deposited as a series of braided fluvial channels in a continental environment. As transgressions commenced from the north, the main valley became progressively flooded and influenced by tidal marine processes, thus over time the fluvial channels developed into a series of meandering, brackish, tidally-influenced channels which form the main clean sand to heterolithic sand and mud reservoirs of the middle member. These channels were then replaced by a series of intertidal flats, bay fills, deltas and shorefaces as the transgression continued, forming the upper member. These marginal marine facies were eventually replaced by the offshore marine and prodelta mudrocks of the Wabiskaw Member.

Within the tributary valley, the middle member of the McMurray Formation is dominantly composed of argillaceous delta plain deposits, but there is occasional preservation of sharp-based, fining-upward, bioturbated tidally-influenced channel deposits that are more typical estuarine channel McMurray reservoirs. The middle member is erosionally overlain by the upper member that is more sand-prone and forms the main reservoir interval in the Thickwood/MacKay area. These sands form more laterally continuous reservoirs and represent vertically and laterally amalgamated proximal deltaic mouth bars that prograded into a brackish bay. The overlaying Wabiskaw Member consists of widespread, offshore marine to prodelta shales resulting from the gradual transgression of the Boreal Sea from the north. As relative sea-level continued to rise, marine influences soon dominated the brackish processes, and progressively onlapped and drowned the Devonian archipelagos to the west.

2.2.1.4 Grand Rapids Formation – Germaine

Cant's (2008) work shows that the Upper Mannville Grand Rapids Formation of the Wabiskaw area of northeastern Alberta contains thick, laterally continuous, composite sand bodies that are partly bitumen-saturated. The Proven-In-Place-Reserves have been estimated to be 8.7 billion cubic meters of 10 – 13 API gravity bitumen. The deposits are at depths of 100m in the northeast to about 300m in the southwest, so the development will use in-situ processes. Authigenic kaolinite and chlorite in pores of the reservoir rocks, tightly cemented concretionary zones, and bottom water (usually) are factors in in-situ development.

The Grand Rapids sands were discharged from deep incised channels that cut the Colony to the Waseca Formations of the Lloydminster area. The NNW trends and discharge locations of these channels were influenced by the solution of the underlying Devonian salts, resulting in some of the largest concentrations of sandstone in the Alberta Basin. Because the sands are discharged from these valleys that shifted laterally because of salt tectonics, they are three-dimensional and shifted laterally. The reservoir bodies are lowstand complexes of shoreface and incised channel sands.

Connelly (2010) shows the separation of sand and shale in the Grand Rapids Formation using the lambda*rho and mu*rho. In this study, rock physical parameters of the Grand Rapids Formation are studied using one well with a full suite of logs available.

2.2.1.5 Bluesky Formation – Peace River

Based on the work by Thomas et al (2002), the exploitable bitumen reserves in the Peace River area are found in sandstones of the Ostracod Zone and Bluesky Formation which, through much of the area, unconformably overlie the Mississippian carbonates of the Debolt Formation. The basal Cretaceous deposition took place in a foreland basin setting beginning with the fluvial/non-marine Gething Formation. During the deposition of this unit, a series of north-south trending channel systems drained the basin northward to the Boreal Sea, with their paths controlled by topographic highs present on the underlying unconformity surface. These topographic highs formed an archipelago that ran parallel to the Rocky Mountain disturbed belt and had a significant effect on subsequent depositional patterns. In the Peace River area, the Red Earth Highlands, which formed part of this archipelago, remained emergent throughout the basal Cretaceous time. The Ostracod Zone consists of medium-to coarse-grained chert rich fluvial sands in which very little authigenic clay is found in the pore system. The Bluesky Formation consists of fine-to-medium quartz-rich estuarine sands in which kaolinite is irregularly distributed through the pore network.

Five wells are used from this area in the study. However, there is no shear sonic log available in these wells. The cross-plots of the P wave velocity against density and P impedance against density are made with samples color-coded by gamma ray values. It is noted that density is correlated well with clay content and the P wave velocity has a weak correlation with clay contents. P impedance, the product of P wave velocity and density is correlated with the clay content to some degree.

2.2.1.6 Wabiskaw Member – Birch

The McMurray Formation is absent at a single well, which locates at the north end of the Athabasca oil sands. The Wabiskaw Member is studied. The Wabiskaw Member consists of marine and shoreface sands and interbedded by marine shales.

Table 2.4 lists the figure numbers for the crossplots, relative changes, and correlations of elastic parameters for the six oil sands regions.

Table 2.4 Figures for crossplots, correlation coefficients and relative changes of sand and shale.

Heavy oil field	Elastic parameters vs. gamma ray	Corr. Coef. with gamma ray	Relative change between sand/shale	Elastic parameter pair crossplot
Christina Lake (McMurray)	Figure 2.4	Figure 2.5	Figure 2.6	Figure 2.7
Meadow Creek(McMurray)	Figure 2.8	Figure 2.9	Figure 2.10	Figure 2.11
Mackay River (McMurray)	Figure 2.12	Figure 2.13	Figure 2.14	Figure 2.15
Birch (Wabiskaw)	Figure 2.23	Figure 2.23	n/a	n/a
Germaine (Grand Rapids)	Figure 2.16	Figure 2.17	Figure 2.18	Figure 2.19
Peace River (Bluesky)	n/a	Figure 2.21	n/a	n/a

2.2.2 Discussion on the lithology separation

2.2.2.1 Sensitivity of rock physical parameters to lithology

The sensitivity of each parameter to lithology for the studied oil sands regions is ranked in Table 2.5. Correlation coefficients with gamma ray values are the major factor determining the ranks of the parameters. High correlation coefficients indicate good sensitivities to lithology. The parameters with correlation coefficients greater than 0.6 are ranked as Grade "A"; the parameters with correlation coefficients greater than 0.5 and less than 0.6 are ranked as "A-". Grade "B" is for correlation coefficient between 0.4 and 0.5; Grade "C" is for correlation coefficient between 0.2 and 0.4; Grade "D" is for correlation coefficient less than 0.2.

Table 2.5 Ranks of sensitivity of rock physical parameters to lithology based on correlation coefficient with gamma ray. *-- subjective (without correlation coefficient)

Heavy oil field	ρ	Vp	Vs	Ip	Is	λ	μ	λρ	μρ	Vp/Vs	σ	λ/μ
Christina Lake (McMurray)	A	D	B	A-	D	A-	C	A	D	A-	A-	A-
Meadow Creek (McMurray)	A	D	B	A-	D	A	C	A	D	A-	A-	A-
Mackay River (McMurray)	A	C	B	D	D	D	C	D	D	C	C	C
Birch (Wabiskaw)	C*	A-*		A-*								
Germaine (Grand Rapids)	A-	A	A	B	A	D	A	D	A	A	A	A
Peace River (Bluesky)	A*	C*		A-*								

A few remarks are made on the ranking and cross-plots.

1. Among the 12 parameters investigated here, density is considered the best to indicate the lithology of the McMurray Formation. The correlation coefficient of density and gamma ray values is greater than 0.6 in most of the studied areas. In addition, density shows a strong correlation with lithology in the Grand Rapids Formation in Athabasca and the Bluesky Formation in Peace River.

2. Lambda*rho is reasonably sensitive to the lithology in four regions where shear sonic logs are available to calculate Lame's parameters. Density has a contribution to the sensitivity of lambda*rho.
3. Other parameters, such as Ip, lambda, and Vs, are able to indicate lithology but with greater uncertainties. For instance, P impedance shows a good sensitivity in the McMurray Formation in Christina Lake and the Bluesky Formation in Peace River. In these regions, the correlation coefficient between Ip and gamma ray is between 0.5 and 0.6; Vp is poorly correlated with lithology, but Ip, the product of Vp and density, seems indicating lithology better due to the effect of density. However, this sensitivity to lithology changes from region to region.
4. In the Grand Rapids Formation, many parameters, besides density and lambda*rho, are well-correlated with lithology. This conclusion should be tentative and further studies are needed by using more well data, since only one well from this region is used.
5. The Vp/Vs ratio, Poisson's ratio, and lambda/mu ratio should have the same ability to separate lithology in the oil sands area. They show correlation coefficients of about 0.5 in two regions in Athabasca, although they are not the best lithology indictors among 12 parameters.

The last remark is that some of the above observations seem not to be explained by Figure 2.14. The data used in this figure are from the Mackay River area. The relative changes of density between sand and shale are lower than those in the Christina Lake and Meadow Creek areas. This is due to the difference of the depositional environments in the McMurray Formation between the Mackay River area and other two areas. In the Mackay River area, the reservoir sands differ from typical McMurray reservoirs in that they are more laterally homogenous, do not contain the laterally-extensive and thick interbedded sands and muds referred to as IHS and are deposited by a lateral accretion of point bars in a tidally-influenced channel environment, and do not contain mud plugs with a reflective channel avulsion. The reservoir architecture appears simpler in these deltaic environments, facies bands are more laterally continuous and the clay content is

much lower. The cross-plots of elastic parameters against gamma ray values in Figure 2.12 show that the gamma ray value of the cluster of shale samples is within a range of 75-90 API. These shale samples are very sandy and contain no mud plugs or abandoned channel facies whose gamma ray values are often larger than 100 API. The relative change of most of the elastic parameters for sand and shale in this region is small.

2.2.2.2 Reservoir depth effects on rock physical parameters in the McMurray Formation

The McMurray Formation in Christina Lake and Meadow Creek is at similar depths. The sensitivity of rock physical parameters to lithology for the two regions is close. But if the burial depth of reservoirs changes largely from region to region, the behaviour of rock physical parameters and their sensitivity to lithology are different. Depositional environment change may be a factor, but compaction effects from the burial depth difference are considered as the main reason for the difference. The sensitivity of each parameter can be examined by the cross-plots of them against depth with samples color-coded by gamma ray values for three regions in Figure 2.24. A few remarks can be made based on these cross-plots:

1. Density is little affected by the burial depth. Density varies between 2.00 g/cc and 2.50 g/cc in the three regions.
2. Other elastic parameters are influenced by the compaction: velocities are lower in the shallow burial depth for the same lithology and velocities change with depth follows different trends for sand and shale. The sand and shale are slightly separable for the shallow reservoir by using Vp but the separation is indistinguishable for the deep reservoirs. Vs is slightly better than Vp as a means of separating sand and shale for both the shallow and deep reservoirs.
3. Because of the variation of velocity with depth, other parameters, such as the impedance and Lame's parameters, show variations with depth as well and lithology sensitivity variations with depth.
4. The Vp/Vs ratio, Poisson's ratio and lambda/mu ratio vary with depth, but their sensitivity to lithology is not affected strongly by the depth.

2.2.2.3 Discussion on correlation between density and lithology

Although density shows a strong correlation with lithology in the oil sands reservoirs, density is generally a porosity indicator rather than a lithology indicator. Gray (2011) points out that "*the better correlation with density suggests that this bitumen reservoir behaves like an acoustic medium, i.e. with sand grains floating in a liquid medium (a slurry), which is the way these reservoirs are frequently described; therefore, this significantly better correlation of density than S-impedance makes sense for Athabasca oil sands reservoirs*" Here, this correlation is understood from a different point of view.

1. As discussed in the sub-section 2.2.2.2 "Reservoir depth effects on rock physical parameters in the McMurray Formation", the density variation for clean sands is small for the reservoirs at different burial depth. Clean sand, whose porosity is high, has lower density than shale with low porosity. The difference of density in the bitumen and water is assumed to be neglected so far, and thus the change in rock bulk density is not due to the fluid type difference.
2. The second remark is on the scale of the samples used in the studies. At a millimeter scale the correlation between density and shale volume may be difficult to observe. Well logs are the main data in the study. For the common density logging tools, the minimum bed resolution for true values under the best conditions is 60cm (Rider, 2002). A tool is only capable of making a true measurement of a bed if the bed is thicker than the emitter-receiver distance of the tool, although a bed which is much thinner than a tool's emitter-receiver distance may still be identifiable. However, the value indicated on the log for this bed will only be percentage of the real reading it should give. At the logging tool resolution, the proportion of sand and shale in IHS or sand with mudclasts should be correlated with density of the mixture.
3. Figure 2.25 shows three shale structures after Ellis and Singer (2008); and Figure 2.26 shows the relationships between the porosity (density) and sand fraction (shale volume) for the three shale structures. Samples of well logs from a McMurray reservoir are cross-plotted in the porosity – sand fraction frame (Figure 2.27). The samples fit the laminated shale model better than others. For

laminated shales, the porosity and sand fraction are linearly correlated. The laminated shale is explained by the IHS.

2.2.2.4 Bandlimited elastic parameters for lithology separation

A significant difference between rock physical parameters from well logs or lab measurements and those from seismic data lies in the limited frequency bandwidth of seismic data. To make quantitative estimates of reservoir properties, the low frequency components which are missing in the seismic data are usually obtained from other sources. Seismic data merely provides relative measurements. Therefore, it is necessary to evaluate the relative measurements of rock physical parameters within the seismic bandwidth for the lithology separation and other purposes. In the following, density, the physical parameter with the most sensitivity to lithology, is used to evaluate the loss of sensitivity to lithology due to the limited bandwidth and furthermore to evaluate the feasibility of predicting reservoir heterogeneity using the deterministic attributes containing only the seismic bandwidth when a reliable low frequency model is unobtainable.

In Figure 2.28, four wells with reservoirs in the McMurray Formation are plotted with gamma ray logs, density logs, and the bandlimited density logs. The top and base of the McMurray Formation are marked in the figure. To apply a bandpass filter, all logs are converted into the time domain using time-depth curves obtained from sonic logs. The bandwidth of the filter is 15-120 Hz, which is the typical bandwidth in the conventional surface seismic data in the McMurray Formation in Athabasca. Overall, the bandlimited density (15-120Hz) still predicts lithology reasonably well, although the lack of the DC component makes the density curve vary around zero. Most of the sand and shale interbeds are identifiable on the bandlimited density curves although the lithology boundaries are blurred. The strong contrast at the Devonian and McMurray formation boundary may contribute much on the low frequency components and this should be carefully dealt with when the seismic data are used.

The cross-plots are made for the full bandwidth density, seismic bandwidth density, and low frequency (0-15 Hz) density against gamma ray values for the McMurray interval in Figure 2.29. The correlation coefficients are calculated for each cross-plot and marked in the plot. The correlation coefficient between the seismic bandwidth density and gamma ray values is amazingly close to that between the full bandwidth density and gamma ray values. In contrast, the low frequency (0-15 Hz) density poorly correlates with gamma ray values. This result is encouraging for applying the bandlimited data in the prediction of reservoir heterogeneity if a low frequency model is unable to be reliably built. Figure 2.30 compares other different low cut frequencies used by the filter on density curves. Table 2.6 lists the correlation coefficients of the bandlimited density and gamma ray values. Noted that the 10 - 15 Hz low cut frequencies have little effect on the correlation between the bandlimited density and gamma ray values but using a higher low cut frequency deteriorates the correlation rapidly, indicating the necessity to preserve the low frequency contents in the seismic data. Usually, the frequency content as low as 15Hz should be preserved in the real seismic data.

Table 2.6 Correlation coefficients of bandlimited density and gamma ray.

Low cut frequency (Hz)	Correlation coefficient between gamma ray and bandlimited density (low-cut frequency – 120 Hz)	Correlation coefficient between gamma ray and density with only low frequency (0 – low cut frequency)
0	0.860 (no high-end cut)	n/a
10	0.829	-0.203
12	0.825	-0.047
15	0.811	0.223
20	0.745	0.506

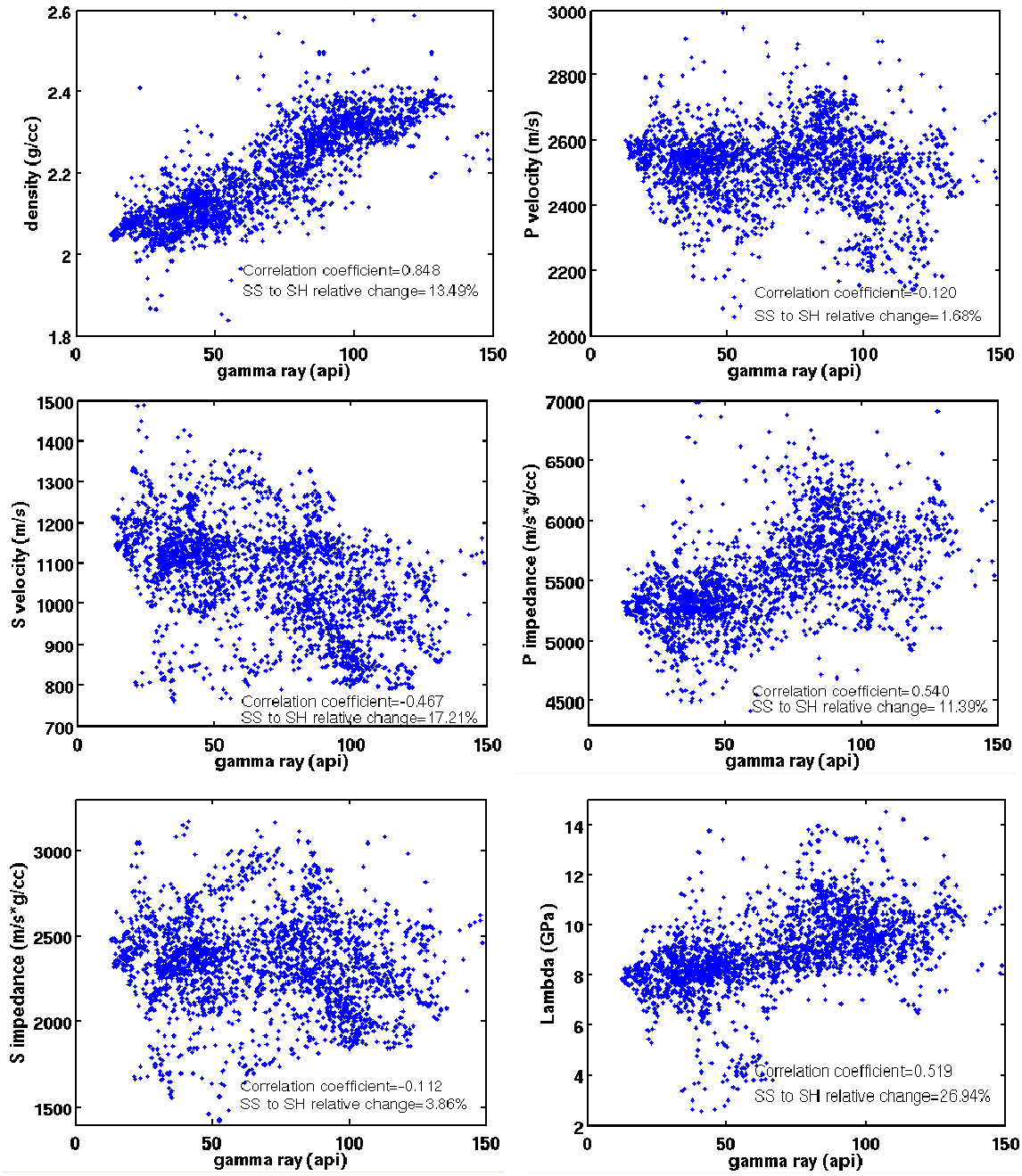

Figure 2.4 Crossplots of rock physical parameters from well logs in Christina Lake against gamma ray values. *(Continued on next page).*

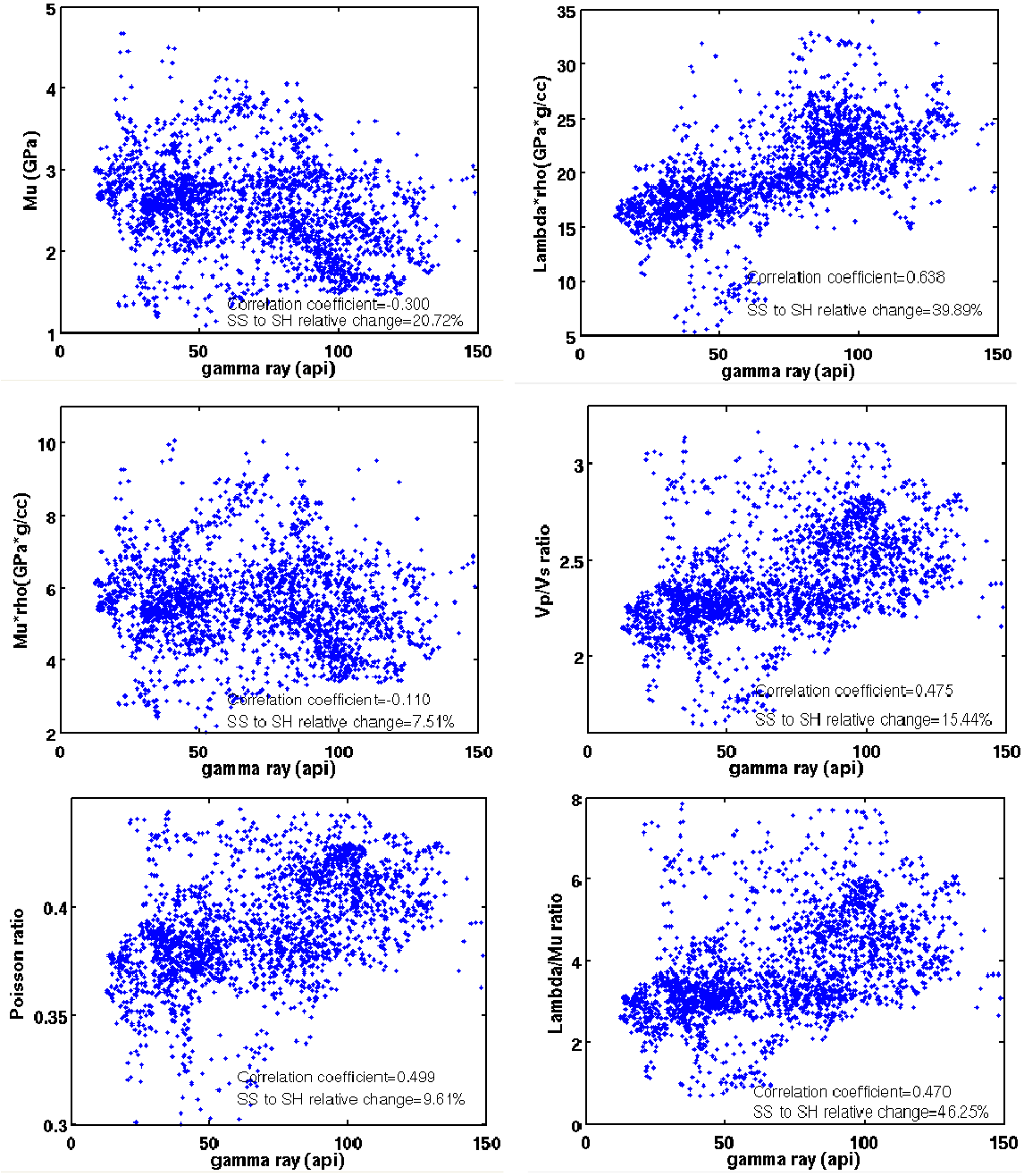

Figure 2.4 *(Continued from previous page)* **Crossplots of rock physical parameters from well logs in Christina Lake against gamma ray values.**

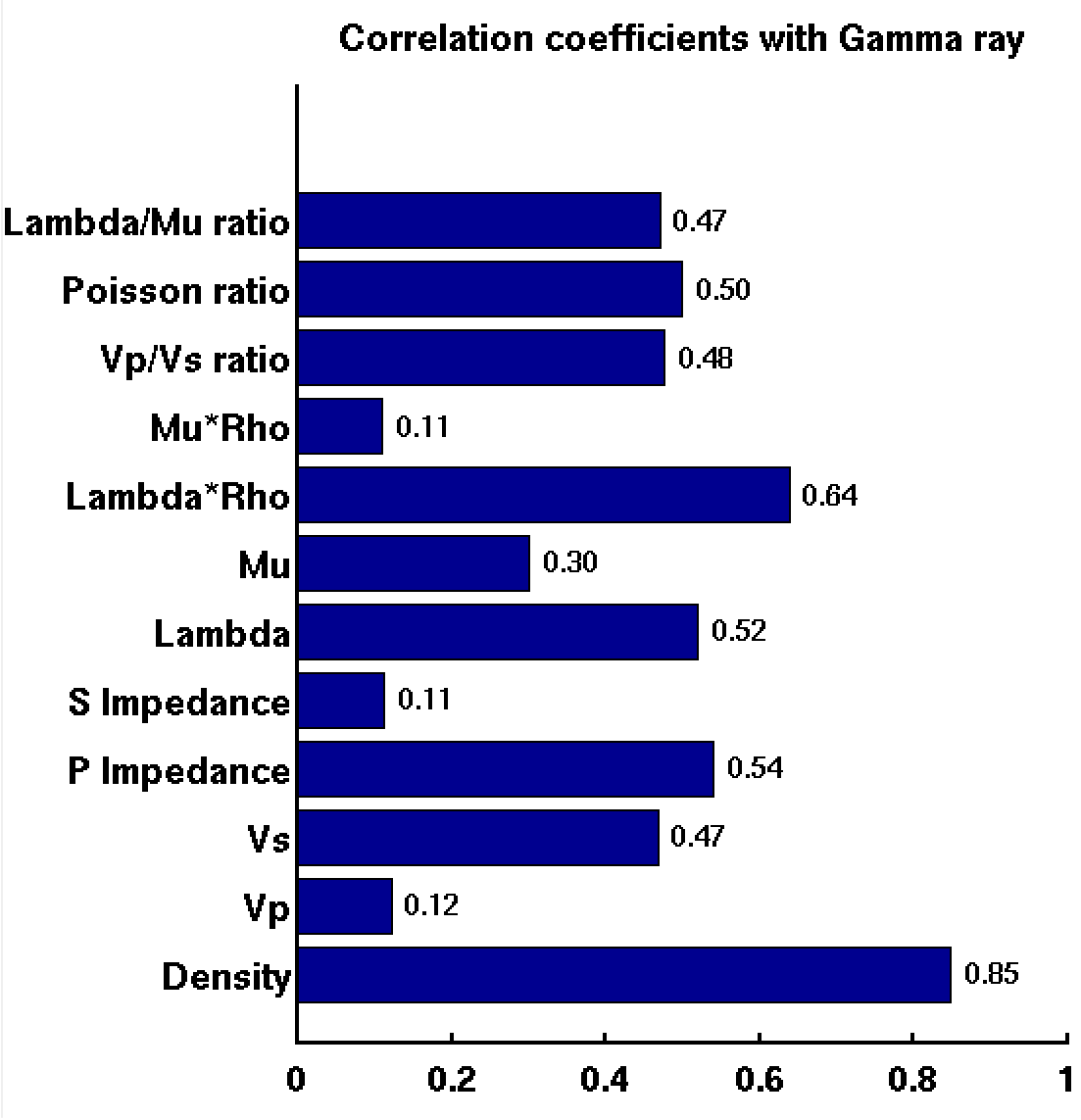

Figure 2.5 Bar chart comparing correlations between rock physical parameters and gamma ray values (Christina Lake). The values labelled on the right of the bars are the correlation coefficients.

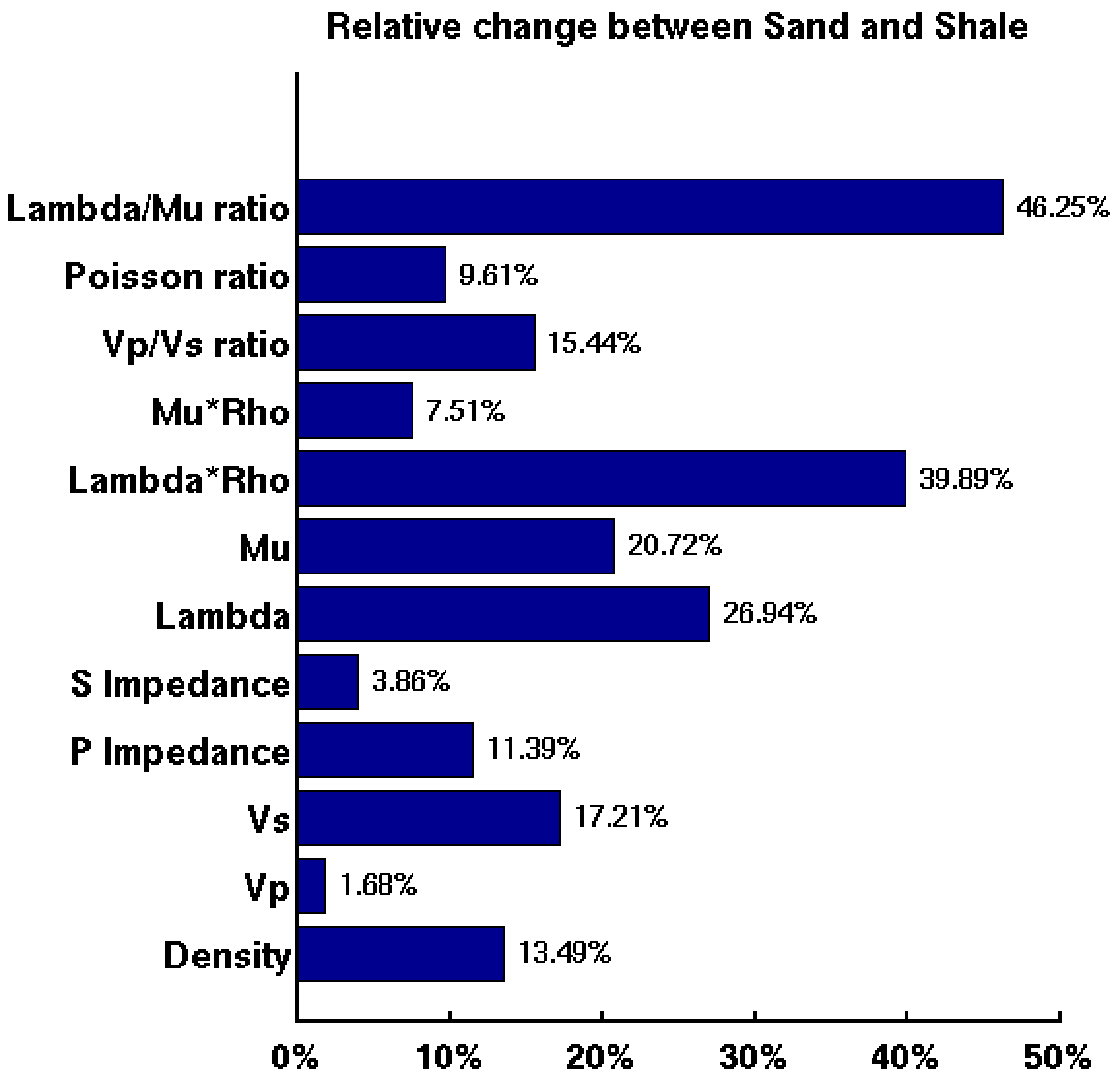

Figure 2.6 Relative changes between sand and shale on each rock physical parameter in Christina Lake.

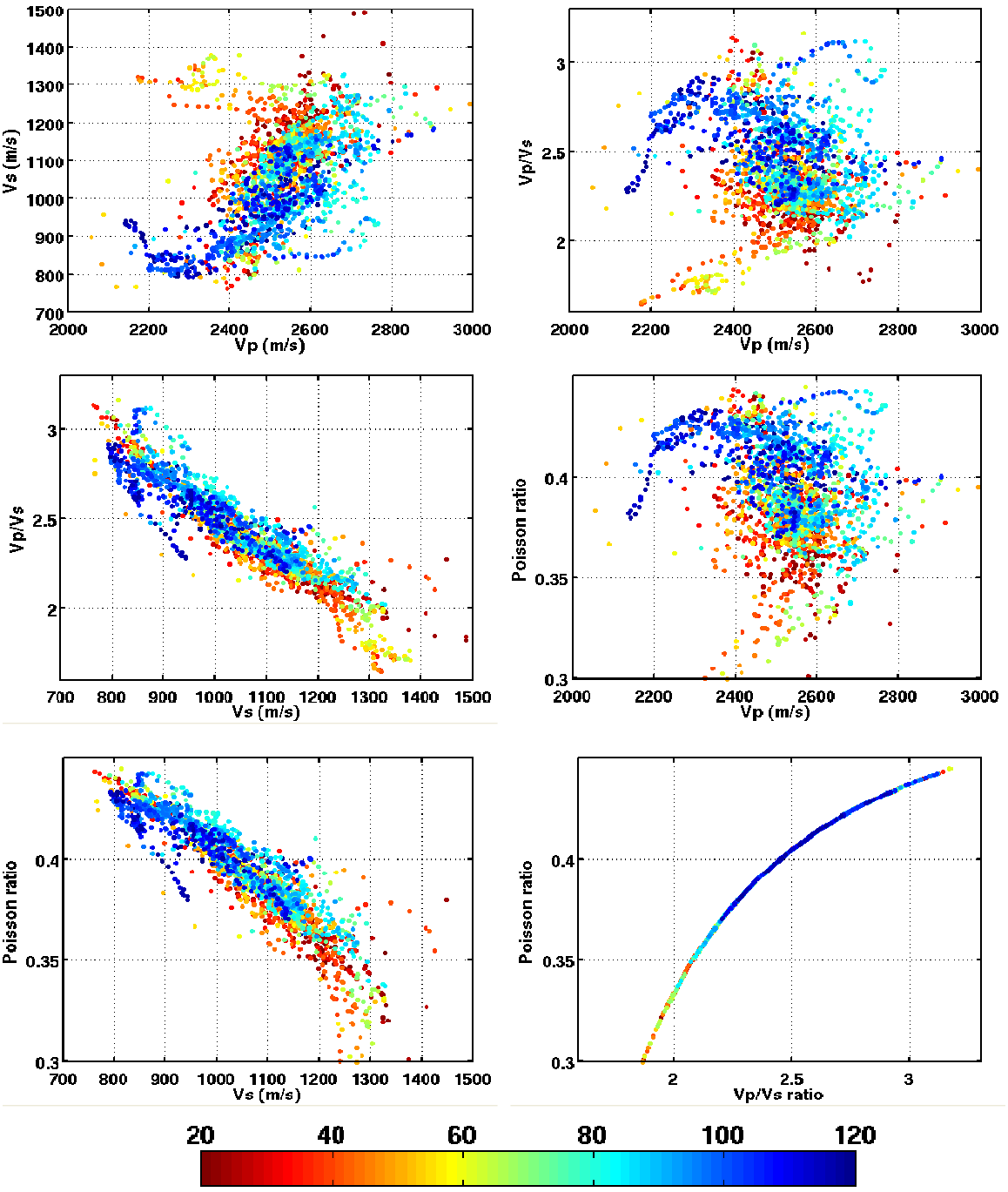

Figure 2.7 Cross plots of various pairs of elastic parameters in Christina Lake with samples color-coded by gamma ray The cross-plot of Poisson's ratio and Vp/Vs ratio in the lower right corner mainly indicates the theoretical relationship between Poisson's ratio and Vp/Vs ratio except the clean sands showing low values on both ratios *(Continued on next page).*

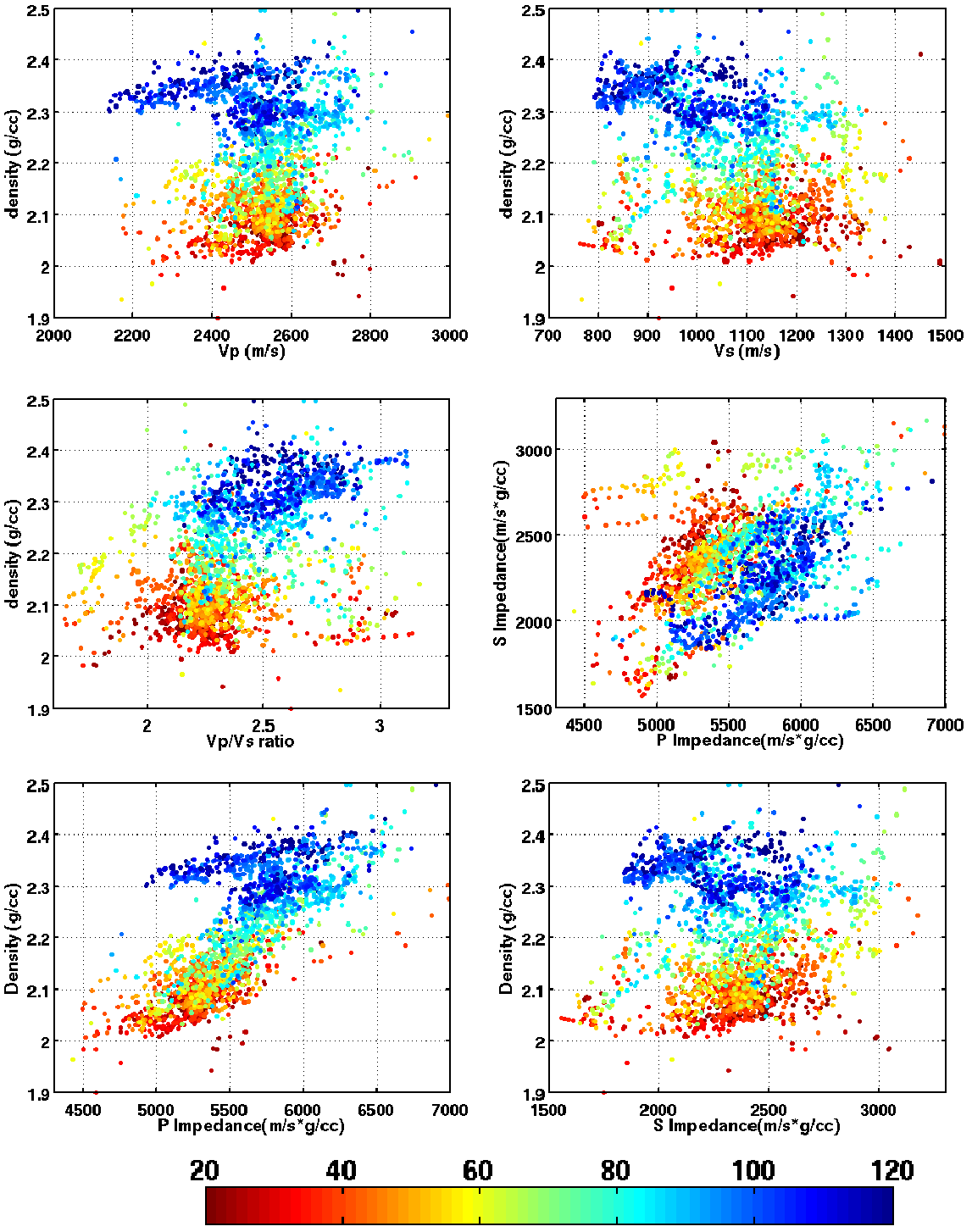

Figure 2.7 *(Continued from previous page)* **Cross plots of various pairs of elastic parameters in Christina Lake with samples color-coded by gamma ray** *(Continued on next page)***.**

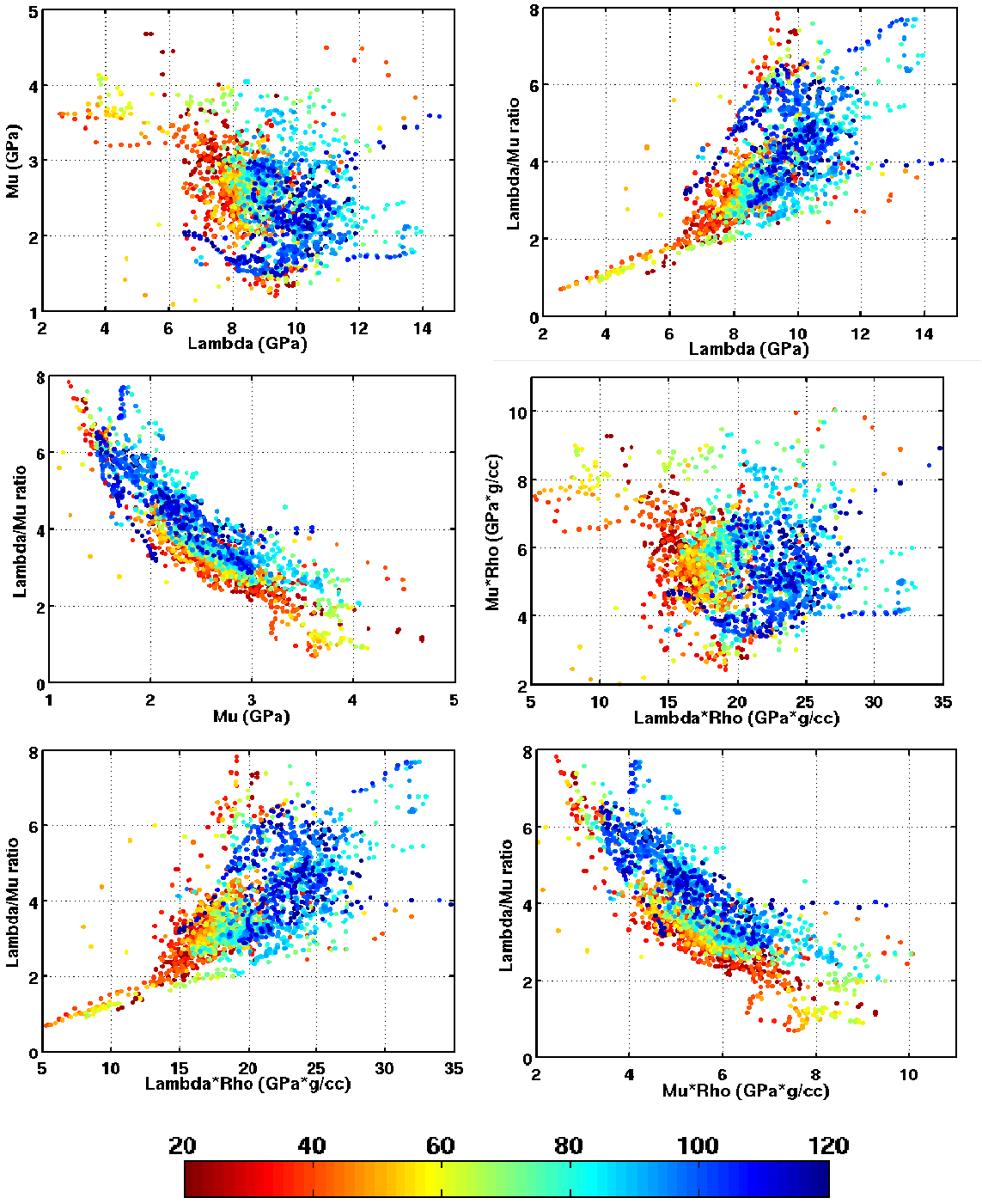

Figure 2.7 *(Continued from previous page)* **Cross plots of various pairs of elastic parameters in Christina Lake with samples color-coded by gamma ray.**

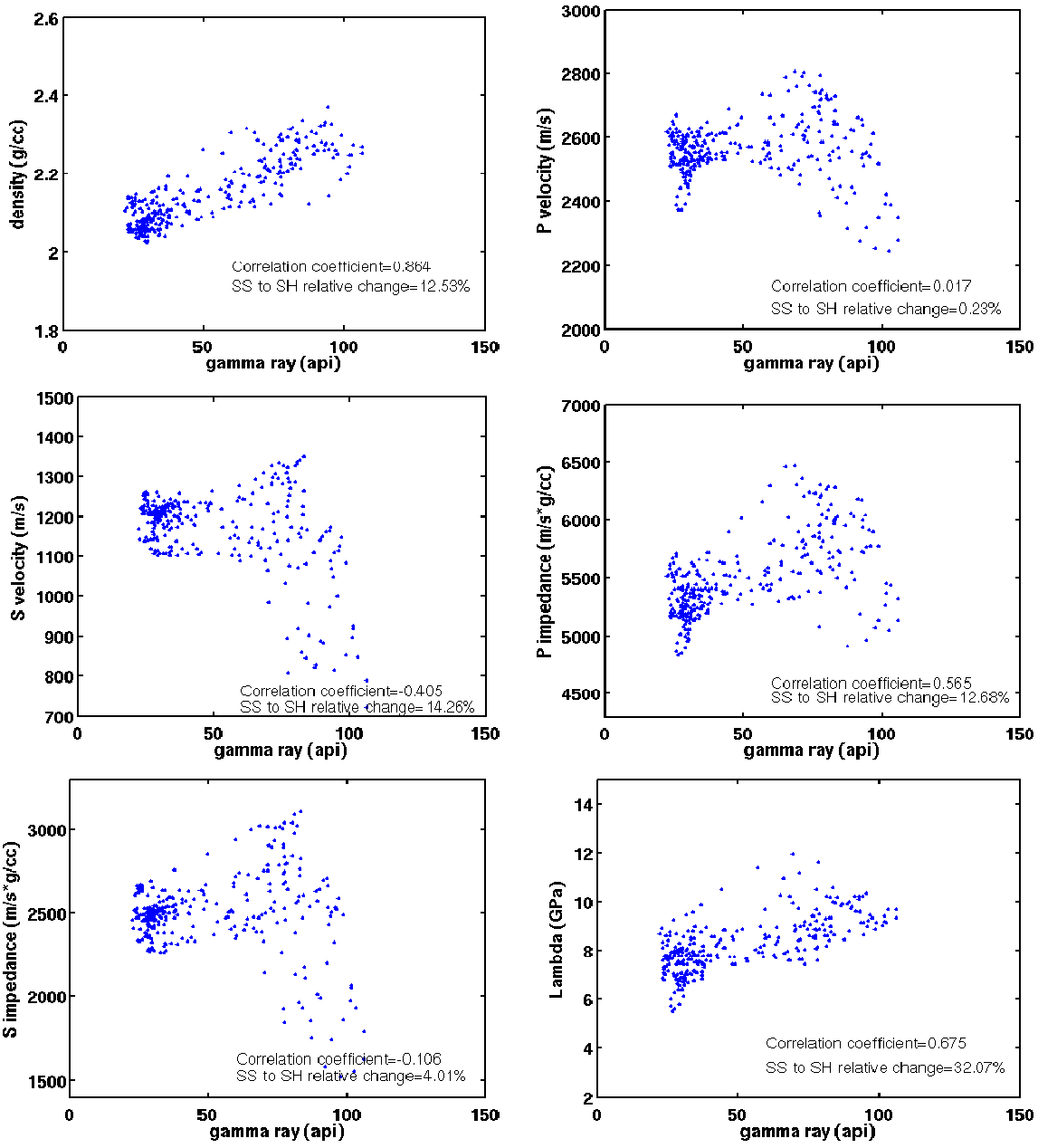

Figure 2.8 Crossplots of rock physical parameters against gamma ray values (Meadow Creek) *(Continued on next page).*

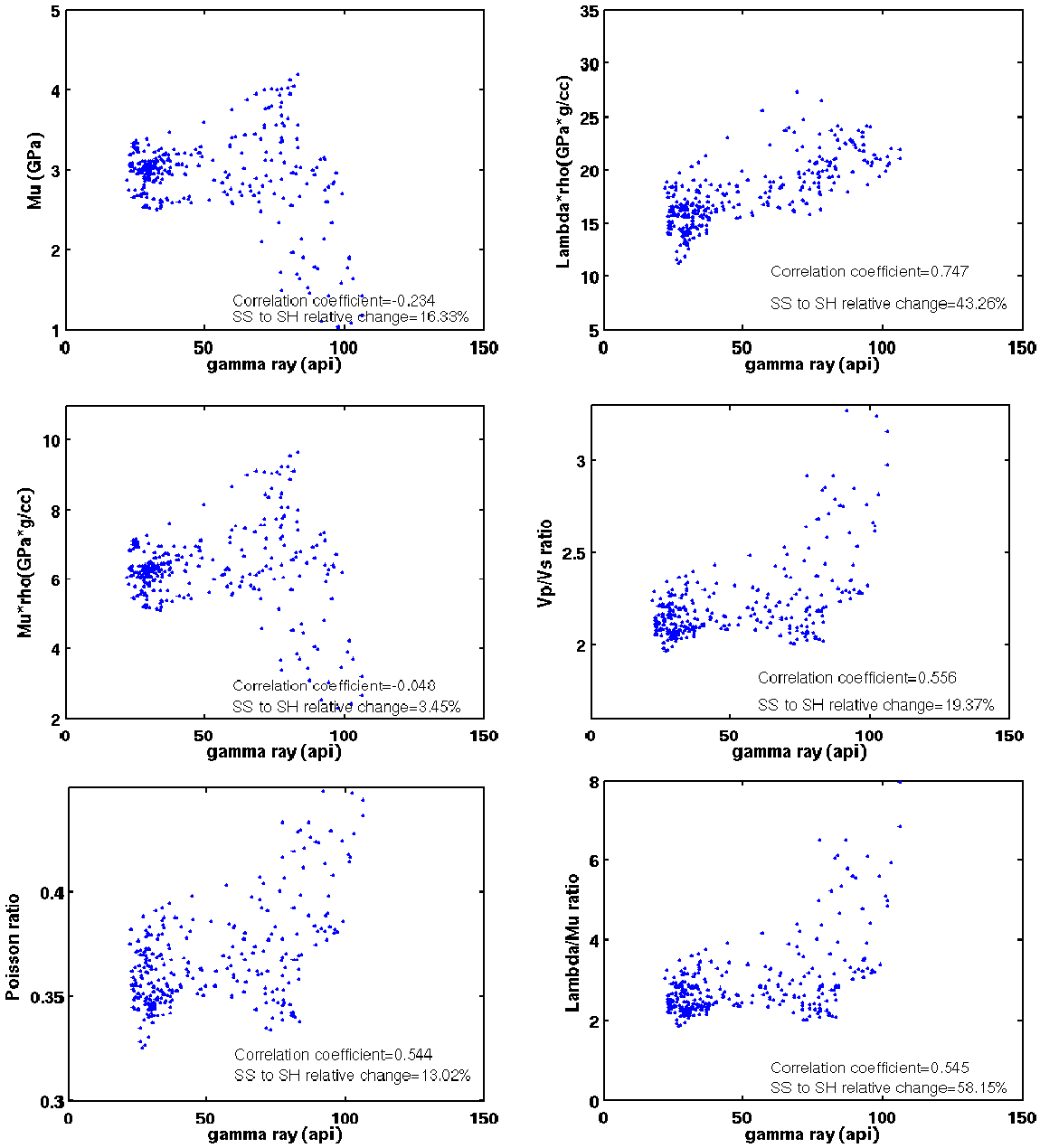

Figure 2.8 *(Continued from previous page)* **Crossplots of rock physical parameters against gamma ray values (Meadow Creek).**

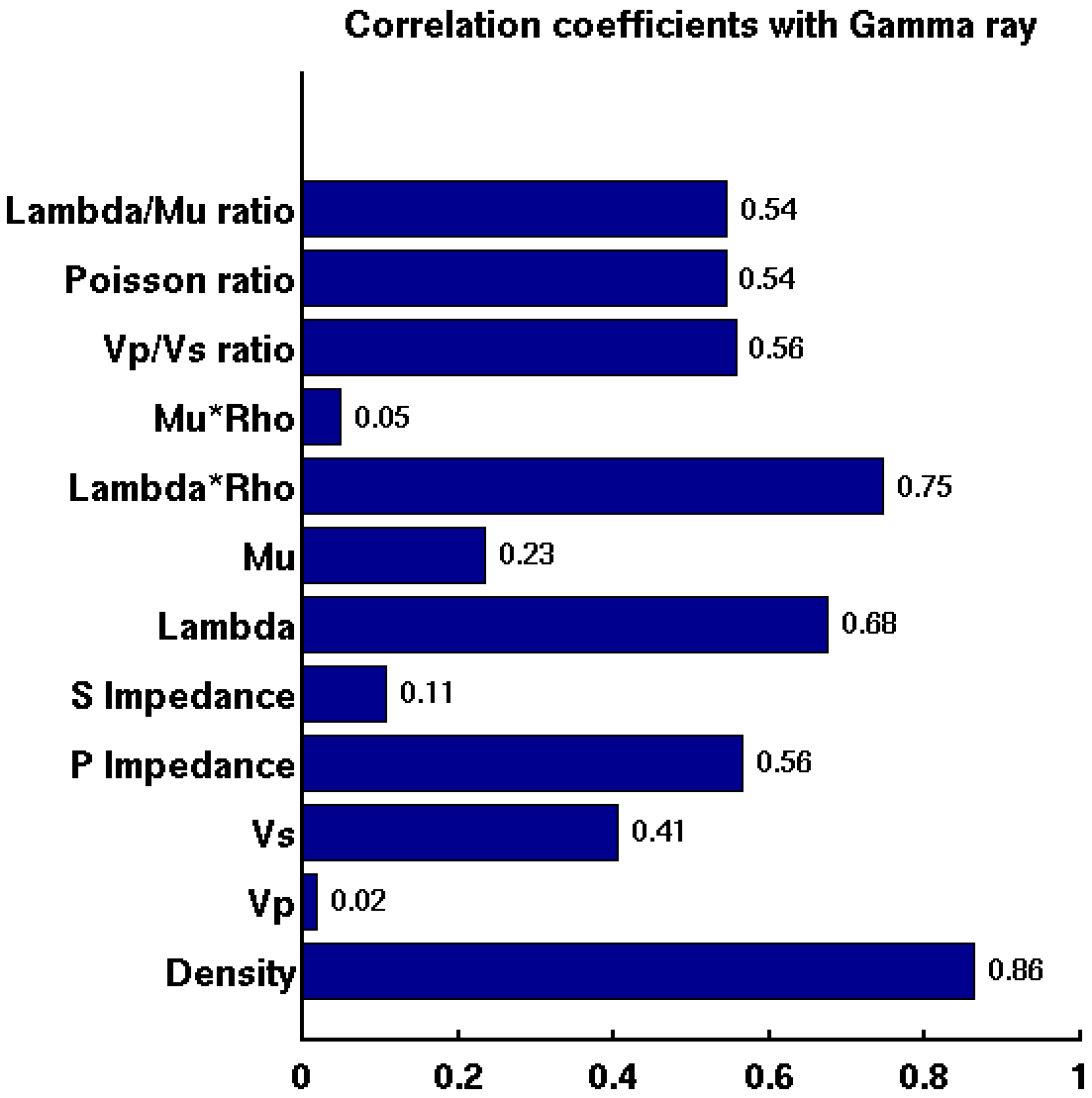

Figure 2.9 Bar chart comparing correlation between rock physical parameters and gamma ray (Meadow Creek). The values labelled on the right of the bars are the correlation coefficients.

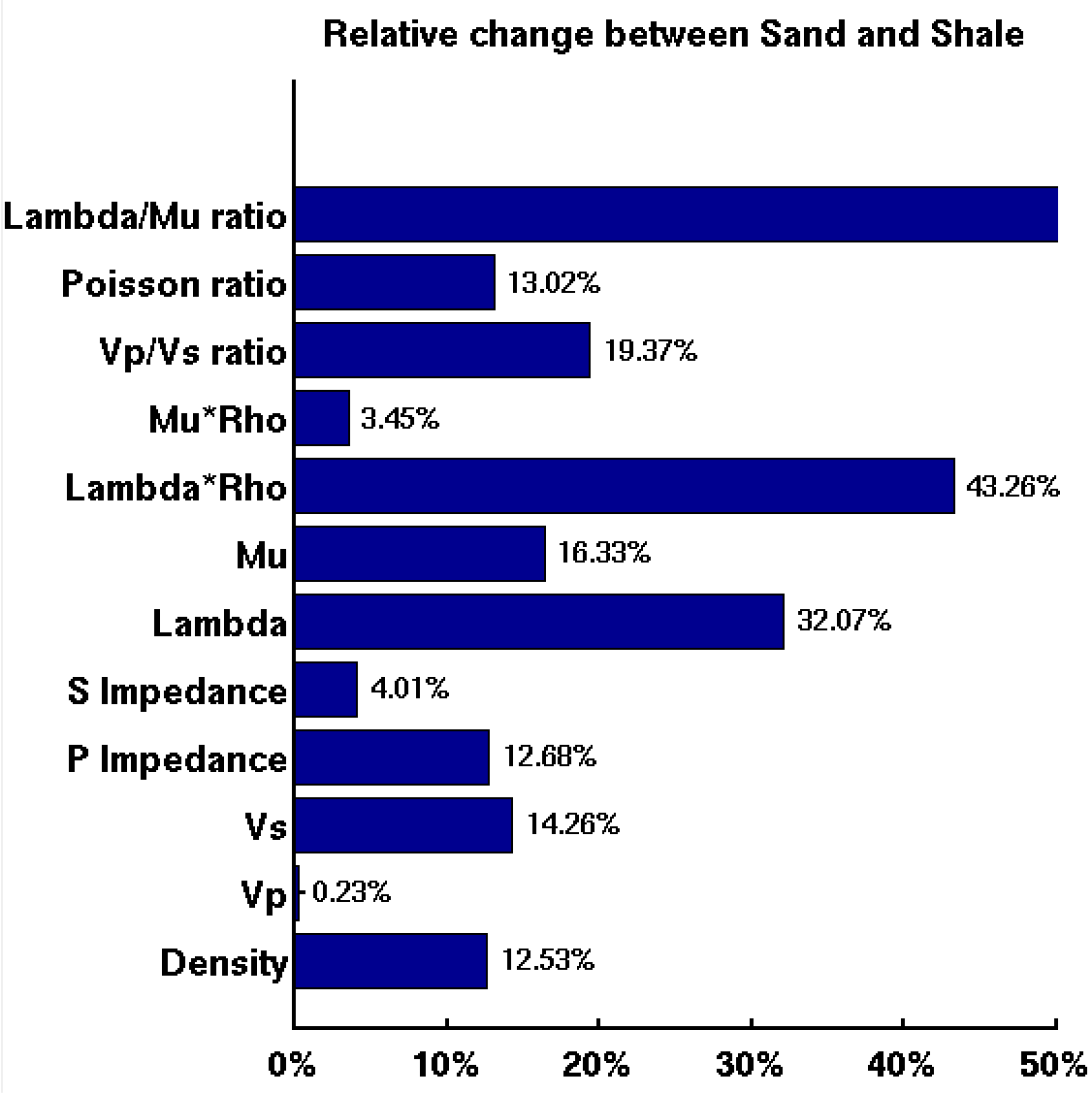

Figure 2.10 Relative changes between sand and shale on each rock physical parameter in Meadow Creek.

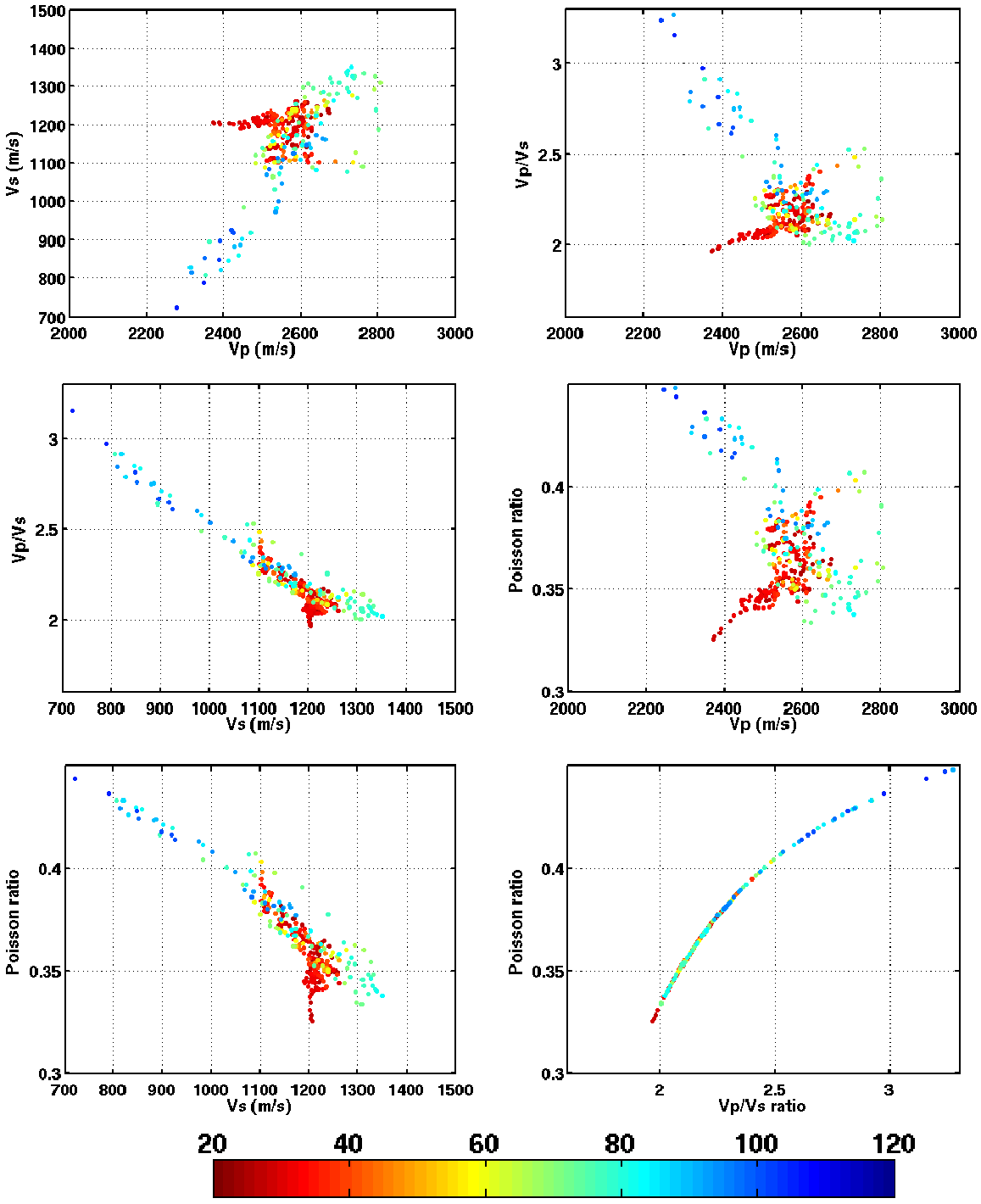

Figure 2.11 Cross plots of various pairs of elastic parameters (Meadow Creek) with samples color-coded by gamma ray. The cross-plot of Poisson's ratio and Vp/Vs ratio in the lower right corner mainly indicates the theoretical relationship between Poisson's ratio and Vp/Vs ratio except the clean sands showing low values on both ratios *(Continued on next page)***.**

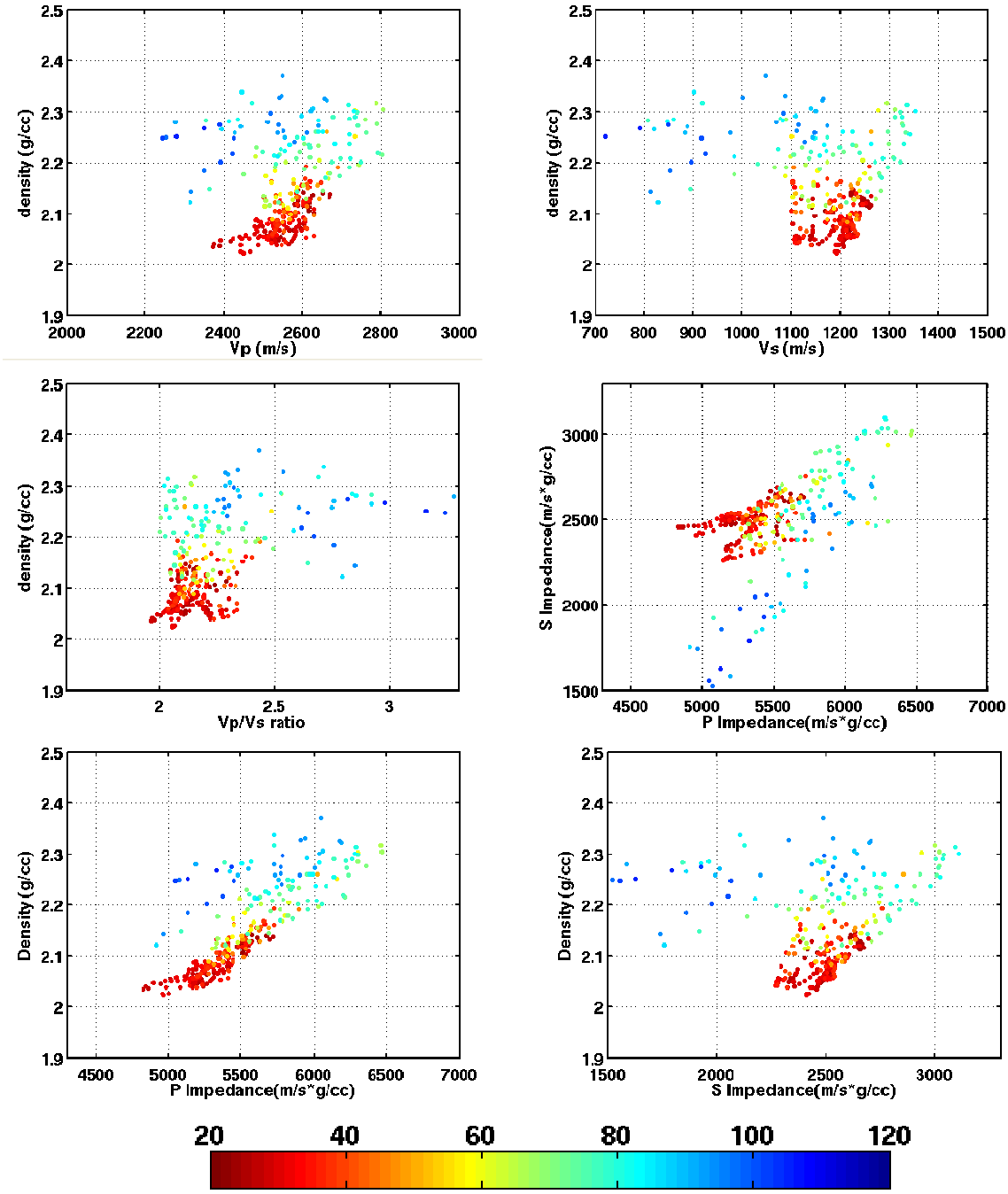

Figure 2.11 *(Continued from previous page)* **Cross plots of various pairs of elastic parameters (Meadow Creek) with samples color-coded by gamma ray** *(Continued on next page).*

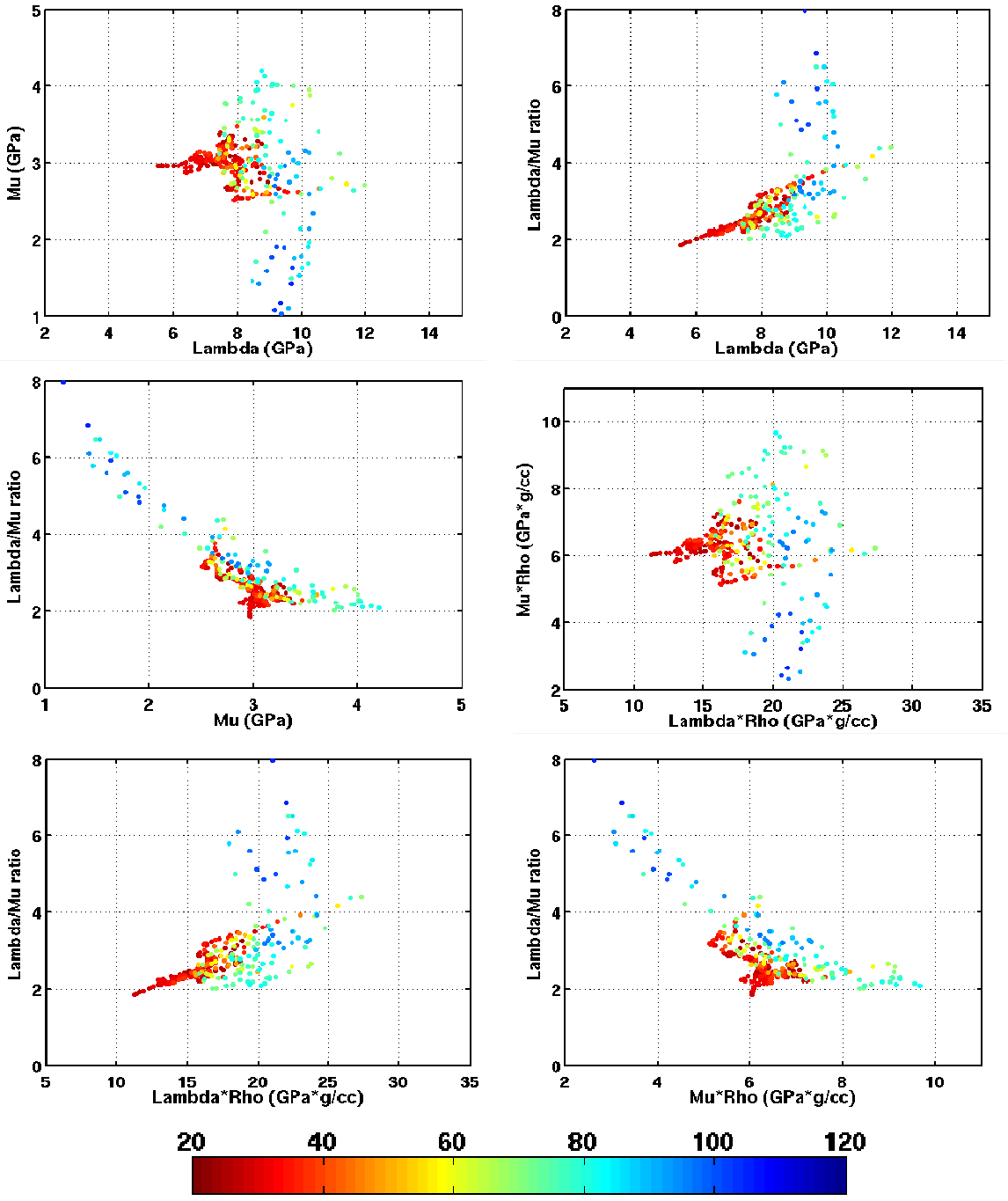

Figure 2.11 *(Continued from previous page)* **Cross plots of various pairs of elastic parameters (Meadow Creek) with samples color-coded by gamma ray.**

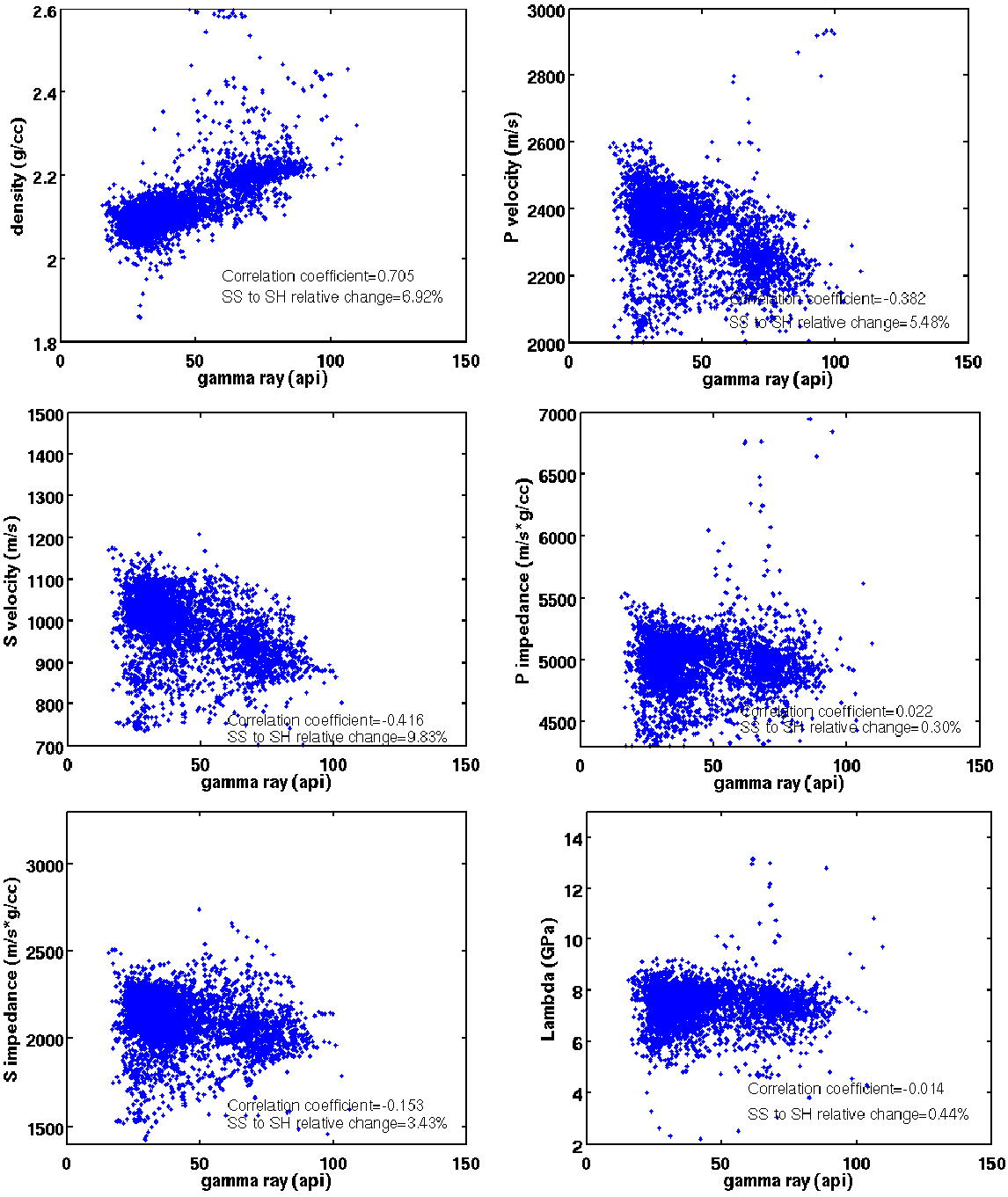

Figure 2.12 Crossplots of rock physical parameters (Mackay River) against gamma ray values. Gamma ray values for most of the samples are less than 95 API *(Continued on next page).*

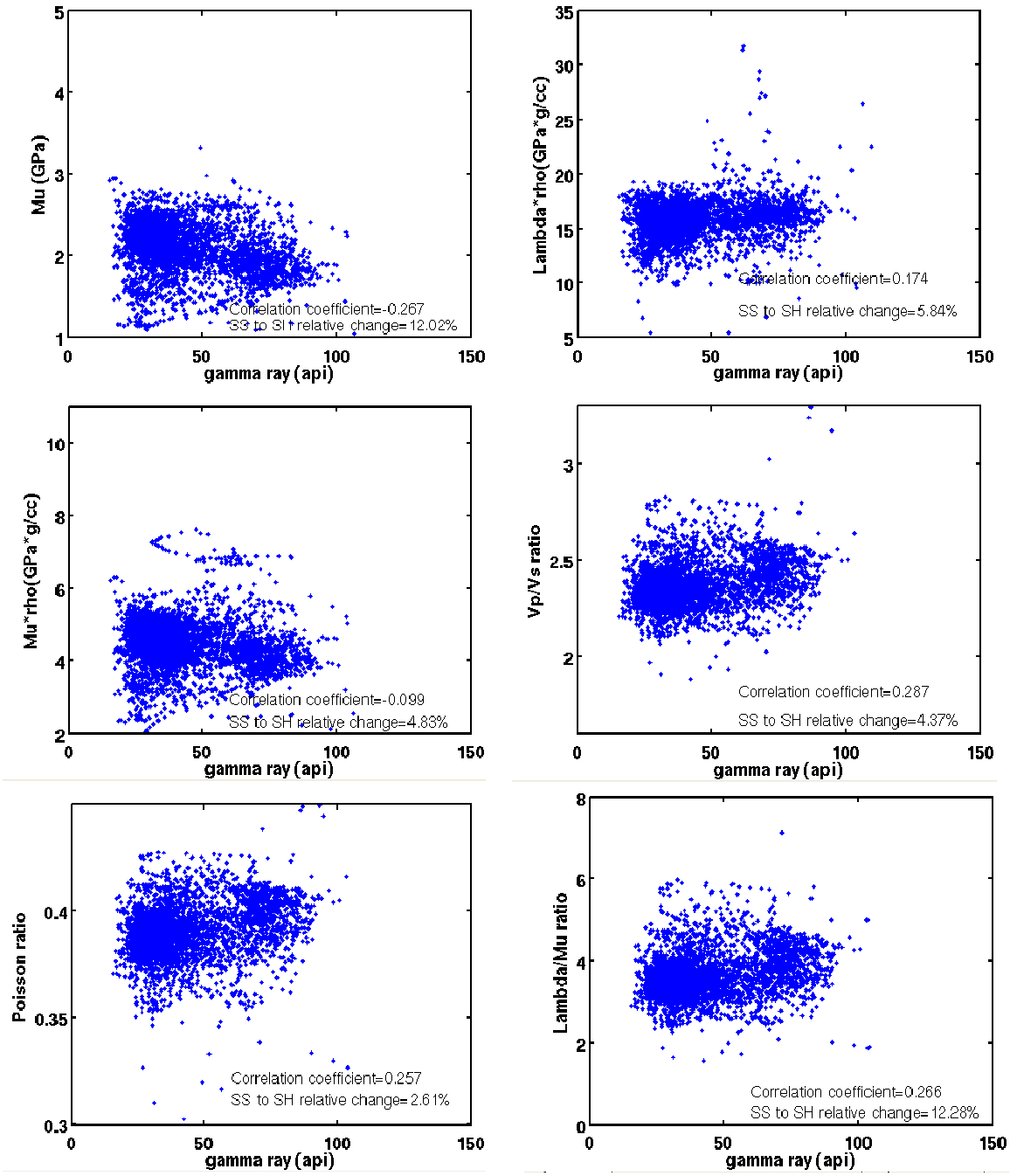

Figure 2.12 *(Continued from previous page)* **Crossplots of rock physical parameters against gamma ray values (Mackay River). Gamma ray values for most of the samples are less than 95 API.**

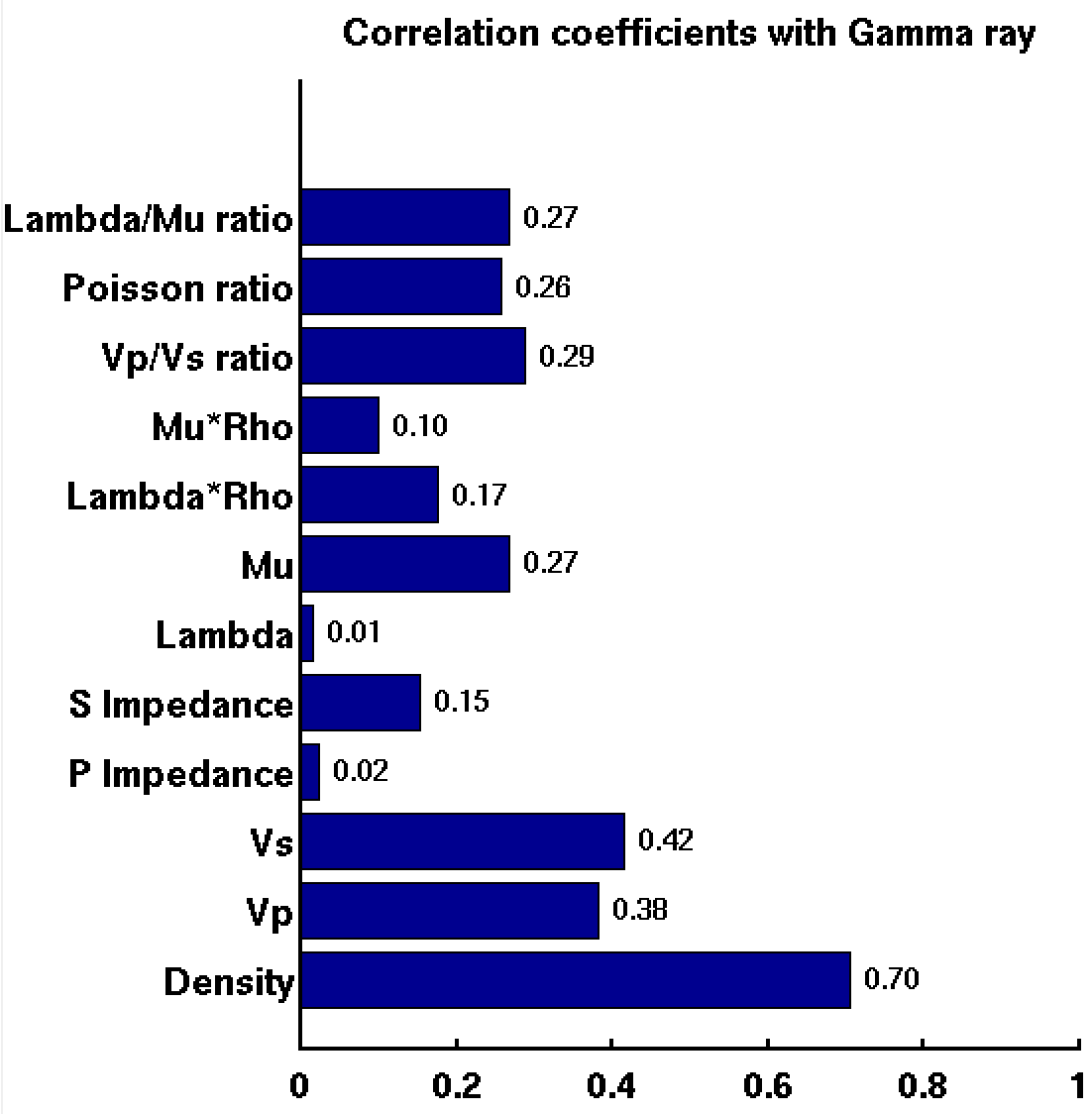

Figure 2.13 Bar chart comparing correlation between rock physical parameters and gamma ray (Mackay River). The values labelled on the right of the bars are the correlation coefficients.

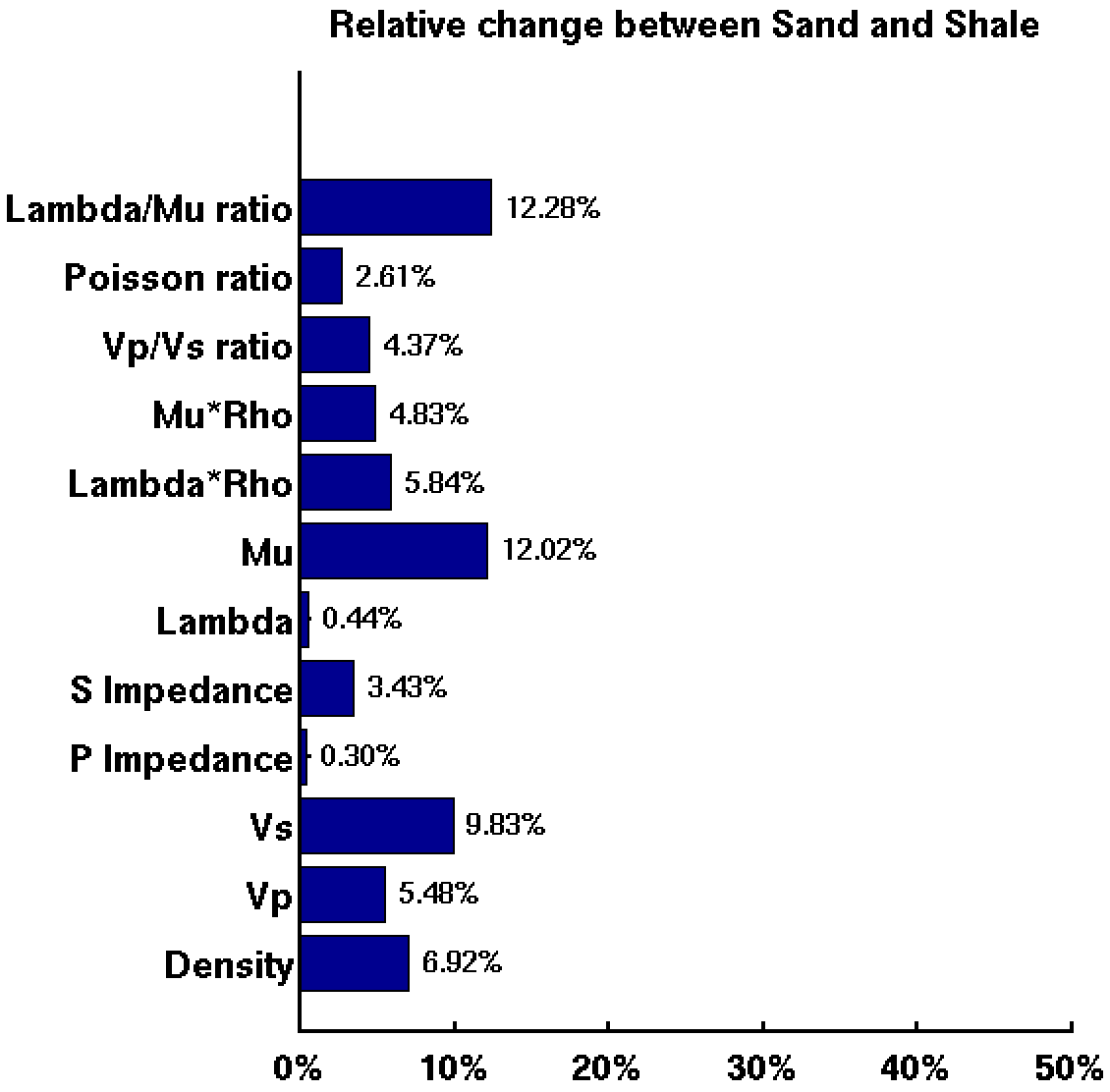

Figure 2.14 Relative changes between sand and shale on each rock physical parameter in Mackay River. The shale class is much sandy in the reservoir, which reduce the difference of elastic properties between sand and shale.

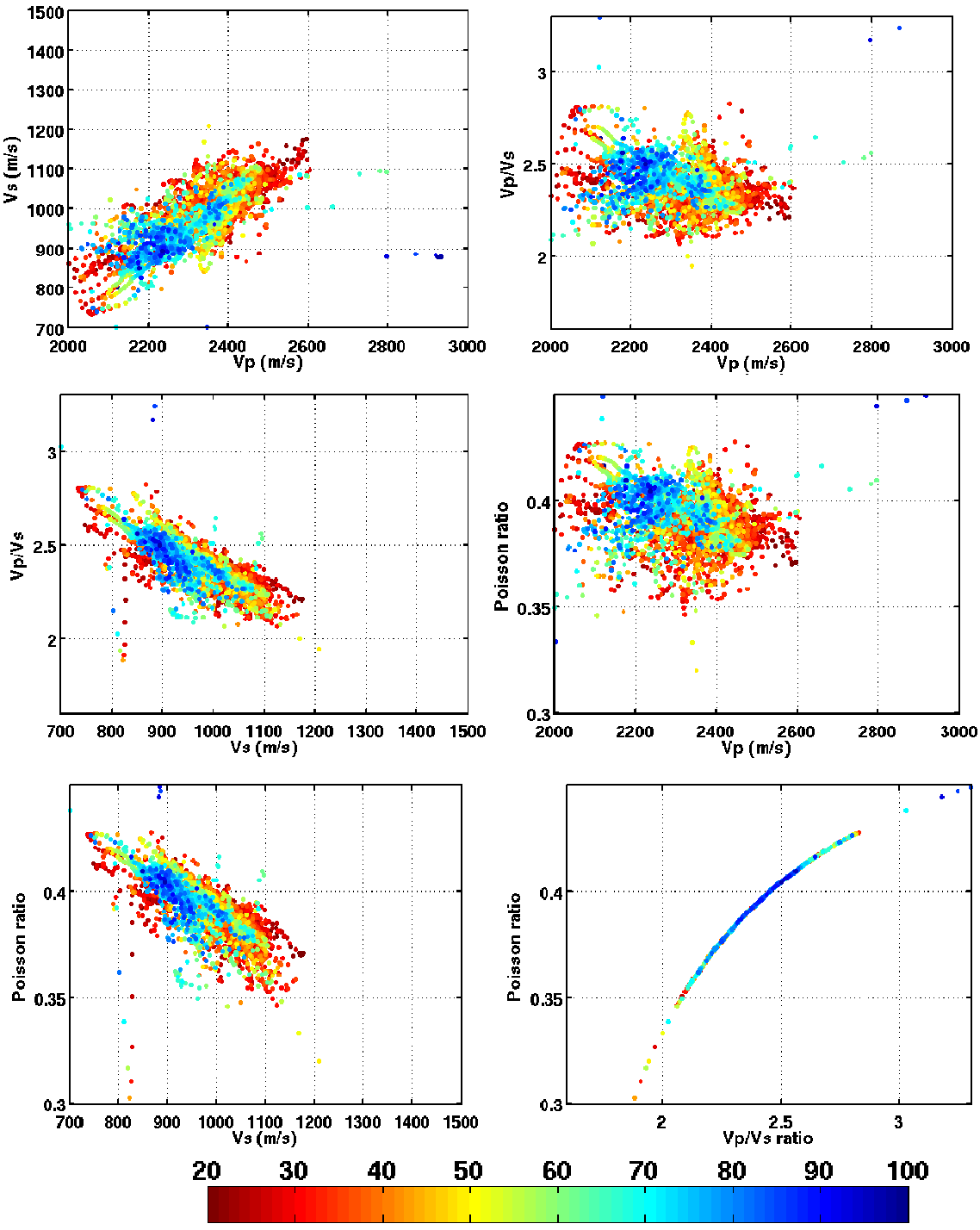

Figure 2.15 Cross plots of various pairs of elastic parameters (Mackay River) with samples color-coded by gamma ray The cross-plot of Poisson's ratio and Vp/Vs ratio in the lower right corner mainly indicates the theoretical relationship between Poisson's ratio and Vp/Vs ratio except the clean sands showing low values on both ratios *(Continued on next page).*

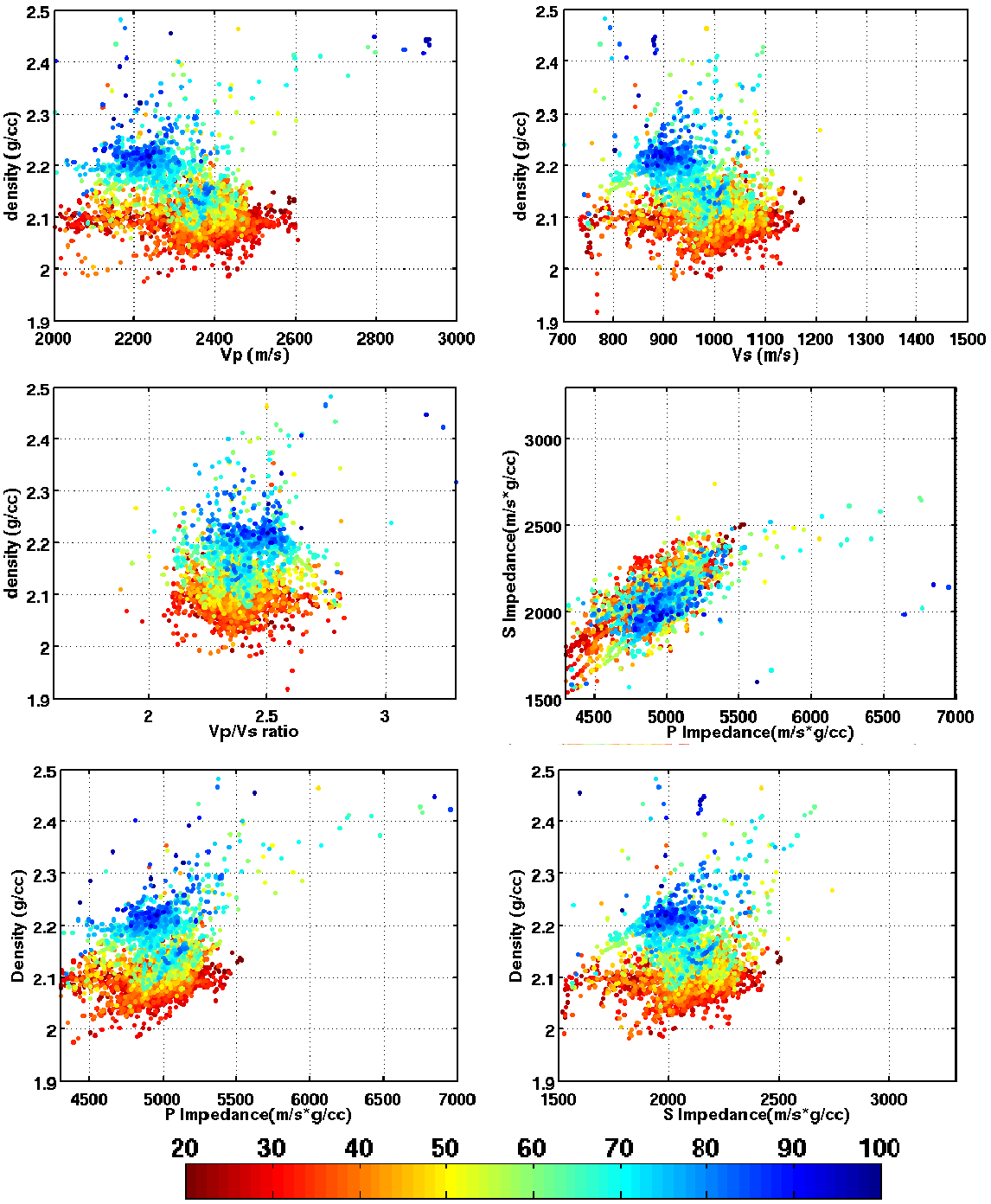

Figure 2.15 *(Continued from previous page)* **Cross plots of various pairs of elastic parameters (Mackay River) with samples color-coded by gamma ray values** *(Continued on next page).*

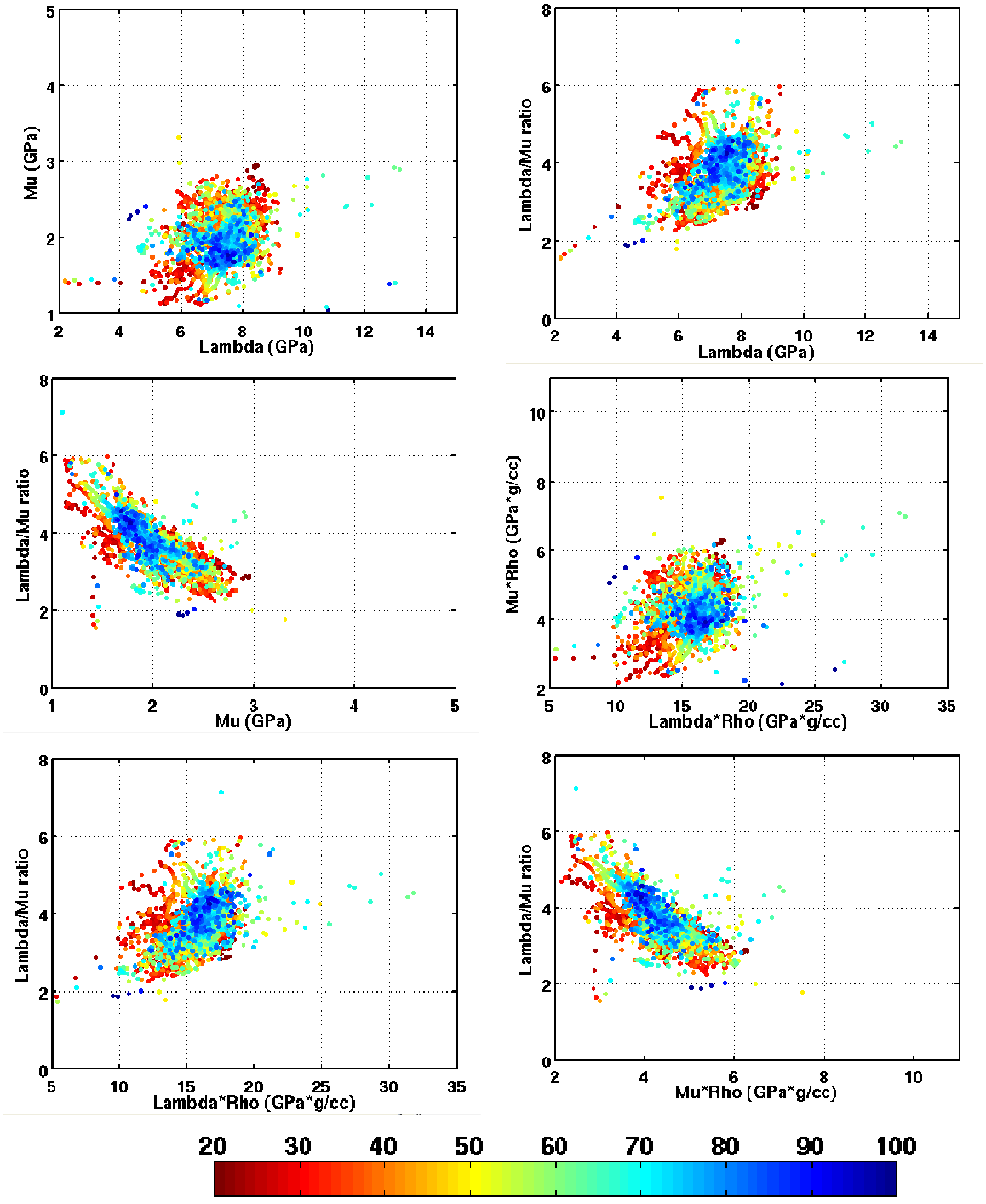

Figure 2.15 *(Continued from previous page)* **Cross plots of various pairs of elastic parameters (Mackay River) with samples color-coded by gamma ray.**

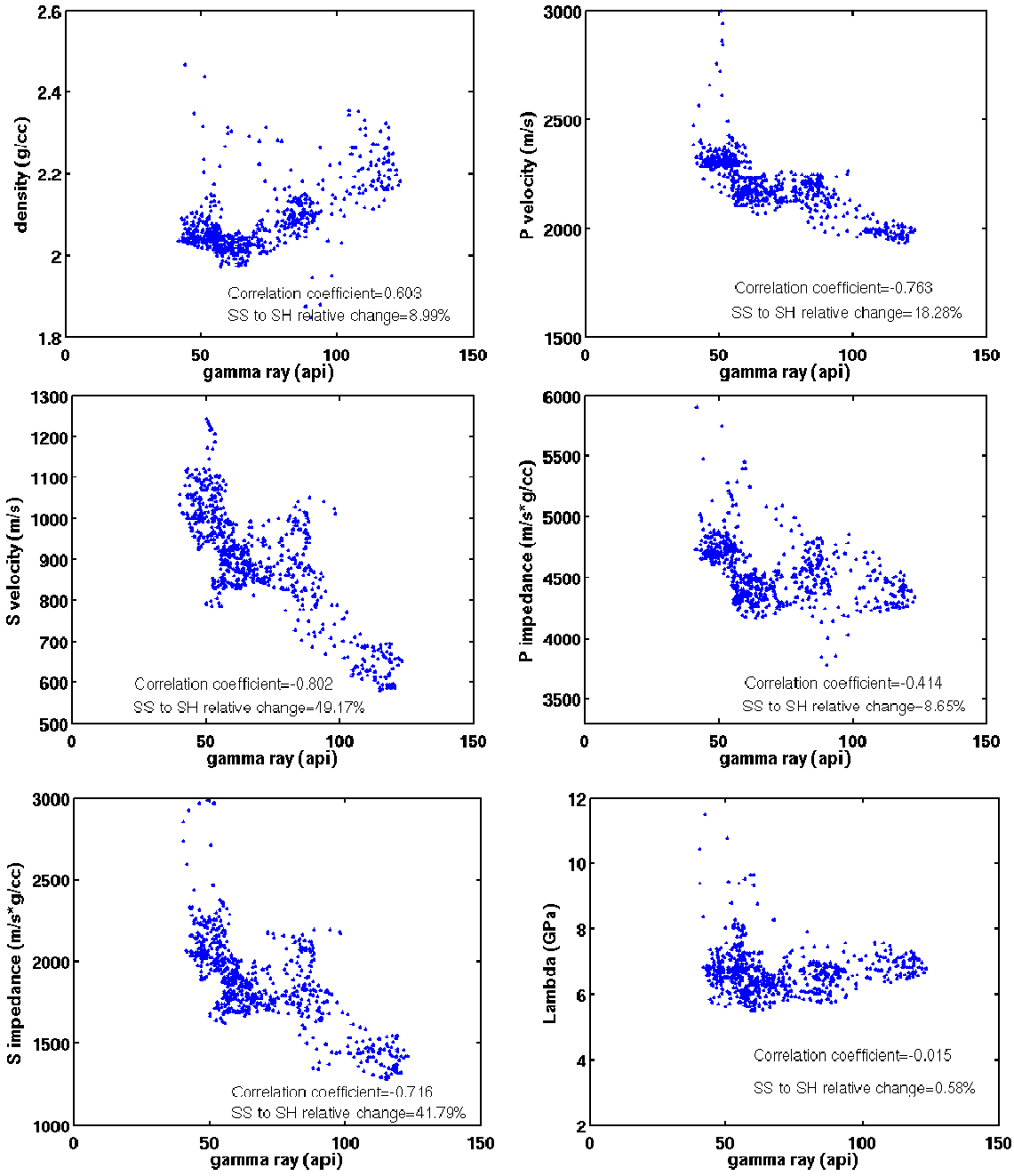

Figure 2.16 Crossplots of rock physical parameters against gamma ray values (the Grand Rapids Formation in Germaine) *(Continued on next page).*

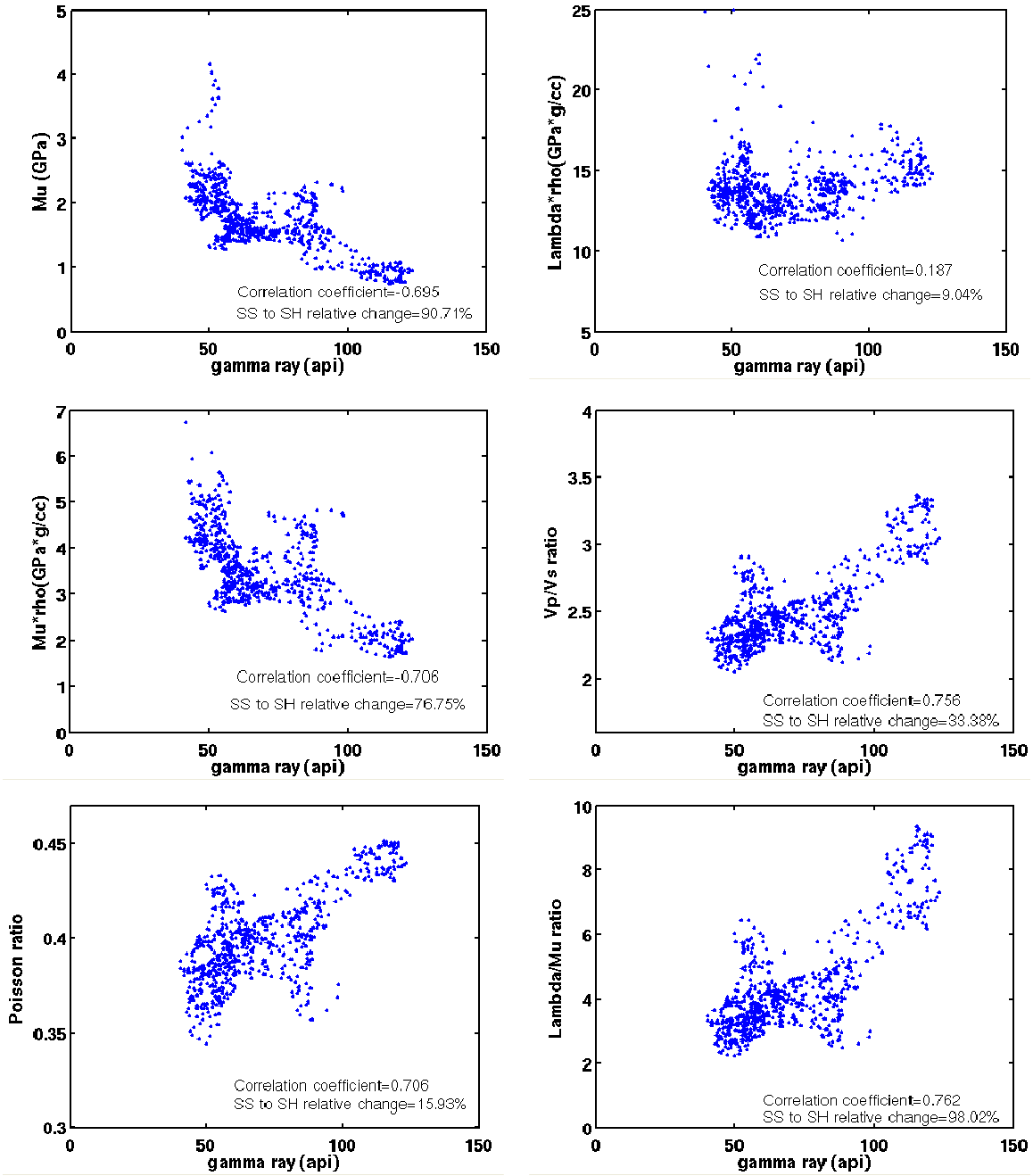

Figure 2.16 *(Continued from previous page)* **Crossplots of rock physical parameters against gamma ray values (the Grand Rapids Formation in Germaine).**

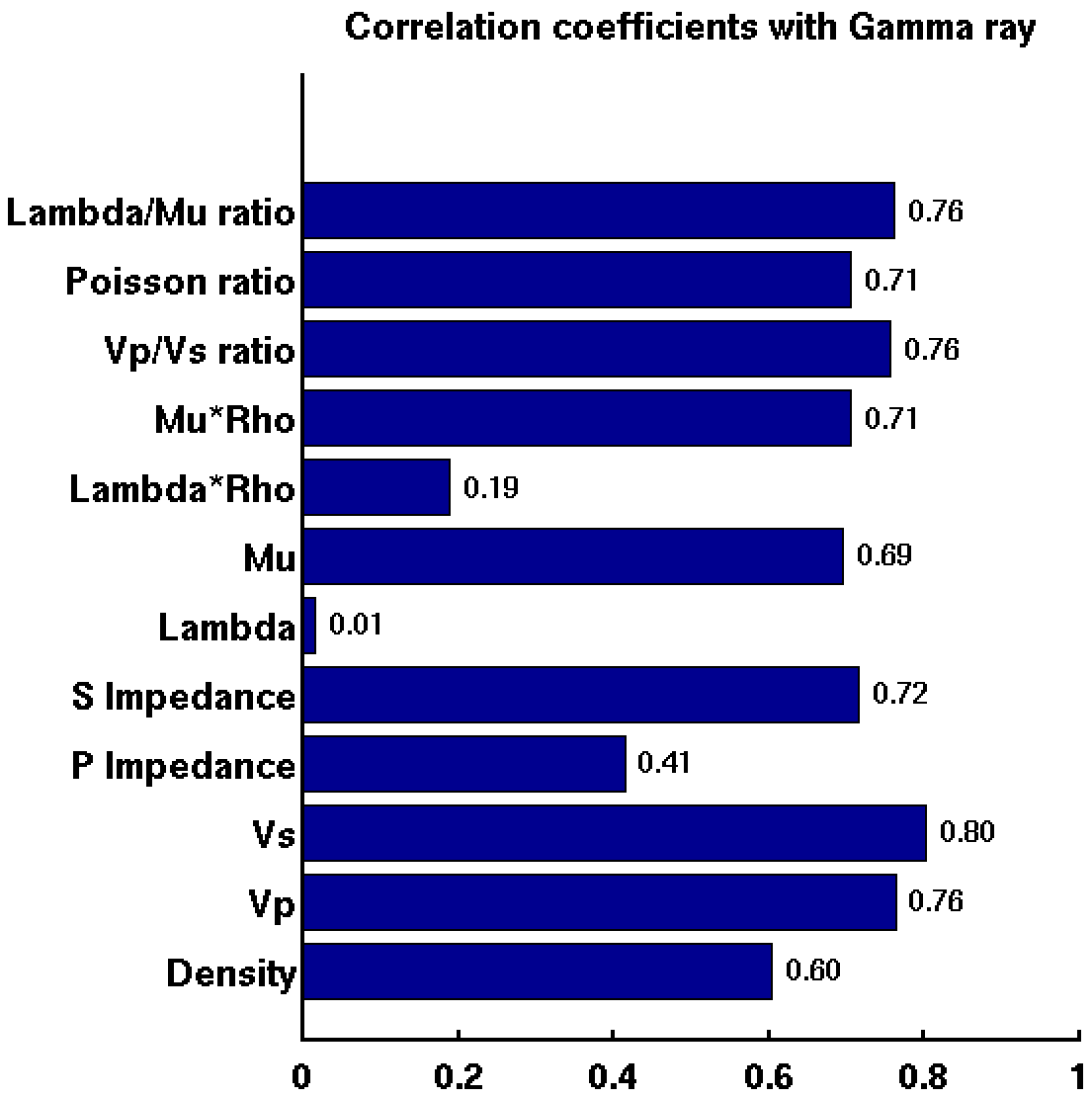

Figure 2.17 Bar chart comparing correlation between rock physical parameters and gamma ray (the Grand Rapids Formation in Germaine). The values labelled on the right of the bars are the correlation coefficients

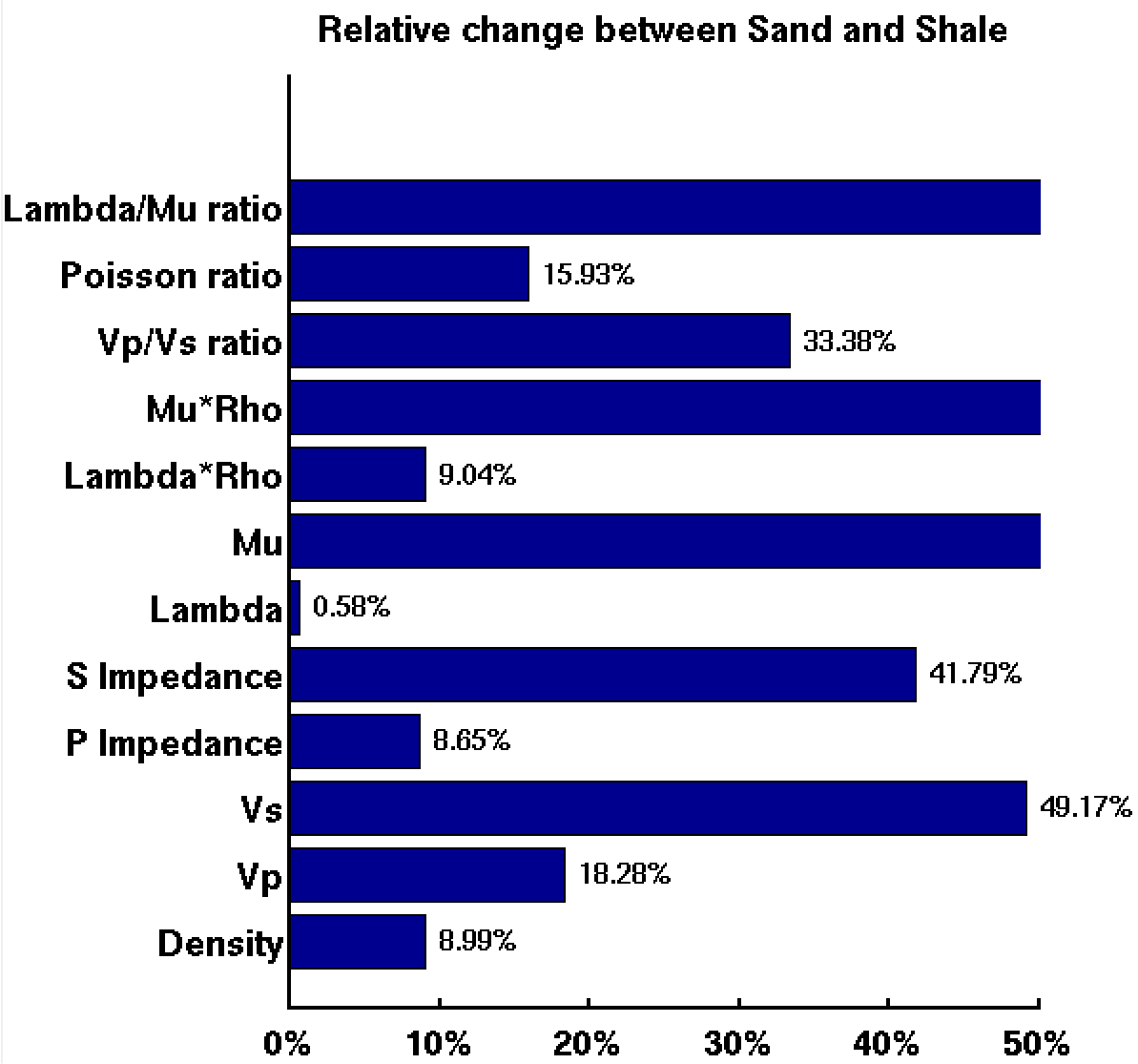

Figure 2.18 Relative changes between sand and shale on each rock physical parameter in the Grand Rapids Formation in Germaine.

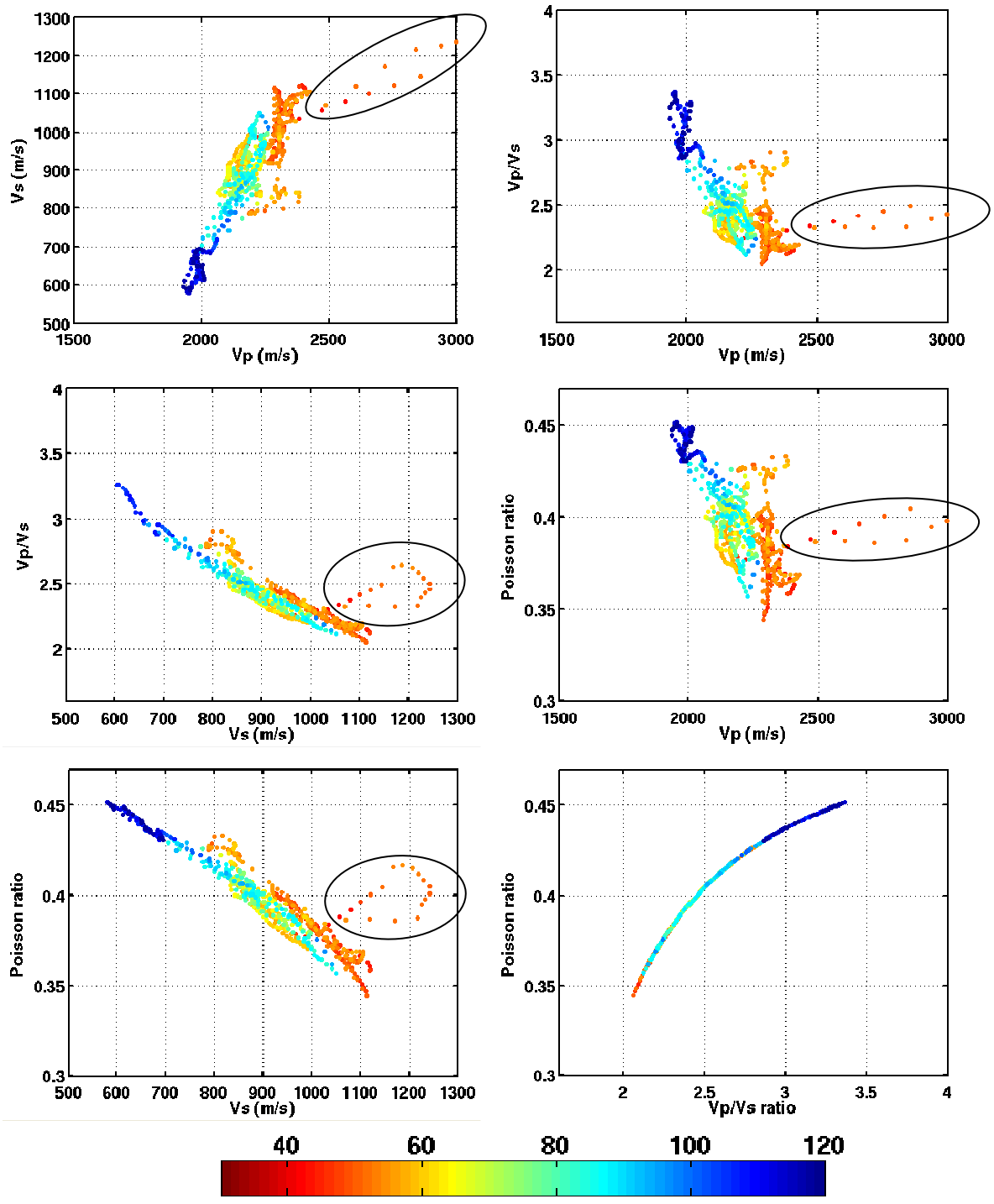

Figure 2.19 Cross plots of various pairs of elastic parameters (the Grand Rapids Formation in Germaine) with samples color-coded by gamma ray The cross-plot of Poisson's ratio and Vp/Vs ratio in the lower right corner mainly indicates the theoretical relationship between Poisson's ratio and Vp/Vs ratio except the clean sands showing low values on both ratios. The outliers in the circles are from a tight concretion *(Continued on next page).*

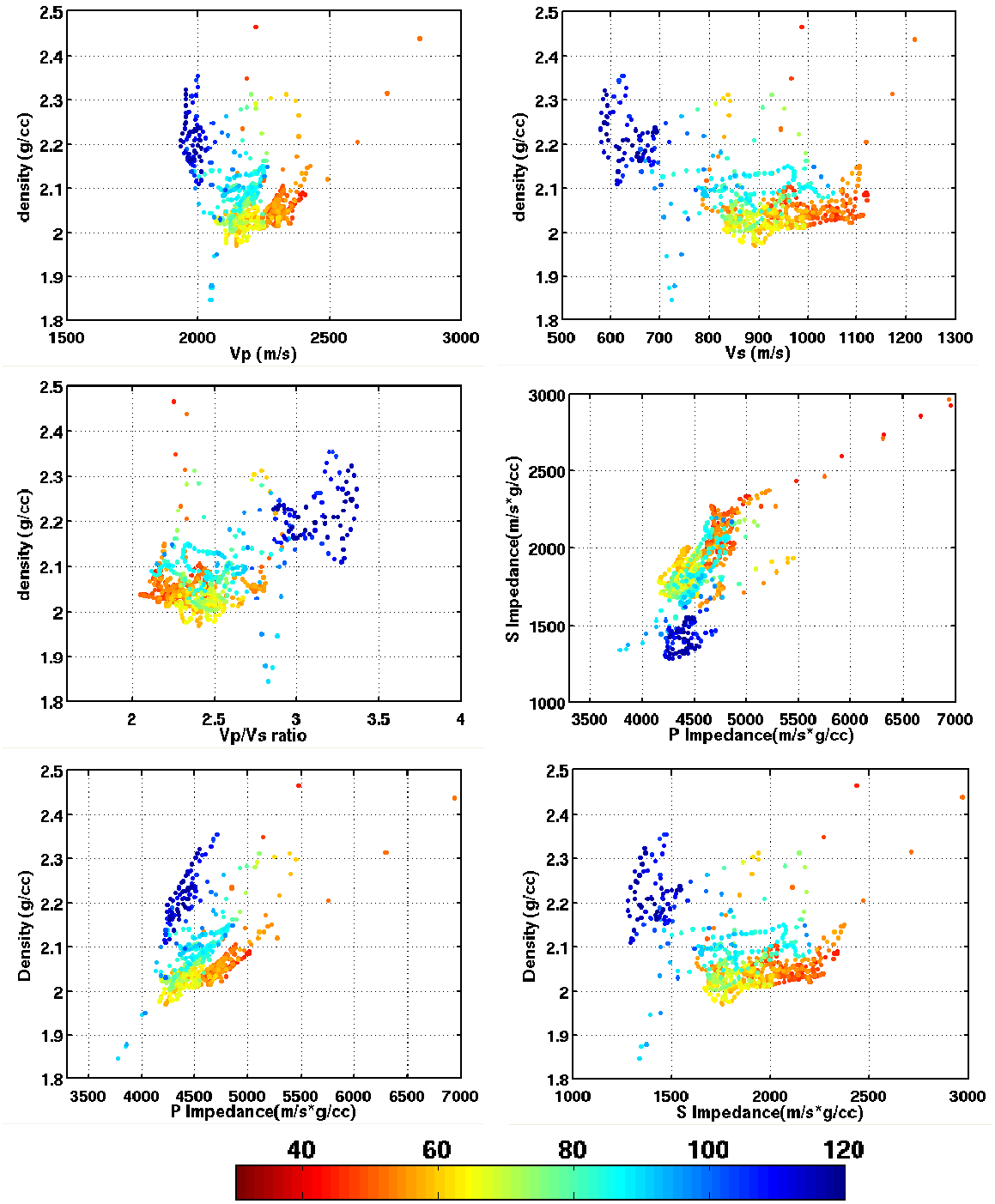

Figure 2.19 *(Continued from previous page)* **Cross plots of various pairs of elastic parameters (the Grand Rapids Formation in Germaine) with samples color-coded by gamma ray** *(Continued on next page).*

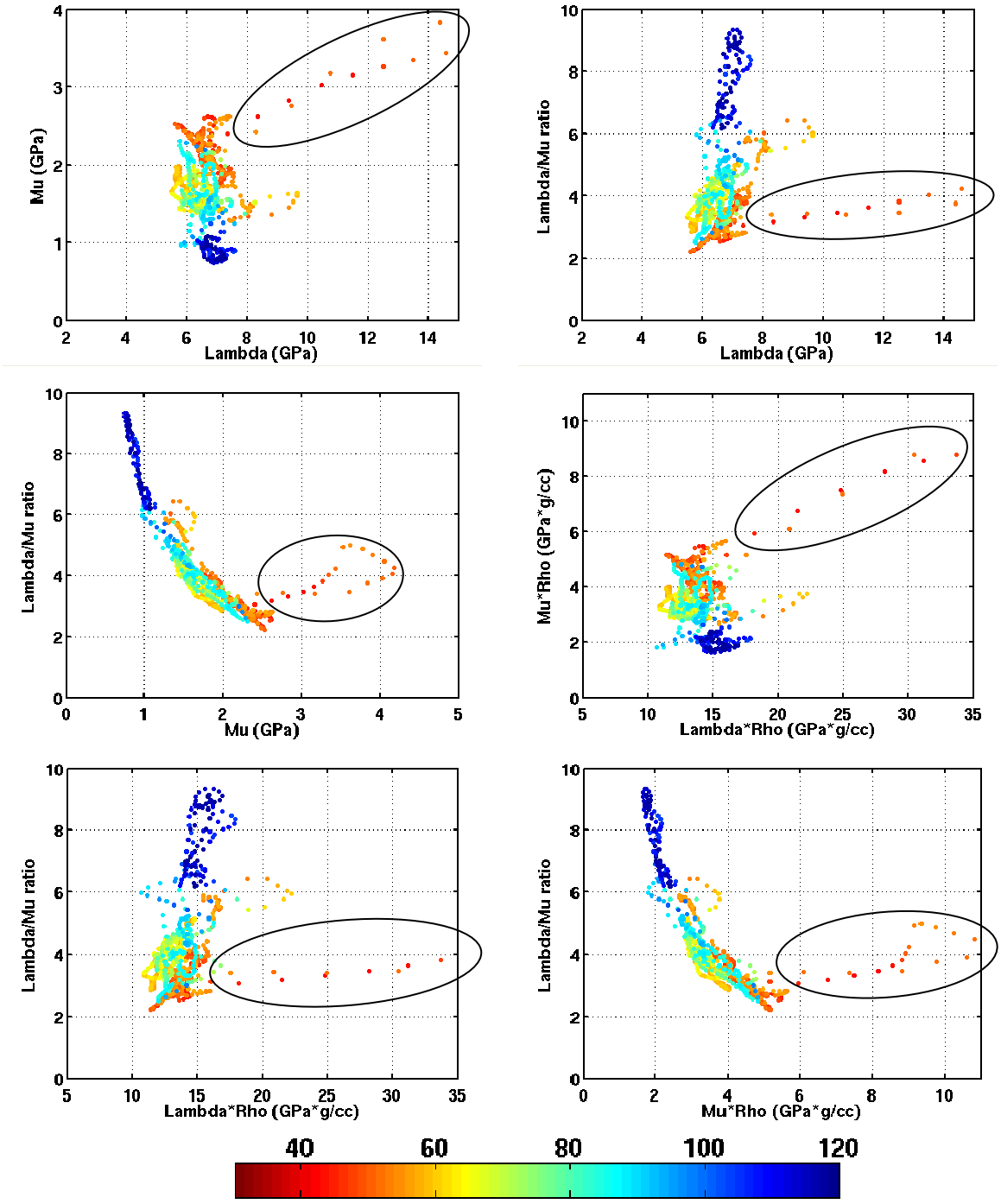

Figure 2.19 *(Continued from previous page)* **Cross plots of various pairs of elastic parameters (the Grand Rapids Formation in Germaine) with samples color-coded by gamma ray. The outliers inside circles are from a tight concretion.**

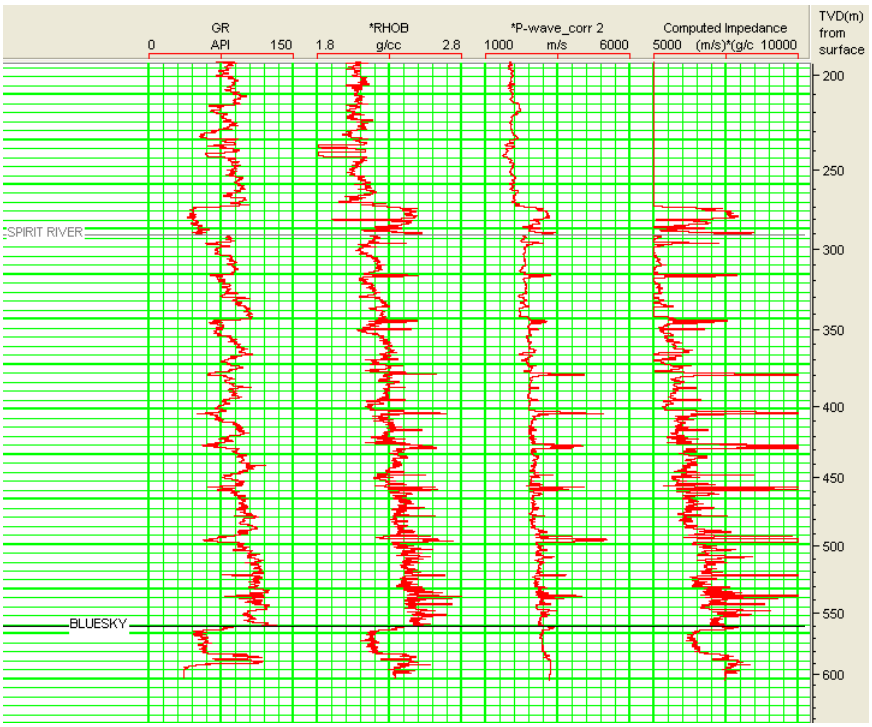

Figure 2.20 A suite of logs for a well in Peace River (the shear sonic is not available). Curves are gamma ray, density, Vp, and P impedance from left to right.

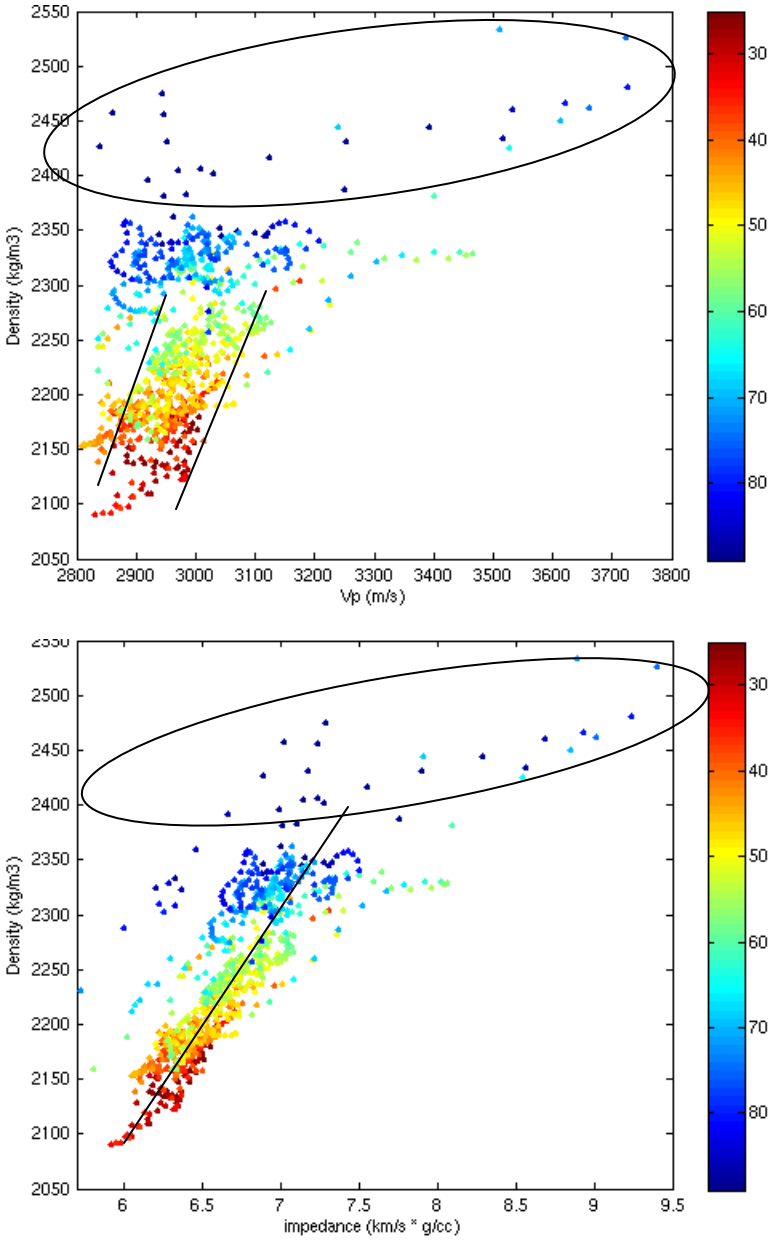

Figure 2.21 Cross-plots of Vp and density (top) and P impedance and density (bottom). Samples are from the Bluesky Formation of five wells in Peace River oil sands area. The color index is for gamma ray values. Samples inside circles are from the formations below the Bluesky and carbonate-dominated.

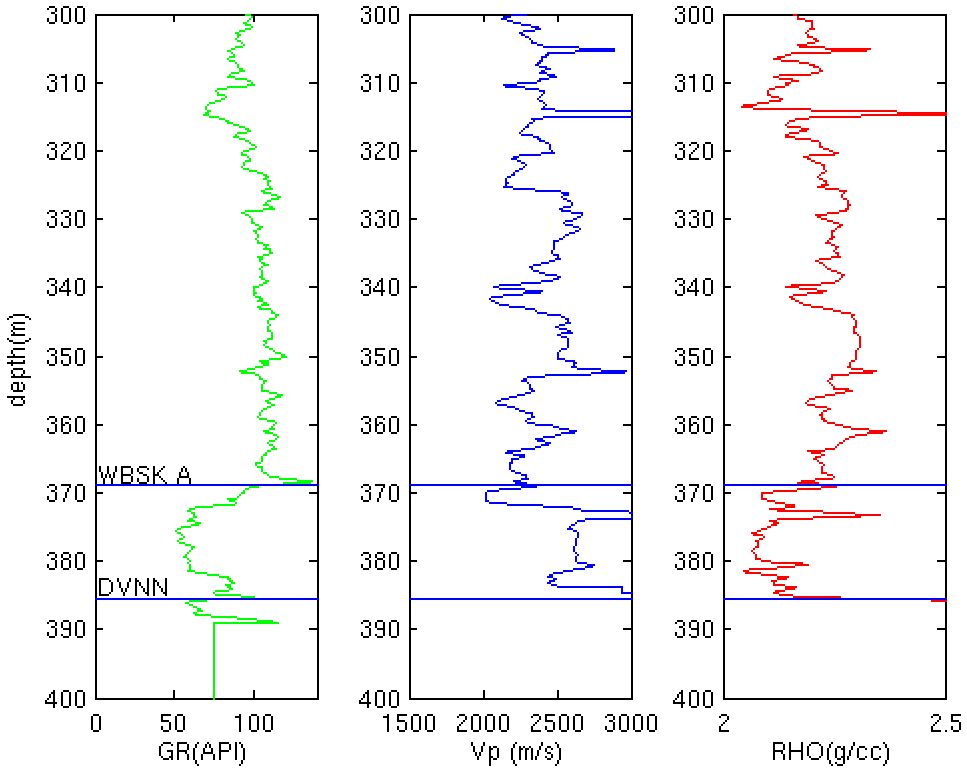

Figure 2.22 A suite of logs from a well in Birch area, North Athabasca. The curves are gamma ray, Vp, and density from left to right. The McMurray Formation is absent at this location. "WBSK" is for the Wabiskaw and "DVNN" is for the Devonian. A tight concretion is within 373-374m.

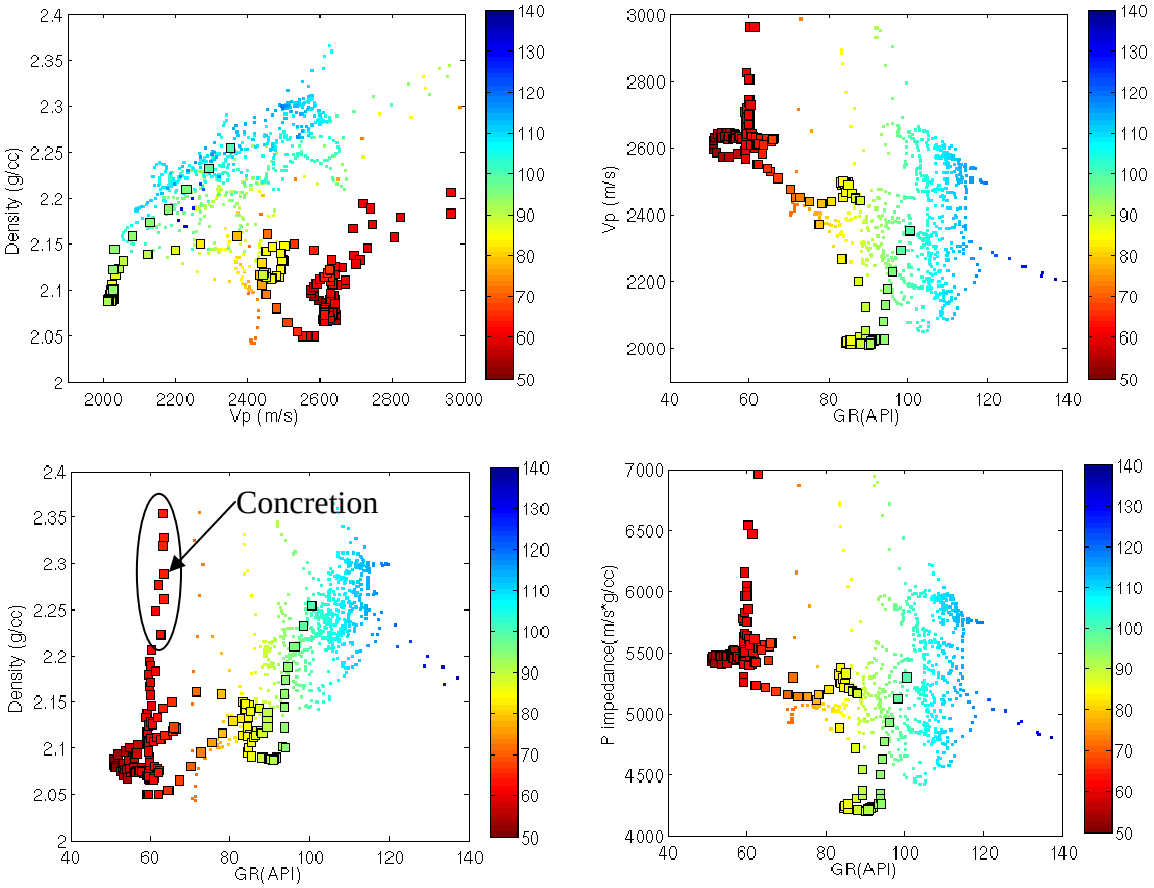

Figure 2.23 Crossplots between density, gamma ray, Vp and P impedance. Samples are from a well (Figure 2.22) in Birch, north Athabasca. The samples marked by squares are from the Wabiskaw Member; other samples are from above the Wabiskaw. Colors are coded by gamma ray values.

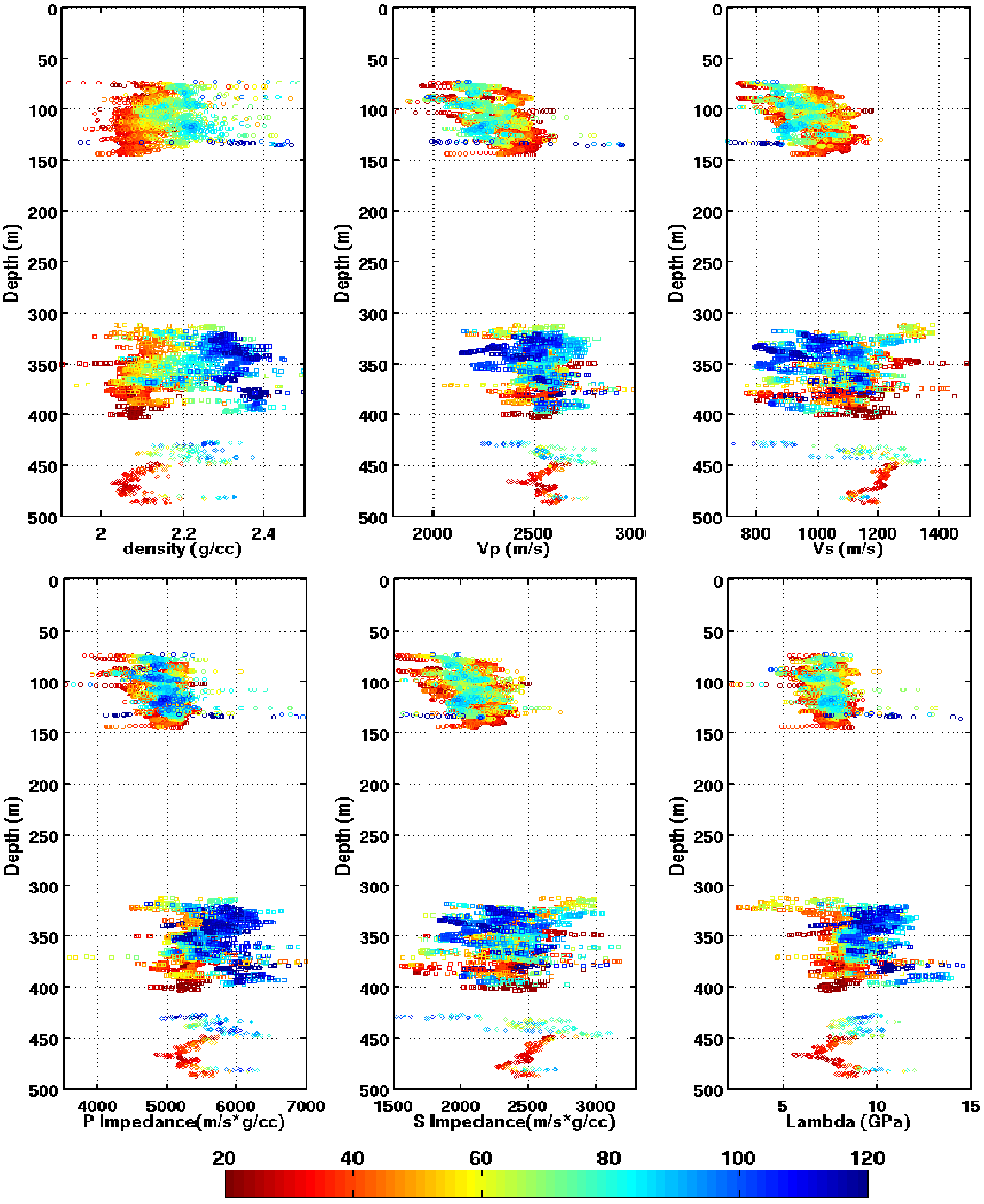

Figure 2.24 cross-plots of elastic parameters with depth with samples color-coded by gamma ray values. Samples are from the McMurray Formation in three reservoirs: two are at similar depth (300-500m) and third one is shallow (50-150m) *(Continued on next page).*

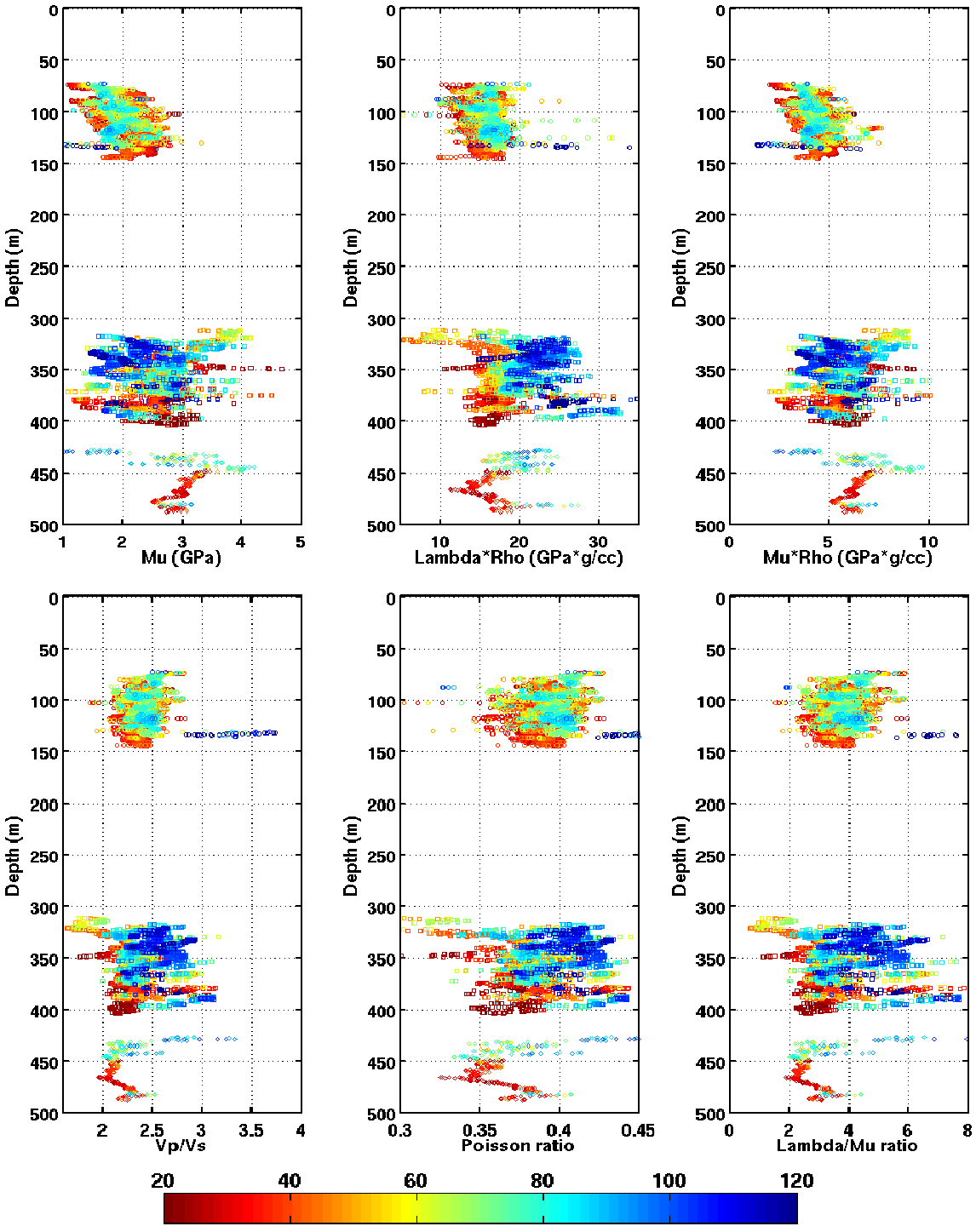

Figure 2.24 *(Continued from previous page)* **Cross-plots of elastic parameters with depth with samples color-coded by gamma ray values. Samples are from the McMurray Formation in three reservoirs.**

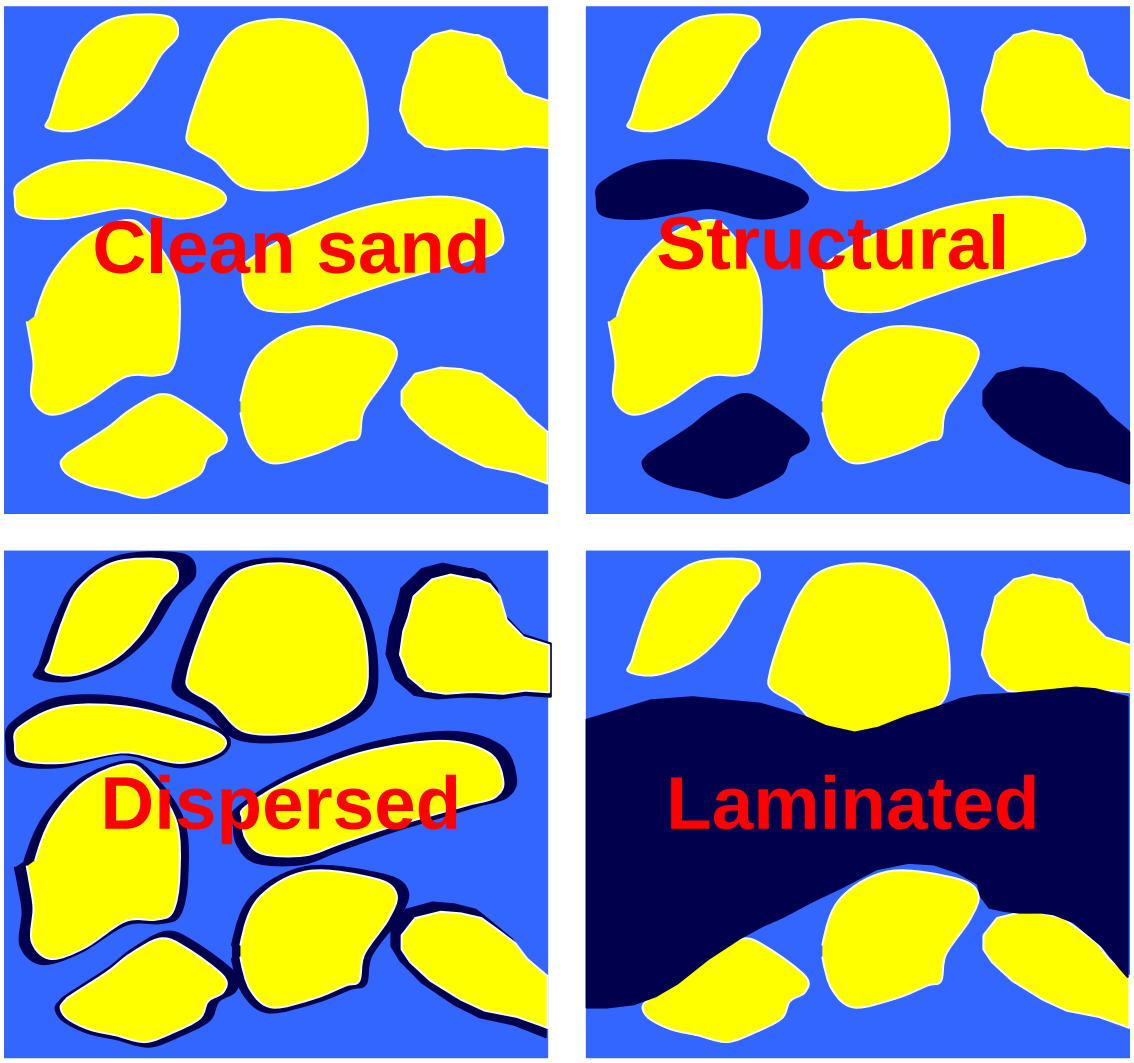

Figure 2.25 Classification of shale by distribution (modified after Ellis and Singer (2008)). The yellow stands for sand grains; the blue color stands for pore space; and the dark color stands for shales.

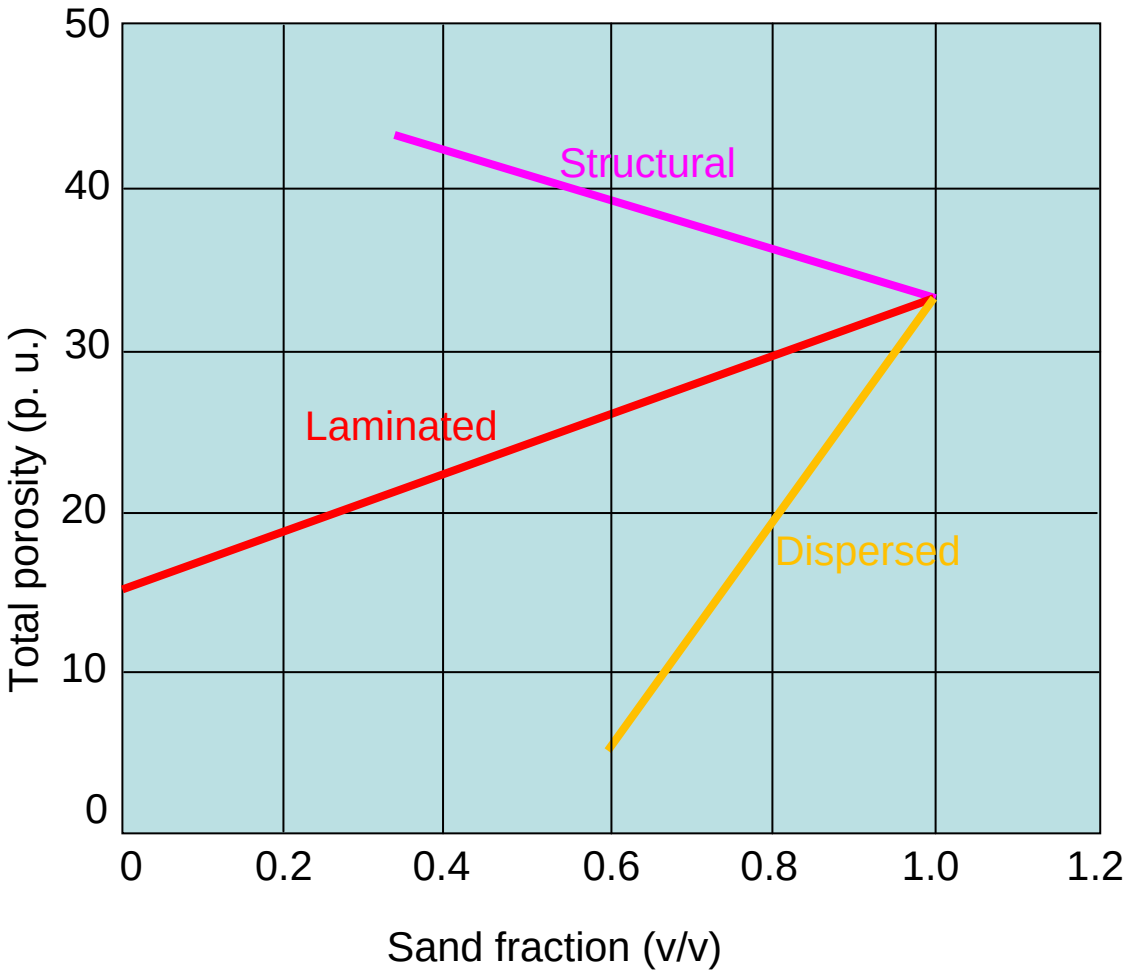

Figure 2.26 Effect of shale distribution when adding a shale with 15% bound water to a sand with 33% porosity (Modified after Ellis and Singer, 2008).

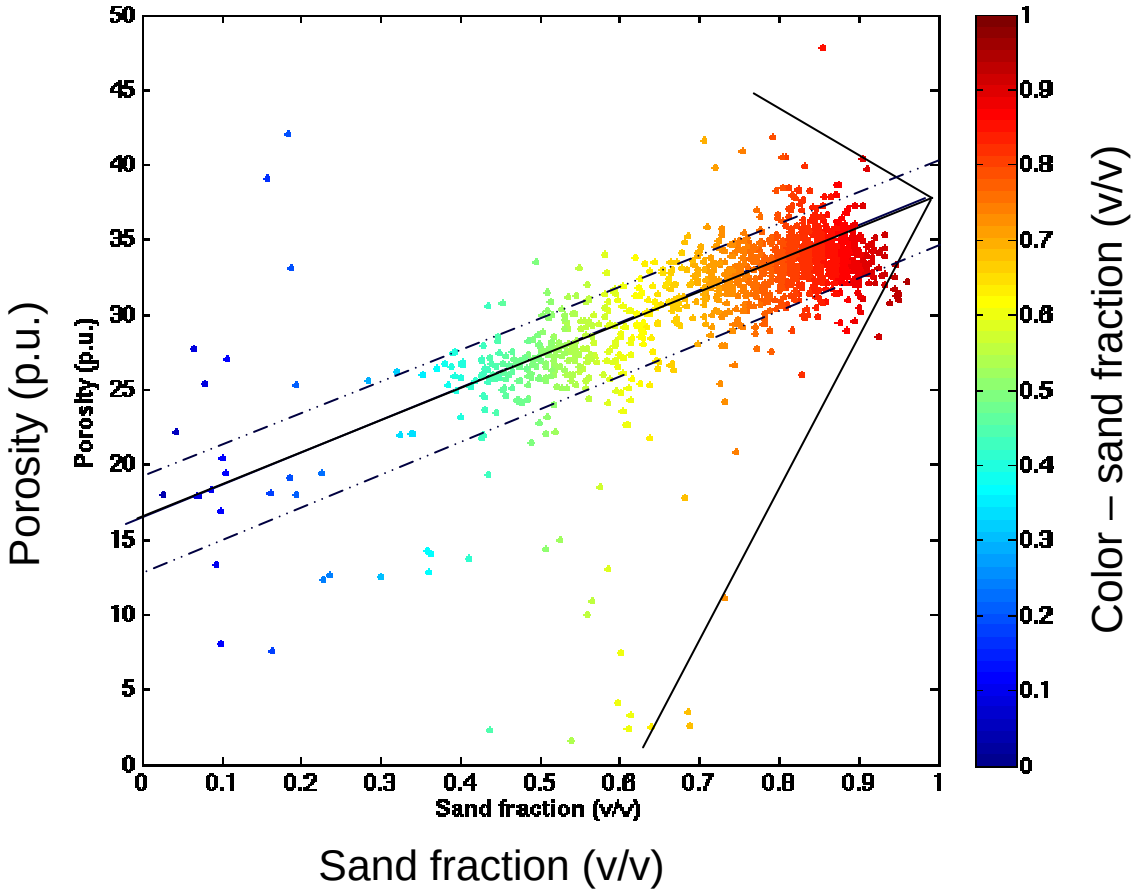

Figure 2.27 Cross plot of sand fraction and porosity. The samples are from a McMurray oil sands reservoir in Athabasca.

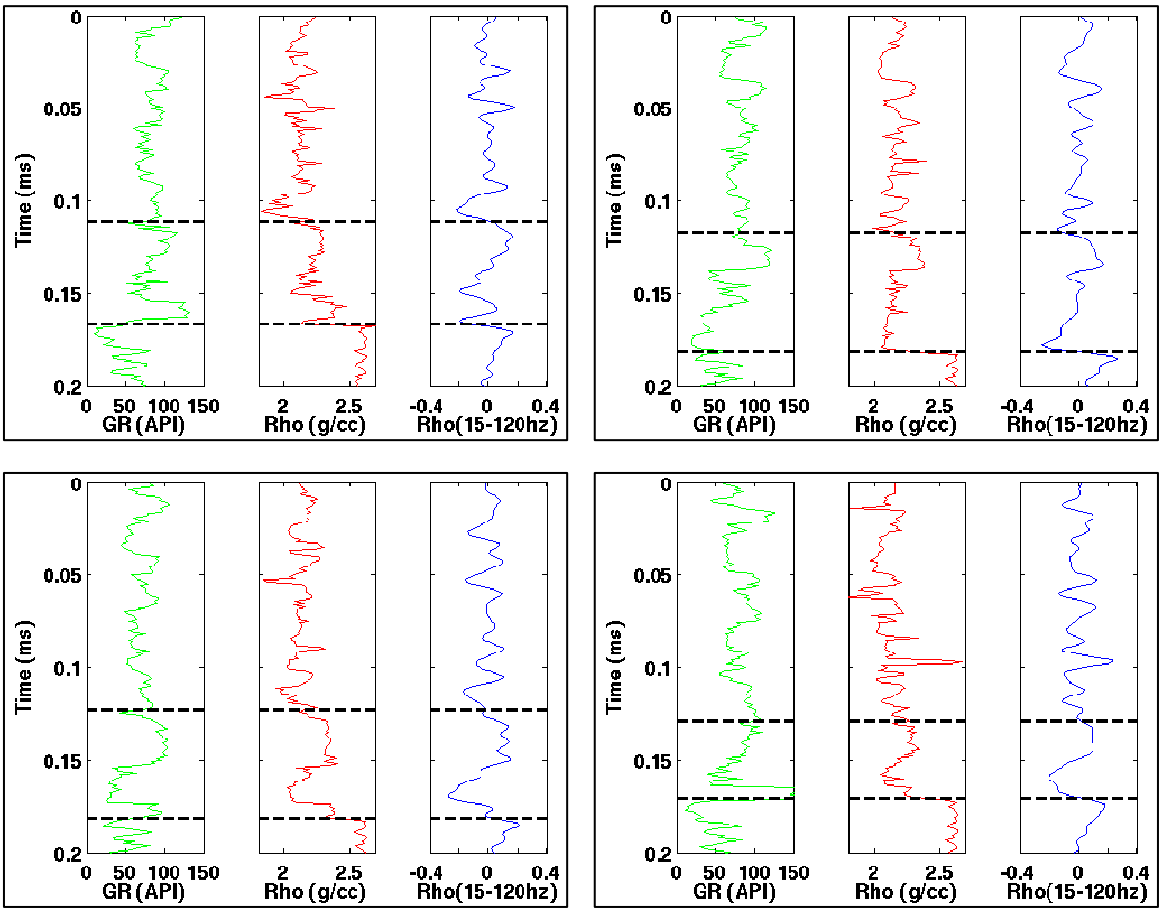

Figure 2.28 Gamma ray, density, bandpass filtered density (15-120Hz) in the time domain from four wells in Athabasca. The top and base of the McMurray Formation are marked by dashed lines.

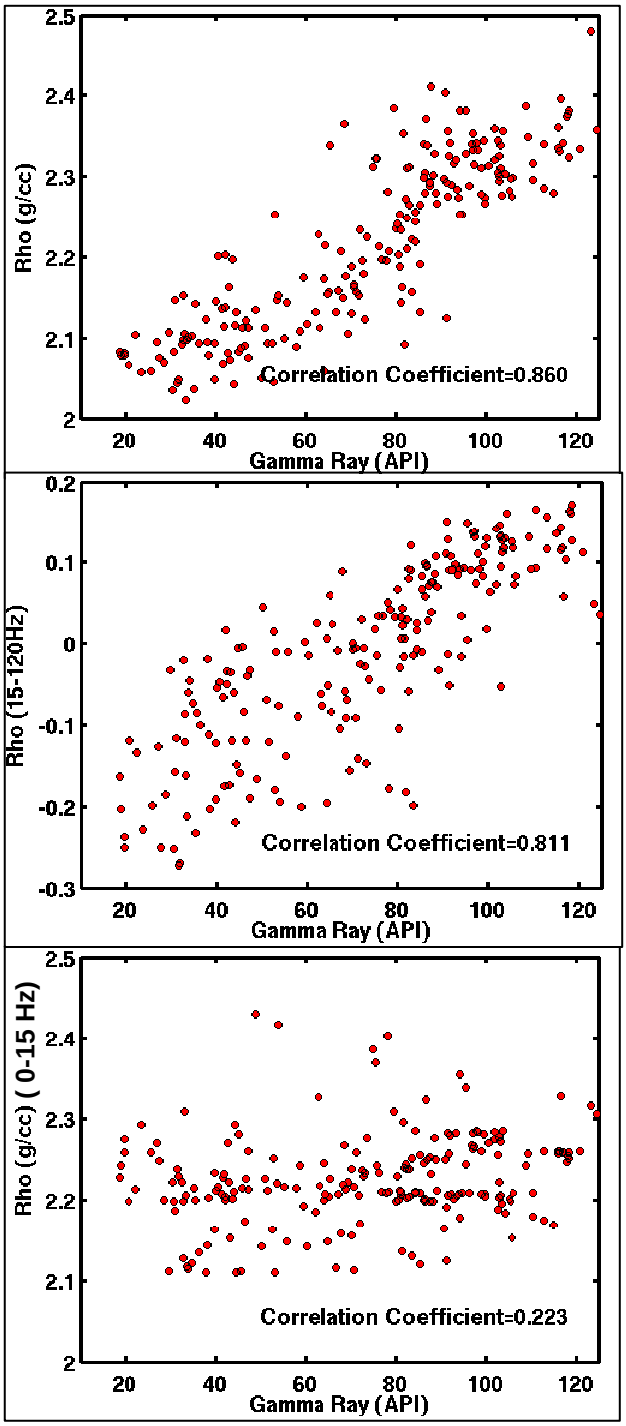

Figure 2.29 Crossplots of gamma ray and density with full bandwidth at the top, seismic bandwidth (15-120Hz) in the middle; and low frequency bandwidth (0-15Hz) at the bottom. Correlation coefficient for each panel is labelled inside the plot. The density and filtered density logs are shown in Figure 2.28. Only samples in the McMurray Formation are used in these cross-plots.

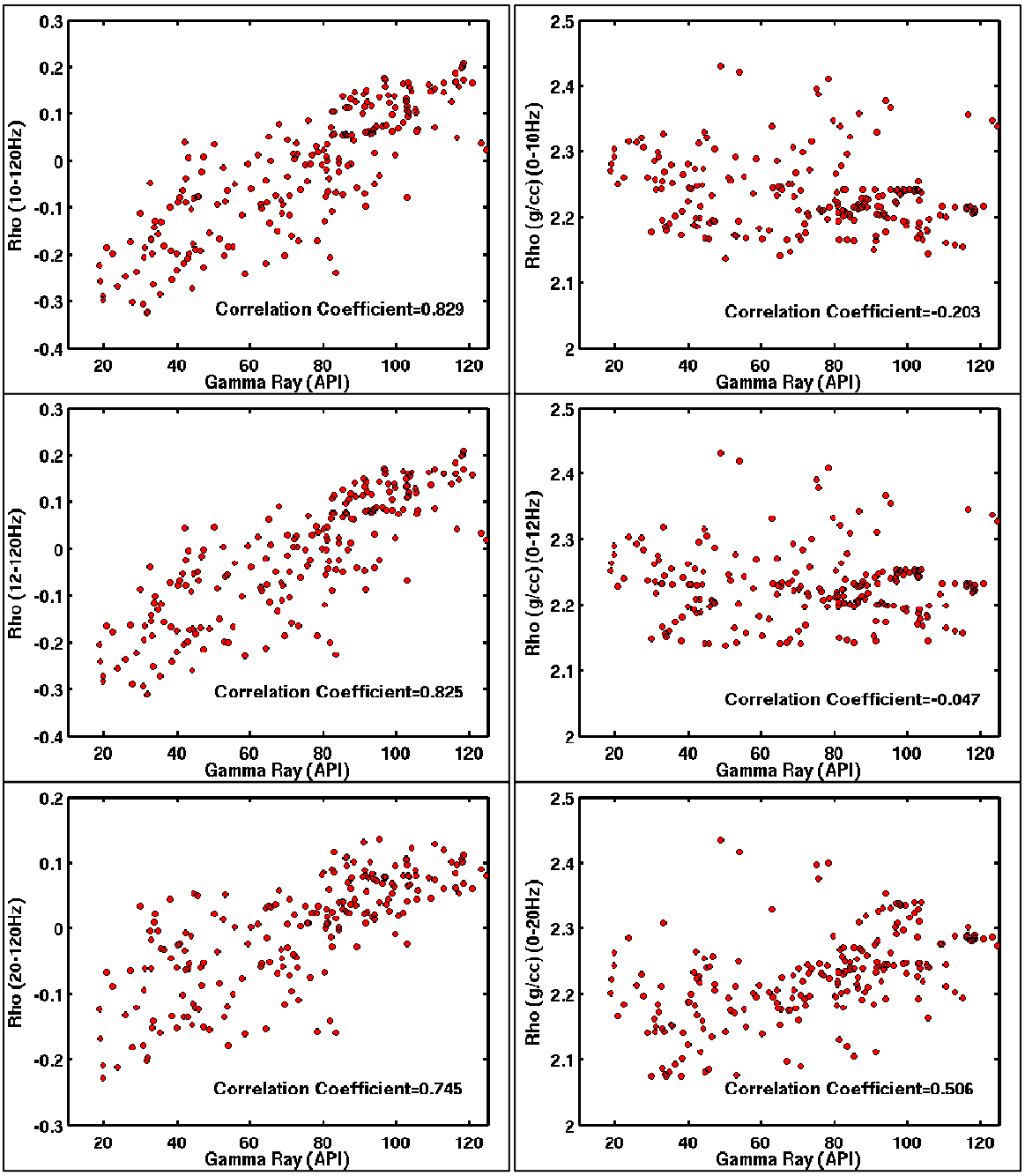

Figure 2.30 Cross plots of gamma ray and density with other frequency bandwidth: 10-120Hz and 0-10 Hz (top), 12-120Hz and 0-12 Hz (middle), and 20-120Hz and 0-20Hz (bottom). The low frequency density (0-12) shows the smallest correlation with gamma ray.

2.3 BITUMEN/WATER SEPARATION IN MCMURRAY FORMATION

The heterogeneity of bitumen distributions is another factor challenging the in-situ bitumen production using the SAGD technology. Highly water saturated sand becomes a thief zone which significantly impacts on the efficiency of steam. In addition to differentiating lithology, it is of the same significance to separate the water saturated and bitumen saturated sand. Bitumen and water saturations behave significantly different on some petrophysical log curves, such as resistivity logs, but high reservoir heterogeneity prevents reliably extrapolating reservoir properties at the borehole to areas far away. To utilize the good lateral resolution of seismic data, the feasibility of applying seismic data on the separation between the water and bitumen saturations should be evaluated using the relationship between rock physical parameters and the saturation of fluids.

For the conventional oil reservoirs, the effects of oil saturation and water saturation are usually of small difference on the seismic response, but when oil is light and with much gas dissolved, the oil saturation shows apparent differences from water saturation on the elastic properties. In the Athabasca oil sands, the crude is bitumen, very heavy oil. The density of bitumen is slightly higher than water at low temperature. According to Mochinaga et al (2006), the density of bitumen in their experiment is about 1.01 g/cc at the temperature of 20 degree Celsius. The density difference between bitumen and water at low temperature is so small that it is impossible to separate bitumen and water saturations based on the seismic response difference due to the density variation. Bitumen at a low temperature behaves like a semi-solid (like glass material – Han et al, 2008). One can assume the bitumen filling the pore has the cementation effect, which makes the rock have stronger incompressibility and rigidity. Based on the study by Kato et al (2008), the bitumen saturated rock has higher P and S velocities at a low temperature (<20 degree Celsius) than at a high temperature (> 20 degree Celsius). But it is ambiguous to link the increase in the P and S velocities with bitumen saturation because the porosity and clay content are also among factors changing P and S velocity.

A similar procedure which is used in the lithology separation study is applied to understand the relationship in the bitumen and water saturation and rock physical parameters. Comparisons between rock physical parameters for the water and bitumen saturations help to find the best rock physical parameters to separate bitumen from water in-situ saturation.

As in textbooks (Rider, 2002; Ellis and Singer, 2008), the water saturation in clean sandstone can be quantitatively estimated from resistivity logs using the Archie's equations. In this study, the water saturation is estimated based on the Archie's equations and resistivity logs following the textbooks.

2.3.1 Results from studies by others

The rock properties of heavy oils have been studied in the laboratory aiming at understanding the heavy oil and heavy oil saturated rocks to help the in-situ thermal production of heavy oils (Han et al, 2008; Mochinaga, 2006; Kato, 2008). One of the major observations is the dependency of bitumen properties on the temperature: bitumen changes from solid to quasi-solid to liquid with the increase of temperature (Han et al 2008). The bitumen bulk density slightly decreases as the temperature rises. Mochinaga et al (2006) record that bitumen density changes from 1.01 g/cc to 0.935 g/cc when the temperature rises from 20ºC to 120ºC. At a cold reservoir temperature, e.g. 20ºC, the bulk density of bitumen is 1.01g/cc, which is very close to the brine water density. The phase change of bitumen with temperature affects the P and S wave propagation in the bitumen-saturated formations. Therefore Vp, Vs, and Vp/Vs ratio are significant for the thermal production monitoring and even possibly the separation between high and low bitumen saturations. Mochinaga et al (2006) and Kato et al (2008) record the Vp/Vs ratio changes at various in-situ thermal production stages. As shown in Figure 2.31 from a study by Kato et al (2008) on the steam injection into oil sands reservoirs, the Vp/Vs ratio of an 80% bitumen saturated reservoir changes from ~2.5 to ~3.7 when the temperature increases from 10ºC to 25ºC under the pressure of 700psi; compared with the P velocity, the S velocity contributes more to the change of the Vp/Vs ratio.

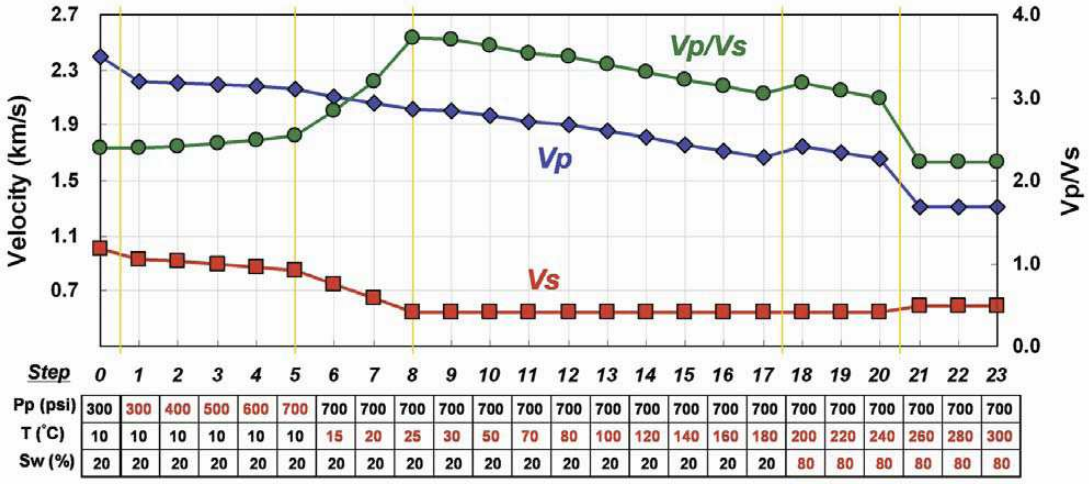

Step	0	1	2	3	4	5	6	7	8	9	10	11	12	13	14	15	16	17	18	19	20	21	22	23
Pp (psi)	300	300	400	500	600	700	700	700	700	700	700	700	700	700	700	700	700	700	700	700	700	700	700	700
T (°C)	10	10	10	10	10	10	15	20	25	30	50	70	80	100	120	140	160	180	200	220	240	260	280	300
Sw (%)	20	20	20	20	20	20	20	20	20	20	20	20	20	20	20	20	20	20	80	80	80	80	80	80

Figure 2.31 Sequential P and S velocities and Vp/Vs ratio changes induced by steam injection. Pore pressure changes occur from step 1-5, and temperature changes from step 5 to 23. Adjacent to the injector well, the movable bitumen is large replaced by hot water at step 18 and water phase changes from liquid to steam at step 21 (Source: Kato, 2008).

2.3.2 Water and bitumen separation by elastic parameters.

In Figure 2.32, a suite of logs of a heavy oil well show the Vp/Vs ratio difference between bitumen and water saturations. Two zones are picked with very close gamma ray and porosity values; the resistivity logs indicate high water saturation in the lower zone and high bitumen saturation in the upper zone. The gas effect is not apparent based on the neutron and density porosity logs. The Vp/Vs ratio is about 2.2 for the water saturated zone but it is about 1.8 for the bitumen saturated zone. The Vp/Vs ratio or Poisson's ratio can be used to separate the water and bitumen separation as shown in this figure. Since the Vp/Vs ratio should not be the only parameter showing the separation for water and bitumen, there should be other elastic parameters indicative of the water and bitumen separation, but this is not discussed further in this study.

In Figure 2.33, the density and Poisson ratio are cross-plotted against gamma ray values and samples are color-coded by the water saturation. Samples are from the McMurray Formation in Athabasca. In the cross-plot of density and gamma ray data, one cannot notice a large difference of density between the highly water saturated clean sand

samples in the dark blue and highly bitumen saturated clean sand samples in bright red. But the Poisson ratio clearly shows a difference between them. Poisson's ratio may be caused by the change of porosity in the clean sandstone, but in this example, the highly bitumen saturated and highly water saturated clean sandstones overlie together in the density-gamma ray cross-plot, indicating their porosities are close. Therefore, the difference on the Poisson's ratio that is mentioned above is possibly caused by the bitumen and water saturations. The water saturated sand samples have slightly larger Poisson's ratio than the bitumen saturated sand samples. The difference of the Poisson's ratio or Vp/Vs ratio is possibly useful in identifying highly bitumen saturated zones if the reservoir is still at a cold temperature.

Bitumen is highly viscous in the semi-liquid or liquid phase. Because of the complex viscoelastic nature of bitumen, the rock physical parameters of bitumen are affected by dispersions and temperatures. The observation on the changes of the Vp/Vs ratio due to the fluid type change is based on the wireline logs from the chosen area only. The physical mechanism of this difference should be studied further using more data from other regions in the Athabasca oil sands.

2.3.3 Seismically separate bitumen and water

The above discussion is based on the well logs and lab measurements, suggesting that it is possible to separate between the water and bitumen if the Vp/Vs or Poisson's ratio and porosity can be obtained reliably. We notice an apparent difference on the Vp/Vs or Poisson's ratio between the water and bitumen saturated rocks. The difference is larger if the reservoir temperature is below the bitumen liquid point (Han et al, 2008) -- low-pressure cold bitumen tends to have a low Vp/Vs ratio in the rock. However, most of these measurements of velocities are made using the ultra-sonic or high frequency sonic waves. Since applying seismic method is the focus of this thesis, the observations from the lab and well log data regarding the Vp/Vs ratio for the heavy oil and water separation need to be validated for the measurements by using the seismic wave frequency. A study by Han et al (2008) certainly shows that the sensitivity of state change of bitumen on the

elastic parameters (the Vp/Vs ratio) is lower when the frequency of wave is as low as the seismic wave frequencies. Figure 2.34 which was plotted by Han et al (2008) shows that the liquid point temperature for the 6 API bitumen is 25ºC and for the 9 API bitumen is 20ºC when the frequency is 100Hz, and the liquid point temperature is even lower when the frequency is lower. When the temperature is above the liquid point, bitumen behaves more like water and the separation between them is difficult. It indicates that the ability of the Vp/Vs ratio to separate bitumen and water saturations by using seismic data may not be as strong as seen in the examples in which the lab or well log data are used. The seismic wave attenuation caused by the high viscosity of bitumen possibly helps identify highly bitumen-saturated zones (Lines et al 2008; Vasheghani et al 2010).

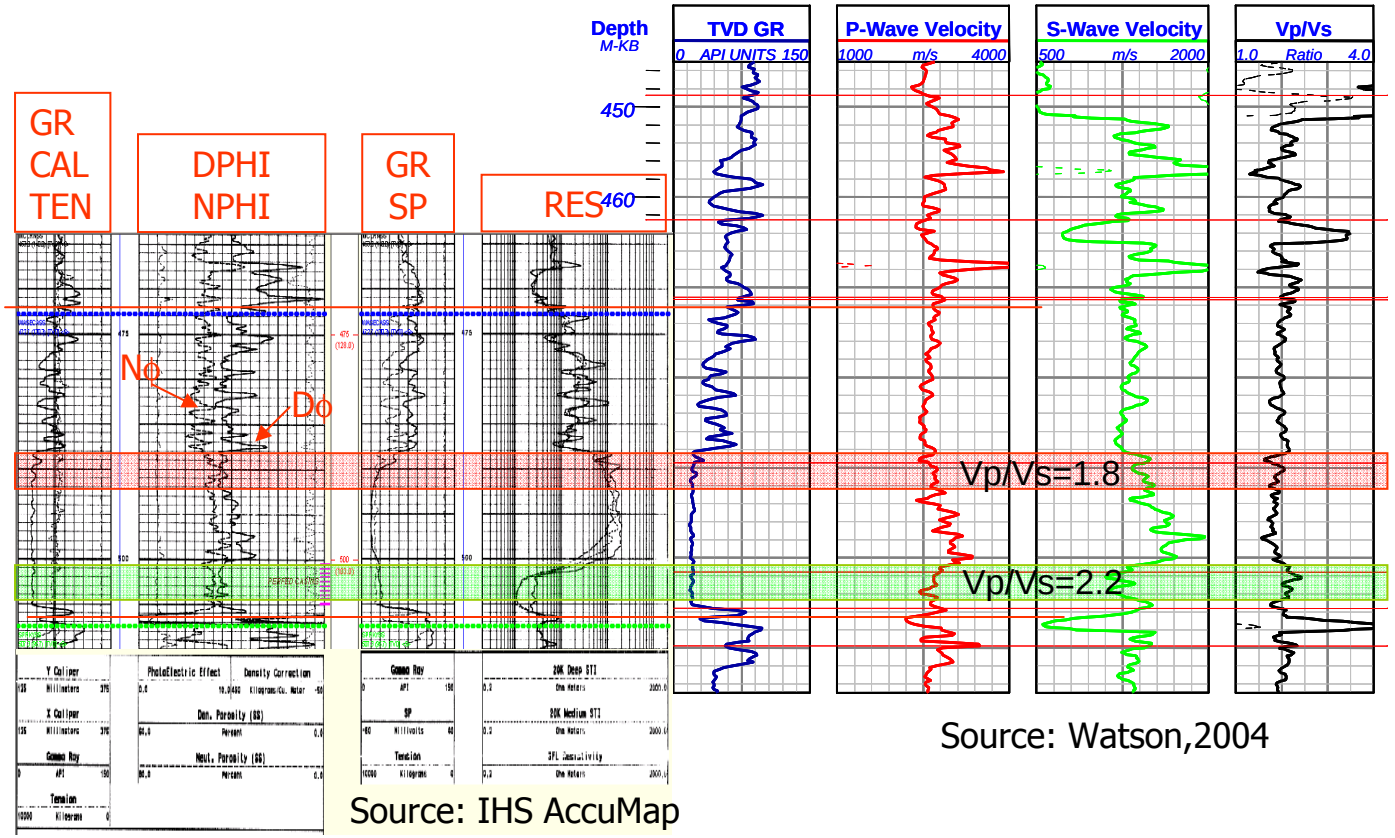

Figure 2.32 A well from a conventional heavy oil production region in the WCSB: the porosity of wet (shaded in green) and oil (shaded in red) zones are very close and it is about 33%, based on density porosity curves. Both zones are clean sands. Both Vp and Vs of wet sands are lower than those of oil sands, but Vp/Vs ratio is higher in wet sands.

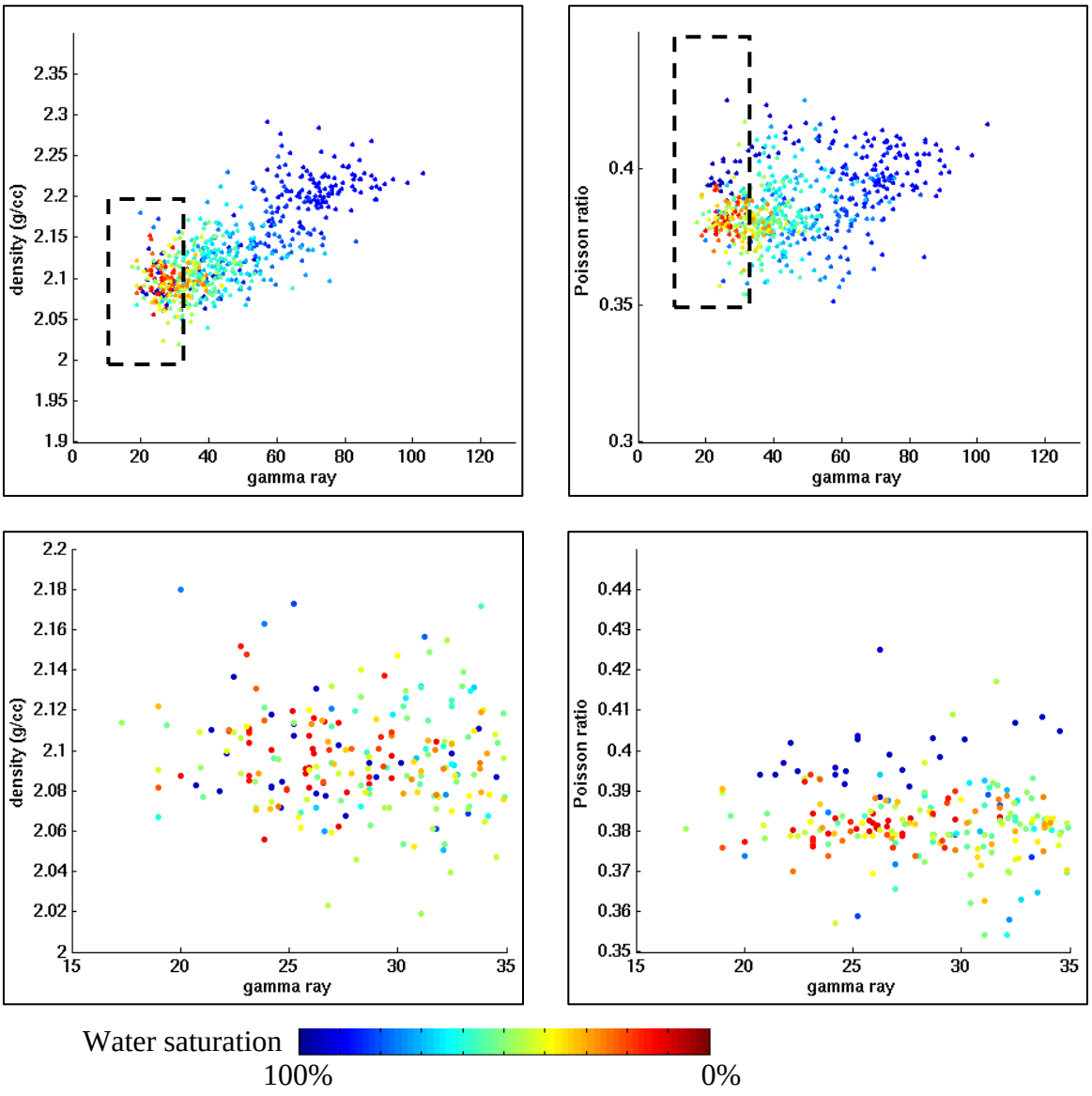

Figure 2.33 Cross-plots of density with gamma ray (left panels) and Poisson's ratio with gamma ray (right panels). The bottom panels are the enlarged portions highlighted by the dash-lined boxes on the top panels. Samples are color-coded by water saturation.

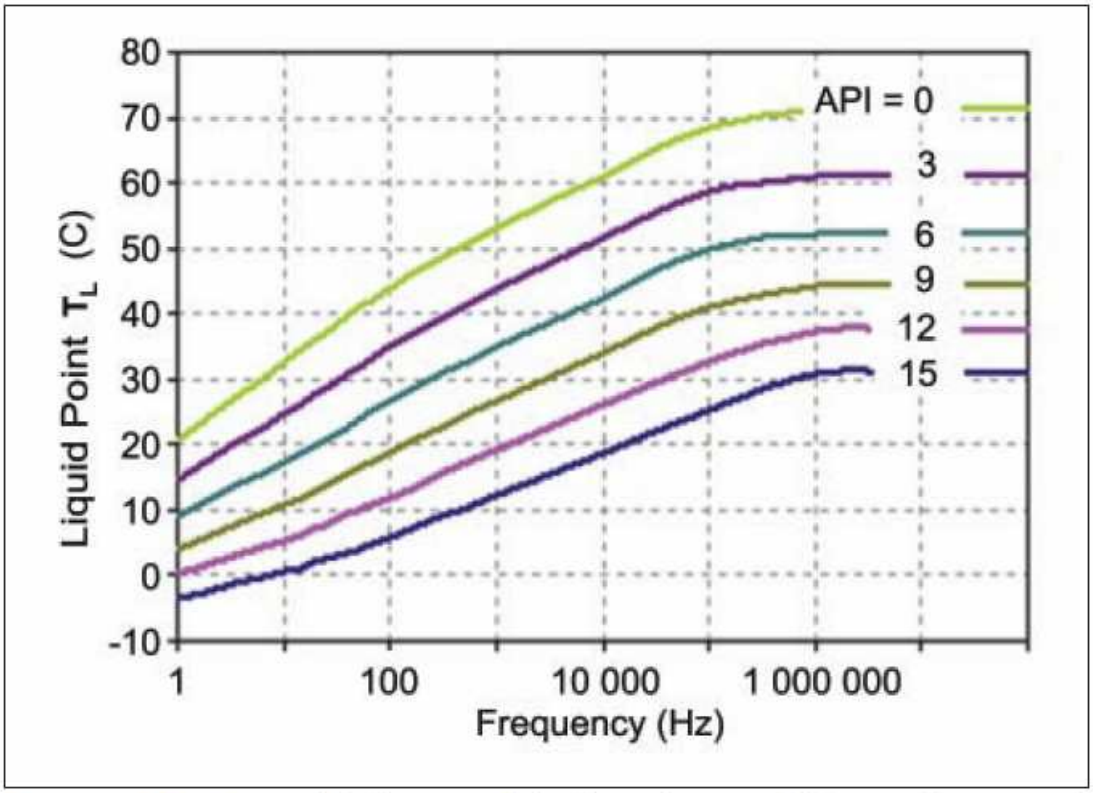

Figure 2.34 Expected behaviour of the liquid point (TL) as a function of the density of the oil (API) and the measurement frequency (Source: Han et al, 2008).

2.4. FACIES PROBABILITIES

The study of rock properties and reservoir properties helps to define the probability of facies and fluids. The probability distributions of facies and fluids, usually in the form of probability density functions (PDFs) are critical for the lithology and fluid classification in the integration of multi-types of information, including rock properties, reservoir properties, seismic data, inversion, and geostatistics, and all kinds of uncertainties related to the used attributes.

Some facies data from core analyses in the Athabasca oil sands are available for understanding the relationships between rock physical parameters and facies. There are 2300 well log samples within core intervals and they are classified into 10 facies. Histograms for each facies against gamma ray values are drawn in Figure 2.35. There are much more samples falling within the facies of trough cross-bedded sand, sandy point

bar, and abandoned channel facies. The statistical analysis of these three facies along with shale volumes (based on gamma ray values) should be reliable but it is difficult to be statistically meaningful for other facies because of the limited sample population for these facies. To make statistical estimates, the log samples are re-grouped into three classes, sand (trough cross-bedded sand, sand with mud-clasts, and sandy point bar), shale (muddy point bar, abandoned channel, and lake mudstone), and shoreface (shoreline sand with mud, shoreline mud with sand, and marine mudstone). Statistical means and deviations for these three classes and the Wabiskaw Member are calculated for the gamma ray values and eight rock physical parameters (Table 2.7). The statistical characters of the distributions are graphically shown in Figure 2.36. Table 2.8 lists the correlation coefficients between the rock physical parameters and gamma ray values, including and excluding shoreface. Table 2.8 also shows that the density, Ip, Vp/Vs ratio, and lambda*rho are correlated well with the shale volume, with correlation coefficients of larger than 0.5. Table 2.9 shows the correlation coefficients between the velocity and density and the impedance and density for the McMurray Formation: the correlation coefficients between the Vp and Vs and between the Ip and Is are 0.4~0.5, which are not strong correlations. The Vp-density and Is-density pairs are nearly uncorrelated, and Vs and density have a negative correlation coefficient. But Ip and density are correlated well, which suggests Ip is able to indicate lithology reasonably for this region.

2.5.1. Quadratic discriminant analysis

In the AVO analysis, cross-plotting of a pair of elastic parameters, such as lambda*rho and mu*rho, is commonly used to separate and classify the fluids types and lithofacies. This practice is discriminant analysis in mathematics. A quantitative evaluation is done in this section on the ability of multi-parameters (pairs visualized in the crossplots) to separate sand from shale in the oil sands by using the cored log samples. The multi-variate Gaussian distribution is assumed for the sand and shale clusters in each cross-plot. The multi-variate Gaussian probability distribution is defined as

$$\mathbf{p} = (2\pi)^{-\mathbf{k}/2}\left|\Sigma\right|^{-1/2}\exp\left(-\frac{1}{2}(\mathbf{x}-\mu)^{\mathbf{T}}\Sigma^{-1}(\mathbf{x}-\mu)\right), \tag{2.9}$$

where **x** is the vector of multi elastic parameters for individual samples, and μ is the vector of mean values of elastic parameters for, and Σ is the covariance matrix. Avseth (2000) uses the minimum of the Mahalanobis distance to perform the quadratic discriminant analysis (QDA). The Mahalanobis distance is defined as $(\mathbf{x}-\mu)^{\mathbf{T}}\Sigma^{-1}(\mathbf{x}-\mu)$, which is the exponent in the multi-variate normal distribution definition – equation (2.9). Since the covariance determinant term i.e. $|\Sigma|^{-1/2}$ is still the lithofacies related, it is reasonable to include it for classifying lithofacies. Here the likelihood ratio (Wikipedia) between sand and shale is used to define the ability of parameters to separate sand and shale:

$$\frac{|\Sigma_{\mathbf{Sand}}|^{-1/2}\exp\left(-\frac{1}{2}(\mathbf{x}-\mu_{\mathbf{Sand}})^{\mathbf{T}}\Sigma_{\mathbf{Sand}}{}^{-1}(\mathbf{x}-\mu_{\mathbf{Sand}})\right)}{|\Sigma_{\mathbf{Shale}}|^{-1/2}\exp\left(-\frac{1}{2}(\mathbf{x}-\mu_{\mathbf{Shale}})^{\mathbf{T}}\Sigma_{\mathbf{Shale}}{}^{-1}(\mathbf{x}-\mu_{\mathbf{Shale}})\right)} \tag{2.10}$$

where Σ_{sand} and Σ_{shale} are the covariance matrices of two (or more than two) elastic parameters for the classes of sand and shale based on the measurements of sand and shale samples.

According to the work by Avseth (2000), the quadratic discriminant analysis (QDA) is very close to neural networks in identifying and classifying lithofacies, though the latter is slightly better but requires much more computational effort. If a normal distribution is not good at describing the lithofacies, neural networks should be the better choice for classifications.

The ability of pair parameters to separate sand from shale is quantified using the samples in Figure 2.35 and Figure 2.36 based on the likelihood ratio equation (2.10). The ratio of the likelihood of sand projected onto the sand probability distribution to the likelihood of sand projected onto the shale probability distribution is used to quantify the ability of separation: a large ratio indicates a good separation. Five pairs of elastic parameters are listed in Table 2.10, although other pairs of parameters can be evaluated if necessary. The cross-plots of four pairs of parameters, Vp-Vs, Ip-Is, λρ–μρ, and ρ–Vp/Vs, are in Figure

2.36. As seen in Table 2.10, the density and the Vp/Vs ratio are certainly the best pair of parameters to separate sand and shale. Other three pairs of parameters (Ip-Is, $\lambda\rho-\mu\rho$, and Ip-Vp/Vs) have the similar ability to separate sand from shale. The Vp and Vs pair seems not as good as other pairs. These observations are limited to the data used in this analysis so far. They may be slightly different if the analysis is applied on the data from other areas.

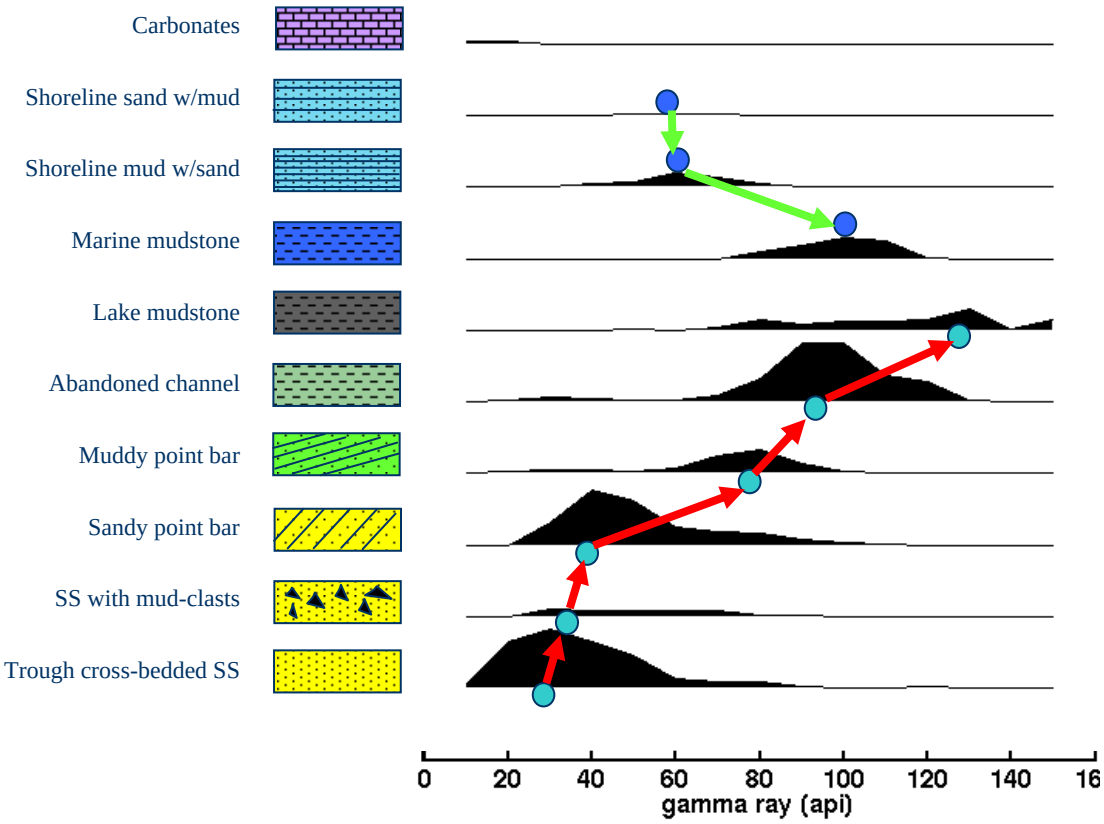

Figure 2.35 Relationship between lithofacies and gamma ray based on core data. In this study, there are 2300 log samples with facies data from core analysis. The samples are classified into 10 facies labelled and represented by rectangles with various filling colors and patterns on the left. On the right side of each facies, there is a chart (filled by black color) showing the distribution of samples along the gamma ray. All distribution charts use the same vertical scale. The dots indicate the gamma ray value for the peak sample count for each facies. Arrows indicate the change from the sandy to the shaley. This figure shows that facies generally correlate with lithology (gamma ray), but the spreading of samples along gamma ray indicates that the facies and lithology are not equal. The uncertainty also comes from the resolution and subjective reason in core analysis and well logging.

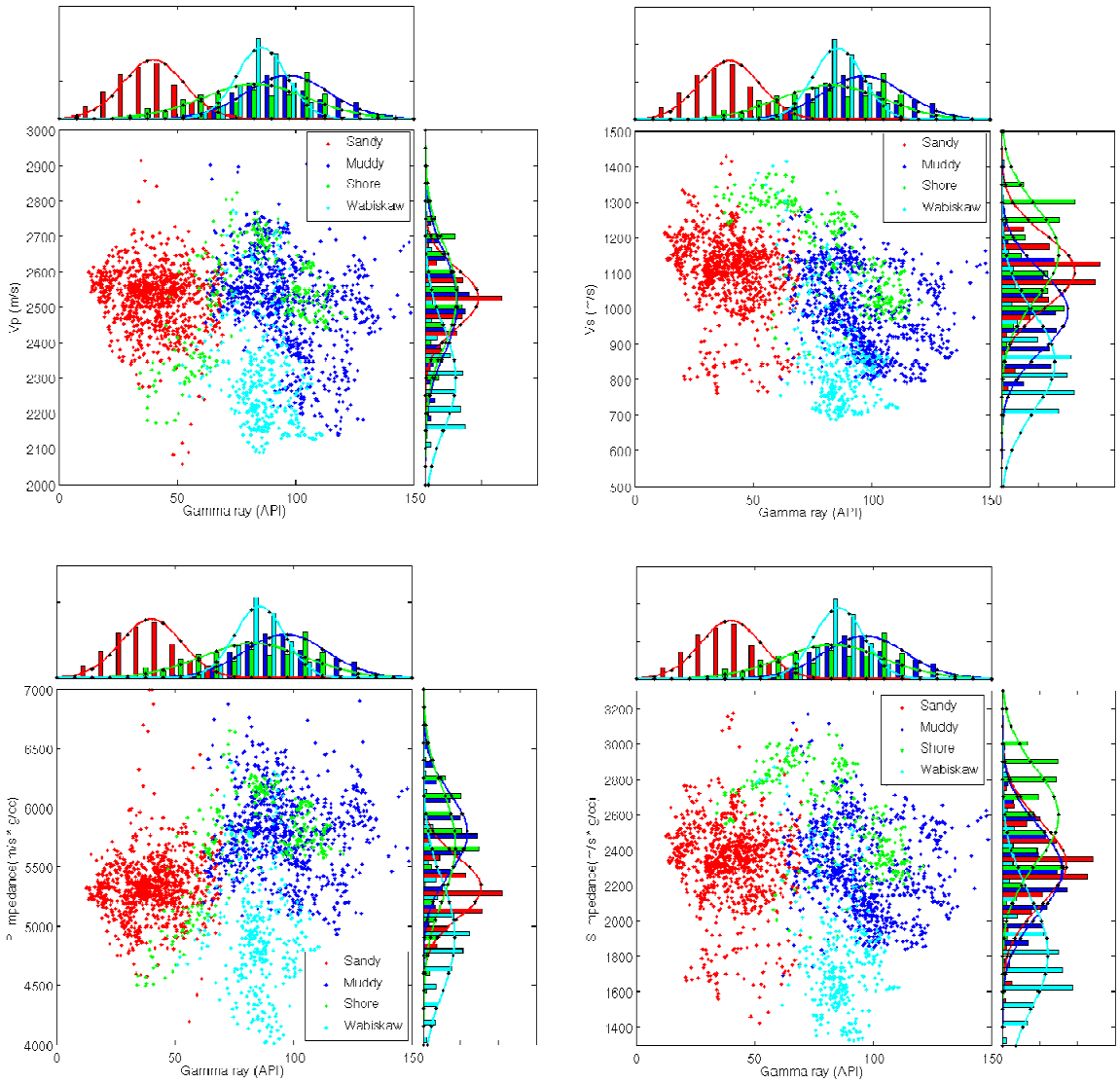

Figure 2.36 Cross plots of between elastic parameters and gamma ray showing separation and distribution of each facies along the parameters. On the top and on the right side of each cross plot are the distributions of samples over horizontal and vertical axes using barcharts: the colors of the bars are corresponding to the same colors used by the samples in the cross plot, and the length of bars is proportional to the number of samples falling within the corresponding interval of elastic parameter or gamma ray. The colored bell-shaped curves on the top or on the right side fits a normal distribution for each facies and are used to indicate the separation between facies and validity of normal distribution *(continued on next page)***.**

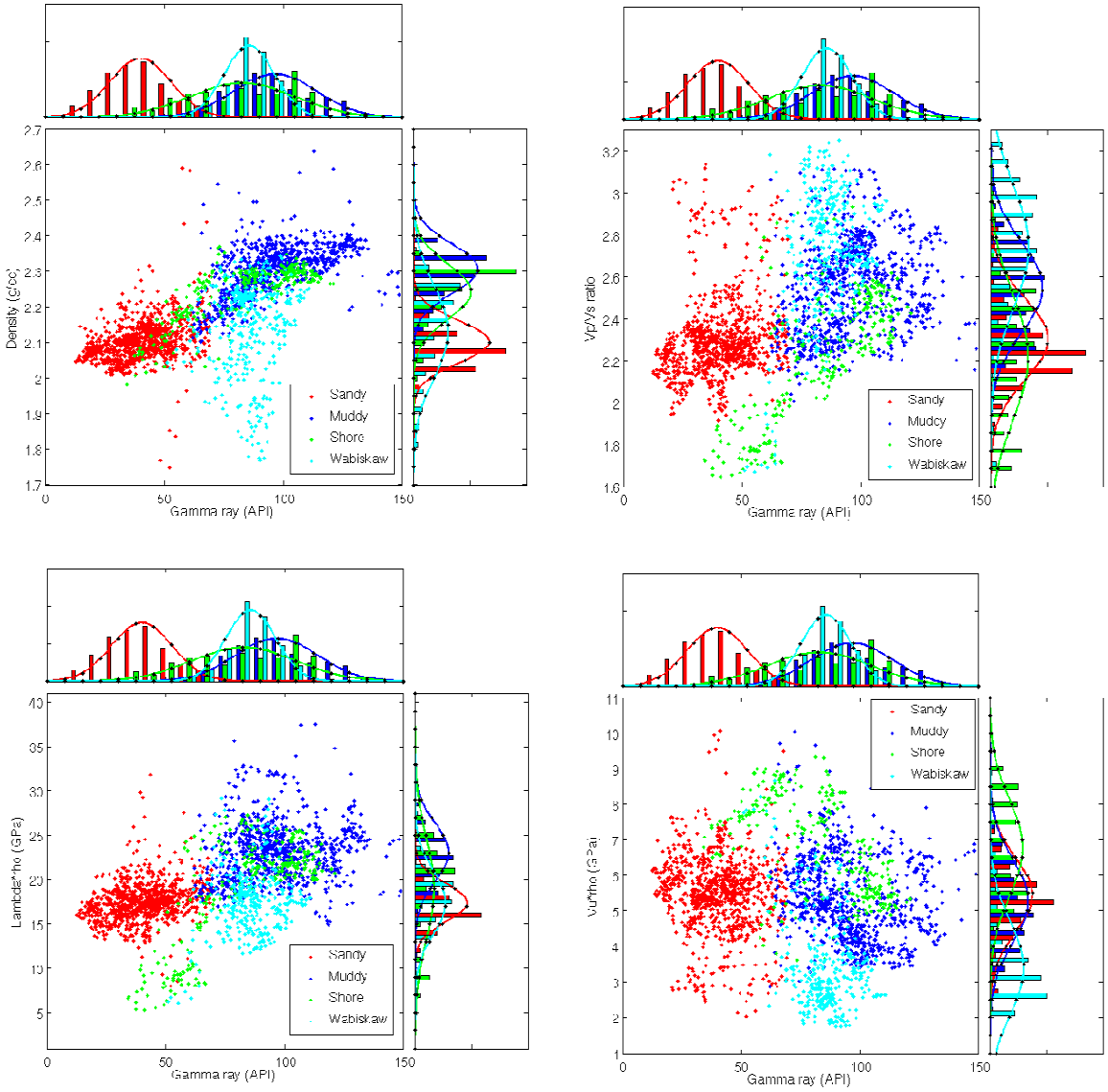

Figure 2.36 *(continued from previous page)* **Cross plots of between elastic parameters and gamma ray showing separation and distribution of each facies along the parameters.** *(continued on next page)***.**

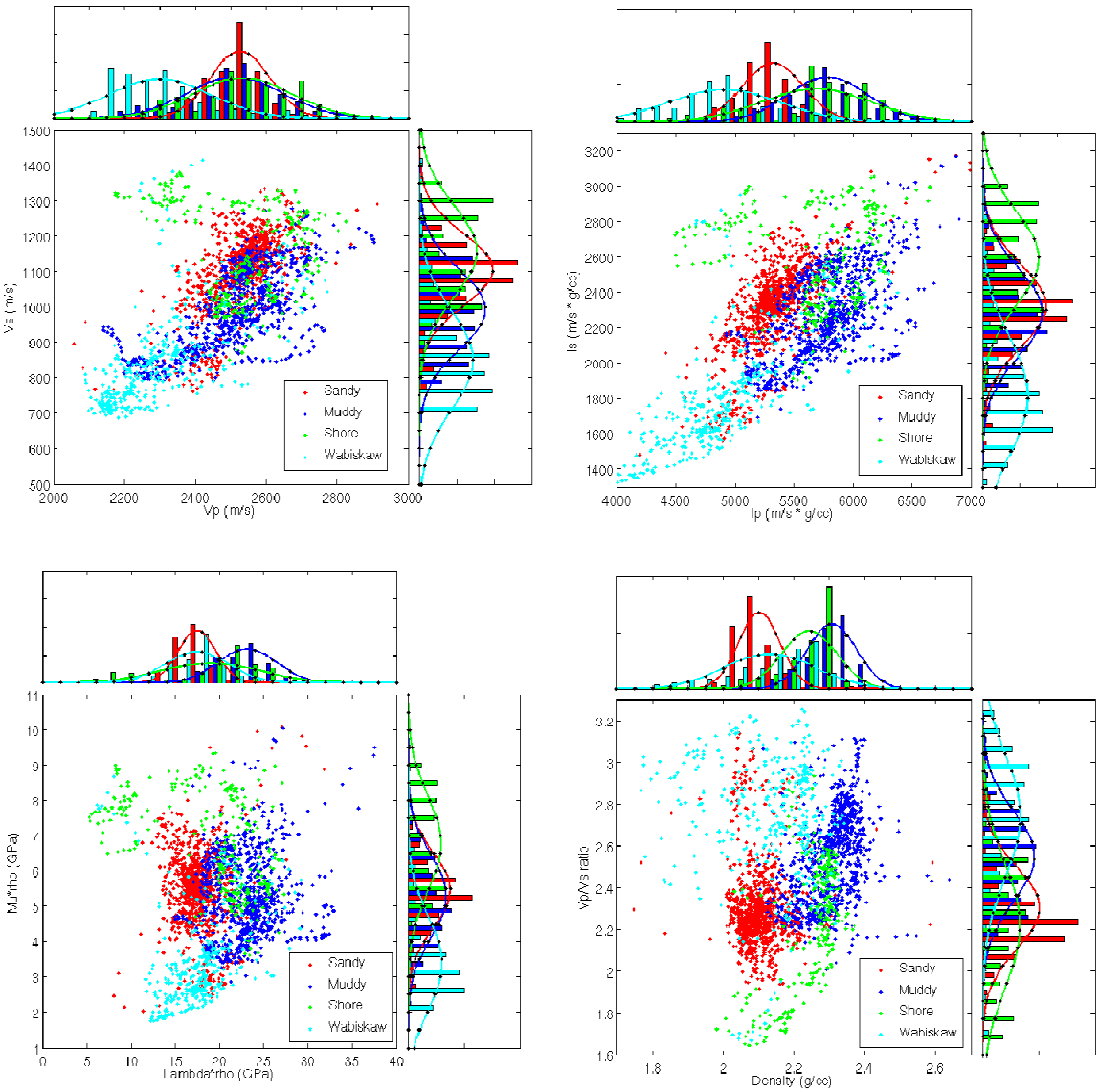

Figure 2.36 *(continued from previous page)* **Cross plots of between elastic parameters and gamma ray showing separation and distribution of each facies along the parameters.**

Table 2.7 Mean values and standard deviations of elastic parameters and gamma ray for the McMurray and Wabiskaw Formations.

	Sand		Shale		Shore		Wabiskaw	
	Mean	Deviation	Mean	Deviation	Mean	Deviation	Mean	Deviation
GR (API)	39.98	12.83	96.68	17.38	82.94	22.02	85.82	10.52
ρ (g/cc)	2.102	0.0591	2.307	0.0693	2.243	0.0777	2.132	0.129
Vp (m/s)	2526	84	2511	137	2533	140	2299	144
Vs (m/s)	1106	102	993	113	1158	130	851	139
Vp/Vs	2.304	0.195	2.552	0.216	2.219	0.298	2.746	0.295
Ip (m/s*g/cc)	5322	256	5785	339	5689	457	4911	467
Is (m/s*g/cc)	2325	234	2288	248	2592	264	1816	327
λρ(GPa*g/cc)	17.43	2.136	23.11	3.31	18.99	5.801	17.47	3.634
μρ(GPa*g/cc)	5.461	1.053	5.294	1.164	6.790	1.355	3.405	1.317

Table 2.8 Correlation coefficients of elastic parameters against gamma ray for the McMurray Formation.

	ρ	Vp	Vs	Ip	Is	Vp/Vs	λρ	μρ
McMurray(all facies)	0.86186	-0.11079	-0.46865	0.54596	-0.1006	0.48069	0.64446	-0.096936
McMurray(no Shore facies)	0.86463	-0.18567	-0.53278	0.5371	-0.14348	0.54255	0.6871	-0.14023

Table 2.9 Correlation coefficients between velocity and density (left) and between impedance and density (right) for the McMurray Formation.

	Vs	Rho
Vp	0.4718	0.0559
Vs		-0.3712

	Is	Rho
Ip	0.4085	0.7533
Is		0.0666

Table 2.10 Quantifying ability of pair parameters to separate sand from shale

Parameter pair	Vp - Vs	Ip - Is	$\lambda\rho - \mu\rho$	Ip – Vp/Vs	ρ – Vp/Vs
Ratio of likelihood	7.99	29.5	26.1	26.4	2390223

2.5 AVO FEASIBILITY

The rock property study shows the feasibility of applying seismic data (pre-stack and post-stack) in the lithology separation:

1. Density is one of the best lithology sensitive seismically derivable parameters; however, density is commonly considered as less reliable due to the ill-posed nature of the AVO inversion. The density extraction from seismic data requires large incident angles and good quality data.
2. The rock property study shows that besides density, other parameters such as lambda*rho and P impedance have reasonably good sensitivity to lithology although their sensitivity may vary with reservoirs and geological settings.
3. Correlation coefficients of the ratios (Vp/Vs ratio, Poisson's ratio and lambda/mu ratio) and lithology are about 0.50, showing the average sensitivity in the lithology indication.
4. Density can be used to predict the lithology if it is able to be extracted from seismic data with a reasonable reliability. If not, an integration of a number of parameters is necessary to balance the sensitivity and uncertainty.

Here a simple modeling is made to show the AVO response at a sand and shale interface. The velocity and density for the sand and shale are provided by the mean values in Table 2.7 for the McMurray Formation. The contributions of Vp, Vs, Ip, Is, and density to the AVO response are calculated using the following two equations, which are three-term linear AVO equations.

$$\mathbf{r}(\theta) = \frac{1}{2}[1 - 4\frac{\overline{\mathbf{Vs}}^2}{\overline{\mathbf{Vp}}^2}\sin^2\theta]\frac{\Delta\rho}{\bar{\rho}} + \frac{1}{2}\frac{1}{\cos^2\theta}\frac{\Delta\mathbf{Vp}}{\overline{\mathbf{Vp}}} - 4\frac{\overline{\mathbf{Vs}}^2}{\overline{\mathbf{Vp}}^2}\sin^2\theta\frac{\Delta\mathbf{Vs}}{\overline{\mathbf{Vs}}} \quad (2.11)$$

$$\mathbf{r}(\theta) = \frac{1}{2}[4\frac{\overline{\mathbf{Vs}}^2}{\overline{\mathbf{Vp}}^2}\sin^2\theta - \tan^2\theta]\frac{\Delta\rho}{\bar{\rho}} + \frac{1}{2}\frac{1}{\cos^2\theta}\frac{\Delta\mathbf{Ip}}{\bar{\mathbf{Ip}}} - 4\frac{\overline{\mathbf{Vs}}^2}{\overline{\mathbf{Vp}}^2}\sin^2\theta\frac{\Delta\mathbf{Is}}{\bar{\mathbf{Is}}} \quad (2.12)$$

where $\mathbf{r}(\theta)$ is the angle dependent reflectivity, $\overline{\mathbf{Vp}}$, $\bar{\mathbf{Ip}}$, $\overline{\mathbf{Vs}}$, $\bar{\mathbf{Is}}$ and $\bar{\rho}$ respectively are the average P-wave velocity, P impedance, S-wave velocity, S impedance, and density across the interface, $\Delta\mathbf{Vp}$, $\Delta\mathbf{Ip}$, $\Delta\mathbf{Vs}$, $\Delta\mathbf{Is}$, and $\Delta\rho$ are the changes in P-wave velocity, P impedance, S-wave velocity, S impedance, and density, and θ is the average angle of incidence and transmission. The reflectivities with angle using the above two equations are shown in Figure 2.37. The contributions of each term in the equations are plotted within the figure. The reflectivity is for the interface of shale overlying sand. Overall, $\mathbf{r}(\theta)$ increases with angle. The effect of density term changes rapidly when the angle is larger than 30 degree.

Here is a comment on the indication of the correlation between elastic parameters on the AVO inversion. The correlations between Vp, Vs, and density and Ip, Is, and density have been shown in Table 2.10 in the previous section; and it is noted that in the studied region the correlations between each other are not strong except Ip and density. The poor correlation between the parameters is of importance for the application of the Bayesian constraint in the AVO inversion. As shown in Chapter 3 in more detail, the correlation coefficients are essential part of the covariance matrix of the model parameters to be obtained by the inversion. In the Bayesian constraint inversion, the correlation coefficients between parameters play an important role in controlling the relationships between parameters in the solution. The analysis in this section shows the correlation between velocity, density, and impedance is not strong; this indicates the AVO inversion can be stabilized by the correlation but without a high fidelity in the solution.

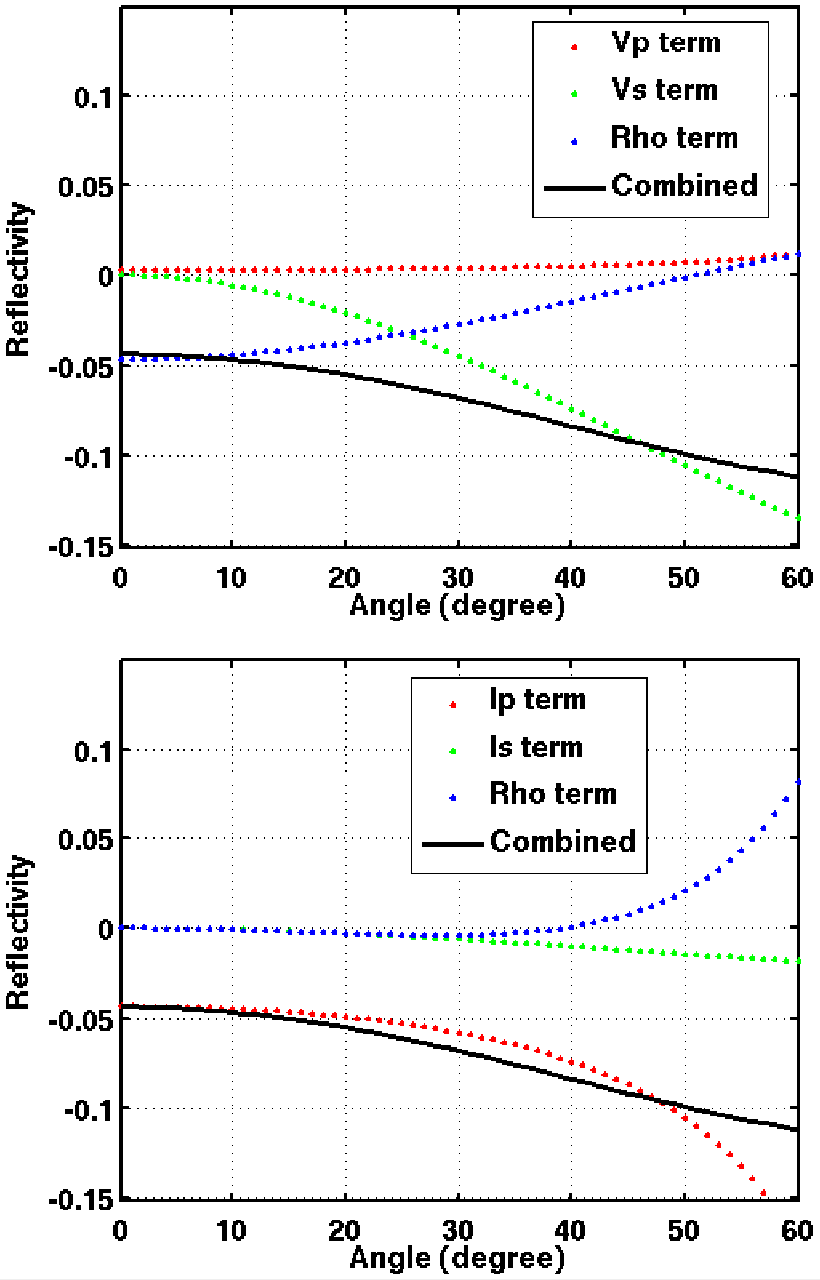

Figure 2.37 Reflectivity with angles at an interface of shale overlying sand in the McMurray Formation. Top panel uses the 3-term AVO equation expressed by velocity and density; bottom panel uses the equation expressed by impedance and density.

2.6 CONCLUSIONS

The majority of Chapter 2 is dedicated to the rock property study on the lithology separation of oil sands reservoirs. Qualitative and quantitative analyses have been done on the sensitivity of the seismically derivable elastic parameters to the lithology. The AVO feasibility for the prediction of lithology heterogeneity and the water and bitumen separation are discussed. The analysis is mainly based on wireline logs and available core data. The conclusions can be drawn in the following.

1. Density is one of the best of 12 parameters to indicate lithology for the McMurray Formation; in addition, density shows a strong correlation with lithology in the Grand Rapids Formation in Athabasca and the Bluesky Formation in Peace River.
2. Lambda*rho is reasonably sensitive to the lithology in all four regions where the shear sonic logs are available to calculate Lame's parameters.
3. Other parameters, such as Ip, lambda, and Vs, are able to indicate lithology but with uncertainties. For instance, the P impedance shows a good sensitivity in the McMurray Formation in Christina Lake and the Bluesky Formation in Peace River. In these regions, Vp is poorly correlated with the lithology, but Ip, the product of Vp and density, is correlated with lithology better because of density. However, their sensitivity to lithology changes from region to region.
4. In the Grand Rapids Formation, many parameters, besides density and lambda*rho, are correlated well with lithology. This conclusion should be tentative and more studies are needed by using more well data, because only one well from this region is used.
5. The Vp/Vs ratio, Poisson's ratio, and lambda/mu ratio should have the same ability to separate lithology in the oil sands area. They show correlation coefficients of about 0.5 in two regions in Athabasca. The ratio for sand is generally lower than for shale.
6. A quadratic discriminant analysis quantitatively defines the separation of sand and shale by using a pair of elastic parameters. Density and Vp/Vs are one of the best pairs of parameters to separate sand from shale.

7. Density is little affected by the burial depth. Density varies between 2.00 g/cc and 2.5 g/cc from the clean sand to the shale. Other elastic parameters are influenced by the compaction: Velocities are lower in the shallow burial depth for the same lithology and the velocities change with depth follows different trends for sand and shale. Sand and shale are slightly separable for the shallow reservoir on Vp but the separation is not distinguishable for the deep reservoirs. Vs is slightly better than Vp to separate sand and shale for the deep reservoirs.
8. Because of the variation of velocity with depth, other parameters, such as impedance and Lame's parameters, show variations with depth and sensitivity variations to lithology with depth.
9. Ratio parameters vary with depth, but their sensitivity to lithology is not affected by the depth.
10. Most of the study in rock properties uses physical measurements from lab or well logging which are absolute values, while the seismic data are positive-negative values due to missing low frequencies. Therefore, any promising ability of physical parameters to identify facies/fluids is compromised when these parameters are derived from seismic data. The background trend (low frequency) added into the seismic inversion dominates the centers of facies clusters in any cross-plots of seismically derived attributes, such as lambda*rho and mu*rho, which are combined to detect gas saturation effectively (Goodway et al, 1997). If the sand background trend is assigned to a shale formation (this happens often), the shale would be classified as sand when we use the rock property cross-plot templates or knowledge based methods. It is very necessary to study the bandlimited physical parameters for the facies/fluids classification. That is one reason why some AVO users mainly stick to the intercept-gradient crossplots and interpretation templates based on them. The bandlimited rock physical parameters are studied, showing the feasibility of using the bandlimited parameters to predict lithologies.
11. Water and bitumen (cold) show some differences on some seismically derivable parameters (such as the Vp/Vs ratio, Poisson's ratio). But the separation of water

and bitumen saturation in the reservoirs by using seismic data is difficult if not impossible.

The study provides the physical basis for the deterministic and conventional interpretation of reservoir heterogeneity of the Athabasca oil sands, and evaluates the rock physical parameters sensitive to the lithology and fluid variation. But due to the complicated nature of reservoir, such as the combination of shale volume and porosity changing, the uncertainty exists in using a limited number of parameters to describe reservoir heterogeneity. More statistical methods or ANN (Hampson et al, 2001) should be applied to adopt more variables in the analysis. In the statistical analysis of the reservoir characterization, the sensitivity study conducted in this thesis provides the physical basis and the deterministic and conventional interpretation provides the initial solution and control of quality for the statistical prediction of reservoir properties.

CHAPTER 3: APPLICATION OF AVO IN HEAVY OILS RESERVOIR CHARACTERIZATION

3.1 INTRODUCTION

Detection of hydrocarbon reservoirs is the most important application of AVO. Increasing AVO is typically pronounced in gas-bearing sediments; and also in some oil-bearing sediments, for example, turbidite sands such as the Late Tertiary deltaic sediments in the Gulf of Mexico (especially during the 1980s-1990s, see Allen & Peddy, 1993), West Africa, and other major deltas around the world. Most major companies use AVO routinely to reduce risks in exploration and to better define the extent and composition of existing hydrocarbon reservoirs.

With the advance of the AVO theory, methods, and practices, the AVO analysis is not limited to indications of hydrocarbon for gas reservoirs but also applied to identify lithologies and to measure hydrocarbon saturation: published examples from the Gulf Coast and Africa (Kelly and Skidmore, 2001; Van Koughnet, 2003) show that the bulk density attributes extracted from AVO can be practically used to differentiate the economic gas reservoirs from non-economic ones. Tonn (2002, 2010), Bellman (2008), Roy et al (2008), and Xu and Chopra (2008) use seismic attributes extracted from AVO to predict reservoir lithology heterogeneity in the heavy oil fields in the West Canada Sedimentary Basin (WCSB). Behura et al (2010) separate the fully and partially gas saturated reservoirs by applying a non-linear AVO inversion. These applications indicate the potentials of AVO applications other than being ‘bright spot’ direct hydrocarbon indicators. With the advance of seismic data acquisition and processing and the better understanding of rock properties of reservoirs, more useful parameters, including bulk density, can be obtained from AVO with more reliability. Discussions made in Chapter 2 on the reservoir heterogeneity of heavy oils in the WCSB show the feasibility of seismic methods to predict this heterogeneity with the help of a rock property study on

seismically derivable elastic parameters sensitive to lithology. If the seismic data quality is good enough, it is possible to predict the reservoir heterogeneity of oil sands from the seismic data reliably.

In the Athabasca oil sands, the distribution of bitumen varies due to a high degree of facies heterogeneity throughout the deposit. This strong lithological heterogeneity makes interpreting geology and estimating the bitumen distribution difficult based on the well controls and geological study only. The surface seismic data plays an important role in characterizing the subsurface heterogeneity because the seismic data provides a lateral and vertical coverage and a link to rock properties through AVO. The seismic data has been applied in the prediction of reservoir heterogeneity in heavy oils. In spite that the deterministic lambda*rho and mu*rho attributes obtained from the AVO inversion are used in the reservoir lithology prediction (Bellman, 2007; Tonn, 2010), many applications of surface seismic data in Athabasca use the attributes derived from seismic data for statistical and neural-network predictions (Tonn, 2002; Anderson et al., 2005, Dumitrescu et al, 2005; Gray et al, 2006; Dumitrescu et al, 2009). In these statistical applications, relationships between the seismic attributes and lithology are derived at the well-control points by a multivariate analysis or non-linear method (artificial neural networks (ANN)) and then the lithology between wells is predicted from the seismic attributes by using these relationships. When the uncertainty is high in the deterministic prediction, the statistical method should be considered for the estimation of uncertainty; however, interpreters often find these statistical methods are more tedious and time-consuming and less straightforward than conventional techniques. Chapter 3 works on developing reliable AVO inversion techniques to extract single or a limited number of AVO attributes from seismic data to predict the lithological heterogeneity in heavy oil reservoirs. The attributes by this method can be used directly in the interpretation as typical AVO attributes and used as the input to the statistical methods or non-linear methods as well as the post-stack inversion.

This chapter begins with a review of basis of the AVO analysis and inversion, makes remarks on the Bayesian constraint AVO inversion, and implements the techniques to improve the AVO inversion. Two case studies in the Athabasca heavy oils are presented to demonstrate the effectiveness of the improved AVO inversion in the prediction of reservoir lithological heterogeneity in heavy oils.

3.2 AVO ANALYSIS

A number of papers on AVO theory, method, practices, and case studies have been published in journals and conferences. Here a brief review on the basic theory of AVO is made as an introduction to the key theoretical derivations of the methodology presented in this thesis.

3.2.1 AVO basic theory

AVO analysis in the industry is based on Zoeppritz equations and their approximations.

3.2.1.1 Zoeppritz equations

In seismology, Zoeppritz equations describe how seismic waves are transmitted and reflected at media boundaries between two different layers of earth. The solutions of Zoeppritz equations (Aki and Richards, 1980) are the plane wave reflection and transmission coefficients as functions of the elastic parameters of both sides of the interface and the angles of incidence and transmission. Zoeppritz equations are the basis of AVO (Amplitude Variations with Offset) or more properly AVA (Amplitude Variations with Angle) since the elastic parameters can be inferred from the amplitude variation with angle. Zoeppritz equations are derived for the idealized situation of two half-spaces in a welded contact. The AVO analysis has been extended to anisotropic media (Ruger, 2002). The regional differential stress in the Athabasca oil sands area introduces anisotropy of the overburden formations. The anisotropy due to the stress differentials affects the integrity of caprocks of heavy oil reservoirs. The analysis and use of the anisotropy requires more effort on the seismic data processing (Bale et al, 2009, Whale et al, 2009; Cary et al 2010). Multi-component and 3D seismic data can help

define the anisotropy in the formations. Regional stress differentials are certainly critical to the design of horizontal drillings in the production. However, only the isotropic AVO is discussed in the thesis because there is no 3D seismic data or multi-component seismic data available for the current study. The seismic anisotropy in the oil sands will be studied in the future.

3.2.1.2 Linear approximation of Zoeppritz equations

Solutions of Zoeppritz equations involve complex matrix multiplications and are nonlinear. A number of studies have simplified the Zoeppritz equations by linearizing them namely Bortfeld (1962), Richards and Frasier (1976), Aki and Richards (1980). The linearization of approximations requires that the fractional perturbations in elastic parameters are small (<<1). Aki and Richards (1980) published the linearized approximations for all the reflection and transmission coefficients. The linearized reflection coefficients are expressed as linear functions of the elastic parameter contrasts and the trigonometric functions of angles. Those linearized approximations provide great insights into the linear links between the reflection coefficients and elastic parameter contrasts and build the foundation for obtaining elastic parameters from the angle-dependent reflectivities on the seismic data – AVO/AVA. In the following is the reflection coefficient for the P wave incidence and P wave reflection, after Aki and Richards (1980)

$$\mathbf{r}(\theta) = \frac{1}{2}\left(1 - 4\gamma^2 \sin^2\theta\right)\frac{\Delta\rho}{\rho} + \frac{1}{2\cos^2\theta}\frac{\Delta\alpha}{\alpha} - 4\gamma^2 \sin^2\theta\frac{\Delta\beta}{\beta}. \qquad (3.1)$$

where $\mathbf{r}(\theta)$ is the angle-dependent reflectivity, α, β, and ρ are the average P-wave velocity, S-wave velocity, and density, and γ is the ratio of S-wave velocity and P-wave velocity, i.e. β/α ratio, $\Delta\alpha/\alpha$, $\Delta\beta/\beta$, and $\Delta\rho/\rho$ are the changes in the P-wave and S-wave velocities and density across the interface, and θ is the average angle of incidence and transmission across the interface. The expression in equation (3.1) reveals the dependency of the angle-dependent reflectivity on elastic parameters in a more simple way than the complex Zoeppritz equations.

3.2.1.3 AVO inversion

Equation (3.1) is the fundamental equation of the AVO analysis. The elastic parameter contrasts in the equation, $\Delta\alpha/\alpha$, $\Delta\beta/\beta$, and $\Delta\rho/\rho$, can be estimated when at least three reflectivities at different angles are observed. This is called the three-parameter AVO inversion or three-term AVO inversion. In addition to be expressed by the parameter set of $\Delta\alpha/\alpha$, $\Delta\beta/\beta$, and $\Delta\rho/\rho$, the equation can be rewritten as various linear formats using different sets of parameters, such as $\Delta Ip/Ip$, $\Delta Is/Is$, and $\Delta\rho/\rho$ (Ip and Is are P and S wave impedances – Gidlow et al 1992, Fatti et al, 1994) and $\Delta\lambda/\lambda$, $\Delta\mu/\mu$, and $\Delta\rho/\rho$ (λ and μ are Lame's parameters – Gray et al, 1999). These different formats can be linearly transformed from each other (Downton and Lines, 2001, Downton, 2005) and therefore would not introduce more disadvantages or advantages for the stability or reliability of the AVO inversion. By a further approximation after the density term is dropped or combined into other two terms via velocity-density relationships (like the Gardner's relationship), two-parameter equations are obtained, such as the Shuey's two-term equation or intercept-gradient equation, the weighted stacks (Smith and Gidlow, 1987), the Gidlow-Fatti two-term equation using impedance reflectivities, and the approximation using the reflectivities of Lame's parameters (Gray et al, 1999). The intercept-gradient two-term equation has been popular since the beginning of the AVO application. In many practices of the AVO inversion it is assumed that every time sample on seismic data represents the reflectivity from a single interface. The time sample by time sample AVO inversion apparently ignores the band-limited feature of seismic data. If the wavelet is uniform at different angles or offsets, the sample by sample inversion is valid in general. If the wavelet changes with offset due to the tuning and stretching in data processing, the time sample by time sample AVO inversion should be realized carefully.

3.2.1.4 Impedance inversion

Impedance is specifically referred to the product of velocity and density. But the impedance in the above title "impedance inversion" means any elastic parameters derivable from the seismic data. The impedance inversion refers to converting reflectivities of elastic parameters to elastic parameters comparable with well logs. The

result from the impedance inversion contains a full bandwidth (at least the DC and low frequencies plus the seismic bandwidth) or a limited bandwidth same as in seismic data. The latter is called the colored impedance inversion, after Lancaster and Whitcombe (2000).

Outputs of the AVO inversion are the reflectivities of density and velocity or impedance. These attributes contain the same frequency bandwidth as in the seismic data and show the contrasts of elastic parameters at medium interfaces. For the purpose of quantitative measurements of reservoirs, one needs to convert these band-limited contrasts at formation interfaces into the elastic parameters of formation layers, since these layer based parameters make more sense if they are comparable with well logs and correlated with formations. Typically, both the low and high frequencies are missing in seismic data, limiting the resolution of the seismic data. If the AVO inversion which extracts band-limited attributes is an ill-posed problem, then the impedance inversion which derives the full bandwidth is a non-unique problem. The reduction of non-uniqueness in the impedance inversion depends on the integration of interpretation and well controls, which should involve iterative geological and rock property model building processes.

P and S wave velocities or impedances and density can be regarded as basic parameters because they are directly related to the seismic data, but the reservoir properties such as porosity, saturation, and permeability are more desired in the reservoir characterization. Through the stochastic inversion, the relationship between reservoir properties and elastic parameters can be incorporated into the AVO inversion, becoming a mega inversion. This will be discussed in Chapter 4.

3.2.1.5 Linear vs. nonlinear

It is claimed (Behura et al, 2010) that using the nonlinear format of Zoeppritz equations provides a better result for the inversion. No doubt nonlinear forms should be used when the post-critical incidence or large contrast is included in the inversion. However, the linear inversion is widely used in the study because linear inversions are usually more

stable than nonlinear ones and those three-term equations are very close to the full Zoeppritz equation when the contrast is small and the angle of incidence is not extremely wide. The reflectivity attributes, such as P and S reflectivity, intercept and gradient, and fluid factor, are of practical importance in the history of AVO applications. They are still used as the DHIs and data quality control by many interpreters today (Castagna, et al, 1998, Swan, 2007, Hilterman and Zhou, 2009). The full waveform inversion is promising but it needs vast computations and the stability is still of concern. If the robustness is one of the key elements of the reservoir characterization (Connolly, 2010), the linear inversion and conventional AVO analysis are no doubt robust processes.

3.2.1.6 Large angle AVO inversion

The inversion using equation (3.1) is generally ill-posed. The use of large angle data is able to reduce ill-posedness. However, there are issues in the large angle data to deal with: the offset dependent tuning, critical incidence, etc. An angle as large as 60 degrees is suggested by Roy et al (2008) to extract reliable density information for the heavy oil reservoir characterization, although the critical incidence can be an issue for that high incident angle. The inversion method implemented in this thesis suggests using large angles up to 45 degree. The correction of the offset-dependent tuning is studied for conditioning data in the AVO analysis in Chapter 5. The inversion realized in the frequency domain looks after the tuning issue itself.

3.2.2 Typical AVO analysis flow

The early AVO analysis identified AVO anomalies, such as increasing AVO (Ostrander, 1984; Rutherford and Williams, 1989), and frameworks using the intercept and gradient, weight stack and fluid factor were built up soon afterwards (Shuey 1984; Smith and Gidlow, 1987; Gidlow et al, 1992; Fatti et al 1994; Castagna and Smith, 1994; Castagna et al, 1998). These AVO analysis methods look for DHIs on the reflectivity within the seismic bandwidth. To conduct a quantitative reservoir prediction and tie with well logs using the AVO data, the AVO inversion and afterward impedance inversion are combined to produce elastic properties comparable with well logs (Goodway et al 1997;

Connolly 1999). Figure 3.1 shows the flow chart of reservoir characterization using pre-stack seismic data, in which the integration of wells and seismic data is highlighted. Two paths can be followed from the seismic data to reservoir properties in this chart: one is deterministic and other one is stochastic. In the deterministic approach, elastic properties are obtained from the pre-stack seismic data either in a cascaded way or by one step: The AVO inversion/extraction, colored inversion, and addition of low frequency components can be cascaded to form a multi-step process which generates reflectivity attributes and well log like elastic parameters. A one-step deterministic approach generates well log like elastic parameters usually without intermediate attributes. In this chapter, the cascaded deterministic approach can be called the conventional AVO analysis. The conventional AVO analysis is cost-efficient and has advantages. Much of the recent research effort in the industry is being made on the stochastic inversion, attempting to incorporate everything (rock properties, reservoir properties, geostatistics, and seismic data) into a probability modeling and simulation process. Chapter 4 makes a more detailed comparison between the inversion and simulation.

The colored inversion converts seismic data into relative elastic parameters, e.g. P impedance, S impedance, density, Poisson's ratio, Vp/Vs ratio, angle-dependent elastic impedance (Connolly, 1999), and lambda-mu-rho attributes (Goodway et al, 1997). The colored inversion directly transforms the seismic data (reflectivity or contrast) to relative parameters without the contamination by errors that may be introduced by a model or interpretation when they are integrated into the inversion. In addition, the colored inversion is simple to understand and its calculation is cost-efficient.

In the deterministic inversion, an initial model of the elastic parameters should be built in the beginning by using horizons, well logs, and other geological information. The deterministic inversion achieves the broad bandwidth impedance by two approaches: one approach simply merges the colored impedance with other frequency components missing from the seismic data, usually only the low frequency components, which are from an initial model of the elastic parameters; the second approach perturbs the initial

full bandwidth model to make the closeness between the seismic data and synthetic data from the model reach certain criteria to produce the final model, which is regarded as the solution of the inversion. The deterministic inversion can be applied either on the pre-stack data or post-stack data. The method in this chapter mainly focuses on the conventional analysis, which generates reflectivity attributes with the seismic bandwidth, then converts them into the relative impedance, and inverts the reflectivity into impedance by a poststack deterministic inversion. Figure 3.2 shows the flow chart used for the case histories in this chapter. In Chapter 4, the stochastic inversion and other statistical and nonlinear approaches to integrate the attributes generated in this chapter will be discussed.

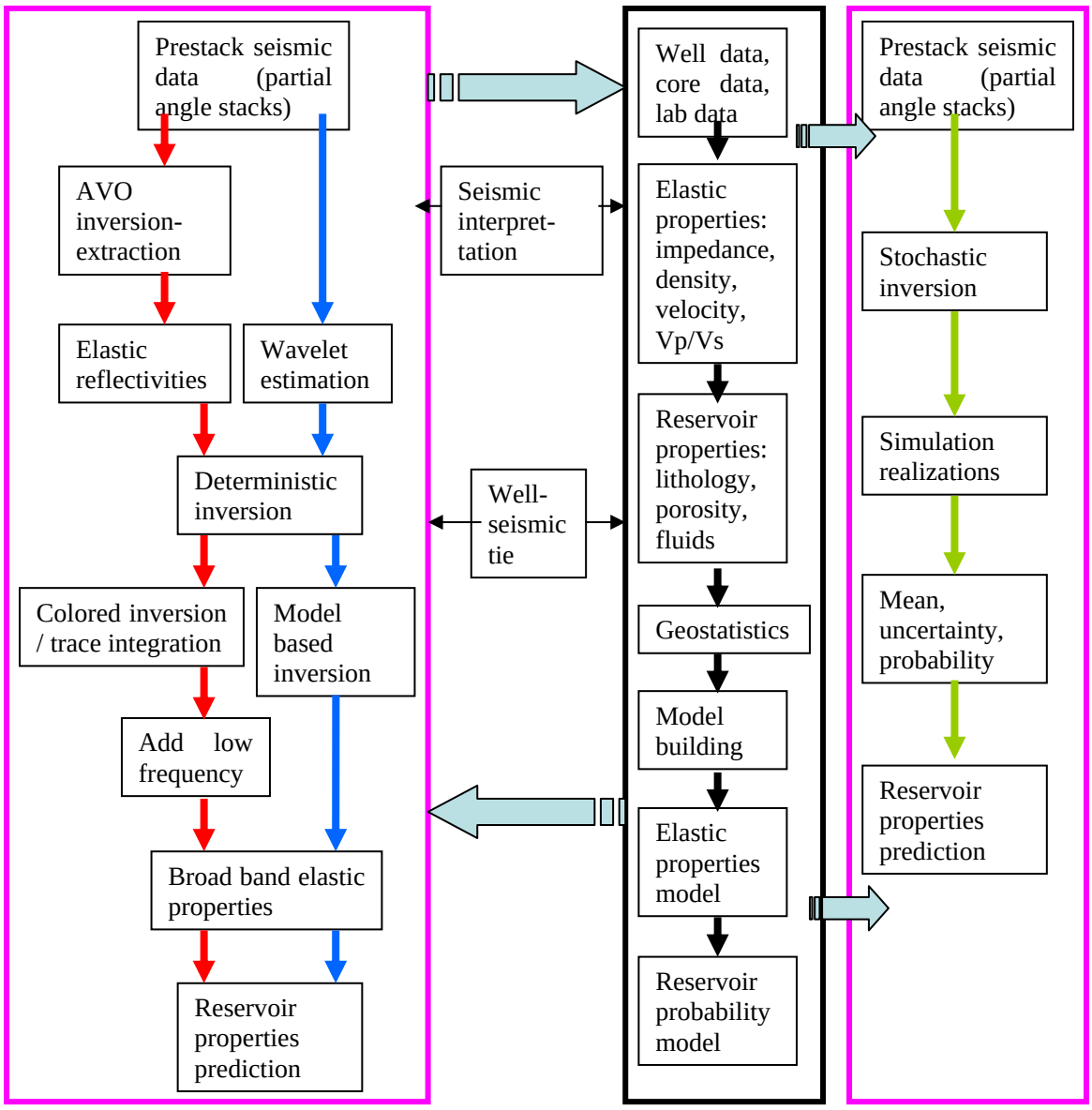

Figure 3.1 Seismic reservoir characterization flow chart. The left purple box includes deterministic inversion methods while the right purple box includes the stochastic inversion method. The box in the middle contains rock properties, reservoir properties, and geostatistics which bridge seismic data with reservoirs and geology. The red arrows in the deterministic approach streamline multi-step inversions while the blue arrows flowchart a one-step deterministic inversion.

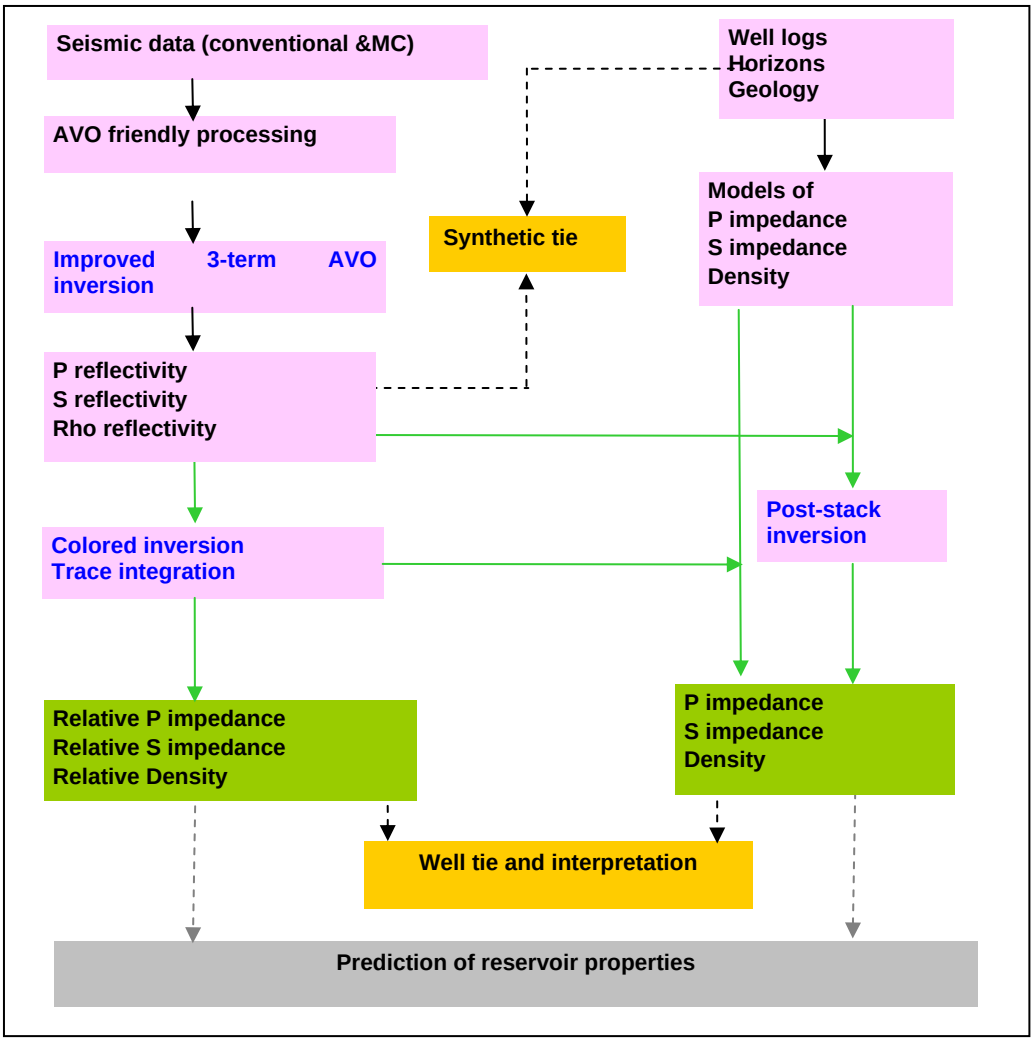

Figure 3.2 Workflow for the Case Histories in Chapter 3. It is a conventional AVO analysis including a deterministic multi-step inversion approach. Although a single iteration of above flow is conducted in practice, the final output of the reservoir properties can be used to build new initial models and therefore a few iterations can be performed for the optimal output.

3.3 EXTRACTION OF ELASTIC PARAMETER REFLECTIVITIES USING AVO INVERSION

Ideally, the inversion should generate elastic parameters or reservoir properties of the formation comparable with well logs. However, as the DHI (Direct Hydrocarbon Indication) was used for decades, the AVO inversion obtains reflectivities of elastic parameters with the seismic frequency bandwidth. Because of its simplicity, quick turnaround, low cost, and seismic data driven nature, it has been popular since the advent

of AVO. *In this thesis, the AVO inversion refers to the extraction of elastic parameter reflectivities from the pre-stack seismic data.* It is sometimes called the AVO extraction. The AVO inversion is commonly done on the time sample basis by using the data at different offsets or angles in a CDP gather after being processed carefully. The implementation is usually done in the time domain sample by sample and the interference due to the limited bandwidth is ignored usually, though the implementation in the frequency domain should better handle the interference and other issues due to the processing, such as the NMO stretching. In spite of its simplicity, the AVO inversion is posed as a complete geophysical inverse problem and has been studied by many academic and industrial geophysicists. A long list of publications can be made on this topic, e.g., Ostrander 1983, Shuey, 1984, Smith and Gidlow, 1987, Gidlow et al, 1992, Fatti et al, 1994, Castagna and Smith, 1994, Castagna et al, 1998, Downton, 2005, Roy et al, 2008, and Xu and Chopra, 2008.

Many geophysical inverse problems are ill-posed or ill-conditioned, and so is the AVO inversion/extraction. The ill-posedness of the AVO inversion has been studied to extract a more reliable and useful parameter from seismic data (Roy et al, 2008, Downton, 2005, Downton and Lines, 2001, Xu and Chopra, 2008). To reduce the uncertainty in the inverse problem, the prior information is often incorporated into the inversion. The Bayes' theorem becomes the natural choice to constrain the inversion using the prior information (Downton and Lines, 2001, Downton, 2005, Roy, 2008). In this chapter, the Bayesian AVO inversion is implemented to extract elastic parameters. The implementation reduces uncertainties in the inversion for the oil sands reservoirs in the WCSB. The use of the Bayesian estimator for the AVO inversion in this thesis is slightly different from that in the industry.

The AVO inversion is based on the angle dependent reflectivity when a plane wave is incident upon an elastic medium interface. The solutions of Zoeppritz's equation are the extract expression of the reflection coefficients with complex formulas. Aki-Richards' approximations to Zoeppritz's equations are widely used in the application of the AVO

analysis due to their simple linearized forms and clear relationships between incident angles and elastic parameter contrasts with the assumption of small elastic property contrasts at the interface. Unless mentioned explicitly, this thesis discusses the P wave incidence and P wave reflection, which are usually assumed by the conventional surface seismic and the vertical component of the multi-component seismic data. A number of formations of the Aki-Richards' approximation with various combinations of the elastic parameter contrasts have been shown in the application of AVO. These formations can be linearly transformed from and to each other (Downton, 2005) and therefore do not improve or deteriorate the ill-posed nature of the inverse problems. The AVO inversion with the Bayesian constraints is derived in the following.

The AVO inversion is commonly done with an angle domain NMO-corrected CDP gather or common-image-point (CIP) gather from the prestack migration (assuming all effects impacting AVO fidelity are rightly corrected). The linearized Aki-Richards' approximation is expressed as

$$\mathbf{r}(\theta) = \frac{1}{2}\left(1 - 4\gamma^2 \sin^2\theta\right)\frac{\Delta\rho}{\rho} + \frac{1}{2\cos^2\theta}\frac{\Delta\alpha}{\alpha} - 4\gamma^2 \sin^2\theta\frac{\Delta\beta}{\beta} \tag{3.2}$$

where $\mathbf{r}(\theta)$ is the angle-dependent reflectivity, α, β, ρ, and γ are the average P-wave velocity, S-wave velocity, density, and β/α ratio, $\Delta\alpha/\alpha$, $\Delta\beta/\beta$, and $\Delta\rho/\rho$ are the changes in the P-wave and S-wave velocities and density across the interface, and θ is the average angle of incidence and transmission across the interface. One of the mostly common approximated forms of the equation (3.2) is the Shuey's two-term equation (Shuey, 1984; Castagna et al, 1998; Swan 1993)

$$\mathbf{r}(\theta) = \mathbf{A} + \mathbf{B}\sin^2\theta \tag{3.3}$$

where **A** and **B** are called the intercept and gradient. Actually **A** is the P impedance reflectivity at a normal incidence and **B** is the combination of the P and S impedance reflectivities.

In practices, the incident angles in the prestack seismic data are estimated through ray-tracing using an interval P-velocity from interpolation of sonic logs or from the output of

seismic velocity analysis. A more commonly used estimation of incident angles is through Walden's approach (1991) with known interval and RMS velocity, and this approach is more computationally efficient than ray-tracing and its accuracy is close to that of ray-tracing. If the reflectivities at many incident angles are known and angles are estimated as described as in the above, $\Delta\alpha/\alpha$, $\Delta\beta/\beta$, $\Delta\rho/\rho$ are the unknown parameters to be inverted by the AVO inversion. The linear AVO inverse problem is written in a matrix form

$$\mathbf{d} = \mathbf{G}\mathbf{m} + \varepsilon \tag{3.4}$$

where $\mathbf{d}$ is the input data vector (offset/angle dependent data samples), $\mathbf{m}=(\Delta\alpha/\alpha, \Delta\beta/\beta, \Delta\rho/\rho)^{T}$, $\mathbf{G}$ is the linear operator determined by the coefficients in equation (3.4) for all angles, and ε is the noise with the assumption of the Gaussian distribution including a zero mean and covariance matrix Σ_{ε} e.g.

$$\varepsilon \sim \mathbf{N}(0, \Sigma_{\varepsilon}). \tag{3.5}$$

If the noise in every measurement is independent, the covariance matrix in equation (3.5) is $\Sigma_{\varepsilon} = \sigma_{\mathbf{N}}^2\mathbf{I}$ -- the dimension of $\mathbf{I}$ is the number of data samples in equation (3.4).

The likelihood function is derived using $\varepsilon = \mathbf{d} - \mathbf{G}\mathbf{m}$ and the PDF of the noise,

$$\mathbf{p} = 2\pi \det(\Sigma_{\varepsilon})^{-1}\mathbf{e}^{-\frac{1}{2}\varepsilon^{\mathbf{T}}\Sigma_{\varepsilon}^{-1}\varepsilon} = 2\pi \det(\Sigma_{\varepsilon})^{-1}\mathbf{e}^{-\frac{1}{2}(\mathbf{G}\mathbf{m}-\mathbf{d})^{\mathbf{T}}\Sigma_{\varepsilon}^{-1}(\mathbf{G}\mathbf{m}-\mathbf{d})} \tag{3.6}$$

The inversion looks for a model $\mathbf{m}$ with which the probability density function (3.6) is maximized. The maximization of equation (3.6) is equivalent to minimizing the objective function

$$\mathbf{J} = (\mathbf{G}\mathbf{m} - \mathbf{d})^{\mathbf{T}}\Sigma_{\varepsilon}^{-1}(\mathbf{G}\mathbf{m} - \mathbf{d}) \tag{3.7}$$

To minimize the objective function $\mathbf{J}$, set the derivative of $\mathbf{J}$ with $\mathbf{m}$ to zero

$$\mathbf{G}^{\mathbf{T}}\Sigma_{\varepsilon}^{-1}(\mathbf{G}\mathbf{m} - \mathbf{d}) = 0 \tag{3.8}$$

Therefore, the least-squares solution or the maximum likelihood solution is

$$\hat{\mathbf{m}} = (\mathbf{G}^{\mathbf{T}}\Sigma_{\varepsilon}^{-1}\mathbf{G})^{-1}\mathbf{G}^{\mathbf{T}}\Sigma_{\varepsilon}^{-1}\mathbf{d}, \tag{3.9}$$

and the covariance of this estimator is

$$\Sigma_{\hat{\mathbf{m}}} = (\mathbf{G}^{\mathbf{T}}\Sigma_{\varepsilon}^{-1}\mathbf{G})^{-1}. \tag{3.10}$$

If $\Sigma_\varepsilon = \sigma_N^2 \mathbf{I}$ is assumed, we have

$$\hat{\mathbf{m}} = (\mathbf{G}^T\mathbf{G})^{-1}\mathbf{G}^T\mathbf{d}, \tag{3.11}$$

and

$$\Sigma_{\hat{\mathbf{m}}} = \sigma_N^2(\mathbf{G}^T\mathbf{G})^{-1}. \tag{3.12}$$

In the covariance equation (3.12), $(\mathbf{G}^T\mathbf{G})^{-1}$ is a measure of the curvature of the prediction error at its minimum. The variance of estimators depends on both the noise in data and the singularity of $(\mathbf{G}^T\mathbf{G})$. Note the effect of $(\mathbf{G}^T\mathbf{G})^{-1}$ on the variance of estimators lies in two aspects:

1. The singularity of $(\mathbf{G}^T\mathbf{G})$ impacts the variance of an estimator. **G** is an n_d x n_m matrix, where n_d is the number of data samples, n_m is the number of the elements in the parameter vector, and n_d is usually greater than n_m, meaning the over-determined. If the samples evenly spread over a certain incident angle range, the singularity (the condition number) of $(\mathbf{G}^T\mathbf{G})$ is nearly independent of the n_d value. Take equation (3.1) as an example. **G** is the matrix consisting of the coefficients (assuming **a**, **b**, and **c**) of three elastic contrasts in equation (3.1) for n_d angles. Therefore, n_m is 3. $(\mathbf{G}^T\mathbf{G})$ is

$$\mathbf{G}^T\mathbf{G} = \begin{pmatrix} \sum_{i=1}^{n_d}\mathbf{a}_i^2 & \sum_{i=1}^{n_d}\mathbf{a}_i\mathbf{b}_i & \sum_{i=1}^{n_d}\mathbf{a}_i\mathbf{c}_i \\ \sum_{i=1}^{n_d}\mathbf{a}_i\mathbf{b}_i & \sum_{i=1}^{n_d}\mathbf{b}_i^2 & \sum_{i=1}^{n_d}\mathbf{b}_i\mathbf{c}_i \\ \sum_{i=1}^{n_d}\mathbf{a}_i\mathbf{c}_i & \sum_{i=1}^{n_d}\mathbf{b}_i\mathbf{c}_i & \sum_{i=1}^{n_d}\mathbf{c}_i^2 \end{pmatrix}.$$

   If n_d data samples evenly spread over a certain angle range, each element in the above matrix is roughly proportional to the square of n_d. The eigenvalues of the matrix are roughly adjusted by n_d, but their ratio (the condition number) is little changed.

2. If more data samples are used in **G**, $(\mathbf{G}^T\mathbf{G})^{-1}$ is scaled down and the variance of the estimator becomes smaller, and so does the uncertainty of the estimates.

3.3.1 Understanding stability of AVO inversion by a modeling study

The least-squares AVO inversion is shown analytically in the last section. This section demonstrates the factors affecting the stability of the AVO inversion using a simple model. Although the AVO inversion is affected by many factors relating to the amplitude fidelity (the AVO theory and the acquisition and processing of the seismic data), the discussion is limited to the signal-to-noise ratio, angle range and sampling because the implementation of the AVO inversion in this chapter focuses on reducing the effects of these factors. The AVO inversion/extraction is applied using the data from modeling. This modeling study provides insights on factors impacting the uncertainty of AVO inversion. The parameters of the geometry of gathers and the signal-to-noise ratio can be controlled and changed easily in the modeling. Well logs (Figure 3.3) are used to generate synthetic offset dependent reflectivities. The shear wave velocity is simply derived from the P wave velocity using mudrock lines in order to make the model contain a strong correlation between the P and S velocities. To exclude the thin-bed effect on AVO, the reflectivity is of full bandwidth. Gathers are generated in the angle domain instead of in the offset domain. Systematic errors such as the NMO stretching are not included in the modeling. To make the visualization convenient, the Shuey's 2 term approximation (intercept and gradient equation) is used for the modeling and inversion. The AVO inversion extracts the intercept and gradient attributes and the crossplots of intercept and gradient attributes are made for the tests for different changes of parameters. Comparisons are made graphically in the crossplotting. The detailed studies of crossplotting intercept and gradient and the indication by crossplots on hydrocarbon anomalies by crossplotting can be found in literature (Castagna and Smith, 1993; Castagna et al, 1998; Simm et al, 2000). This study conducts the following tests:

1. Keeping an angle range of 0 to 40 degree, four different signal/noise ratios are tested: ∞ (no noise), 1, 0.5, and 0.25. Figure 3.4 shows the gathers with different S/N ratios. The crossplots compare the intercept and gradient from the inversions in Figure 3.5.

2. Keeping the signal/noise ratio of 0.25, four different angle ranges are tested: 0-10 degree, 0-20 degree, 0-30 degree, and 0-40 degree. Figure 3.6 compares the crossplots of the intercept and gradient from the inversions of the AVO gathers with different angle ranges.
3. Keeping the signal/noise ratio of 0.25, and the 20 degree angle range, the minimum and maximum angles vary: 0-20 degree, 10-30 degree, and 20-40 degree. The comparison of the inversions from gathers with these variations is made in Figure 3.7.
4. a) Keeping the signal/noise ratio of 0.25 and the angle range of **0-20** degree, the sample number of the inversion varies: 10, 40, 200, and 2000. The crossplot is made in Figure 3.8 for the comparison of the inverted intercept and gradient.

   b) Keeping the signal/noise ratio of 0.25 and the angle range of **0-30** degree, the number of samples in the inversion varies: 10, 40, 200, and 1500. The crossplot is made in Figure 3.9 for the comparison of the inverted intercept and gradient.

The variance of the gradient is calculated using equation (3.12) and plotted in Figures 3.10 and 3.11 for a few variations of parameters.

The reliability of the inversion is evaluated by the shift of samples from the true trend and the scattering of samples in the crossplot of the intercept and gradient. Observations on the reliability of the AVO inversion can be made from these tests as follows:

1. The signal/noise ratio (random noise) does affect the reliability of the inversion but less significantly than other factors. The random noise is simulated in the tests, although the coherent noise and noise bursts generate outliers which should usually be attenuated before the AVO inversion is applied.
2. Increasing the angle range and including as many far angles are effective to make the AVO inversion more reliable. Missing far angles significantly reduces the reliability of the inversion. The large angle processing is a key to improve the reliability of the AVO inversion.

3. Increasing data samples in the AVO inversion reduces the uncertainty of the inversion. The increase of the seismic data fold incurs a larger cost in the acquisition, but the number of samples in the inversion can be increased by using spatial and time windows and using the correlation between neighboring locations. All these means attempt to increase the data to parameters ratio, which will be discussed later in this chapter.
4. The limited angle ranges or lack of the far angle data generates a large deviation from the true trend in the crossplots of the intercept and gradient. The shift of the trend in the crossplotting, suggested by Swan (2007), is possibly caused by the unreasonable offset dependent scaling and is able to be corrected analytically. But the shift of the trend due to the limited angle ranges or the lack of the far angles as discussed in this section should be considered differently. This issue is discussed in more detail in Chapter 5.

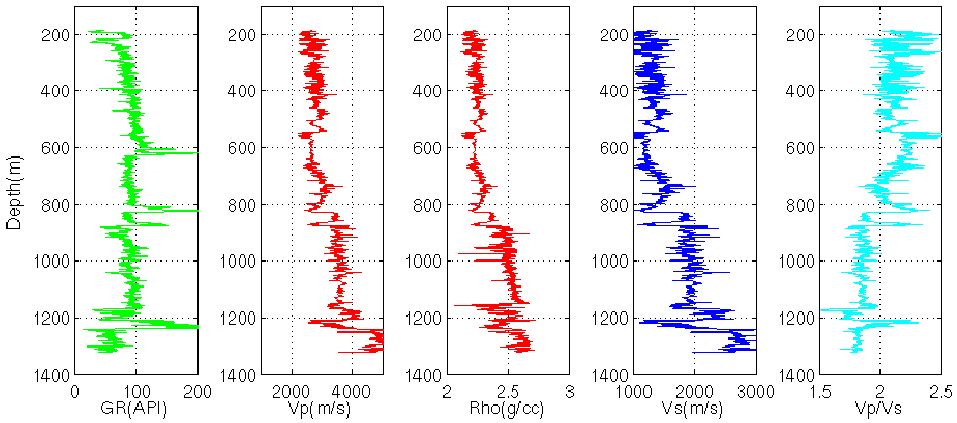

Figure 3.3 Well logs for generating synthetic seismograms. They are, from left to right, gamma ray, P wave velocity (Vp), density, S wave velocity (Vs), and Vp/Vs ratio. Vs is generated from Vp using a single mud-rock line.

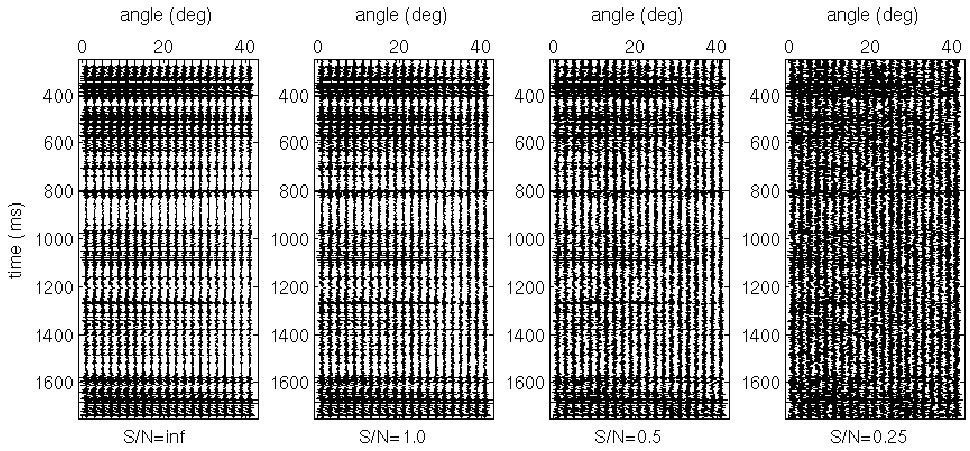

Figure 3.4 Synthetic AVO gathers with different noise levels, from left to right, noise-free, S/N=1, S/N=0.5, and S/N=0.25. Angle range is 0-40 degree.

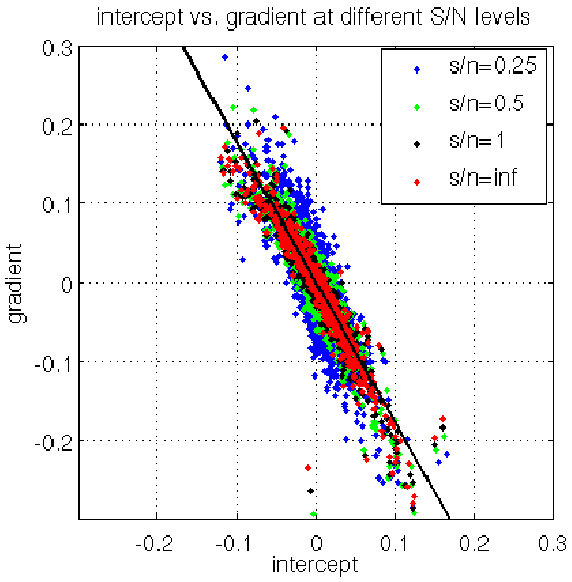

Figure 3.5 Crossplots of intercept and gradient inverted from gathers with various noise levels. When noise level is higher, the samples are deviated from the black trend line and rotated toward vertical axis. Black line is the back ground trend provided by the mud-rock line (same in Figures 3.6-3.9). It is noted that the scattering and trend drift are not large even if the S/N ratio is 0.25.

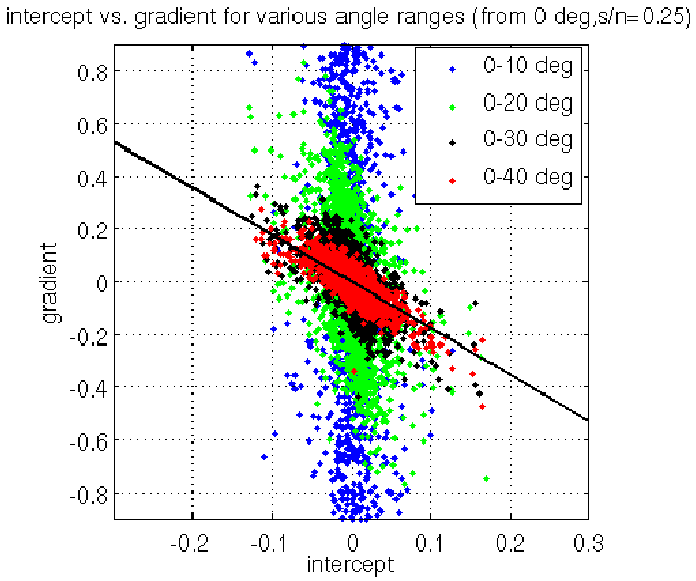

Figure 3.6 Crossplots of intercept and gradient inverted from gathers with different angle ranges (all the angle ranges start from zero degree). When the angle range is smalle (<= 20degrees), the samples deviate from the trend line dramatically.

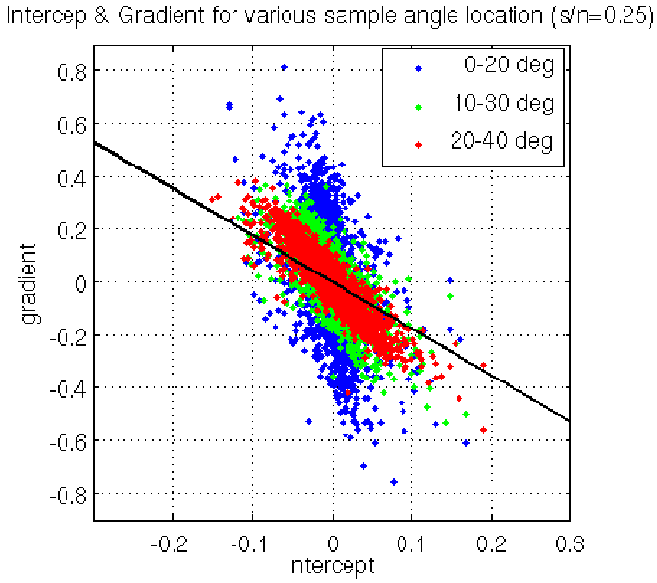

Figure 3.7 Crossplots of intercept and gradient inverted from gathers with the same angle range (20 degrees) but minimum and maximum angles are different. Although angle range is the same, the far angle data samples generate more reliable inversion results.

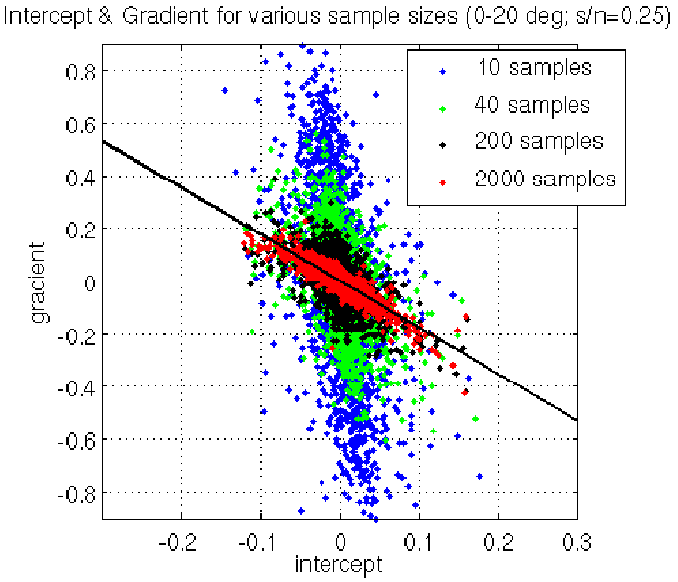

Figure 3.8 Crossplots of intercept and gradient inverted from gathers with the same angle range (0-20 degree) and S/N ratio but different sample numbers. Significantly large sample population generates reliable inversion results.

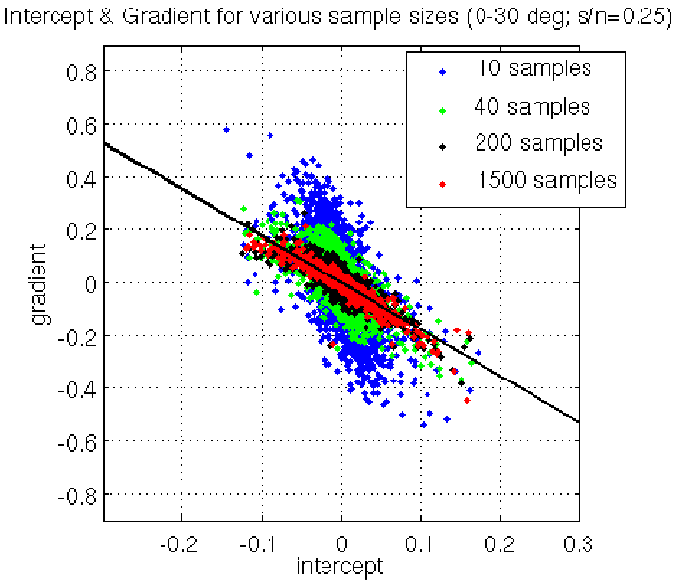

Figure 3.9 Crossplots of intercept and gradient inverted from gathers with the same angle range (0-30 degree) and S/N ratio but different sample numbers. It shows the inversion is stable with the angle range of 0-30 degree and 200 samples or more. In the real data, 200 data samples can be realistic by using superbinning for 2D or 3D data.

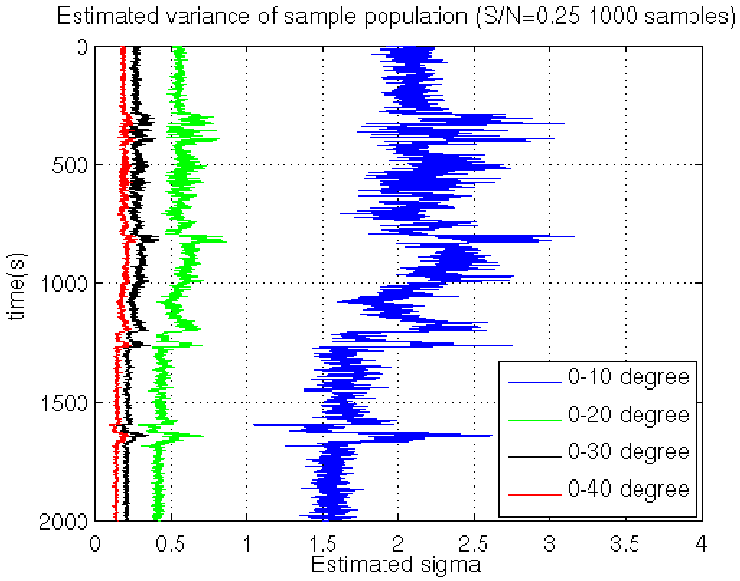

Figure 3.10 Variances of gradient from the AVO inversion with different angle ranges (S/N=0.25, and 1000 samples).

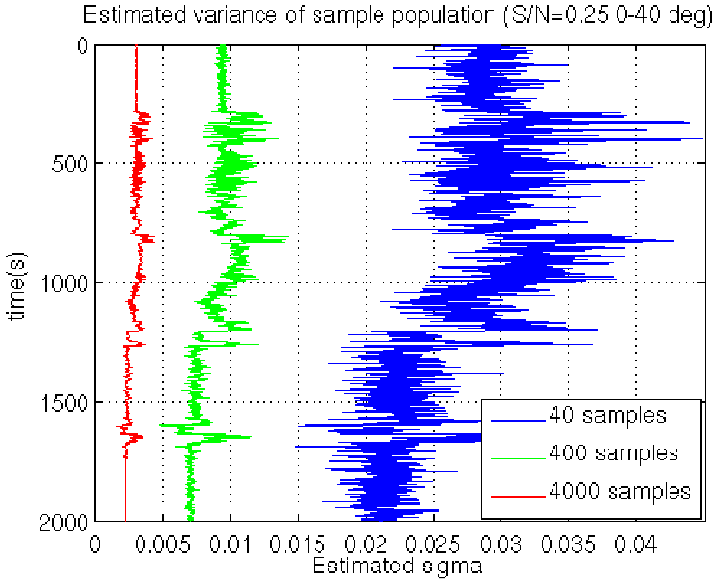

Figure 3.11 Variances of gradient from the AVO inversion with different sample numbers (S/N=0.25 and the 0-40degree angle range).

3.3.2 The *a priori* information and Bayesian constraint

It is noted in the last section that the wide angle, high S/N ratio, and sufficient data samples generate a stable AVO inversion. But the real cases are not often under all of those conditions. Thus when the AVO inversion becomes unstable, the *a priori* information is usually used to constrain the solutions. When *a priori* constraints are

incorporated into the inversion, they are usually expressed in the form of PDFs and the Bayes' inference is a natural choice to construct a joint PDF used by the inversion.

The Bayesian constraint AVO inversion has been applied in the industry for the past decade (Swan 1993; Downton and Lines, 2001; Cassassuce et al, 2004; Downton, 2005; Roy et al, 2008). The method of the AVO inversion used in this chapter is developed on the Bayes' theorem as well.

The Bayes' theorem is expressed as

$$\mathbf{P}(\mathbf{m}\,|\,\mathbf{d}) = \frac{\mathbf{P}(\mathbf{d}\,|\,\mathbf{m})\mathbf{P}(\mathbf{m})}{\mathbf{P}(\mathbf{d})}\ , \tag{3.13}$$

where $\mathbf{P}(\mathbf{d}|\mathbf{m})$ is the likelihood function and $\mathbf{P}(\mathbf{m})$ is the prior probability density function. The denominator $\mathbf{P}(\mathbf{d})$ is a normalization function which may be dropped if only the shape of the PDF is of interest. After $\mathbf{P}(\mathbf{d})$ is dropped, equation (3.13) becomes

$$\mathbf{P}(\mathbf{m}\,|\,\mathbf{d}) = \mathbf{P}(\mathbf{d}\,|\,\mathbf{m})\mathbf{P}(\mathbf{m})\,. \tag{3.14}$$

When the model $\mathbf{m}$ is assumed to follow a multi-variate Gaussian distribution with the mean of $\overline{\mathbf{m}}$ and covariance of $\Sigma_{\mathbf{m}}$, e.g. $\mathbf{m} \sim \mathbf{N}(\overline{\mathbf{m}}, \Sigma_{\mathbf{m}})$, its probability density function (PDF) is

$$\mathbf{P}(\mathbf{m}) = 2\pi \det(\Sigma_{\mathbf{m}})^{-1} \mathbf{e}^{-\frac{1}{2}(\mathbf{m}-\overline{\mathbf{m}})^{\mathbf{T}} \Sigma_{\mathbf{m}}^{-1} (\mathbf{m}-\overline{\mathbf{m}})}\,. \tag{3.15}$$

If the error or misfit in the data follows a normal distribution, the likelihood PDF $\mathbf{P}(\mathbf{d}|\mathbf{m})$ is

$$\mathbf{P(d|m)=}\ 2\pi \det(\Sigma_{\varepsilon})^{-1} \mathbf{e}^{-\frac{1}{2}(\mathbf{Gm}-\mathbf{d})^{\mathbf{T}} \Sigma_{\varepsilon}^{-1} \varepsilon (\mathbf{Gm}-\mathbf{d})} \tag{3.15b}$$

The joint (*a posteriori*) PDF $\mathbf{P}(\mathbf{m}|\mathbf{d})$ is

$$\mathbf{P(m|d)=P(d|m)P(m)=}\ 2\pi \det(\Sigma_{\varepsilon})^{-1} \mathbf{e}^{-\frac{1}{2}(\mathbf{Gm}-\mathbf{d})^{\mathbf{T}} \Sigma_{\varepsilon}^{-1} \varepsilon (\mathbf{Gm}-\mathbf{d})} . 2\pi \det(\Sigma_{\mathbf{m}})^{-1} \mathbf{e}^{-\frac{1}{2}(\mathbf{m}-\overline{\mathbf{m}})^{\mathbf{T}} \Sigma_{\mathbf{m}}^{-1} (\mathbf{m}-\overline{\mathbf{m}})} \tag{3.16}$$

A solution with the maximum *a posteriori* (MAP) probability density function is usually obtained by the minimization of the following objective function (the sum of the exponents in equation (3.16))

$$\mathbf{J} = (\mathbf{Gm} - \mathbf{d})^{\mathbf{T}} \Sigma_{\varepsilon}^{-1} (\mathbf{Gm} - \mathbf{d}) + (\mathbf{m} - \overline{\mathbf{m}})^{\mathbf{T}} \Sigma_{\mathbf{m}}^{-1} (\mathbf{m} - \overline{\mathbf{m}}). \quad (3.17)$$

The minimization of **J** derives the following maximum *a posteriori* solution,

$$\hat{\mathbf{m}} = (\mathbf{G}^{\mathbf{T}} \Sigma_{\varepsilon}^{-1} \mathbf{G} + \Sigma_{\mathbf{m}}^{-1})^{-1} \mathbf{G}^{\mathbf{T}} \Sigma_{\varepsilon}^{-1} \mathbf{d} + (\mathbf{G}^{\mathbf{T}} \Sigma_{\varepsilon}^{-1} \mathbf{G} + \Sigma_{\mathbf{m}}^{-1})^{-1} \Sigma_{\mathbf{m}}^{-1} \overline{\mathbf{m}}. \quad (3.18)$$

If $\Sigma_{\varepsilon} = \sigma^2 \mathbf{I}$ is assumed, equation (3.18) becomes

$$\hat{\mathbf{m}} = (\mathbf{G}^{\mathbf{T}} \mathbf{G} + \sigma^2 \Sigma_{\mathbf{m}}^{-1})^{-1} \mathbf{G}^{\mathbf{T}} \mathbf{d} + (\mathbf{G}^{\mathbf{T}} \mathbf{G} + \sigma^2 \Sigma_{\mathbf{m}}^{-1})^{-1} \sigma^2 \Sigma_{\mathbf{m}}^{-1} \overline{\mathbf{m}}. \quad (3.19)$$

Note $\hat{\mathbf{m}}$ is used to represent the estimated model **m**, or the MAP estimator. It includes two terms – the data term $(\mathbf{G}^{\mathbf{T}} \mathbf{G} + \sigma^2 \Sigma_{\mathbf{m}}^{-1})^{-1} \mathbf{G}^{\mathbf{T}} \mathbf{d}$ and prior term $(\mathbf{G}^{\mathbf{T}} \mathbf{G} + \sigma^2 \Sigma_{\mathbf{m}}^{-1})^{-1} \sigma^2 \Sigma_{\mathbf{m}}^{-1} \overline{\mathbf{m}}$. The MAP estimator is the interpolation between the prior term and data term. When $\sigma \rightarrow 0$, $\hat{\mathbf{m}} \rightarrow (\mathbf{G}^{\mathbf{T}}\mathbf{G})^{-1}\mathbf{G}^{\mathbf{T}}\mathbf{d}$, which is the least-squares solution, and when $\sigma \rightarrow \infty$, $\hat{\mathbf{m}} \rightarrow \overline{\mathbf{m}}$, which is the statistical mean of the model (usually an initial model in practice). Both the data term and prior term are important to construct the Bayesian estimator. An example in an oil sands model in the next chapter (Chapter 4) will show that the sum of the data term and prior term makes more sense.

3.3.3 Examining a commonly used solution of Bayesian AVO inversion

In the common applications of the Bayesian constraint on the AVO inversion/extraction (Demirbag et al, 1993; Swan 1993; Downton and Lines, 2001, Downton, 2005; Roy et al, 2008, Cassassuce et al, 2004), the second term in equation (3.19), the prior term, is dropped with an assumption of zero mean of reflectivities and the solution becomes

$$\hat{\mathbf{m}} = (\mathbf{G}^{\mathbf{T}} \mathbf{G} + \sigma_{\mathbf{N}}^2 \Sigma_{\mathbf{m}}^{-1})^{-1} \mathbf{G}^{\mathbf{T}} \mathbf{d}, \quad (3.20)$$

which is actually the data term of the Bayesian estimator. This data term estimator is investigated in more detail shortly.

In the AVO inversion/extraction, one of the significant issues with the unconstrained least-squares estimator, $(\mathbf{G}^{\mathbf{T}} \mathbf{G})^{-1} \mathbf{G}^{\mathbf{T}} \mathbf{d}$, is the large uncertainty due to the strong

singularity of $\mathbf{G^T G}$ if the offset of the seismic data is limited or more parameters are inverted. The strong singularity usually comes from the fact that the magnitude of the first column elements in $\mathbf{G}$ is much larger than of the second or third column. $\sigma^2\Sigma_\mathbf{m}^{-1}$ regularizes $\mathbf{G^T G}$, making the inversion stable by increasing the small eigenvalues in $\mathbf{G^T G}$. Taking the two term AVO approximation for example, the $\Sigma_\mathbf{m}$ is expressed as

$$\Sigma_\mathbf{m} = \begin{pmatrix} \sigma_1^2 & \rho\sigma_1\sigma_2 \\ \rho\sigma_1\sigma_2 & \sigma_2^2 \end{pmatrix} = \sigma_1^2 \begin{pmatrix} 1 & \rho\sigma_2/\sigma_1 \\ \rho\sigma_2/\sigma_1 & \sigma_2^2/\sigma_1^2 \end{pmatrix}, \tag{3.21}$$

where σ_1 and σ_2 are the variances (standard deviations) of the two parameters and ρ is the correlation coefficient of the two parameters. The inverse of $\Sigma_\mathbf{m}$ is

$$\Sigma_m^{-1} = \frac{1}{\sigma_1^2} \begin{pmatrix} 1 & \rho\sigma_2/\sigma_1 \\ \rho\sigma_2/\sigma_1 & \sigma_2^2/\sigma_1^2 \end{pmatrix}^{-1} \tag{3.22}$$

If the data is noisy, making σ_N/σ_1 large, or $\mathbf{G^T G}$ is very singular because the angle range or the data samples are limited (e.g., ~10 offsets/angles), then $\mathbf{G^T G} + \sigma_\mathbf{N}^2\Sigma_\mathbf{m}^{-1}$ should be dominated by $\sigma_\mathbf{N}^2\Sigma_\mathbf{m}^{-1}$. The data term estimator becomes

$$(\mathbf{G^T G} + \sigma_\mathbf{N}^2\Sigma_\mathbf{m}^{-1})^{-1}\mathbf{G^T d} \rightarrow \eta \begin{pmatrix} \sum_{\mathbf{i}=1}^{\mathbf{M}} \mathbf{a_i d_i} \\ \rho\dfrac{\sigma_2}{\sigma_1} \sum_{\mathbf{i}=1}^{\mathbf{M}} \mathbf{a_i d_i} \end{pmatrix}, \tag{3.23}$$

where η is a scalar, $\mathbf{a_i}$'s are the elements in first column in $\mathbf{G^T}$ and $\mathbf{d_i}$'s are the data samples. The first element in this vector is the weighted stack of the data (for the intercept-gradient solution, the first element is the stack of data since $\mathbf{a_i}$ =1), and the second element is the scaled first element by a constant which is the off-diagonal element of $\Sigma_\mathbf{m}$ after normalized by σ_1^2 – in equation (3.21). If the two parameters in the model are uncorrelated, $\Sigma_\mathbf{m}$ becomes a diagonal matrix making the solution close to the damped least-squares estimator, and the second parameter is forced to be close to zero. These are demonstrated by a series of tests by using synthetic examples in Figures 3.12-3.16, where the intercept and gradient are inverted from the data with 20 angles, the S/N ratio of 0.25, and the 0-20 degree angle range – a singular case. As the prior constraint, the covariance

matrix for these tests is derived from well logs used in modeling AVO gathers and defined as follows

$$\Sigma_{\mathbf{m}} = \begin{pmatrix} \sigma_{\mathbf{A}}^2 & -0.962\sigma_{\mathbf{A}}\sigma_{\mathbf{B}} \\ -0.962\sigma_{\mathbf{A}}\sigma_{\mathbf{B}} & \sigma_{\mathbf{B}}^2 \end{pmatrix}, \tag{3.24}$$

where σ_A and σ_B are the standard deviation of **A** (intercept) and **B** (gradient) and σ_B/σ_A=1.91. The correlation coefficient between **A** (intercept) and **B** (gradient) is -0.962.

The correlation coefficient in the covariance matrix is modified by changing the true value (0.962) of the model to three different values: 0.8, 0.5 and 0.0. The intercept and gradient from the constraint and unconstraint inversions and from the model are cross-plotted in Figures 3.12-3.15. In addition the damped least-squares solution (the diagonal elements in the covariance matrix are identical and the off-diagonal elements are zeros) is generated and the comparison is made in Figure 3.16. The straightforward least-squares solution (without damping) is in blue color in these figures. These tests show that

1. To make the solution of the inversion follow the same trend as the model, the correlation coefficient of the model parameters in the covariance matrix has to be very high. A large correlation coefficient forces the solutions of the inversion to be much more correlated than the model;
2. Although the correlation coefficient can be reduced to generate a crossplot with the scattering of samples similar to that of the model, the trend of the samples from inversions is deviated from the trend of the model;
3. When the correlation coefficient is forced to zero, the solution is like that of the damped least-squares;
4. The covariance matrix plays an important role in the Bayesian constrained AVO inversion. Correlation coefficients and variance ratio of the model parameters control the fidelity of the solution.

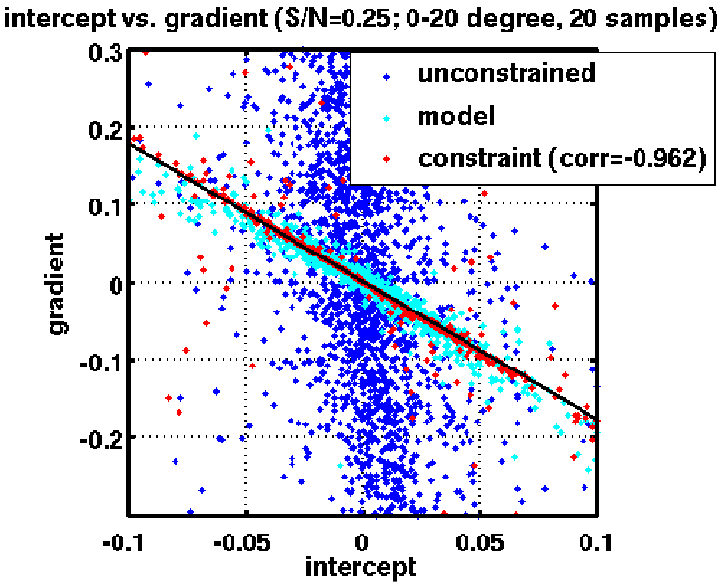

Figure 3.12 Cross-plot of the intercept and gradient of the model and the solutions of the unconstraint inversion and constraint inversion in which the constraint matrix Σ_m is calculated from the model intercept and gradient (correlation coefficient is -0.962).

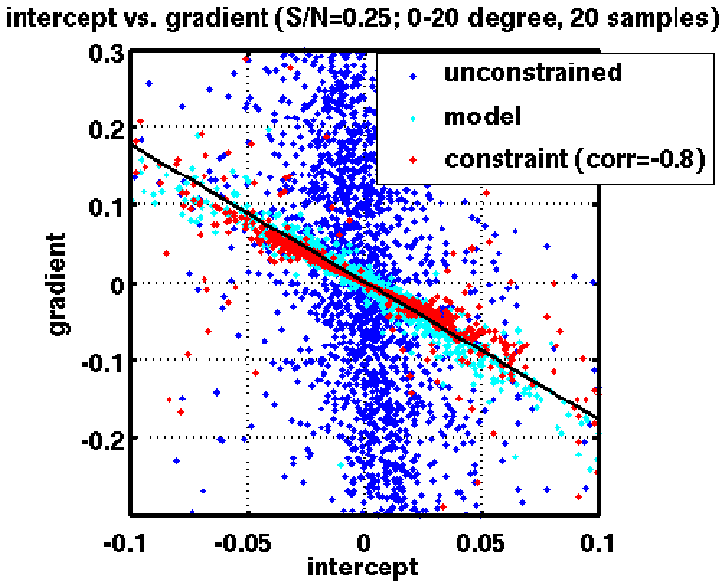

Figure 3.13 Cross-plot of the intercept and gradient of the model and the solutions of the unconstraint inversion and constraint inversion in which the correlation coefficient in constraint matrix Σ_m is changed to -0.8.

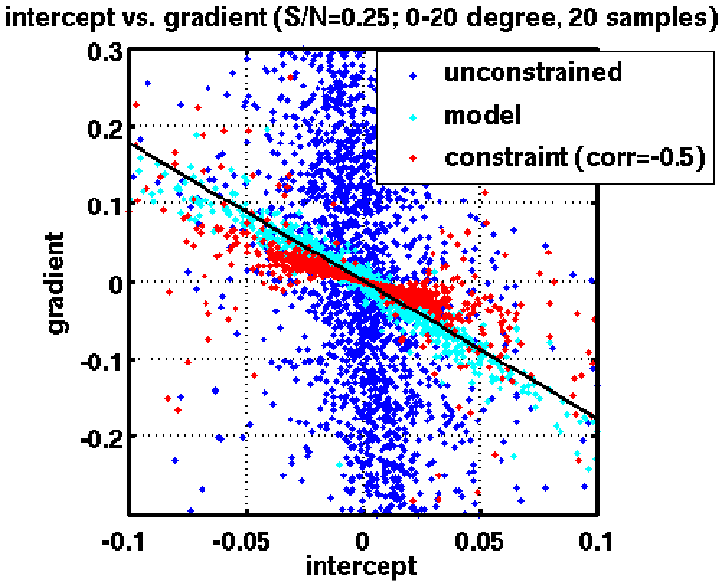

Figure 3.14 Cross-plot of the intercept and gradient of the model and the solutions of the unconstraint inversion and constraint inversion in which the correlation coefficient in constraint matrix Σ_m is changed to -0.5 (S/N=0.25, 0-20 degree angle range and 20 samples).

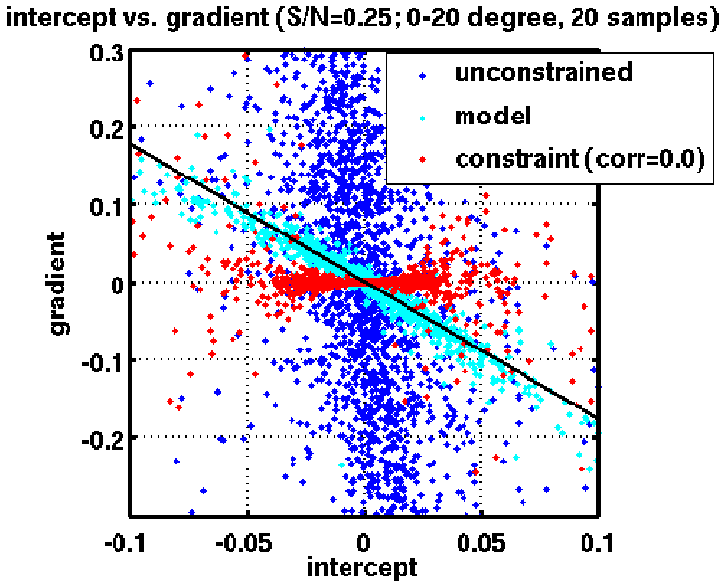

Figure 3.15 Cross-plot of the intercept and gradient of the model and the solutions of the unconstraint inversion and constraint inversion in which the correlation coefficient in constraint matrix Σ_m is changed to 0.0 (S/N=0.25, 0-20 degree angle range and 20 samples).

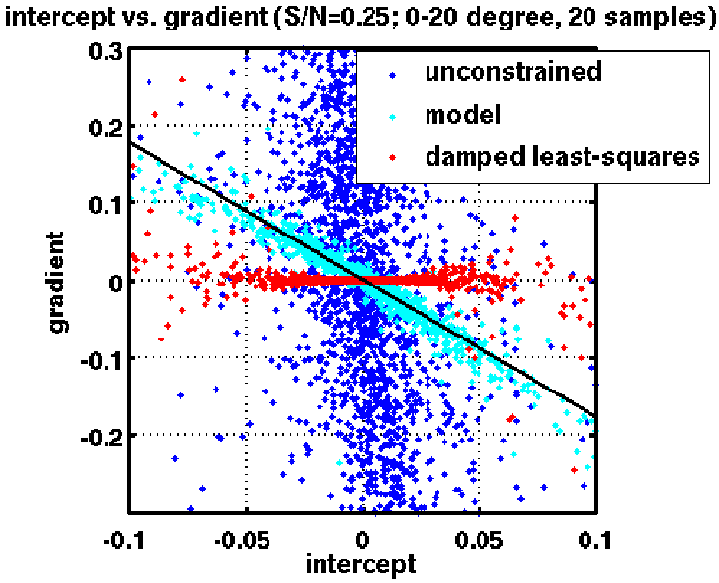

Figure 3.16 Cross-plot of the intercept and gradient of the model and the solutions of the unconstraint inversion and damped least-squares inversion (S/N=0.25, 0-20 degree angle range and 20 samples).

From the above discussion and illustration, we note that the constraints in the estimator $(\mathbf{G}^{\mathbf{T}}\mathbf{G}+\sigma_{\mathbf{N}}^{2}\Sigma_{\mathbf{m}}^{-1})^{-1}\mathbf{G}^{\mathbf{T}}\mathbf{d}$ stabilize the AVO inversion when the AVO inversion is significantly unstable. The constraints make the solution fall into the ballpark of the true answers; however, the correlation coefficient between the model parameters has an important impact on the fidelity of the solution. The constraints generate smaller gradients in the intercept-gradient AVO inversion when the noise/signal ratio is large. But if the correlation between parameters is weaker, we see the trend of the solutions of the inversion deviates from the trend of the model parameters. If the correlation between parameters is weak, usually in unconsolidated oil sands, we should pay more attention to the use of this estimator $(\mathbf{G}^{\mathbf{T}}\mathbf{G}+\sigma_{\mathbf{N}}^{2}\Sigma_{\mathbf{m}}^{-1})^{-1}\mathbf{G}^{\mathbf{T}}\mathbf{d}$. A few remarks are made here:

1. The mean of seismic amplitudes is close to zero within a large data time window because of the band limited frequency. However, the AVO inversion derives the reflectivity at each interface. The mean of reflectivities at multi interfaces should not be equivalent to the mean of the reflectivities at the individual interfaces. Thus the prior term of the model should not be assumed to be zero.

2. For the highly noisy data and a zero prior term assumption, the estimator $(\mathbf{G}^{\mathbf{T}}\mathbf{G}+\sigma_{\mathbf{N}}^{2}\Sigma_{\mathbf{m}}^{-1})^{-1}\mathbf{G}^{\mathbf{T}}\mathbf{d}$ results in gradients close to zero in the intercept-gradient analysis.
3. It is important to construct a reasonable prior term for the Bayesian AVO inversion. The prior term may be estimated from the prior covariance matrix (the diagonal elements) and an initial value of one or two parameters for the model, for example, the P wave reflectivity is close to the stack of the data. Building the initial model requires the interpretation of the data through an iterative process. Although an initial model can be built based on well logs, it is recommended to estimate the initial model mainly from data itself. The well logs are mainly used to provide the statistical relationships between elastic parameters in the form of covariance matrix.

3.3.4 Derivation of the Bayesian estimator by joint Gaussian distribution

The solution of the Bayesian constraint AVO inversion (3.19) can be derived from the joint Gaussian distribution of the data and prior model. The MAP solution can be obtained by maximizing the PDF of the joint Gaussian distribution of the data, *a priori* model parameters, and theory (relationship between the model and data). The basis of the multivariate Gaussian distribution and conditional distribution is shown in Figure 3.17. The uncertainty of the Bayesian estimator can be derived handily through the derivation of the joint Gaussian distribution.

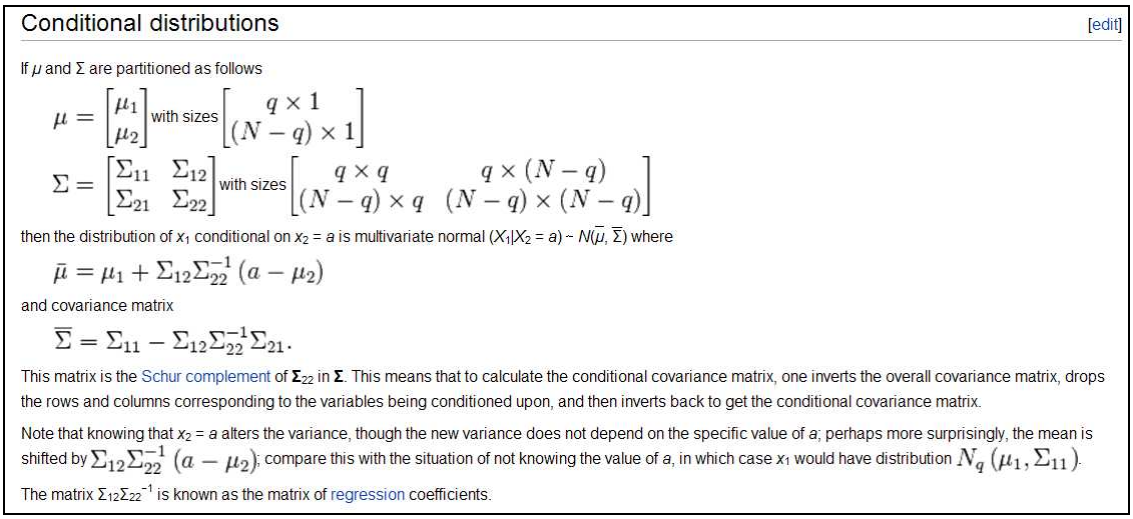

Conditional distributions [edit]

If μ and Σ are partitioned as follows

$$\mu = \begin{bmatrix} \mu_1 \\ \mu_2 \end{bmatrix} \text{ with sizes } \begin{bmatrix} q \times 1 \\ (N-q) \times 1 \end{bmatrix}$$

$$\Sigma = \begin{bmatrix} \Sigma_{11} & \Sigma_{12} \\ \Sigma_{21} & \Sigma_{22} \end{bmatrix} \text{ with sizes } \begin{bmatrix} q \times q & q \times (N-q) \\ (N-q) \times q & (N-q) \times (N-q) \end{bmatrix}$$

then the distribution of x_1 conditional on $x_2 = a$ is multivariate normal ($X_1|X_2 = a$) ~ $N(\bar{\mu}, \bar{\Sigma})$ where

$$\bar{\mu} = \mu_1 + \Sigma_{12}\Sigma_{22}^{-1}(a - \mu_2)$$

and covariance matrix

$$\bar{\Sigma} = \Sigma_{11} - \Sigma_{12}\Sigma_{22}^{-1}\Sigma_{21}.$$

This matrix is the Schur complement of $\mathbf{\Sigma}_{22}$ in $\mathbf{\Sigma}$. This means that to calculate the conditional covariance matrix, one inverts the overall covariance matrix, drops the rows and columns corresponding to the variables being conditioned upon, and then inverts back to get the conditional covariance matrix.

Note that knowing that $x_2 = a$ alters the variance, though the new variance does not depend on the specific value of a; perhaps more surprisingly, the mean is shifted by $\Sigma_{12}\Sigma_{22}^{-1}(a - \mu_2)$; compare this with the situation of not knowing the value of a, in which case x_1 would have distribution $N_q(\mu_1, \Sigma_{11})$.

The matrix $\Sigma_{12}\Sigma_{22}^{-1}$ is known as the matrix of regression coefficients.

Figure 3.17 Conditional multivariate normal distribution (Source: Wikipedia)

In the AVO inversion, we define the normal distribution of a model as $\mathbf{m} \sim \mathbf{N}(\overline{\mathbf{m}}, \Sigma_{\mathbf{m}})$ and that of the noise as $\varepsilon \sim \mathbf{N}(0, \Sigma_{\varepsilon})$ and the data and model have a relationship of $\mathbf{d} = \mathbf{G}\mathbf{m} + \varepsilon$, and the data $\mathbf{d}$ follows a normal distribution as

$\mathbf{d} \sim \mathbf{N}(\overline{\mathbf{d}}, \Sigma_{\mathbf{d}})$,

where $\overline{\mathbf{d}} = \mathbf{G}\overline{\mathbf{m}}$, and $\Sigma_{\mathbf{d}} = \mathbf{G}\Sigma_{\mathbf{m}}\mathbf{G}^{\mathbf{T}} + \Sigma_{\varepsilon}$.

If the model is conditional to the data, we have the joint distribution as

$$\begin{bmatrix} \mathbf{m} \\ \mathbf{d} \end{bmatrix} \sim \mathbf{N}\left(\begin{bmatrix} \overline{\mathbf{m}} \\ \overline{\mathbf{d}} \end{bmatrix}, \begin{bmatrix} \Sigma_{\mathbf{m}} & \Sigma_{\mathbf{m},\mathbf{d}} \\ \Sigma_{\mathbf{d},\mathbf{m}} & \Sigma_{\mathbf{d}} \end{bmatrix} \right) \tag{3.25}$$

where

$$\Sigma_{\mathbf{m},\mathbf{d}} = \Sigma_{\mathbf{m}}^{\mathbf{T}}\mathbf{G}^{\mathbf{T}}. \tag{3.26}$$

The distribution for $\mathbf{m}$ conditioning to $\mathbf{d}$ is Gaussian, therefore

$$\mathbf{p}(\mathbf{m} \mid \mathbf{d}) \sim \mathbf{N}(\overline{\mathbf{m}}_{\mathbf{m}|\mathbf{d}}, \Sigma_{\mathbf{m}|\mathbf{d}}) \tag{3.27}$$

$$\overline{\mathbf{m}}_{\mathbf{m}|\mathbf{d}} = \overline{\mathbf{m}} + \Sigma_{\mathbf{m},\mathbf{d}}\Sigma_{\mathbf{d}}^{-1}(\mathbf{d} - \overline{\mathbf{d}}) = \overline{\mathbf{m}} + \Sigma_{\mathbf{m}}^{\mathbf{T}}\mathbf{G}^{\mathbf{T}}(\mathbf{G}\Sigma_{\mathbf{m}}\mathbf{G}^{\mathbf{T}} + \Sigma_{\varepsilon})^{-1}(\mathbf{d} - \mathbf{G}\overline{\mathbf{m}}). \tag{3.28}$$

It can be proved equation (3.28) is equivalent to equation (3.19) – the maximum *a posteriori* solution (Menke, 1989; Tarantola, 2005). The covariance of the estimate (3.28) is

$$\Sigma_{\mathbf{m|d}} = \Sigma_{\mathbf{m}} - \Sigma_{\mathbf{m,d}}\Sigma_{\mathbf{d}}^{-1}\Sigma_{\mathbf{d,m}} = \Sigma_{\mathbf{m}} - \Sigma_{\mathbf{m}}^{\mathbf{T}}\mathbf{G}^{\mathbf{T}}(\mathbf{G}\Sigma_{\mathbf{m}}\mathbf{G}^{\mathbf{T}} + \Sigma_{\varepsilon})^{-1}\mathbf{G}\Sigma_{\mathbf{m}}. \quad (3.29)$$

The *a posteriori* distribution (3.27), in an explicit analytical form, contains the complete solution of the inversion, including the uncertainty. In much of the literature, Σm is assumed to be a symmetrical matrix (Menke, 1989; Tarantola, 2005).

3.3.5 Uncertainty analysis

The uncertainty of the Bayesian constraint inversion can be estimated by equation (3.29).

3.3.6 Distributions other than the Gaussian

The Gaussian probability distribution is mathematically most tractable (Duijndam, 1988a). The assumption of the Gaussian distribution makes the implementation of the inversion be formulated elegantly. However, a Gaussian distribution is not perfectly describing the prior or noise distribution in some cases and other distributions have been considered (Downton, 2005, Alemie and Sacchi, 2010, Duijndam, 1988a). The use of a double exponential or Laplace distribution leads to more robust l_1-norm estimators. The prior model PDF of a Laplace distribution is formulated as

$$\mathbf{p(m)} = \frac{1}{2^{\mathbf{n}/2}\,|\,\mathbf{C}\,|^{1/2}}\mathbf{e}^{-\sqrt{2}|\mathbf{C}^{-1/2}(\mathbf{x}-\mu)|} \quad (3.30)$$

where **n** is the number of parameters and μ and **C** are the mean and covariance matrix respectively.

The Cauchy distribution has been applied in the AVO inversion (Lin et al, 2008; Alemie and Sacchi, 2010). The Cauchy distribution is a long tail distribution. The incorporation of a Cauchy prior distribution leads to the sparsity in the solution.

3.4 IMPROVING AVO INVERSION FOR OIL SANDS RESERVOIR CHARACTERIZATION

The Bayesian AVO inversion incorporates the prior information such as rock properties into the inversion, stabilizes the inversion, and balances the seismic data and the rock

properties based on the stability need. In this sense, rock properties play an important role in generating a reliable solution. Some modifications of the Bayesian AVO inversion (equation (3.19)) are made based on the experience in applications of oil sands reservoir rock properties. The implementation of the modified Bayesian AVO inversion is carefully designed with the following considerations:

1. The AVO inversion/extraction can be performed on the time sample by time sample basis, if the wavelet variation with angle is neglectable. However, the wavelet does change with angle, and this change cannot be neglected if a large angle AVO inversion is performed. Implementation is based on time windows in this chapter to deal with the wavelet variation with angle in the real seismic data.
2. Spatial windowing is also used to reduce the uncertainty, which effectively increases the number of samples in the inversion.
3. Inversion is realized in the frequency domain. Reliabilities of the inversion for different frequency components are different because of the wavelet and noise difference. Usually the solution at the dominant frequency provides a constraint for more noisy or ill-posed frequency components.
4. The implementation of inversion in the frequency domain easily makes the solution include the low frequency components of the initial model. The information outside of seismic bandwidth is non-unique in the inversion, and this will mainly studied in the next chapter. The AVO inversion in this chapter mainly works within the frequency bandwidth of seismic data.
5. The maximum angle in the inversion for the density estimation in the case histories is chosen to be 40-45 degree for the oil sands reservoirs. Roy et al (2008) suggest a far angle of 60 degree in their case study on the oil sands. An angle larger than 45 degree requires a high fidelity processing and a question is raised on the issue of critical incidence at large angle. For the unconsolidated formations as in heavy oil reservoirs, the density variation is usually large, though less-correlated to the variations of P or S wave velocities. This makes the S/N ratio for the density contrasts relatively larger than normally thought and makes it possible

to extract the density information from the prestack data with relatively good quality. This is also reported by others (Tonn, 2010).

3.4.1 Potential of AVO in mapping heavy oil reservoir heterogeneity in the WCSB

Although AVO is still a good indicator for the top gas of reservoirs and has good uses in the in-situ development and monitoring in the heavy oils in the WCSB, one of the most desirable uses of AVO should be describing reservoir heterogeneities – lithological and geological heterogeneities, which is critical for the efficient open-pit mining and in-situ development of bitumen. AVO applications in the reservoir characterization for heavy oils have been traceable for the past decade (Downton and Lines, 2001; Tonn 2002; Gray et al, 2004; Anderson et al 2005; Bellman 2008; Roy et al 2008; Xu and Chopra, 2008; Dumitrescu and Lines, 2009; Tonn, 2010; Connelly, 2010). It is commonly understood that the density parameter is sensitive to the clay content in the heavy oil reservoirs in the WCSB and is able to map the reservoir lithological heterogeneity. However, unlike the AVO application for identifying the gas saturation in the unconsolidated sandstone, the lithology separation of the interbedded sand and shale appears more difficult.

3.4.2 Reducing uncertainty and prediction error in AVO inversion/extraction

Based on the discussion on $(\mathbf{G}^{\mathbf{T}}\mathbf{G}+\sigma_{\mathbf{N}}^{2}\Sigma_{\mathbf{m}}^{-1})^{-1}\mathbf{G}^{\mathbf{T}}\mathbf{d}$, we note that it prevents errors spreading wildly but the correlation coefficient in the covariance matrix may shift the trend in the inversion results from the rock property trends. To further constrain the solution to follow the rock property trend, it is necessary to include the prior term instead of dropping it.

In this chapter, the complete Bayesian estimator is adopted as follows to perform the Bayesian constraint AVO inversion,

$$\hat{\mathbf{m}}=(\mathbf{G}^{\mathbf{T}}\mathbf{G}+\sigma^{2}\Sigma_{\mathbf{m}}^{-1})^{-1}\mathbf{G}^{\mathbf{T}}\mathbf{d}+(\mathbf{G}^{\mathbf{T}}\mathbf{G}+\sigma^{2}\Sigma_{\mathbf{m}}^{-1})^{-1}\sigma^{2}\Sigma_{\mathbf{m}}{}^{-1}\overline{\mathbf{m}}\,. \tag{3.31}$$

This solution is a mix of the data influence and the prior model. The weights on both are flexibly chosen and adjusted by the signal to noise ratio, the singularity of $\mathbf{G}^{\mathrm{T}}\mathbf{G}$, and the sample population in the data **d**.

Downton and Lines (2001) adopt an approach to estimate signal and noise ratios in their data term only solution, which nicely handles the signal-noise-ratio and scaling between the prior covariance of the model and data. The formula used by Downton and Lines (2001) is copied here:

$$\hat{\mathbf{m}} = (\mathbf{G}^{\mathbf{T}}\mathbf{G} + \frac{2(\mathbf{Gm}-\mathbf{d})^{\mathbf{T}}(\mathbf{Gm}-\mathbf{d})}{(\mathbf{N}-1)\mathbf{m}^{\mathbf{T}}\Sigma_{\mathbf{m}}^{-1}\mathbf{m}}\Sigma_{\mathbf{m}}^{-1})^{-1}\mathbf{G}^{\mathbf{T}}\mathbf{d}, \tag{3.32}$$

where **N** is the sample number of the data. The final solution is obtained by using an initial model and a few iterations of updating (Downton and Lines, 2001). A similar treatment on the signal to noise ratio is adopted by Alemie and Sacchi (2010) as well.

Let's re-visit the estimator of the Bayesian constraint AVO inversion:

$$\hat{\mathbf{m}} = (\mathbf{G}^{\mathbf{T}}\mathbf{G} + \sigma^2\Sigma_{\mathbf{m}}^{-1})^{-1}\mathbf{G}^{\mathbf{T}}\mathbf{d} + (\mathbf{G}^{\mathbf{T}}\mathbf{G} + \sigma^2\Sigma_{\mathbf{m}}^{-1})^{-1}\sigma^2\Sigma_{\mathbf{m}}{}^{-1}\overline{\mathbf{m}} \tag{3.33}$$

In this equation, we assume the prior term and data term are perfectly scaled. Since the seismic data **d**, initial model $\overline{\mathbf{m}}$, and covariance matrix $\Sigma_{\mathbf{m}}$ are usually from different sources, the magnitudes of the data, model, or covariance have to be calibrated. In the implementation in this thesis, the initial model $\overline{\mathbf{m}}$ is derived from data, therefore, has the same magnitude as the seismic data but the covariance matrix is from well logs and so a constant scalar is applied on it to match the magnitude of seismic data. In equation (3.33), $\sigma^2\Sigma_{\mathbf{m}}^{-1}$ is commonly considered in practice as the combination of the noise-to-signal ratio and covariance of model parameters from the prior information (Cassassuce at el, 2004, Downton, 2005, Downton and Lines, 2001, Roy et al, 2008). The covariance of model parameters in the AVO inversion is derived from well logs and it needs multiple wells or time/depth segments. The essence of this covariance is the variances of parameters and the correlation coefficients between them. Although the covariance has been used as the prior constraint in the AVO inversion without deliberations on how to relate it to the signal-to-noise ratio (Downton 2005, Roy et al, 2008), it is worth it to be pointed out that the covariance should be normalized by the variance of the first model parameter (usually the P wave reflectivity at normal incidence). It is acceptable that the noise-to-signal ratio

is estimated locally at the time sample where the AVO inversion is conducted. But a global noise-to-signal ratio is suggested for a more stable solution for the entire data.

In general, the AVO application works well in stratigraphic areas with little or mild structures. In such areas, the rock properties within the same formation and seismic characters at the same formation boundary show a strong lateral correlation. Conventionally, the AVO inversion is applied on the data at every common depth point (CDP). Commonly, supergathers (or common offset stack gather, Ostrander gather) are used in the AVO interpretation and inversion. A supergather is generated by stacking a group of neighboring CDP gathers into a single CDP gather. The supergather has a higher S/N ratio than the single CDP gather, and is useful for quality-control and scanning AVO anomalies and sometimes is used in the AVO inversion for poor quality data. Although supergathers improve the quality of data and the reliability of AVO inversion, the number of neighboring CDPs should not be large otherwise the quality might be poor when the local dips exist. Even if the event is flat, the small geological lateral variation, where the AVO anomalies are small but very important, may be smeared by the supergathers. It is better to apply the inversion on multi-lateral locations simultaneously to honor the stratigraphical lateral correlation to make the AVO inversion more robust without damaging geological characters. With pre-stack time migration (PSTM) becomes a common process in seismic data processing, the gathers generated by PSTM are used by AVO analysis as well. PSTM positions reflections to correct subsurface locations and improves the signal/noise ratio in the output gathers. Applying the AVO inversion on a group of neighboring PSTM gathers simultaneously can honor the lateral continuity of the geology as well.

3.4.2.1 Initial model for the prior term

An initial model is used by the prior term in equation (3.19) and should be defined carefully. Building an initial model usually requires the *a priori* information on the geology, lithology, and rock property trends in the studied area. The implementation of the AVO inversion in this thesis emphasize including reliable information from data in

the initial model. Local mud-rock lines provide an analytical relationship between two parameters in the two-term AVO inversion, such as two term Shuey's approximation of the Zoeppritz equation. The near offset or full offset stack is close to the AVO intercept, which should be a good prior term. The two-parameter AVO inversion should be more stable than the three-parameter AVO inversion. For the three-term inversion, the solution of the two-parameter AVO inversion and local rock physical relationships provide the *a priori* information of the initial model. This becomes one of the important characteristics in the conventional AVO analysis and application in the case histories in heavy oils in the WCSB in this thesis. Building a reliable model needs much interpretation and an iterative process.

3.4.3 Utilizing stratigraphy in AVO inversion

In the stratigraphic settings, any location should not be isolated from neighboring locations. The use of lateral stratigraphic correlations should improve the robustness of the AVO inversion. Brac et al (1988) are amongst the first to incorporate the lateral geological constraint in the post-stack impedance inversion. In their formulation of the objective function, the geological constraint term is controlled by an empirical lateral length controlling the smoothness of the final model and its variation along the stratigraphic horizons. In their constrained AVO inversion, Tonellot et al (1999) define the prior term in the objective function using a covariance matrix exponentially weighted by the distance along the stratigraphic horizons. Similar to what is done by Tonellot et al (1999), Buland et al (2003) assume the lateral coupling of the model diminishes exponentially and define a correlation function by the covariance of the model parameters weighted by the exponential function of the distance between the current and neighboring CDP locations. The above exponential spatial covariance operator has been suggested by Tarantola (2005) as well. Bosch et al (2009) cast the inverse problem in the Bayesian framework with incorporating the prior information from geostatistics: the simple co-kriging estimate and its covariance that result from the geostatistical interpolation of the well log data.

In the following the derivation of the constraint for the AVO inversion on multiple spatial locations in a neighborhood is given. The time domain expression and subsequently the frequency domain one are derived. Assume there are N spatial locations in a neighborhood to be inverted simultaneously by the AVO inversion. For the i^{th} location, the angle-dependent data vector is $\mathbf{d}_i$, the noise vector is $\mathbf{n}_i$, and the model parameter vector is $\mathbf{m}_i$, and the linear AVO equations form the matrix $\mathbf{G}_i$. The linear inverse problem is posed as

$$\begin{pmatrix} \mathbf{G}_1 & 0 & \cdot & \cdot & \cdot & 0 \\ 0 & \mathbf{G}_2 & 0 & \cdot & \cdot & \cdot \\ \cdot & 0 & \cdot & \cdot & \cdot & \cdot \\ \cdot & \cdot & \cdot & \cdot & \cdot & \cdot \\ \cdot & \cdot & \cdot & \cdot & \cdot & 0 \\ 0 & \cdot & \cdot & \cdot & 0 & \mathbf{G}_N \end{pmatrix} \begin{pmatrix} \mathbf{m}_1 \\ \mathbf{m}_2 \\ \cdot \\ \cdot \\ \cdot \\ \mathbf{m}_N \end{pmatrix} = \begin{pmatrix} \mathbf{d}_1 + \mathbf{n}_1 \\ \mathbf{d}_2 + \mathbf{n}_2 \\ \cdot \\ \cdot \\ \cdot \\ \mathbf{d}_N + \mathbf{n}_N \end{pmatrix}, \tag{3.34}$$

Equation (3.33) can be rewritten in the form of super-matrices and super-vectors, which are expressed in a large font size as follows.

$$\mathbf{Gm} = \mathbf{d} + \mathbf{n} \tag{3.35}$$

Each individual $\mathbf{m}_i$ includes three elastic parameters related to the P and S impedance and density. The covariance matrix $\mathbf{\Sigma_m}$ for the three parameters can be obtained from the prior information. If $\mathbf{d}_i$'s in the window are picked to follow the stratigraphy, a strong correlation should exist between them. Therefore, the covariance between $\mathbf{m}_i$ and $\mathbf{m}_j$, should combine the correlation between them and the constraints of rock properties. It takes a form of $r_{ij}\,\mathbf{\Sigma_m}$, where r_{ij} is the correlation coefficient with a reasonable value coming from the *a priori* information. The super covariance is

$$\mathbf{\Sigma_m} = \begin{pmatrix} \Sigma_\mathbf{m} & \mathbf{r}_{12}\Sigma_\mathbf{m} & \cdot & \cdot & \cdot & \mathbf{r}_{1n}\Sigma_\mathbf{m} \\ \mathbf{r}_{21}\Sigma_\mathbf{m} & \Sigma_\mathbf{m} & \mathbf{r}_{23}\Sigma_\mathbf{m} & \cdot & \cdot & \cdot \\ \cdot & \mathbf{r}_{32}\Sigma_\mathbf{m} & \cdot & \cdot & \cdot & \cdot \\ \cdot & \cdot & \cdot & \cdot & \cdot & \cdot \\ \cdot & \cdot & \cdot & \cdot & \cdot & \mathbf{r}_{n-1,n}\Sigma_\mathbf{m} \\ \mathbf{r}_{n1}\Sigma_\mathbf{m} & \cdot & \cdot & \cdot & \mathbf{r}_{n,n-1}\Sigma_\mathbf{m} & \Sigma_\mathbf{m} \end{pmatrix} \tag{3.36}$$

The implementation in this chapter uses the stack volume to extract the correlation coefficient r_{ij} between neighboring locations. The Bayesian estimator for a mini-cube of data can be derived using equations (3.34)-(3.36) and an initial model.

3.4.4 AVO inversion in frequency domain

A linearized form is preferred to apply AVO inversion in the frequency domain. The data, recorded as a function of the source-receiver distance (offset), must be transformed from the offset domain to the angle domain. This transform can be completed by using a common-angle migration, ray tracing, or the popular approximate offset-angle relations based on a smooth background velocity model (Walden, 1991).

3.4.4.1 Bayesian constraint AVO inversion in the frequency domain

The linear PP AVO equation (3.1) is re-written in the time domain as follows,

$$\mathbf{r}(\mathbf{t},\theta) = \mathbf{a}(\mathbf{t},\theta)\frac{\Delta\alpha}{\alpha} + \mathbf{b}(\mathbf{t},\theta)\frac{\Delta\beta}{\beta} + \mathbf{c}(\mathbf{t},\theta)\frac{\Delta\rho}{\rho} \tag{3.37}$$

Where α, β, and ρ are the average P-wave velocity, S-wave velocity, and density, $\Delta\alpha/\alpha$, $\Delta\beta/\beta$, and $\Delta\rho/\rho$ are the changes in the P-wave and S-wave velocities and density across the interface, and θ is the average angle of incidence and transmission across the interface, and **a**, **b**, and **c** symbolically stand for the coefficients of the velocity and density contrasts in equation (3.1). To formulate a linear equation in the frequency domain, an assumption is made that **a**, **b**, and **c** are independent of time. This assumption is usually valid if the time window is not large and the lithology change is not dramatic (The changes from clastics to carbonates should be large ones). Under such an assumption, equation (3.37) can be formulated in the frequency domain as follows,

$$\tilde{\mathbf{r}}(\mathbf{f},\theta) = \mathbf{a}(\theta)\tilde{\mathbf{r}}_{\alpha}(\mathbf{f}) + \mathbf{b}(\theta)\tilde{\mathbf{r}}_{\beta}(\mathbf{f}) + \mathbf{c}(\theta)\tilde{\mathbf{r}}_{\rho}(\mathbf{f}), \tag{3.38}$$

where $\tilde{\mathbf{r}}_{\alpha}$, $\tilde{\mathbf{r}}_{\beta}$, and $\tilde{\mathbf{r}}_{\rho}$ are the contrasts of the P and S velocities and density in the frequency domain. Equation (3.38) shows the frequency components are independent on each other. Therefore, a linear inverse problem can be posed for each frequency as follows,

$$\tilde{\mathbf{r}}(\mathbf{f},\theta) = \tilde{\mathbf{G}}(\theta)\tilde{\mathbf{m}}(\mathbf{f}) + \tilde{\varepsilon}(\mathbf{f}), \tag{3.39}$$

where '~' represents in the frequency domain.

If the prior model is defined by $\begin{pmatrix} \overline{\mathbf{m}}(\mathbf{t}) \\ \Sigma_{\mathbf{m}}(\mathbf{t}) \end{pmatrix}$ in the time domain, then it is defined as $\begin{pmatrix} \tilde{\overline{\mathbf{m}}}(\mathbf{f}) \\ \tilde{\Sigma}_{\mathbf{m}}(\mathbf{f}) \end{pmatrix}$ in the frequency domain, where the $\tilde{\overline{\mathbf{m}}}(\mathbf{f})$ can be obtained through the Fourier transform of $\overline{\mathbf{m}}(\mathbf{t})$ and the $\tilde{\Sigma}_{\mathbf{m}}(\mathbf{f})$ can be obtained from $\Sigma_{\mathbf{m}}(\mathbf{t})$, which is derived as follows.

The rock property prior information $\Sigma_{\mathbf{m}}$ is expressed as

$$\Sigma_{\mathbf{m}} = \begin{pmatrix} \sigma_1^2 & \rho_{12}\sigma_1\sigma_2 & \rho_{13}\sigma_1\sigma_3 \\ \rho_{12}\sigma_1\sigma_2 & \sigma_2^2 & \rho_{23}\sigma_2\sigma_3 \\ \rho_{13}\sigma_1\sigma_3 & \rho_{23}\sigma_2\sigma_3 & \sigma_3^2 \end{pmatrix} = \sigma_1^2 \mathbf{C}_{\mathbf{m}}, \tag{3.40}$$

where σ_1, σ_2, and σ_3 are variances (or standard deviations) of elastic parameters, ρ_{12}, ρ_{13}, and ρ_{23} are the correlation coefficients between these elastic parameters, and

$$\mathbf{C}_{\mathbf{m}} = \begin{pmatrix} 1 & \rho_{12}\sigma_2/\sigma_1 & \rho_{13}\sigma_3/\sigma_1 \\ \rho_{12}\sigma_2/\sigma_1 & \sigma_2^2/\sigma_1^2 & \rho_{23}\sigma_2\sigma_3\sigma_1^2 \\ \rho_{13}\sigma_3/\sigma_1 & \rho_{23}\sigma_2\sigma_3/\sigma_1^2 & \sigma_3^2/\sigma_1^2 \end{pmatrix}. \tag{3.41}$$

$\mathbf{C}_{\mathbf{m}}$ can be defined by the rock properties and regarded as stationary if the mud-rock line change is small within a certain depth/time range (Downton and Lines, 2001). Then, we have

$$\Sigma_{\mathbf{m}}(\mathbf{t}) = \sigma_1^2(\mathbf{t})\mathbf{C}_{\mathbf{m}} \tag{3.42}$$

and

$$\tilde{\Sigma}_{\mathbf{m}}(\mathbf{f}) = \tilde{\sigma}_1^2(\mathbf{f})\mathbf{C}_{\mathbf{m}} \tag{3.43}$$

The linear inversion can still be performed for each frequency component with the Bayesian constraints. The estimator of the Bayesian constraint inversion in the frequency domain is

$$\tilde{\hat{\mathbf{m}}}(\mathbf{f}) = (\tilde{\mathbf{G}}^{\mathrm{T}}\tilde{\mathbf{G}} + \tilde{\sigma}^2\tilde{\Sigma}_{\mathbf{m}}^{-1})^{-1}\tilde{\mathbf{G}}^{\mathrm{T}}\tilde{\mathbf{d}} + (\tilde{\mathbf{G}}^{\mathrm{T}}\tilde{\mathbf{G}} + \tilde{\sigma}^2\tilde{\Sigma}_{\mathbf{m}}^{-1})^{-1}\tilde{\sigma}^2\tilde{\Sigma}_{\mathbf{m}}^{-1}\tilde{\overline{\mathbf{m}}}, \tag{3.44}$$

and the covariance of the estimator is

$$\tilde{\tilde{\Sigma}}_{\tilde{\tilde{\mathbf{m}}}} = \tilde{\tilde{\Sigma}}_{\mathbf{m}} - \tilde{\tilde{\Sigma}}_{\mathbf{m}}\tilde{\mathbf{G}}^{\mathbf{T}}(\tilde{\mathbf{G}}\tilde{\tilde{\Sigma}}_{\mathbf{m}}\tilde{\mathbf{G}}^{\mathbf{T}} + \tilde{\tilde{\Sigma}}_{\mathbf{m}})^{-1}\tilde{\mathbf{G}}\tilde{\tilde{\Sigma}}_{\mathbf{m}} \ . \tag{3.45}$$

The equivalent to equations (3.34)-(3.36) in the frequency domain can be derived in a similar way to include the lateral correlation of multiple CDP locations.

To implement AVO inversion in the frequency domain, data need to be sorted into the angle domain, and the coefficients of the unknowns in the linear AVO equation need to be time-independent within the window of the inversion. But the frequency domain AVO inversion has advantages:

1. The AVO inversion is performed on every frequency component independently, but relationships exist between the frequency components so that the frequency components with high reliabilities can constrain other less reliable components. The inversion can be done in a bootstrapping manner.
2. The issue of the wavelet variation with angle is resolved naturally in the frequency domain. The loss due to the tuning for high frequency components at a far angle (see Chapter 5) can be handled by the inversion in the frequency domain.

3.4.4.2 Considerations in implementation in the frequency domain for Athabasca oil sands

In the implementation of the frequency domain AVO inversion, a target oriented approach is adopted for the Athabasca oil sands. The window includes the Clearwater Formation to the top of the Paleozoic. The reflection of the Cretaceous and Paleozoic interface is usually the strongest in Athabasca. To avoid its dominance in the frequency spectra, this interface is modeled beforehand and replaced with zero reflection. The Paleozoic and Cretaceous data are inverted separately and the results are welded afterwards.

3.4.5 Conditions for reliable three-parameter AVO inversion

In the above, the theory of the constraint AVO inversion and the improvement of reliabilities in the inversion are discussed. However, it is worth it to be kept in mind that

the three-term linear AVO inversion is typically ill-conditioned. To make good use of the three-parameter AVO inversion, we have to meet the requirements on seismic data and reservoir properties:

1. Reliable AVO inversion needs good quality data, long offsets and a high signal/noise ratio. This requires better data processing, especially the techniques to recover far offset data that work on the residual moveout, anisotropy, high frequency loss, and coherent noises.
2. Based on the rock property study, the density contrast at the target zone is large in oil sands reservoirs. Most heavy oil reservoirs are buried in unconsolidated sandstones with porosity larger than 28%; therefore, the density contrast between reservoir and non-reservoir should be strong, compared with in tight clastic formations. Thus, it is possible to obtain the density information from seismic data with a better reliability. This is also observed by peers working on oil sands reservoirs in Athabasca (Tonn, 2010).
3. The method presented here can be applied in any geological setting, but it shows a better feasibility to detect the lithology variation in heavy oil reservoirs in the WCSB where the contrasts of the bulk density due to the lithology facies variation are usually large, reducing the uncertainty in the inversion.

3.4.6 A synthetic example

A synthetic AVO angle gather with a 0-40 degree angle range is used to compare different inversion methods: the least-squares, Bayesian constraint inversions (data term only but with extract covariance of the model reflectivities), and the improved Bayesian constraint inversion. The comparison is made in Figure 3.18. The amplitude ratio of the signal and noise is 2 to 1 in the gather. Well logs derive the rock property covariance matrix, which is

$$\mathbf{C_m} = \begin{pmatrix} \sigma_{\mathbf{rp}}^2 & \mathbf{r}_{\mathbf{ps}}\sigma_{\mathbf{rp}}\sigma_{\mathbf{rs}} & \mathbf{r}_{\mathbf{p}\rho}\sigma_{\mathbf{rp}}\sigma_{\mathbf{r}\rho} \\ \mathbf{r}_{\mathbf{ps}}\sigma_{\mathbf{rp}}\sigma_{\mathbf{rs}} & \sigma_{\mathbf{rs}}^2 & \mathbf{r}_{\mathbf{s}\rho}\sigma_{\mathbf{rs}}\sigma_{\mathbf{r}\rho} \\ \mathbf{r}_{\mathbf{p}\rho}\sigma_{\mathbf{rp}}\sigma_{\mathbf{r}\upsilon} & \mathbf{r}_{\mathbf{s}\rho}\sigma_{\mathbf{rs}}\sigma_{\mathbf{r}\rho} & \sigma_{\mathbf{r}\upsilon}^2 \end{pmatrix} = \sigma_{\mathbf{rp}}{}^2 \begin{pmatrix} 1.000 & 2.418 & 0.2546 \\ 2.418 & 6.709 & 0.5102 \\ 0.2546 & 0.5102 & 0.1455 \end{pmatrix}. \qquad (3.46)$$

where $\sigma_{\mathbf{rp}}$, $\sigma_{\mathbf{rs}}$, and $\sigma_{\mathbf{r\rho}}$ are the standard deviations of P and S reflectivity ($\mathbf{r_p}$ and $\mathbf{r_s}$) and density reflectivity ($\mathbf{r}_\rho$) derived from well logs, and $\mathbf{r_{ps}}$, $\mathbf{r_{p\rho}}$ and $\mathbf{r_{s\rho}}$. are the correlation coefficients between P, S, and density reflectivities. The correlation coefficient between the P and S reflectivities, $\mathbf{r_p}$ and $\mathbf{r_s}$, is 0.9336, which is very high; the correlation coefficient between P impedance and density reflectivities, $\mathbf{r_p}$ and $\mathbf{r_\rho}$, is 0.6648; and the one between S impedance and density reflectivities, $\mathbf{r_s}$ and $\mathbf{r_\rho}$, is 0.5164.

This synthetic example shows the Bayesian inversion is able to extract the reliable density reflectivity from AVO gathers when the data quality is good, the angle is large enough up to 40 degrees and P and S impedance reflectivities are highly correlated. It is noted that even the data term-only Bayesian solution is reasonably good in spite of the lack of accuracy for small reflections.

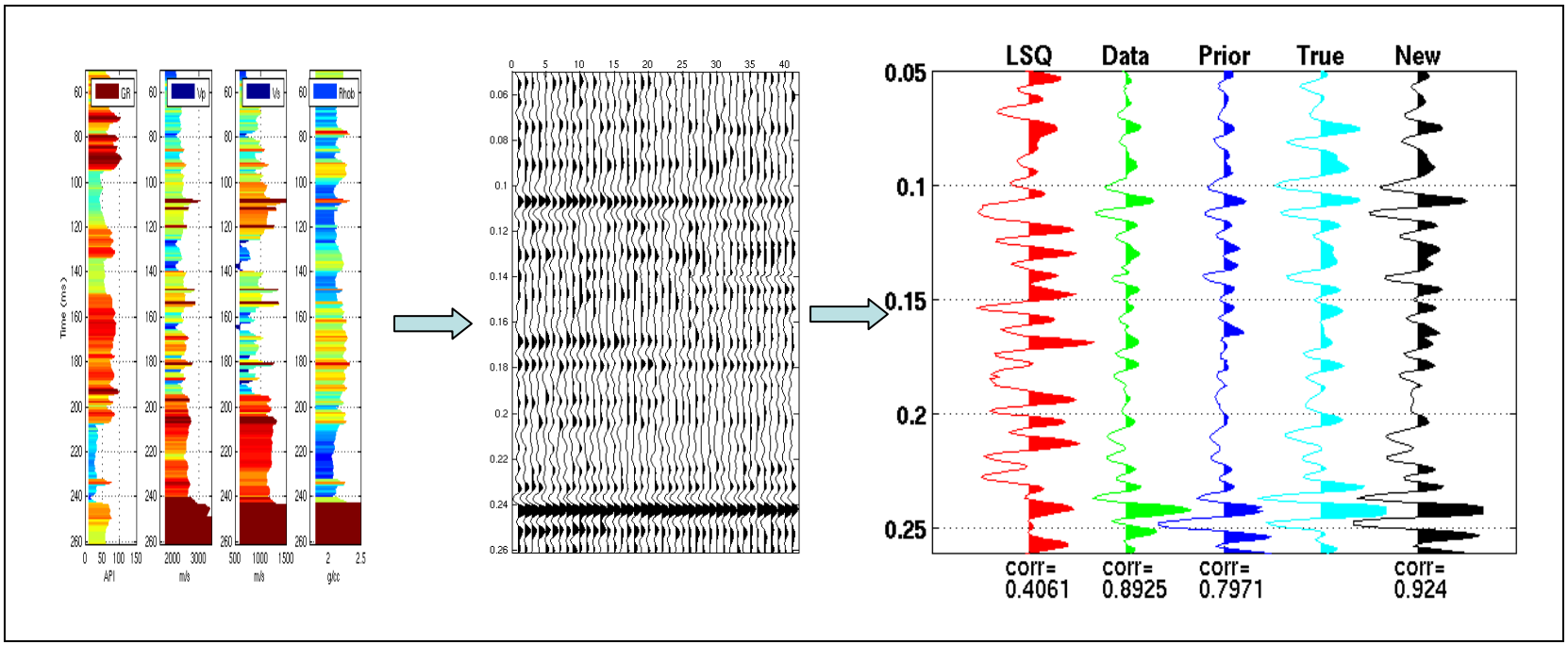

Figure 3.18 Comparison of density reflectivity derived by application of different AVO inversion methods on a synthetic gather. Well logs to generate the synthetic gather are shown on the left panel. The synthetic gather in the middle panel (inclusive of noise) is sorted with respect to the angle and the range of angles used is from 0° (left) to 40° (right). On the right panel, the red trace is density reflectivity obtained from the application of least-squares inversion and scaled down three times for display; the green trace is obtained after application of the Bayesian-constrained AVO inversion—data term only (equation 3.19); the blue trace is obtained after application of the Bayesian-constrained AVO inversion—prior term only (equation 3.19); the cyan trace is the true density reflectivity calculated from the density log; and the black trace on the extreme right is obtained by the application of the improved three-term Bayesian AVO inversion. The correlation coefficients between the inverted and true density reflectivities are marked under each inverted trace. The black trace on the right has the highest correlation coefficient.

3.5 EXTENSION TO MULTI-COMPONENT AVO INVERSION/EXTRACTION

3.5.1 Multi-component AVO inversion/extraction

Multi-component seismic acquisition introduces more data and information and promises more reliable AVO extraction/inversion (Stewart, 1990; Larsen, 1999; Margrave et al, 2001). It has been noted that joint PP and PS inversion is able to generate more robust rock property estimates; however, the use of PS data in the AVO analysis is challenged by issues in data processing, such as the statics issue in the shear wave onshore data and the resolution and quality issues in the converted wave data. The mix of advantages and challenges in the joint PP and PS use in the reservoir characterization makes it an interesting topic. Discussion on a reliable joint PP and PS AVO inversion is made in this section and the application on real multi-component seismic data will be done in the future.

Stewart (1990) uses the following objective function to jointly extract P wave velocity, S wave velocity contrasts $\Delta\alpha/\alpha$ and $\Delta\beta/\beta$ from the PP and PS datasets.

$$\varepsilon = \sum_{i=1}^{\#offsets} \left(R^{pp} - a\frac{\Delta\alpha}{\alpha} - b\frac{\Delta\beta}{\beta} \right)^2 + \left(R^{ps} - c\frac{\Delta\alpha}{\alpha} - d\frac{\Delta\beta}{\beta} \right)^2 , \tag{3.47}$$

where

$$a = \frac{1}{8}\left(1 - \frac{4\beta^2}{\alpha^2}\sin^2\theta + \frac{4}{\cos^2\theta} \right),$$

$$b = -\frac{4\beta^2}{\alpha^2}\sin^2\theta,$$

$$c = -\frac{\alpha\tan\varphi}{8\beta}\left(1 - \frac{2\beta^2}{\alpha^2}\sin^2\theta + \frac{2\beta}{\alpha}\cos\theta\cos\varphi \right),$$

$$d = \frac{\alpha\tan\varphi}{2\beta}\left(\frac{4\beta^2}{\alpha^2}\sin^2\theta - \frac{4\beta}{\alpha}\cos\theta\cos\varphi \right).$$

The R^{pp} and R^{ps} in the above equation are defined as (Stewart, 1990):

$$R^{pp}(\theta) \sim \frac{1}{2}\left(1 - 4\frac{\beta^2}{\alpha^2}\sin^2\theta\right)\frac{\Delta\rho}{\rho} + \frac{1}{2\cos^2\theta}\frac{\Delta\alpha}{\alpha} - \frac{4\beta^2}{\alpha^2}\sin^2\theta\frac{\Delta\beta}{\beta},$$

$$R^{ps}(\theta) \sim \frac{-\alpha\tan\varphi}{2\beta}\left[\left(1 - \frac{2\beta^2}{\alpha^2}\sin^2\theta + \frac{2\beta}{\alpha}\cos\theta\cos\varphi\right)\frac{\Delta\rho}{\rho}\right.$$

$$\left. - \left(\frac{4\beta^2}{\alpha^2}\sin^2\theta - \frac{4\beta}{\alpha}\cos\theta\cos\varphi\right)\frac{\Delta\beta}{\beta}\right], \tag{3.48}$$

where θ is the average of P wave angle of incidence and transmission through the interface, φ is the average of S wave angles of reflection and its associated transmission angle. In addition, Gardner's relationship between the density and P wave velocity, $\rho \sim k\alpha^{1/4}$ and $\frac{\Delta\rho}{\rho} \sim \frac{1}{4}\frac{\Delta\alpha}{\alpha}$, is used to convert the density term Δρ/ρ in Rpp and Rps into a P velocity term Δα/α.

From the objective function (3.47), the solution of the inversion becomes the weighted stack of the PP and PS data. Margrave et al (2001) show the advantage of the joint weighted stacks of PP and PS data by the uncertainty analysis and application of the joint inversion in real data cases. The above objective function is extended to include a third unknown – density Δρ/ρ (Larsen, 1999). The published application (Larsen, 1999, Margrave et al 2001) of the joint inversion mainly shows the superior results of P and S impedances derived from the joint PP and PS data. In addition, the time sample based implementation of the joint PP and PS AVO inversion is suggested by these researchers (i.e. time-slicing the 3D data). It is suggested in this thesis that joint inversion be implemented in the frequency domain. In addition, the reliability of the three-parameter joint inversion is investigated because it is more appealing to extract the reliable density information from the joint inversion for lithology discrimination in heavy oils in the WCSB.

3.5.2 Evaluation of stability of joint PP and PS inversion

The joint PP and PS AVO inversion can be expressed using matrices and vectors. The PP and PS linear inverse problems are expressed individually as

$\mathbf{d}_1=\mathbf{G}_1\mathbf{m}+\mathbf{n}_1$ for PP

and

$\mathbf{d}_2=\mathbf{G}_2\mathbf{m}+\mathbf{n}_2$ for PS.

where $\mathbf{d}_1$ and $\mathbf{d}_2$ are respectively the PP and PS AVO data, $\mathbf{m}$ is the model, $\mathbf{n}_1$ and $\mathbf{n}_2$ are respectively the noise in the PP and PS AVO data, and $\mathbf{G}_1$ and $\mathbf{G}_2$ are matrices determined by the angles and linear AVO equations for PP and PS data. It is assumed that $\mathbf{n}_1$ and $\mathbf{n}_2$ follow the same Gaussian distribution e.g. $\varepsilon \sim \mathbf{N}(0,\Sigma_\varepsilon)$. $\mathbf{d}_1$ and $\mathbf{d}_2$ may have different sample numbers. The least squares inversion minimizes the following objective function.

$$\mathbf{J}=\left\|\mathbf{G}_1\mathbf{m}-\mathbf{d}_1\right\|^2+\left\|\mathbf{G}_2\mathbf{m}-\mathbf{d}_2\right\|^2 \tag{3.49}$$

or

$$\mathbf{J}=\left\|\begin{pmatrix}\mathbf{G}_1\\ \mathbf{G}_2\end{pmatrix}\mathbf{m}-\begin{pmatrix}\mathbf{d}_1\\ \mathbf{d}_2\end{pmatrix}\right\|^2. \tag{3.50}$$

The least squares solution is

$$\hat{\mathbf{m}}=(\mathbf{G}_1^{\mathrm{T}}\mathbf{G}_1+\mathbf{G}_2^{\mathrm{T}}\mathbf{G}_2)^{-1}(\mathbf{G}_1^{\mathrm{T}}\mathbf{d}_1+\mathbf{G}_1^{\mathrm{T}}\mathbf{d}_1). \tag{3.51}$$

The covariance of this estimator is

$$\Sigma_{\hat{\mathbf{m}}}=\sigma_{\mathbf{n}}^2(\mathbf{G}_1^{\mathrm{T}}\mathbf{G}_1+\mathbf{G}_2^{\mathrm{T}}\mathbf{G}_2)^{-1} \tag{3.52}$$

To understand the advantage of the joint PP and PS inversion on improving the stability, one can compare the condition number of $\mathbf{G}_1^{\mathrm{T}}\mathbf{G}_1+\mathbf{G}_2^{\mathrm{T}}\mathbf{G}_2$ with those of $\mathbf{G}_1^{\mathrm{T}}\mathbf{G}_1$ and $\mathbf{G}_2^{\mathrm{T}}\mathbf{G}_2$.

Table 3.1 Velocities and density above and below an interface to test the PP and PS joint inversion (after Larsen, 1999).

Layer	α (m/s)	β (m/s)	ρ (g/cc)
1	3000	1500	2.294
2	4000	2000	2.465

Using the elastic parameters for an interface in Table 3.1 (Source: Larsen, 1999), we design a model of PP and PS reflections at the interface assuming a 0-35 degree angle range for the PP data and the maximum PS incident angle of 45 degree. If only P and S reflectivities are inverted, the condition numbers of the $\mathbf{G}^T\mathbf{G}$ matrix, the ratio of the largest to the smallest eigenvalues, for the PP only, PS only, and joint PP and PS inversions are respectively 48.5, 14.0, and 2.75. We note that the joint PP and PS inversion decreases the condition number rapidly, which stabilizes the inversion. If three parameters are inverted from the joint PP and PS AVO, the condition numbers of $\mathbf{G}^T\mathbf{G}$ matrix for the PP only, PS only, and joint PP and PS inversion are respectively 3.19×10^4, 2.39, and 7.02. The density solution should have a similar uncertainty by using the joint PP and PS inversion or PS inversion.

3.5.3 Joint multi-component AVO inversion with prior information

The l_2 norm objective function of the joint PP and PS inversion is expressed as

$$\mathbf{J} = \mathbf{C}_{\mathbf{PP}} \left\| \mathbf{G}_{\mathbf{PP}}\mathbf{m} - \mathbf{d}_{\mathbf{PP}} \right\|^2 + \mathbf{C}_{\mathbf{PS}} \left\| \mathbf{G}_{\mathbf{PS}}\mathbf{m} - \mathbf{d}_{\mathbf{PS}} \right\|^2 + \mathbf{C}_{\mathbf{m}} \left\| \mathbf{m} - \mathbf{m}^{\mathbf{prior}} \right\|^2 \tag{3.53}$$

where $\mathbf{d_{PP}}$ and $\mathbf{d_{PS}}$ stand for the PP and PS data, and $\mathbf{C_{PP}}$, $\mathbf{C_{PS}}$, and $\mathbf{C_m}$ represent the covariance of the PP and PS data and the model respectively. $\mathbf{m^{prior}}$ is the prior model. $\mathbf{G_{PP}}$ and $\mathbf{G_{PS}}$ are the theory of the PP and PS AVO, usually the linear approximations of Zoeppritz equations.

3.5.4 Discussions on the PP-PS joint inversion

3.5.4.1 Preference in the frequency domain

PP and PS datasets contain different frequency bandwidths. Usually, the PS bandwidth is not as wide as the PP bandwidth even if all these bandwidths are measured in the PP travel time domain. The joint AVO inversion should only be applied on the bandwidth contained in both components, if the typical time domain sample-by-sample implementation of the AVO inversion is applied. It should be more reasonable that the joint PP and PS inversion is applied for the frequencies contained in both the PP and PS

data while the PP AVO inversion is only applied in the high frequency contained only in the PP data.

3.5.4.2 Amplitude scaling discrepancy of PP and PS

The PP and PS data usually pass through different processing flows. This may cause the scaling of both datasets not proportional to the true energy partition ratio of the PP and PS waves. The amplitudes of the PP and PS data can be calibrated by modeling (Margrave et al, 2001).

3.5.5 A synthetic example

The PP and PS joint AVO inversion discussed in this section is tested by a synthetic example. Figures 3.19 and 3.20 show the well logs and synthetic PP and PS angle gathers: the joint inversion is applied on the noise-free gathers and random-noise-added gathers. When the PS gathers are generated, the PP travel time is used to avoid the uncertainty caused by the error in the registration of the PS time to the PP time. A 100 Hz high-end frequency and a 0-35 degree incident angle range are used for the inversion on the PP angle gather. There are two sets of PS angle gathers – both contain a 0-45 incident angle range but different high-end frequencies: 100 Hz and 60 Hz. The application of the joint PP and PS inversion is done in both the time (on a time-sample by time-sample basis) and frequency domains (on a frequency-sample by frequency-sample basis) by a straightforward least squares method. The results of the joint inversion are shown in Figure 3.21. For the PP and PS gathers containing same high end frequency (100Hz), the joint inversion generates identical results for both in the time and frequency domains by using either noise-free or noisy gathers. The second test is the Bayesian constraint joint PP (100Hz) and PS (60Hz) inversion: the joint inversion is applied only on <=60 Hz portion; for the high frequency contained only in the PP data, a covariance matrix from the low frequency solutions and a prior model generated from the PP data are used to constrain the PP AVO inversion, and this generates a superior inversion result to those from time domain or without constraints. In Figure 3.21, four panels of traces are displayed: Panel (a) is the solution of joint PP and PS inversion from noise free data

without any constraints; Panel (b) is the solution of joint PP and PS inversion from noisy data without any constraints. The inversion is applied both in the time domain and in the frequency domain for the test in Panels (a) and (b) and outputs from both domains are identical. Panel (c) shows the constrained joint PP and PS inversion in the frequency domain, but the constraints are only applied on the PP inversion for the frequency higher than 60 Hz. Panel (d) is also for constrained joint inversion in the frequency domain – the constraints are applied on all frequency components. There are nine traces in each panel: the first three traces are the bandlimited Vp reflectivity from the well log, the joint inversion of the 100 Hz PP and 100 Hz PS gathers, and the joint inversion of the 100 Hz PP and 60 Hz PS gathers respectively; the second group of three traces are the bandlimited Vs reflectivity and ordered as same as the Vp reflectivity from the well log, the joint inversion of the 100 Hz PP and 100 Hz PS gathers and the joint inversion of the 100 Hz PP and 60 Hz PS gathers; the third group of three traces are the bandlimited density reflectivity and ordered as the same as the Vp and Vs reflectivities. The correlation coefficients of the inverted and true reflectivities in Figure 3.21 are calculated and listed in Table 3.2

Table 3.2 Correlation coefficients of the inverted and true reflectivities in Figure 3.21

		Noise free data, no constraint	Noisy data, no constraint	Noisy data, only high frequency PP constraint	Noisy data, all frequency constraint
Vp reflectivity	100 Hz PP + 100 Hz PS	1.0000	0.9098	0.9098	0.9098
	100 Hz PP + 60 Hz PS	0.9829	0.9269	0.8740	0.9098
Vs reflectivity	100 Hz PP + 100 Hz PS	1.0000	0.9481	0.9481	0.9481
	100 Hz PP+ 60 Hz PS	0.8344	0.7540	0.9198	0.9423
Density reflectivity	100 Hz PP + 100 Hz PS	1.0000	0.7434	0.7434	0.7434
	100 Hz PP + 60 Hz PS	0.3400	0.3770	0.6196	0.8455

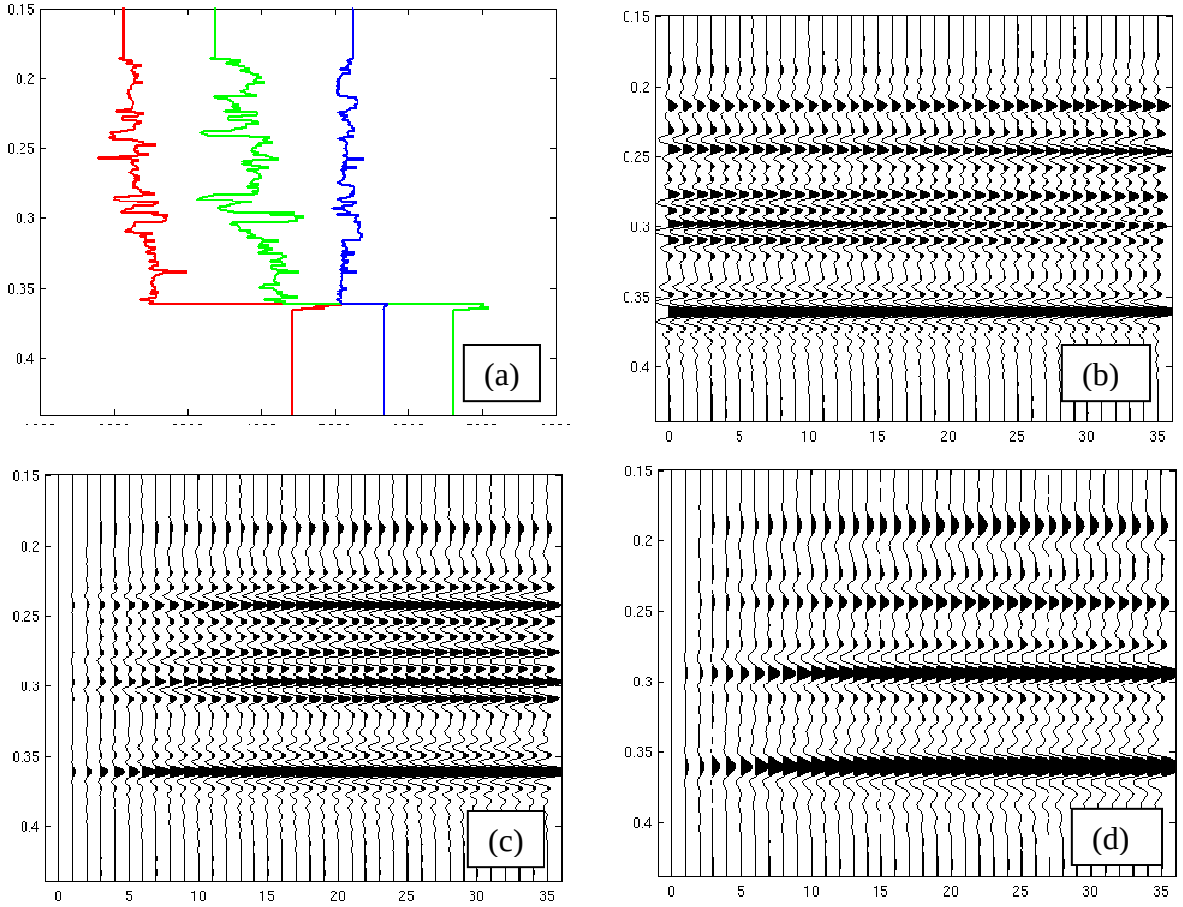

Figure 3.19 PP and PS AVO gathers. (a) well logs for generating synthetic gathers: red – Vp, green – Vs, and blue – density; (b) PP angle gather with 36 traces, 100 Hz high-end frequency and 0-35 degree incident angle range; (c) PS angle gather with 36 traces, 100 Hz high-end frequency and 0-45 degree incident angle range; (c) PS angle gather with 36 traces, 60 Hz high-end frequency and 0-45 degree incident angle range. All gathers are registered to PP traveltime exactly in angle domain.

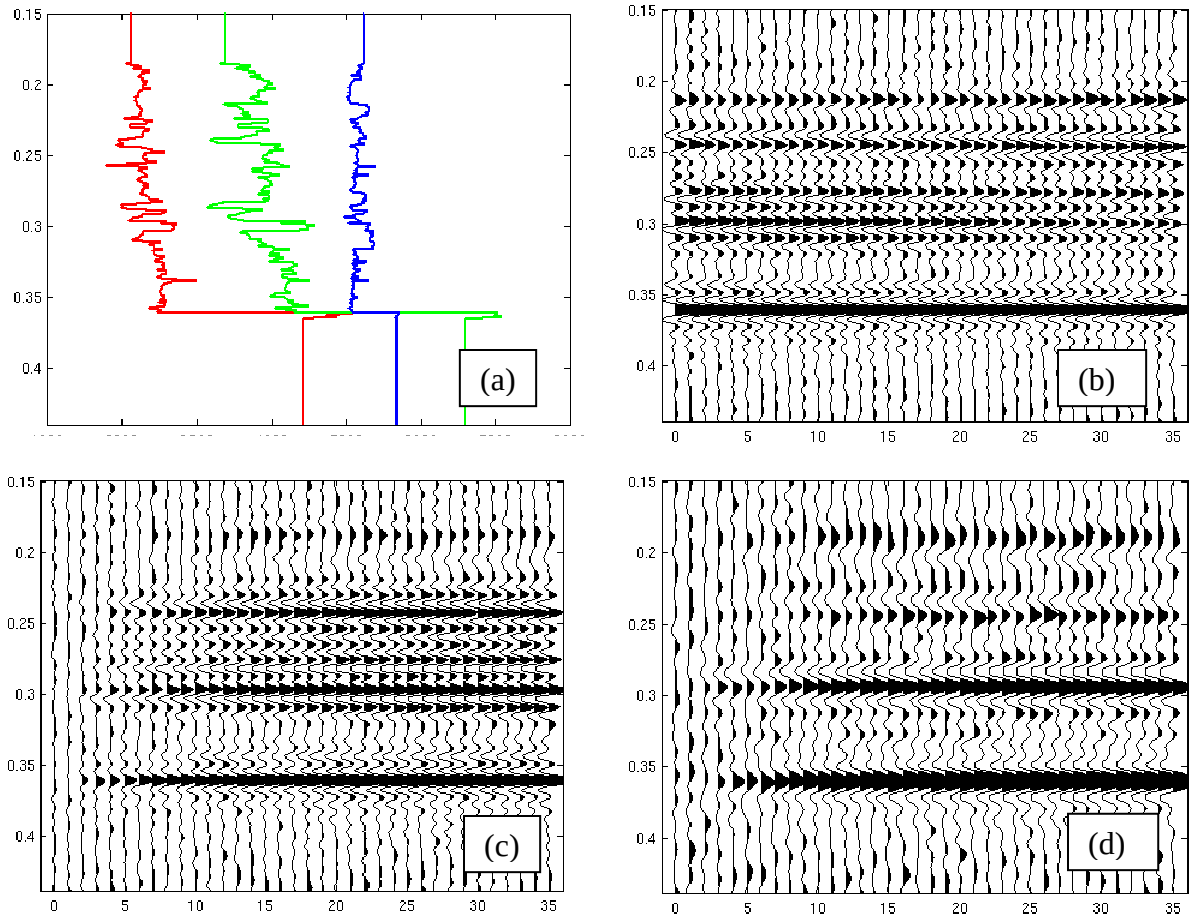

Figure 3.20 PP and PS AVO gathers with noise added. (a) well logs for generating synthetic gathers: red – Vp, green – Vs, and blue – density, same as in Figure 3.19 (a); (b), (c), and (d) are the PP, PS angle gathers arranged as the same as in Figure 3.19 except that random noise is added in the gathers.

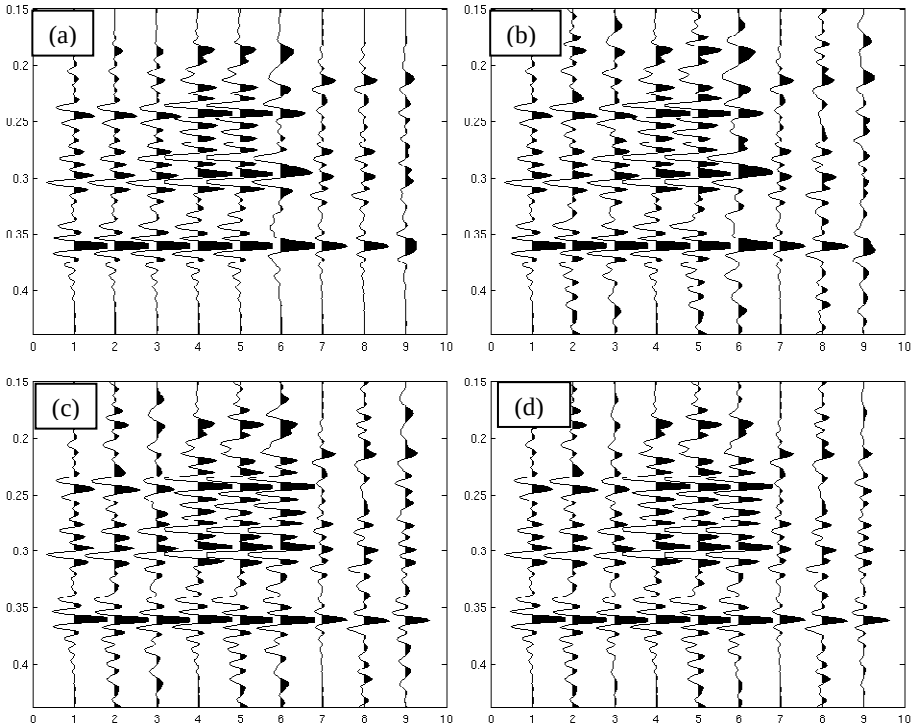

Figure 3.21 Joint PP and PS inversion results: (a) time or frequency domain inversion of noise free data; (b) time or frequency domain inversion from noisy data; (c) frequency domain solution – constraint applied on 60-100Hz when 60 Hz PS data is used; (d) frequency domain solution – constraint applied on all frequency when 60 Hz PS data is used. On each of these four panels, the first three traces are P reflectivities from the model, joint inversion of 100Hz PP and 100Hz PS gathers, and joint inversion of 100Hz PP and 60Hz PS gathers; the second three traces are S reflectivities from the model, joint inversion of 100Hz PP and 100 Hz PS gathers, and joint inversion of 100Hz PP and 60Hz PS gathers, and the third three traces are density reflectivities from the model, joint inversion of 100Hz PP and 100 Hz PS gathers, and joint inversion of 100Hz PP and 60Hz PS gathers.

3.6 CASE HISTORIES

Two case studies are used to demonstrate the effectiveness of the AVO inversion in the prediction of oil sands reservoir heterogeneities in Athabasca. The first case demonstrates the complete process of the AVO analysis. In the second case the reservoir heterogeneity predicted by the AVO inversion is confirmed by blind well tests.

A two-step approach to understand the heterogeneity of Athabasca oil-sand reservoirs is adopted. The first step involves a rock property study to understand the relationship between lithology and the related rock parameters and pick lithology-sensitive rock parameters that can be seismically derived. The second step derives the chosen parameters from the seismic data using the improved AVO inversion presented in this chapter.

Figure 3.2 already shows the workflow for mapping reservoir heterogeneity using the seismic data in the studied areas. This workflow is based mainly on the conventional P-wave surface seismic, though it can be extended to incorporate the multi-component seismic data. As stated earlier, due to the heterogeneity within the formation and a weak correlation between the seismic (P impedance and reflectivity) and lithology, “normal” attempts at geologic interpretation usually prove futile. We address this problem by using the AVO attributes from surface seismic data. Since the oil sands reservoir is shallow and seismic data usually have a sufficiently high resolution in shallow zones, it was expected that reasonably convincing estimates of reservoir heterogeneity could be obtained. The inversion is performed and analyzed in a deterministic way and it works for estimating the lithology-sensitive density reflectivity attribute provides the good quality control and validation with well ties. However, it should not in any way discourage the application of statistical methods for the same goal. When more than a couple of seismic attributes with good correlations with reservoir properties are available, neural-network approaches could determine reservoir properties within the interval of interest.

3.6.1 Case 1

A real data example in this case demonstrates the use of the workflow and reliability of the improved 3-parameter AVO inversion. The data is from the Birch area in the north Athabasca and was provided by Arcis Corporation. Gamma ray, sonic, and density logs are available in the well for QC the result and the post-stack impedance inversion (Figure 3.22). The shear wave velocity is predicted from the P wave velocity using local mudrock lines. The McMurray Formation is absent at this well location. The objective of the study is to predict the heterogeneity within the Wabiskaw Member, in which there are marine and shoreface sands interbedded by marine shales. The cross-plots between the available logs are made in Figure 3.23. The cross-plots show that the density and Vp have a similar sensitivity to lithology inside the Wabiskaw but their variations with gamma ray values are opposite: the sand has higher P velocities but lower density than the shale in the Wabiskaw Member. No shear log is available in the study region and pseudo-shear log is predicted from the nearby area data.

A good quality 2D line crossing the well is used in the analysis. The high cut frequency for the signal is up to 130 Hz and the maximum angle of 41 degree for AVO inversion is chosen. The AVO inversion generates P, S reflectivity (impedance contrasts) and density reflectivity with the seismic frequency bandwidth. The synthetic P, S, and density reflectivities are generated from the well logs with a single wavelet and compared with the corresponding reflectivities at the well location from the AVO inversion. In Figure 3.24, the synthetic and real data comparisons are made. In the figure, the correlation of the seismic data and log curves is made and the correlation coefficients between synthetics and the real data are marked. The correlation coefficients are close for three kinds of reflectivities and reasonably good within a 300 ms time window. In the figure, a few arrows mark locations where the density variation is opposed to the P impedance variation, and the inverted P and density reflectivities are apparently different, matching the synthetics. The special implementation of the AVO inversion preserves these anomalies deviated from the background trend.

Figures 3.25-3.33 display a set of attributes derived by the key steps in the workflow: reflectivities, colored attributes (the layered attributes with the seismic bandwidth), and full-band attributes. Reflectivity and relative impedance and relative density are 100% seismic data driven, while the impedance and density are partly dependent on models derived from the well logs and interpretation (horizons). It is noted that the formation boundaries and anomalies derived on the relative P impedance and relative density at the well location are very close to those on the P impedance and density logs.

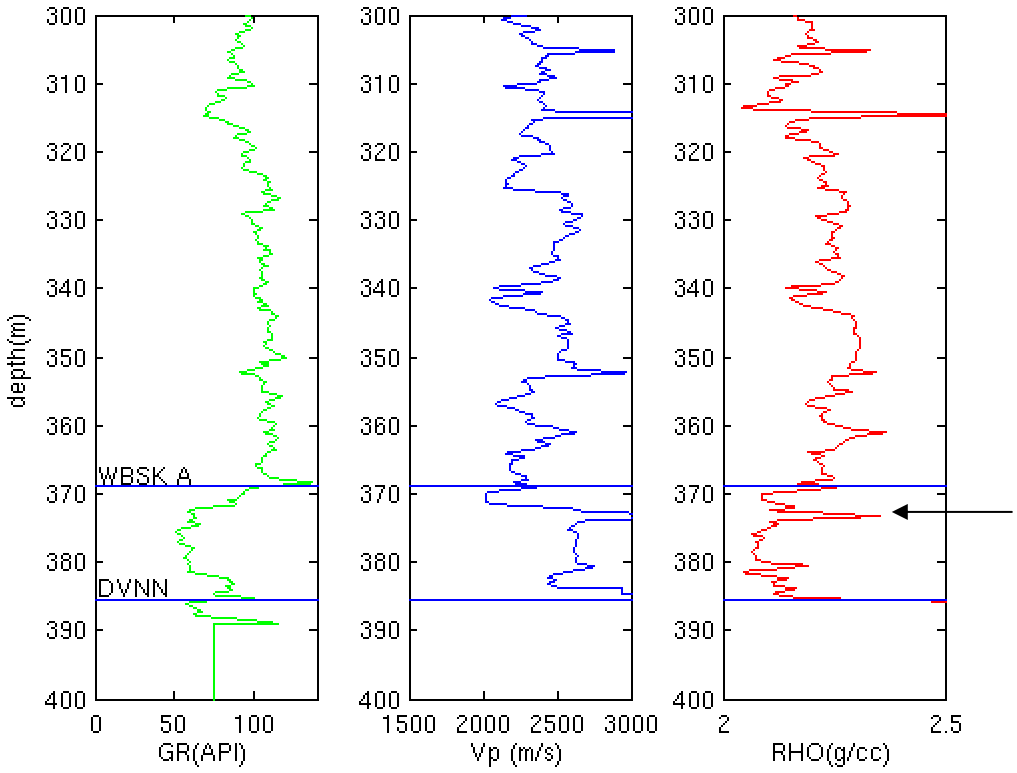

Figure 3.22 Log curves of the well used in Case 1: gamma ray, Vp, and density. "WBSK A" marks the top of the Wabiskaw Member of the Clearwater Formation; "DVNN" marks the top of the Devonian Formation. The arrow indicates a tight streak inside the Wabiskaw member.

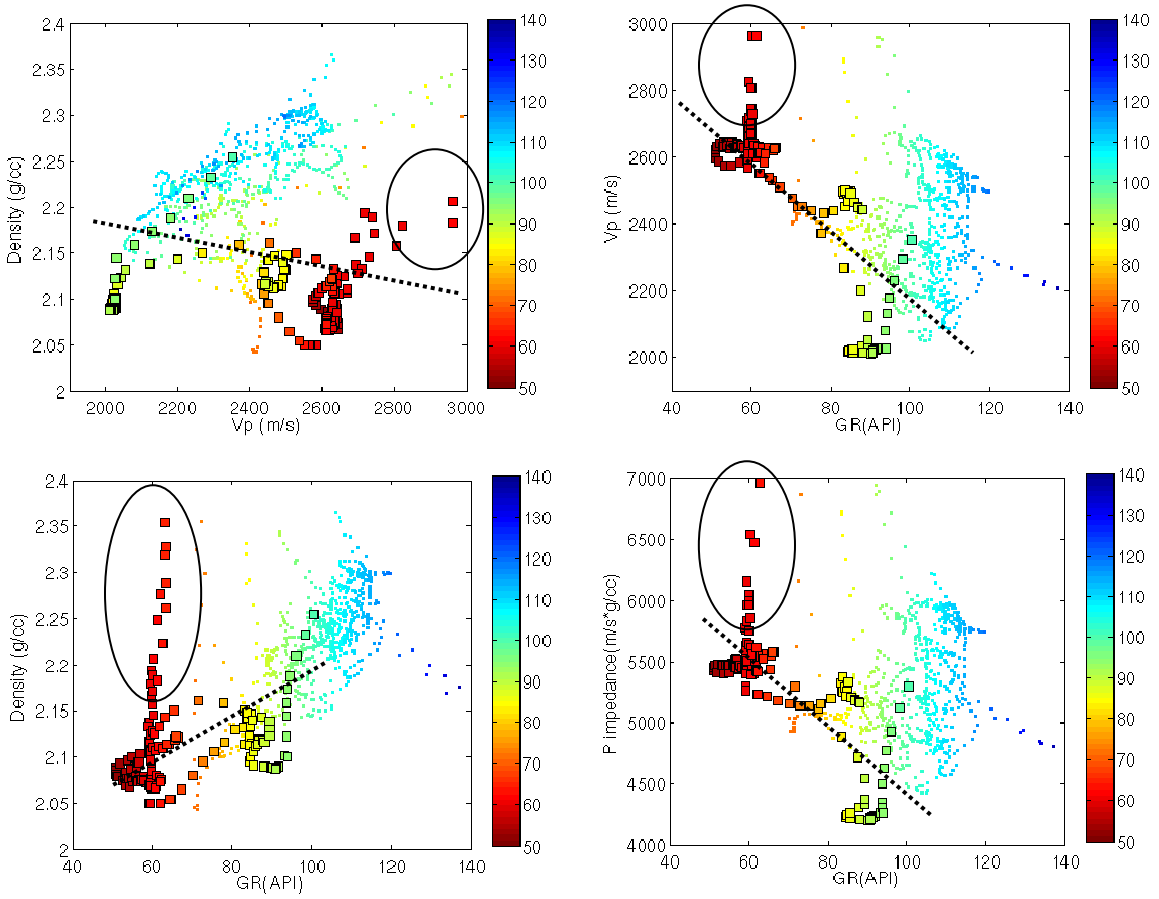

Figure 3.23 Crossplots of Vp and density, gamma ray and Vp, gamma ray and density, and gamma ray and P impedance from the portion of logs shown in Figure 3.19. The squares are samples within the Wabiskaw Member. Tiny dots are samples from above the Wabiskaw. A thin tight layer at the top of sand generates large scattering in the plots (in circles). In spite of that, the sensitivity of lithology to velocity, impedance and density can be observed. Samples in the circles are from the tight streak shown in Figure 3.22. The dash lines roughly indicate the trend between parameters and gamma ray within the target – the Wabiskaw Member.

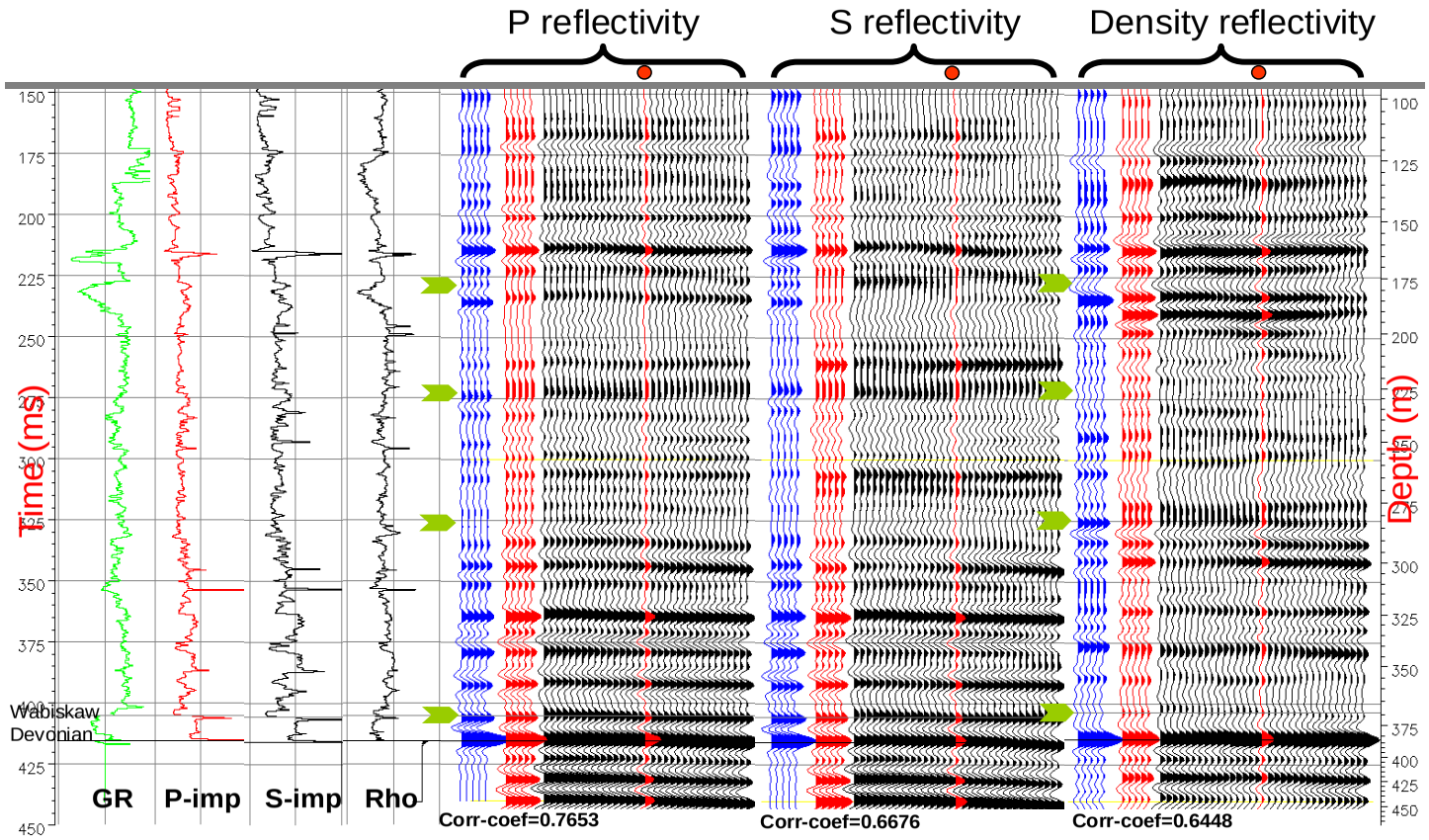

Figure 3.24 Correlation between synthetics from wells and reflectivities from inversion: Blue traces are synthetic reflectivities from P, S impedance and density well logs. Black traces are small portions of P and S reflectivities and density reflectivity sections from AVO inversion close to the well and well location is marked by the red traces in the middle of the sections. Reflectivity traces at the well location are duplicated five times and drawn beside corresponding synthetic traces for comparison (the red traces). Correlation coefficients within the time window are shown for the three reflectivities.

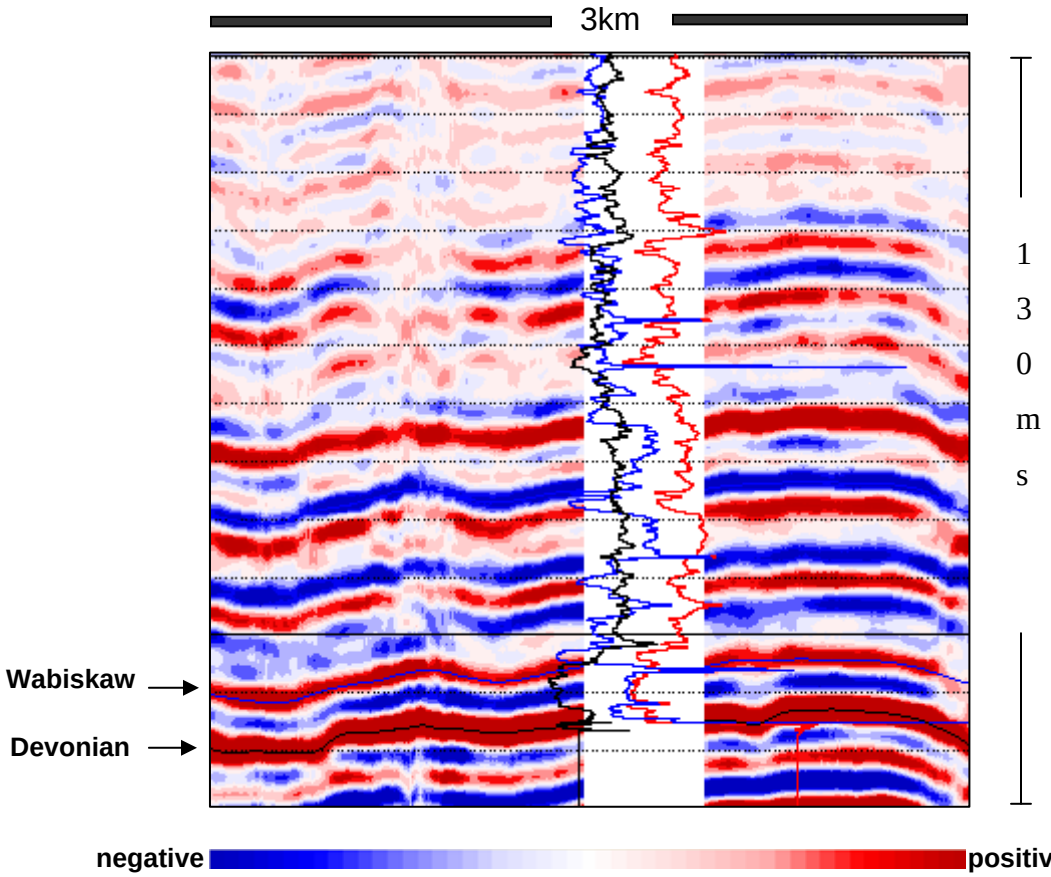

Figure 3.25 P reflectivity from the AVO inversion. Log curves overlaid: black – gamma ray, red – density, and blue – P impedance. The time interval in 130 ms and sections are 3 kilometers long (Data courtesy Arcis Corp).

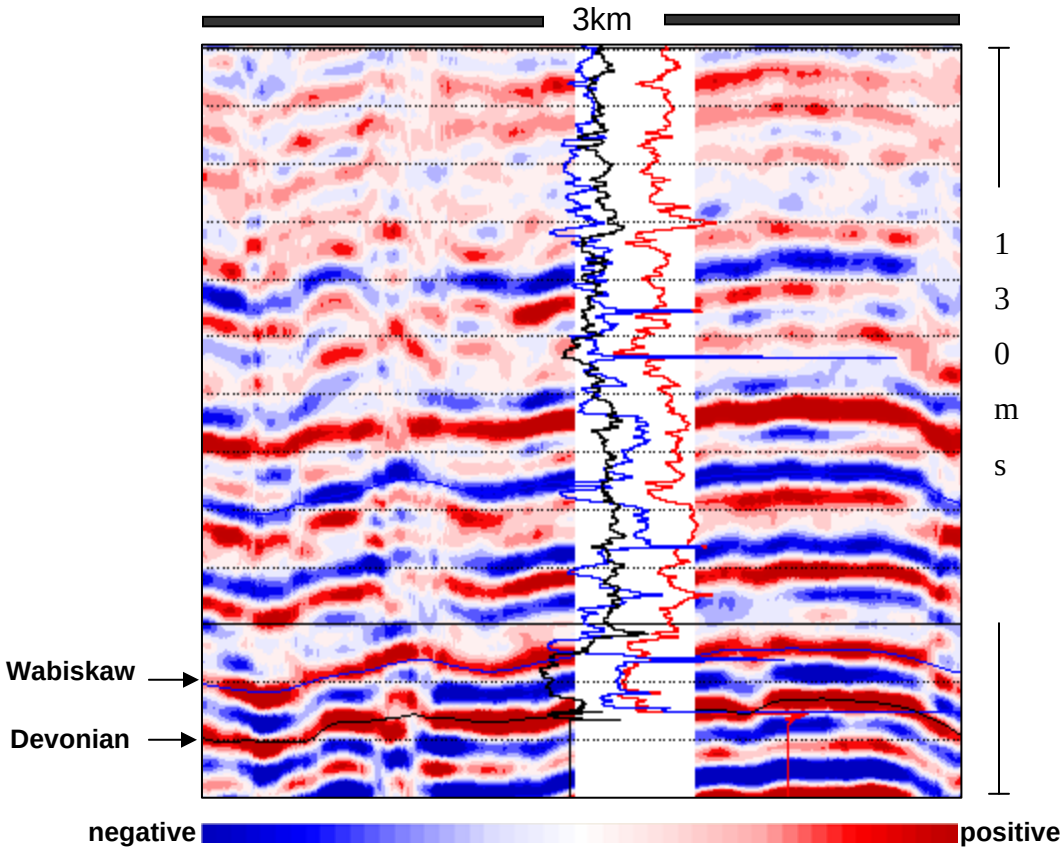

Figure 3.26 S reflectivity from the AVO inversion. Log curves overlaid: black – gamma ray, red – density, and blue – P impedance. The time interval in 130 ms and sections are 3 kilometers long (Data courtesy Arcis Corp).

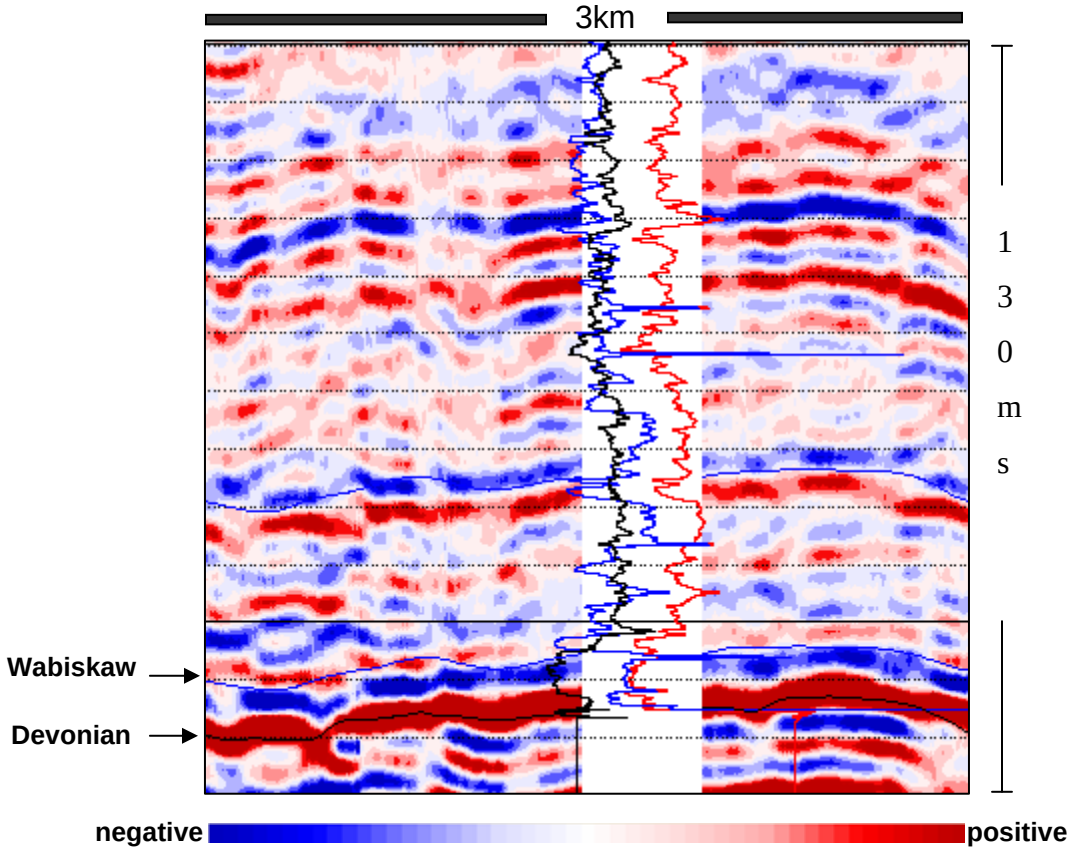

Figure 3.27 Density reflectivity from the AVO inversion. Log curves overlaid: black – gamma ray, red – density, and blue – P impedance. The time interval in 130 ms and sections are 3 kilometers long (Data courtesy Arcis Corp).

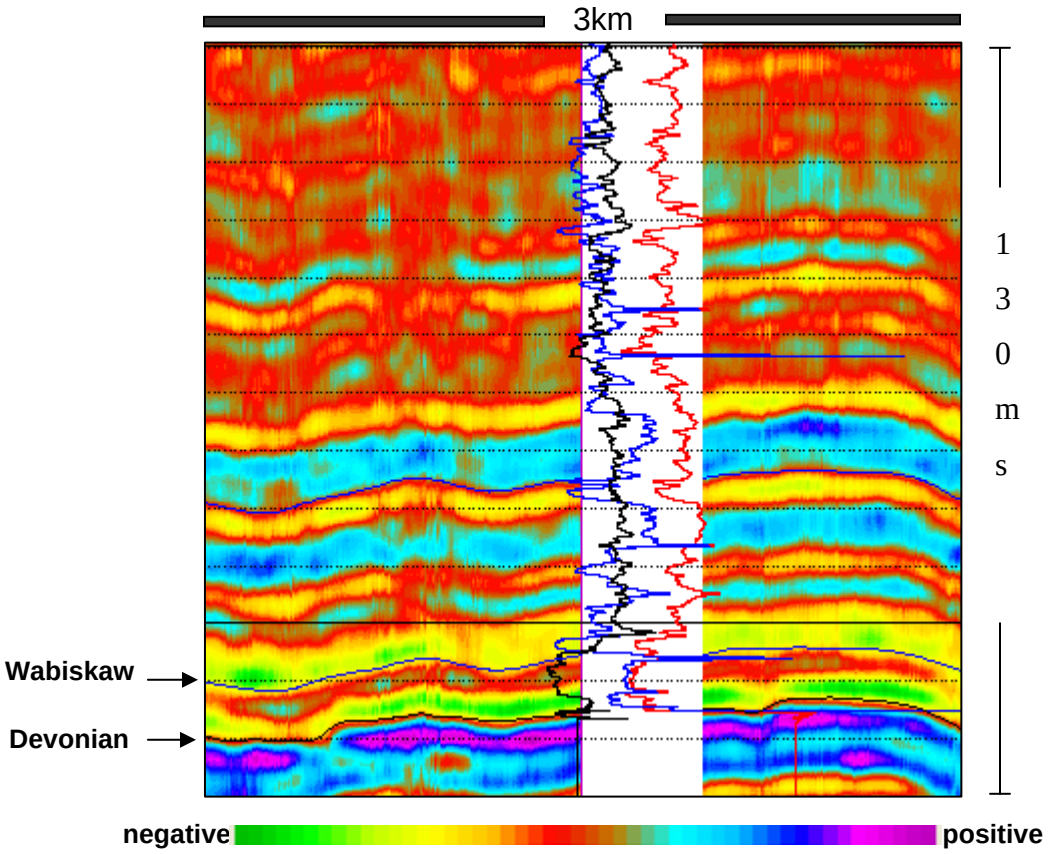

Figure 3.28 Relative P impedance converted from P reflectivity. Log curves overlaid: black – gamma ray, red – density, and blue – P impedance. The time interval in 130 ms and sections are 3 kilometers long.

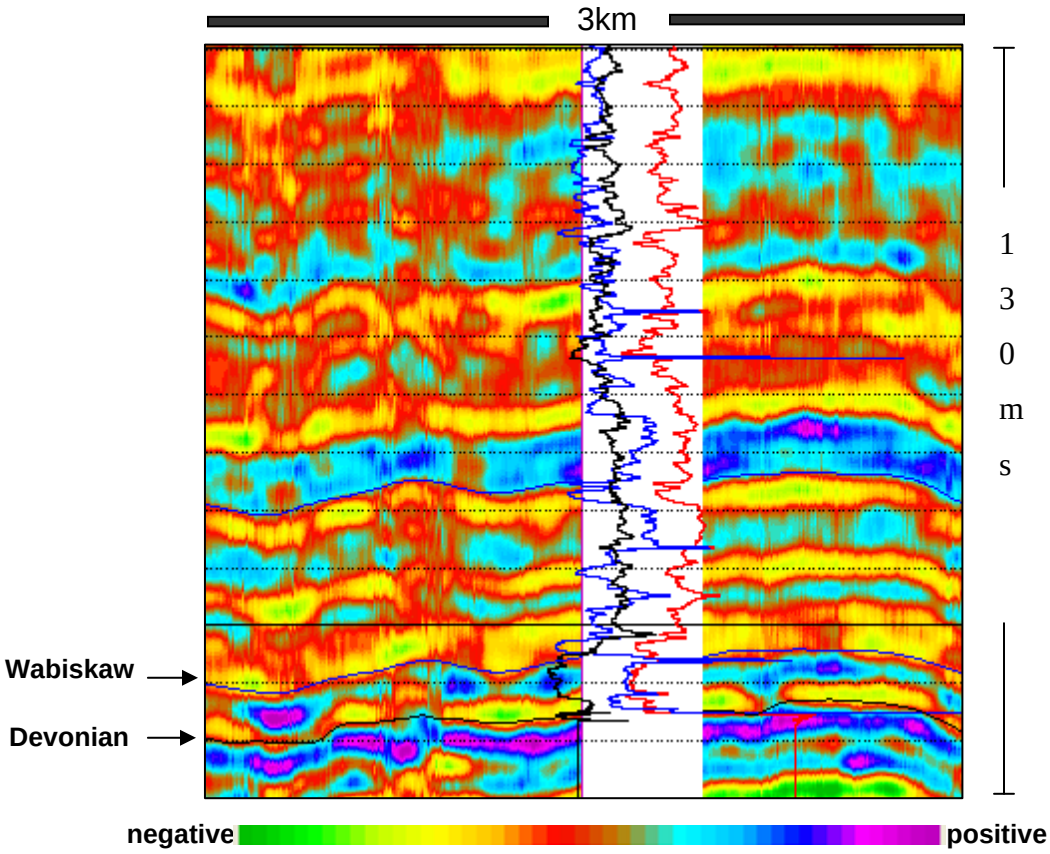

Figure 3.29 Relative S impedance converted from S reflectivity. Log curves overlaid: black – gamma ray, red – density, and blue – P impedance. The time interval in 130 ms and sections are 3 kilometers long.

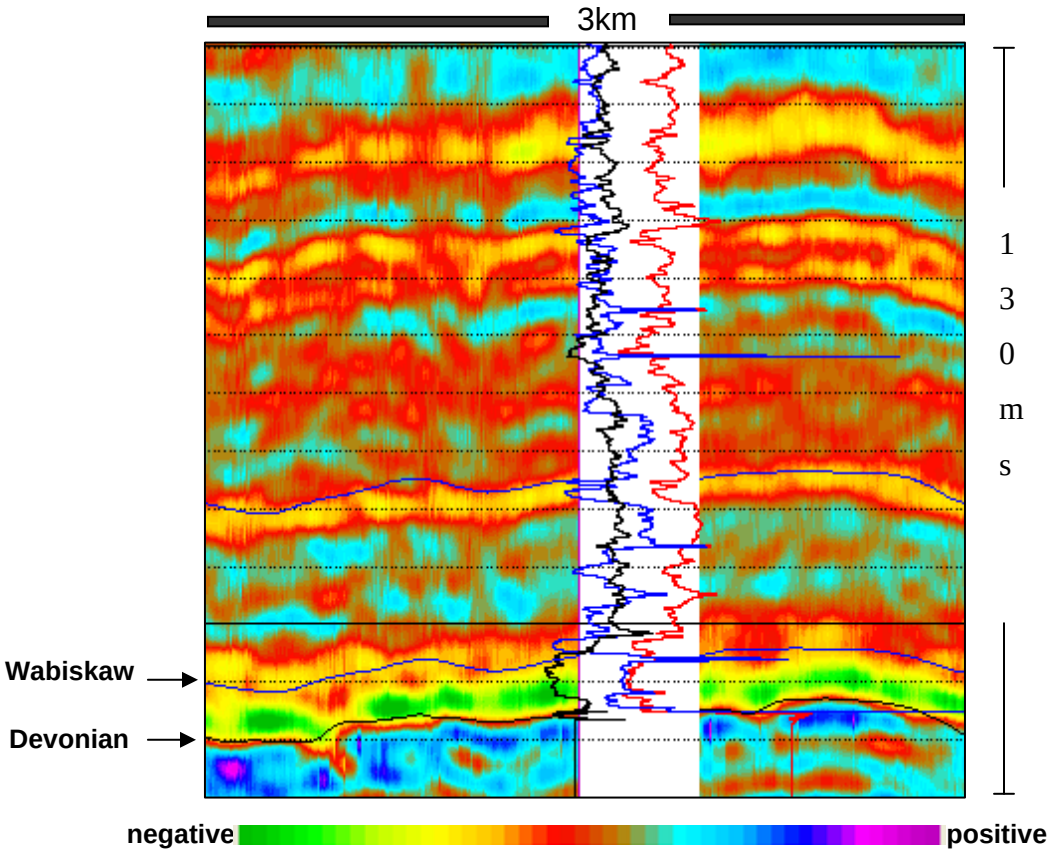

Figure 3.30 Relative density converted from density reflectivity. Log curves overlaid: black – gamma ray, red – density, and blue – P impedance. The time interval in 130 ms and sections are 3 kilometers long.

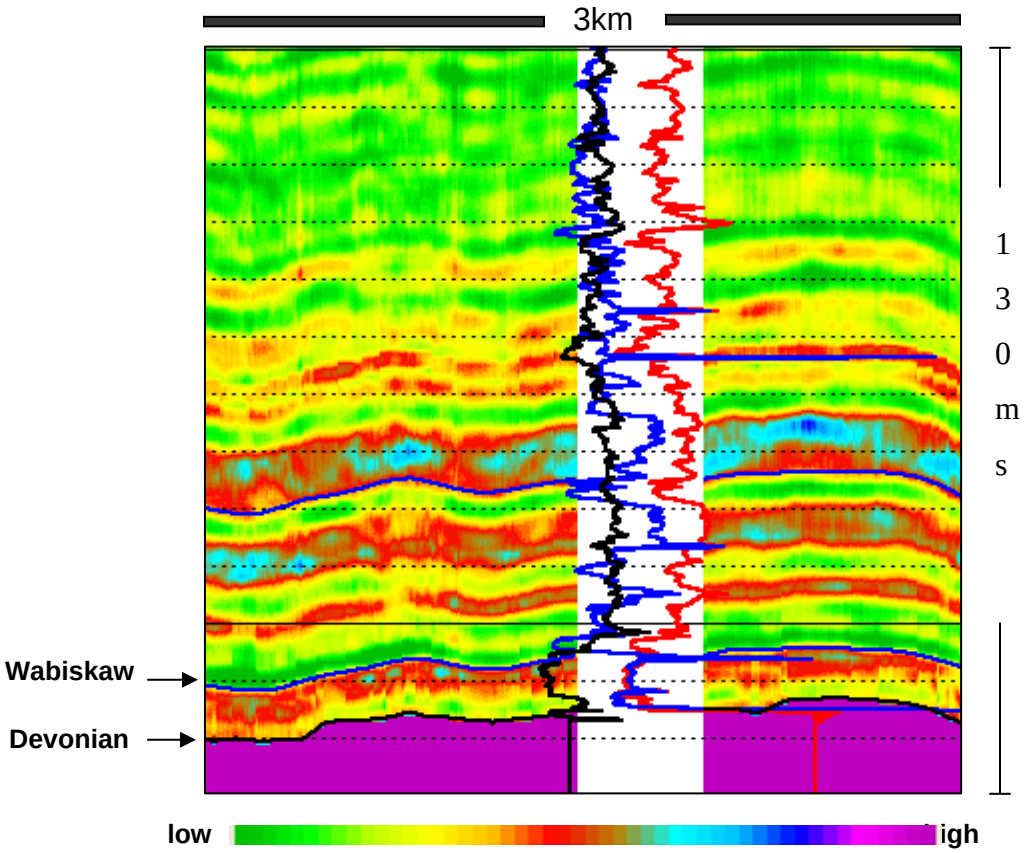

Figure 3.31 P impedance from impedance inversion. Log curves overlaid: black – gamma ray, red – density, and blue – P impedance. The time interval in 130 ms and sections are 3 kilometers long.

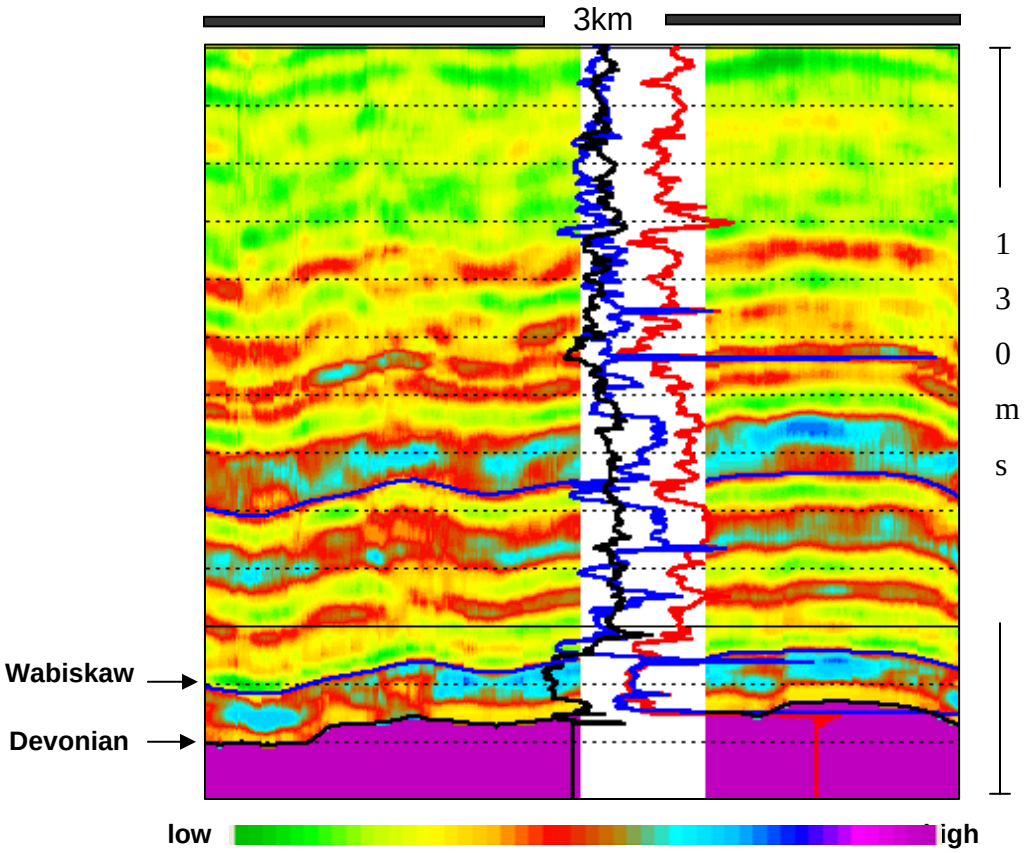

Figure 3.32 S impedance from impedance inversion. Log curves overlaid: black – gamma ray, red – density, and blue – P impedance. The time interval in 130 ms and sections are 3 kilometers long.

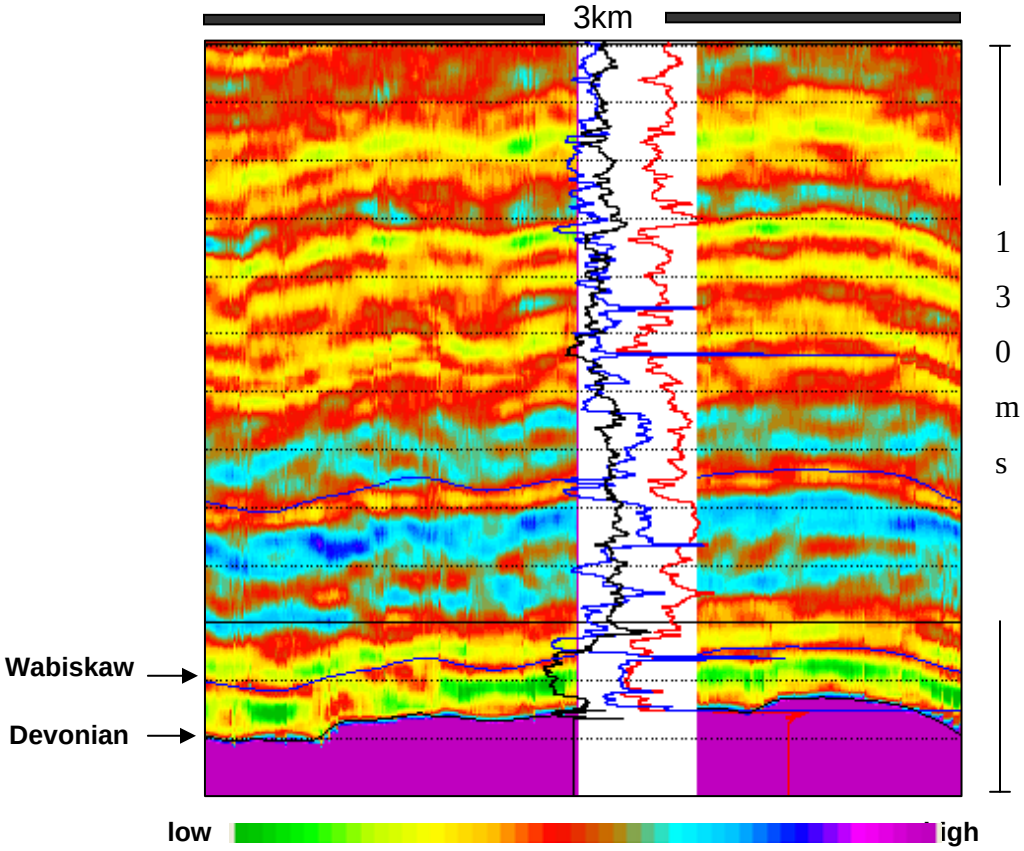

Figure 3.33 Density from impedance inversion. Log curves overlaid: black – gamma ray, red – density, and blue – P impedance. The time interval in 130 ms and sections are 3 kilometers long.

3.6.2 Case 2

A 2D seismic line from a heavy oil production region in Athabasca is used in this case. The seismic data was provided by an anonymous company. Well controls are available for the impedance inversion and blind tests. The reservoir is in the McMurray Formation.

3.6.2.1 Geological settings

The McMurray Formation consists of middle and upper members, which are overlain by the Wabiskaw Member of the Clearwater Formation. The lower member of the McMurray Formation was never deposited in the tributary valley because of limited accommodation space in these thinner and structurally elevated tributary valleys when compared with the main trunk valley. Where preserved in the main valley, the lower member of the McMurray Formation was deposited as a series of braided fluvial channels in a continental environment. As transgressions commenced from the north, the main valley became progressively flooded and influenced by tidal marine processes, thus over time the fluvial channels developed into a series of meandering, brackish, tidally-influenced channels which form the main clean sand to heterolithic sand and mud reservoirs of the middle member. These channels were then replaced by a series of intertidal flats, bay fills, deltas and shorefaces as the transgression continued, forming the upper member. These marginal marine facies were eventually replaced by offshore marine and prodelta mudrocks of the Wabiskaw Member.

Within the tributary valley, the middle member of the McMurray Formation is dominantly composed of argillaceous delta plain deposits, but there is occasional preservation of sharp-based, fining-upward, bioturbated tidally-influenced channel deposits that are typically estuarine channel McMurray reservoirs. The middle member is erosionally overlain by the upper member that is more sand-prone and forms the main reservoir interval in the study area. These sands form more laterally continuous reservoirs and represent vertically and laterally amalgamated proximal deltaic mouth bars that prograded into a brackish bay. The overlaying Wabiskaw Member consists of widespread, offshore marine to prodelta shales resulting from the gradual transgression of

the Boreal Sea from the north. As the relative sea-level continued to rise, marine influences soon dominated the brackish processes, and progressively onlapped and drowned the Devonian archipelagos to the west.

The McMurray Formation is abruptly overlain by 5 meters of laminated, dark grey, silty clayshale with zones of moderated to small-sized traces and layers of light-gray bioturbated siltstone, assigned to the base of the Wabiskaw Member. Some silts are normally-graded and sharp-based. The shales are widespread, and are believed to have been deposited in an offshore marine to distal prodelta environment. The marine shales are sharply and erosively overlain by muddy sand of the Wabiskaw Member. The sands are ~5 meters thick, lower to very fine grained, and contain 30 to 40% mud. They are interpreted as forced regressive distal delta-front lobes. As marine transgression ensued, the distal delta-front became replaced with offshore marine, bioturbated claystones.

The reservoir sands differ from typical McMurray reservoirs in that they are more laterally homogenous, do not contain the laterally-extensive and thick interbedded sands and muds referred to as IHS and are deposited by a lateral accretion of point bars in a tidally-influenced channel environment, and do not contain mud plugs with a reflective channel avulsion. The reservoir architecture appears simpler in these deltaic environments, facies bands are more laterally continuous and the clay content is much lower. It is predicted that SAGD development will be well-suited to these types of reservoirs.

3.6.2.2 Rock property analysis

Rock property analysis in a given area is important for, firstly, the determination of those rock parameters that may exhibit some useful lithology-correlated relationship and, then, using this relationship to estimate such attributes from seismic data. In Figure 3.34 is the crossplotting of different pairs of parameters for the McMurray Formation reservoir which is at a depth of about 100 m. Figure 3.34(a) shows a strong linear correlation between the bulk density and gamma ray values. Clean sand samples have average

densities of 2.075 g/ cc with average gamma-ray values of API 25, whereas the shale has an average density of 2.24 g/cc with average gamma ray value of API 85. If a linear relationship between the gamma ray value and shale volume (Vshale) is assumed, then Vshale can be estimated from density by using the relation Vshale = (density - 2.075)/0.165. Figure 3.34(b) reveals a weak correlation between the gamma ray (shale volume) and Vp/Vs ratio. Since the P impedance can be more reliably derived from seismic data, it is always desirable to look for any strong correlation between the impedance and another rock parameter of interest. However, as seen in Figures 3.34(c) and 3.34(d), the P impedance is unable to indicate lithology variations; since in this case the shale and the sandstone have similar P-wave impedance values as shown by the uncorrelated gamma ray and the P impedance scatter.

3.6.2.3 Inversion results

The 2D seismic profile running through 11 wells in the study area was taken through an amplitude-preserved AVO processing flow. In Figure 3.35 it is the cross-section of gamma ray logs of 9 wells on the 2D seismic line. The best quality reservoir is between the well 5 and well 7. The thickest bitumen pay locates between well-6 and well 7. The Clearwater Formation and the Wabiskaw shale and mudstone form the caprocks for the reservoir. From the well 7 to the well 8 and further right the Wabiskaw D mudstone is more sandy and become relatively poor caprock.

The data quality of the seismic was reasonably good and the usual noise problems in terms of ground rolls and other wave modes were skillfully tackled using adaptive and iterative noise-attenuation schemes. The surface elevation variation along the profile is about 45 m, and this is of the same order as the reservoir depth variation of 55–90 m. This elevation variation was a significant factor regarding the amplitude recovery and the stability of the AVO inversion at the reservoir level. Care was exercised for the amplitude recovery and super-binning was part of the data conditioning for the AVO inversion. Figure 3.36 shows a stacked section for the seismic profile with the zone of interest indicated. Figure 3.37 shows log curves and synthetics for a typical well and their

correlation with the derived P impedance and density reflectivities from the seismic data. The correlation between the two pairs of reflectivities is reasonably good and encouraging. The sections of P impedance and density reflectivities are shown in Figure 3.38; the major events such as the Wabiskaw and Devonian tops are consistent on both sections; however, the apparent difference is seen inside the reservoir. Figure 3.39 shows the results of different AVO attributes derived as per the workflow. Only the density attributes are shown because the P impedance is not sensitivity to the lithology heterogeneity as shown in the rock property analysis and there is no good correlation between P impedance attributes and reservoir heterogeneity on the real data as well. The density reflectivity derived after the AVO inversion is shown in Figure 3.39(a). The relative density was derived from the density reflectivity after the simple trace integration without using density logs from wells, and this result (Figure 3.39(b)) indicates the richest sand areas (dark green) are in the middle of the McMurray Formation with a good seal cap in the upper McMurray around wells 5 and 6. These are verified by the overlain gamma-ray log curves.

Next, the density logs from all the wells except wells 3 and 7 (not available at the time) were used to generate a density model. A model-based poststack inversion was performed on the density reflectivity utilizing the density model to generate a density section (Figure 3.39(c)). This section has a higher resolution than the relative density and better matches with the log curves. The linear relationship indicated on the crossplot between the density and gamma ray values (Figure 3.34(a)) was used to transform the derived density section into a Vshale section (Figure 3.39(d)). Two recently drilled wells (3 and 7) were used in a blind test; well 3 is mainly shaley within the McMurray and the density inversion result verifies this. Well 7 has good sand in the middle McMurray, but a sandy cap in the upper McMurray. These results are clearly confirmed on the inverted density (Figure 3.39(c)) and the derived Vshale sections (Figure 3.39(d)). The same results are seen on the relative density sections. All four derived density estimate sections in Figure 3.39 yield encouraging confirmation with well logs and exhibit a believable lateral variation in reservoir heterogeneity within the target zone.

In Figure 3.40, the portion of the density attributes between the Well 4 and Well 8 is highlighted. It is noted that the relative density, which is the 100% seismic data drive, provides the primary trend of reservoir heterogeneity. The low frequency incorporated in the full band density and shale volume provides a secondary source of the reservoir heterogeneity. This confirms the conclusion drawn in Chapter 2 that the seismic band attributes are able to predict reservoir heterogeneity with a relatively high confidence.

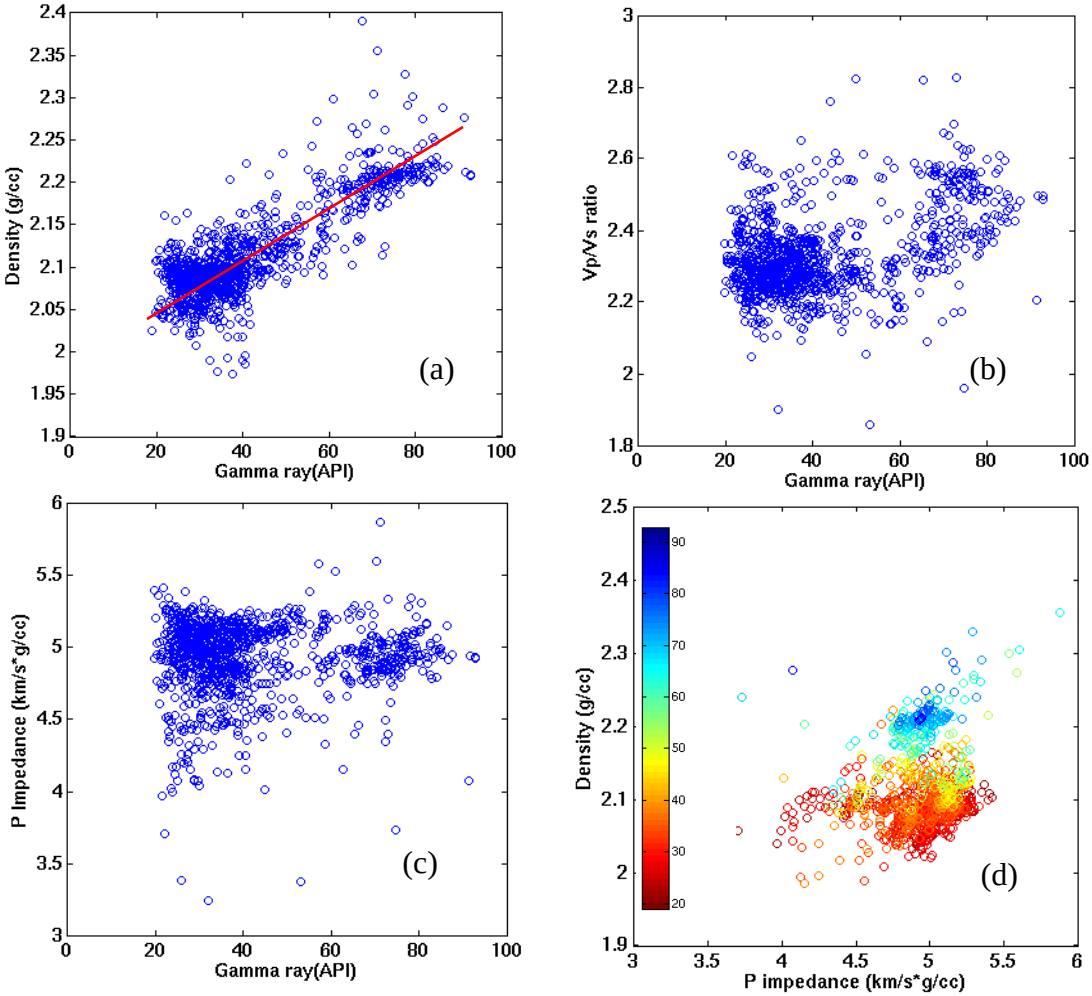

Figure 3.34 Crossplots of (a) density vs gamma-ray, (b) Vp/Vs ratio vs gamma ray, (c) P-impedance vs gamma ray, and (d) density vs P-impedance, with colors coded by gamma-ray values. Data samples come from McMurray formation in four wells in the study area of Athabasca oil sands. The reservoir is at a depth of 100 meters. A linear relationship between density and gamma ray (red line in Figure 3.34(a)) can be used to estimate V-Shale (or pseudo gamma ray) from density.

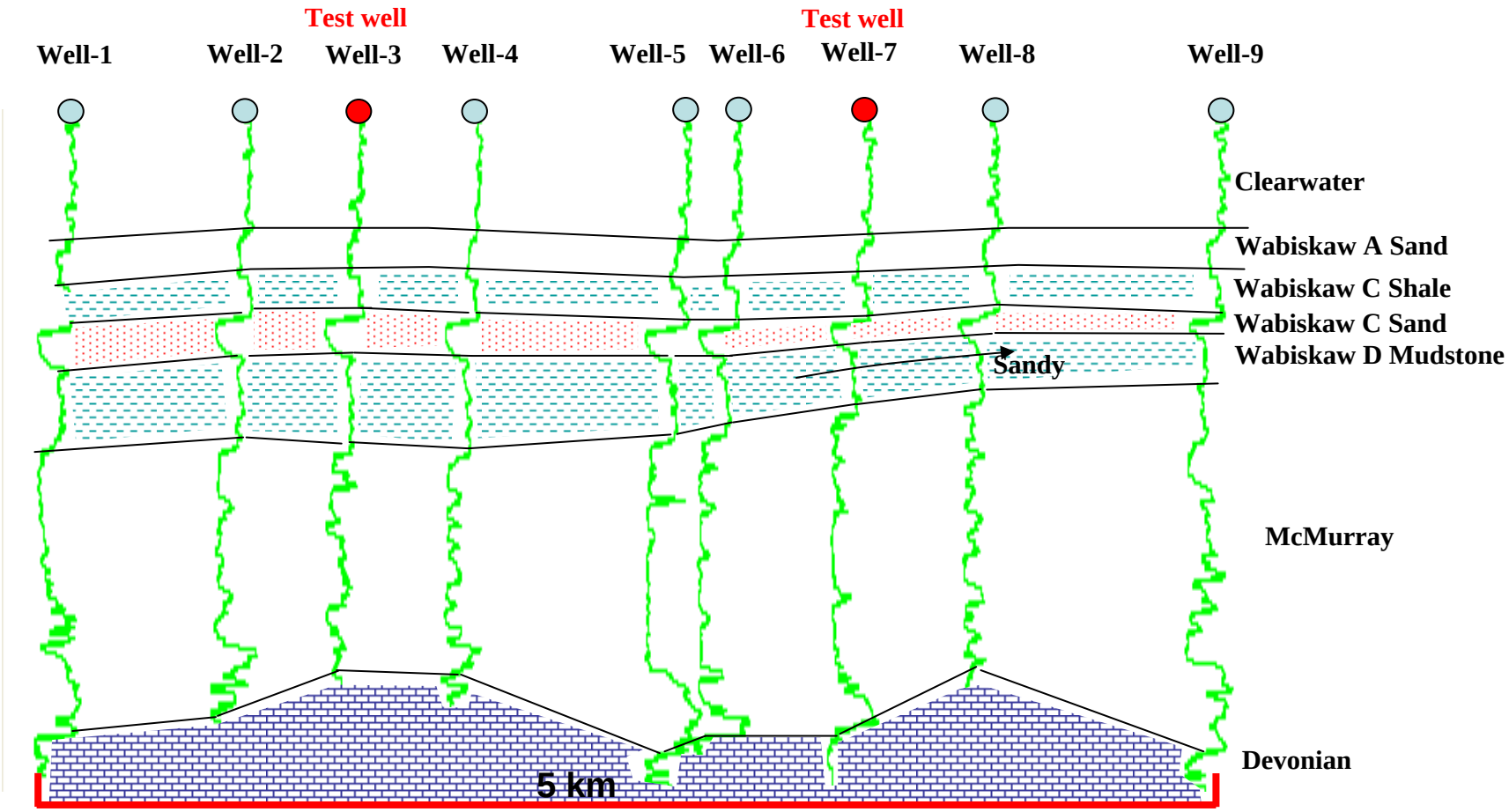

Figure 3.35 Cross-section of gamma ray logs of the wells on the 2D seismic line. The best quality reservoir is between the well 5 and well 7. The thickest bitumen pay locates between well-6 and well 7. The Clearwater Formation and the Wabiskaw shale and mudstone form the caprocks for the reservoir. From the well 7 to the well 8 and further right the Wabiskaw D mudstone is more sandy and is relatively poor caprock.

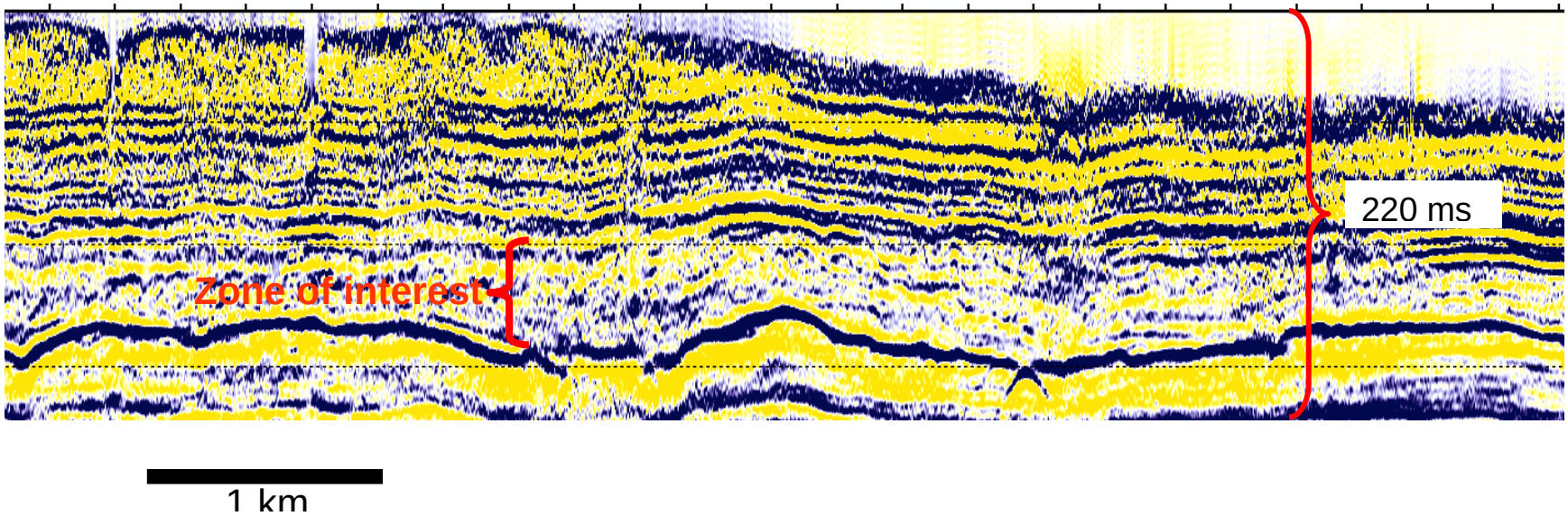

Figure 3.36 Stack section showing the zone of interest. The processing was done using a commercial seismic data processing package – FOCUS, a product from Paradigm Geophysical (Data courtesy an anonymous company).

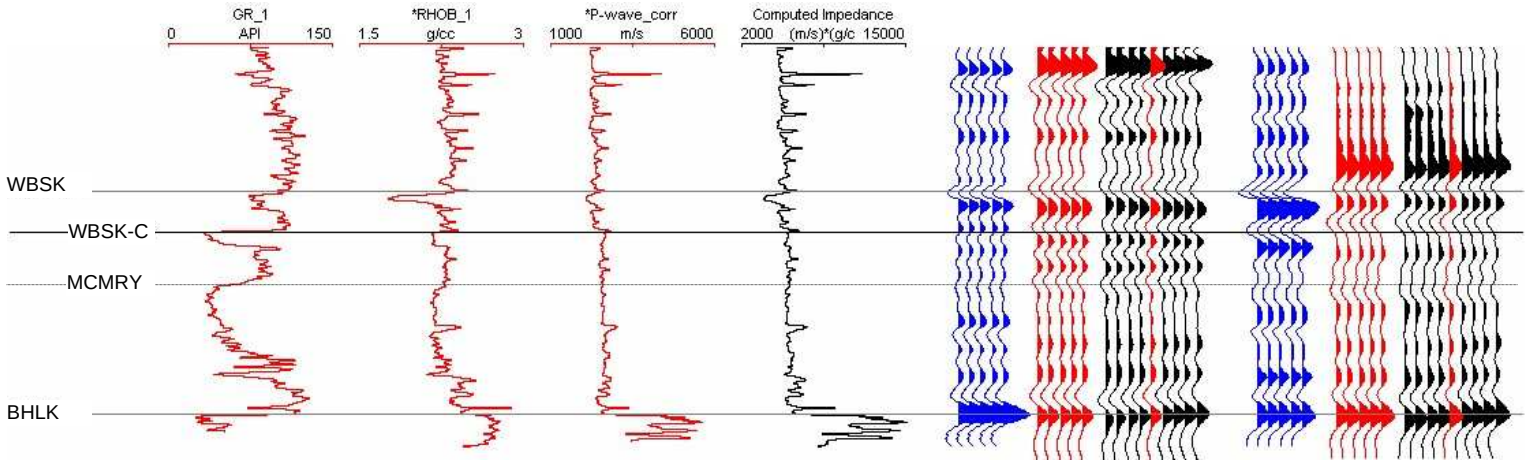

Figure 3.37 Synthetic tie with AVO derived reflectivities. Blue traces are synthetic reflectivity; red traces are inverted reflectivity at well location; black traces are portion of inverted reflectivity section at well location. Left group of traces are P reflectivity and right group of traces are density reflectivity.

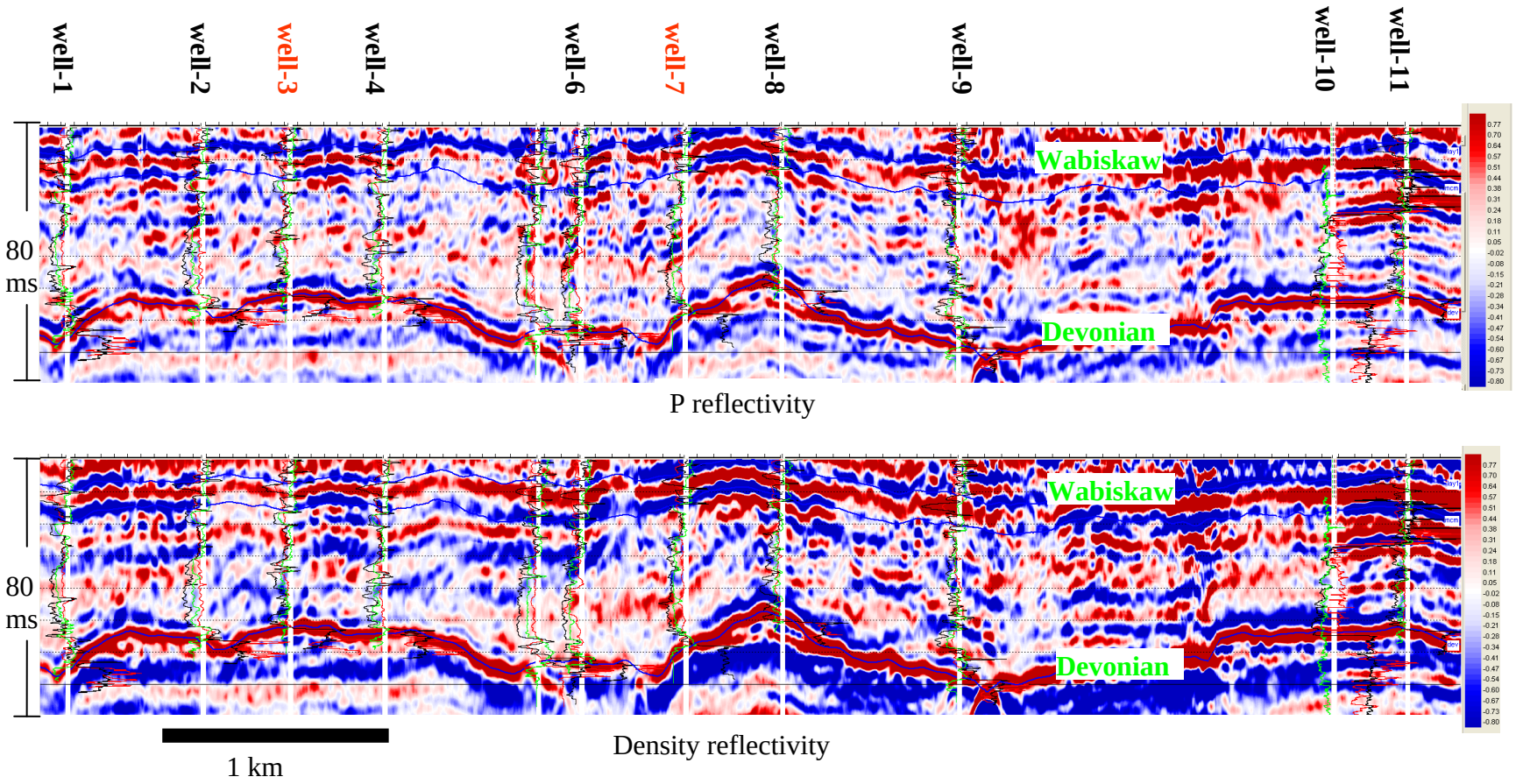

Figure 3.38 P impedance and density reflectivities sections from the AVO inversion.

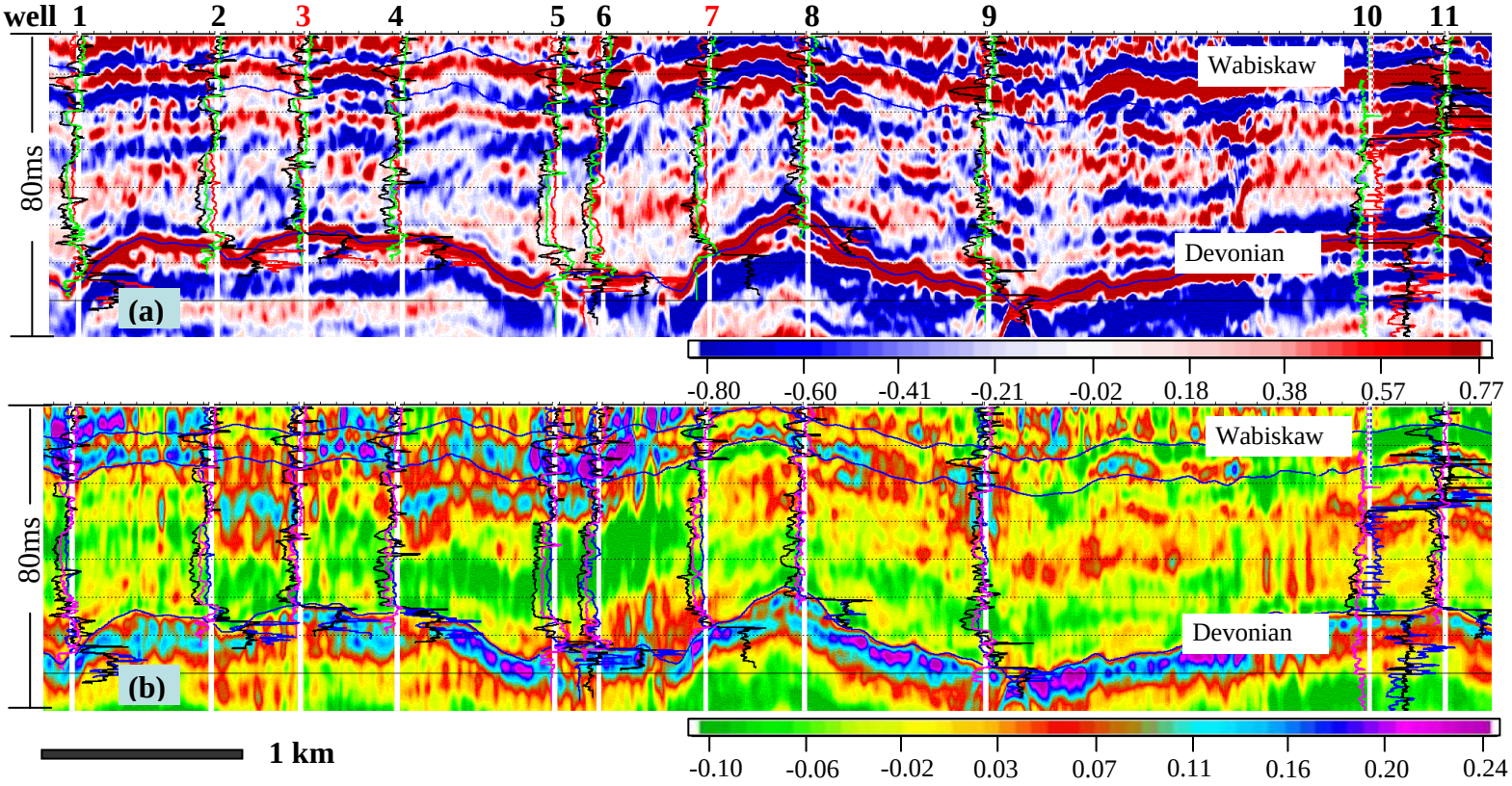

Figure 3.39 Top panel (a) is the density reflectivity; second panel (b) is the colored density—the trace-integration version of density reflectivity; third panel (c) (on next page) is the density section from model based inversion; bottom panel (d) is V-shale transformed from density in the third panel using the linear relationship between density and gamma ray shown in Figure 1a. Log curves are overlaid on the section. In panels (b), (c), and (d), the black curves are density logs, the purple are gamma ray logs, and the blue are impedance logs. No density logs are used in the derivation of (b),and density logs from all wells except well 3 and well 7 and horizons are used to generate a density model to derive (c) from (a) using model-based post-stack inversion -- the Hampson-Russell Strata software package *(continued on next page).*

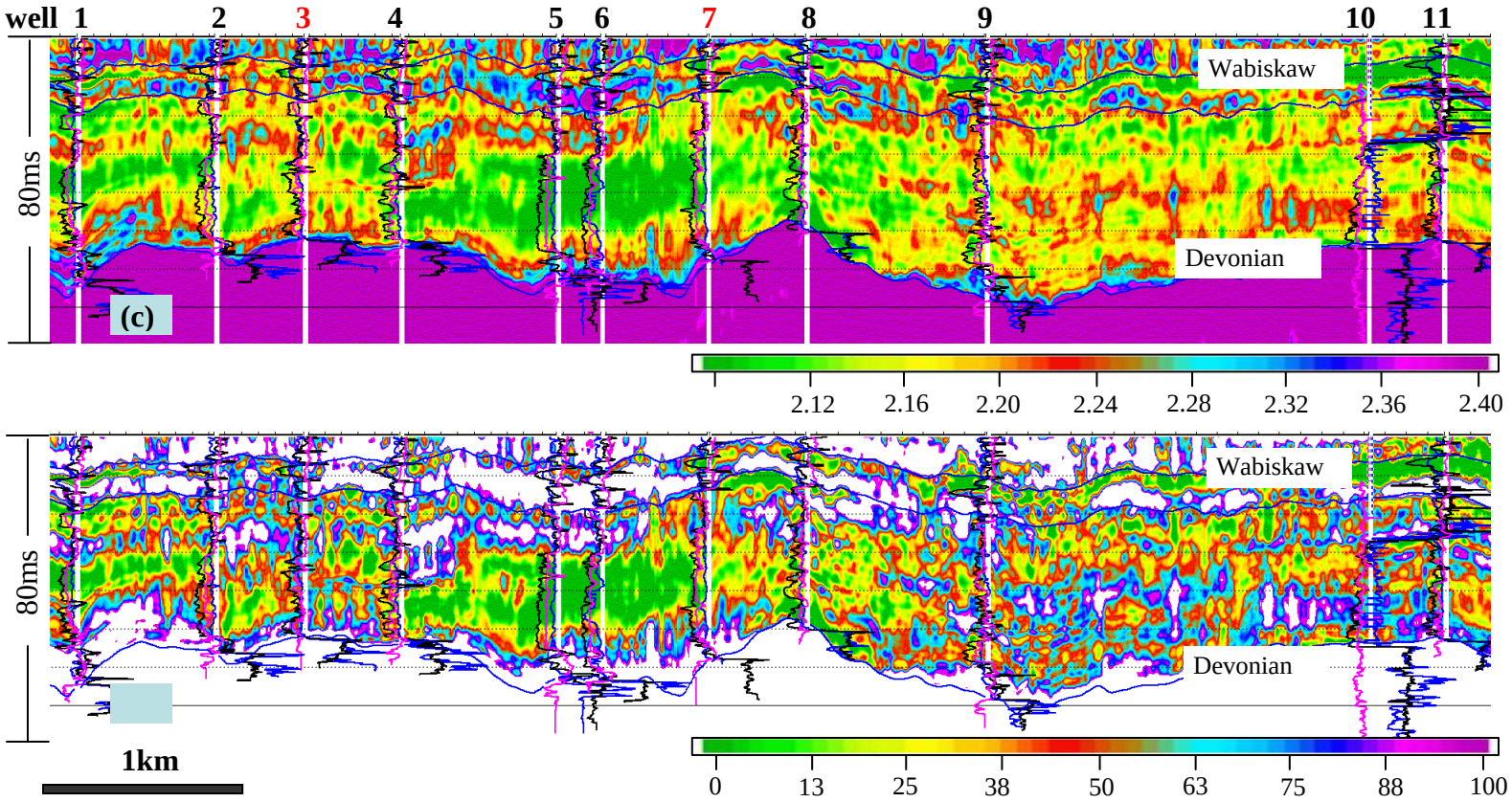

Figure 3.39 *(continued from previous page)* **The middle McMurray is usually the reservoir while the upper McMurray is cap rock. The richest sand areas (dark green) within mid-McMurray are around wells 5 and 6 with good shaley cap rocks in upper McMurray, and these are verified by gamma-ray logs of both wells. Recently drilled well 3 and well 7 are served as blind well tests. Well 3 is mainly shaley within McMurray and the density inversion result verifies this. Well 7 is drilled at the edge of the richest sand zone and its reservoir also matches the inversion results. In addition, the sandy cap rock within upper McMurray in well 7 is convincingly predicted by the inversion.**

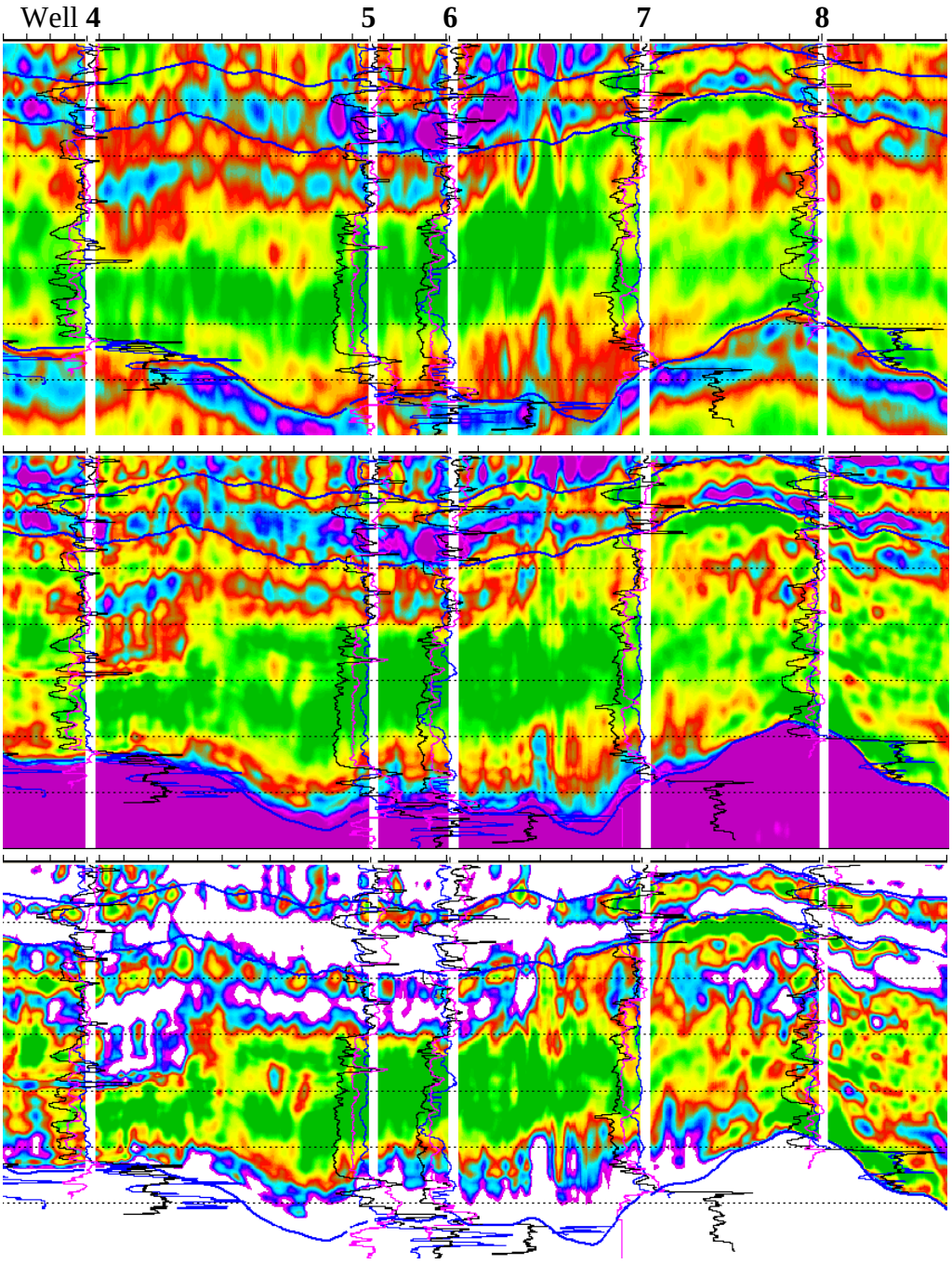

Figure 3.40 Enlarged portions of relative density, density and shale volume between wells 4 and 8. Top panel: relative density (seismic frequency bandwidth); middle panel: full bandwidth density (from model based inversion); bottom panel: shale volume. Color codes are same as in Figure 3.39. The sections are displayed in the Hampson-Russell Strata software package.

3.7 CONCLUSIONS

Chapter 3 discusses the AVO inversion for the PP data based on the approximation of Zoeppritz equation and its applications on the prediction of lithology heterogeneity of heavy oil reservoirs in the WCSB; the improvements on the PP and PS joint inversion are briefly discussed and illustrated by a synthetic example. With the better understanding of ill-posedness in the AVO inversion, improvements make the inversion more robust and more applicable in the oil sands reservoir characterization. The commonly used Bayesian AVO inversion is evaluated and the additional constraint from the data-driven rock physical interpretation is introduced for a more reliable and theoretically reasonable solution.

The estimator of the Bayesian AVO inversion used by many industrial peers is $(\mathbf{G}^{\mathbf{T}}\mathbf{G}+\sigma_{\mathbf{N}}^{2}\Sigma_{\mathbf{m}}^{-1})^{-1}\mathbf{G}^{\mathbf{T}}\mathbf{d}$, with an assumption of zero mean of the model parameters. However, the assumption of zero mean is not correct. Therefore, the estimator of the Bayesian AVO inversion used by the implementation in the thesis is

$$\hat{\mathbf{m}}=(\mathbf{G}^{\mathbf{T}}\mathbf{G}+\sigma^{2}\Sigma_{\mathbf{m}}^{-1})^{-1}\mathbf{G}^{\mathbf{T}}\mathbf{d}+(\mathbf{G}^{\mathbf{T}}\mathbf{G}+\sigma^{2}\Sigma_{\mathbf{m}}^{-1})^{-1}\sigma^{2}\Sigma_{\mathbf{m}}{}^{-1}\overline{\mathbf{m}}\,.$$

Some modifications on this estimator are made for more reliable solutions for oil sands reservoirs. The Bayesian AVO inversion is realized in the frequency domain in this thesis to be more robust and to better deal with the tuning. Spatial correlation on the stacked data is used to constrain the inversion, which is as effective as the supergather -- increasing the signal-to-noise ratio or sample number.

The conventional AVO analysis is used for the oil sands reservoir characterization. In the conventional AVO analysis, the reflectivity, colored impedance, and well-log-like impedance are all derived in multi-steps. The outputs from every step are all useful in the interpretation and data quality control.

Two case studies are shown in this chapter to demonstrate the effectiveness of the reliable AVO inversion and the characterization of oil sands reservoir lithology heterogeneity. The case studies show that besides the typical P and S wave attributes, the AVO

inversion derives density attributes from the PP data with relatively high reliability. In the second case study, the prediction of lithology in the McMurray Formation in Athabasca is confirmed by blind well tests. The bandlimited density from the AVO inversion provides key information for the lithology prediction.

Chapter 3 has discussions on the joint PP and PS AVO inversion. The joint PP and PS inversion reduces the ill-posedness of PP AVO inversion. The frequency bandwidth difference in the PP and PS data needs to be considered by the joint inversion. The frequency domain implementation of the joint PP and PS inversion is suggested and illustrated by synthetic tests. The application of the suggested joint inversion will be done in the future when both components of data are available and processed appropriately.

3.7.1 Discussion

In this chapter, methodologies are addressed to derive reliable lithology sensitive attributes from the pre-stack seismic data. Due to the limited bandwidth and in particular the absence of low frequencies in the seismic data, it is difficult to directly recover the absolute-value attributes from the seismic data. All the inversion with an absolute impedance output therefore requires a constraint or prior information, which is usually obtained from interpolation of well logs and guided by the picked horizons. After the inversion, this prior information is embedded in the resulting estimates. The background model sometimes dominates the overall understanding of the inversion results and drifts interpretation (e.g. cross-plotting of elastic parameters), and therefore, the artifacts introduced by the interpolation between wells can be misleading in the subsequent interpretation. As advocated by Connolly (2010), methods should be robust and practical as the request for reservoir characterization; the bandlimited AVO attributes are important and should be used as in the initial interpretation in the reservoir characterizations.

3.7.2 Use of output of AVO inversion

The AVO inversion discussed in Chapter 3 is seismic data driven. It is implemented on a time sample basis in time domain or time window basis in the frequency domain. Rock property and lateral correlation constraints are used to reduce the uncertainty of the inversion. Besides the direct use of the output in the interpretation, a post-stack inversion scheme is suggested as a joint P, S impedance (or velocity) and density inversion. This scheme replaces the one-step the full bandwidth pre-stack seismic inversion (discussed in Chapter 4) with a two-step process: the AVO inversion and the joint post-stack inversion. The author believes one-step and two-step inversion schemes should generate very close results. The advantage of the two-step is reducing the computing time on the synthetic pre-stack seismogram generation and fitting with the real data. If the problem is posed in a Bayesian framework with the assumption of Gaussian distributions, the objective function of the joint P and S impedance and density post-stack inversion should be

$$\mathbf{J} = \mathbf{J}_{\mathbf{d}} + \mathbf{J}_{\mathbf{m}} = \left\| \begin{pmatrix} \mathbf{r}_{\mathbf{P}} \\ \mathbf{r}_{\mathbf{S}} \\ \mathbf{r}_{\rho} \end{pmatrix} - \begin{pmatrix} \mathbf{W}_{\mathbf{P}} & & \\ & \mathbf{W}_{\mathbf{S}} & \\ & & \mathbf{W}_{\rho} \end{pmatrix} \begin{pmatrix} \mathbf{D} & & \\ & \mathbf{D} & \\ & & \mathbf{D} \end{pmatrix} \begin{pmatrix} \mathbf{m}_{\mathbf{P}} \\ \mathbf{m}_{\mathbf{S}} \\ \mathbf{m}_{\rho} \end{pmatrix} \right\|^2_{\mathbf{C}_{\mathbf{d}}^{-1}} + \left\| \begin{pmatrix} \mathbf{m}_{\mathbf{P}} \\ \mathbf{m}_{\mathbf{S}} \\ \mathbf{m}_{\rho} \end{pmatrix} - \begin{pmatrix} \overline{\mathbf{m}}_{\mathbf{P}} \\ \overline{\mathbf{m}}_{\mathbf{S}} \\ \overline{\mathbf{m}}_{\rho} \end{pmatrix} \right\|^2_{\mathbf{C}_{\mathbf{m}}^{-1}} . \tag{3.54}$$

The details of the above equation will be explained in Chapter 4. The rock property and geometrical constraints (lateral and vertical, or geostatistical) can be incorporated in the prior term in the above equation, and other PDFs of the model and bound limits can be incorporated as well.

3.7.3 Future work

Seismic anisotropy and the AVO inversion on the multi-component seismic data for heavy oil reservoirs will be worked on in the future.

CHAPTER 4: QUANTITATIVE PREDICTION OF RESERVOIR HETEROGENEITY

4.1 INTRODUCTION

In the previous chapter, developments are made on the AVO inversion to extract seismic attributes to predict reservoir lithology heterogeneity. Lithology-sensitive AVO attributes are derived by the AVO inversion which is mainly a seismic data driven process and results in bandlimited seismic attributes used to map reservoir lithology heterogeneity with the help of rock properties; the methodology is addressed to deal with ill-posedness/ill-condition in the AVO inversion. By carefully dealing with the uncertainty and constraints, the AVO inversion is effective to extract lithology-sensitive seismic attributes and the effectiveness is demonstrated by case studies. However, seismic data mainly provides relative changes of the elastic parameters or reservoir properties; the absolute values, the low frequency contents, are missing in the seismic data. A quantitative prediction of reservoir properties usually needs well-log-like full frequency bandwidth data. To obtain the absolute rock physical parameters from the seismic data, low frequency contents and the background trend of elastic parameters and reservoir properties have to come from sources other than the seismic data and be integrated with the seismic data.

This chapter shows the study on the quantitative prediction of reservoir properties for heavy oil reservoirs and the developments on the impedance inversion in a Bayesian framework in which the elastic properties of reservoir are converted from the seismic data. Since it is not possible to conduct a detailed study on the relationship between elastic properties and reservoir properties, such as saturation and facies, the inversion does not include reservoir properties.

4.1.1 Structure of Chapter 4

Section 4.2 reviews quantitative predictions of reservoir properties. Beginning with reviews of the inversion methods, Section 4.3 shows the developments of the impedance inversion in a Bayesian framework in this thesis. Using a realistic oil sands model, Section 4.4 demonstrates the Bayesian inversion. Section 4.5 draws conclusions for this chapter.

4.2 QUANTITATIVE PREDICTION OF RESERVOIR PROPERTIES USING SEISMIC DATA: INVERSION AND SIMULATION

Quantitative prediction of reservoir properties is the ultimate goal of reservoir characterization. Reservoir properties, such as porosity, facies, permeability, fluid types and saturation are critical quantities for the reservoir assessment, development, and production. Seismic data in the reservoir characterization provides a geometrical description of reservoirs and estimates of the elastic properties, from which the reservoir properties can be predicted.

The inversion of acoustic and elastic properties from the seismic data is a key step in a classical procedure to predict reservoir properties. With recent developments in the industry, reservoir properties are derived from seismic data by a single step called stochastic simulation. However, the derivation of elastic properties by inversion is still the typical use of seismic data in the reservoir characterization due to the close relationships between the elastic parameters and seismic data. In addition, the inversion of elastic properties from seismic data can be posed as a simpler linear problem with the reasonable Gaussian assumption. Since the seismically related elastic properties usually can be characterized by mono-modal probability density functions, the inversion of elastic properties is relatively simple and the analytical estimate and covariance can be given by a generalized linear inversion or common nonlinear least-squares methods such as Newton’s if less linear forward model operators are used. When the reservoir properties have complex statistical distributions which cannot be handled by a simple linear inversion, the costly stochastic simulation or nonlinear approaches are used in the

industry. The developments on the quantitative prediction of reservoir properties in this chapter focus on improving the inversion of elastic properties by incorporating the prior information for missing low frequency contents in seismic data. Projection of elastic properties onto reservoir classes is another important step, in which multi-modal of probability densities of reservoir properties has to be considered, but it is not covered in this thesis.

Seismic inversion is a classical topic and has been studied for decades. There are good commercialized seismic inversion packages in the industry. But study on seismic inversion (and AVO) is being carried out in the industry and academia, and papers on inversions are published on most recent issues of Geophysics and other major journals. In addition to the developments on core functions of the Bayesian inversion, the work in this thesis implements many basic and supportive functions for the inversion, which build a foundation for the improvement of the inversion for oil sands heterogeneities in the future.

Non-inversion methods to predict reservoir properties include the geostatistical approach (Doyen, 1988) and multi-variate analysis and nonlinear methods such as the neural network (Hampson et al, 2001). Neural networks have been applied in the prediction of reservoir properties in the heavy oils in the WCSB (Tonn, 2002; Anderson et al, 2005; Dumitrescu et al 2005; Dumitrescu et al 2009). In a neural network analysis, relationships between seismic attributes and reservoir properties are derived at wells by training the neural network. The correlations between seismic attributes and reservoir properties are used to rank the attributes. Sometimes the physical link between them is often secondary.

The stochastic inversion (simulation actually) and its applications in the reservoir characterization are seen in many publications in the recent decade (Varela et al 2003; Gunning and Glinski, 2004; Francis, 2005; Contraras et al, 2005; Hansen et al, 2005, 2006; Gonzalez 2006; Merletti and Torres-Verdin 2006; Bosch et al 2007; Spikes 2008; Soni et al 2008; Buland et al 2008; Hansen and Mosegaard, 2008; Bosch et al 2009;

Olvmoen and Omre; 2010; Olvmoen et al 2010; Sams and Saussuss, 2010). The stochastic inversion is usually defined as the counterpart of the deterministic inversion. The following is a brief review on the deterministic inversion, stochastic inversion and procedure of the stochastic simulation.

4.2.1 Deterministic inversion vs. stochastic inversion

The deterministic and stochastic inversions are defined in the industry by Bosch et al (2010), "*the inversion of seismic data for elastic properties can be posed as a deterministic problem or as a stochastic problem, i.e., model random parameters characterized by probability densities (Russell, 1988) summarizes two of the widely used deterministic or optimization-based methods of seismic inversion for elastic properties: sparse-spike techniques and model-based inversion*." and by Francis (2005, 2006a, and 2006b), "*conventional seismic inversion is often referred to as deterministic inversion. A better description would be best estimate inversion. The word deterministic should properly refer to a model from which predictions are determined directly through a functional (physical) relationship. The best estimate refers to a model in which the objective is to minimize the error in the prediction. Well known examples would include linear regression and geostatistical procedures such as kriging. Conventional seismic inversion minimizes the difference between the forward convolution of a wavelet with a reflectivity model and the seismic trace*." Both definitions classify the deterministic inversion as optimization-based methods and the stochastic inversion as probability-based parameter modeling. In fact, the maximum *a posteriori* probability solution under the mono-modal Gaussian probability distribution can be regarded as an optimization method in spite of the fact that the stochastic simulation can be performed as well. Therefore, it is preferred in this thesis to distinguish between inversion (optimization) and simulation.

Another difference between the deterministic and stochastic inversions is addressed by a few researchers, e.g. Francis (2005) and Sams and Saussus (2010): the histogram of output by the deterministic inversion has a smaller variation than impedances observed at

wells. I believe one reason for the smaller deviation from the deterministic inversion is that the deterministic inversion usually only incorporates low frequencies in the initial model (or constant hard bounds) and the solution within the seismic frequency bandwidth is controlled by seismic data. The stochastic simulation generates log like results containing frequencies up to the Nyquist frequency. However, since the simulation draws models to be conditioned to the seismic data, the bandlimited nature of the seismic data certainly impacts on the uncertainty of the final solution of the simulation thus with a frequency dependency. This should be an interesting topic worth studying.

In spite of the difference of the deterministic inversion and stochastic simulation, the estimates of the model by two methods are often very close for the real data (Francis, 2005; Sams and Saussus, 2010), for instance, the similar mean net pays by two inversions in Figure 4.1.

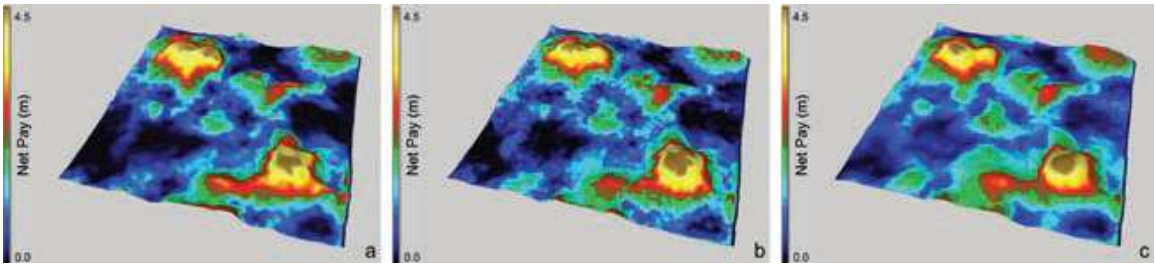

Figure 4.1 The mean net pay from (a) deterministic inversion, (b) the initial model, and (c) geostatistical inversion (Source: Sams and Saussus, 2010a).

4.2.2 Stochastic simulation

Haas and Dubrule (1994) introduce the geostatistical inversion in which Sequential Gaussian Simulation (SGS) is applied to generate many realizations constrained by seismic stacked data. In their inversion scheme, every spatial location is simulated to be conditional to the well controls, seismic data, and the model at the locations where simulation is completed previously. Because the kriging estimation is applied for every simulation, it is a time-consuming process. The most recent geostatistical inversion is applied on the pre-stack data (usually the partial angle stacks to reduce the computation time) when AVO and elastic parameters are popularly used in the industry and the

probability of petrophysical and rock physical properties are used in the posterior PDF of the reservoir properties using the Bayes' theorem (Varela et al 2003; Gunning and Glinski, 2004; Francis, 2005; Contraras et al, 2005; Hansen et al, 2005, 2006; Gonzalez 2006; Merletti and Torres-Verdin 2006; Bosch et al 2007; Spikes 2008; Soni et al 2008; Buland et al 2008; Hansen and Mosegaard, 2008; Bosch et al 2009; Olvmoen and Omre; 2010; Olvmoen et al 2010; Sams and Saussuss, 2010). The running time of simulations depends on the sampling of the posterior PDF: a full Monte Carlo sampling or a biased one e.g. the Sequential Gaussian Simulation (SGS) or Markov Chain Monte Carlo (MCMC). The latter sampling speeds up the simulation process.

Typical stochastic inversion is not difficult to understand: a model is drawn from the posterior PDF and conditioned to the seismic data by fitting the seismic data and synthetic data from the model. If the synthetic is close enough to the seismic data, models are accepted as realizations. To generate a realization, making a synthetic and comparing it with the seismic data may need to be repeated many times. If the geostatistics is used in the model, the kriging or co-kriging estimate is commonly used. A full simulation requires updating the kriging estimate for every new node in a 3D grid in the simulation, which takes much more time as well. A compromised approach is only performing the kriging estimation once using the initial data and using the same kriging estimate for all nodes (Haas and Dubrule, 1994). Francis (2005, 2006a, 2006b) proposes an alternative stochastic inversion, which is actually the hybrid of the simulation and deterministic inversion: a realization conditional to the well data and geostatistics is generated at first; using this realization as the initial model; a generalized linear inversion is applied to update the initial model to fit the seismic data; and the updated model is output as the final realization.

The stochastic inversion is usually costly. A large number of realizations are needed to produce the meaningful mean and variance of the reservoir properties. The minimum number of realization have been the discussions in the literature: 10 realizations are recommended by Torres-Verdin et al. (1999); 10 realizations by Varela et al. (2003); 50-

100 realizations by Rowbotham et al, (1998); 15 realizations by Sams and Saussus (2010); 100 realizations by Francis (2005); 10 realization by Debeye et al (1996). Although recommended by some authors, a dozen of realizations should be difficult to describe the statistics of the model. A realistic number of realizations are possibly 50-100. To save costs, a biased sampling method is usually adopted, for example, the Markov Chain Monte Carlo method.

A remark is made here that the model is with full bandwidth of frequencies but the seismic data is bandlimited. To condition the model to the seismic, only the seismic bandwidth in the model needs to be updated for the data fitting. It is worth a study to design the simulation by drawing models in the frequency domain to save costs in the generation of synthetic seismic data.

4.2.3 Bayesian inversion and stochastic simulation

By assuming Gaussian distributions for the prior probability density and for the errors in the data and by using a linear forward-model operator, the Bayesian inference yields a posterior probability density that is also Gaussian. In this situation, the mean and covariance of the posterior probability density are analytical (Menke, 1989; Buland et al, 2003; Tarantola 2005). If the estimator and deviation of the estimator can be determined analytically, the average and uncertainty of the realizations of the simulation should converge to the estimator and its deviation when the number of realizations is large enough (Francis, 2005; Bosch et al 2010). The analytical mean and covariance define the complete model space; in the meantime, the analytical mean stands for the MAP solution of the inversion while the covariance describes the uncertainty of the solution. Therefore the analytical Bayesian estimator and covariance is a most cost-efficient simulation result. Whenever Gaussian PDFs are available, the analytical solution should be honoured as much as possible. Elastic properties and errors in the seismic data are often observed as mono-modal Gaussian distributions, but the reservoir properties follow multi-modal distributions. Instead of simulating the reservoir properties conditioned to the seismic data, it is a cost-efficient and robust process to transform the seismic data to

elastic properties by an analytical estimator and subsequently simulate the reservoir properties conditional to the elastic properties (Figure 4.2)

Other efforts have been made in the industry to combine the simulation and linear inversion (Francis, 2005; Hansen et al, 2005 and 2006; Hansen and Mosegaard, 2008). Francis's approach is by using the simulation to generate an initial model for the subsequent generalized linear inversion whose output is a realization. Hansen et al (2005, 2006) use previous simulated nodes to update the prior information for the linear inversion until all nodes are completed and many realizations can be generated by randomly picking initial models or simulated nodes.

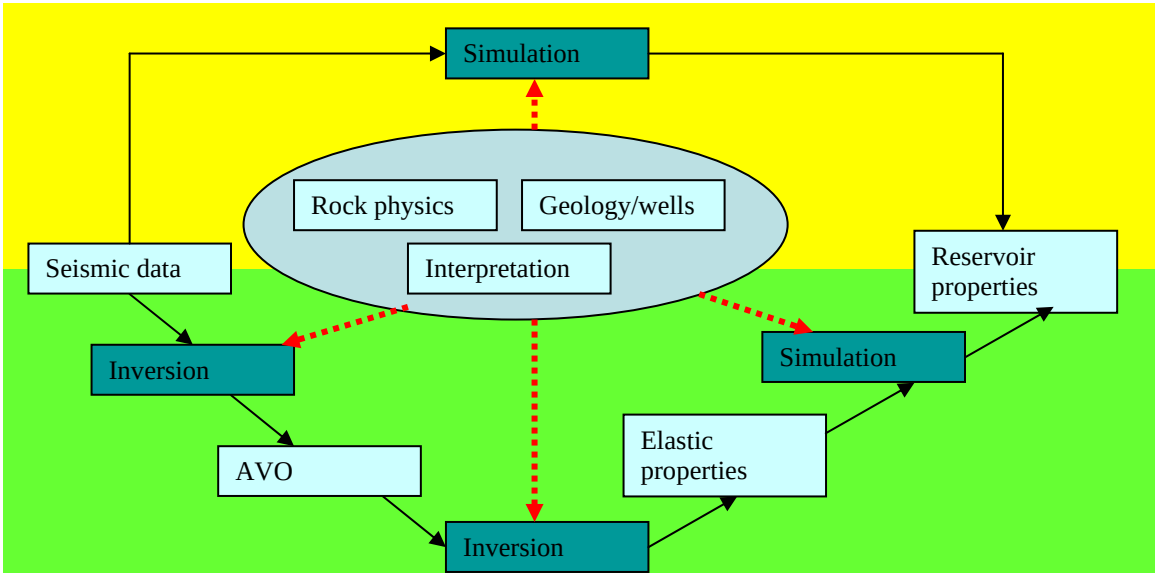

Figure 4.2 Two approaches to transform seismic data to reservoir properties by help of rock properties, geology, wells and interpretation. In the yellow area, the stochastic simulation is a one-step approach; the green area highlights a multi-step approach including the inversion, AVO, and simulation.

4.3 INVERSION

Non-uniqueness and ill-posedness are often combined in geophysical inverse problems (Lines and Treitel, 1985). Different geophysical data can be inverted together, like electrical-magnetic, seismic, and gravity, with the inter-relationship between different data linked to a common model. In the seismic inversion, the strong non-uniqueness exists in the prediction of elastic parameters beyond the seismic bandwidth. If the AVO is

included in the inversion, the ill-posedness is another issue to deal with. Starting with a brief review of a few typical seismic inversion methods in the history, this section describes the developments of the Bayesian seismic inversion.

4.3.1 Methods of inversion

Seismic data is the bandlimited reflectivities. A well-accepted relationship between the reflectivity and impedance (here the impedance is referred to a more general term for the P and S wave impedances, velocity, density, Lame's parameters, elastic impedance, etc.) is as follows

$$\mathbf{r} = \frac{\mathbf{I}_2 - \mathbf{I}_1}{\mathbf{I}_2 + \mathbf{I}_1} = \frac{\Delta \mathbf{I}}{2\mathbf{I}} = \mathbf{d}(\ln \mathbf{I}), \tag{4.1}$$

where $\mathbf{r}$ is the reflection coefficient and $\mathbf{I}$ is the impedance, $\mathbf{I}_1$ and $\mathbf{I}_2$ are the impedance of upper and lower sides of a reflection interface, $\mathbf{d}$ is for difference, and "ln" stands for natural logarithm. .

4.3.1.1 Bandlimited inversion

The bandlimited inversion is a basic method to convert the interface seismic data into the interval impedance data for the convenience for interpretations. The bandlimited inversion includes the trace integration (Lindseth, 1979) and the colored inversion (Lancaster and Whitcombe, 2000). The trace integration takes the form of

$$\mathbf{I}_2 = \frac{1+\mathbf{r}}{1-\mathbf{r}} \mathbf{I}_1 \tag{4.2}$$

Lindseth (1979) uses the trace integration to generate the bandlimited impedance and combines it with a smooth low frequency background impedance to create a smoothed well log-like impedance profile. The trace integration should be applied on the data with balanced spectra. Scaling is needed to tune the bandlimited impedance to the corresponding impedance range.

Colored inversion is used as a fast-track application in the reservoir characterization (Lancaster and Whitcombe, 2000). A global operator is estimated from the well logs and seismic traces by matching seismic spectra with those of the impedance logs. The

operator applies the spectral shaping and phase rotation on the seismic traces to generate bandlimited impedance. The scaling issue is automatically handled by the operator, which is bandlimited itself. The color inversion seems to be more robust than the trace integration. The example in Figure 4.3 shows the bandlimited impedance from the trace integration and colored inversion.

The bandlimited impedance from a trace integration or colored inversion is only the relative impedance, containing positive and negative data values like seismic data. But the inversion modifies phases and boosts the low frequency amplitude so that the bandlimited impedance is more desirable to the stratigraphic interpretation and lithology analysis. In addition, the bandlimited inversion is nearly the 100% data driven. It provides a quality control for other inversions and has been the initial stage of more complicated seismic reservoir characterizations and welcomed by many interpreters (Hernandez et al, 2009; Lazaratos and David, 2009; Robinson and Davis, 2010). The bandlimited inversion from the AVO attributes in Chapter 3 shows its ability in identifying lithologies for the heavy oil reservoirs: the frequency bandwidth of seismic data in the heavy oil areas in the WCSB is usually wide and the bandlimited impedance is of high resolution.

Although some researchers relate the trace integration results to relative impedance and colored inversion results to colored impedance, both of them are called relative impedance in this thesis. Combining the relative impedance with the smooth low frequency background impedance generates the absolute impedance for reservoir property prediction in the initial first look.

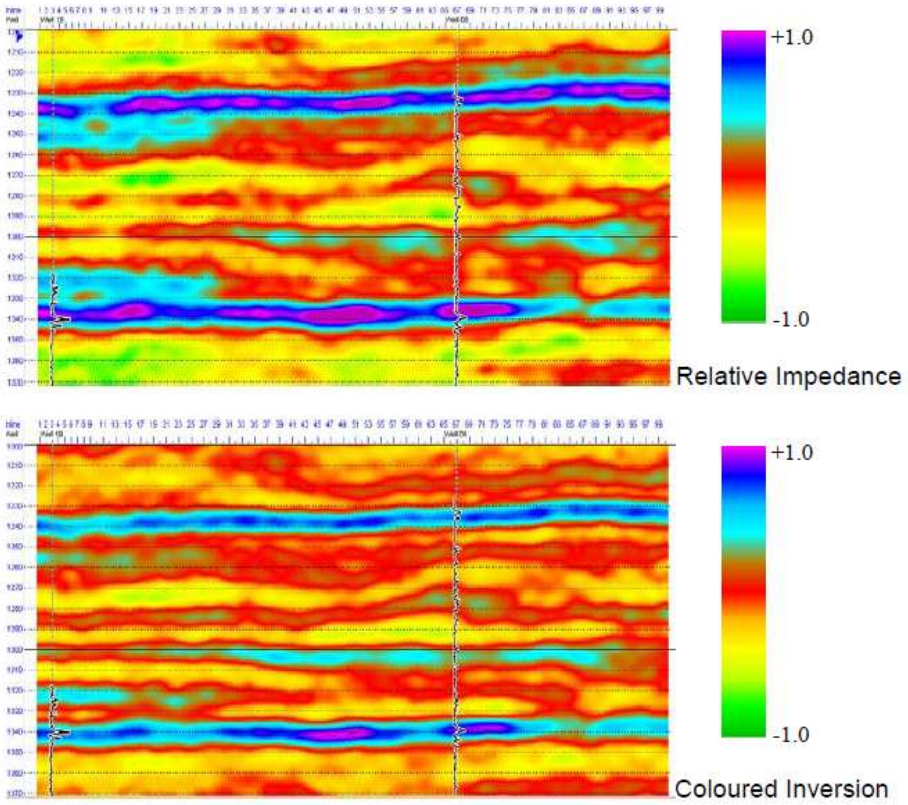

Figure 4.3 Trace integration vs. colored inversion (Source: Earthworks)

4.3.1.2 Sparse spike inversion

The non-uniqueness of the solution of the seismic impedance inversion comes from the bandlimited nature of seismic data (e.g. the missing of low frequency components). The incorporation of geological interpretation and rock property measurements is an important step in the seismic inversion. Sparse spike inversion is one of the inversion methods incorporating constraints to reduce the non-uniqueness in the solution. Oldenburg et al (1983) introduce the minimum structure assumption in their inversion, which generates a minimum number of non-zero reflectivities (sparse spikes) in the inverted traces. The objective function is the sum of l_1 norm of reflectivities such as

$$\mathbf{J=\Sigma|r_i|}. \quad (4.3)$$

A linear programming algorithm is used to solve the optimization min(J) by using seismic data as a constraint and the impedance boundaries as an inequality in the linear

programming algorithm. The optimization gives rise to high-resolution sparse reflectivities.

The sparse spike inversion generates sparse-spike reflectivities with a full bandwidth with the help of the l_1 norm minimization and background constraints, but it fully honours the seismic data. As noted by Francis (2005), the seismic bandwidth portion of the resulting impedance (after filtering) from the sparse spike inversion is almost indistinguishable from the relative impedance from the integration of traces.

Using the l_1 norm or other constraints to generate the sparse reflectivity in the objective functions for the inversion is widely used in the industry (e.g. Sacchi and Ulrych 1996, the Laplace probability distribution -- Duijndam, 1988a and 1988b; the Cauchy probability distribution -- Alemie and Sacchi, 2011).

4.3.1.3 Constrained model inversion

Starting with an initial model of impedance, the model-based inversion adjusts the model to make the best match between the synthetic seismogram and real seismic data and outputs the final model as a solution. Wavelets and convolution models are usually used in an objective function:

$$\mathbf{d=w*r} \tag{4.4}$$

where **d** is the seismic trace, **w** is the wavelet, and **r** is the reflectivity. The reflectivity is defined as the difference of logarithmic impedance,

$$\mathbf{r=ln(I_2)-ln(I_1)}. \tag{4.5}$$

The objective function based on l_2 norm in the matrix form is as follows

$$\mathbf{J=||d-WDz||^2=(d-WDz)^T(d-WDz),} \tag{4.6}$$

where **z** is the logarithmic impedance vector and **D** is the derivative matrix. A straightforward least-squares solution of the minimization of the above objective function is given as

$$\mathbf{z=(D^TW^TWD)^{-1}D^TW^Td.} \tag{4.7}$$

Alternatively, a conjugate-gradient optimization is applied to impose bounds on the solution and stabilize the low frequency (Russell, 1988; Russell and Hampson, 1991; Hampson-Russell software documentation).

Additional regularization terms are usually included in the objective function to restrict the possible solutions to those that satisfy additional criteria, such as a fixed mean layer thickness, smoothness, or a condition of lateral continuity (Sacchi and Ulrych, 1996; Theune et al, 2010).

4.3.1.4 Bayesian inversion

The AVO inversion in Chapter 3 uses the Bayesian constraints to help stabilize the inversion. In this chapter, the Bayesian framework provides constraints to reduce the non-uniqueness in converting the seismic data to impedance. This study focuses on looking for the means and covariance of models with high reliabilities. The prior models from petrophysics and geostatistics have been used by many listed in the beginning of this chapter. In this study, the prior model from geostatistics is not discussed because of the lack of data for reliable variograms, but the prior information of rock property measurements and local geology is included in the inversion.

In a Bayesian framework, the probabilities density function (PDF) of the reservoir model is conditioned to various information including seismic data, petrophysics, geostatistics, and so on. The key to apply the Bayes' rule is to represent the information in the form of probability density function (PDF). The PDF of the reservoir properties (*a posteriori*) are the product of PDFs of all information. The PDFs are usually made with the assumption of normal distributions, including a mean and covariance. The objective of the inversion is to look for a set of reservoir properties, with which the *a posteriori* PDF is maximum (MAP).

In the following, the derivation of the MAP estimate and uncertainty with the Gaussian probability distribution is made. If the model **m** is assumed to follow a multi-variate Gaussian distribution, $\mathbf{m} \sim \mathbf{N}(\overline{\mathbf{m}}, \Sigma_{\mathbf{m}})$, its probability density function (PDF) is

$$\mathbf{p}(\mathbf{m}) = 2\pi \det(\Sigma_{\mathbf{m}})^{-1} \mathbf{e}^{-\frac{1}{2}(\mathbf{m}-\overline{\mathbf{m}})^{\mathbf{T}} \Sigma_{\mathbf{m}}^{-1} (\mathbf{m}-\overline{\mathbf{m}})}. \tag{4.8}$$

The error in the data is usually assumed to follow a Gaussian distribution, i.e. $\varepsilon \sim \mathbf{N}(0, \Sigma_{\mathbf{d}})$. Therefore the likelihood PDF is

$$\mathbf{P(d|m)=}\, 2\pi \det(\Sigma_{\varepsilon})^{-1} \mathbf{e}^{-\frac{1}{2}(\mathbf{Gm}-\mathbf{d})^{\mathbf{T}} \Sigma_{\varepsilon}^{-1} \varepsilon (\mathbf{Gm}-\mathbf{d})} \tag{4.9}$$

The maximum *a posteriori* (MAP) solution is equivalent to the one which minimizes the following objective function

$$\mathbf{J} = (\mathbf{Gm}-\mathbf{d})^{\mathbf{T}} \Sigma_{\varepsilon}^{-1} (\mathbf{Gm}-\mathbf{d}) + (\mathbf{m}-\overline{\mathbf{m}})^{\mathbf{T}} \Sigma_{\mathbf{m}}^{-1} (\mathbf{m}-\overline{\mathbf{m}}). \tag{4.10}$$

Minimizing **J** derives the MAP solution as follows,

$$\hat{\mathbf{m}} = (\mathbf{G}^{\mathbf{T}} \Sigma_{\varepsilon}^{-1} \mathbf{G} + \Sigma_{\mathbf{m}}^{-1})^{-1} \mathbf{G}^{\mathbf{T}} \Sigma_{\varepsilon}^{-1} \mathbf{d} + (\mathbf{G}^{\mathbf{T}} \Sigma_{\varepsilon}^{-1} \mathbf{G} + \Sigma_{\mathbf{m}}^{-1})^{-1} \Sigma_{\mathbf{m}}^{-1} \overline{\mathbf{m}}. \tag{4.11}$$

If $\Sigma_{\varepsilon} = \sigma^2 \mathbf{I}$ is assumed, the above estimator becomes

$$\hat{\mathbf{m}} = (\mathbf{G}^{\mathbf{T}} \mathbf{G} + \sigma^2 \Sigma_{\mathbf{m}}^{-1})^{-1} \mathbf{G}^{\mathbf{T}} \mathbf{d} + (\mathbf{G}^{\mathbf{T}} \mathbf{G} + \sigma^2 \Sigma_{\mathbf{m}}^{-1})^{-1} \sigma^2 \Sigma_{\mathbf{m}}^{-1} \overline{\mathbf{m}}. \tag{4.12}$$

The uncertainty of the estimate is

$$\Sigma_{\mathbf{m|d}} = \Sigma_{\mathbf{m}} - \Sigma_{\mathbf{m,d}} \Sigma_{\mathbf{d}}^{-1} \Sigma_{\mathbf{d,m}} = \Sigma_{\mathbf{m}} - \Sigma_{\mathbf{m}}^{\mathbf{T}} \mathbf{G}^{\mathbf{T}} (\mathbf{G} \Sigma_{\mathbf{m}} \mathbf{G}^{\mathbf{T}} + \Sigma_{\varepsilon})^{-1} \mathbf{G} \Sigma_{\mathbf{m}}. \tag{4.13}$$

Note $\hat{\mathbf{m}}$ is used to represent the estimated **m**, or the MAP estimator. The estimator is the weighted average between the prior term and data term. If $\sigma \rightarrow 0$, $\hat{\mathbf{m}} \rightarrow (\mathbf{G}^{\mathbf{T}}\mathbf{G})^{-1}\mathbf{G}^{\mathbf{T}}\mathbf{d}$, which is the least-squares solution, and if $\sigma \rightarrow \infty$, $\hat{\mathbf{m}} \rightarrow \overline{\mathbf{m}}$, which is the statistical mean of the model (usually the prior model in practice).

Other types of probability distributions can be incorporated into the Bayesian inversion. Sacchi and Ulrych (1996) compare four different regularizations (Lp criterion, the Cauchy criterion, the Sech criterion, and the Huber criterion) in the objective function in the acoustic impedance inversion. These criteria were used in the robust waveform inversions to diminish the influence of outliers in the seismic inversion. l_1 norm criterion is used in the sparse spike inversion (Oldenburg et al, 1983), reviewed in 4.4.1.2. The

Cauchy criterion is also seen being used in the Bayesian inversion for reservoir characterization recently (Lin et al 2008; Alemie, 2010; Alemie and Sacchi, 2011).

4.3.1.5 Uncertainty of inversion

Solutions of the seismic inversion are associated with uncertainties which come from:

1. Measurement errors in seismic data and well logs.
2. Errors incurred by seismic data processing.
3. Approximate wave-equation model (Convolutional model is a commonly used assumption in the seismic inversion).
4. Uncertainties associated with rock physical elastic properties and reservoir properties.

Quantifying uncertainties helps us to estimate our risks. Quantifying all uncertainties in reservoir characterization is important and should be an interesting topic to study in the future.

4.3.2 Developments of the Bayesian inversion in this thesis

The implementation of the Bayesian impedance inversion in this chapter is designed with the following characteristics:

1. The model parameters in the inversion are impedance instead of logarithmic impedance. Logarithmic impedance is commonly used in the impedance inversion (equation (4.1)), which requires the elastic properties log-Gaussian distributed (Buland and Omre, 2003). An approximation with a reasonably good accuracy makes the impedance be the unknowns in the inversion so that the Gaussian assumption can be used.
2. Volume based inversion scheme: multi lateral locations of formations are inverted simultaneously. In a 3D data volume, the input for the inversion is defined by a local area, such as 5 bin x 5 bin. The result in the center bin is the final output. Move to next adjacent location and invert a new local area. When the entire dataset is iterated, the data at each lateral location has been used multiple times. Therefore, the inversion is a computing intensive process.

3. Inversion is designed as a joint post stack P and S impedance and density inversion. The bandlimited P and S impedance and density reflectivities are generated by the AVO inversion, in which the ill-posedness is strong and the solution is stabilized by constraints. The output of the AVO inversion becomes the input of the impedance inversion. Inverting the bandlimited P and S impedance and density instead of prestack data costs less computation time.
4. Rock property constraints are included. Well logs are studied to derive the statistics of rock properties.
5. Bounds of elastic parameters are applied to limit the outlier caused by the Gaussian assumption and l_2 norm terms in the objective function.
6. Lateral correlation is used as the prior information in the volume based inversion.
7. The geometrical attributes, AVO attributes, and neural network are used to build the initial model for the inversion.

It is assumed the noise in the data follows the Gaussian distribution. The Cauchy or Laplace distribution makes the solution more robust and will be studied in the future.

4.3.2.1 Impedance vs. logarithmic impedance

The reflection coefficient is commonly expressed as the difference of logarithmic impedance (Oldenburg et al, 1983; Buland and Omre 2003; Buland et al 2003; Hampson-Russell software documentation), which causes inconvenience for the inversion: (1) the exponentials of the inversion solutions need to be calculated to obtain the impedance; (2) the probability distribution functions of model parameters need to be log-Gaussian or log-Cauchy etc. A separate statistical analysis of rock properties is required to derive the PDFs of the logarithmic parameters. In the following, it is shown that the trace integration with a scaling can be used in the impedance inversion to replace the logarithmic impedance.

The reflection coefficient is defined as follows

$$\mathbf{r_i} = \frac{\mathbf{I_{i+1}} - \mathbf{I_i}}{\mathbf{I_{i+1}} + \mathbf{I_i}}. \tag{4.14}$$

The impedance is inverted from the above reflection coefficient as follows

$$\mathbf{I_i} = \mathbf{I_0} \prod_{\mathbf{j}=1}^{\mathbf{i}} \frac{1+\mathbf{r_j}}{1-\mathbf{r_j}} \tag{4.15}$$

With an assumption of small reflection coefficients, equation (4.15) can be expressed as

$$\mathbf{I_i} = \mathbf{I_0}\left(1 + \sum_{\mathbf{j}=1}^{\mathbf{i}} 2\mathbf{r_j}\right). \tag{4.16}$$

The accuracy of the approximation in equation (4.16) is compared with the accurate equation (4.15) in Figure 4.4 by using a synthetic trace generated from well logs.

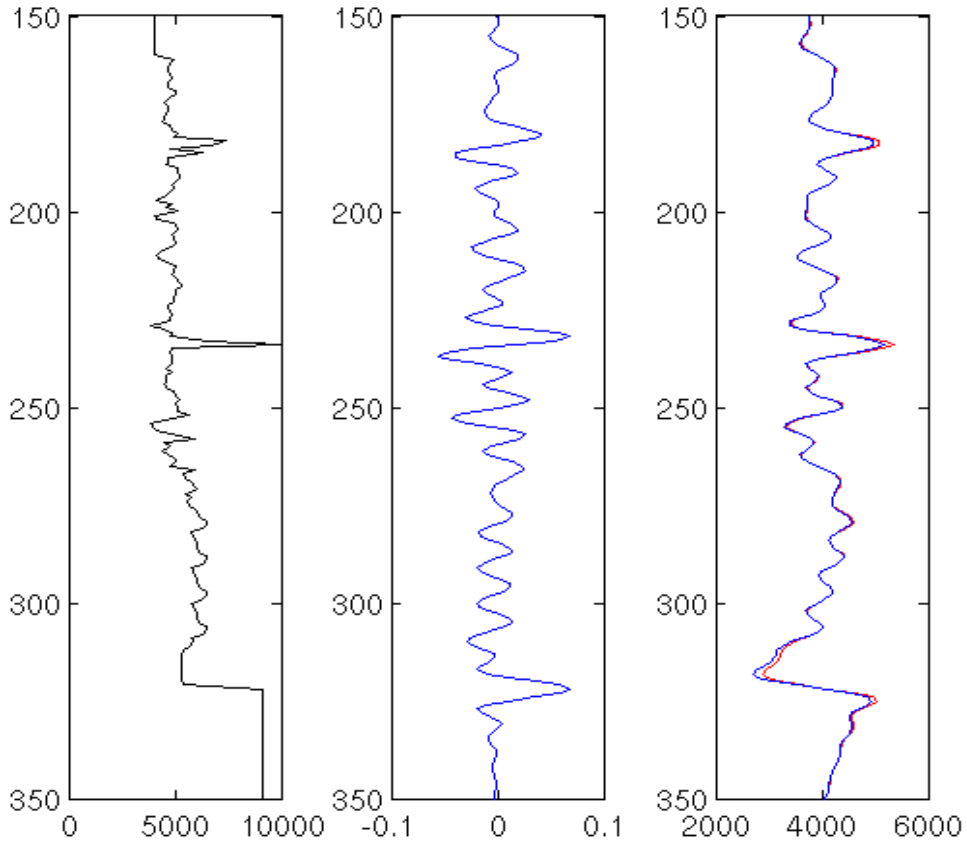

Figure 4.4 Accuracy of trace integration: left – impedance curve; middle – synthetic seismic trace with 10-150 Hz bandwidth; right – band limited impedance inverted from the middle panel (red by equation (4.15) and blue by equation (4.16)).

Equation (4.16) is expressed in the form of matrices as follows

$$\begin{bmatrix} \mathbf{I}_1 \\ \mathbf{I}_2 \\ \mathbf{I}_3 \\ \vdots \\ \mathbf{I}_n \end{bmatrix} = \mathbf{I}_0 + 2\mathbf{I}_0 \begin{bmatrix} 1 & & & & \\ 1 & 1 & & & \\ 1 & 1 & 1 & & \\ \vdots & \vdots & \vdots & \ddots & \\ 1 & 1 & 1 & \cdots & 1 \end{bmatrix} \begin{bmatrix} \mathbf{r}_1 \\ \mathbf{r}_2 \\ \mathbf{r}_3 \\ \vdots \\ \mathbf{r}_n \end{bmatrix}, \tag{4.17}$$

or

$$\mathbf{I= I_0+2I_0Lr.} \tag{4.18}$$

The impedance inversion can be derived from the above equation (4.18).

$$\mathbf{r} = \frac{1}{2\mathbf{I}_0}\mathbf{L}^{-1}(\mathbf{I}-\mathbf{I}_0) = \frac{1}{2\mathbf{I}_0}\mathbf{L}^{-1}\mathbf{I}\,. \tag{4.19}$$

L is an integral matrix and $\mathbf{L^{-1}}$ is the derivative matrix in the equations (4.18) and (4.19). $\mathbf{I_0}$ in the equations acts as a scaling. Equation (4.19) linearizes the relationship between the reflection coefficient and the impedance. Using equation (4.19), the inversion derives an output of impedance instead of logarithmic impedance. The scalar of $(1/2I_0)$ can be provided as the prior information.

4.3.2.2 Lateral and vertical constraints

The model parameters are derived for a window in the impedance inversion. The correlation between the time samples is necessary to be considered. Besides, the correlation between rock physical parameters must be incorporated as well. The lateral correlation of the geology has been considered in Chapter 3, and it is also incorporated in the impedance inversion.

Vertical correlation

An exponential function is used in the industry to reduce the dependency when two formations are far away vertically. It is assumed in this thesis that there is strong independency between the parameters at different depths. The covariance matrix is close to a matrix whose off-diagonal elements reduce their magnitude rapidly as they are away from the diagonal elements.

Lateral correlation

Brac et al (1988) are among the first to introduce stratigraphic constraints in their post stack inversion, Tonellot et al (1999) apply stratigraphic constraints in the prestack seismic inversion. In the methods by both Brac et al and Tonellot et al, the exponential covariance operates as a part of the prior information and is a function of the lateral distance guided by horizons and stratigraphic knowledge. The spatial exponential covariance is also suggested by Tarantola (2005). A spatial exponential covariance defines the lateral correlation acting as an exponential variogram in the geostatistical prediction. It is used in the prestack inversion by Buland et al (2003) and Buland and Omre (2003). The exponential function defining lateral correlations is usually global and uniform in the above applications.

Due to the strong geological heterogeneity in the oil sands reservoir and the limit of well spacing, a global exponential function to define the lateral geology is not appropriate in the IHS facies, one of the causes of reservoir geological heterogeneity. In Chapter 3, multi-lateral locations are inverted in the AVO inversion in which the correlation between neighboring locations is used. The time window used by the AVO inversion is small enough to limit the correlation within local geological features. In the impedance inversion, the time window is longer than the window used in the AVO inversion. The correlation from the entire inversion window cannot reflect the local change of geology. Thus in the impedance inversion, the correlation is estimated for multiple segments within the time window. Its mathematical expression is shown in next section.

Rock property constraint

Many researchers have been investigating the rock physical constraints in Bayesian inversion (Downton and Lines, 2001; Tonellot et al, 2001; Buland and Omre 2003; Downton, 2005; Cassassuce et al, 2004; Roy et al 2008). Here a similar methodology is adopted for the incorporation of rock property constraints, which is in form of covariance matrix of elastic properties usually determined from well logs or local rock properties. The diagonal elements of the covariance matrix are the squares of the standard deviation

of each parameter, and the off-diagonal elements are the product of standard deviations of each pair of two parameters and the correlation coefficient between the two. The covariance matrix is symmetrical.

4.3.2.3 Use of output of AVO inversion

The prestack seismic data (or partial angle stacks) are usually the input to the elastic parameter inversion in the industry. Therefore the ill-posedness and non-uniqueness are reduced simultaneously by the inversion. It takes much time to invert the prestack data, whose data volume is usually large. Here, a slightly different scheme of the elastic parameter inversion is chosen: the elastic parameters are derived from the results of the AVO inversion by using a joint post stack impedance inversion. Therefore, transforming pre-stack seismic data to impedance becomes a two-step approach: the AVO inversion and joint post-stack impedance inversion. The two-step approach handles the ill-condition and non-uniqueness in two separate steps and the use of post-stack data (P, S, and density reflectivities) reduces the computation cost. It should output results equivalent to or close to those by the one-step approach.

If the problem is posed in the Bayesian framework with an assumption of the Gaussian distribution, the objective function of the joint P and S impedance and density post-stack inversion should be

$$\mathbf{J} = \mathbf{J_d} + \mathbf{J_m} = \left\| \begin{pmatrix} \mathbf{r_P} \\ \mathbf{r_S} \\ \mathbf{r}_\rho \end{pmatrix} - \begin{pmatrix} \mathbf{W_P} & & \\ & \mathbf{W_S} & \\ & & \mathbf{W}_\rho \end{pmatrix} \begin{pmatrix} \mathbf{D} & & \\ & \mathbf{D} & \\ & & \mathbf{D} \end{pmatrix} \begin{pmatrix} \mathbf{m_P} \\ \mathbf{m_S} \\ \mathbf{m}_\rho \end{pmatrix} \right\|^2_{\mathbf{C_d}^{-1}} + \left\| \begin{pmatrix} \mathbf{m_P} \\ \mathbf{m_S} \\ \mathbf{m}_\rho \end{pmatrix} - \begin{pmatrix} \overline{\mathbf{m}}_\mathbf{P} \\ \overline{\mathbf{m}}_\mathbf{S} \\ \overline{\mathbf{m}}_\rho \end{pmatrix} \right\|^2_{\mathbf{C_m}^{-1}} . \tag{4.20}$$

where $\mathbf{r_p}$, $\mathbf{r_s}$, and $\mathbf{r}_\rho$ are the vectors of P, S, and density reflectivities generated by the AVO inversion, $\mathbf{m_p}$, $\mathbf{m_s}$, and $\mathbf{m}_\rho$ are vectors of models of P and S impedance and density, $\overline{\mathbf{m}}_\mathbf{P}$, $\overline{\mathbf{m}}_\mathbf{S}$, and $\overline{\mathbf{m}}_\rho$ are the vectors of initial models (or prior model) of P and S impedance and density, $\mathbf{W}_P$, $\mathbf{W}_S$, and $\mathbf{W}\rho$ are the matrices containing shifted wavelet for P, S, and density reflectivities, $\mathbf{D}$ is the derivative matrix, and $\mathbf{C_d}$ and $\mathbf{C_m}$ are respectively the covariance for the noise and covariance for the model. The objective function $\mathbf{J}$ consists

of two parts: the data part $\mathbf{J_d}$ and the prior part $\mathbf{J_m}$. The rock physical, geometrical (lateral and vertical, or geostatistical) and other constraints can be incorporated in the prior term in the above equation. Other distributions of the model and bound limits can be applied as well. The wavelet matrices $\mathbf{W}_P$, $\mathbf{W}_S$, and $\mathbf{W}\rho$ are usually identical if the offset-dependent amplitude of prestack data is preserved and calibrated in the processing, i.e., $\mathbf{W}_P=\mathbf{W}_S=\mathbf{W}\rho=\mathbf{W}$, where W is defined as

$$\mathbf{W}=\begin{pmatrix} \mathbf{w}_1 & 0 & \cdots & 0 \\ \mathbf{w}_2 & \mathbf{w}_1 & & \\ \vdots & \mathbf{w}_2 & \ddots & \\ \mathbf{w}_{\mathbf{n_w}} & \vdots & \ddots & \vdots \\ 0 & \mathbf{w}_{\mathbf{n_w}} & & \mathbf{w}_1 \\ 0 & 0 & \ddots & \mathbf{w}_2 \\ \vdots & \vdots & & \vdots \\ 0 & 0 & \cdots & \mathbf{w}_{\mathbf{n_w}} \end{pmatrix}, \tag{4.21}$$

where n_w is related to the time samples in the definition of a wavelet, and the number of columns is same as the number of samples in the $\mathbf{r_p}$, $\mathbf{r_s}$, or $\mathbf{r}_\rho$ vector.

The derivative matrix **D** is defined as,

$$\mathbf{D}=\begin{pmatrix} -1 & 1 & 0 & \cdots & 0 \\ 0 & -1 & 1 & \ddots & \vdots \\ \vdots & \ddots & -1 & 1 & 0 \\ 0 & 0 & \cdots & -1 & 1 \end{pmatrix}, \tag{4.22}$$

which contains n_d row and n_d+1 columns, where n_d is the length of the $\mathbf{r_p}$, $\mathbf{r_s}$, or $\mathbf{r}_\rho$ vector.

4.3.2.4 Objective function

The objective function of seismic inversion in a Bayesian framework generally includes two parts: the data part (likelihood) – $\mathbf{J_d}$ and model part (prior) – $\mathbf{J_m}$, i.e. the following equation in which a Gaussian distribution is assumed for the noise and model.

$$\mathbf{J}=\mathbf{J_d}+\mathbf{J_m}=\left\|\mathbf{d}-\mathbf{f}(\mathbf{m})\right\|_{\mathbf{C_d}^{-1}}^{2}+\left\|\mathbf{m}-\overline{\mathbf{m}}\right\|_{\mathbf{C_m}^{-1}}^{2}. \tag{4.23}$$

The model part $\mathbf{J_m}$ in the above equation can include a series of terms, e.g., rock properties, geostatistics, and other constraints on the model. Since the definition of the objective function is analytical, an optimal solution should be obtained and the

covariance of the estimator should be defined as well. If the inversion problem is nonlinear, there are possibly multi local maxima of the objective function and nonlinear optimizations need to be applied, e.g. Sen and Stoffa (1991), Mallick (1995) and Ma (2002).

4.3.2.4.1 Linearized forward modeling

Research has been made in the industry to transform the seismic data to reservoir properties in a one step process, in which the complicated relation between the reflection data of seismic and reservoir properties is hidden in either the deterministic inversion or mostly stochastic inversion. Ulvmoen and Omre (2010) and Ulvmoen et al (2010) predict lithology/fluid properties from the prestack seismic data and well observations by using the Bayesian inversion in which a forward modeling generates the synthetic prestack seismic from the lithology/fluid changes. Similar methodologies are applied by others, e.g., Larsen et al (2006). It is assumed that the Bayesian inversion looks after all models and relationships between the elastic parameters and reservoir properties or between the seismic data and elastic parameters. However, a multi-step inversion or simulation process provides more quality controls and interpretation with intermediate results.

The data part in the objective function (4.23) is

$$\mathbf{J_d} = \left\| \mathbf{d} - \mathbf{f}(\mathbf{m}) \right\|_{\mathbf{C_d}^{-1}}^{2}, \tag{4.24}$$

where **f(m)** the forward modeling can be linearized by the following equation if the reservoir properties and elastic properties are linearly linked.

$$\begin{bmatrix} \mathbf{d}(\theta_1) \\ \cdot \\ \cdot \\ \cdot \\ \mathbf{d}(\theta_{\mathbf{n}_\theta}) \end{bmatrix} = \begin{bmatrix} \mathbf{W}_1 & & & \\ & \cdot & & \\ & & \cdot & \\ & & & \mathbf{W}_{\mathbf{n}_\theta} \end{bmatrix} \begin{bmatrix} \mathbf{c}(\theta_1, \mathbf{P}) & \mathbf{c}(\theta_1, \mathbf{S}) & \mathbf{c}(\theta_1, \rho) \\ \cdot & \cdot & \cdot \\ \cdot & \cdot & \cdot \\ \cdot & \cdot & \cdot \\ \mathbf{c}(\theta_{\mathbf{n}_\theta}, \mathbf{P}) & \mathbf{c}(\theta_{\mathbf{n}_\theta}, \mathbf{S}) & \mathbf{c}(\theta_{\mathbf{n}_\theta}, \rho) \end{bmatrix} \begin{bmatrix} \mathbf{D} & & \\ & \mathbf{D} & \\ & & \mathbf{D} \end{bmatrix}$$

$$\times \begin{bmatrix} \mathbf{R}(\mathbf{P}, \phi) & \mathbf{R}(\mathbf{P}, \mathbf{V_{sh}}) & \mathbf{R}(\mathbf{P}, \kappa) \\ \mathbf{R}(\mathbf{S}, \phi) & \mathbf{R}(\mathbf{S}, \mathbf{V_{sh}}) & \mathbf{R}(\mathbf{S}, \kappa) \\ \mathbf{R}(\rho, \phi) & \mathbf{R}(\rho, \mathbf{V_{sh}}) & \mathbf{R}(\rho, \kappa) \end{bmatrix} \begin{bmatrix} \phi \\ \mathbf{V_{sh}} \\ \kappa \end{bmatrix} \tag{4.25}$$

where $\mathbf{d}(\theta_i)$'s are the angle dependent traces, $\mathbf{W_i}$'s are the angle dependent wavelets ($\mathbf{W_i}$ is a matrix of wavelet, defined similarly as in equation (4.21)), **c**'s are the coefficients in the AVO equations, **D** is the derivative matrix, and **R**'s are the relationships to link reservoir properties (ϕ,$\mathbf{V}_{sh}$, and κ) to elastic properties (Ip, Is, and ρ). Equation (4.25) is formulated into a simple expression as follows by hiding the details inside the matrices and vectors.

$$\mathbf{d=[W][A][D][C]v} \tag{4.26}$$

where **v** is the vector for reservoir properties, **C** is the matrix converting reservoir properties (ϕ,$\mathbf{V}_{sh}$, and κ) into elastic physical parameters (P and S impedance and density), **D** is the derivative matrix to generate reflectivities of elastic parameters (Rp, Rs, Rρ etc.), **A** is the matrix containing the angle information relating to AVO linear equations, **W** is the matrix for wavelet, and **d** is for the traces at various incident angles.

The model **m** can change from reservoir property vector **v** to others. If **m** in **f(m)** is the elastic properties **z=[C]v**, the forward model is

$$\mathbf{d=[W][A][D]z} \tag{4.27}$$

where **z** is the vector of the elastic physical parameters (P and S impedance and density).

If **m** in **f(m)** is the vector of the reflectivity **r=[D][C]v**, the forward model is

$$\mathbf{d=[W][A]r} \tag{4.28}$$

where **r** is the vector of the elastic parameter reflectivity. **A** is a diagonal matrix, and so **W** and **A** can exchange positions resulting in

$$\mathbf{d=[A]r'} \tag{4.29}$$

where **r'=[W]r** is the bandlimited reflectivity with the assumption of angle-invariable wavelet. Equation (4.29) is the forward modeling operator used by the AVO inversion.

Using the forward modeling and l_2 norm, the misfit of data and forward model for the objective function is

$$\left\|\mathbf{d - WADCv}\right\|^2_{\mathbf{C_d^{-1}}}, \tag{4.30}$$

if reservoir properties are the unknowns, and

$$\left\|\mathbf{d}-\mathbf{WADz}\right\|^2_{\mathbf{C}_\mathbf{d}^{-1}} \tag{4.31}$$

if elastic properties are the unknowns, and

$$\left\|\mathbf{d}-\mathbf{WAr}\right\|^2_{\mathbf{C}_\mathbf{d}^{-1}} \tag{4.32}$$

if the reflectivities are the unknowns.

The inversion using equation (4.29) generates the bandlimited reflectivities and the inversion based on equations (4.26) – (4.28) can generate full bandwidth outputs but needs to deal with the non-uniqueness. In spite of different output parameter sets (reservoir properties, elastic properties, and reflectivities) based on these equations, the prior constraint is not limited to using the prior term and covariance of the output parameters. The knowledge of another set of parameters can be used via their relationship with the output parameters. For example, if impedance **z** is the output of inversion, the prior knowledge of reservoir properties **v** and reflectivity **r** can be integrated into the prior term of the objective function in the forms of $\left\|\mathbf{C}^{-1}\mathbf{z}-\bar{\mathbf{v}}\right\|^2_{\mathbf{C}_\mathbf{v}^{-1}}$ and $\left\|\mathbf{Dz}-\bar{\mathbf{r}}\right\|^2_{\mathbf{C}_\mathbf{r}^{-1}}$, where **C**, **D**, **z**, **v**, and **r** are defined as in equation (4.26). An l_1 term such as $\left\|\mathbf{Dz}\right\|$ is usually used for a minimum number of layers.

The linear AVO equations are included in the linearized forward modeling for the impedance inversion discussed in the above. The AVO inversion in Chapter 3 has already used these linear AVO equations. The impedance inversion in this chapter uses the output of the AVO inversion– the bandlimited P and S impedance and density reflectivities and the inversion outputs the full bandwidth P and S impedance and density; and the objective function is already shown in equation (4.20) in 4.3.2.3.

4.3.2.4.2 Angle dependency of the seismic wavelet

If the prestack seismic data or partial angle stacked seismic data is used in the inversion, the angle dependency of wavelets needs to be considered. It was discussed in the AVO inversion (Chapter 3) and will be studied further in the seismic data processing and conditioning (Chapter 5). The angle dependency of wavelet is mainly due to two reasons:

(1) the bandwidths of data at near and far angles are different – the near angle data usually contains wider bandwidth than the far angle data, which suffer from more attenuation and offset-dependent tuning; (2) the preservation of amplitude in the data processing is not perfect which introduces non-geological and non-rock physical amplitude variation with angle and this 'pseudo' AVO can be removed by the variation of wavelets with angle after careful calibration.

It becomes common in the industry to use angle-dependent wavelets in the prestack seismic inversion. Prestack seismic data used in the elastic property inversion is usually passed through seismic processing and the offset-dependent primary reflections are assumed to be recovered and preserved. Ideally, the amplitude difference at the near and far angle data is only caused by rock properties and geology. But the data processing and factors other than rock properties and geology often cause the angle dependency of wavelets. The wavelets at different angles must be calibrated carefully to remove the effect from non-rock properties or non-geology.

4.3.2.4.3 a priori

In general, the model (prior) part in the objective function (4.23) is

$$\mathbf{J_m} = \left\| \mathbf{m} - \overline{\mathbf{m}} \right\|_{\mathbf{C_m}^{-1}}^{2}. \tag{4.33}$$

This equation can be more complex to include all possible constraints of rock properties, lateral and vertical correlations, bounds, sparseness, etc. Each constraint is assumed to follow the exponential probability density function. The prior constraints are the product of all the exponential probability density functions. The prior part in the objective function is the sum of exponents of probability density functions. It should in general be

$$\mathbf{J_m} = \sum_{\mathbf{i}=1}^{\mathbf{N_C}} \mathbf{w_i} \left\| \mathbf{m} - \overline{\mathbf{m}} \right\|_{(\mathbf{C_m}^{-1})_\mathbf{i}}^{\mathbf{p}}, \tag{4.34}$$

where $\mathbf{N}_C$ is the total number of constraint terms, $\mathbf{p}$ indicates l_p norm, which is more general than l_2 norm, and $\mathbf{w}_i$ is the weight on the constraints.

Since the P and S impedance and density are the output of inversion, the rock property constraint is in a form of covariance matrix which is calculated based on well controls. This rock property covariance matrix should be

$$\Sigma_{\mathbf{m}} = \begin{pmatrix} \sigma_{\mathbf{P}}^2 & \sigma_{\mathbf{P}}\sigma_{\mathbf{S}}\mathbf{r}_{\mathbf{PS}} & \sigma_{\mathbf{P}}\sigma_{\rho}\mathbf{r}_{\mathbf{P}\rho} \\ \sigma_{\mathbf{P}}\sigma_{\mathbf{S}}\mathbf{r}_{\mathbf{PS}} & \sigma_{\mathbf{S}}^2 & \sigma_{\mathbf{S}}\sigma_{\rho}\mathbf{r}_{\mathbf{S}\rho} \\ \sigma_{\mathbf{P}}\sigma_{\rho}\mathbf{r}_{\mathbf{P}\rho} & \sigma_{\mathbf{S}}\sigma_{\rho}\mathbf{r}_{\mathbf{S}\rho} & \sigma_{\rho}^2 \end{pmatrix} \tag{4.35}$$

where $\sigma_{\mathbf{p}}$, $\sigma_{\mathbf{s}}$, and $\sigma_{\boldsymbol{\rho}}$ are the standard deviations of P and S impedance and density, and $\mathbf{r}_{\mathbf{PS}}$, $\mathbf{r}_{\mathbf{P\rho}}$ and $\mathbf{r}_{\mathbf{S\rho}}$. are the correlation coefficients between P and S impedance and density. The correlation coefficients $\mathbf{r}_{\mathbf{PS}}$, $\mathbf{r}_{\mathbf{P\rho}}$ and $\mathbf{r}_{\mathbf{S\rho}}$ are closely related to the mudrock line of the P and S velocities and density-velocity relation, such as Gardner's relationship (Downton and Lines, 2001). If the elastic parameters are inverted over a time window, each element in the above covariance is replaced by a matrix, which is close to an identity matrix scaled by the individual elements in the above covariance matrix.

Lateral and vertical correlation as covariance matrix

In AVO analysis using the pre-stack seismic data, a common practice is borrowing adjacent CMP gathers to form a supergather – the superbinning (common offset stacking usually follows). The superbinning essentially increases the samples in the inversion, and it does not take into account the geological changes between adjacent locations. In the inversion implemented in this chapter, the lateral changes at adjacent locations are included. The data at the adjacent CMP locations (a mini-cube in 3D) are inverted simultaneously and the lateral change between locations is defined by a covariance matrix consisting of the correlation coefficients. For simplicity, the lateral constraint matrix is explained by the post-stack acoustic impedance inversion in the next.

Suppose $\mathbf{d}_1$ and $\mathbf{d}_2$ are the vectors representing two adjacent stacked traces with the length of the inversion time window. The acoustic impedance vectors to be inverted are $\mathbf{m}_1$ and $\mathbf{m}_2$. The misfits between the data and forward convolution modeling for two traces are respectively

$$\left\|\mathbf{d}_1 - \mathbf{WDm}_1\right\|^2, \tag{4.36}$$

and

$$\left\|\mathbf{d}_2 - \mathbf{WDm}_2\right\|^2, \tag{4.37}$$

where **W** is the wavelet defined as in equation (4.21) and **D** is the derivative matrix defined as in equation (4.22).

If the noise in all traces follows the same Gaussian distribution, the misfit of the joint inversion on the two traces is

$$\left\|\begin{pmatrix}\mathbf{d}_1\\ \mathbf{d}_2\end{pmatrix} - \begin{pmatrix}\mathbf{WD} & \\ & \mathbf{WD}\end{pmatrix}\begin{pmatrix}\mathbf{m}_1\\ \mathbf{m}_2\end{pmatrix}\right\|^2. \tag{4.38}$$

The covariance matrix to include the vertical and lateral correlations should be

$$\mathbf{C}_{\mathbf{corr}} = \begin{pmatrix}\mathbf{C}_{11} & \mathbf{C}_{12}\\ \mathbf{C}_{21} & \mathbf{C}_{22}\end{pmatrix}, \tag{4.39}$$

where $\mathbf{C}_{11}$ and $\mathbf{C}_{22}$ are the auto correlation matrices of each trace and these matrices consisting of zero off-diagonal elements if the vertical independency is assumed, and $\mathbf{C}_{12}$ and $\mathbf{C}_{21}$ are the cross correlation matrices between two traces and they are identical matrices whose off-diagonal elements are usually small for a mildly structural geology compared with the diagonal elements.

4.3.2.5 A special treatment for Athabasca oil sands

In the Athabasca oil sands, the reservoir is usually in the McMurray Formation, which sits on top of the Devonian Formation. The top portion of the Devonian is usually the high-velocity high-density medium. The seismic reflection at the McMurray-Devonian interface should be much stronger than any reflection above the Devonian. The reflection coefficient can be so large (>0.1) that the small reflectivity assumption for the linear AVO equation is not valid. Strong amplitude imposes a large weight on the optimization of inversion. Secondly, the top portion of the Devonian is usually carbonate rock, while formations above the Devonian are clastic rocks. The rock physical behaviours of clastic rock and carbonate rock are different, and the different rock property statistics may challenge some part of the inversion. To minimize the influence of the Devonian

Formation, the McMurray-Devonian interface is estimated in the beginning, and then the seismic data is split into two parts: above and below the Devonian interface. Inversion is performed on two parts separately and the final result is the merge of the two.

4.3.3 Initial model by integration of interpretation

The Bayesian MAP estimation needs the prior term and covariance of the model. The prior term is usually defined by an initial model in practice. Building the initial model is an important first step. Much effort is needed to reasonably integrate all kinds of prior information besides the seismic data. More than one initial model can be used as constraints with different means and covariance. This makes the prior part in the objective function (equation (4.23)) be $\mathbf{J_m} = \sum_{\mathbf{i}=1}^{\mathbf{N_C}} \mathbf{w_i} \left\| \mathbf{m} - \overline{\mathbf{m}}_\mathbf{i} \right\|_{(\mathbf{C_m}^{-1})_\mathbf{i}}^{\mathbf{p}}$, where N_C is the number of constraint kinds, $\mathbf{w_i}$ is the weight on each constraint, and $\mathbf{p}$ stands for *l*p norm. For example, Bosch et al (2009) use models and uncertainties from the geostatistical estimation and from an elastic property study. Solutions from the probability neural network (PNN) analysis can be used in the initial model, but the uncertainty of PNN predictions needs to be defined. This is a future study.

High frequency components (higher than seismic frequency) are not included in the Bayesian inversion in this study. The Bayesian inference generates a balance between the prior model and fitting the seismic data by the maximum *a posteriori* (MAP) probability.

4.3.3.1 Low frequency content in seismic data

The low frequency component or at least the average of the inverted interval in the solution parameters is important for the quantitative prediction of reservoir properties. This portion of inversion results are usually from sources out of seismic data (i.e. well logs). Pre-stack seismic data contains some low frequency velocity information (Claerbout, 1985) – NMO velocities, but it is usually considered that a large uncertainty exists in using this information so that the use of NMO velocities is rarely seen in the reservoir property prediction. NMO velocities were used in pore pressure prediction in

the past (Swan 2001; Kan and Swan 2001). Suggestion has been made combining other geophysical data, i.e. electromagnetic resistivity data (Mukerji et al, 2009, see Figure 4.5), to estimate the low frequency seismic impedance. Recent efforts on the full waveform inversion (FWI) (Operto et al, 2006; Krebs et al, 2009; Margrave et al, 2011) and the field seismic acquisition (Margrave et al, 2011, Isaac and Margrave, 2011; Lloyd and Margrave, 2011) may provide reliable low frequency velocity contents from the seismic data.

In the following, the low frequency velocity from the NMO velocity (pre-stack time migration velocity) is evaluated using fourteen wells with the sonic logs and nearby RMS velocity in an Athabasca oil sands area in the WCSB. After smoothing by a 100ms window, the RMS velocity is converted to an interval velocity. The velocity from sonic logs is smoothed in the same way. The 100ms smoothing acts as a low pass filter, and its frequency response is shown in Figure 4.6, which indicates most of the 0~5 Hz content is preserved after smoothing. Figure 4.7 compares the smoothed velocities from the well sonic logs and interval velocities from the smoothed RMS velocities at the 14 well locations. The reservoir in the McMurray Formation is approximately 50ms thick, overlaying the Devonian. Since most of the wells don't penetrate deep into the Devonian, the actual smoothing within the reservoir interval for the well logs does not include the Devonian, but it does for the RMS velocity in the seismic. This results in a larger mismatch between two kinds of velocities within the reservoir interval. However, it is encouraging that a good match between the two velocities is seen above the reservoir at most of the wells. The mismatch is partly due to poor check-shot corrections. It is worth it to explore and test the processing procedure to derive low frequency velocity content within the reservoir interval from the NMO or PSTM velocity in the future. It is suggested that the Devonian top must be picked in the velocity analysis and the data below the Devonian should not be used in smoothing. These will be tested in the future.

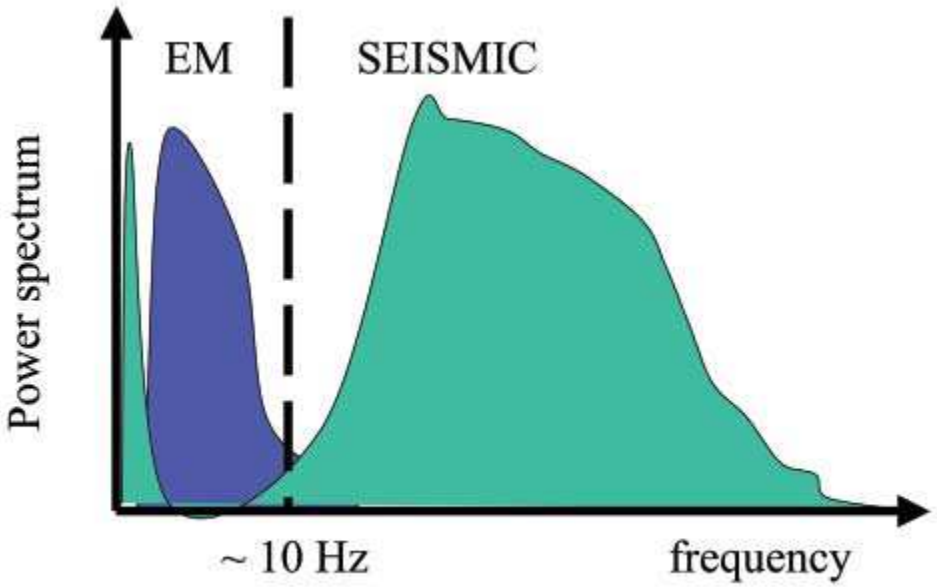

Figure 4.5 The domains where seismic data and CSEM (controlled source electromagnetic(EM)) data contain information about the subsurface. Seismic data lack information about the low frequency (~2-10 Hz) impedance CSEM data contains information in this band about Earth resistivity. (Source: Mukerji et al, 2009). The low frequency information in green (0-2 Hz) is from velocity analysis of seismic data (Claerbout, 1985).

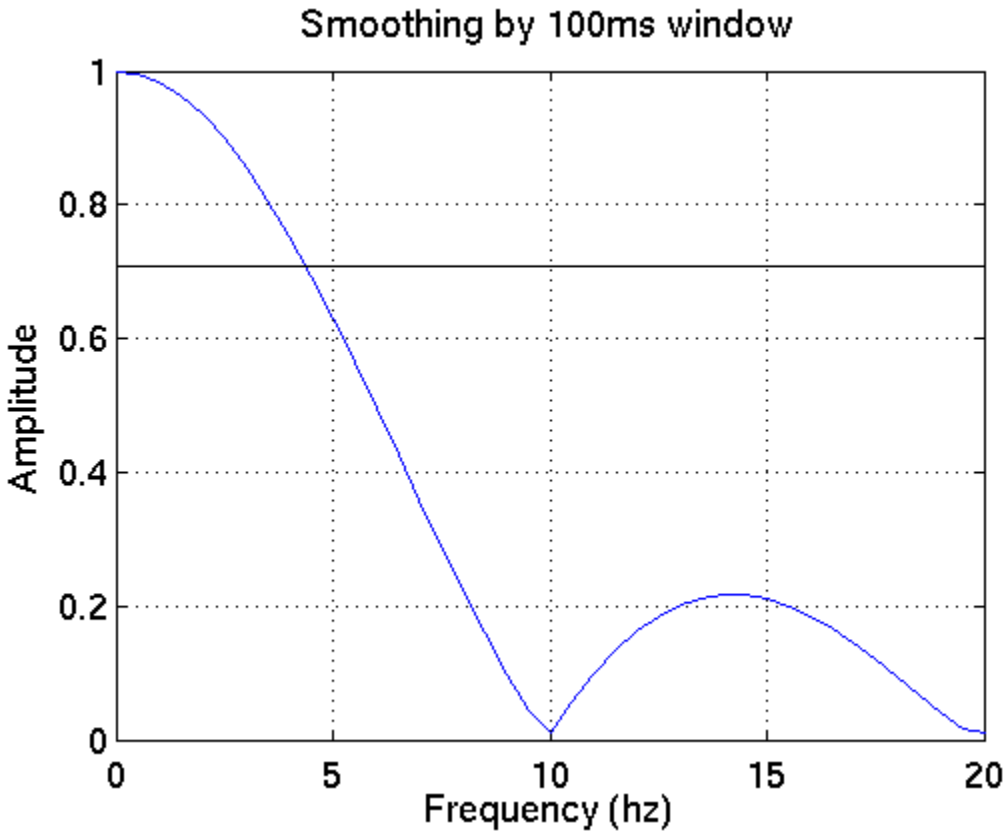

Figure 4.6 Amplitude spectrum of the smoothing operator of 100ms time window. The black line indicates the amplitude value of 0.707.

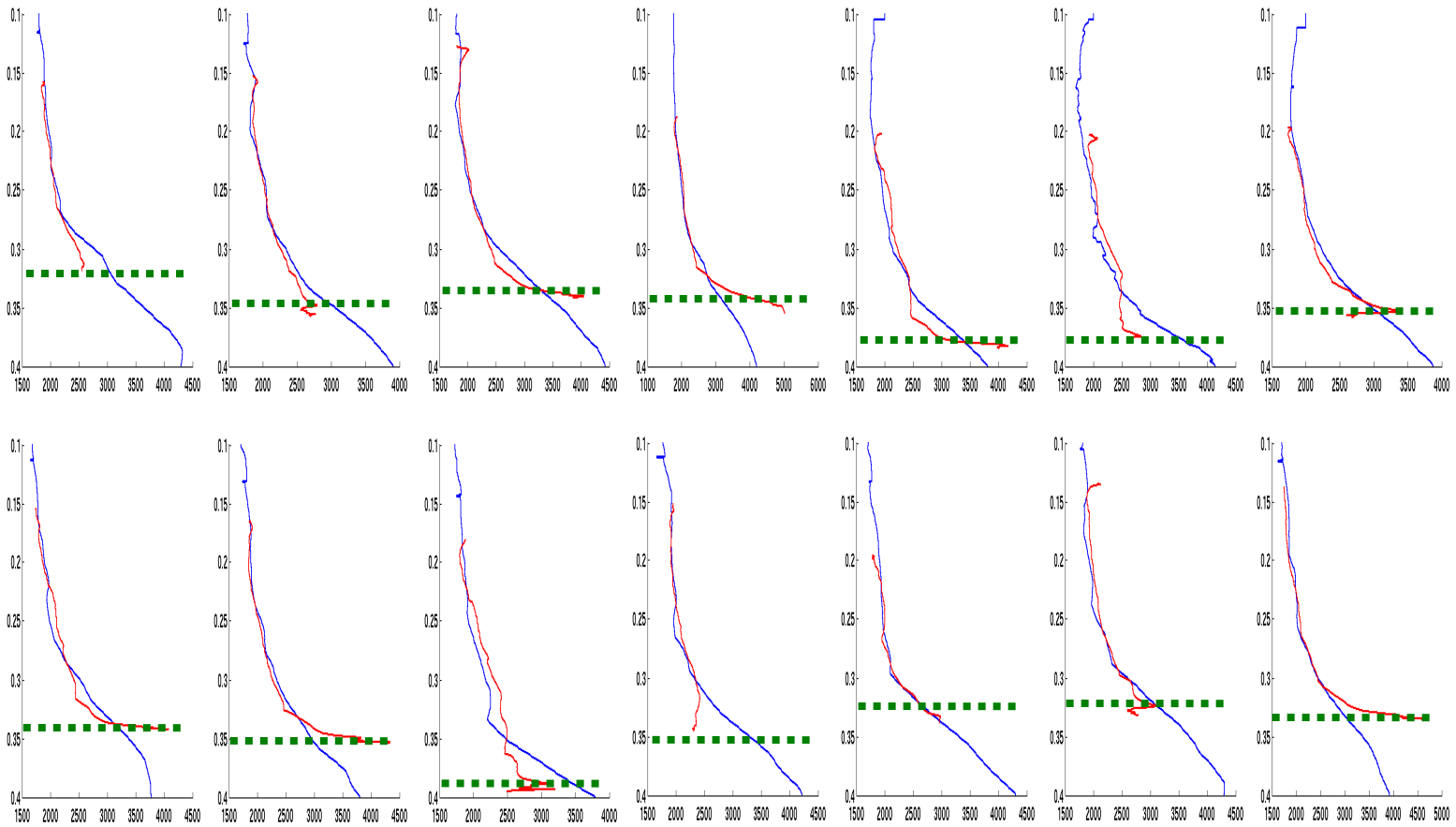

Figure 4.7 Velocity from the well logs (red) and from RMS velocity from seismic (blue). The vertical axis is in time (second) and horizontal axis unit is m/s. Green dash lines indicate the Devonian tops. The reservoir top is about 0.05 second above the Devonian top.

4.3.3.2 Incorporation of seismic attributes

Seismic-derived parameters are called seismic attributes. They can be velocity, amplitude or rate of change of any of these with respect to time or space. Seismic attributes can be classified into “physical attributes” and “geometrical attributes”. Seismic attributes have been used to predict the facies and geometry for decades. Amplitude and amplitude related attributes (such as the instantaneous attributes) and AVO attributes (such P and S impedance, Vp/Vs ratio etc.) are commonly used in the reservoir prediction (Russell et al 1997; Hampson et al, 2001; Tebo and Hart, 2003; Anderson et al, 2005; Dumitrescu et al 2005; Dumitrescu et al 2009; Stright et al 2009). Besides the direct interpretation of these attributes, a suite of seismic attributes can be selected to include those physically meaningful for producing the most effective training set in the artificial neural network for predicting the lithology classes away from the boreholes. Stratigraphically significant attributes can capture changes in waveform shape that are caused by changes in stratigraphy (Hart, 2008). Using models, Hart (2008) finds the secondary derivative of seismic data is better than the seismic amplitude to describe clinoforms (Figure 4.8). Although without a low frequency content (usually with big uncertainties), the relative impedance is used by many interpreters and in practice is one of the best seismic attributes (Cooke et al, 1999).

No doubt, the facies not only change the rock physical properties, causing the seismic amplitude variation vertically, but also they should form distinct lateral patterns. These lateral patterns affect the geometrical and textural characters of seismic data. The seismic attributes showing the lateral patterns relating to the inclined heterolithic stratification (IHS) in the McMurray Formation will provide help in the facie predication. As observed by Fustic (2207) and Fustic et al; (2007), the IHS in the McMurray Formation shows dips on the dipmeter logs. The dip attribute from seismic data is possibly one of such attributes able to help define the IHS in the McMurray Formation. Geometrical attributes, such as coherency, homogeneity, and texture, have been applied in the reservoir characterization (Chopra and Marfurt 2007; Gao 2011). The use of geometrical attributes in oil sands reservoirs is occasionally found in practice (Dumitrescu and Lines, 2009).

Therefore, the 3D seismic data and geometrical or textural attributes are investigated in this section to look for the attributes sensitive to the lateral patterns related to lithofacies.

In this study, the volume-based geometrical attributes are generated for an oil sands reservoir model by using software packages (both commercialized and developed by university consortia). Those attributes include texture attributes, similarity, curvature attributes, local dips, etc. A dozen of the attributes and combinations of them are studied to search the attributes with good correlation with lithology, but such an attribute is hardly found. In general, these geometrical attributes are noisy, containing a low vertical resolution and blurring the formation boundary. A program is coded in the study to calculate local dips from seismic data. With carefully choosing time and spatial windows, the program works better than other available packages. This shows that the geometrical attribute algorithms have to be customized for the needs of oil sands heterogeneity. So other attribute algorithms will be programmed in the future for better reliability and hopefully more attributes good at describing the reservoir geometry.

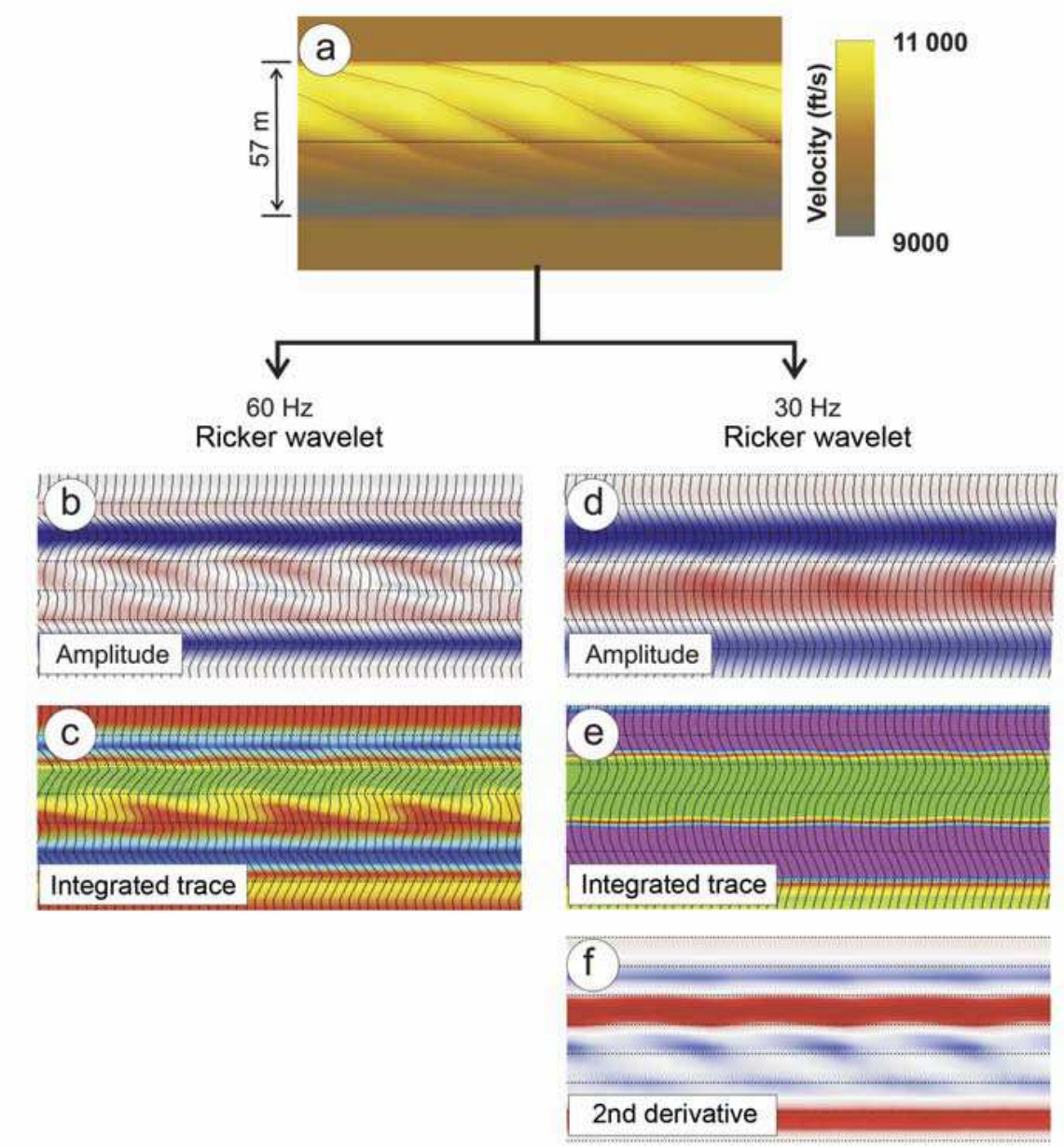

Figure 4.8 (a) Geologic model of a prograding succession of clinoforms. (b) Predicted amplitude response using a 60-Hz Ricker wavelet. (c) Integrated trace (relative acoustic impedance) attribute derived from the amplitude data shown in (b). (d) Predicted amplitude response using a 30-Hz Ricker wavelet. (e) Integrated trace (relative acoustic impedance) attribute derived from the amplitude data shown in (d). (f) Second-derivative attribute derived from the amplitude data shown in (d) (Source: Hart 2008).

4.3.3.3 Initial model

The common procedure in the industry to build an initial model for the impedance inversion is an interpolation using the stratigraphic geometry and the well logs. An initial model for each elastic parameter is built by filling the inter-well volume using a standard interpolation technique. In the initial model built in this thesis, the above process is still carried out as the first step, but the elastic parameters are made constant within the major layers (the McMurray Formation and above and below the McMurray Formation) and the constants of elastic parameters are the average over all reliable well logs. The second step is merging the constant mega layer model with a prediction using the probability neural network (PNN) to generate the final initial model. Therefore only the low frequency content (from smoothing and removal of DC) of PNN prediction is used in the merge. Four attributes are used in PNN to predict elastic properties: relative impedance, dips, time, and lateral correlation on the stack.

PNN is applied in the prediction of heavy oil reservoir properties (Tonn, 2004; Dumitrescu et al, 2006 and 2007; Dumitrescu and Lines, 2008). Although the estimates by PNN are reasonable, the uncertainty of the result is usually not estimated (Gallop, 2006). It is worth it to study this in the future: the uncertainty of the PNN prediction should be expressed in a form of covariance so that the PNN prediction and uncertainty can be used as the mean and covariance by the Bayesian constraint impedance inversion. The PNN analysis has four steps: (i) perform a multi-attribute step-wise linear regression and its validation, (ii) train neural networks to establish the nonlinear relationships between seismic attributes and reservoir properties at well locations, (iii) apply trained neural networks to the 3-D seismic data volume, and (iv) validate results on wells withheld from training.

4.4 EXAMPLE

4.4.1 An Athabasca oil sands reservoir model

A geological model is built for a point bar system in the McMurray Formation. The geology of the McMurray Formation is studied to build a realistic point bar system for

the model in this thesis (the AEUB reports 2000, 2003; Barrett et al, 2010; Cody et al, 2001; Pembicki, 2007; Labrecque et al, 2010; McLennan and Deutsch, 2004; Wynne et al 1994; Nakayama et a 2008; Patruyo et al, 2009; Strobl et al, 2004; Petro-Canada, 2001; Walsh 2008; Webb 2011, and Zou 2005). In some of the literature, the modeling of the point bar systems has been applied, including those in the McMurray Formation (Sarzalejo and Hart, 2006; Patruyo et al, 2009; Willis and Tang, 2010; and Labrecque, 2010).

The McMurray Formation displays a continuum of sedimentary environments, from fluvial in the lower parts, to estuarine in the middle and marine shoreface near the top. A hypothetical depositional model of the McMurray Formation is shown in Figure 4.9 (Bembicki, 2007). The McMurray Formation is subdivided into three members: the lower, middle, and upper McMurray have some consistent lithological expressions. The lower McMurray is generally medium-to-coarse-grained, and massive-appearing to crudely cross-bedded. These beds are most commonly interpreted as having a fluvial nature. The Middle McMurray deposits are dominated by inclined heterolithic stratification (IHS) that is interpreted to represent deposition on tidally influenced point bars. Notably, the middle McMurray contains a brackish-water trace fossil assemblage and is thereby interpreted as representing a fossil estuary. The upper McMurray deposits are variable, but generally contain a comparatively open marine signal. These strata are normally interpreted as shallow, low-energy shoreface deposits and small deltaic complexes (Gingras and Rokosh 2004). The well log cross-section in Figure 4.10 illustrates the lithology variation inside the McMurray Formation. The heterogeneity of the McMurray Formation is illustrated by Figure 4.11 and Figure 4.12.

The oil sands model to test the inversion attempts to depict a point bar system in the McMurray Formation. It includes fluvial channels in the lower McMurray Formation, point bars in the middle McMurray Formation, and marine deposition in the upper McMurray. The point bars are typical in the McMurray Formation in the Athabasca oil sands and have been studied by many in the past (Flach and Mossop, 1985; Fustic et al

2007; Labrecque, 2010; Walsh 2008, Strobl, 2011 (Figures 4.13-4.16)). These studies provide geometrical characteristics of the point bar systems in the McMurray Formation.

4.4.1.1 Model 3D geometrical parameters

The McMurray Formation channel and point bar geomorphological parameters derived by Labrecque (2010) are referred to define the geometrical parameters for the point bar system in the model. Table 4.1 lists the parameters (Labreque, 2010) of the point bar system from the 3D seismic data in the Long Lake oil sands lease, Athabasca.

Table 4.1 McMurray Formation channel and point bar geomorphological parameters (Source: Labreque, 2010).

Parameter	Value	Method
Point bar thickness (T)	Up to 30-40 m	Measured in core/logs
Channel depth (D)	32-36 m	Measured in core/logs
Dip of IHS beds	8-12°	Measured in dipmeter logs
Channel Width (W)	500-584 m	Measured in 3-D seismic data
W:T ratio (F)	14.4-16.7	Based on well and seismic measurements
Meander Wavelength (λ)	5.5-6.4 km	$\lambda = 11W$ (Leopold and Wolman, 1960)
Point bar length	A) 1.4-3.2 km B) 5.9 km	A) $L = 1/2\lambda$ (Leopold and Wolman, 1960) B) Measured in 3-D seismic data
Sinuosity (S)	A) 1.6-1.7 B) 2.4	A) $S = 3.5F^{-0.27}$ (Chorley et al., 1984) B) Estimated from seismic; Neilsen, 2008

Figure 4.17 shows the map view of the 3D point bar for the model. A line (A-B) is marked along the accretion direction of the point bar. Line AB in Figure 4.18 shows the cross section of the point bar.

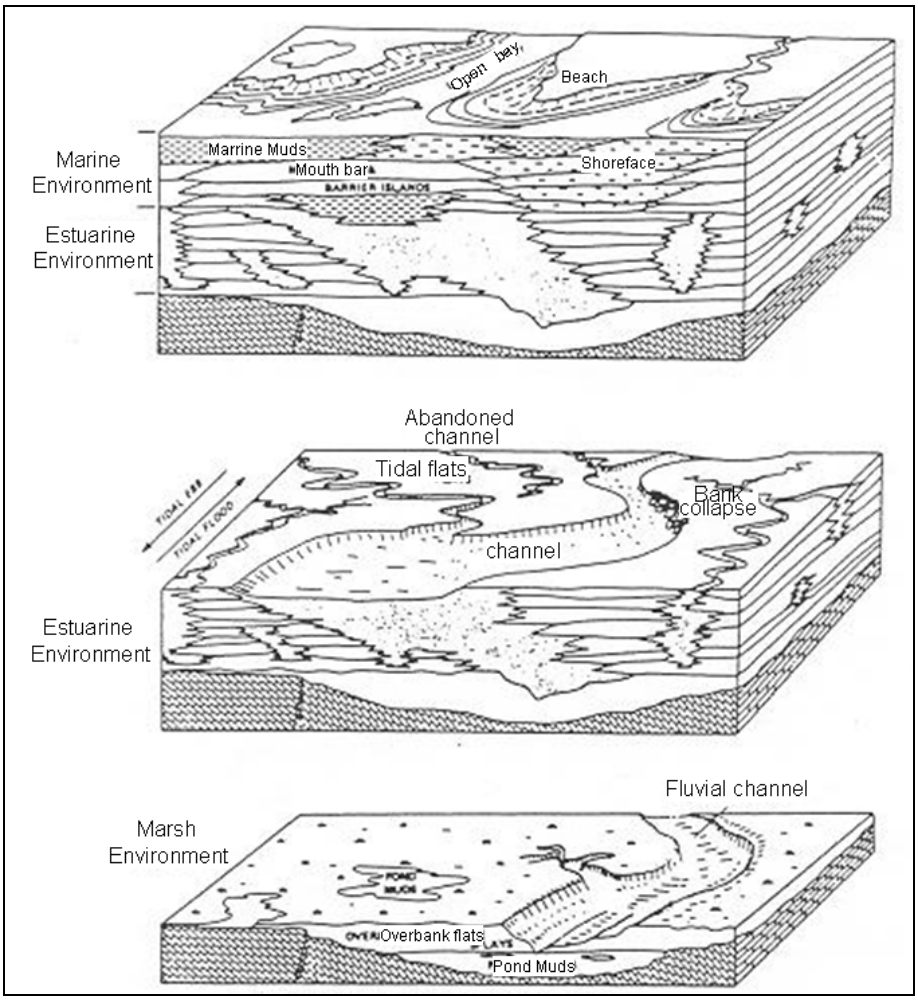

Figure 4.9 Hypothetical depositional model of the McMurray Formation (After Dembicki, 2007)

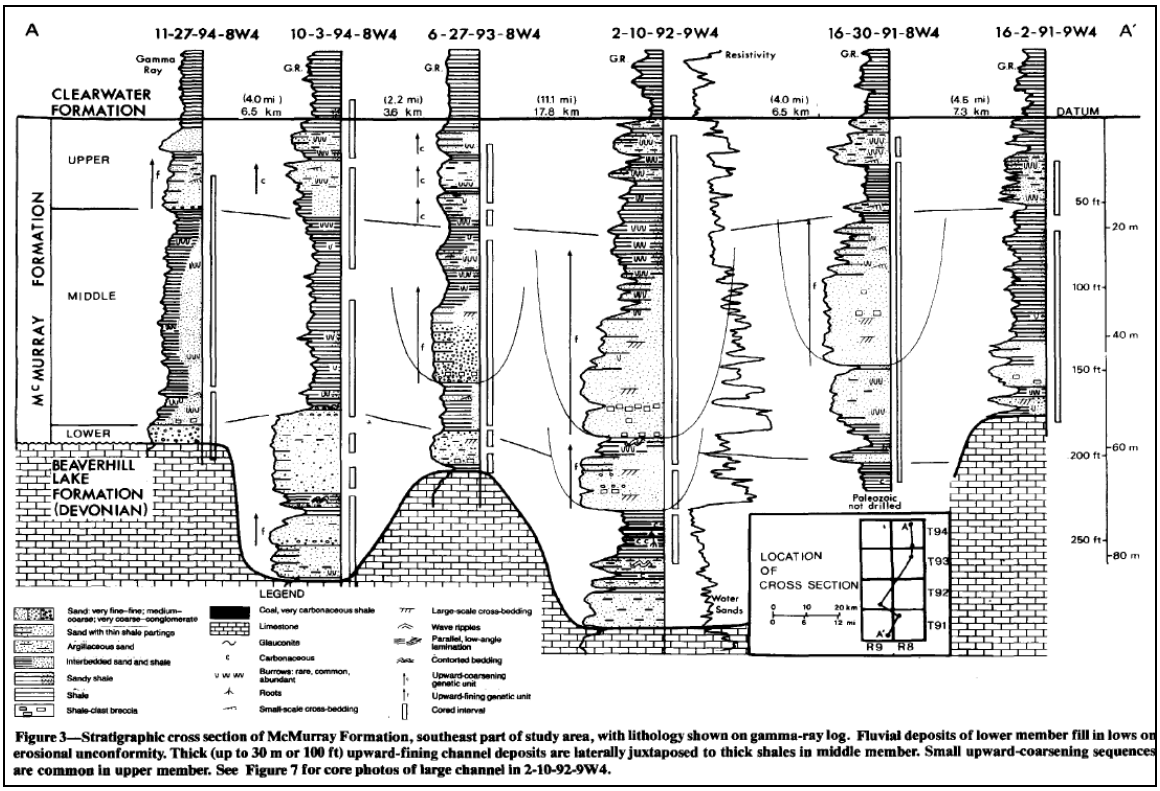

Figure 3—Stratigraphic cross section of McMurray Formation, southeast part of study area, with lithology shown on gamma-ray log. Fluvial deposits of lower member fill in lows on erosional unconformity. Thick (up to 30 m or 100 ft) upward-fining channel deposits are laterally juxtaposed to thick shales in middle member. Small upward-coarsening sequences are common in upper member. See Figure 7 for core photos of large channel in 2-10-92-9W4.

Figure 4.10 Stratigraphic cross section of the McMurray Formation (Source: Flach and Mossop, 1985).

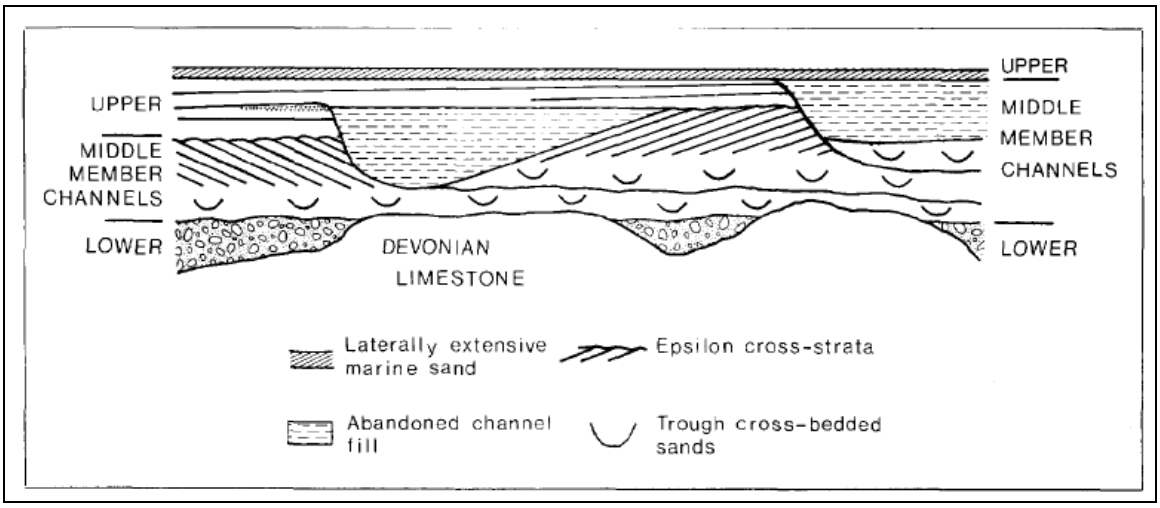

Figure 4.11 Cross section of the McMurray Formation (Source: Flach and Mossop, 1985).

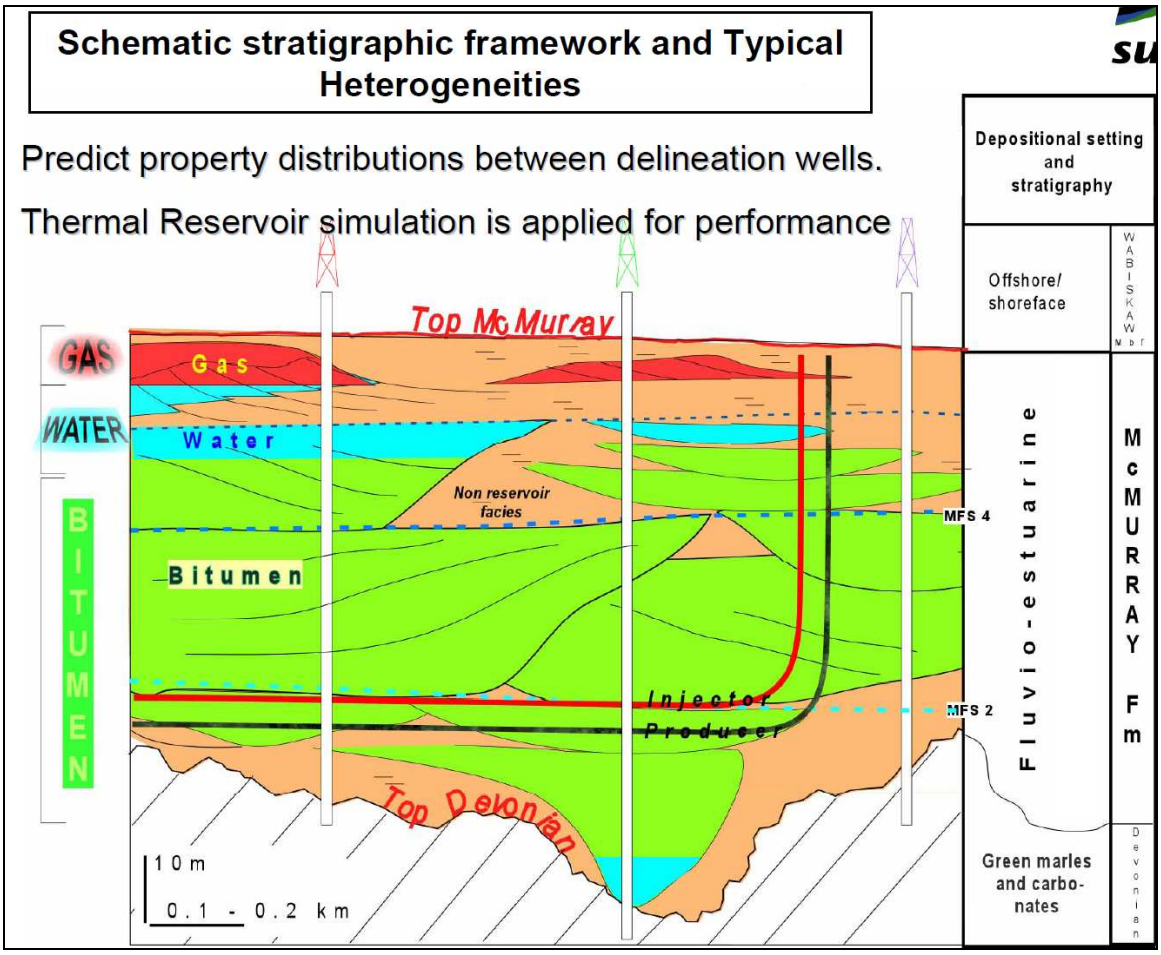

Figure 4.12 Illustration of reservoir heterogeneity and impact on in-situ production of bitumen in the McMurray Formation (Source: Garner et al, 2005).

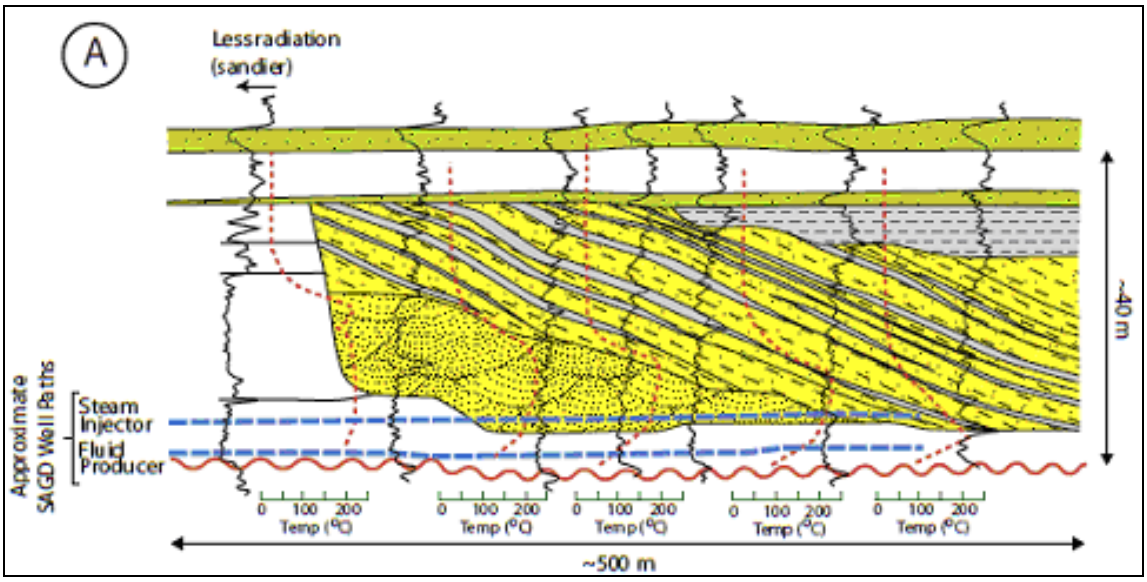

Figure 4.13 Stratigraphic cross-section a point bar in the McMurray Formation (Source: Labrecque, 2010).

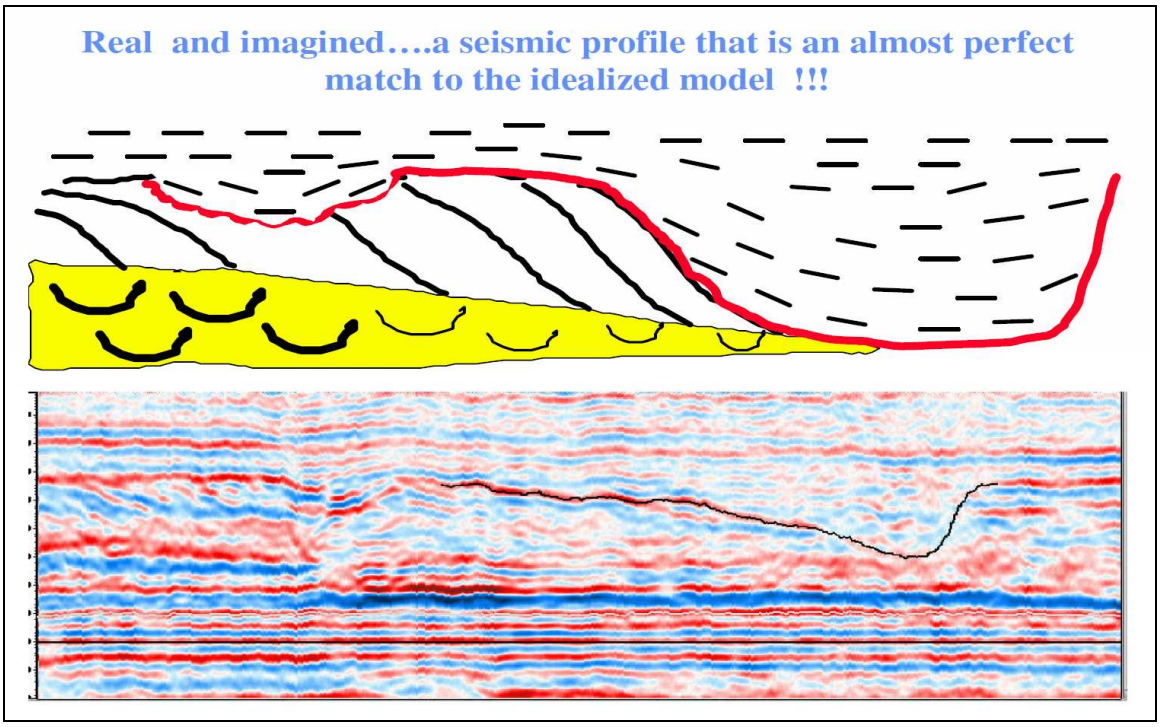

Figure 4.14 Example of point bar with seismic profile (Source: Walsh, 2008)

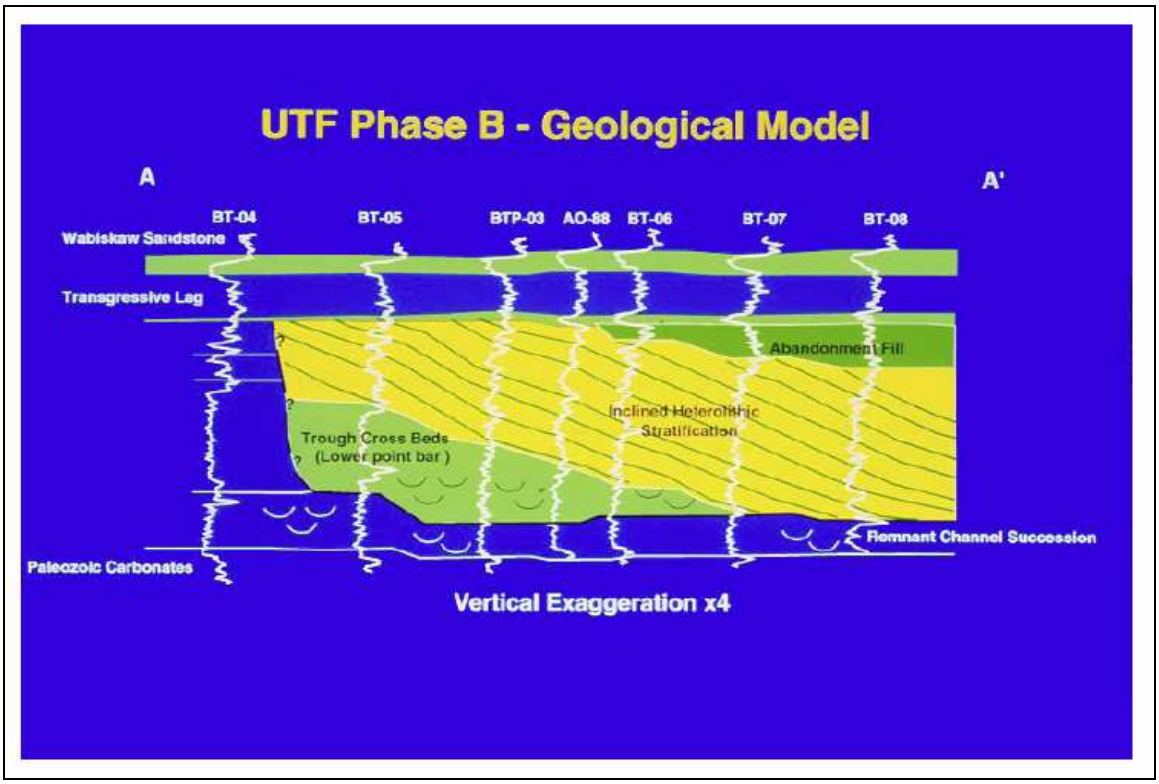

Figure 4.15 Geological model for a cross-section in a point bar system (Source: Strobl, 2011)

Figure 4.16 Time slice of 3D seismic amplitude, showing point bars in the McMurray Formation (Source: Fustic et al, 2007).

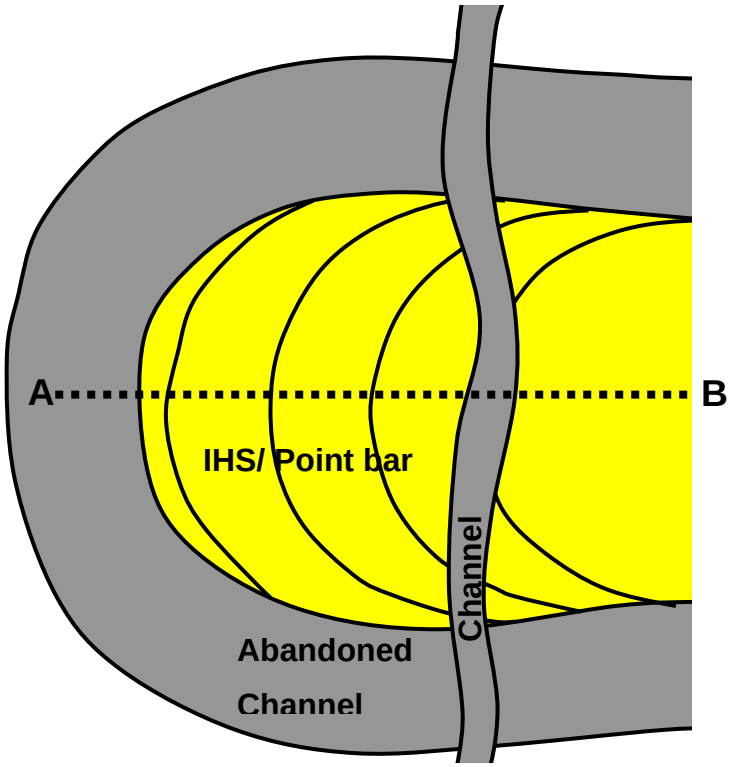

Figure 4.17 A point bar system used in the modeling and inversion. Cross section A-B is shown in Figure 4.18.

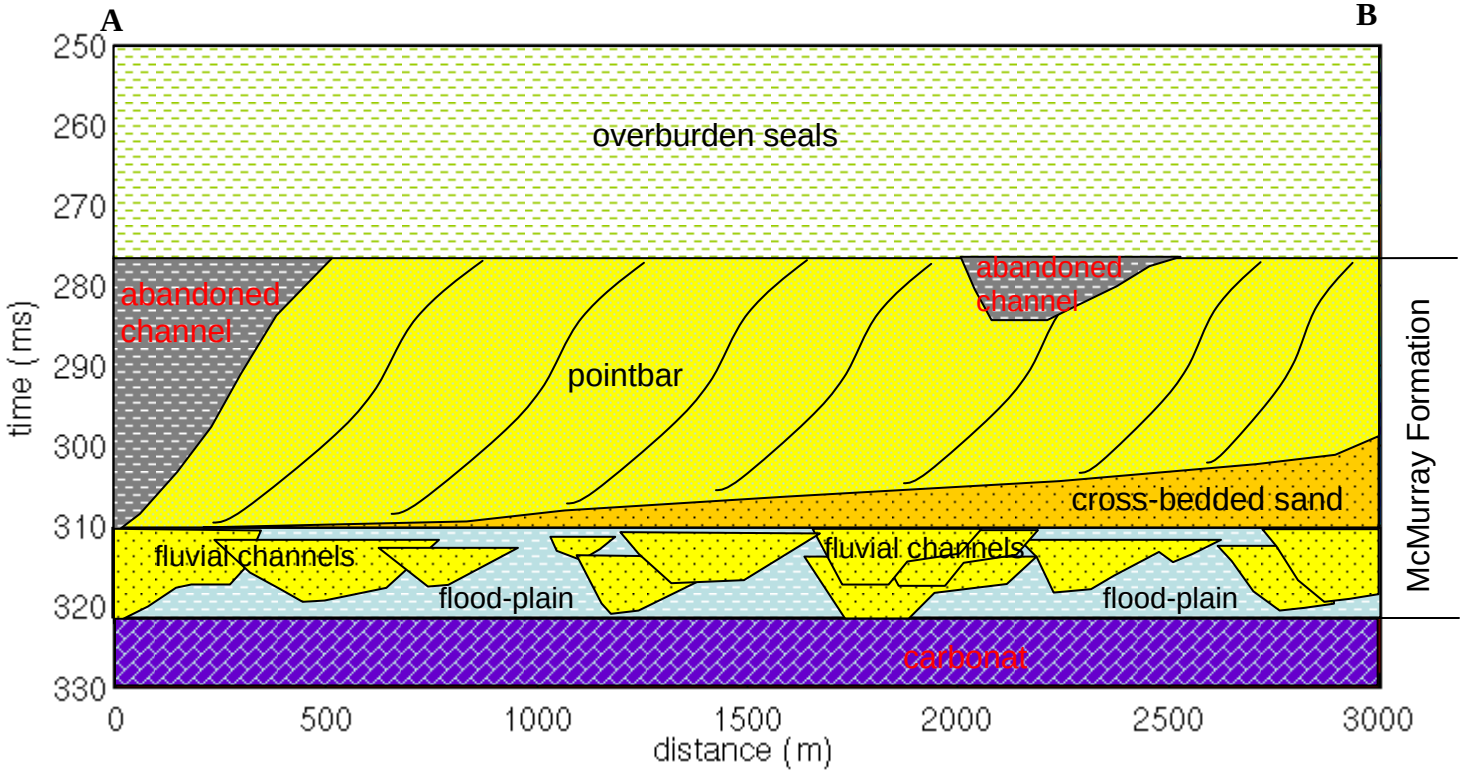

Figure 4.18 Cross section A-B (marked in Figure 4.17) showing facies in the McMurray Formation.

4.4.1.2 Rock physical measurements vs. facies

Cross-plots in Figure 4.19 show the elastic parameters of three facies in the McMurray Formation: cross-bedded sand, point bar (IHS), and abandoned channel. The elastic properties are used to populate the geological model for generating the model dataset. Figures 4.20 – 4.22 are the profiles of P and S velocities and density for the cross-section AB as labelled in Figure 4.18.

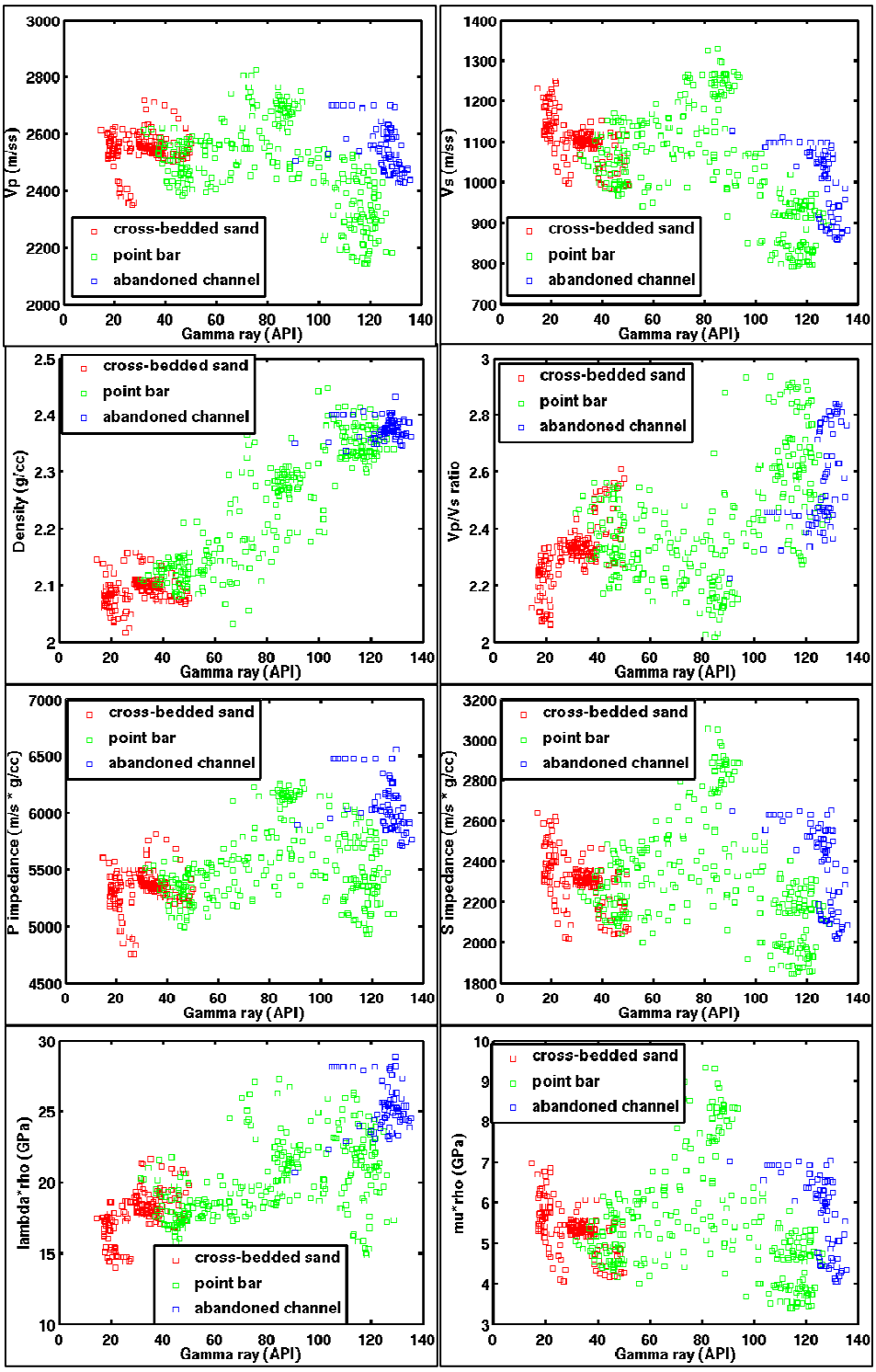

Figure 4.19 Elastic parameters for three facies in McMurray formation: cross-plots against gamma ray *(continued on next page).*

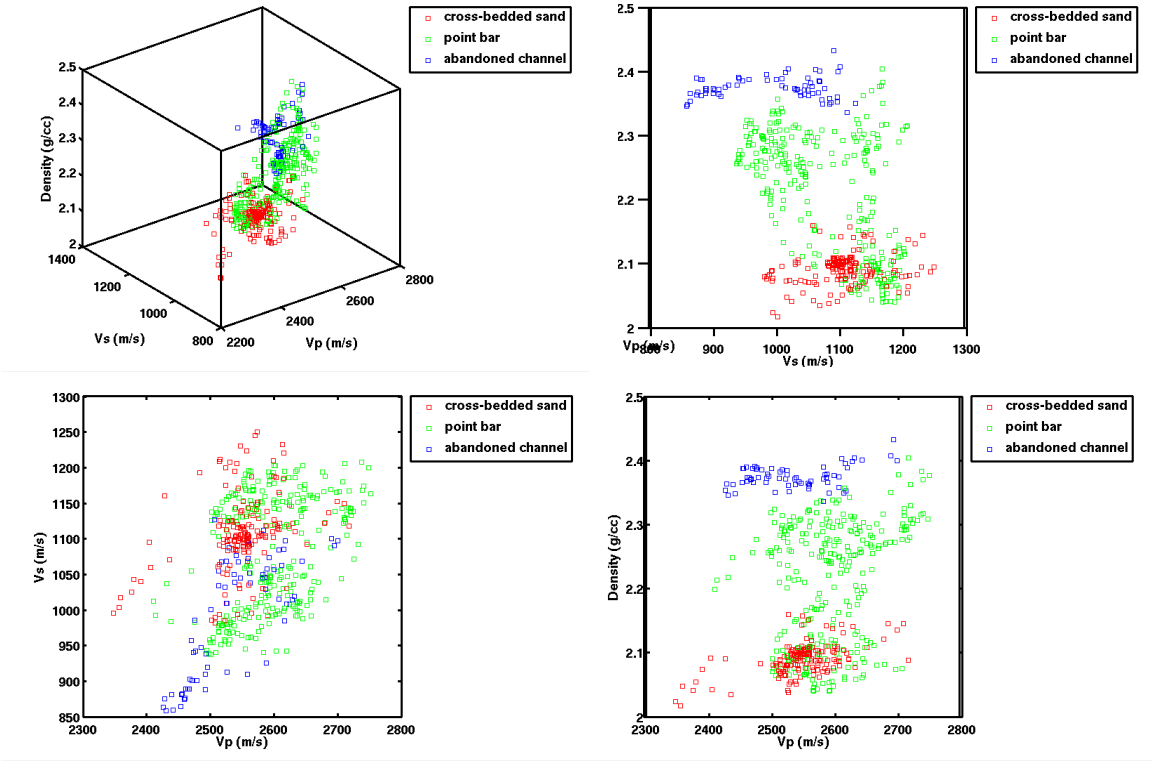

Figure 4.19 *(continued from previous page)* **cross-plots between Vp, Vs, and density for three facies.**

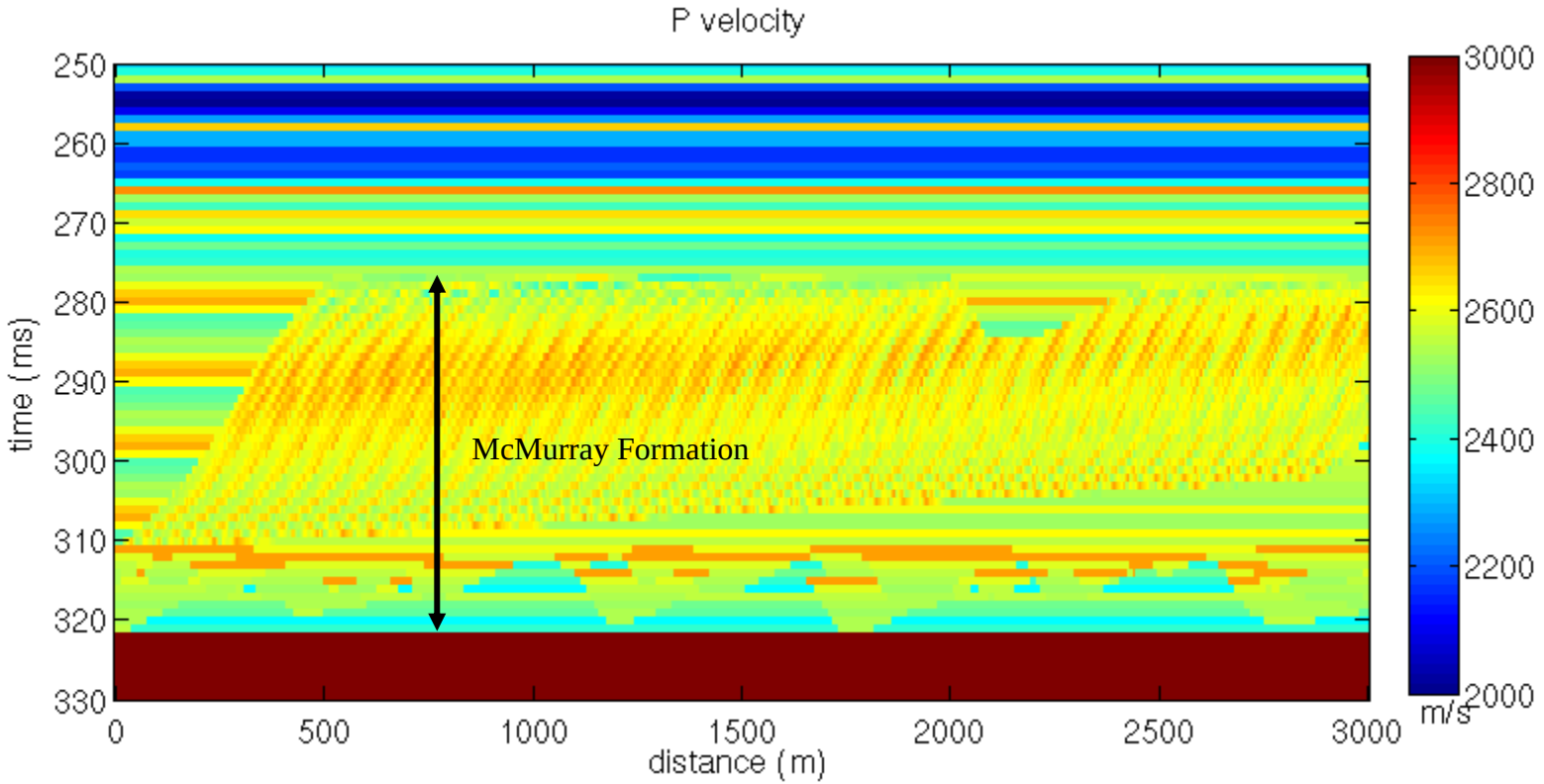

Figure 4.20 P velocity field of the model.

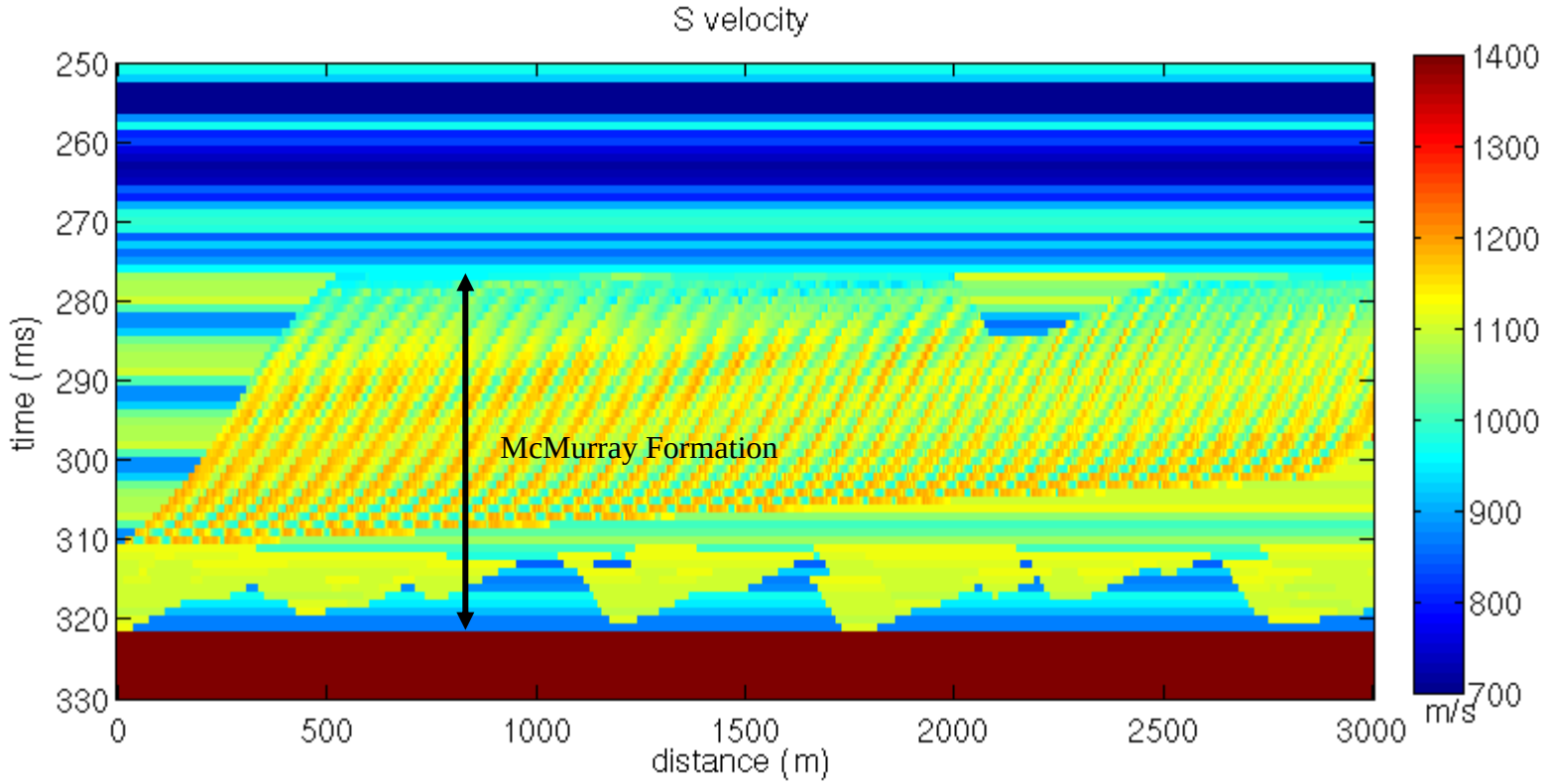

Figure 4.21 S velocity field of the model.

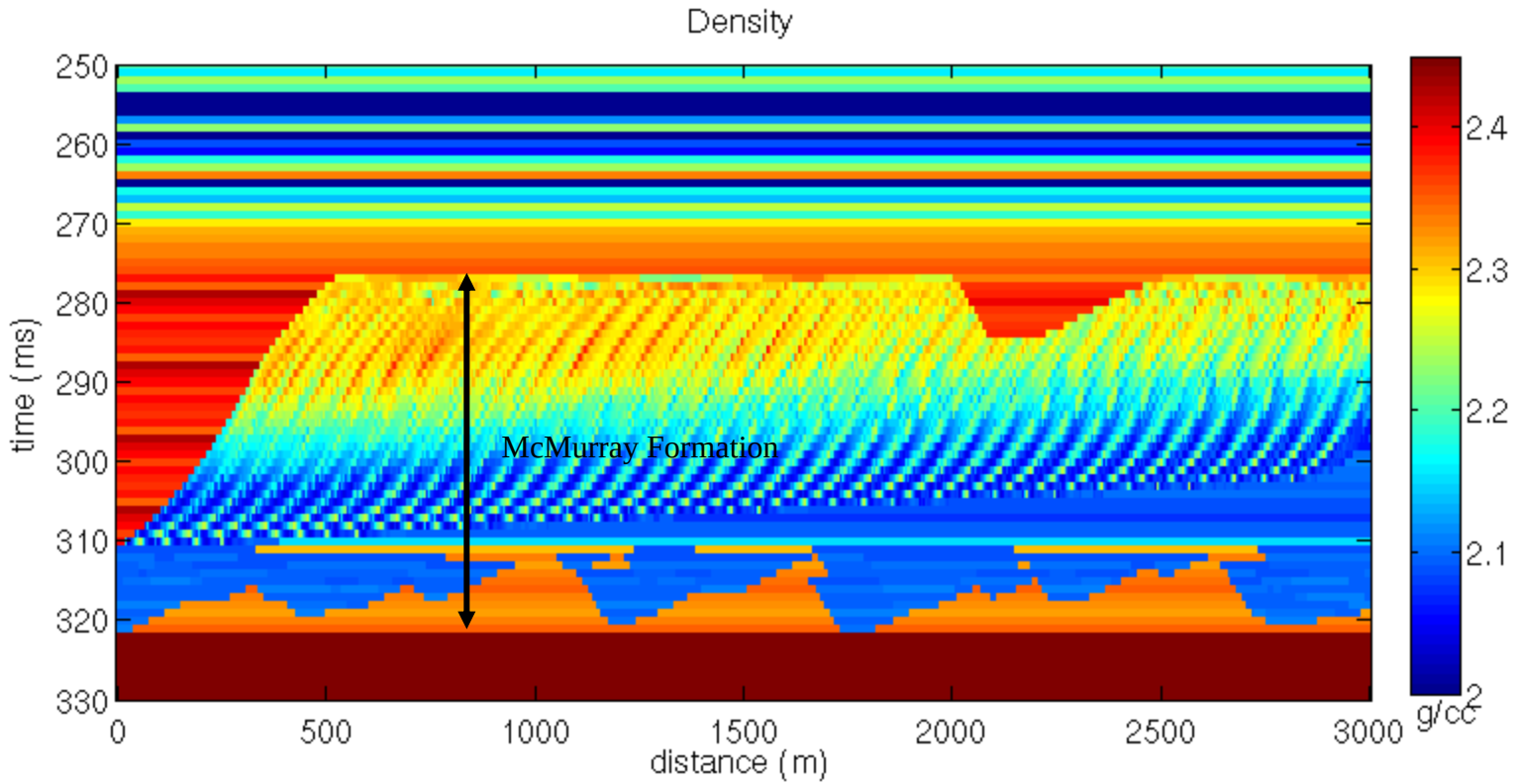

Figure 4.22 Density of the model.

4.4.1.3 Synthetic data

AVA gathers are generated with a 0-45 degree angle range and a 15-150Hz frequency bandwidth. Random noise is added to the synthetic gathers (Figure 4.23 and Figure 4.24). The gathers with random noise are used in the AVO inversion to generate inputs for the joint post stack elastic parameter inversion.

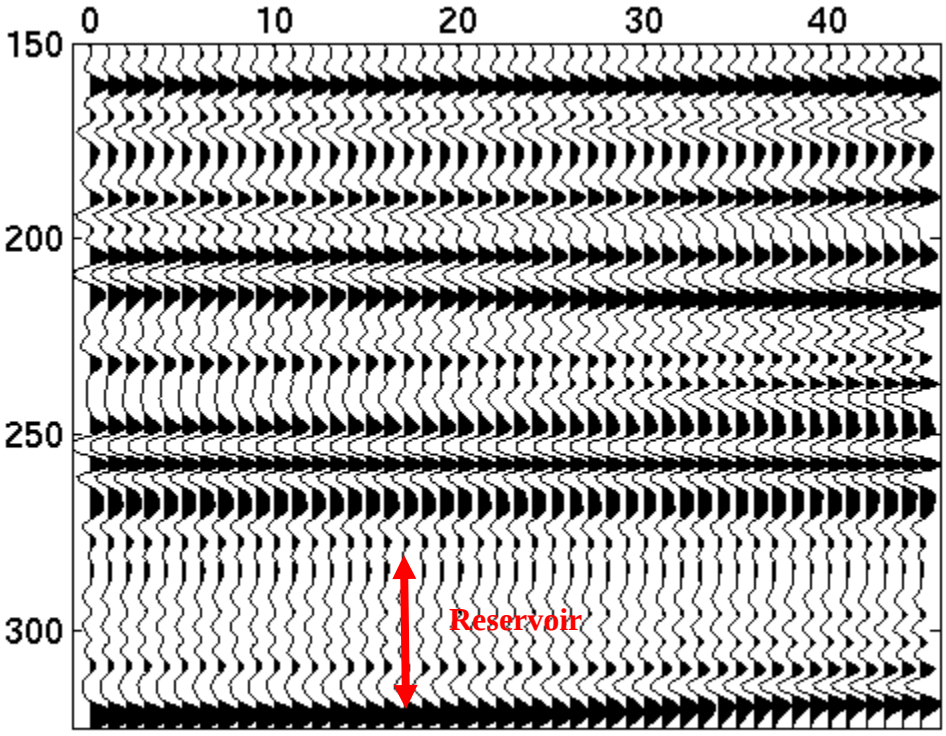

Figure 4.23 Model AVA gather – noise free.

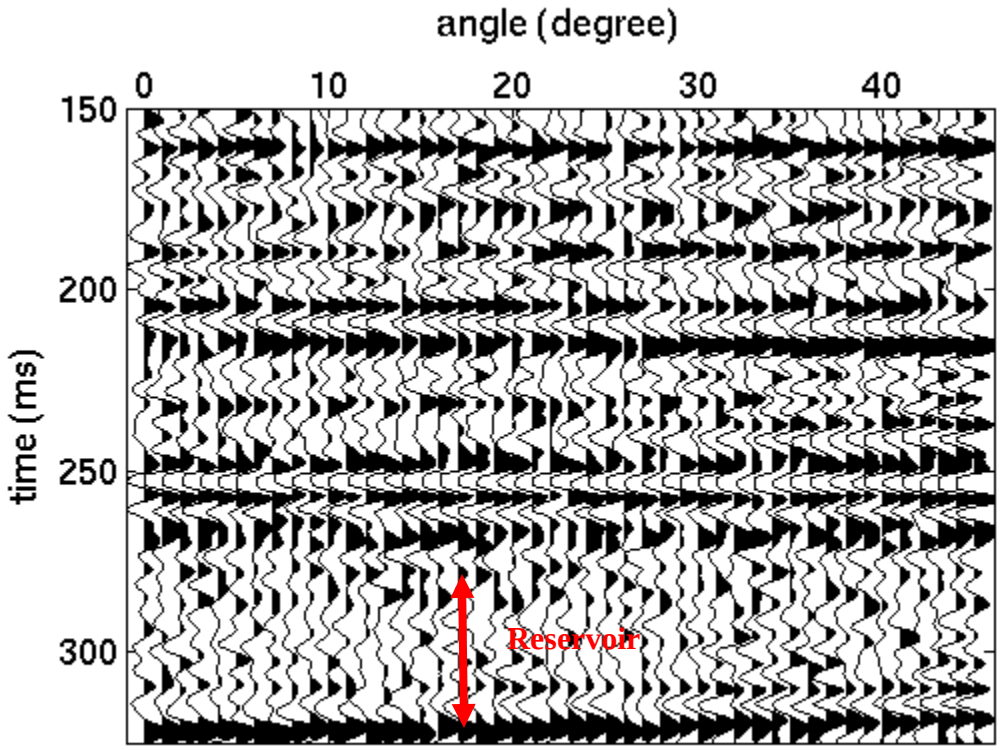

Figure 4.24 AVA gather with noise added – used for inversion.

4.4.2 Workflow

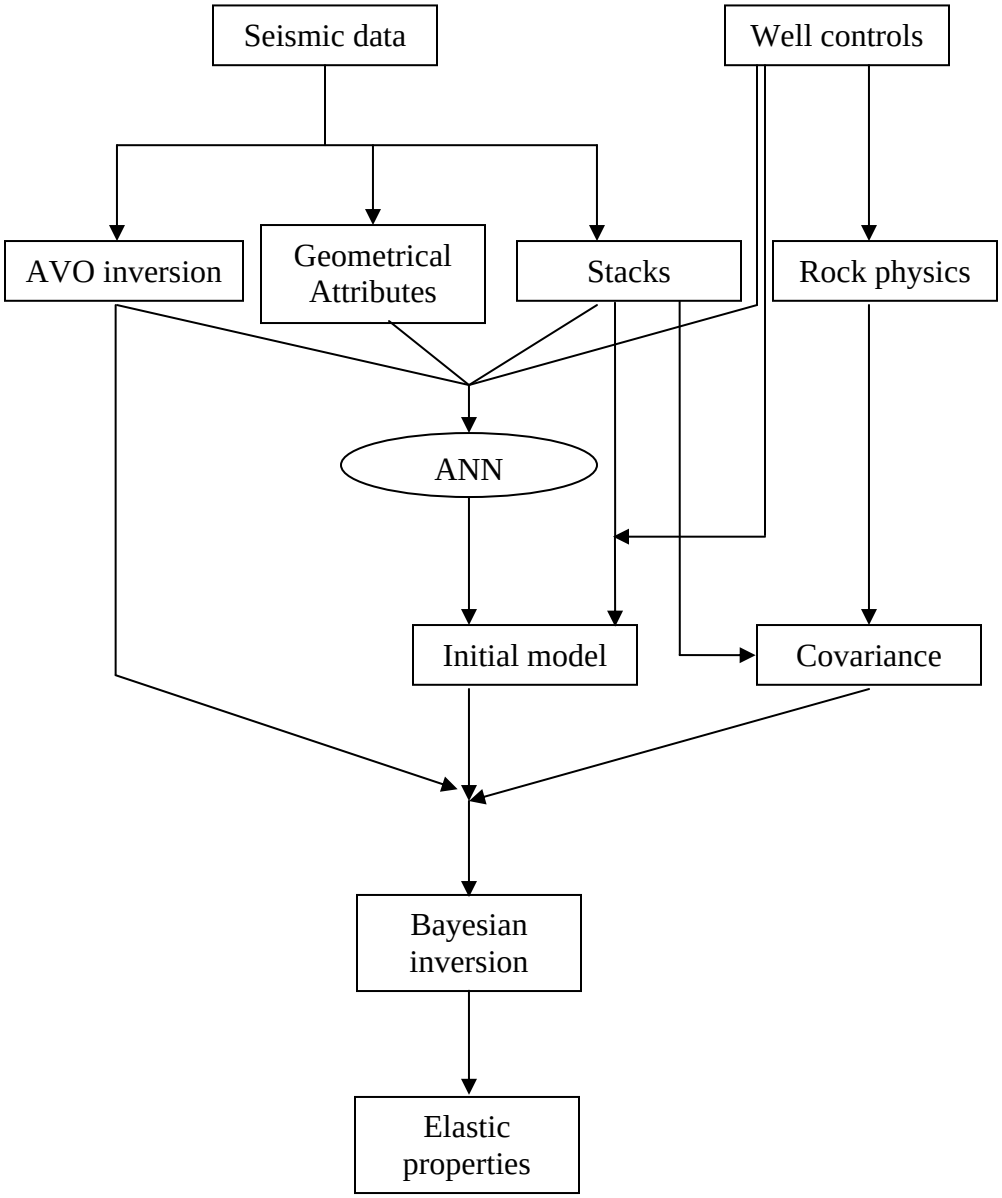

Figure 4.25 Workflow of AVO inversion and joint post-stack elastic property inversion.

Figure 4.25 shows the workflow of the AVO inversion and joint post-stack elastic property inversion:

1. Seismic data generates the stack, AVO attributes, and geometrical attributes.

2. AVO attributes, stacks and geometrical attributes and interpretation are used to generate the initial model of elastic properties with the help of well logs. The initial model also acts as the prior term for the inversion.
3. Stacks, seismic attributes, and well logs are used to generate the rock property covariance and the geometrical covariance.
4. The results of the AVO inversion, covariance, and initial model are input to the Bayesian impedance inversion to generate elastic properties.

4.4.3 AVO inversion

Figures 4.26-4.31 show the results of the AVO inversion and their comparisons with the true bandlimited reflectivities from the model: P impedance reflectivities, S impedance reflectivities, density reflectivities, and Vp/Vs reflectivities. The P and S impedance reflectivities from the AVO inversion show a good match with their corresponding model reflectivities except that the inverted S impedance reflectivities are more noisy. The S/N ratio on the inverted density reflectivities is constrained reasonably well. The inverted density reflectivities show a reasonable match with the model density reflectivities. As density is the key parameter to map the reservoir heterogeneity of heavy oils, the relative density from the inversion and that from the model are compared in Figure 4.31 and the comparison shows a good fidelity of the AVO inversion.

The rock property constraint covariance matrix used in the inversion is

$$\mathbf{C_m} = \begin{pmatrix} \sigma_{\mathbf{rp}}^2 & \mathbf{r}_{\mathbf{ps}}\sigma_{\mathbf{rp}}\sigma_{\mathbf{rs}} & \mathbf{r}_{\mathbf{p}\rho}\sigma_{\mathbf{rp}}\sigma_{\mathbf{r}\rho} \\ \mathbf{r}_{\mathbf{ps}}\sigma_{\mathbf{rp}}\sigma_{\mathbf{rs}} & \sigma_{\mathbf{rs}}^2 & \mathbf{r}_{\mathbf{s}\rho}\sigma_{\mathbf{rs}}\sigma_{\mathbf{r}\rho} \\ \mathbf{r}_{\mathbf{p}\rho}\sigma_{\mathbf{rp}}\sigma_{\mathbf{r}\upsilon} & \mathbf{r}_{\mathbf{s}\rho}\sigma_{\mathbf{rs}}\sigma_{\mathbf{r}\rho} & \sigma_{\mathbf{r}\upsilon}^2 \end{pmatrix} = \sigma_{\mathbf{rp}}{}^2 \begin{pmatrix} 1.000 & 1.833 & 0.2744 \\ 1.833 & 4.368 & 0.3819 \\ 0.2744 & 0.3819 & 0.1821 \end{pmatrix}. \qquad (4.40)$$

where $\sigma_{\mathbf{rp}}$, $\sigma_{\mathbf{rs}}$, and $\sigma_{\mathbf{r\rho}}$ are the standard deviations of P and S reflectivity ($\mathbf{r_p}$ and $\mathbf{r_s}$) and density reflectivity ($\mathbf{r}_\rho$) derived from well logs, and $\mathbf{r_{ps}}$, $\mathbf{r_{p\rho}}$ and $\mathbf{r_{s\rho}}$. are the correlation coefficients between P, S, and density reflectivities. The correlation coefficient between **rp** and **rs** (P and S impedance reflectivities) is 0.877, which is not very high; the correlation coefficient between **rp** and **rρ** (P impedance and density reflectivities) is 0.6431; and the one between **rs** and **rρ** (S impedance and density reflectivities) is 0.4282.

The data term and prior term of the Bayesian estimate of the AVO inversion are shown in Figure 4.30 for the density reflectivity from the model dataset. As we have noted that the synthetic example in Chapter 3 (Figure 3.18) shows a good fidelity in the data term solution of the density reflectivity. However, the data-mean-only solution for this example (Figure 5.30) doesn't show a good match with the model, but the sum of data term and prior term makes more sense. The lower S/N ratio and the sensitivity of solution to the rock property covariance matrix determine the fidelity of the solution if only the data term is included in the solution (Figure 5.30).

4.4.4 Geometrical attributes

Figure 4.32 shows the local dip attributes calculated by the program developed in this study and by a package from a research consortium. Clearly, the dip attribute by the program developed in this study is more meaningful and matches with the lateral accretion shown in the model (Figure 3.18 and Figures 3.20-3.22). The dip attribute calculated by the other package shows random sign reversals on the dips and a low vertical resolution.

4.4.5 Initial model

As discussed in 4.3.3.3, the initial model is a mix of a smoothed ANN output (background is removed) and a background mega-layer model. Ten wells (300m apart) are chosen for the ANN training set in this example. The Hampson-Russell Emerge software package is used for the ANN training and prediction of elastic parameters for the initial model. Figures 4.33 – 4.35 show the mega-layer model and the initial model for the inversion.

4.4.6 Inversion

Figures 4.36 – 4.39 compare the true and inverted elastic properties. Overall, the inversion does a decent job to obtain the three elastic parameters. Major facies can be defined by combining the three parameters. The results of inversion contain frequencies

lower than 150Hz so that the definition of the more detailed geological characters is relatively low. For example, the fine patterns inside the point bar cannot be seen in the inverted attributes. The low frequency contents in the initial model are different from the true; so it is ambiguous for the inverted attribute to define the facies without an accurate back ground trend. For example, the abandoned channel on the left of the inverted density section in Figure 4.38 can be misidentified as the extension of the point bar with a few shale plugs.

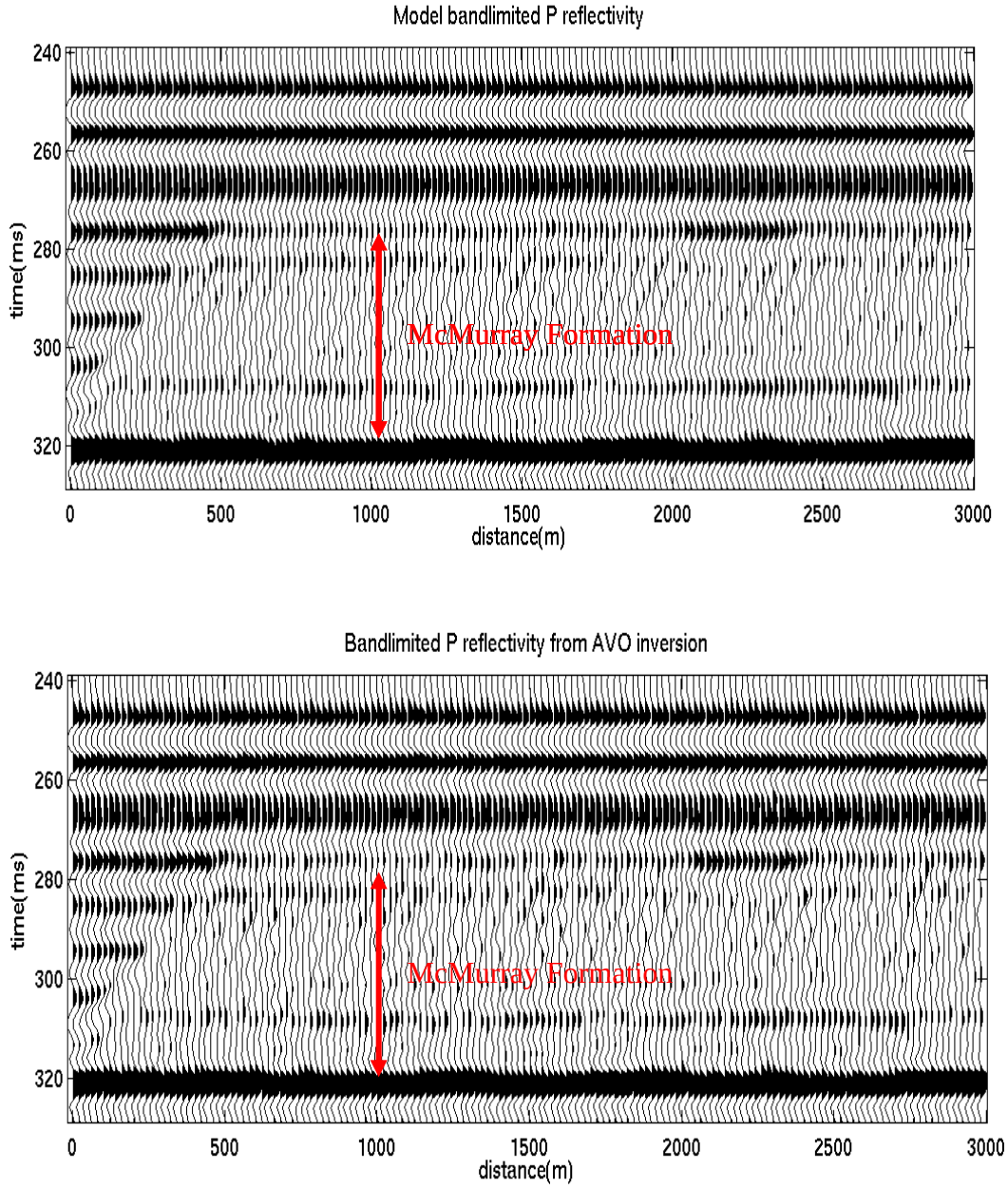

Figure 4.26 True bandlimited P reflectivity and AVO inversion generated P reflectivity.

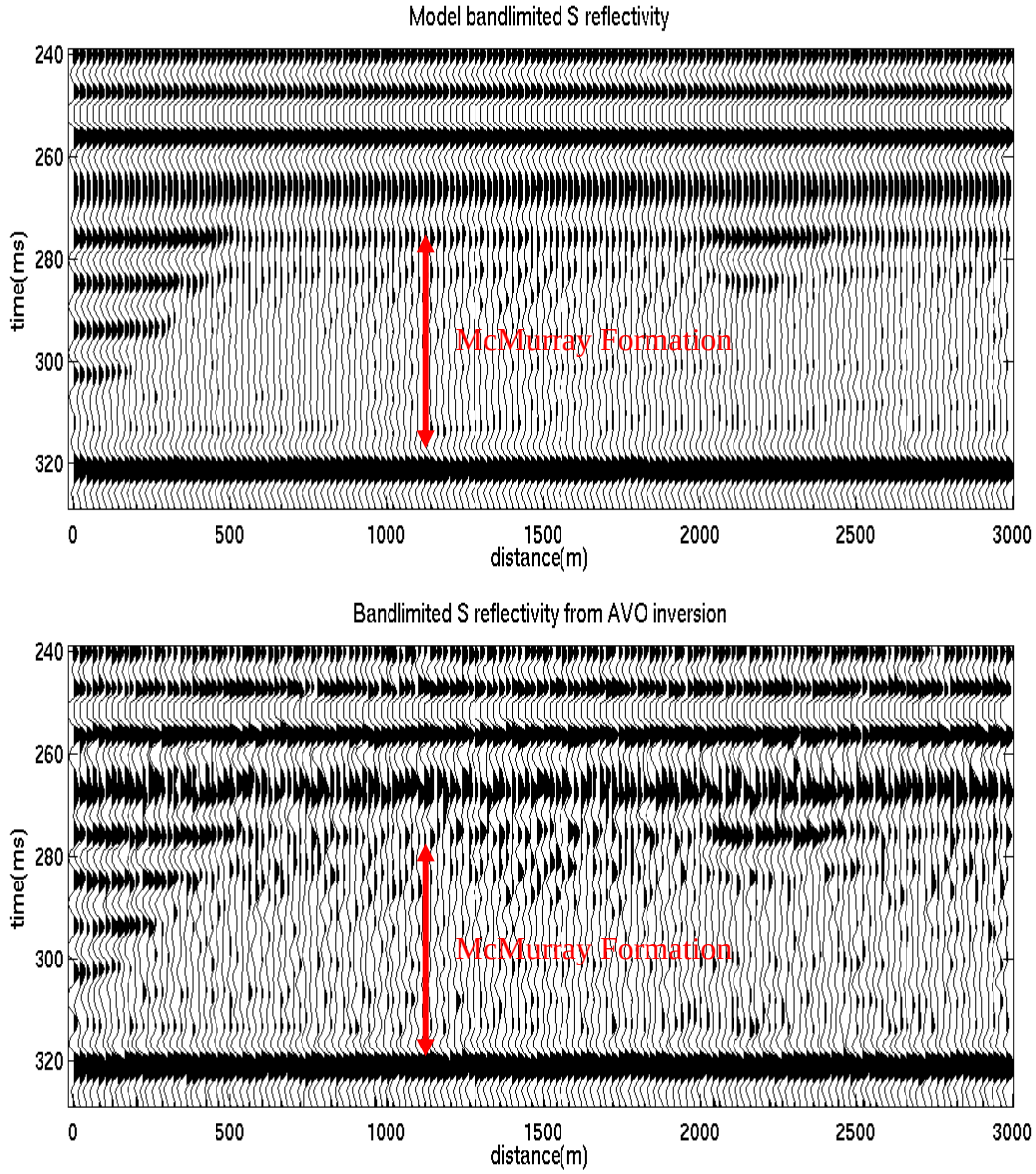

Figure 4.27 True bandlimited S reflectivity and AVO inversion generated S reflectivity.

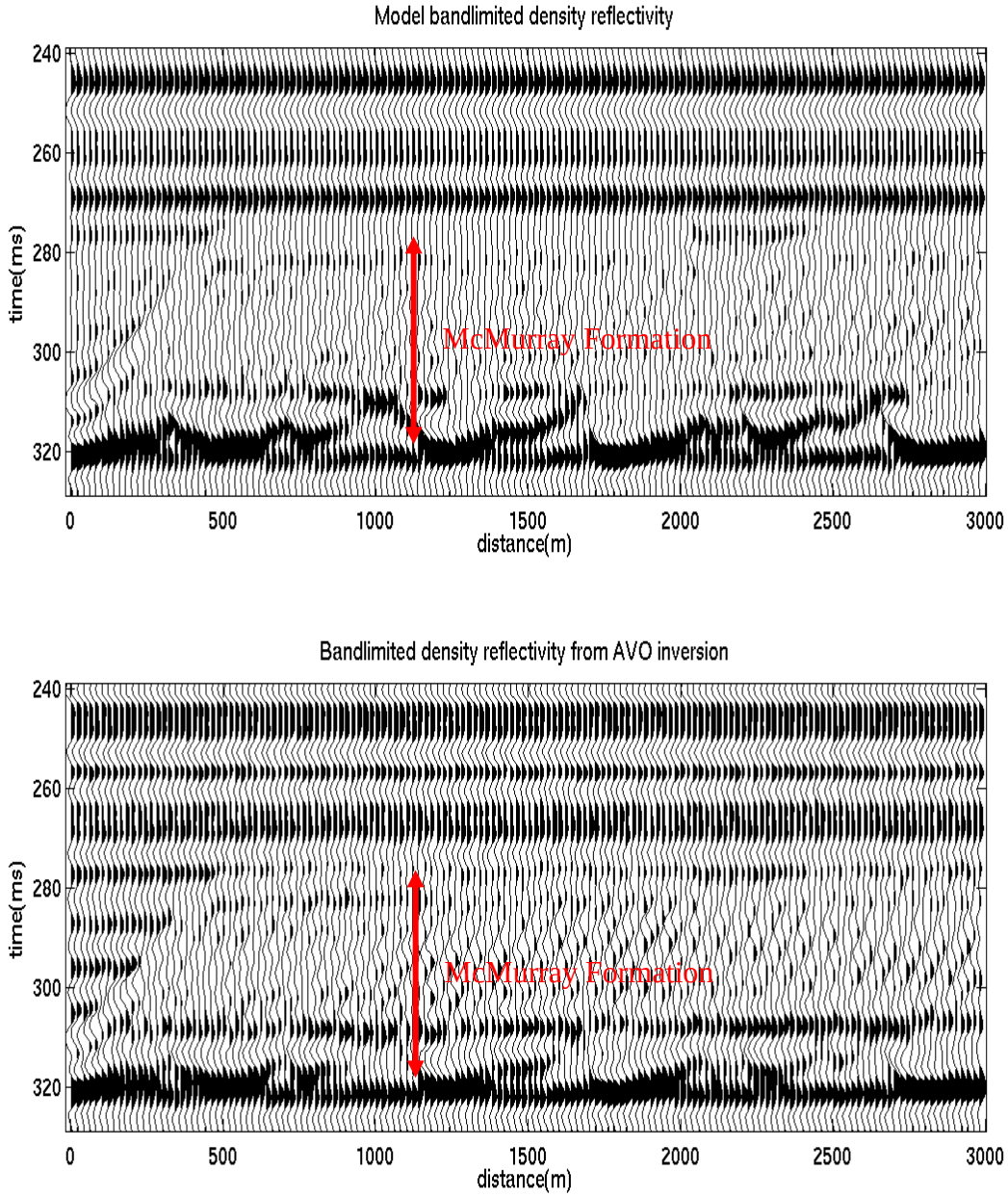

Figure 4.28 True bandlimited density reflectivity and AVO inversion generated density reflectivity.

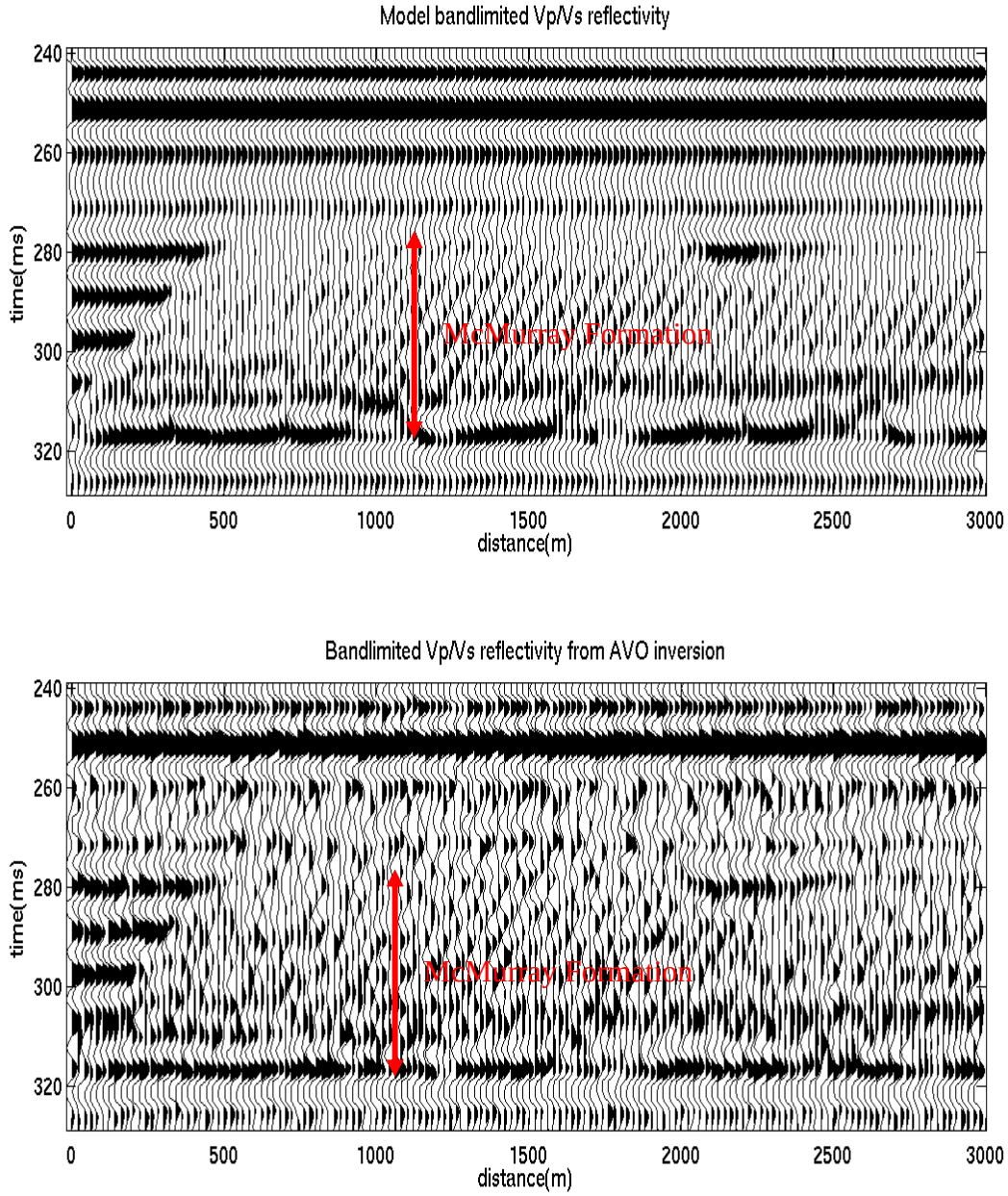

Figure 4.29 True bandlimited Vp/Vs ratio reflectivity and AVO inversion generated Vp/Vs ratio reflectivity.

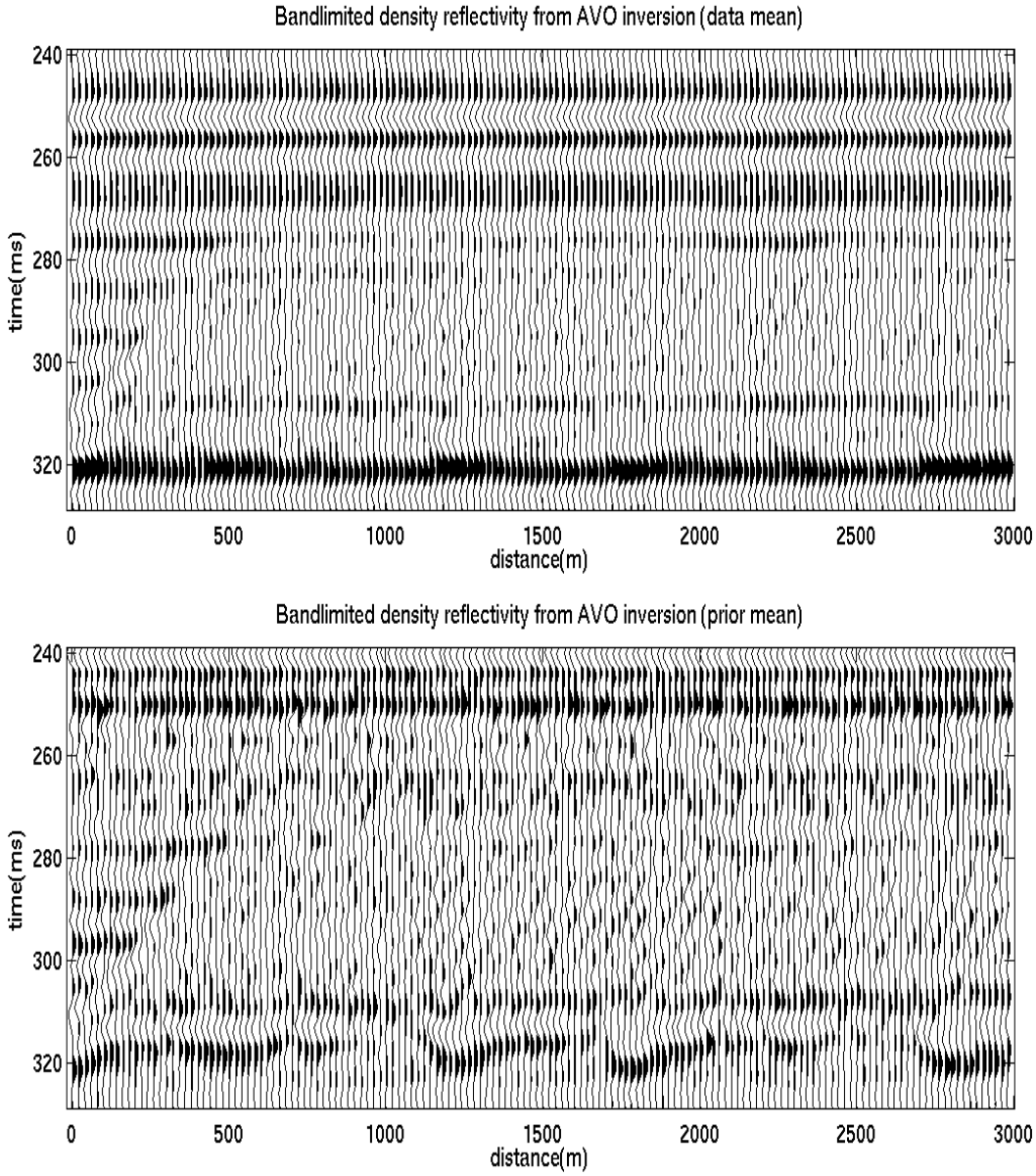

Figure 4.30 Density reflectivity (bandlimited) by AVO inversion: upper panel – data term (in equation (3.19)) in the Bayesian estimate; lower panel – prior term (in equation (3.19)) in the Bayesian estimate. Sum of two panels generates the Bayesian estimate of density reflectivity as shown in lower panel in Figure 4.28.

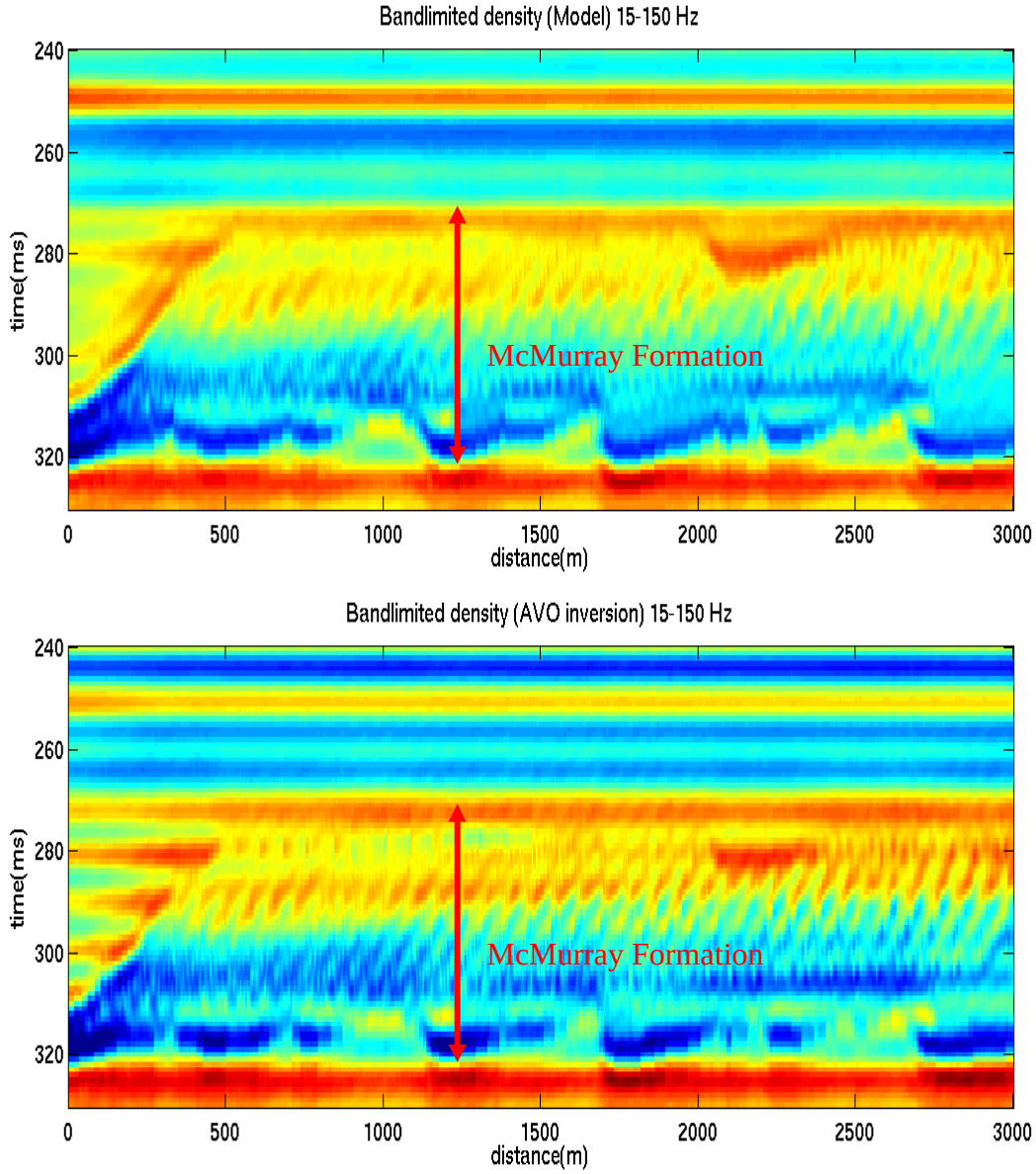

Figure 4.31 True relative density (10-150Hz) and AVO inversion generated relative density (10-150Hz) – The McMurray top is positioned higher in the inverted result.

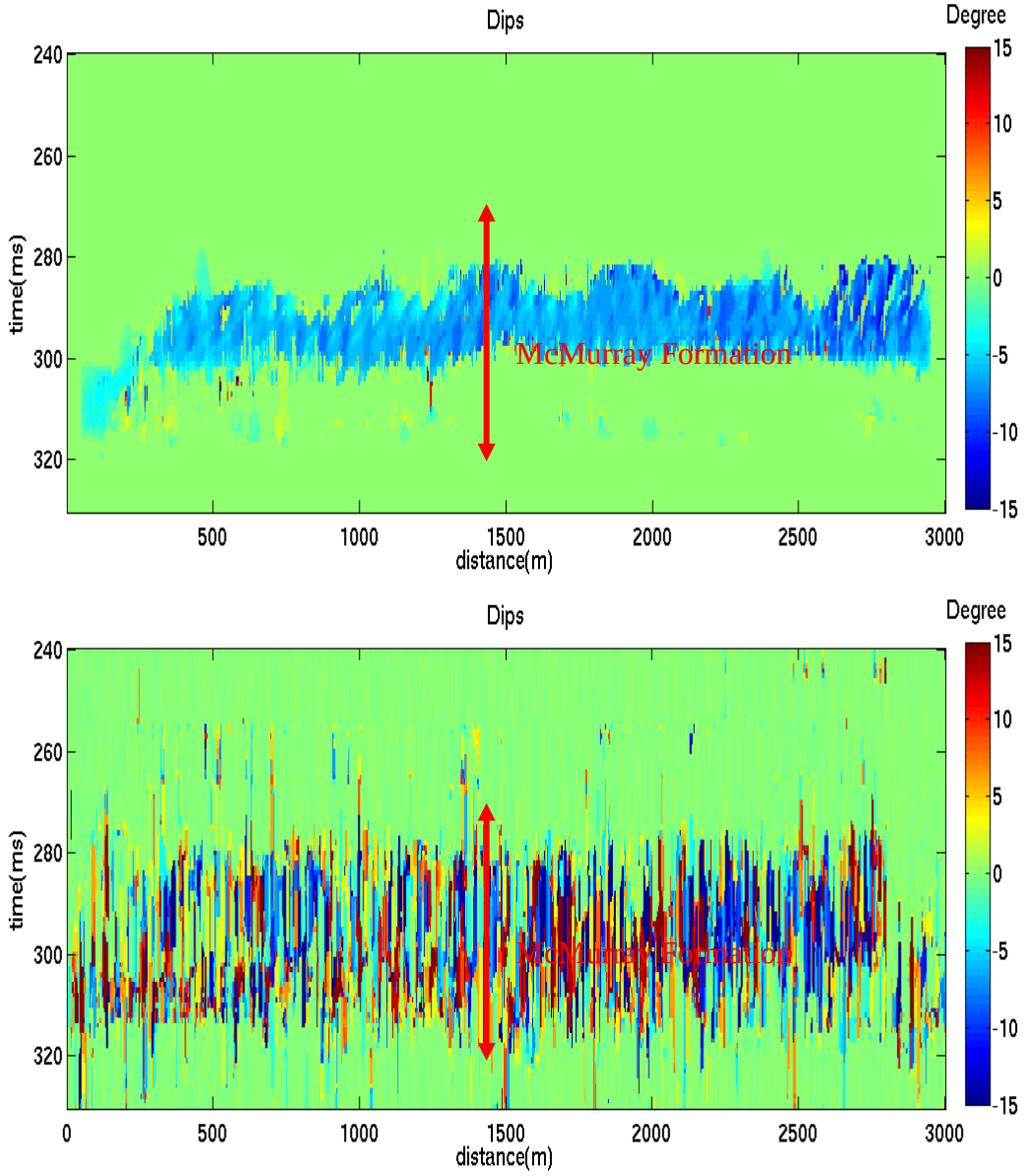

Figure 4.32 dip attributes: the upper is calculated by a program developed in the thesis; the lower is estimated by a package from a research consortium.

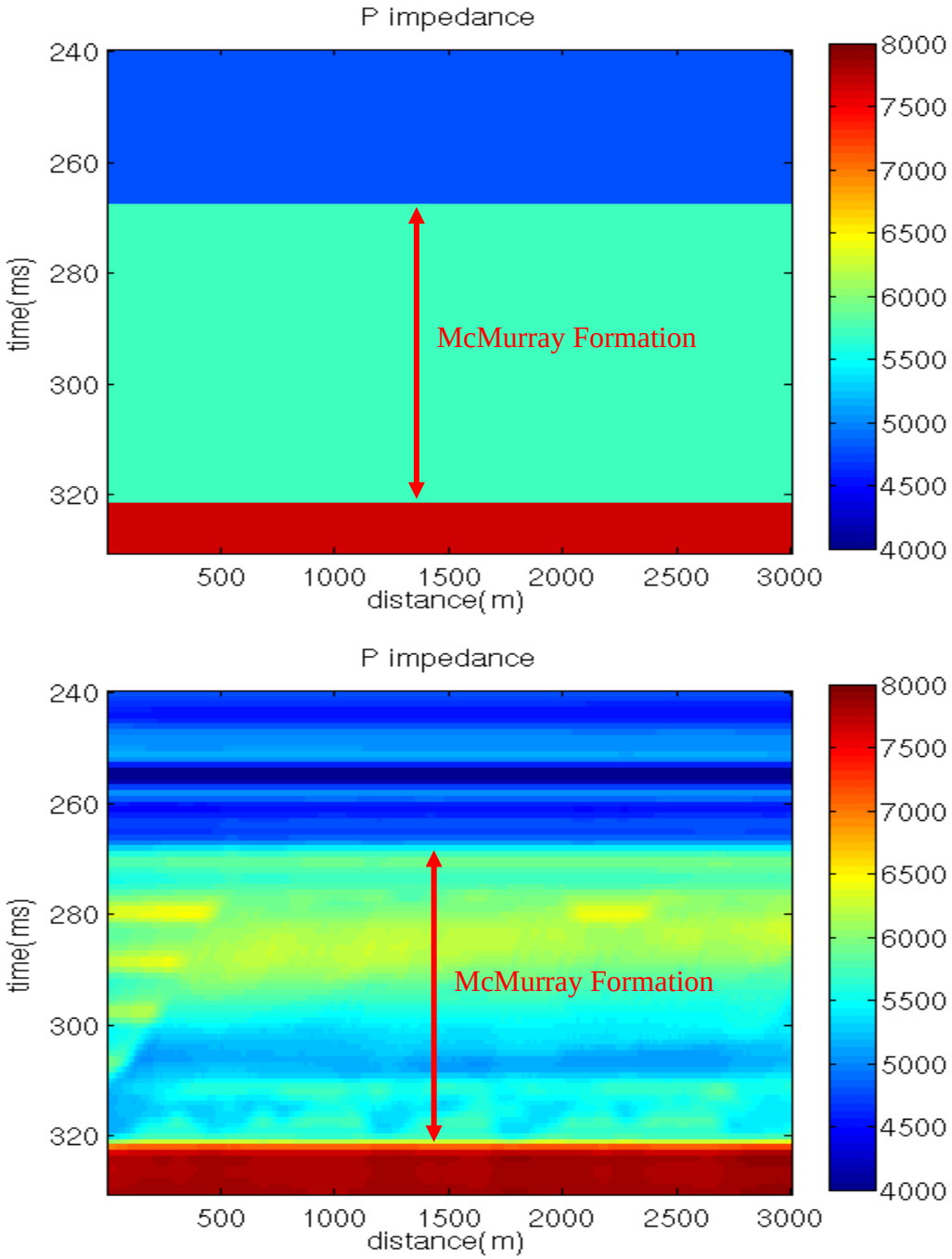

Figure 4.33 Layer model and low frequency model of P impedance.

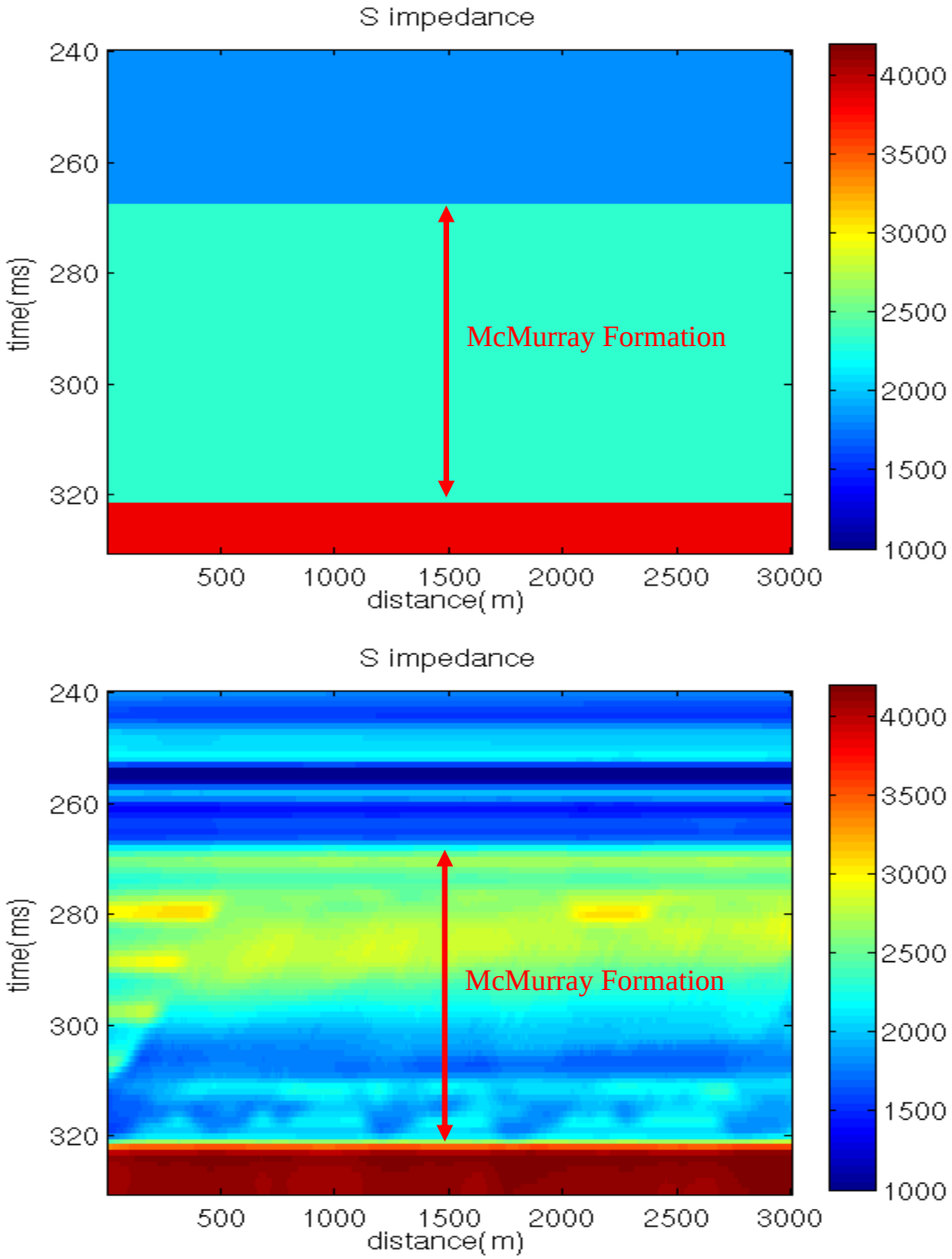

Figure 4.34 Layer model and low frequency model of S impedance

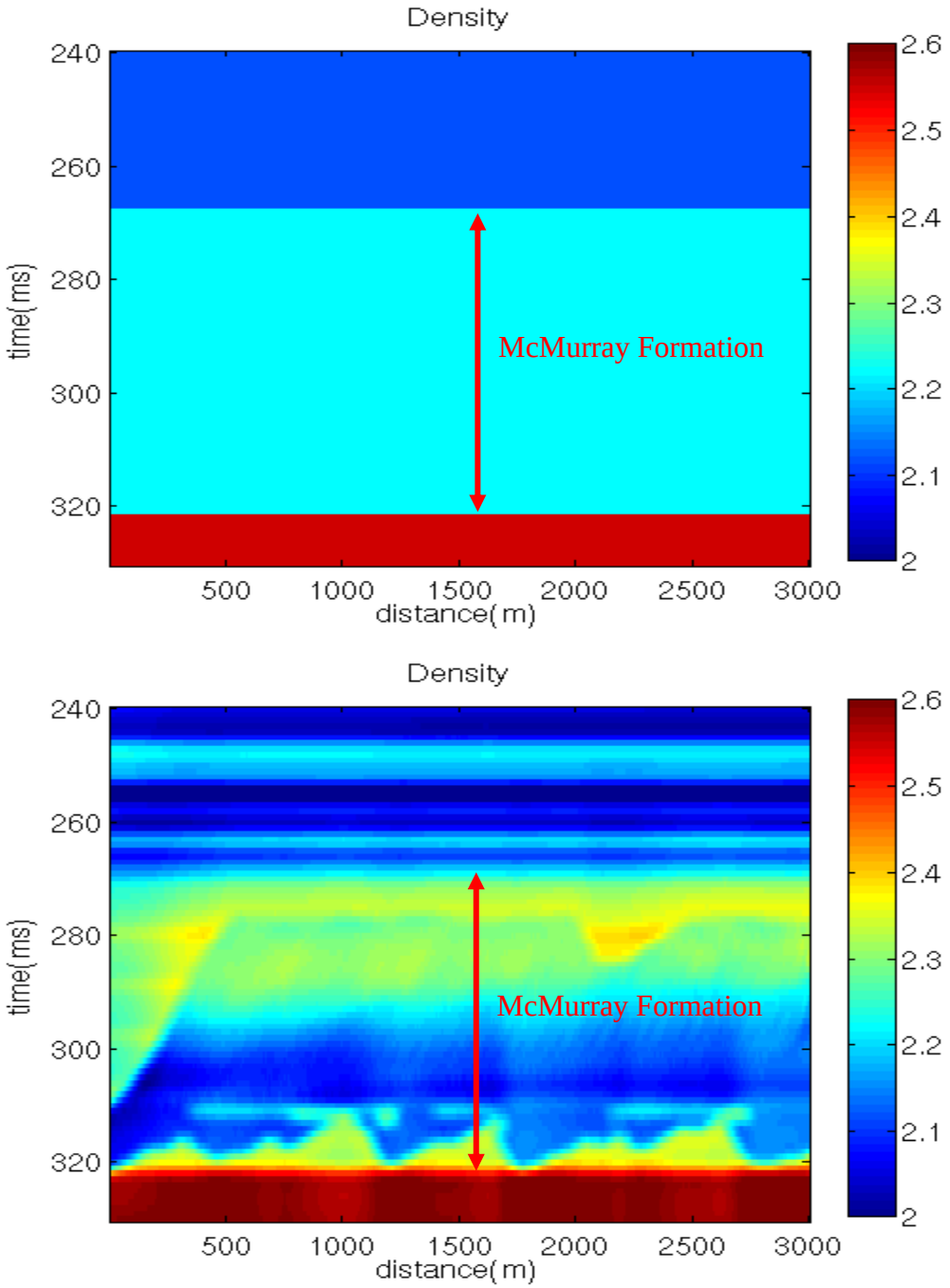

Figure 4.35 Layer model and low frequency model of density.

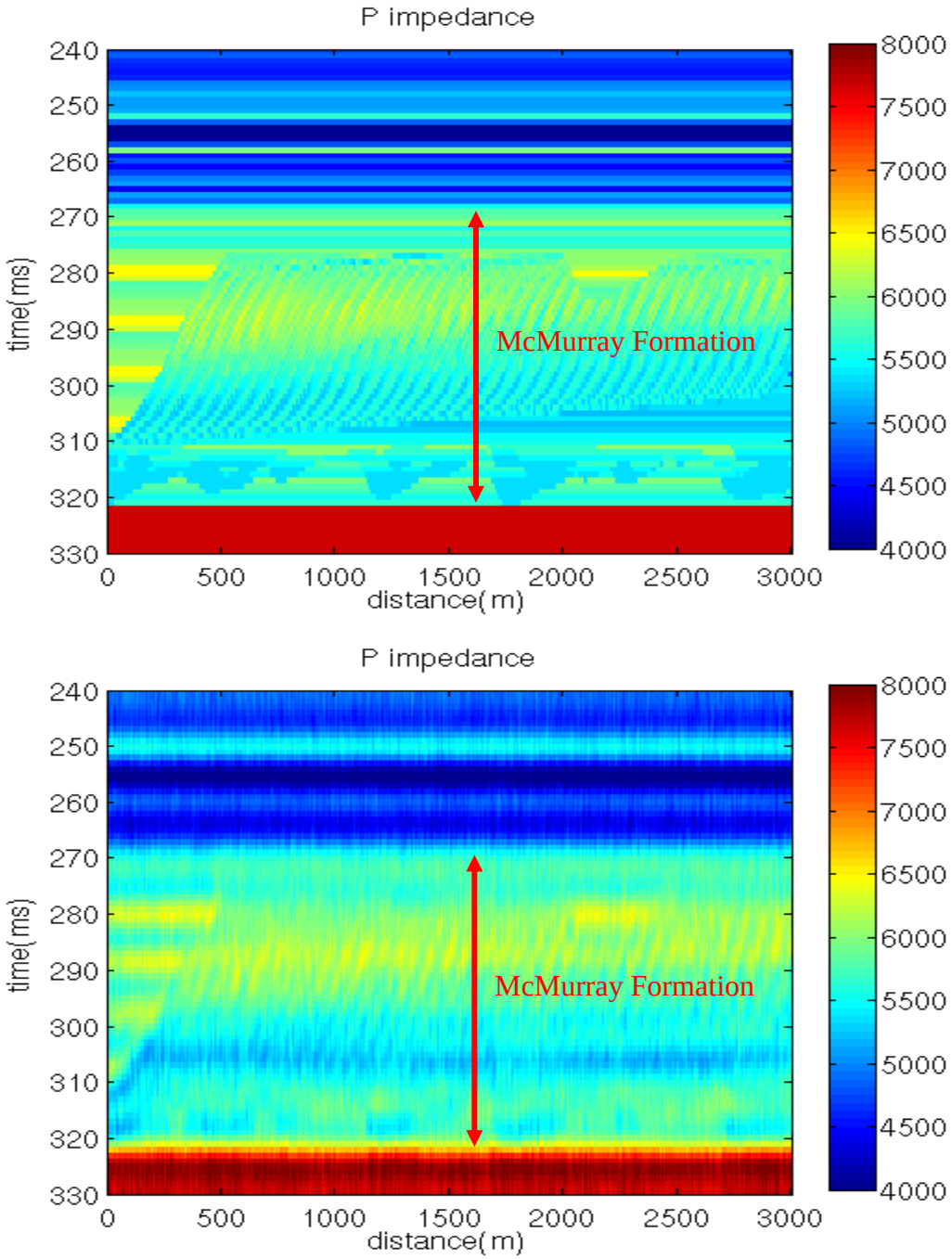

Figure 4.36 True P impedance and inverted P impedance.

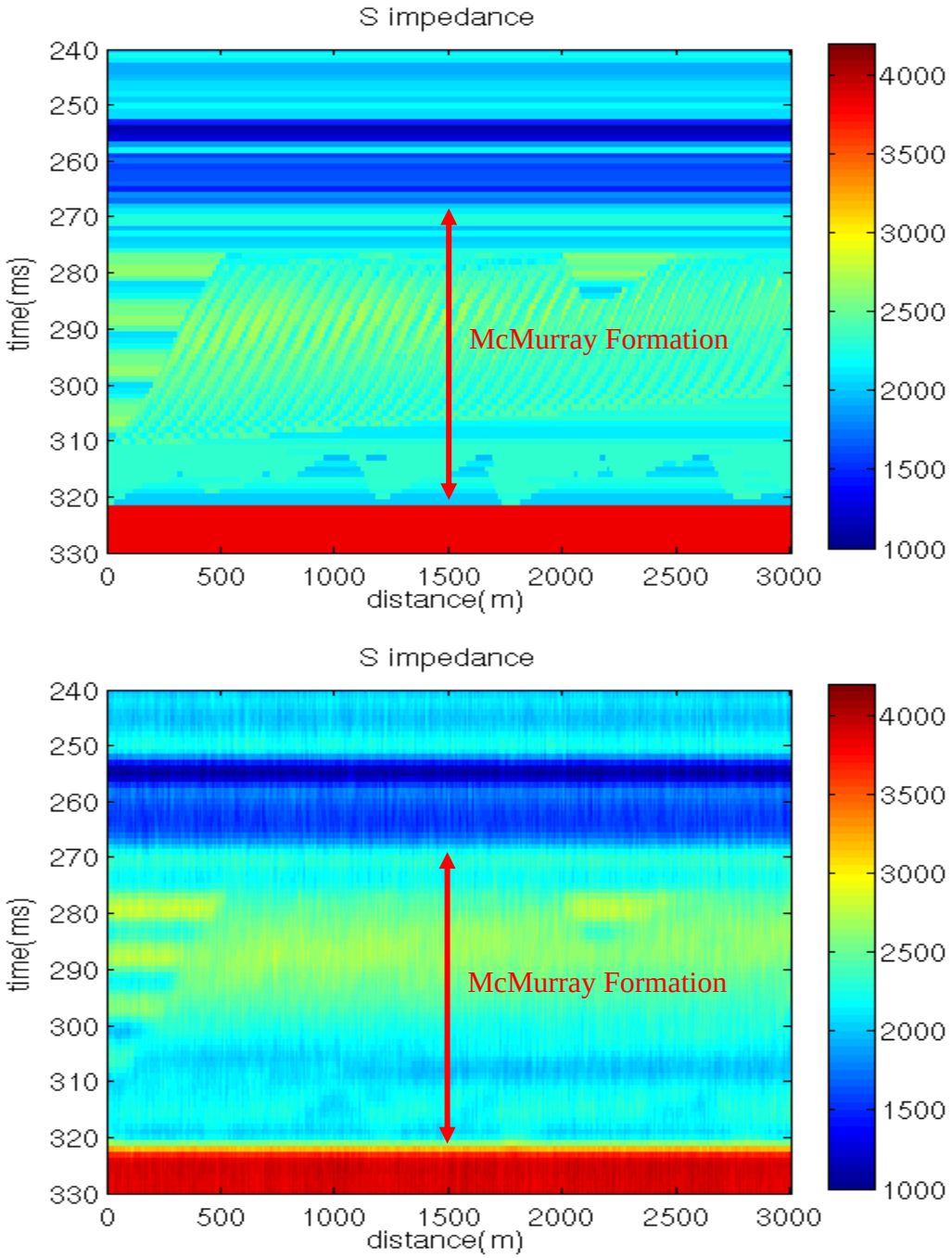

Figure 4.37 True S impedance and inverted S impedance

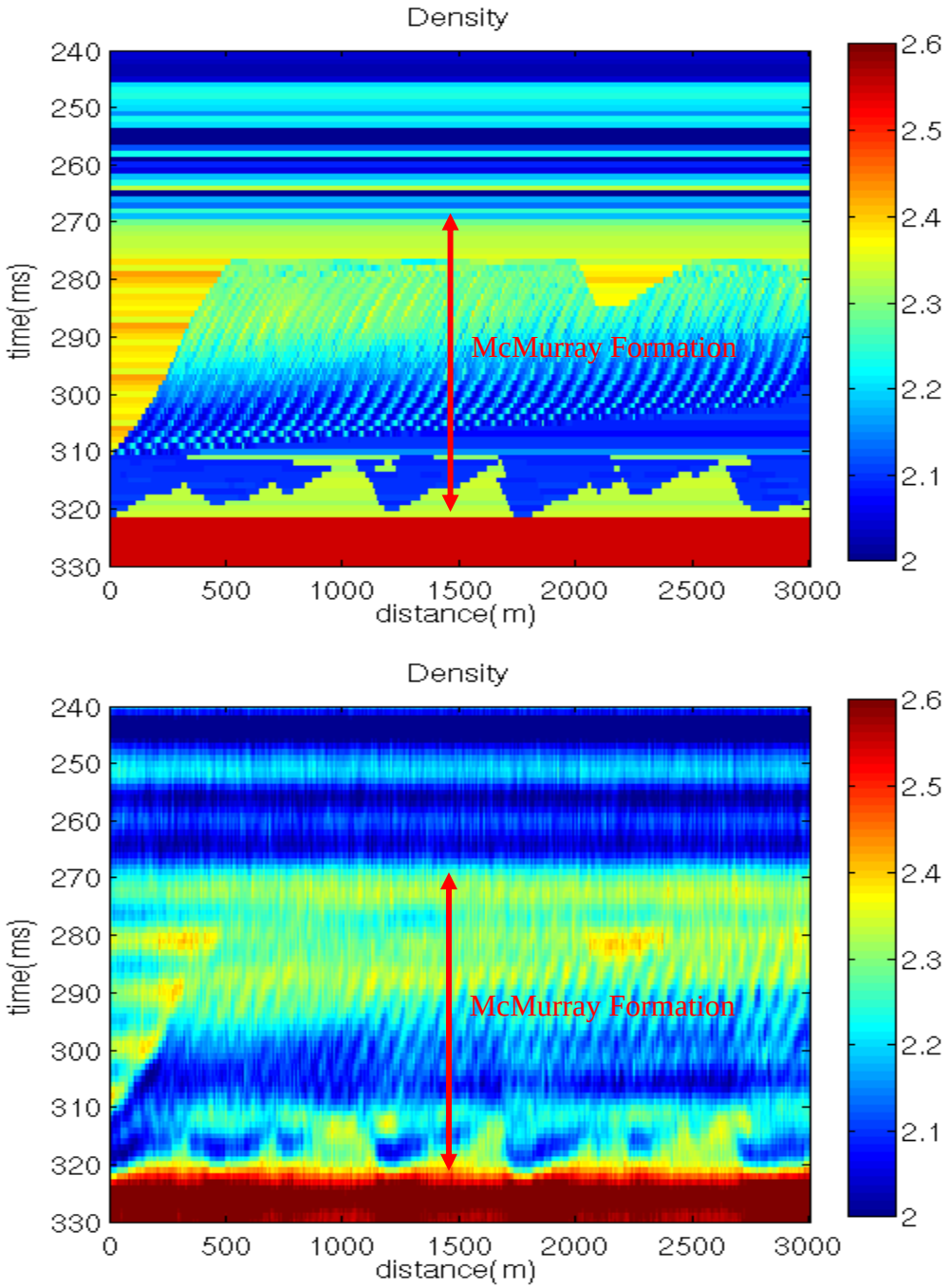

Figure 4.38 True density and inverted density.

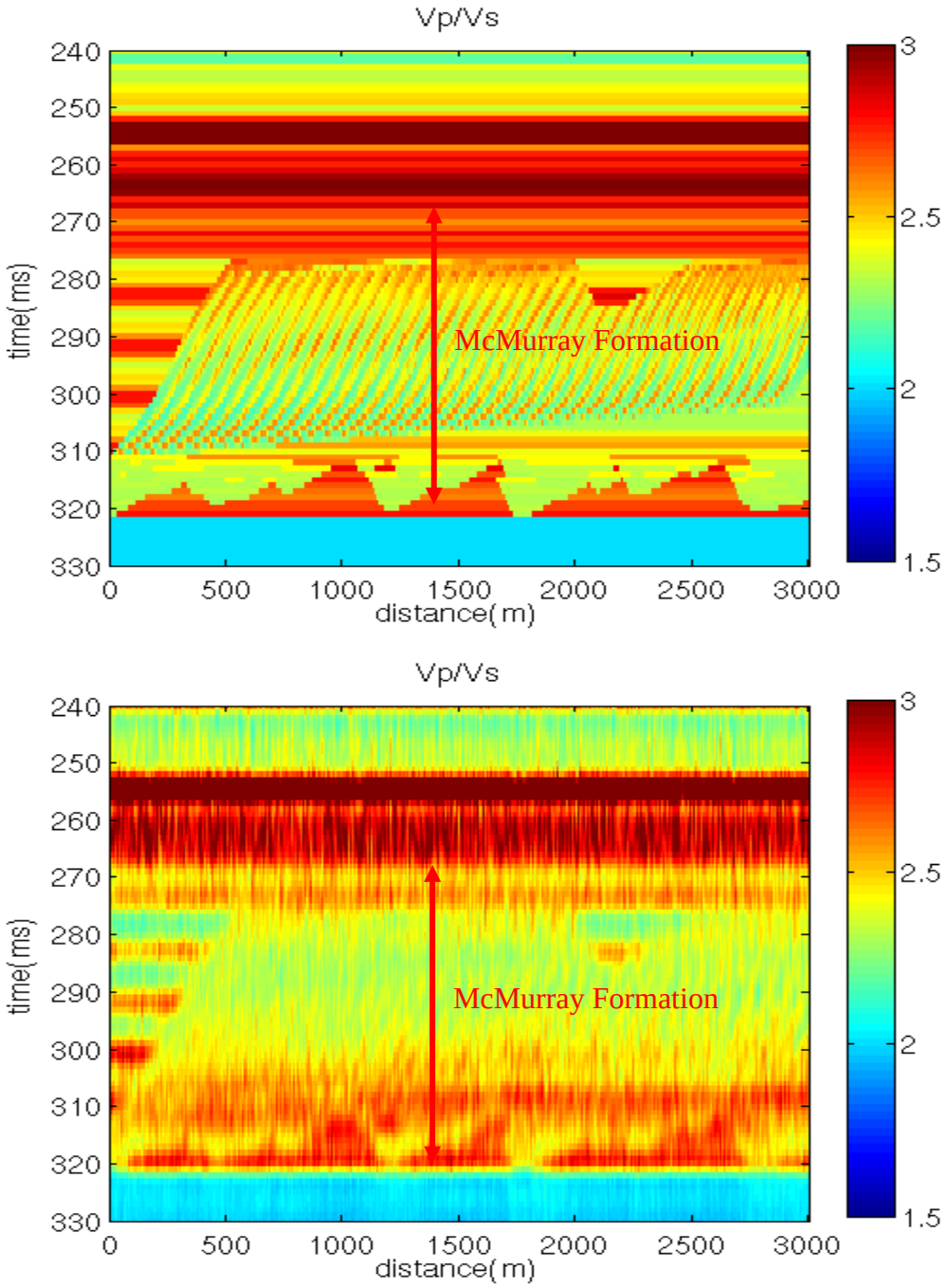

Figure 4.39 True Vp/Vs ratio and inverted Vp/Vs ratio.

4.5 SUMMARY AND DISCUSSION

Beginning with a review on the quantitative prediction of reservoir properties using seismic data, Chapter 4 studies the recent development in the industry on the inversion and simulation and makes developments on the impedance inversion, focusing on incorporating constraints to reduce the non-uniqueness of the solution.

The analytical Gaussian mean and covariance define a complete model space; the analytical mean stands for the MAP solution of the inversion while the covariance describes the uncertainty of the solution. Elastic properties and errors in the seismic data are often observed to follow the mono-modal Gaussian distribution, but the reservoir properties follow multi-modal distributions. Simulating the reservoir properties conditional to the seismic data is costly, but it is possibly a cost-efficient and robust process to transform the seismic data to elastic properties by an analytical estimator and subsequently simulate the reservoir properties conditioned to the elastic properties.

The Bayesian elastic parameter inversion developed in this chapter includes the following major features:

1. The inversion results in impedance instead of logarithmic impedance so that the Gaussian assumption can be used for the probability density functions.
2. The inversion is volume based – multi- lateral locations of formations are inverted simultaneously. The local geological characters constrain the inversion.
3. The inversion is designed as a joint post-stack P and S impedance and density inversion. The bandlimited P and S impedance and density reflectivities are generated by the AVO inversion, in which the ill-posedness is strong and the inversion is stabilized by the constraints. The result of the AVO inversion becomes the input of the impedance inversion. Using the P and S impedance and density reflectivities instead of the prestack data in the inversion costs less computation time.
4. Rock property constraints are included. Well logs are studied to derive the statistics of rock properties.

5. Seismic geometrical attributes have been studied for heavy oil reservoir characterization and building the initial model for the inversion. Due to the limitation of the software package, algorithms to calculate effective attributes for oil sands reservoirs have to be programmed and only a couple of attributes are coded and applied for the initial modeling building in the study. An initial model is built by mixing the mega layer model and the smoothed prediction of PNN from multiple attributes.

A geological model with a point bar system in the McMurray Formation is built based on a comprehensive study of publications on the Athabasca oil sands. The geological model includes point bars, abandoned channels, and fluvial channels in the McMurray Formation. The rock properties of oil sands reservoirs are used to populate the point bar model and to generate elastic properties for the modeling. Synthetic data with random noise is generated from the elastic property volumes of the model. The two-step inversion (AVO inversion + joint post-stack inversion) is applied on the data, showing the reliability of the method to map the reservoir heterogeneity. The method is able to derive the three elastic parameters with reasonable reliability. Considering the band limit of seismic data and uncertainty in low frequency content, the method is good for further improvement.

4.5.1 Future work

There is much to study for converting seismic data to elastic properties/reservoir properties. In the future, the research will carry on the following work with focus on the application in the heavy oil reservoirs in the WCSB.

1. Uncertainty of the probability neural network (and neural network classification);
2. Feasibility of using the low frequency contents in the NMO/migration velocity;
3. Application of the inversion developed in this chapter on real seismic data;
4. Probability distributions other than the Gaussian one;
5. Uncertainty quantification of the inversion developed in this chapter;
6. Program coding for the geometrical seismic attributes for heavy oil reservoirs.

CHAPTER 5: SEISMIC DATA PROCESSING AND CONDITIONING FOR RESERVOIR CHARACTERIZATION

5.1 INTRODUCTION

When the seismic data is applied in reservoir characterization, including direct hydrocarbon indication and extracting elastic parameters, the reliability of the results critically depends on the quality of the seismic data: the signal-to-noise ratio, reliable amplitude correction fulfilling the elastic parameter extraction, and intrinsic rock physics basis behind the data. Although studies have been published on how to prepare seismic data (processing and conditioning) for AVO and elastic inversion (Yu, 1985; Ursin, 1990; Gulunay, et al, 2007; Swan, 1997, 2001, and 2007; Roy et al, 2005; Singleton, 2008), a massive amount of studies and papers are on the rock properties, AVO analysis, inversion and application in reservoir characterization. J. Castagna (2001) states “Perhaps the most important (but least discussed or studied) aspect of AVO inversion is the prestack amplitude correction or calibration that is applied to the data prior to inversion. It remains to be proven that deterministic amplitude calibration applied pre-drill is generally adequate for quantitative inversion. In most cases, some form of statistical amplitude balancing is required (Rutherford, 1993; Ross and Beale, 1994)”.

Seismic wave propagation and the change of amplitude during propagation are much more complicated than the assumption made by the commonly-used AVO analysis. The AVO analysis is mainly based on the plane wave propagation, isotropy, pre-critical incidence, linearization of Zoeppritz equation, etc., although some efforts have been made on considering more complex assumptions, such as the spherical wave (Ursenbach et al, 2007), the anisotropic AVO (Ruger, 2002,) and the full Zoeppritz equation (Behura et al, 2010). In this chapter, the focus is on seismic data processing and conditioning for the conventional AVO analysis and inversion. In seismic exploration, the seismic data processing is usually specialized and finished by the seismic data processing services

providers, while the AVO analysis and inversion is usually completed by oil and gas companies or the specialized services groups. Even though not impossible, it is difficult to interactively perform the data processing and AVO analysis to adjust the parameters and correct the improper data amplitude modifications in the processing for AVO due to the independence between processing service providers and end users of data for AVO in the oil and gas companies. In addition, good quality statics corrections for onshore seismic data and multiple attenuations for offshore seismic data require expertise, experience, technologies, and computer powers, which stop the users of AVO from processing seismic data from field data to guarantee that AVO is preserved. In many cases, the seismic pre-stack data delivered to the AVO analysts may have been distorted (severely sometimes); the AVO analysts have to exploit these data with care and still make the most possible use of them. In the first part of this chapter, the AVO friendly processing is studied, and the second part is dedicated to how to condition the pre-stack data for the AVO analysis.

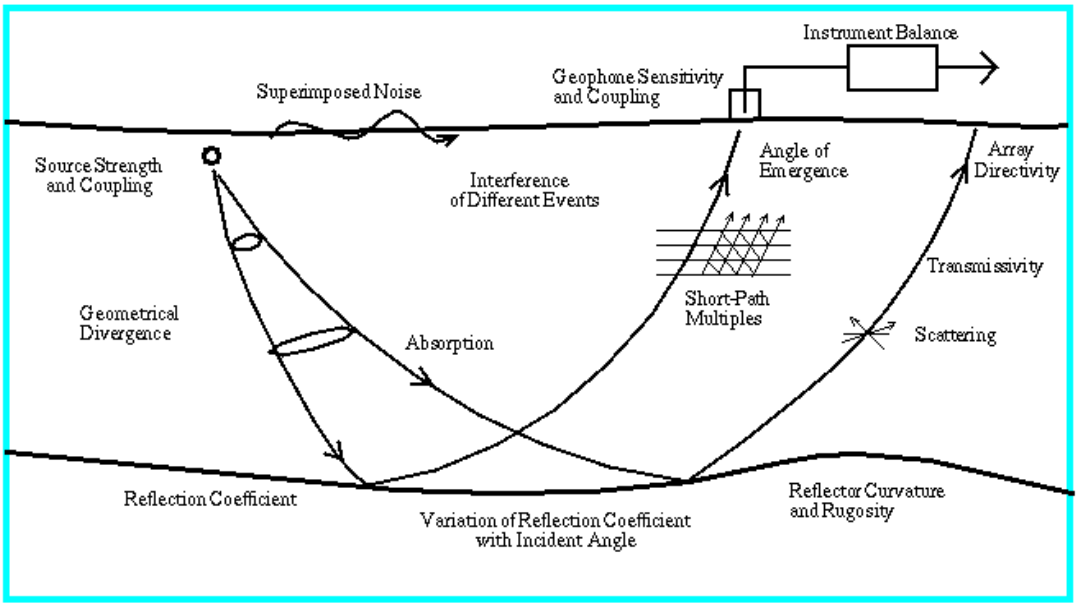

Figure 5.1 Factors affecting amplitude of seismic wave (Sheriff, 1975)

The process of seismic wave propagation is complex, and the amplitude change of the seismic wave is mostly due to the complex subsurface rocks and fluid saturated in the rocks. Rocks are more anelastic than elastic, with the attenuation due to heat loss,

dispersion, and some anelastic effects. The seismic data recorded on the earth's surface is more reliable in describing structures or stratigraphic cycles than extracting elastic parameters. The most effective approaches in the seismic data processing for the best structural image and resolution are usually still statistical with simple assumptions. Sheriff (1975) lists several broad categories of factors which affect amplitude variations with offset including data collection, wave propagation effects, data processing and geologic factors (Figure 5.1). The main purpose of the conventional seismic data processing is imaging the stratigraphic and structural subsurface using seismic data. The conventional seismic processing seeks high resolutions and high signal/noise ratios. These goals can be achieved in the conventional processing by experienced personnel and highly efficient signal processing algorithms. Deconvolution, filtering, stacking, spectral balancing and whitening, and migration are among the tools to obtain good quality subsurface imaging. Trace-by-trace operations are effective in correcting many factors affecting amplitude, including difference of source strength and geophone coupling in the data acquisition and attenuation in the wave propagation. Stacked seismic data is used in the interpretation while the amplitude fidelity in the pre-stack data is usually neglected in the use of conventional seismic data processing. When the value of AVO in exploration and production has been found by interpreters, the quality of pre-stack data, especially the preservation of AVO, becomes more and more important. While the stacks from the AVO preserved data are of high quality for structural and stratigraphic imaging, they are usually hard to surpass the conventional processing results done by a same data processor. It is common that the conventional processing is used for the structural and stratigraphic interpretation but the amplitude-preserved pre-stack data is used for the AVO analysis. Since AVO and elastic parameter extraction from seismic data are the main study in the thesis, AVO friendly data processing for the AVO analysis will be discussed in this chapter. In this thesis, "AVO friendly processing" is used to represent this kind processing. Processing for the AVO purposes is called different names in the industry: AVO friendly processing, AVO compliant processing, true amplitude processing, and others. Conventional processing is called "relative amplitude processing" sometimes as opposed to "true amplitude processing". In this chapter, AVO friendly

processing flow for the land seismic data is explained and illustrated by data examples for key steps in the flow. And some special topics, including migration and 3D data issues, are discussed. The second part of this chapter is dedicated to the data conditioning for the AVO analysis and includes the amplitude QC and fix, residual NMO removal, and NMO stretching and tuning correction.

5.2 AVO FRIENDLY SEISMIC DATA PROCESSING

Like the conventional seismic data processing, the AVO friendly processing corrects the factors which cause seismic data (pre-stack) to deviate from the assumptions of AVO by recovering the amplitude attenuation due to wave propagation and compensating the difference of sources and receivers. Unlike the conventional seismic data processing, AVO friendly processing avoids using trace-by-trace operation and attempts to correct those non-geologic or non-AVO factors by using a deterministic approach or a combination of deterministic and statistical approaches. A surface-consistent approach rather than trace-by-trace approaches is usually coded in the tools used in the AVO friendly processing.

The seismic source is usually a point source and generates spherical waves theoretically. Spherical wave propagation is accompanied with amplitude attenuation due to the geometrical spreading: its amplitude is proportional to the reciprocal of distance from the source in an elastic uniform 3D medium. Therefore, the amplitude recovery can be done by estimation of the distance that waves travel from source, which requires the reliable velocity field of subsurface for traveltime calculation. Earth media are inelastic other than elastic; heat loss occurs in the wave propagation. The quality factor (Q) model is constructed to compensate for the inelastic loss. Defining the elastic and inelastic model to recovery amplitude loss is classified as a deterministic approach. Although much effort is made on the deterministic amplitude recovery, statistical recovery is still the main workhorse in the processing industry. Figures 5.2-5.7 compare two approaches for the amplitude recovery on shot gathers. The statistical approach uses an exponential function (exponent of 2 in this example) of travel time to recover all amplitude loss; the

deterministic approach proceeds step by step removing geometrical spreading, compensating attenuation due to heat loss, correcting the directivity of wave emergence at surface and correcting the array effect due to the grouping of geophones. The processing and visualization of Figures 5.2-5.7 are done in FOCUS, a seismic processing system from Paradigm Geophysical. In the deterministic approach, the corrections of geometrical spreading and absorption are the most effective in changing the amplitude of gathers. The amplitude recovery and AVO restoration in general seem having little difference on the results produced by both approaches, but the deterministic approach requires much effort in building an earth model.

An AVO friendly processing flow contains many steps used by the conventional processing as well. Those steps are important in generating high quality final results for both the structural/stratigraphic interpretation and AVO analysis. They include trace editing, statics analysis, deconvolution, noise attenuation, velocity analysis, NMO correction, stacking, and migration. In the AVO friendly processing, any trace-by-trace operation should be avoided. Instead, many iterations of surface-consistent scaling combined with various noise attenuations are introduced. Sometimes, a surface-consistent frequency boosting is performed to correct the inefficiency of the surface-consistent deconvolution in order to match the resolution with that on the conventional processing deliverables.

Figures 5.8-5.17 use examples to demonstrate the amplitude improvements by key steps in an AVO friendly processing flow. The flow chart on side of each of these figures only shows the key steps reflecting the AVO friendly processing philosophy. The processing and visualization of Figures 5.8-5.17 are done in FOCUS, a seismic processing system from Paradigm Geophysical. The flow is based on land seismic data processing; marine data processing is not discussed in this thesis. In the example used here, four iterations of noise attenuation and surface-consistent scaling are applied. Statics, velocity, and other operations are not shown in the flow chart, but they are essential in both the conventional and AVO friendly processing.

Seismic data processing with its history of nearly a century includes much more than what are covered in this thesis. Many interesting and challenging topics are still under study, like de-multiples, migration, and signal enhancement (forever).

Noise attenuation in seismic data processing should be applied for better signal-to-noise ratio. Random noise, airblast, cable noise, energy bursts, ground rolls, and other coherent noise are usually mitigated by different approaches. Multi-channel data is usually needed to identify noise and preserve signal. Pre-stack data can be sorted into different sorting domains to iteratively attack noise: shot, receiver, offset plan, cross-spread, etc. If coherent noise aligns well in appropriate sorting domain, many conventional processing tools, such as f-k filter, are efficient to remove the noise. Retrieval of subtle signal removed by noise attenuation tools becomes a trend in the seismic data processing industry (Choo et al, 2004): no matter how sophisticated the noise attenuation tools are, there are always damages on signal. Noise attenuation is usually applied after the data is scaled surface—consistently to have the signal (reflections) keep a good lateral amplitude continuity. Iterations of noise attenuation are necessary in various processing stages with spectral variation in the data.

To summarize, the principles in the AVO friendly processing include:

1. Utilizing surface consistent process, e.g. surface-consistent deconvolution, surface-consistent scaling etc.
2. Performing noise attenuation. High signal-noise ratio is important for the AVO analysis.
3. Avoiding trace by trace operations, which may destroy AVO fidelity.
4. Iterative multi-steps of signal and AVO enhancements.
5. Applying the best conventional processing results, such as statics and velocity analysis.

Prestack time migration (PSTM) is already a standard step in the processing flow nowadays. Although the AVO preservation in the PSTM has been discussed for the time being, the output of PSTM has been used by many analysts, because the use of PSTM removes the effects of diffractions, enhances the signal-to-noise ratio, bins the 3D gathers for the AVO analysis with great flexibilities, and avoids the structural mismatch between interpretations based on the migrated data and AVO results from the un-migrated data.

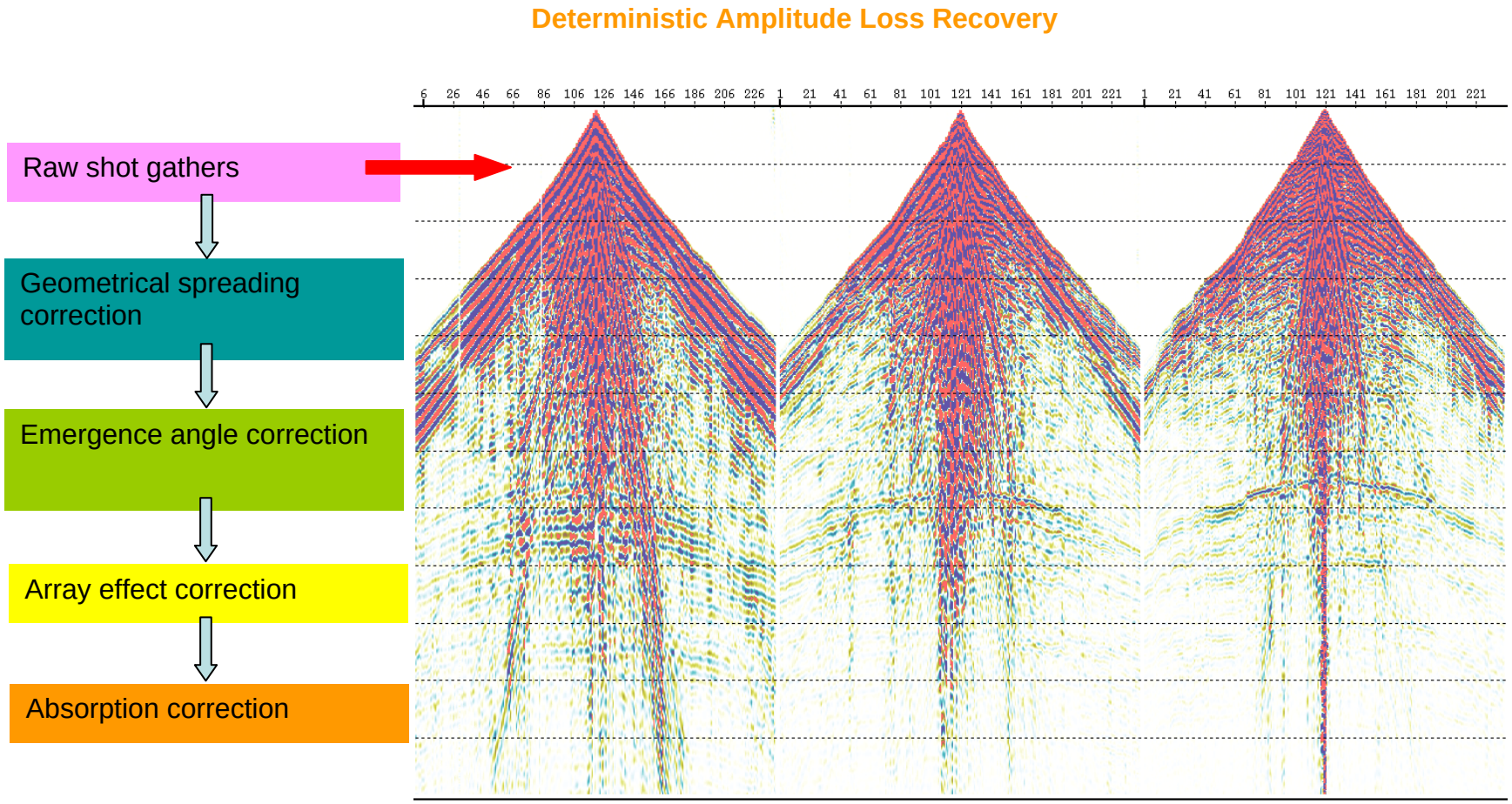

Figure 5.2 Three raw shot gathers (Data courtesy Arcis Corp).

Deterministic Amplitude Loss Recovery

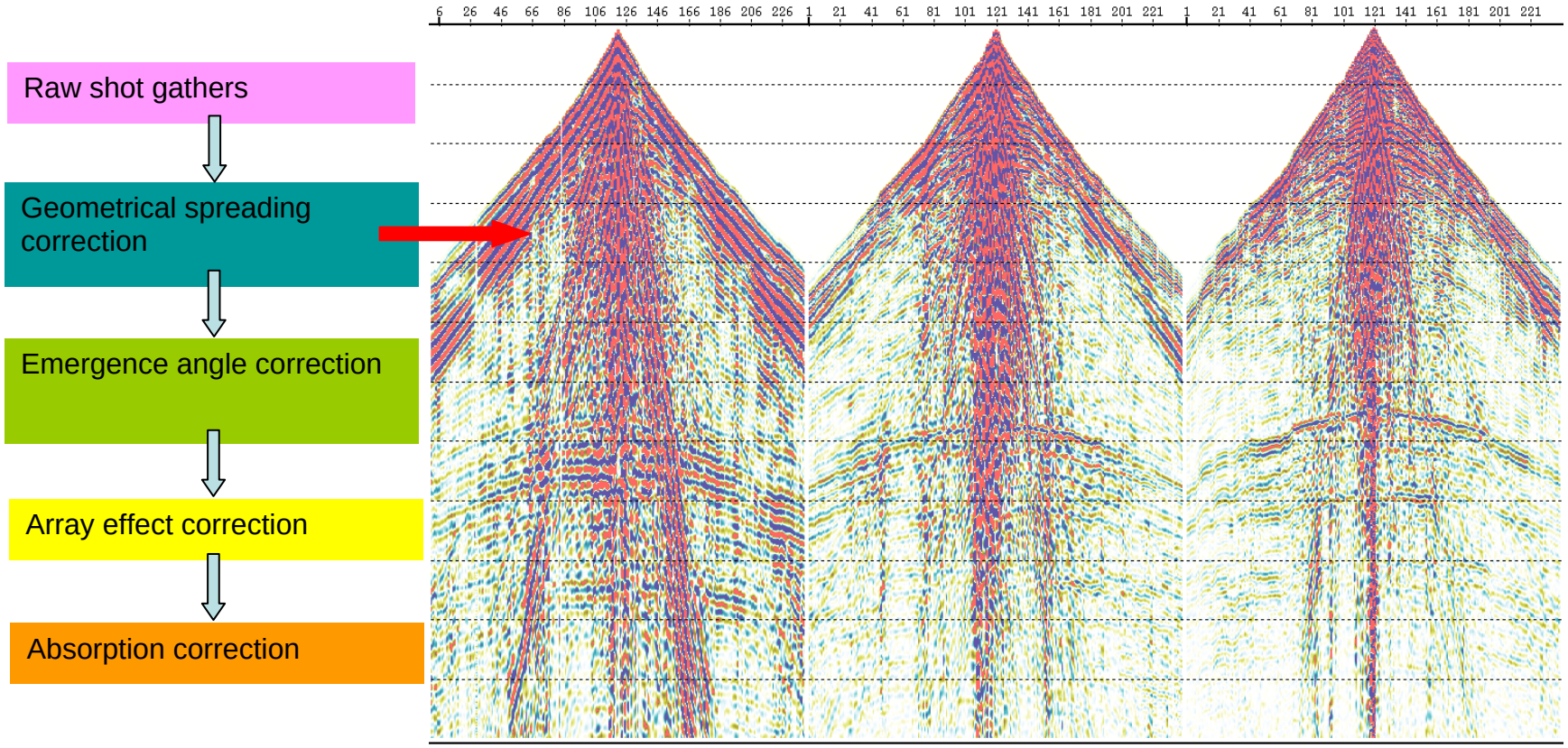

Figure 5. 3 Shot gathers after geometrical spreading correction.

Deterministic Amplitude Loss Recovery

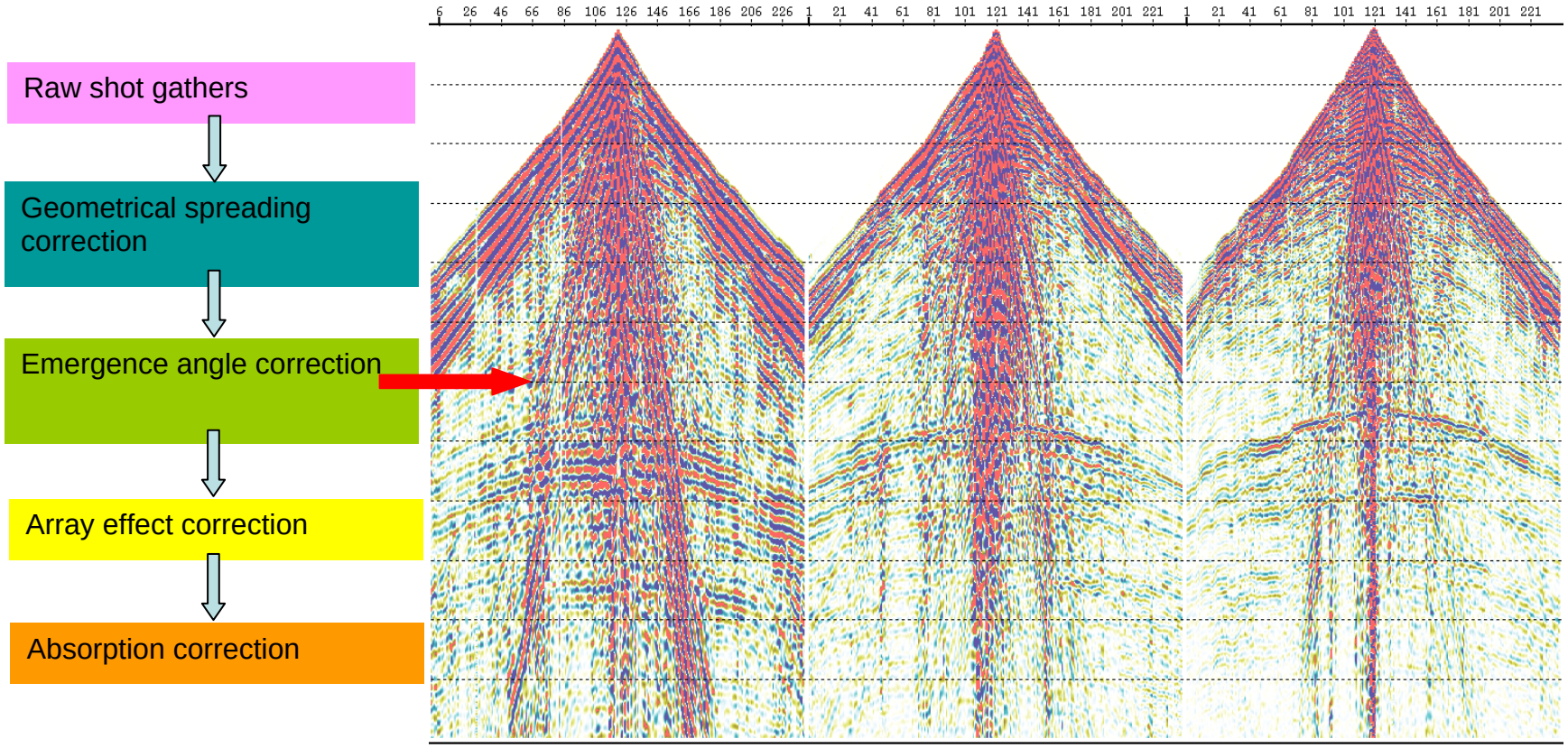

Figure 5 4 Shot gathers after geometrical spreading correction and emergence angle correction.

Deterministic Amplitude Loss Recovery

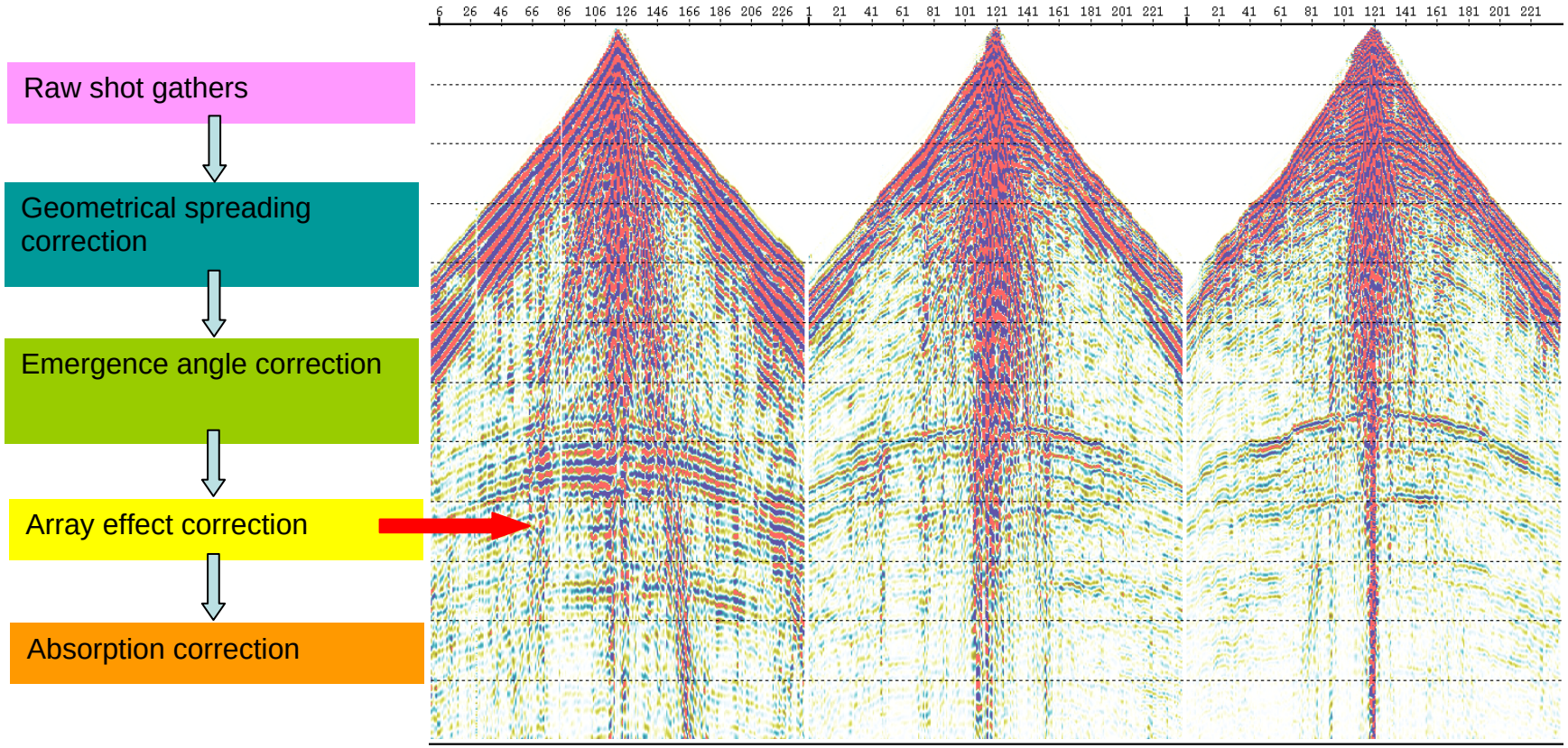

Figure 5.5 Shot gathers after geometrical spreading correction, emergence angle correction, and array effect correction.

Deterministic Amplitude Loss Recovery

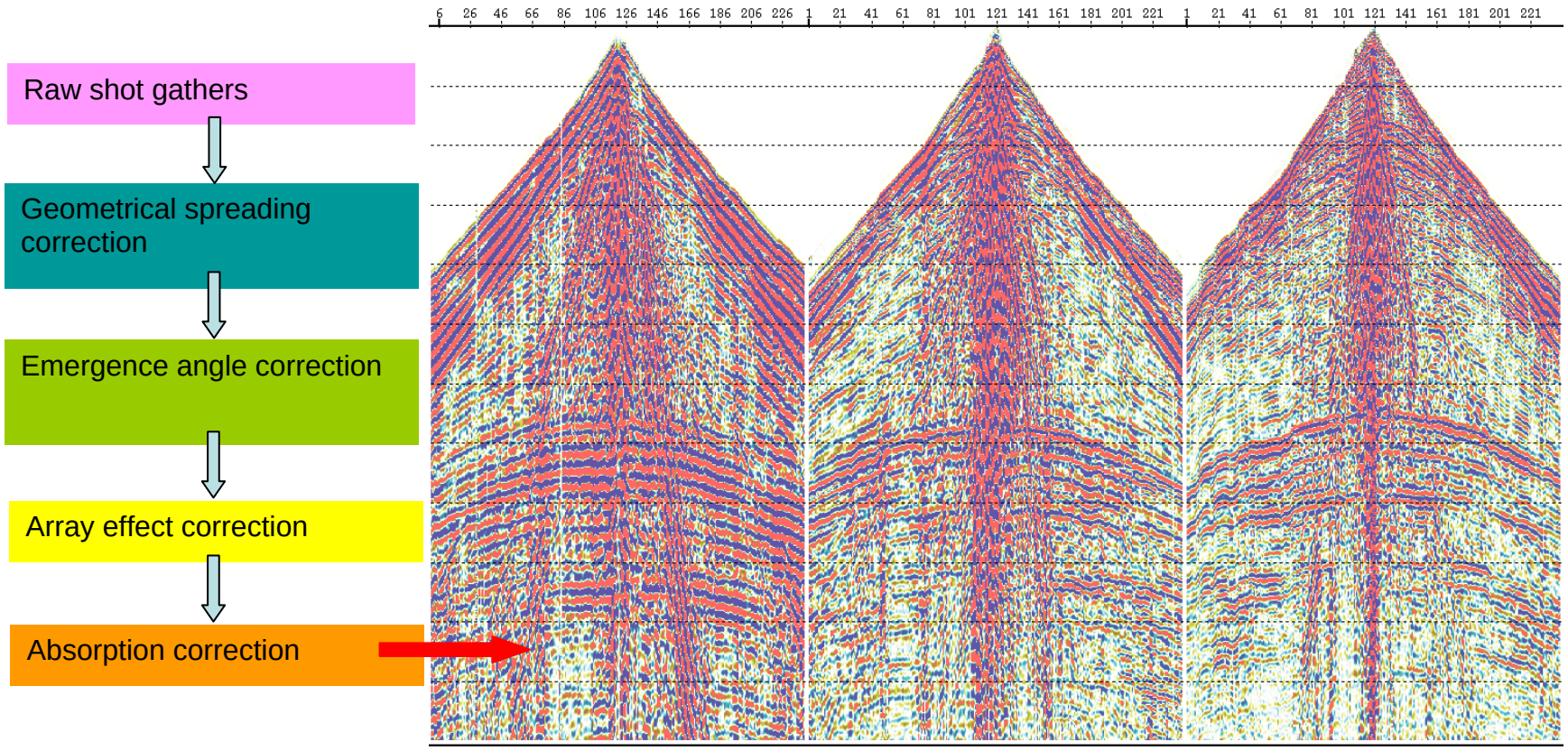

Figure 5.6 Shot gathers after geometrical spreading correction, emergence angle correction, array effect correction, and absorption correction.

Relative Amplitude Loss Recovery

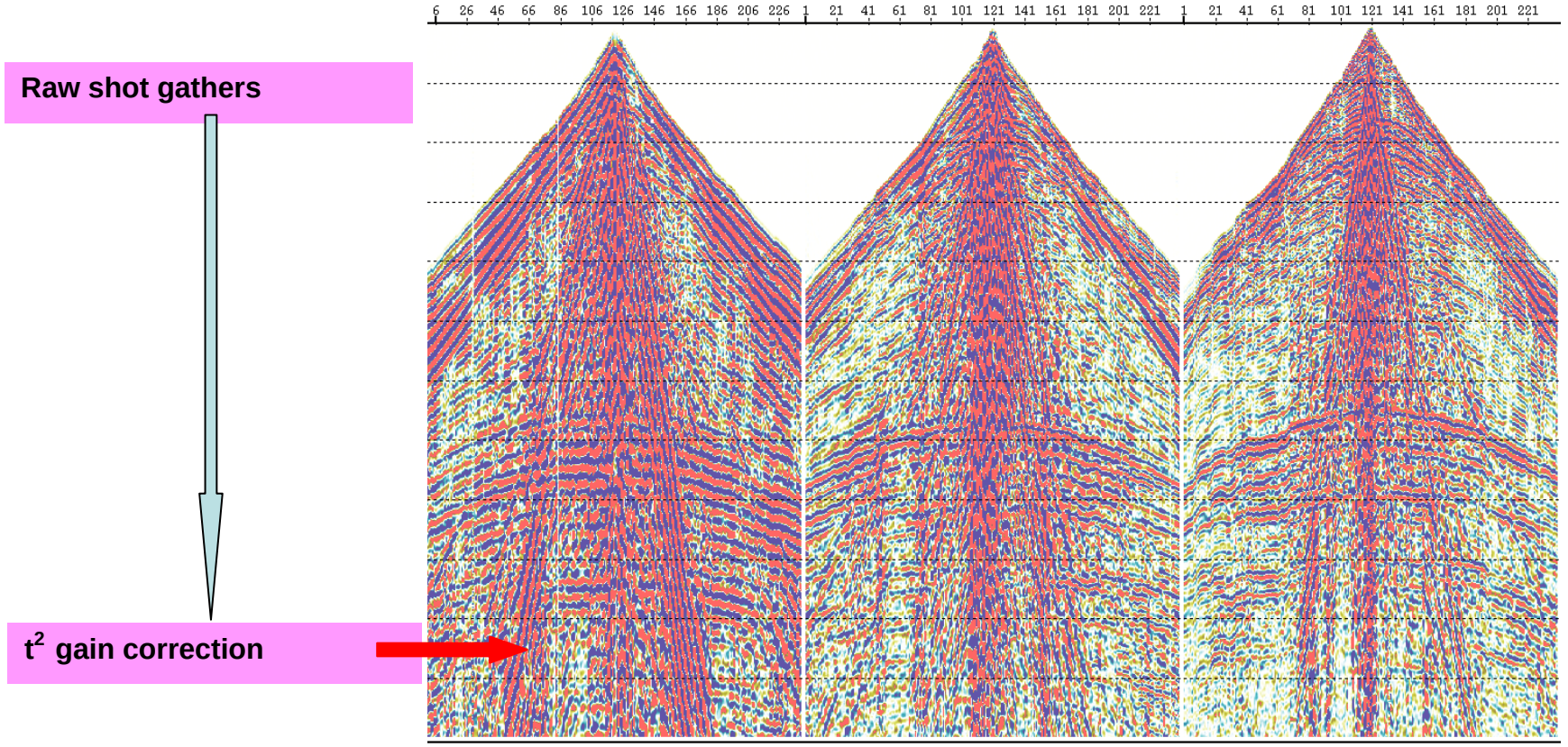

Figure 5.7 Shot gathers after amplitude recovery using t^2 gain correction.

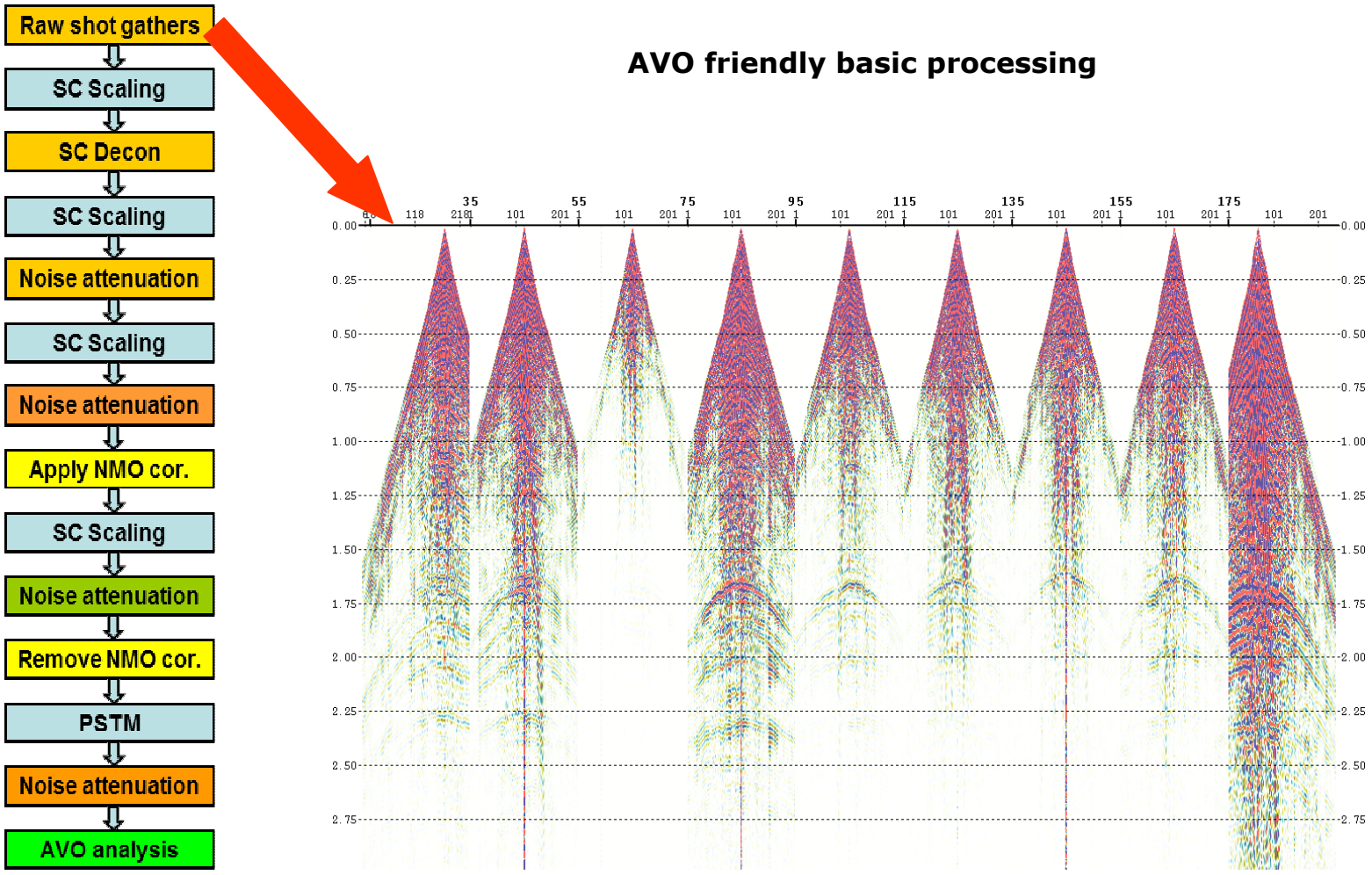

Figure 5.8 Raw shot gathers for a 2D line (Data courtesy Arcis Corp).

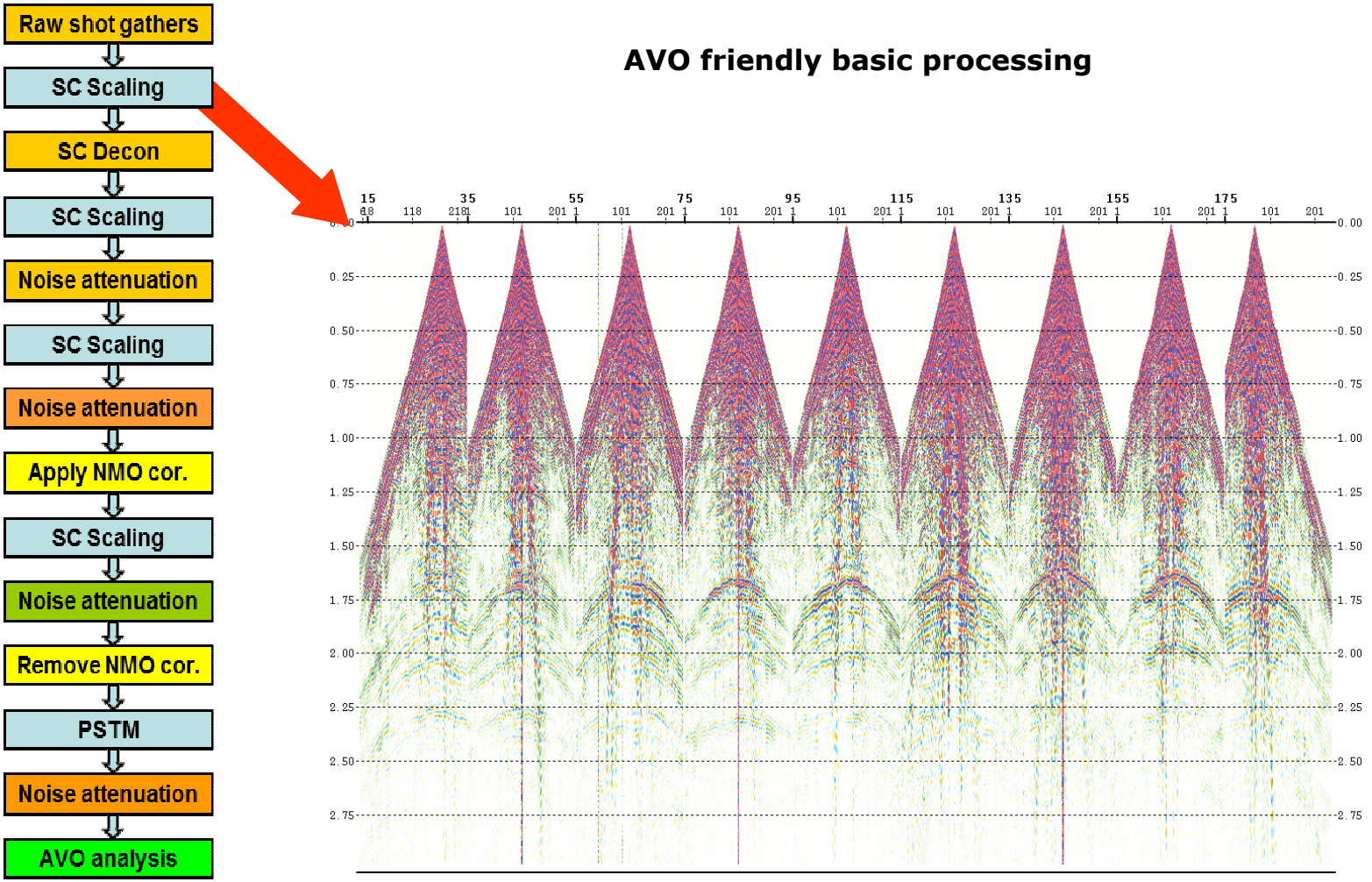

Figure 5.9 shot gathers after the 1st surface consistent scaling.

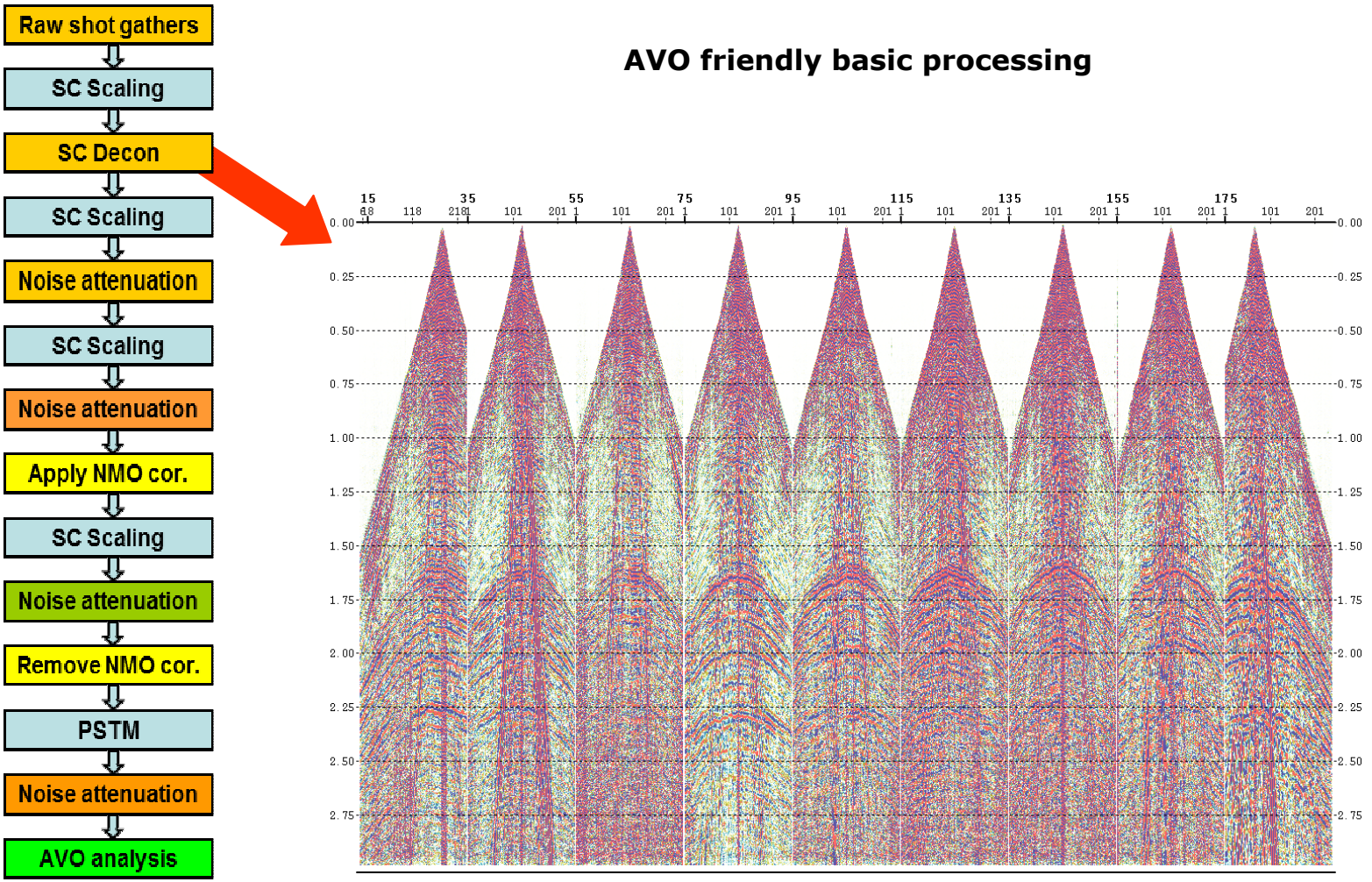

Figure 5.10 shot gathers after the 1st surface consistent scaling and surface consistent deconvolution.

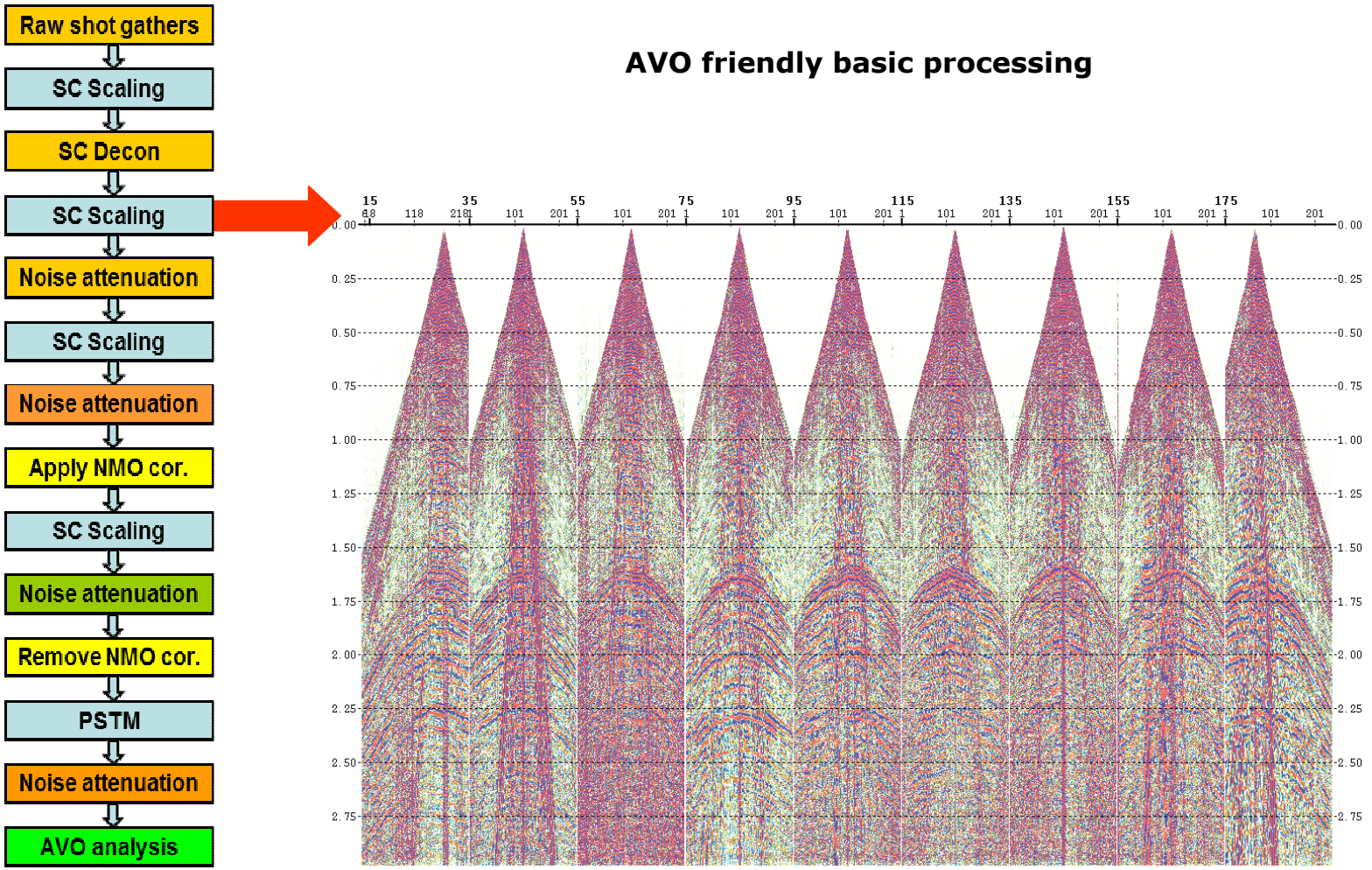

Figure 5.11 shot gathers after the 1st surface consistent scaling, surface consistent deconvolution, and 2nd surface consistent scaling.

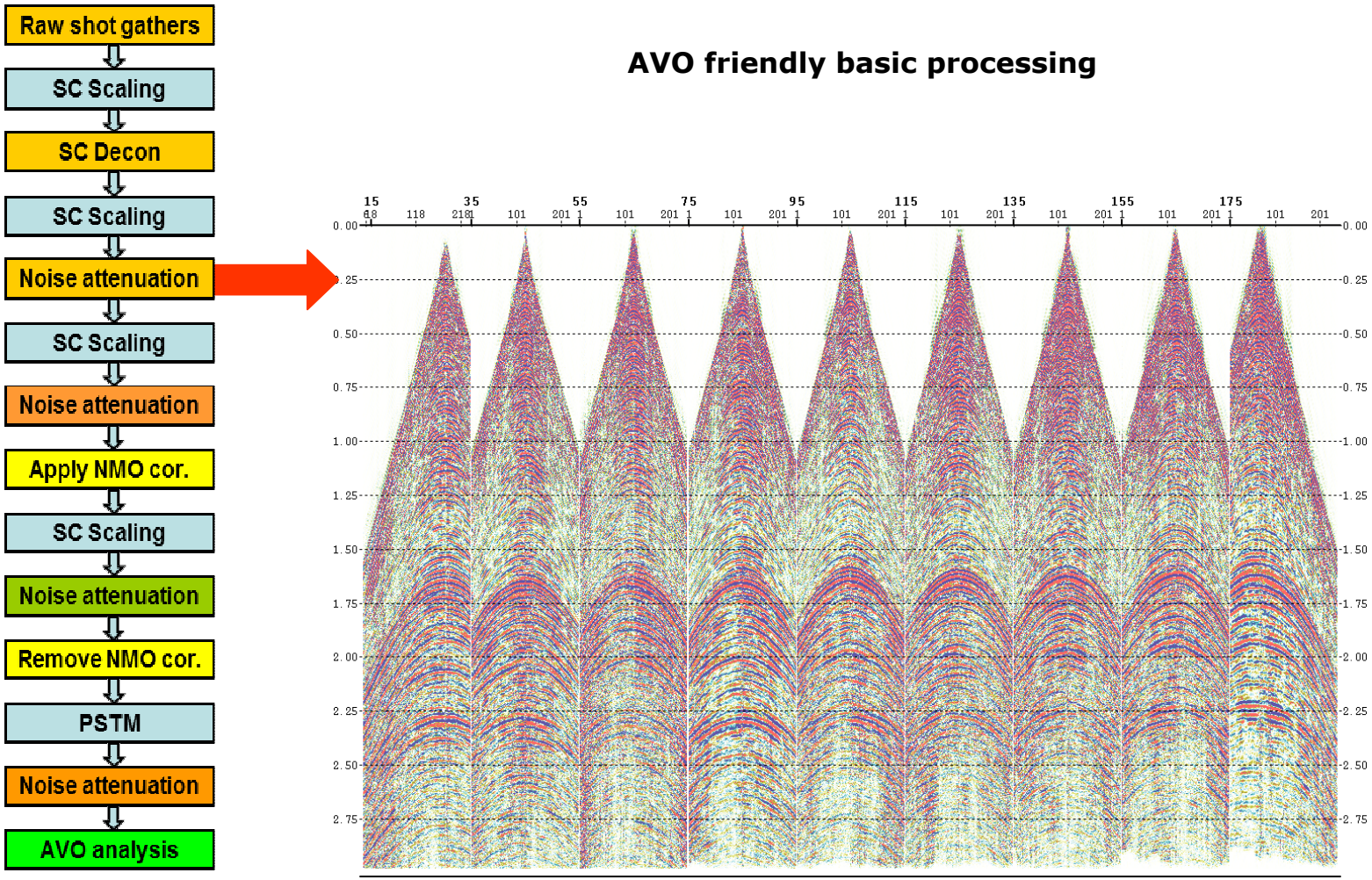

Figure 5.12 shot gathers after the 1st surface consistent scaling, surface consistent deconvolution, 2nd surface consistent scaling, and 1st noise attenuation.

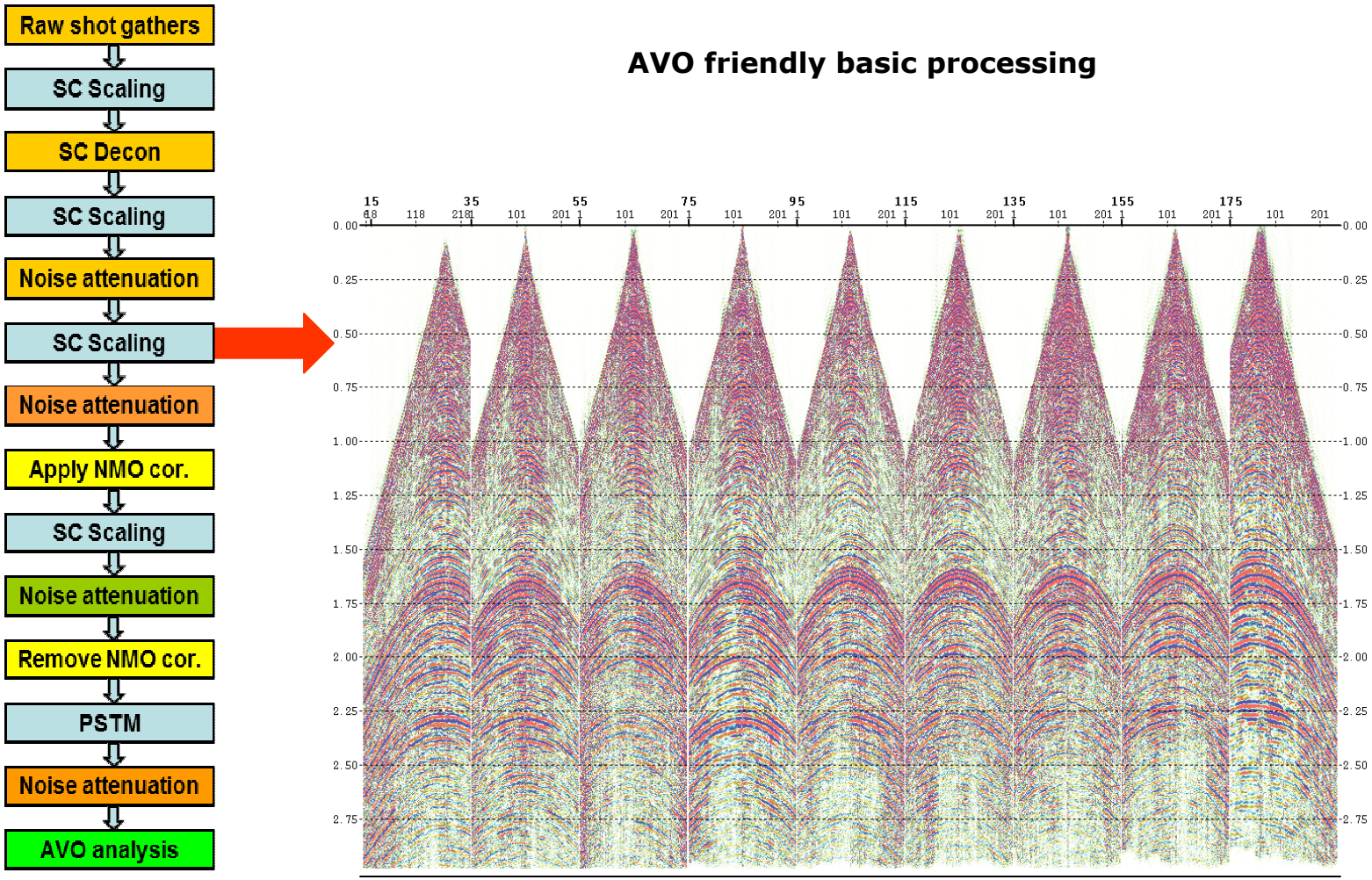

Figure 5.13 shot gathers after the 1st surface consistent scaling, surface consistent deconvolution, 2nd surface consistent scaling, 1st noise attenuation, and 3rd surface consistent scaling.

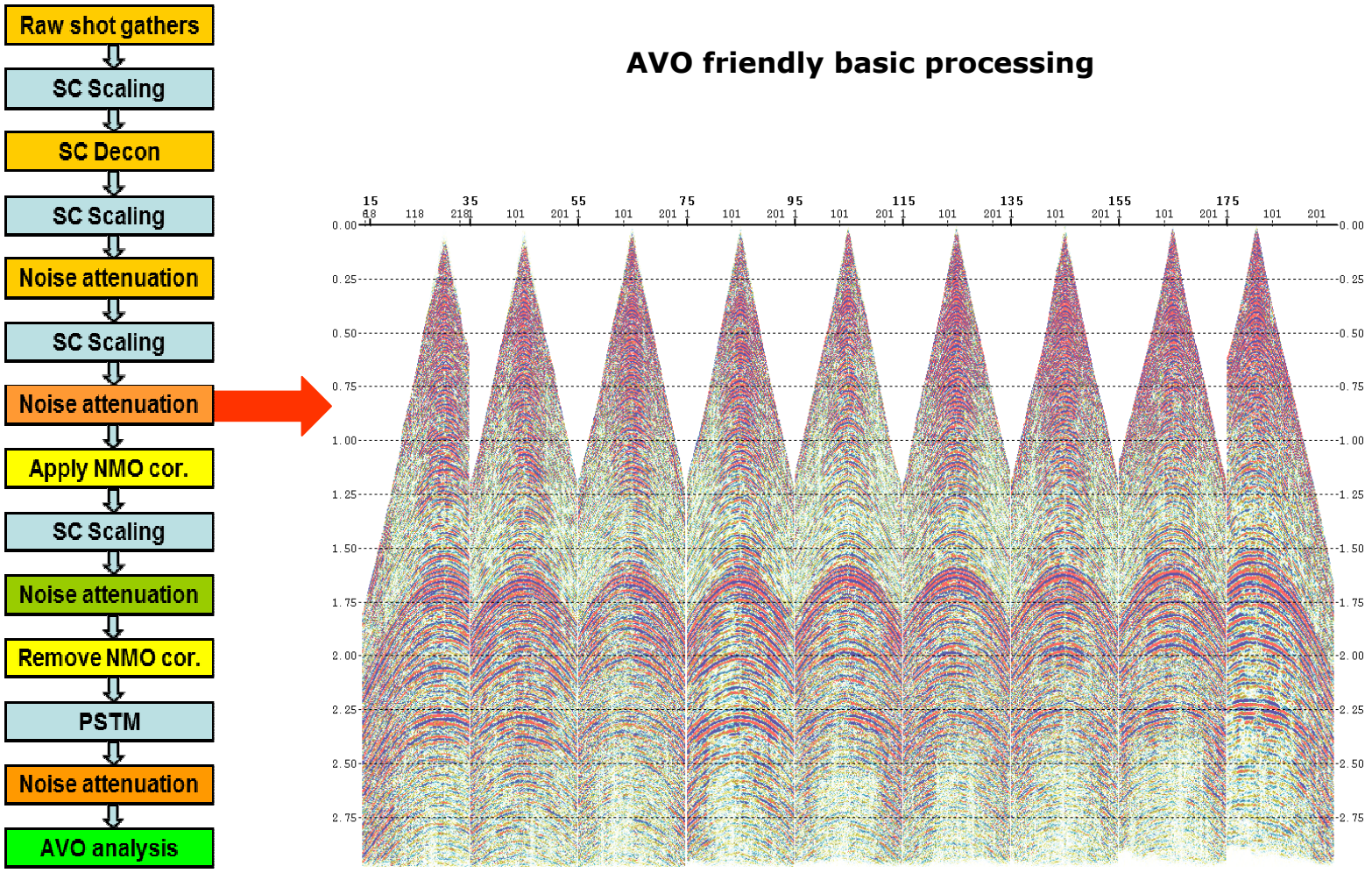

Figure 5.14 shot gathers after the 1st surface consistent scaling, surface consistent deconvolution, 2nd surface consistent scaling, 1st noise attenuation, 3rd surface consistent scaling, and 2nd noise attenuation.

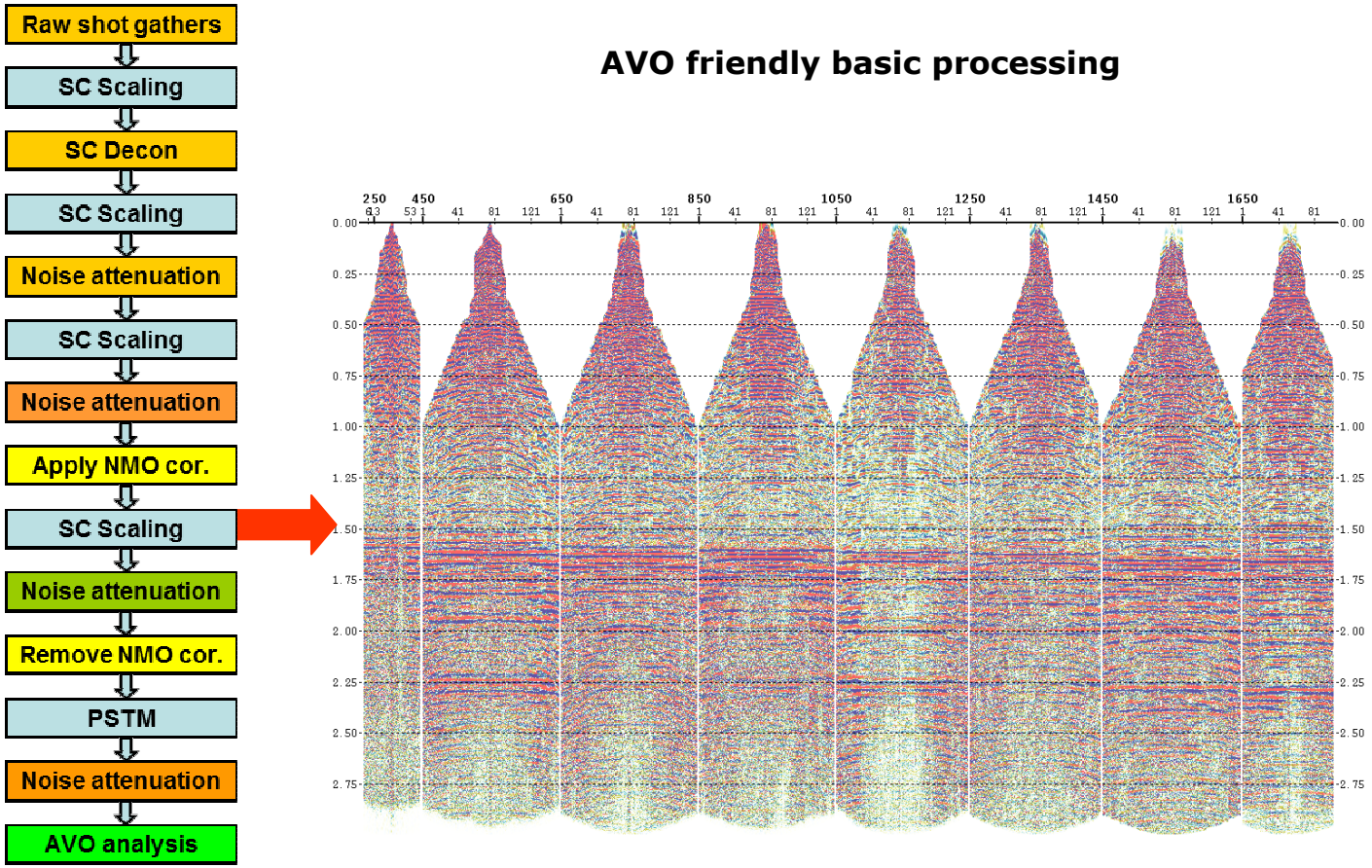

Figure 5.15 CDP gathers after the 1st surface consistent scaling, surface consistent deconvolution, 2nd surface consistent scaling, 1st noise attenuation, 3rd surface consistent scaling, 2nd noise attenuation, and 4th surface consistent scaling.

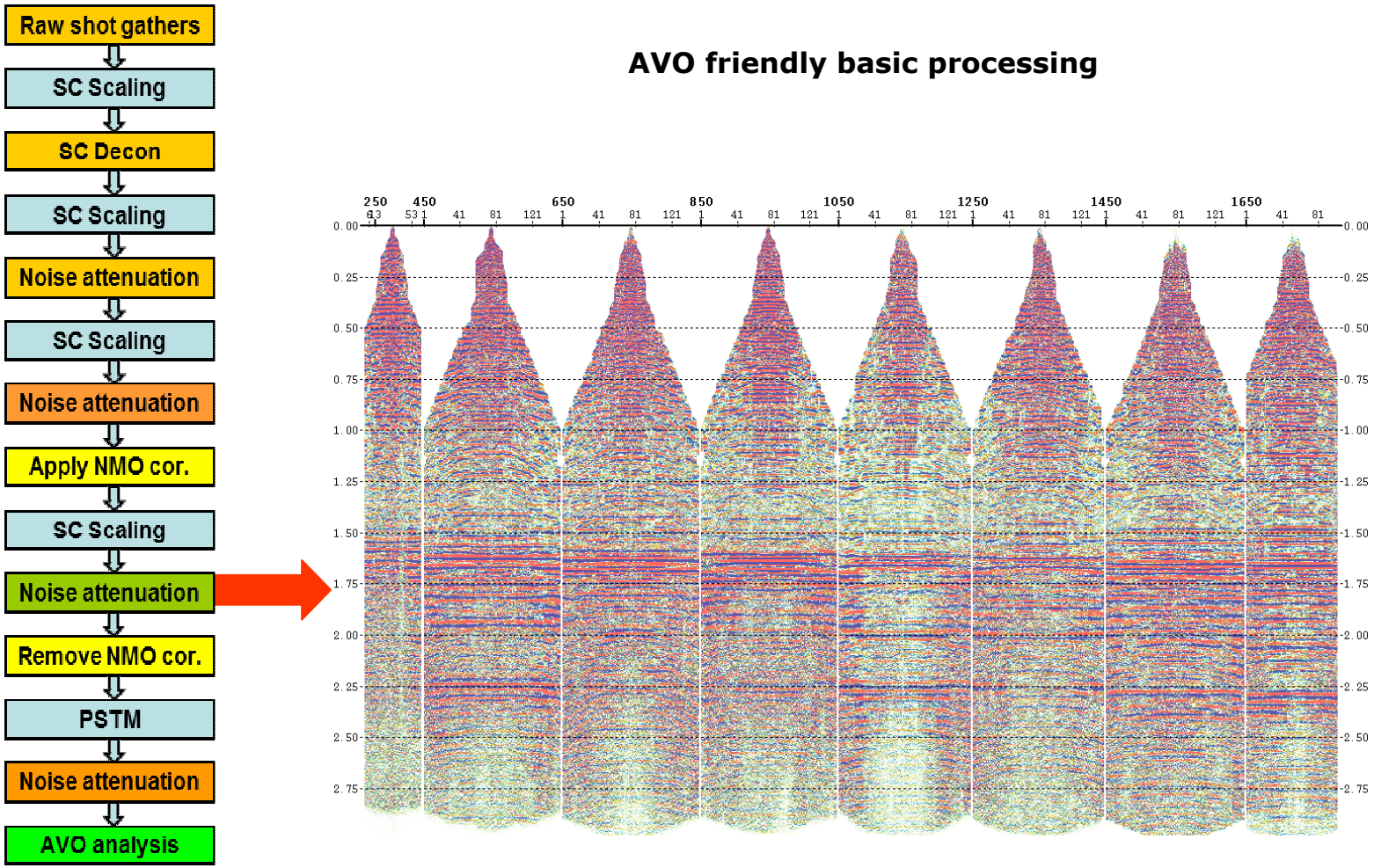

Figure 5.16 CDP gathers after the 1st surface consistent scaling, surface consistent deconvolution, 2nd surface consistent scaling, 1st noise attenuation, 3rd surface consistent scaling, 2nd noise attenuation, 4th surface consistent scaling, and 3rd noise attenuation.

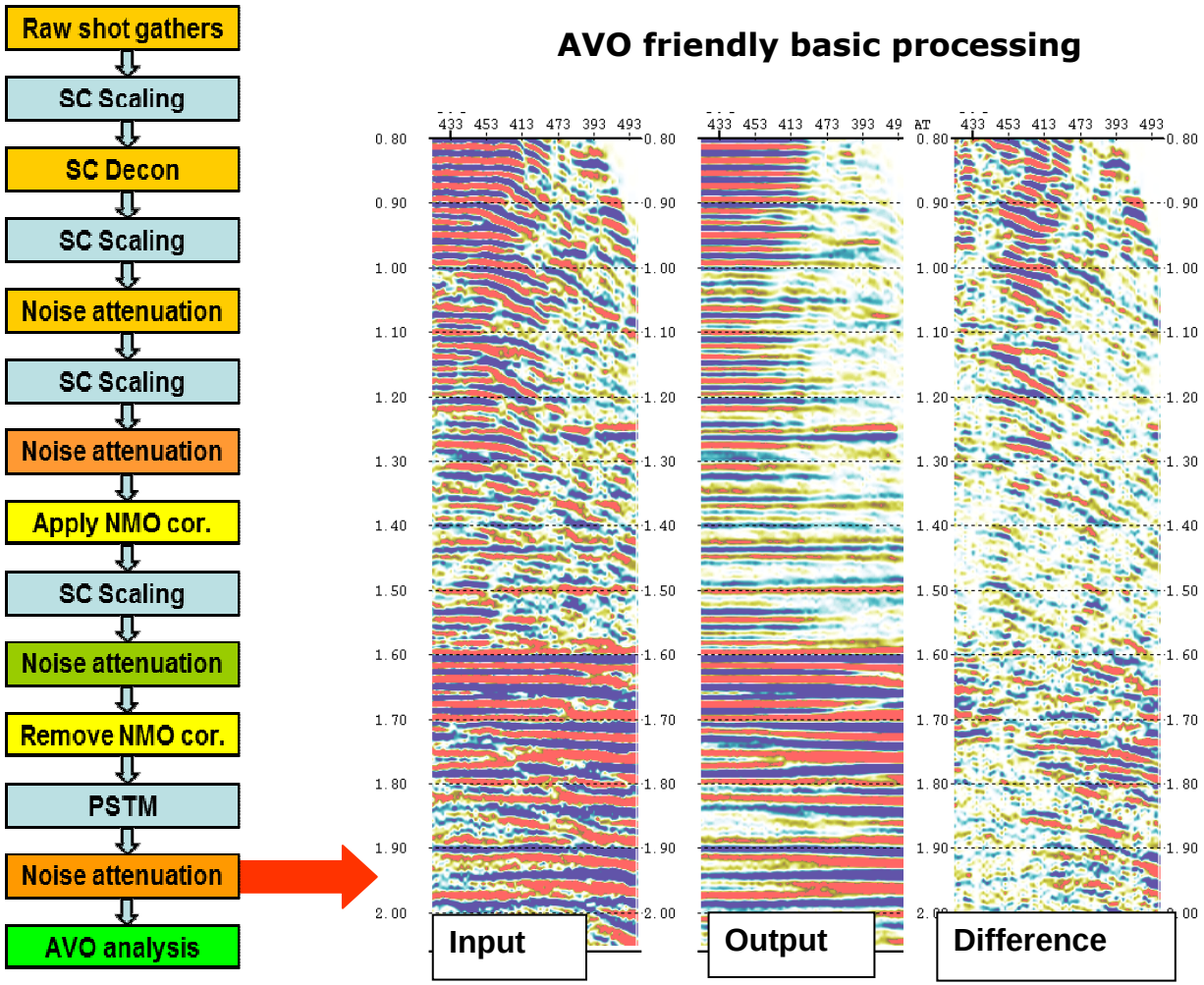

Figure 5.17 PSTM gathers showing the 4th noise attenuation.

5.3 CONDITIONING PRE-STACK DATA FOR AVO ANALYSIS

We can think of the preparation of seismic data for AVO as a two-stage process. Stage 1 is the basic seismic data processing and Stage 2 is conditioning the prestack data for the AVO needs. Stage 1 is usually finished in processing workshops. The industry has agreed on the necessities to preserve amplitude for the AVO analysis by choosing processing streams to maintain the integrity of data and improve the signal-to-noise ratio. After data is delivered from processing workshops, further conditioning of data is needed for the quantitative AVO analysis. The data conditioning corrects more effects distorting AVO, improves the signal-to-noise ratio, and generates high quality gathers for the AVO interpretation and inversion. Many of these need to be customized for individual projects and they are not able to be stream-lined or delivered by processing workshops. As part of the AVO data conditioning, the AVO QC, calibration, and fixing should be done by the AVO practitioners.

In the AVO data conditioning stage, AVO specialists evaluate the data quality and AVO preservation and apply corrections to improve the AVO fidelity and the reliability of AVO analysis. In the next of this chapter, a few examples will show the application of corrections and regularization to improve the AVO fidelity and reliability.

Signal enhancement is always important for any use of seismic data. Although the noise attenuation is not discussed in this chapter, attenuation of random and coherent noises in the prestack data helps reduce the uncertainty in the AVO analysis and impedance inversion.

5.4 NMO STRETCHING AND OFFSET-DEPENDENT TUNING CORRECTION

Wavelet stretching due to NMO correction of seismic gathers causes problems in AVO. Coupled with the degrading action of wavelet stretching during NMO correction is the offset-dependent tuning for thin beds. Even though the tuning is inherent in the data before NMO correction, its effect on AVO is more obvious on the NMO corrected data. This section expands an early study (Xu and Chopra, 2007b) for an analytical

understanding of the NMO stretching and thin-bed tuning and their correction to improve the AVO fidelity. Based on these studies, NMO stretching and thin-bed tuning corrections are implemented in a practical fashion for the production AVO analysis. Both synthetic and real data examples show that these corrections are necessary for performing a reliable AVO analysis.

5.4.1 Induction

Effects of normal moveout (NMO) on the stacking and AVO analysis and their correction have been studied for over three decades. Dunkin and Levin (1973) were among the earliest who noticed that the NMO procedure stretches wavelet waveforms, and they derived an analytical relationship to link the spectral changes due to NMO correction and the velocity and offset. Lin and Phair (1993), Swan (1997), and Dong (1999) attempt to quantify the effect of the offset-dependent tuning on AVO and suggest solutions for correcting the AVO gradient, a commonly used indicator for hydrocarbon anomalies. Castoro et al (2001) analytically explain the wavelet stretching and offset-dependent tuning and provide a practical procedure to correct them. More recent researchers (Lazaratos and Finn, 2004, Roy et al, 2005, Perez and Marfurt, 2006) have focused their attention to the stretching effect during processing of data, as stretching and its resultant AVO biasing exist in the large incident angle data from depth migration. Lazaratos and Finn (2004) follow Dunkin and Levin (1973) and correct the stretching on the offset gathers by applying an inverse spectral shaping filter. Roy et al (2005) find an analytical derivation for wavelet stretching in migration depending only on reflection angle in the layered media. Perez and Marfurt (2006) seek a more robust implementation for correcting wavelet stretching after common-angle migration by combining the studies by Roy et al (2005) and Lazaratos and Finn (2004).

When the offset range is limited to the near offset for generating stack sections, the necessity of applying stretching and tuning corrections can not be seen by many interpreters. However, when the far offset data are used in the AVO analysis, the stretching and tuning do bias observations. The out-of-phase AVO artifact due to

stretching and tuning can lower the reliability of AVO and waste time. Based on the above-mentioned studies, correction to the wavelet stretching and offset-dependent tuning is designed and implemented. Both synthetic and real data examples are used to test the effectiveness of the implementations. The real data example shows the necessity of applying the stretching and tuning corrections prior to the AVO analysis.

5.4.2 Wavelet stretching and offset dependent tuning

5.4.2.1 Pulse/wavelet stretching

Dunkin and Levin (1973) consider the effect of NMO on an isolated pulse, which can be thought as the seismic record from a single reflector. They provide an analytical expression of pulse spectral compression due to the NMO correction, which is given as equation (5.1),

$$\tilde{\mathbf{g}}_0(\mathbf{f}) = \mathbf{a}\,\tilde{\mathbf{g}}(\mathbf{af}), \tag{5.1}$$

where $\tilde{\mathbf{g}}_0$ is the spectrum of NMO corrected pulse, $\tilde{\mathbf{g}}$ is the spectrum of uncorrected pulse, and **a**, as shown in equation (5.2), is a function of offset **X**, velocity **V**, time at zero offset $\mathbf{t_0}$, and time **t** at offset **X**:

$$\mathbf{a} = \frac{\mathbf{t}}{\mathbf{t}_0}\left(1 - \frac{\mathbf{X}^2}{\mathbf{V}^3\mathbf{t}_0}\frac{\mathbf{dV}}{\mathbf{dt}_0}\right)^{-1}. \tag{5.2}$$

From equation (5.2), we notice that **a** is usually greater than 1.0 because **t** is always bigger than $\mathbf{t_0}$ and NMO velocity rarely decreases with time. Therefore, NMO correction compresses the pulse bandwidth to 1/**a** times the original and amplifies the amplitude by scale of **a** in the meantime. Obviously, one can correct the distortion due to NMO by reversing the process shown in equation (5.1). As noticed by Roy et al (2005), **a** is non-stationary and requires velocity information. They study the wavelet stretching in the angle domain data, which is often seen in depth migration and suggest a stationary stretching factor as shown in equation (5.3),

$$\mathbf{W}_\theta(\mathbf{f}) = \frac{1}{\cos\theta}\mathbf{W}_0\left(\frac{\mathbf{f}}{\cos\theta}\right), \tag{5.3}$$

where $\mathbf{W}_\theta$ is the wavelet spectrum at reflection angle θ, and $\mathbf{W}_0$ is the wavelet spectrum at the zero reflection angle.

A single interface model as shown in Figure 5.18 is used to demonstrate the NMO stretching and its correction on a pulse. Shuey's 2-term AVO approximation is used in the modeling. AVO intercept and gradient are inverted from (i) an ideal gather (no stretching at all), (ii) the NMO corrected gather, and (iii) the NMO corrected gather after wavelet stretching correction. The above gathers are shown in Figure 5.18 in both time and frequency domains. Cross-plot is generated for the intercept and gradient extracted from these gathers by using Shuey's 2-term AVO approximation. Artifacts due to the rough interpolation implementation in NMO correction can be seen and they can be reduced by sophisticated interpolation algorithms. The ideal cross-plot of intercept and gradient is like a straight line passing through the origin (green line in Figure 5.18(i)). But the NMO correction gives rise to out-of-phase side lobes which biases the cross-plot of intercept and gradient. In Figure 5.18 (d), (h) and (i) the wavelet stretching and AVO distortion due to NMO correction is corrected reasonably well. The intercept and gradient derived from the stretching-corrected gather fall along the line passing origin in the cross-plot with invisible deviations from the true trend line.

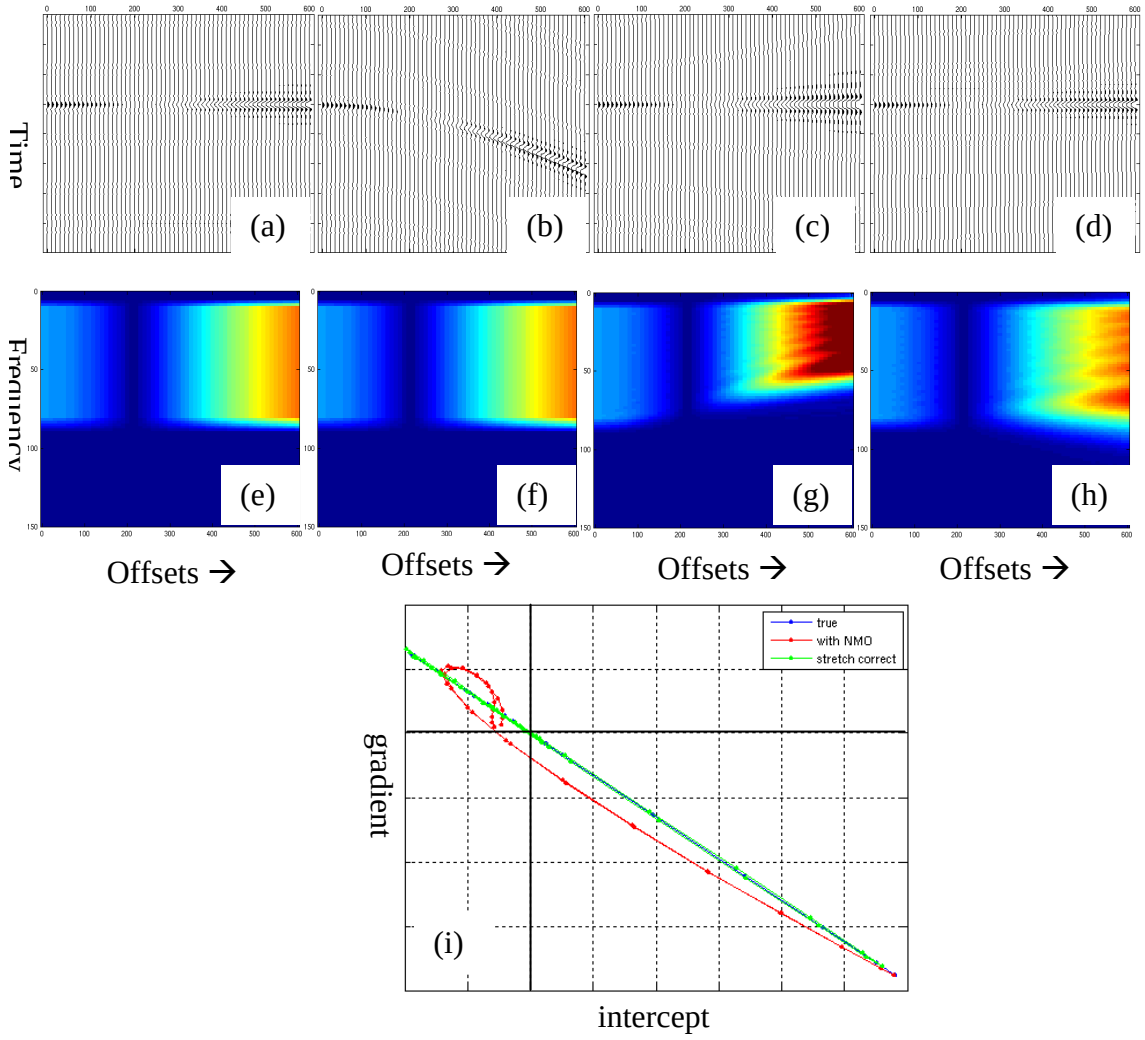

Figure 5.18 A single interface model is used to illustrate stretching of NMO and correction of stretching. Shown here are (a) – the ideal offset gather, modeled without NMO differential time; (b) – gather with NMO differential time; (c) – gather after NMO correction applied on (b); (d) – stretching corrected gather based on equation (5.3). (e), (f), (g), and (h) are the amplitude spectrum (frequency –offset domain) for t-x gathers in (a), (b), (c), and (d). AVO intercept and gradient are calculated using gathers in (a), (c), and (d) respectively, and cross-plotted in (i).

5.4.2.2 Offset-dependent tuning

In the AVO analysis, besides considering the effect of tuning due to the thickness of a reservoir, the offset dependent tuning also needs to be considered. This is because the waveform interference in the offset domain is influenced not only by the layer thickness but also by the differential moveout. Figure 5.19 shows diagrams to explain the offset-

dependent tuning based on convolution assumption. In the left red box, two close reflectivities without AVO show differential moveout – the travel time difference decreases as the offset increases. As a result of this, tuning causes a spectrum expansion. If the incident angle is assumed as constant θ, the far offset trace can be derived from the near offset trace by $T_{far}(f) = T_{near}(f\cos\theta)$. If AVO is taken into account, the far offset trace may not be simply derived from the near offset trace with a cosine mapping, but the spectral expansion is still significant. In the processing of seismic data, the same wavelet is usually assumed to apply on both the near and far offset traces. The wavelet frequency response is illustrated in the blue box in Figure 5.19 and high-cut frequency – f_c is assumed. As per convolution model, the spectrum of the output trace is the product of spectra of pulse wavelet and reflection coefficient series. The output bandwidth is limited by the wavelet bandwidth. This is illustrated in the right green box, from which we can see that due to the high cut of wavelet spectrum, some of the high-frequency components at the far offset trace are lost while their equivalents still exist in the near offset trace. As a result, the far offset trace loses resolution even before the NMO correction is applied. Since the offset-dependent tuning causes spectral expansion, a wider frequency bandwidth is required for a trace with tuning than the one without tuning to keep the same resolution of reflector series. However, the filtering effect of earth and the application of band limited filters in the processing makes the bandwidth of the far offset traces same as or narrower than that of the near offset traces.

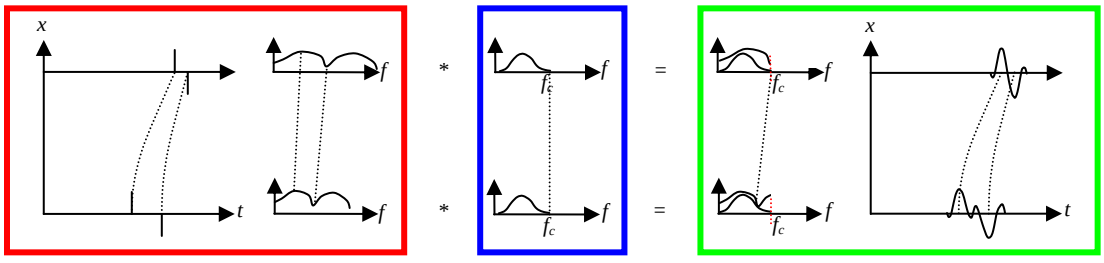

Figure 5.19 Diagram of a convolution model with tuning effect. In the left red box, two close reflectivities without AVO show offset dependent tuning. The wavelet frequency response is illustrated in the blue box in the middle and high-cut frequency – f_c is assumed. In the right green box, tuning lowers the resolution at far offset trace after same wavelet is applied.

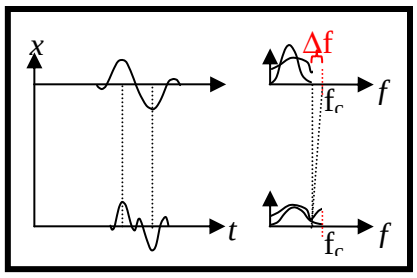

Figure 5.20 NMO correction stretches the waveform at far offset and compresses the spectrum resulting in the magnification of low frequency components.

Figure 5.20 shows a diagram to illustrate the fact that NMO correction compresses the spectra of the wavelet and reflector series. The NMO correction modifies the pulse spectrum in the same way shown in the last section, and thus, the spectral compression in the NMO correction aligns the existing frequency components at the far offset trace with those at the near offset traces.

To generate high resolution stacking and preserve AVO, both the near offset and far offset traces need to keep the same bandwidth and it is required to restore AVO for every component. One of the choices is to reduce the near offset trace bandwidth to that of the far offset trace after spectral shape is corrected for wavelet stretching, as illustrated in Figure 5.21 (a). However, such a choice could lower the resolution of the near offset trace and stacked section and is not readily accepted by interpreters. An alternative choice is to extrapolate the bandwidth of the far offset trace to match that of the near offset traces, as shown in Figure 5.21 (b). When AVO exists, the spectral shape at the far offset may not necessarily match that at the near offset, and so the extrapolation of high frequency components at the far offset traces needs the use of AVO knowledge or assumptions, which may come from the gather itself.

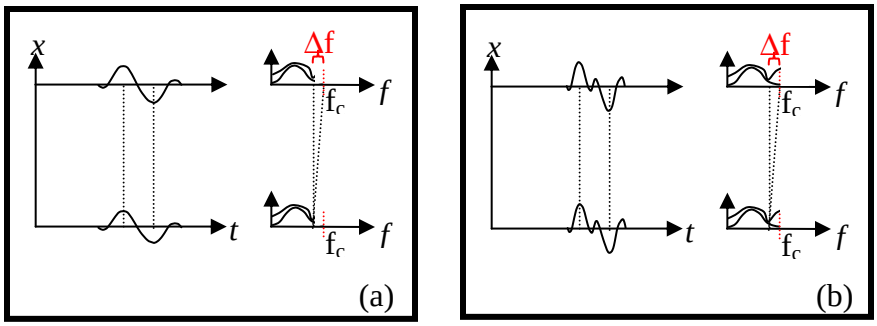

Figure 5.21 Illustration of two choices for removing tuning effect: (a) after wavelet stretching correction, the high frequency component at near offset traces is cut to match at far offset trace. Therefore, stretching is removed with a loss of resolution but bandwidth matches. (b) the lost high frequency components at far offset due to tuning can be recovered by using other sources of information, such as AVO relationship from *a priori*, or other reliable components of data within the same gather.

5.4.2.3 Wavelet stretching and tuning correction

The wavelet stretching and offset-dependent tuning corrections can be done separately in the frequency domain. The wavelet stretching needs to be applied prior to the tuning correction. The offset domain gathers are more commonly used in the AVO analysis than the angle domain gathers but the stretching factor is non-stationary in the offset domain. If the time window is small enough for a mildly-changed velocity field, a stationarity assumption can be made (Castoro et al, 2001, Lazaratos and Finn, 2004). It is more practical to use overlapping time windows and averaging as suggested by Lazaratos and Finn. Tests have to be done to look for an optimal window size for the stationarity assumption and computing efficiency.

The wavelet stretching correction is based on equation (5.1) or (5.3). It needs to be borne in mind that the wavelet stretching correction can only restore the usable frequency band at the far offset trace, which is narrower than at the zero offset trace. The high frequency loss due to tuning is compensated in next step. When the wavelet doesn't have a box car spectral shape, wavelets need to be estimated first. The amplitude ratio of non-stretching wavelet and stretched wavelet is used to scale the far offset data in the frequency domain. This procedure is suggested by Castoro et al (2001). A non-stretching wavelet can be

estimated from the zero or stacked near offset data, and the stretched wavelet can be calculated by the stretching factor equation (5.1) or (5.3). The far offset data can provide a stretched wavelet, and from it the non-stretching wavelet can be derived based on equation (5.1) or (5.3). The results from the above two options should reconcile well when data quality and processing flows are reasonable. Some AVO-unfriendly processes, such as trace-to-trace whitening after the NMO correction, certainly make this fail.

Compensation of the high frequency loss due to tuning can not be achieved by deconvolution kind of approaches used by Castoro, et al, 2001 and Roy et al, 2005 because there is no high frequency signal left after filtering and NMO correction when the stretching is severe (e.g. the portion below dash line in Figure 5.22 (d)). The lost high frequency components at the far offset can be estimated from the near offset data where the corresponding high frequency components exist by an AVO inversion approach if the stationary assumption is used for small time window or ideally for angle gathers. If the range of the far offsets with loss of high frequency is large, the AVO inversion would be less reliable. Using the local mud-rock line, as well as the intercept attributes, the gradient can be determined. The reflectivity at larger offsets can then be calculated using the intercept and calculated gradient. In the absence of a reliable local mud-rock line, the ratio of the intercept and gradient can be estimated statistically from the reliable low frequency components in the analyzed time window after the wavelet stretching correction.

5.4.3 Examples

A few synthetic and real data examples are used to show the effectiveness of the NMO stretching and tuning correction to restore the high fidelity AVO.

5.4.3.1 Synthetic examples

Figure 5.22 shows the NMO stretching on a synthetic gather and its spectral change. The gather is modeled without AVO effect. On the spectrum for the NMO-corrected gather on the far offset traces, low frequency components are amplified and high frequency

components are missing due to the tuning plus band pass filtering. NMO correction correctly aligns the low frequency components.

Figure 5.23 and Figure 5.24 show the stretching and tuning correction on two synthetic gathers: one without AVO effect, and one with strong AVO. The gather has a 400 ms time window. The useful signal zone is about 250ms thick. A single window is used to calculate the stretching factor. Improvement on the stretching correction could be achieved (such as aliasing on Figure 5.24 (d)) if overlapping time window and averaging (used by Lazaratos and Finn, 2004) and more optimal parameters were used. The gathers resulting from the stretching and tuning corrections closely match the ideal gathers. More importantly, the AVO distortion is fixed by the stretching and tuning corrections.

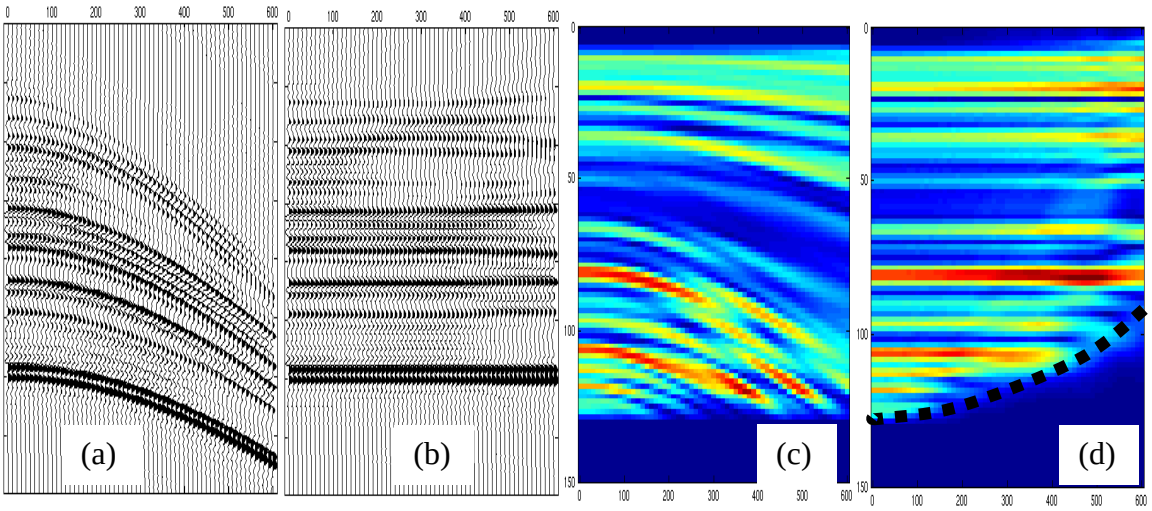

Figure 5.22 NMO correction on an offset domain gather. (a) Offset domain gather before NMO correction, with no AVO effect in the modeling; (b) the same gather as in (a) after NMO correction; (c) amplitude spectrum of gather in (a) before NMO correction. (d) amplitude spectrum of gather in (b) after NMO correction. Hot colors represent high values; and cold colors low values. The shape of outside edge of the spectrum after NMO correction on (d) approximately follows a $\cos\theta$ curve (see the black dot line).

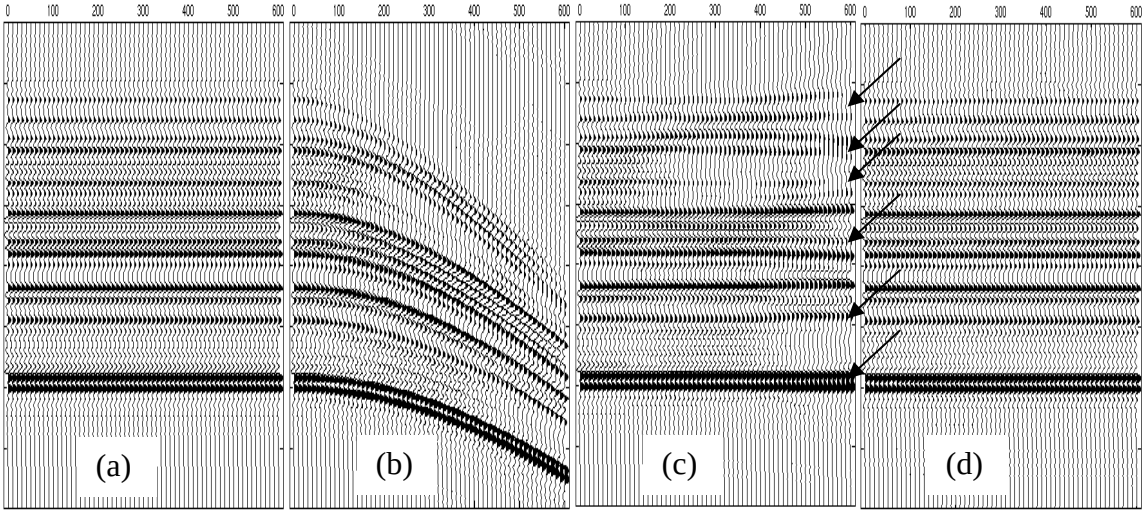

Figure 5.23 NMO stretching and tuning correction for an offset gather without AVO effect. (a) ideal gather, no stretching, no time normal moveout. (b) before NMO correction; (c) after NMO correction. Stretching can be seen. (d) after stretching and tuning correction applied on (c). Resolution loss can be seen on far offset after NMO correction in (c). Arrows indicate several obvious stretching

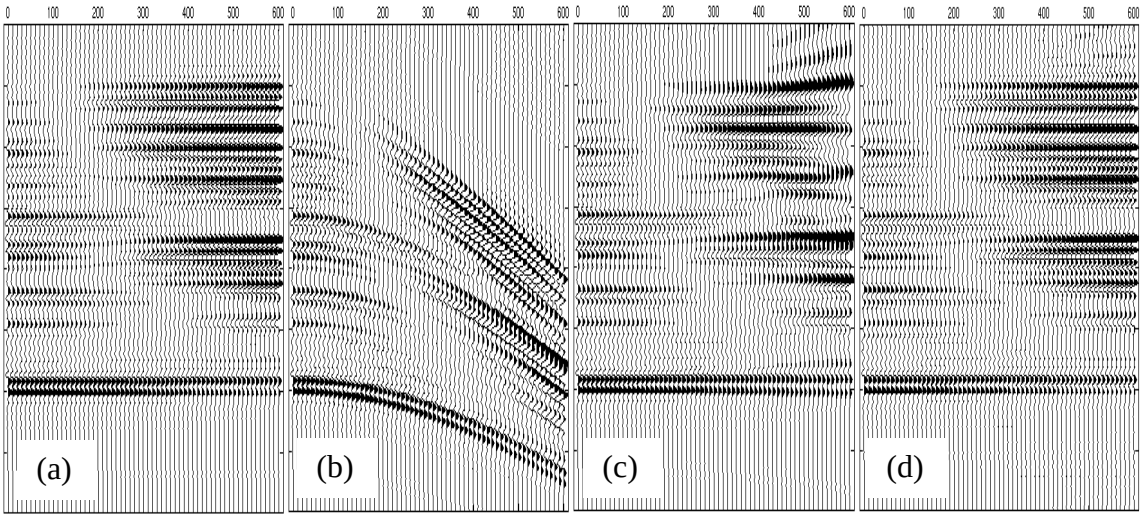

Figure 5.24 NMO stretching and tuning correction for an offset gather with strong AVO effect. (a) ideal gather, no stretching, no normal moveout applied. (b) before NMO correction; (c) after NMO correction. Stretching can be seen. (d) after stretching and tuning correction applied on (c). AVO is restored at far offset traces after stretching and tuning corrections.

5.4.3.2 Real data example

A real dataset from Alberta, Canada was used to test the NMO stretching and offset-dependent tuning correction. The data was provided by Arcis Corporation. Data was processed in an AVO friendly fashion and NMO correction was applied. Figure 5.25 shows an NMO corrected CDP gather to demonstrate the effectiveness of corrections. An NMO corrected CDP gather is shown in Figure 5.25 (a) and a black arrow indicates the reservoir target. The amplitude spectrum for this CDP gather is shown in Figure 5.25 (b). Note the high frequency loss at far offset due to the offset-dependent tuning and the enrichment of low frequency at the far offset due to the NMO stretching. The box in dotted line indicates the frequency band weakly affected by the offset-dependent tuning. Figure 5.25 (c) is the gather after a band pass filter defined by the dot-line box in Figure 5.25 (b) and a red arrow indicates a reference event showing the increasing AVO, although the modeling shows a dimming AVO at this geological marker. The gather in Figure 5.25 (d) is generated by applying the NMO stretching correction only on the gather in Figure 5.25 (c). The amplitude increasing AVO on the reference marker event (red arrow) is reduced. Figure 5.25 (e) shows the gathers after the compensation of high frequency components on the far offset traces. An increasing AVO can be seen clearly at the reservoir target indicated by the black arrow. The reference marker indicated by the red arrow shows a dimming AVO, which matches AVO modeling.

In Figure 5.26, stack sections and AVO attributes from the same dataset are shown. Figure 5.26 (a) shows the stacked section without stretching and tuning correction, and the enlarged version for the portion inside the black box is shown in Figure 5.26 (b); Figure 5.26 (c) is the stacked section from the gathers with stretching and tuning correction applied and the enlarged portion in the black box is shown in Figure 5.26 (d). Because the tuning correction compensates the high frequency components for the far offset traces, the resolution on the stack section is enhanced. The arrows in Figure 5.26 (b) and (d), the stacked sections, indicate the definition of some of the reflection events improved by the stretching and tuning correction. The intercept and gradient attributes are extracted from the gathers with and without stretching and tuning correction. Figure

5.26 (e) shows the product of the intercept and gradient without stretching and tuning correction; the same product from data after the stretching and tuning correction is shown in Figure 5.26 (f). The black arrows indicate the reservoir target. As a weak class III AVO (or Class II-b) is expected at reservoir targets, a positive product of intercept and gradient should be seen at the reservoir zone while most of other portion of the section should have negative product values. Although the reservoir, indicated by black arrows, can be found on both Figure 5.26 (e) and (f), it is more consistent and standout on Figure 5.26 (f). The larger overall value on Figure 5.26 (e) than (f) can be explained by the fact that the tuning generates larger gradient when the thickness of thin layers is larger than 1/12 wavelength for a dimming AVO (see the derivation by Lin and Phair, 1993). Obvious artifact anomalies can be seen on Figure 5.26 (e) at the geological marker indicated by the red arrows. This marker has a strong impedance contrast and wavelet stretching generates strong out-of-phase side lobes, which generates artifact AVO anomaly—positive product of intercept and gradient. These artifact anomalies are reasonably removed by the stretching and tuning correction.

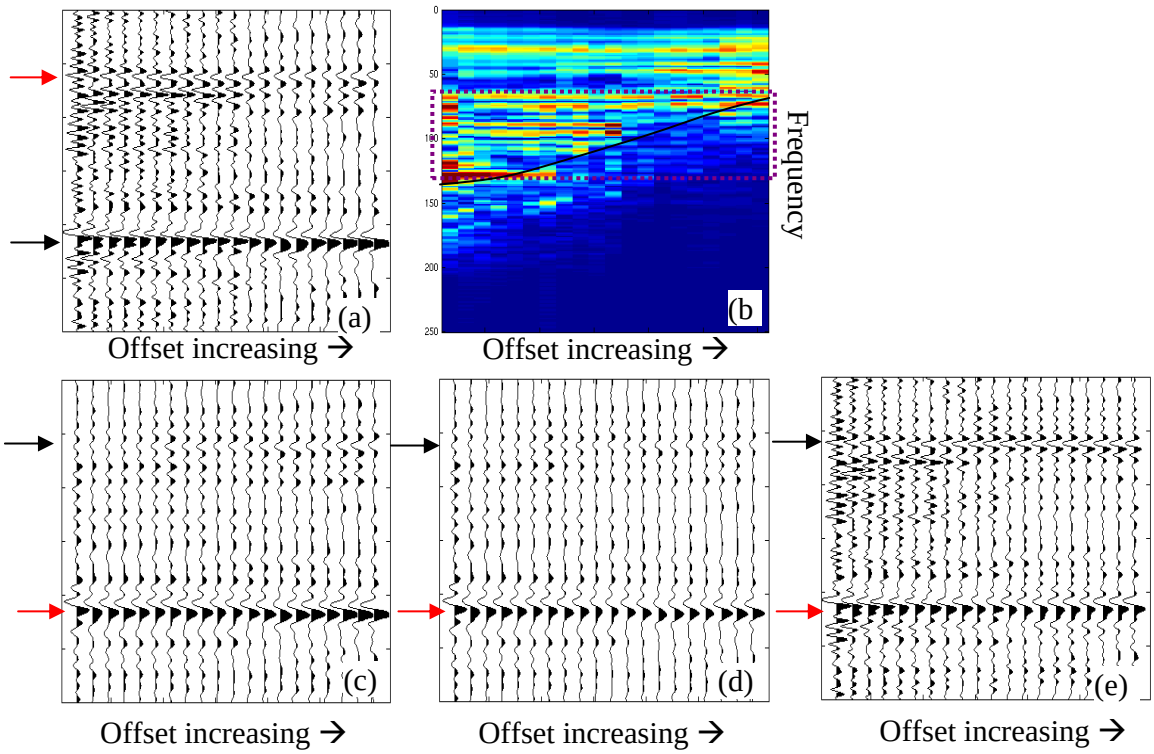

Figure 5.25 NMO stretching effect and correction on a CDP gather from a real seismic dataset. Figure (a) is the NMO corrected CDP gather and the reservoir target is indicated by the black arrow. (b) is the amplitude spectrum for the gather in (a). Dotted line box indicates that the frequency components within it are weakly affected by offset-dependent tuning. (c) is the gather after band pass filter defined by the dotted line box in (b) and a red arrow indicates a reference event showing increasing AVO. (d) is generated by applying stretching correction on gather (c). The increasing AVO on reference marker event (red arrow) is weaker. (e) is the final stretching corrected gather after tuning on far offset traces.

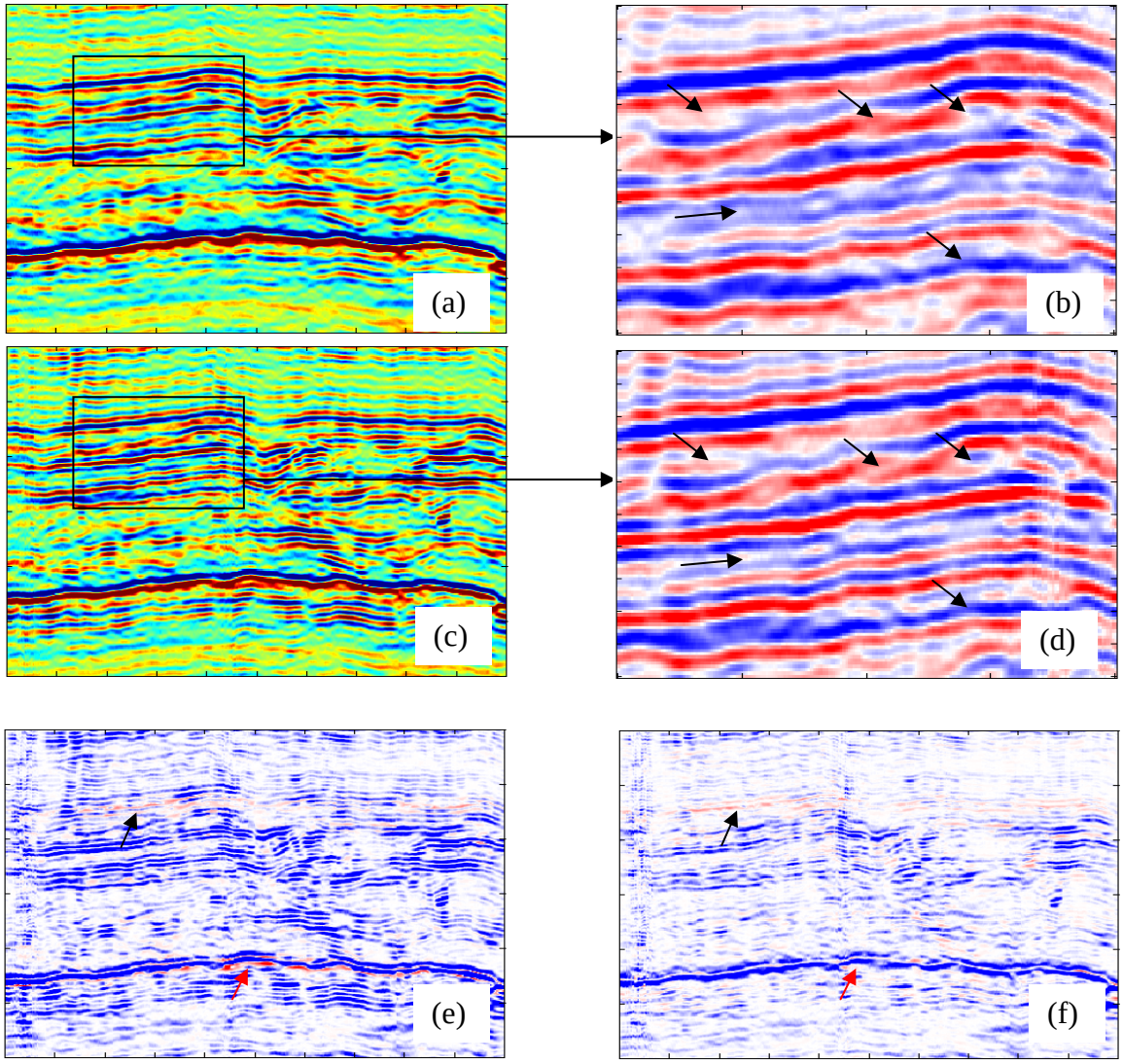

Figure 5.26 Comparison of real data sections with and without stretching and tuning correction. Figure (a) is a stacked section without correction, and the enlarged version for the portion inside the black box is shown in (b); (c) is the stacked section from stretching and tuning correction applied gathers and the enlarged portion in the black box is shown in (d); (e) is the product of intercept and gradient without stretching and tuning correction; (f) is the product of intercept and gradient with stretching and tuning correction (Data courtesy Arcis Corp).

5.4.4 Conclusions and discussion on NMO stretching and tuning correction

There are two main reasons for the loss of AVO fidelity in the NMO correction: one is a low frequency amplification due to the wavelet stretching, and the other one and also more important is the intrinsic loss of high frequencies due to filtering during wave

propagation and processing for the offset-dependent tuning events. The wavelet stretching can be restored by a relatively deterministic approach, but the high frequency loss due to tuning and filtering requires an AVO guided frequency extrapolation in order to preserve AVO. This study suggests a stretching and tuning correction. The model and real data examples demonstrate the necessity of applying corrections for stretching and tuning for performing a reliable AVO analysis.

5.4.4.1 AVO without NMO

Because of the negative effects of NMO on AVO analysis, the AVO analysis before NMO has been studied (Downton and Lines, 2002, 2003). In their approach, the NMO is incorporated into the AVO inversion. Although the wavelet stretching is not an issue in it, the high frequency loss due to tuning is not solved and still affects the final AVO results. In addition, flattened gathers with high fidelity AVO are not required with their approach, but important for the QC and interpretation.

5.4.4.2 Practical considerations

The stretching and tuning distortions are more severe for the NMO corrected wide angle traces. As wide angle data is more promising for the determination of more elastic parameters, stretching and tuning correction become crucial for reliable AVO analysis. If the angle is limited to a smaller range, say 0-30 degree, stretching and tuning correction seems less significant for many geological settings. However, it is certainly important for improving the resolution and AVO fidelity if there are large and sharp vertical velocity variations near the reservoirs, especially if the reservoir porosity sits within a tight formation and beneath a lower impedance shale layer. This is often seen in the Western Canadian Sedimentary Basin (WCSB). The real data from the WCSB shown in the above section have an approximated largest angle of 39 degrees and the application of correction on it provides more reliable AVO analysis results.

5.5 RESIDUAL NMO REMOVAL

Velocity analysis is not able to be conducted at every lateral location in the seismic data. Velocity via interpolation between control points of velocity analysis corrects most of the normal moveout in the data between control points. But lateral stratigraphic or structural variation changes velocity field which is not able to be predicted by interpolation perfectly. The velocity error causes non-flattened events and needs to be corrected for an optimal AVO analysis. NMO correction is usually hyperbolic, which is able to flatten data in the near to mid offset range but fails in the far offset (>30degree). The anisotropy is also attributed to the inability of the common hyperbolic NMO correction to flatten the far offset data. To make a high resolution stacked image, the far offset data beyond a time-offset function (mute function) is not used in many processing projects. Based on author's experience, most of the processing contractors choose muting function falling within the incident angles 25-30 degrees for the reservoirs in the WCSB to discard the strongly stretched and unflattened far offset data to achieve the best resolution in the stacked data. However, the AVO analysis requires wide angles; a stable AVO inversion needs angles of larger than 30 degrees (even up to 60 degrees, Roy et al, 2008). Therefore, the far offset traces must be flattened. A high order NMO correction and anisotropic NMO correction are able to flatten events at a much far offset, but these incur more cost, which may make many processing projects use only common hyperbolic NMO correction. Swan (2001) suggests a method to correct residual NMO to flatten events on the prestack gathers. This method is practical and effective. Kan and Swan (2001) also find a use of residual NMO correction in the pore pressure prediction besides flattening gathers. One needs to evaluate the effectiveness of this method on very far offset data, but the method should work well on the correction of velocity errors on medium to far offset data. Here, an example shows the effectiveness of Swan's residual NMO correction. A commercial package – AVEL, developed by Fusion Geophysical, is used to make automatic residual NMO correction with the Swan's method.

In Figure 5.27, CDP gathers are applied NMO correction by a velocity with 5% error on the central location. The error is introduced on purpose to test Swan's automatic velocity

correction. Figure 5.28 shows the CDP gathers after the automatic velocity correction, and Figure 5.29 overlays CDP gathers before and after the automatic velocity correction. It is noticed that the automatic velocity correction is effective.

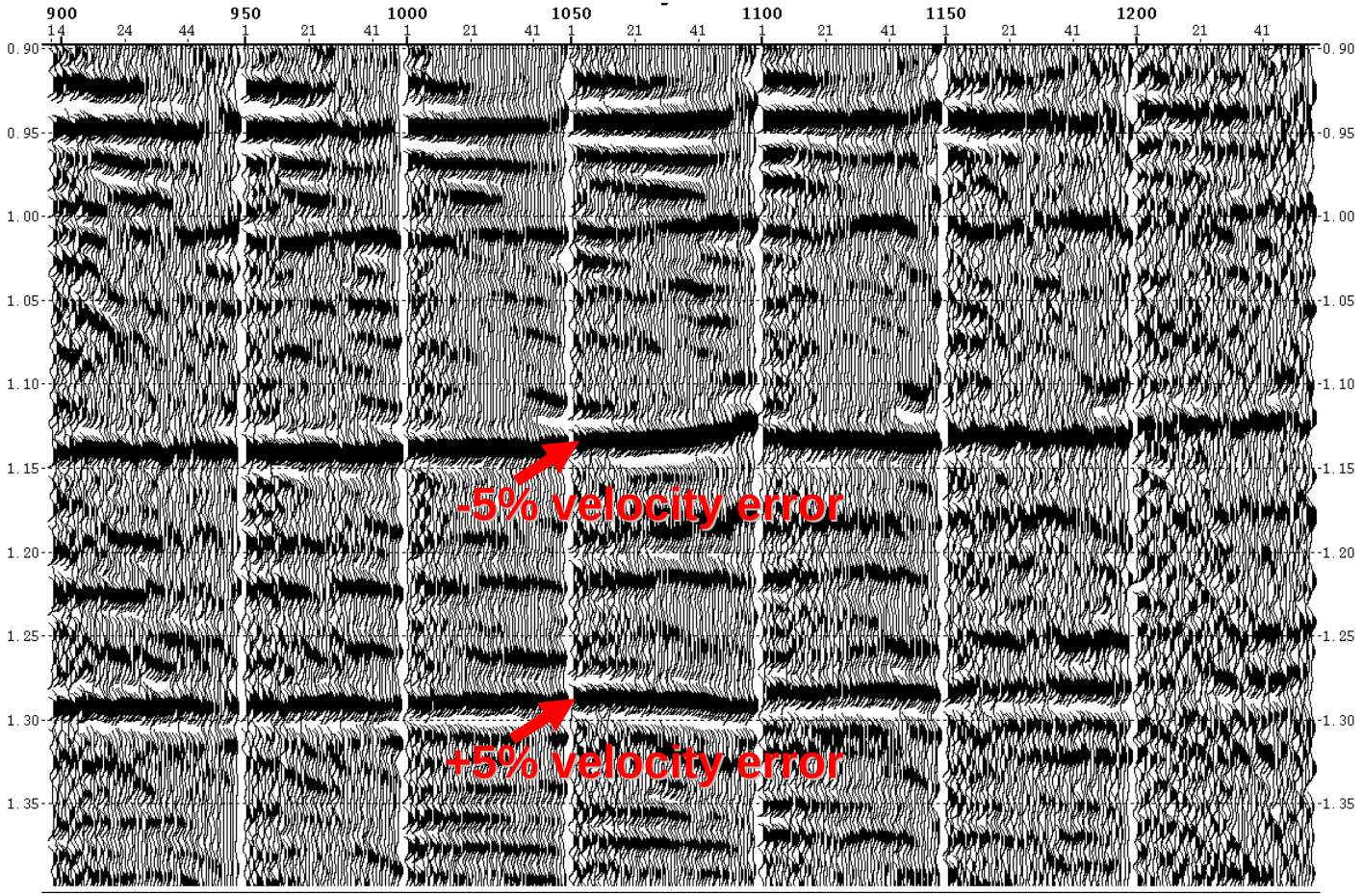

Figure 5.27 CDP gathers after NMO correction by velocity with 5% error on two events at the center CDP gather (Data courtesy Arcis Corp).

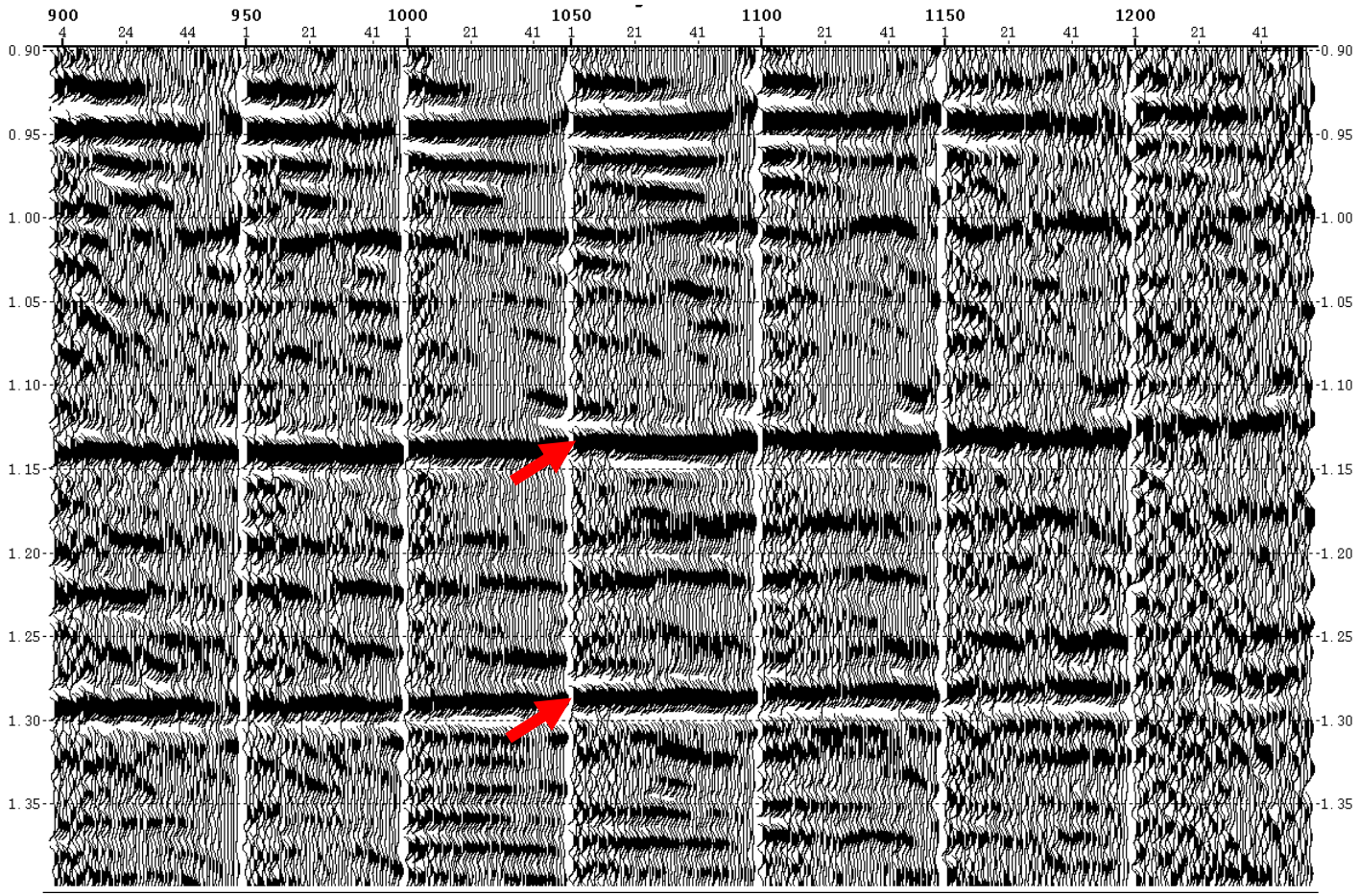

Figure 5.28 CDP gathers after automatic velocity correction.

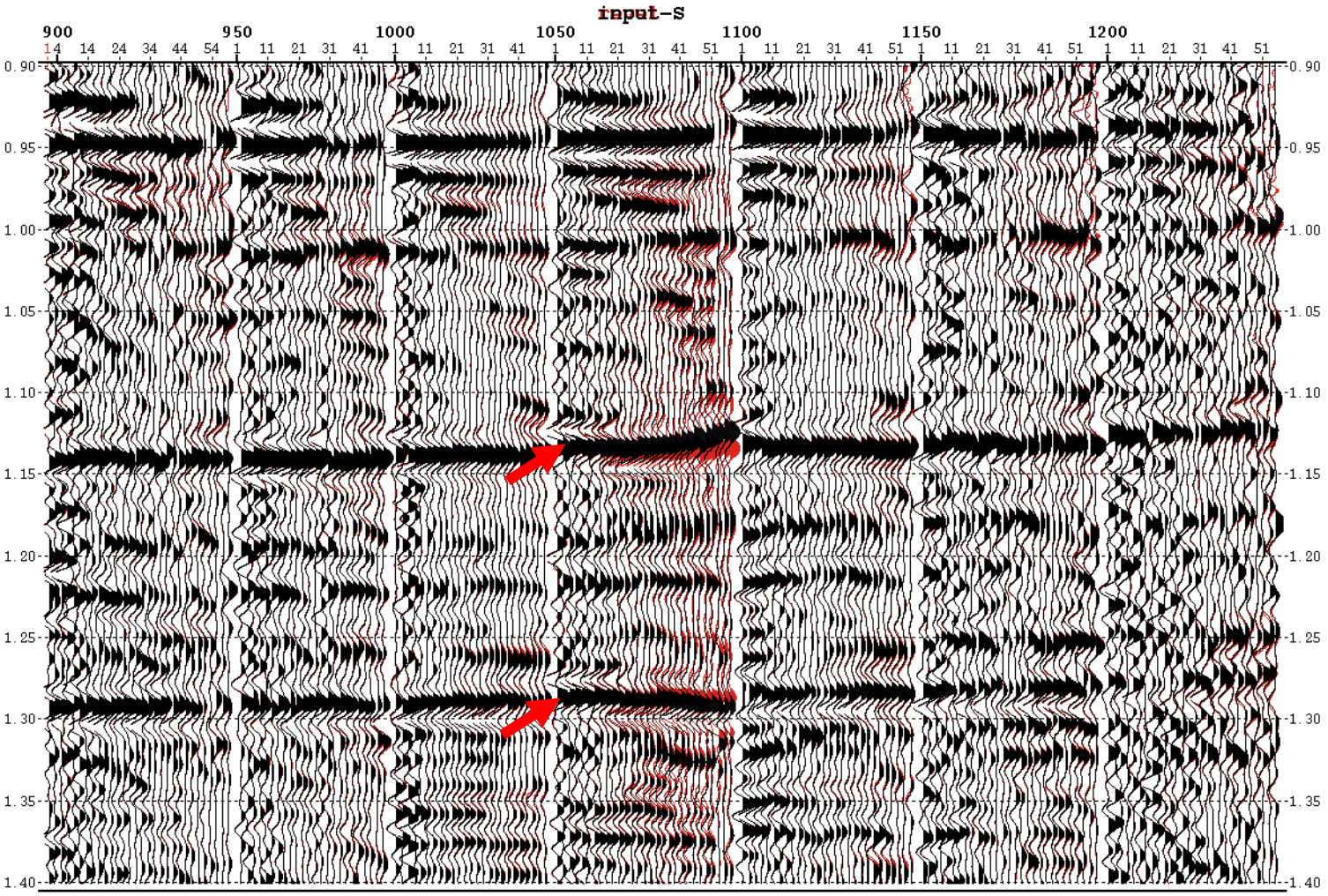

Figure 5.29 Overlaid CDP gathers before (black) and after (red) Swan automatic velocity correction.

5.6 AVO QC AND FIX

AVO friendly processing addresses surface consistent operations. Offset dependent operations, such as offset-dependent scaling and spectral balancing, are not recommended usually. However, even the processing that follows the AVO friendly processing flow does not guarantee AVO is recovered to match well controls, rock properties, or geology. Sometimes, AVO application specialists need to apply a smooth offset dependent scaling (boldly). The scalar should be estimated from the high quality component of the data and should have to be global (or areal sometimes) and the estimate of scalars should be guided by the rock property statistics.

AVO modeling enables ones to understand the AVO variation due to the rock physical property change, and also provides diagnostics to quality-control the AVO preservation in the processing. Most of the modeling in practice uses the Zoeppritz equation or its approximations. Fully elastic (or inelastic) modeling, including all waves instead of only P to P reflection waves, sometimes helps explain real data better than the Zoeppritz equation based modeling. Because the AVO analysis is based on Zoeppritz equation, the quality control and conditioning of the data are able to be completed by the simplified approach handily. The QC and fix of AVO are usually defined by a large lateral coverage and time window other than only well control and target formation.

5.6.1 AVO behaviour under the mudrock-line

This section discusses the fidelity of AVO affected by the offset dependent scaling. Swan (2002, 2006) analytically shows an approach to correct the background shift by using the intercept and gradient for AVO interpretation. These background shifts are attributed to residual move-out and incorrect offset dependent scaling. In Swan's approach, the two term intercept-gradient equation is used to derive the background shift correction. The two term Shuey's equation incurs greater error when wide angle (>30 degree) but the derivation of correction is relatively convenient to derived by this two term equation. Certainly, it is necessary to expand the correction to wide angle and other two or three parameter equations analytically or empirically. As we have seen in Chapter 3, the

background shift of intercept and gradient is not only due to AVO anomalies but also because of the noise, angle range and sample population size. Here, the simple intercept-gradient equation is used to demonstrate the background shift correction and offset dependent scaling correction.

In the AVO friendly processing, operations affecting offset-dependent amplitude variation include the geometrical spreading correction and attenuation corrections. The choice of parameters for these operations depends on the experience of data processors. Sometimes, other offset-dependent amplitude scaling is applied by data processors with scalars estimated globally or locally. Although these operations are able to correct the imbalance between offsets, calibrating the global AVO behaviour is suggested. In the processing, it is a basic goal to make a reflection amplitude balance for the data in the shallow or deep and in the near or far offset. This is done by the quality-control (usually visually) of a processor even in an AVO friendly surface consistent flow. Although the amplitude of reflections is determined by local rock property statistics and geology, it is appropriate to understand the generic amplitude behaviour along offsets using the basis rock property statistics. Suppose a series of formations are all clastic rocks, and then the reflection coefficients normalized by the normal incident reflection coefficient can be expressed analytically. This is derived in the following if the mudrock line and density-velocity Gardner's relationship are assumed:

$$\mathbf{V_P} = \mathbf{a}\mathbf{V_S} + \mathbf{b} \tag{5.4}$$

$$\rho = 1.741 \cdot \mathbf{V_P}^{0.25} \tag{5.5}$$

$$\frac{\mathbf{R}(\theta)}{\mathbf{R_P}} = 1 + \left(1 - \frac{6.4}{\mathbf{a}}\frac{\mathbf{V_S}}{\mathbf{V_P}} - 1.6 \cdot \frac{\mathbf{V_S}^2}{\mathbf{V_P}^2}\right)\sin^2(\theta) \tag{5.6}$$

where **a** and **b** are the gradient and intercept in an assumed linear relationship between Vp and Vs, and R(θ) is angle dependent reflectivity and Rp is normal incident reflectivity. R(θ)/Rp can be regarded as the normalized angle-dependent reflectivity. The reflection coefficient in equation (5.6) depends on the Vs/Vp ratio, and is graphically shown in Figure 5.30 for three different Vp/Vs ratios. It shows that the amplitude dims with angle generally. But the decreasing trend is reversed at the far angle (>30) if a more

accurate equation than Shuey's is used or there is a large deviation from mudrock lines. Figure 5.31 models an AVA gather from well logs. The Vs is predicted from Vp using a mud-rock line. The average amplitude within a one-second time window and the amplitude prediction by equation (5.6) are compared in Figure 5.32. They match well up to the 30 degree angle.

The test in Figure 5.31 and Figure 5.32 is based on a perfect mud-rock line between Vp and Vs. However, if the derivation of Vp and Vs from a perfect mud-rock line is realistic, the match between the theoretical average AVO based on mudrock line and from actual data is compromised, and so the match cannot reach very far angles. Figure 5.33 shows real logs for modeling an AVA gather. The good match between two amplitude curves is up to the 20-25 degree angles only (Figure 5.34).

These tests are based on a single reflection interface and ideal conditions. For the real data, the comparison is preferably done in the frequency domain.

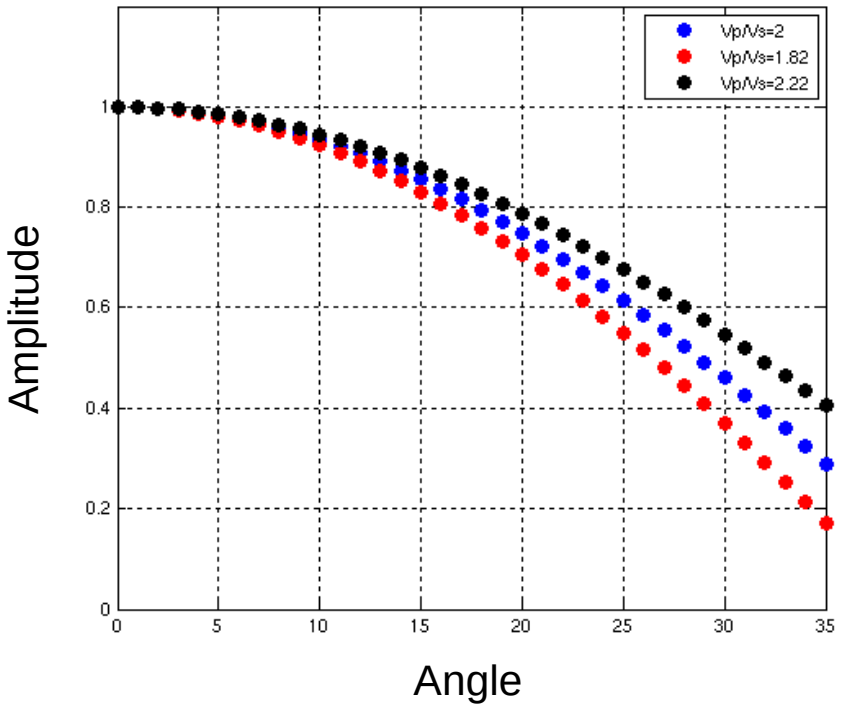

Figure 5.30 Normalized AVOs estimated by a given mudrock line (Castagna) and different Vp/Vs ratios.

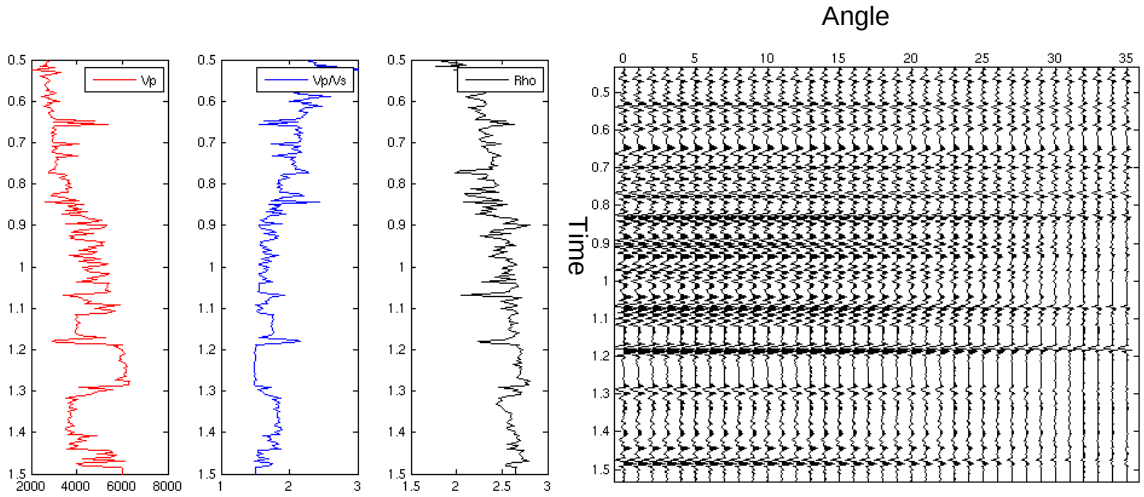

Figure 5.31 Vp, Vp/Vs and density (mudrock line is assumed), and model angle gather. Amplitude dims with angle.

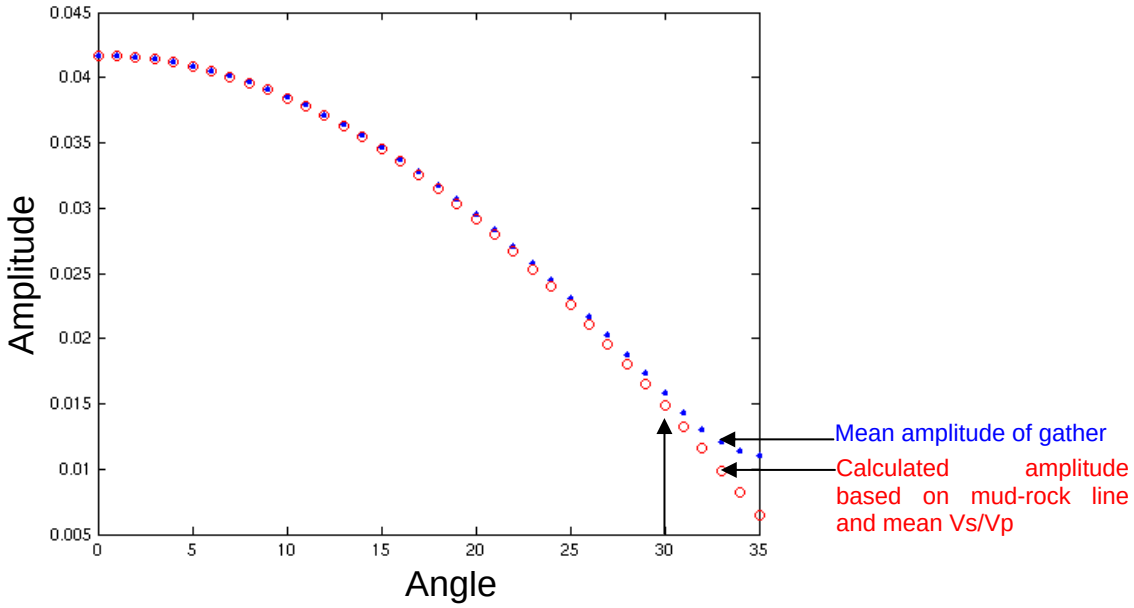

Figure 5.32 Average AVA in Figure 5.31 within 1000ms window and normalized AVA based on the mudrock line (average Vp/Vs ratio within 1000ms window is used). They have a close match up to 30 degree of angle.

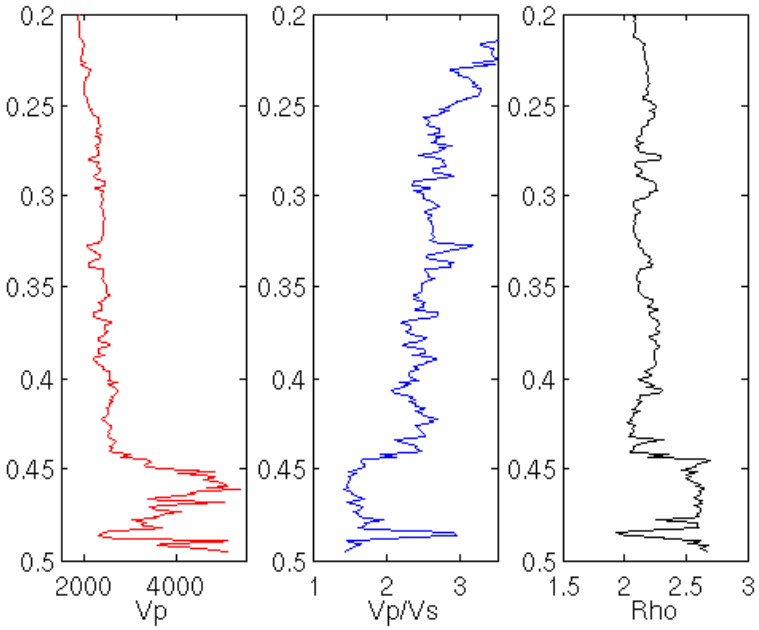

Figure 5.33 Well logs with real shear velocity – cross-plot of Vp and Vs shows scattering.

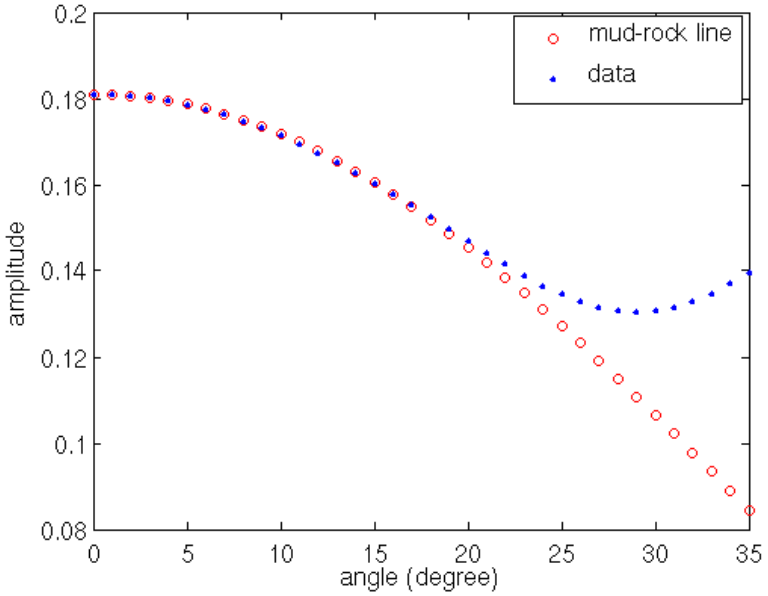

Figure 5.34 Average AVA from modeled data using logs in Figure 5.33 within 300ms window and normalized AVA based on mudrock line (average Vp/Vs ratio within 200ms window is used). They closely match up to 20-25 degree of angle only.

When the AVO modeling is used to calculate the offset/angle dependent scalars, care must be taken by using good well logs with a high correlation with seismic data. The calibration is applied on good signal data and large window (angle domain is preferred) with frequency dependence (the tuning effect and strong attenuation on seismic data are difficult to model).

5.6.2 Example of fixing poor AVO preservation

Sometimes an AVO practitioner must make use of the data with poor AVO preservation because the re-processing is not possible. In this situation, a trace-by-trace scaling would be used to make the global or areal average AVO behavior within a large valid window follow an average theoretical AVO response.

The seismic data and well information in this example are from the northwest China with the show right from an anonymous provider. The example shows the AVO fix is applied on the data with poorly preserved AVO and the subsequent AVO analysis result is reasonable and confirmed by later drilling. Figure 5.35 shows a few CDP gathers, and almost every event on the gathers has a strongly increasing AVO, which is wrong. The possible reason for this is a trace-by-trace balance was applied after muting by careless processors.

Figure 5.36 shows the correlation between a conditioned CDP gather and a model AVO gather from the well at the CDP location. The well has tight gas reservoirs. The correlation is reasonably good.

The AVO inversion is applied after the amplitude is fixed by a global offset-dependent scaling and the post-stack inversion is applied subsequently to derive P and S impedance. Poisson's ratio is calculated from the P and S impedance and shown in Figure 5.37, in which the green to yellow colors show a low Poisson's ratio and indicate gas saturation. Well A is a high quality gas well and is used in the AVO calibration and the inversion of P and S impedance. The variation of Poisson' ratio generally matches with the gas

saturation at well A. Well B and Well C were drilled with the help of Poisson's ratio section. Well B is a high quality gas well in the area, and well C is an average quality gas well. The predication of reservoirs based on Poisson's ratio from AVO matches the two later drilled wells.

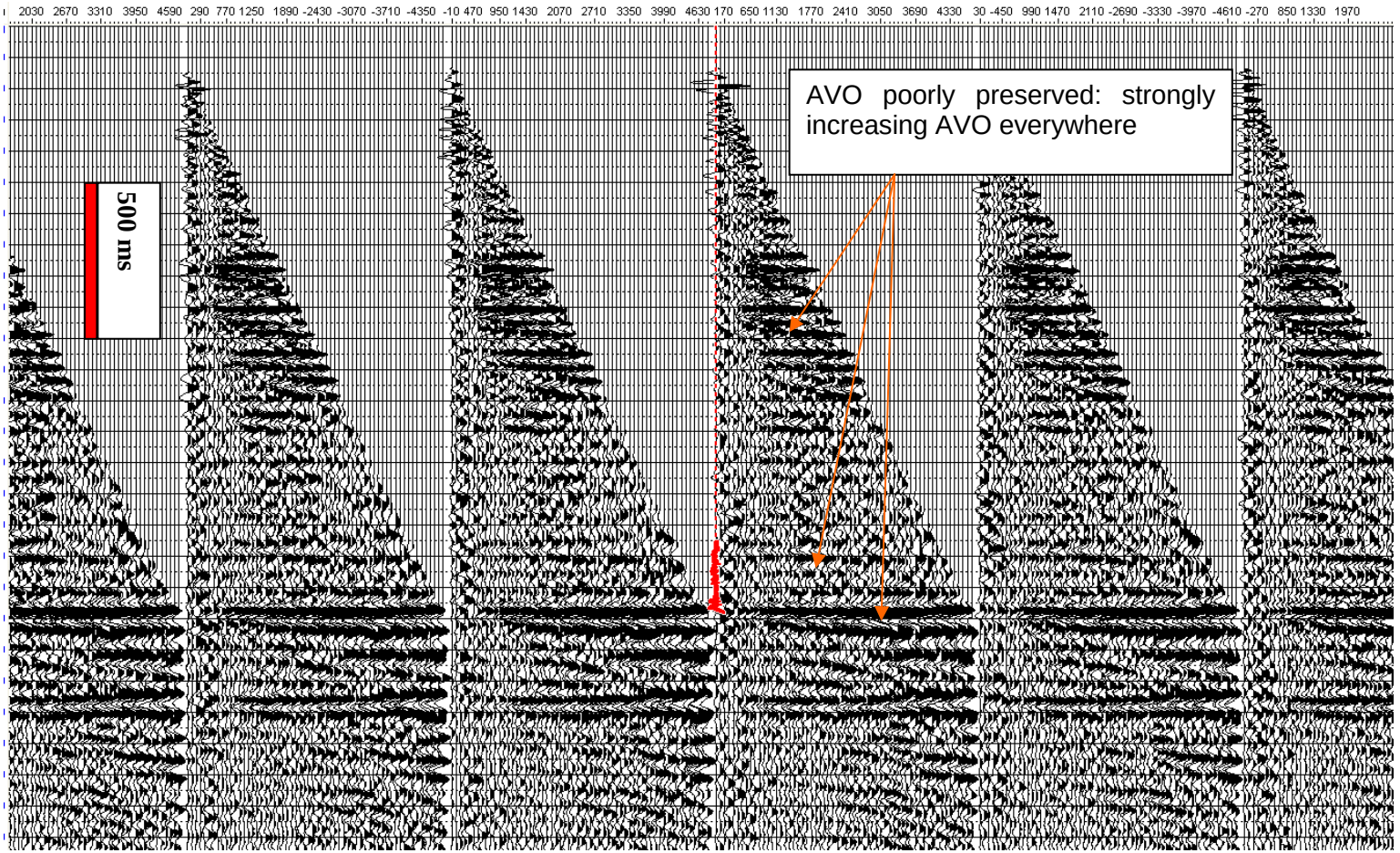

Figure 5.35 CDP gathers delivered from processing workshop for the use of AVO analysis. AVO increasing with offset can be seen from top to bottom of the gathers. The processing is not able to review and make correction to the amplitude. The possible cause to the abnormal amplitude behaviour is a long window AGC applied after muting.

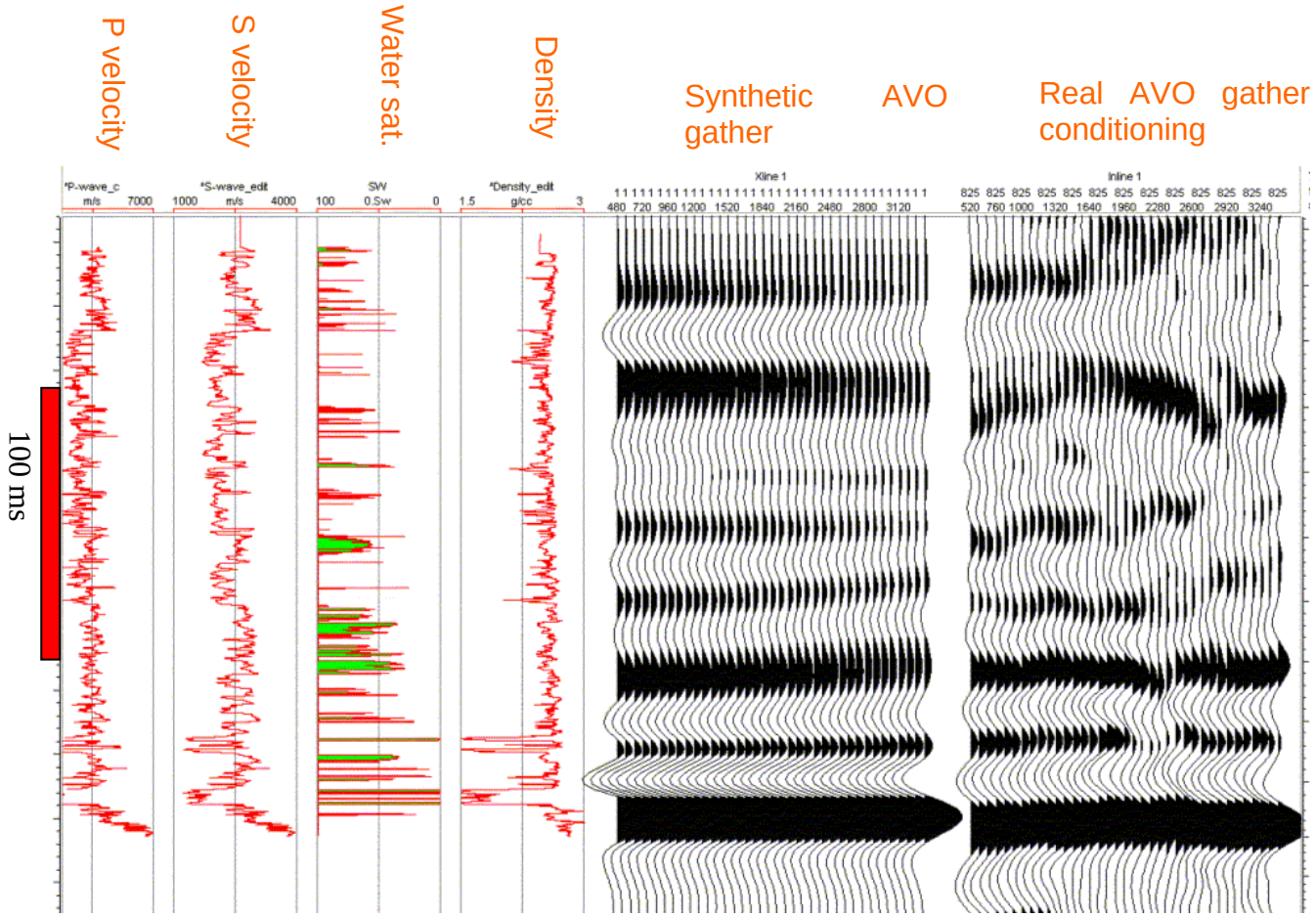

Figure 5.36 Well logs, synthetic AVO gather and real seismic CDP gather at well location after fixing of the amplitude. The reservoir is gas-saturated thin sand beds as shown by green color. Although the AVO correlation between synthetic and real data is not excellent, reasonable AVO match can be seen on key tops and bases of key gas charged layers.

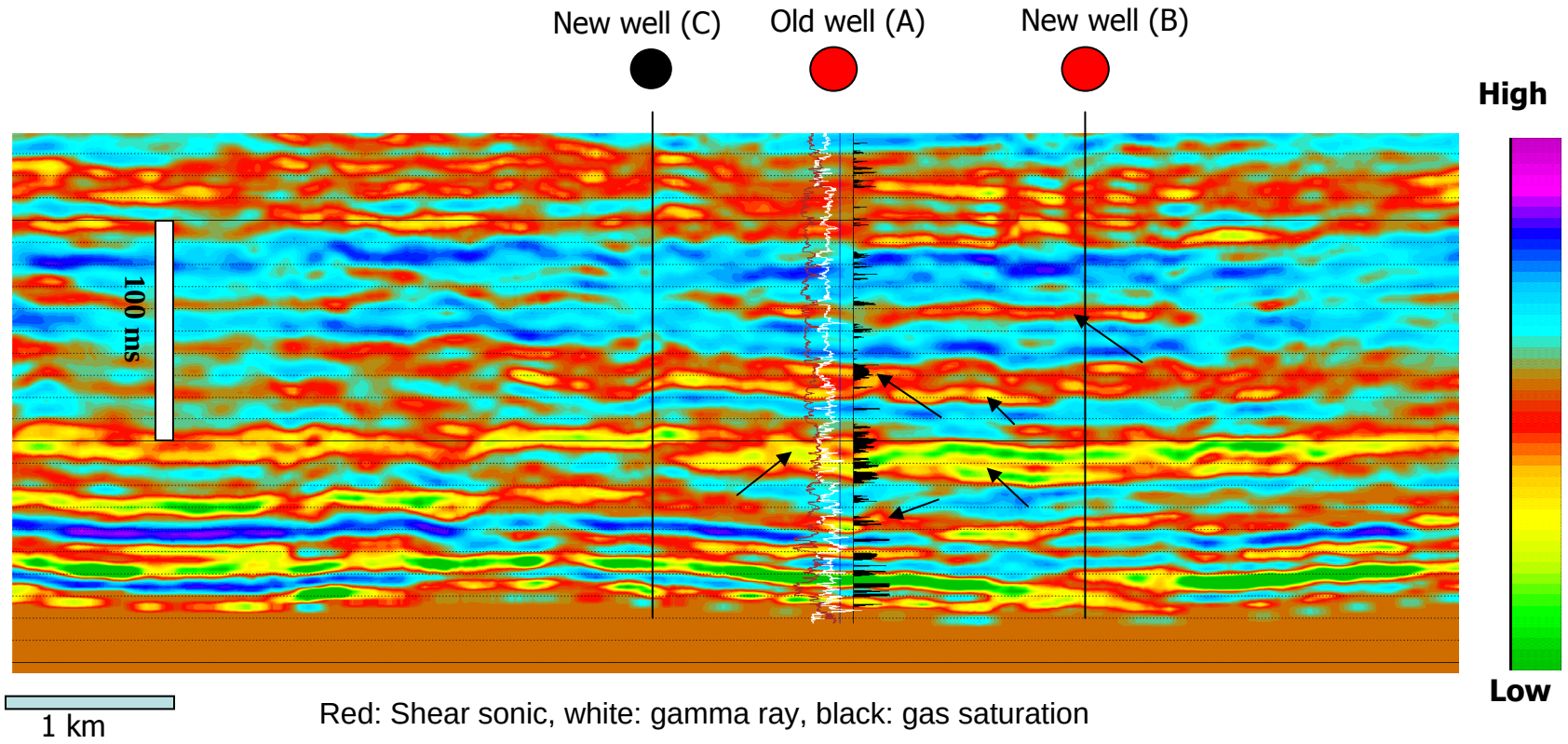

Figure 5.37 Possion's ratio section from AVO analysis using amplitude corrected data. Low Poisson's ratio indicates high gas saturation. The middle well (with good reservoir) is used in the calibration of AVO and inversion. The reservoir is multi-layer tight sands. Two wells are drilled on each side of the old well. The reservoir in the left well is not as good as the middle well, but the right well is a good one. The reservoir quality confirms the Poisson's ratio section.

5.7 ISSUES WITH 3D DATA

AVO is usually understood based on the layered earth model and 2D seismic geometry. When the 3D seismic data is widely used in the AVO analysis, the AVO analysis of 3D data is applied on modified gathers with more 2D sense (e.g. superbinning followed by common offset stack, or migrated gathers (common imaging point gathers)). Although this practice is followed in a conventional AVO analysis flow and is convenient to be understood, the geometry of 3D acquisition and its commonly-seen irregularity in the real acquisition may generate different AVO results. As an expansion of an early study (Xu and Chopra, 2007a) in the following, the adaptive superbinning is introduced to balance the fold distribution over offsets in 3D data so that the result of the AVO inversion is more meaningful. Superbinning is usually used in the data with little structure in spite that the Pre-Stack Time Migration (PSTM) becomes more and more routine even in the non-structural geology. Variable output bin spacing is addressed in the 3D pre-stack time migration. There may be other pitfalls in the 3D AVO, but only the adaptive superbinning and variable bin spacing in PSTM are discussed in this section.

5.7.1 3D supergathers

For the 2-D surface seismic data, the fold and offset are usually found to have a one-to-one correlation. But in a 3D CDP gather, the fold is generally low for the near and far offsets and traces with the intermediate offsets dominate the overall fold. In the 3-D AVO analysis, the AVO inversion uses the gathers with evenly spaced offsets which are generated from supergathers followed by partial offset/angle stacking or PSTM. This study shows these kinds of binning will lower the reliability of AVO inversion for the 3D AVO analysis and an approach is presented to generate supergathers adaptively to overcome the effect of 3D fold imbalance. The real data example shows the benefit from this adaptive supergather to improve the reliability of the AVO inversion.

3-D surface seismic data has many useful features which include fine sampling, better resolution, better and accurate visualization and volume interpretation of structural and stratigraphic features. All these help in providing a vivid picture of the geologic features

in the subsurface. These characteristic qualities of 3D seismic data, coupled with the fact that 3-D prestack time or depth migration yield accurate imaging of subsurface features, represent sufficient ground and reason to expect AVO analysis to be carried out on 3-D data

In a typical AVO flow that is used on prestack data, especially for stratigraphic objectives, after the data has been put through an AVO friendly processing (that restores true amplitudes), supergathers (gathers generated by collecting traces from adjacent CMPs) and Ostrander gathers (gathers generated from supergathers by stacking traces with similar offset intervals) are generated. Next, AVO attribute pairs are extracted, such as Rp and Rs or intercept and gradient, etc. While the interpretation can be directly carried out on the intercept and gradient attributes, Rp and Rs attributes are put through impedance inversion and extraction of LMR (Lambda-Mu-Rho) attributes which are then interpreted. Such a processing flow is followed for 2-D as well as 3-D datasets without differentiation though there are more traces in a 3-D dataset than a 2-D dataset.

However, there are many differences between the two. For the 2-D surface seismic data, the fold and offset are usually found to have a one-to-one correlation. Unfortunately, this is not true for most 3-D seismic datasets. Figure 5.38 shows some gathers from a 3-D dataset, where the offset variation is shown in red and the fold variation in blue. We notice at a glance that for the near and far offsets, the fold is low and traces with the intermediate offsets dominate the overall fold in this set of gathers. It is advisable to try and understand the impact of such a fold variation with offset on the extraction of AVO attributes.

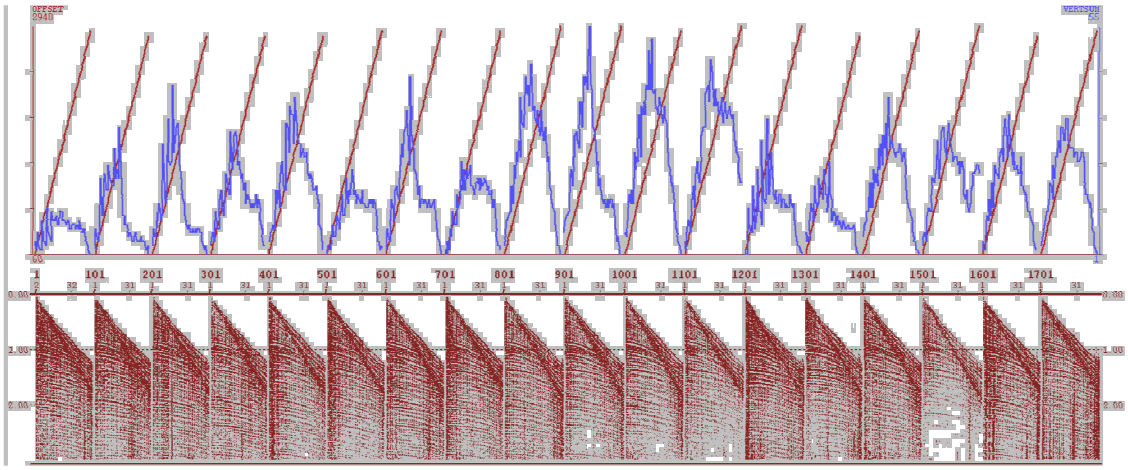

Figure 5.38 Example of fold (indicated in blue) versus offset (indicated in red) distribution in a 3-D dataset. Fold is low at near and far offsets (Data courtesy Arcis Corp).

To investigate this, synthetic gathers were generated using log data as input. Figure 5.39 shows the log curves and an angle domain gather generated from them. Two gathers were generated with the same number of traces in each and a 0-30 degree angle coverage, but their fold distributions were different, more like 3-D and 2-D and indicated as A and B and shown in Figure 5.40. Random noise was added to these two gathers. These gathers represent the supergathers in real seismic data, and so for convenience they are referred to as the 3-D and 2-D supergathers. Next, the Ostrander gathers were generated from the two supergathers by stacking traces with the same angle into a single trace.

As the objective is to understand the effect of the fold variation with offset on AVO attributes, P-reflectivity (Rp) and S-reflectivity (Rs) were extracted from the gathers using the Fatti's approximation of Zoeppritz equation and least-squares fitting, and the results were compared.

Figure 5.41 shows two panels: the left panel compares the S-reflectivity extracted from the different gathers, while the right panel compares the P-reflectivity. Trace 1 represents the true answer, trace 2 is from the 3-D supergather, trace 3 is from the Ostrander gather, trace 4 is from the 3-D Ostrander gather with weights based on the local fold applied in a

least squares sense, trace 5 is from the 2-D supergather and trace 6 from 2-D Ostrander gather.

Left panel comparison: Comparing traces 2 and 5, we notice that the 2-D supergather appears to be more reliable. Comparison of traces 2, 3 and 4 indicates that the Ostrander gathers (trace 3) on the 3-D appears generating worse results than the supergather (trace 2). However, the weighted Ostrander gather (trace 4) tends to improve the result. For the 2-D case, only subtle differences can be noticed (trace 5 and trace 6) on the results of Ostrander gathers and supergathers.

Right panel comparison: Comparison of the different P-reflectivity traces shows that they all look quite similar, with the exception of trace 3, corresponding to Rp extracted directly from the 3-D Ostrander gather.

The above observations may be summarized as follows:

1. Although useful for quality control and the understanding of AVO responses, Ostrander gathers (superbinning followed by partial offset stacking) may not improve the AVO inversion/extraction for the 3-D data.
2. An even fold distribution with offset/angle results in a better extraction of AVO attributes.

The above exercise on the synthetic data has demonstrated that while generating supergathers in 3-D seismic data is necessary to improve the signal-to-noise ratio, its drawback is that events get smeared, which could be a problem for subtle AVO anomalies. To address the issue of uneven fold distributions in supergathers, an adaptive approach for supergathering is suggested. It entails borrowing of traces from adjacent CMP locations depending on the fold distribution and so include an effect of an even fold distribution with offset.

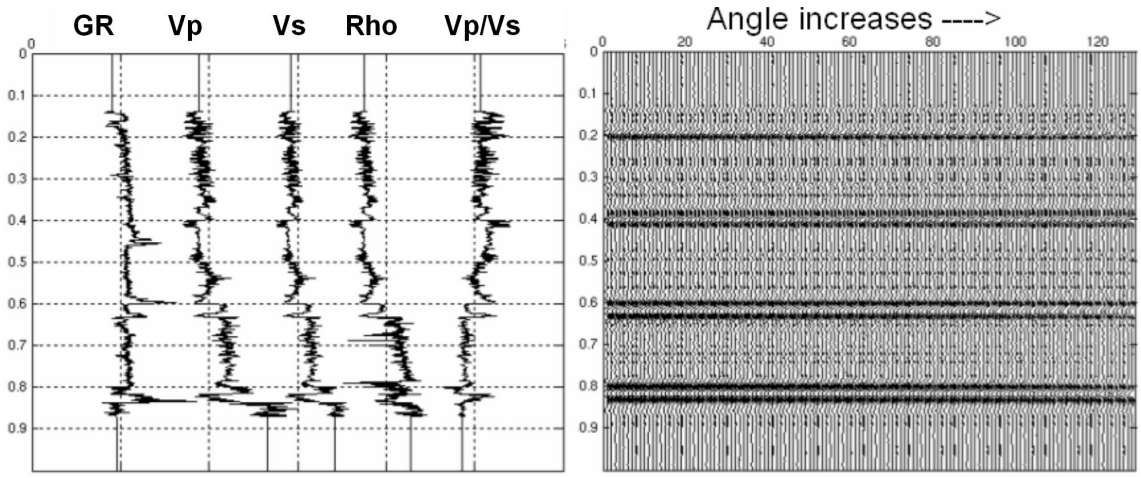

Figure 5.39 A synthetic gather (right) generated from the log curves shown to the left.

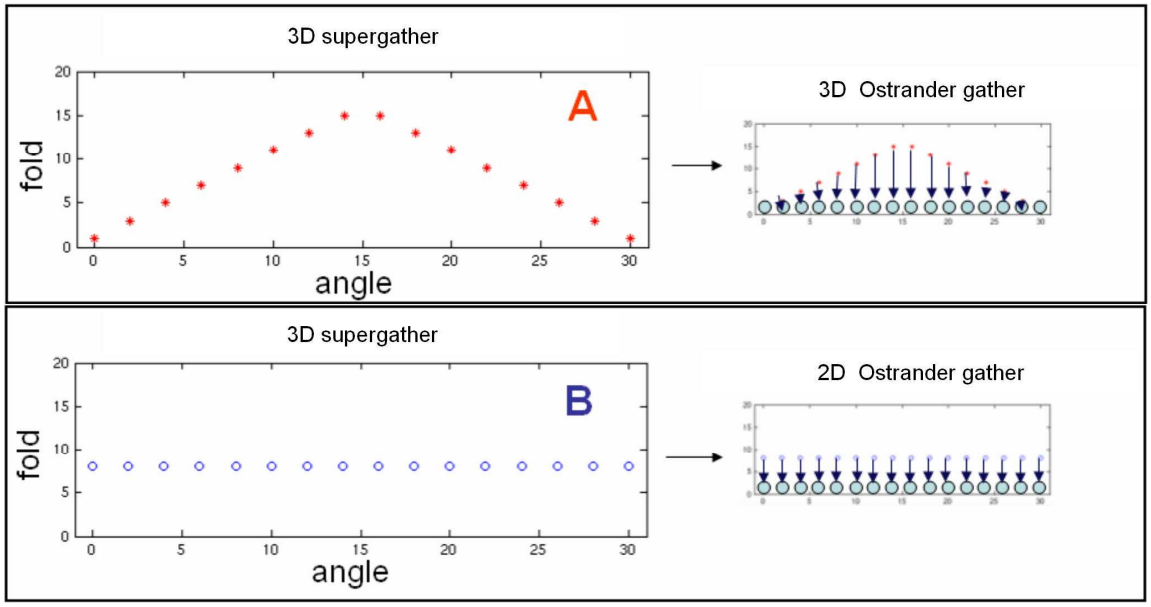

Figure 5.40 Fold distribution shown for the 3-D and 2-D supergathers as well as for the Ostrander gathers derived there from.

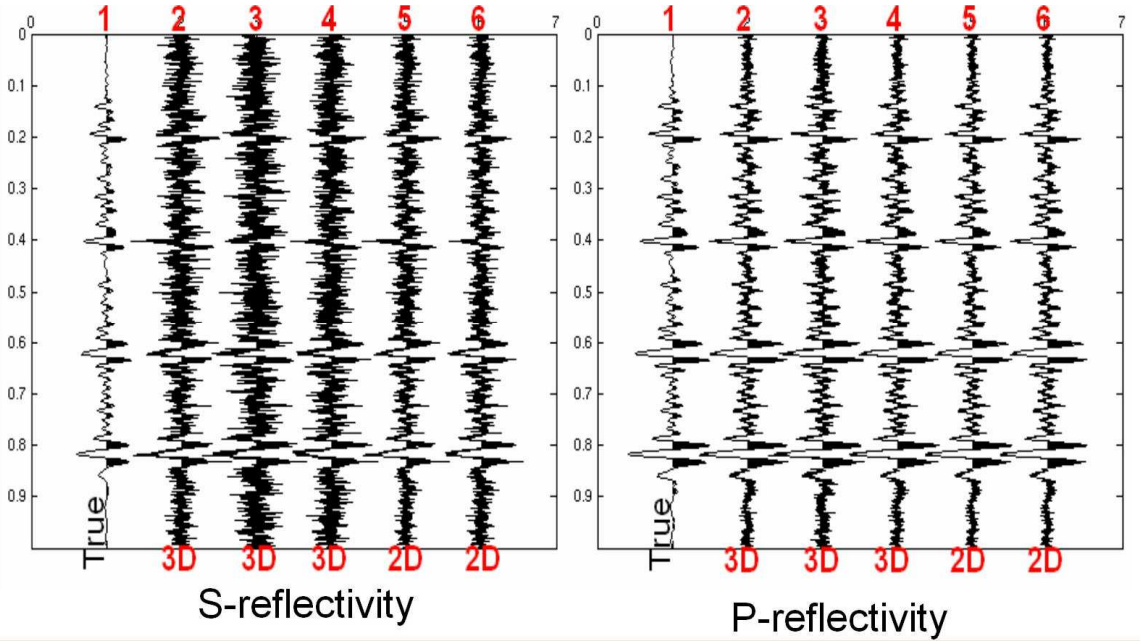

Figure 5.41 Comparison of P-reflectivity and S-reflectivity extraction from different supergathers and Ostrander gathers.

The adaptive supergather approach mentioned above was applied on a 3-D seismic data volume from Alberta, Canada, to see the impact it has on the extraction of AVO attributes. The seismic data is provided by Arcis Corporation. Figure 5.42 shows the survey map for the 3-D seismic volume, and also indicates the location of a gas well and a dry well on it. It may be noticed that the top left corner has a fold higher than the rest of the survey.

To make a fair comparison, the AVO extraction was done on three different types of gathers:

(a) 3 x 3 supergathers,
(b) Ostrander gathers generated from 3x3 supergathers, and
(c) Adaptive supergathers.

Figure 5.43 shows the horizon slices extracted from the P-reflectivity inverted from these three types of gathers at the target level. Though the noise level and acquisition footprint patterns are somewhat more pronounced, the P-reflectivity from the Ostrander gathers

(Figure 5.43b) is as good as that inverted from the supergathers (Figure 5.43a). P-reflectivity inverted from the adaptive supergathers retains most of the character seen on the other two and more, but its noise level and footprint is subdued.

In Figure 5.44, the fluid factor horizon slices at the target level are compared, for (a) 3x3 supergather and (b) adaptive supergather. The red color is indicative of the potential pay. Notice that the fluid factor display in Figure 5.44(a) from the 3x3 supergather shows anomalies in the form of round red patches which do not match the production data from the two wells. The equivalent display from the adaptive supergathers shown in Figure 5.44(b) provides a much better match with well production. Besides this match with production data, the sizes of the anomalies seen on both displays are quite different, Figure 5.44(a) showing stronger anomalies except the one around the gas well.

In an attempt to understand the difference in the anomalies caused by different supergather schemes, a reliability analysis of the AVO inversion was carried out. The reliability was defined as a function of geometry parameters, data error and uncertainty in the extraction. Figure 5.45 shows the equivalent horizon slices to those shown in Figure 5.44, with again the red color indicating higher unreliability. Apparently, the adaptive supergathers improve the reliability for different portions as shown in black rings on the slices. Comparing the reliability maps with the fluid factor maps, it is seen that reliability difference has a good correlation with the fluid factor difference.

Figure 5.42 Surface map for a 3-D data volume from Alberta, Canada. Two wells (one is a gas well and the other is dry) are in survey (Data courtesy Arcis Corp).

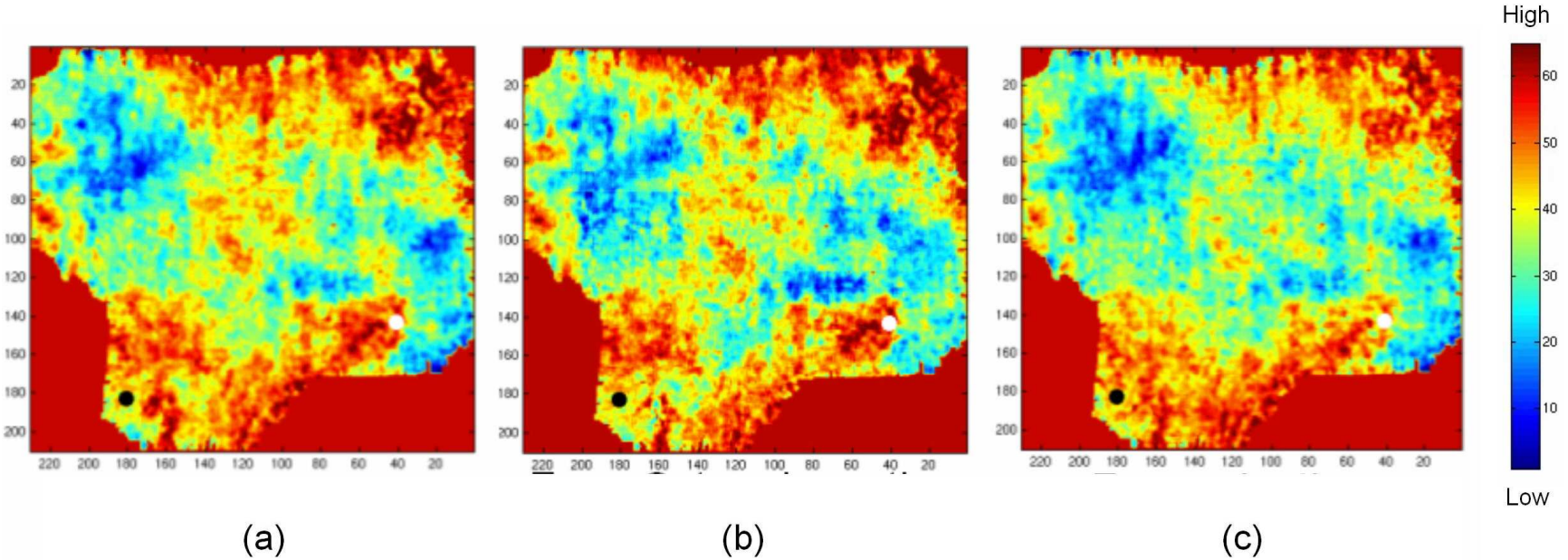

Figure 5.43 P-reflectivity horizon slices from three different types of gathers (a) 3x3 supergather (b) Ostrander gather derived from the 3x3 supergather, and (c) adaptive supergather (Data courtesy Arcis Corp).

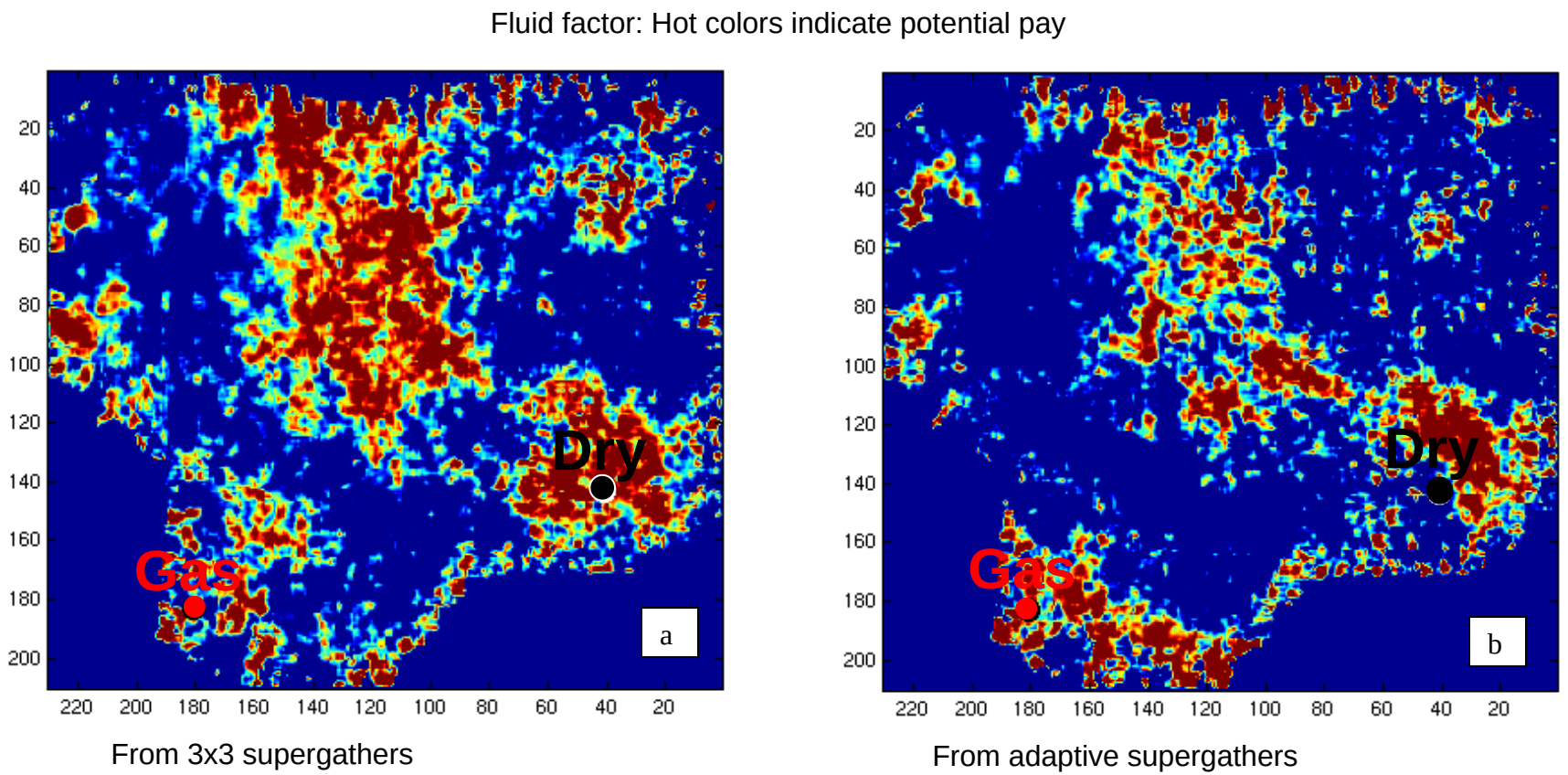

Figure 5.44 Comparison of fluid factor horizon slices from (a) 3x3 supergathers (b) adaptive supergathers. The quality of the results is determined by how good the match between the anomalies and well production (gas or dry). The right result shows a better match (Data courtesy Arcis Corp).

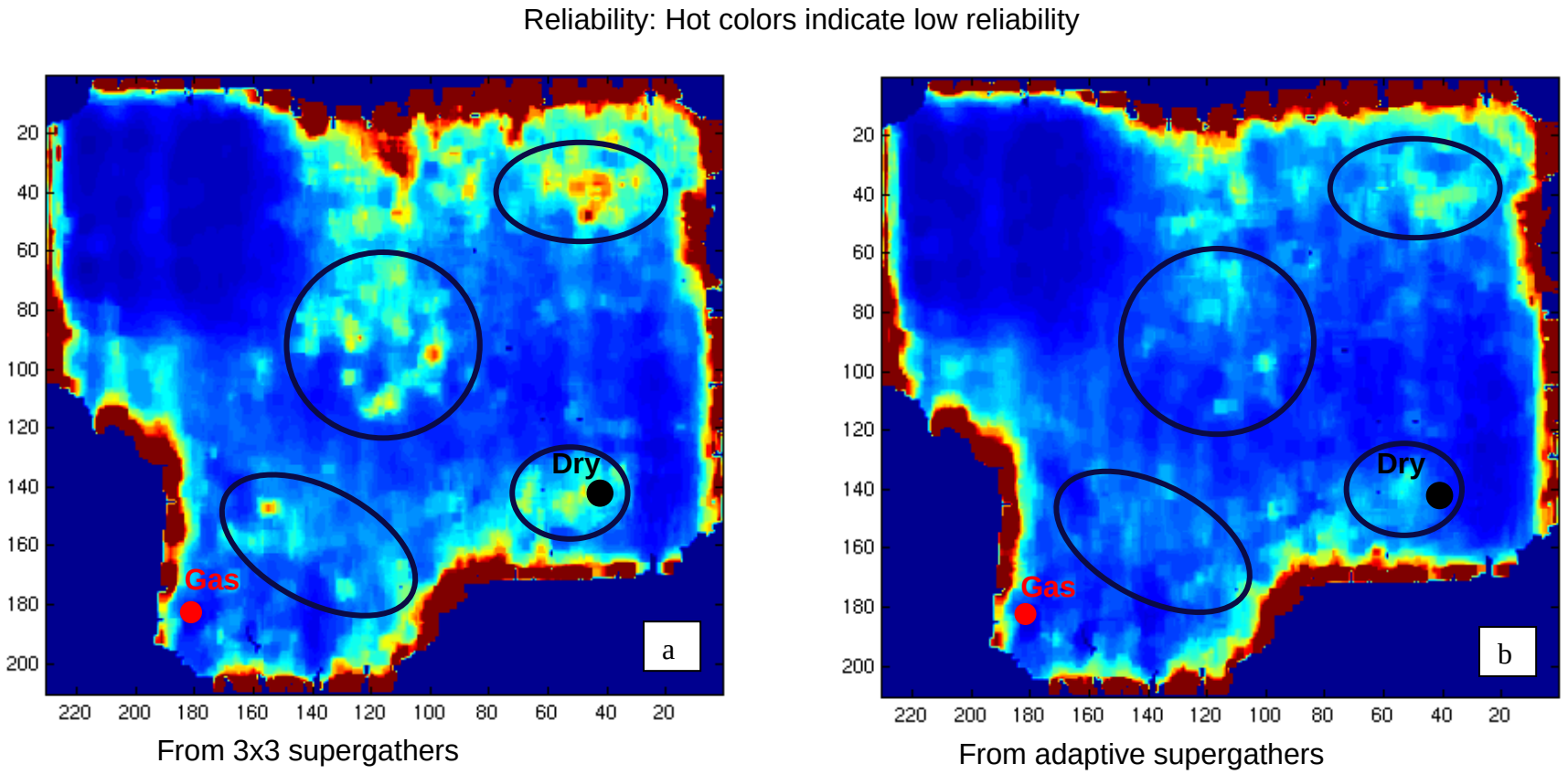

Figure 5.45 Comparison of reliability horizon slices from (a) 3x3 supergathers (b) adaptive supergathers (Data courtesy Arcis Corp).

5.7.2 PSTM for 3D data

Surface conditions and cultural and environmental factors in 3D data acquisition often leave holes and deviation from regular grids in the final geometry of the data. In addition, the receiver lines and shot lines in 3D surveys are often spaced a few times wider than the CMP bin sizes used by the processing. To overcome the sparseness of lines and fill holes in a 3D survey, study and practice are seen in the industry using a five-dimensional (commonly inline, xline, offset, azimuth, and frequency dimensions -- 5D) interpolation. 5D interpolation generates pseudo receiver or shot lines in between original lines and increases data volumes which is a great advantage in generating better output of prestack migration. 5D interpolation is also able to generate data with random acquisition layouts. Although 5D interpolation increases data volume without incurring acquisition cost, the computational cost increases and the amplitude and structure accuracy of interpolated data is worth to investigate. In this sub-section, a few examples of PSTM gathers from 3D data show pitfalls in the use of PSTM in AVO. They show that a careful definition of output bin spacing in the PSTM may improve the AVO analysis on the PSTM output even without 5D interpolation applied on the input data.

In Figure 5.46, three PSTM gathers are shown; on the top of each gather, a blue line shows the offset and a red line (labelled “INTERP”) flags if there are traces within that bin in the original CMP gather (0 for empty original bins; 1 for bins containing traces originally). The left panel is a PSTM gather in which offset bins are equally spaced and AVO is poor preserved especially for the traces with the top red line flagged zero. The middle panel shows the PSTM gather with a variable bin spacing; the spacing is calculated globally using the nominal fold of the data; AVO on the middle panel gather is much better than the one on the left panel with equally spaced bins; but the variable spacing is global and there are still some local deviations from it: the zero flags on the top red line show the empty original bins while red arrows on the gather indicate the timing and amplitude of events at these locations are still abnormal. The gather on the right panel is generated from the middle gather by discarding the traces with empty original

bins. AVO analysis using the right panel gather should result in more reasonable attributes.

Another example in Figure 5.47 shows the effect of output gather binning in the PSTM as well: the left PSTM gather has equally spaced bins and the bin number is close to the nominal fold of 3D data. Migration artifacts can be seen on the near offset bins and the AVO and offset amplitude consistency are poorly preserved. The right PSTM gather with variable bin spacing preserves better AVO for the near to mid-far offset traces.

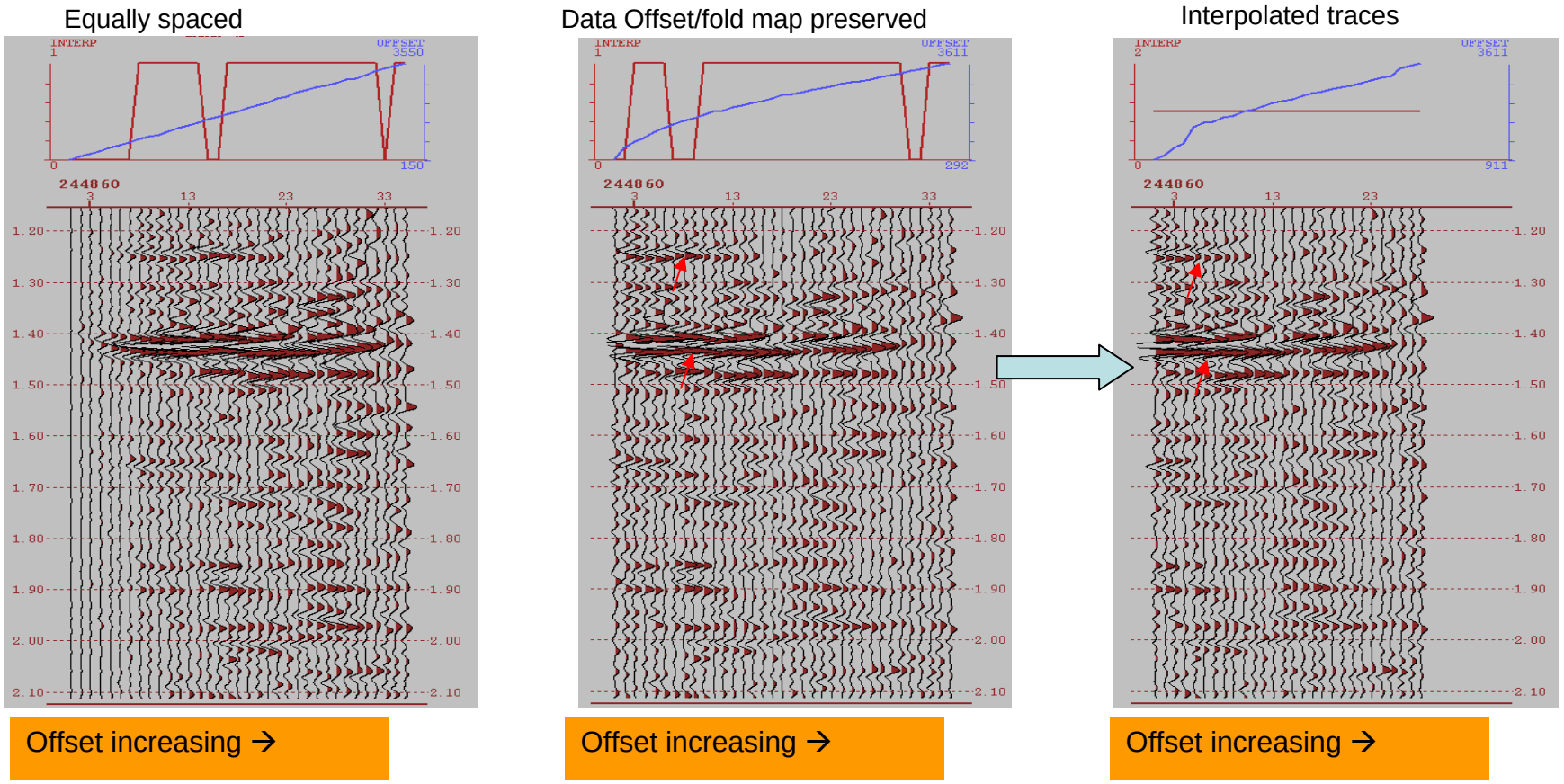

Figure 5.46 PSTM gathers with equally spaced bins (left), variable bins with nominal fold (middle), and variable bins with nominal fold and removal of originally empty bins (right) (Data courtesy Arcis Corp)

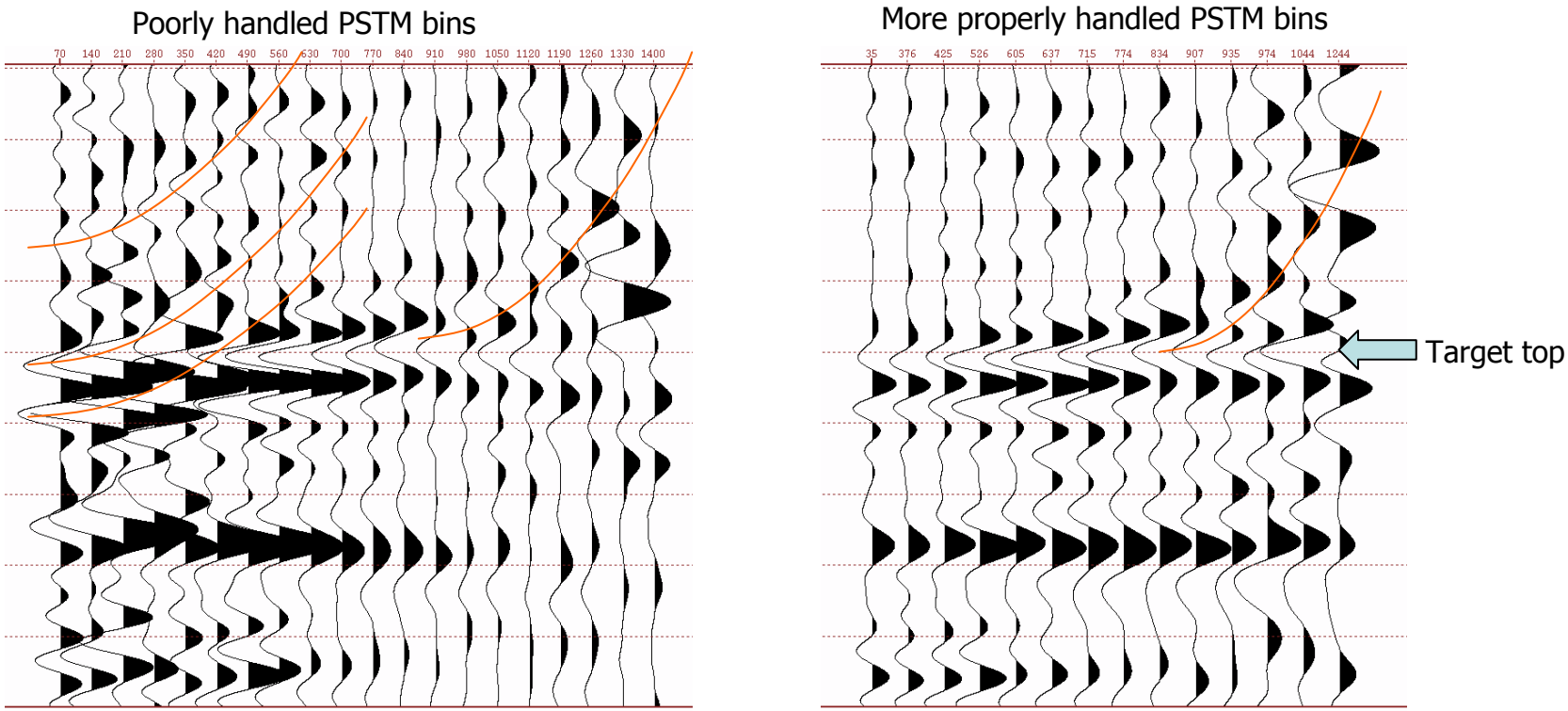

Figure 5.47 Left PSTM CDP gather has equally spaced bins and bin number is close to the nominal fold of 3D data. Migration swings can be seen on the near offset bins and AVO and offset amplitude consistency are poorly preserved. The right PSTM gather is better with variable bin spacing within the gather to balance the input trace numbers to generate every bin. Both gathers have migration swings at far offset (Data courtesy Arcis Corp).

5.8 SUMMARY

Seismic data for reservoir characterization is required passing through the AVO friendly processing and careful conditioning afterwards. The AVO friendly processing consists of iterations of noise attenuations and surface consistent data balancing. Data examples demonstrate the comparison for the deterministic amplitude recovery and relative amplitude recovery and AVO friendly processing flow. Studies have been made on the seismic data conditioning for reservoir characterization, including the offset dependent tuning and NMO stretching correction, residual NMO correction, AVO QC and fix and the issues with 3D data.

The AVO friendly processing consists of iterations of noise attenuations and surface consistent data balancing. The deterministic amplitude recovery makes theoretical sense but requires reliable velocity and attenuation models. The relative amplitude recovery is robust and at most times results in a similar amplitude restoration as the deterministic inversion. The principles in AVO friendly processing include:

1. Utilizing surface consistent process, e.g. surface-consistent deconvolution, surface-consistent scaling etc.
2. Performing noise attenuation. High signal-noise ratio is important for the AVO analysis.
3. Avoiding trace by trace operations, which may destroy AVO fidelity.
4. Iterative multi-steps of signal and AVO enhancements.
5. Applying the best conventional processing results, such as statics and velocity analysis.

Studies have been made on data conditioning for reservoir characterization, including the offset dependent tuning and NMO stretching correction, residual NMO correction, and AVO QC and fix. The issues with 3D data are addressed.

An original method based on inversion is designed for correcting the offset-dependent tuning and NMO stretching effect. The NMO stretching can be analytically corrected, but

the offset-dependent tuning is inherent in the seismic wave propagation through the field of velocity increasing with depth. Although the tuning effect is usually coupled with NMO stretching, the information loss at the far offset exists before the NMO correction is applied. The frequency bandwidth at the far offset is equivalent to or most times less than that at the near offset. To correct the tuning and stretching, high frequency components at the far offsets need to be compensated, which is done by an inversion implemented in the frequency domain. The inversion is an ill-posed problem, which is constrained by the low frequency or dominant frequency components wherever there is no information loss. The synthetic and real data examples show the method is able to correct the tuning and stretching effect with high fidelity.

Adaptively superbinning 3D data is another development to balance the fold distribution in the irregular geometry of 3D acquisition. The real data example shows the adaptive supergathering improves the reliability of AVO inversion, confirmed by the match of reservoirs at the well controls in a real data example.

AVO preservation needs to be quality controlled before the data is used in the reservoir characterization. Relationships in rock properties (mud-rock lines) provide general AVO trends for calibration of amplitudes. Improper AVO scaling by processing can be fixed by the offset-dependent scaling with cares, which is demonstrated by a real data example.

In addition, the residual NMO removal using Swan’s method and issues with bin spacing in the pre-stack time migration of 3D data are discussed in this chapter and demonstrated by examples.

This page is left blank intentionally.

CHAPTER 6: CONCLUSIONS

This thesis develops seismic prediction of the heavy oil reservoir heterogeneity in the Western Canadian Sedimentary Basin (WCSB). The thesis starts with studies on rock properties of oil sands reservoirs in Athabasca to find the qualitative and quantitative relationships between the lithology and seismically derivable elastic parameters in reservoirs, which determines the feasibility of seismic applications. With an understanding of rock properties, developments are made on seismic methods to derive the lithology sensitive elastic parameters for the qualitative and quantitative prediction of reservoir lithology heterogeneity. Seismic data processing and conditioning for reservoir characterization have been studied.

6.1 ROCK PROPERTIES OF HEAVY OIL RESERVOIRS

Qualitative and quantitative analyses have been done on (1) the seismically derivable elastic parameters and their sensitivities to the lithology (shale volume), (2) the feasibility of prediction of the lithology heterogeneity, and (3) the water and bitumen separation. The analyses are mainly based on the wireline logs and core data. The conclusions can be drawn for these studies in the following.

1. Density is one of the best of 12 parameters to indicate the lithology for the McMurray Formation, Athabasca. In addition, density shows a strong correlation with lithology in the Grand Rapids Formation in Athabasca and the Bluesky Formation in Peace River.
2. Lambda*rho is reasonably sensitive to the lithology in all four regions where the shear sonic logs are available to calculate Lame's parameters.
3. Other parameters, such as Ip, lambda, and Vs, are useful to indicate lithology. For instance, P impedance shows a good sensitivity in the McMurray Formation in Christina Lake and the Bluesky Formation in Peace River. In these regions, Vp is poorly correlated with lithology, but Ip, the product of Vp and density, shows a

good correlation with lithology because of the effect of density. However, this sensitivity of Ip changes from region to region.

4. In the Grand Rapids Formation, many parameters, besides density and lambda*rho, are correlated well with lithologies. This conclusion should be tentative and more studies are required to include more well data, because only one well from that region is used.
5. The Vp/Vs ratio, Poisson's ratio, and lambda/mu ratio should have the same ability to separate lithologies in the oil sands reservoirs. The correlation coefficients between the gamma ray value and each of these ratios are about 0.5 in two regions in Athabasca.
6. Quadratic discriminant analysis quantitatively defines the separation of sand and shale by using pairs of elastic parameters.
7. Density is little affected by the burial depth. Density varies between 2.00 g/cc and 2.5 g/cc from the clean sand to shale in the reservoir. Other elastic parameters are influenced by the compaction. Velocities are lower in the shallow burial depth for the same lithology; the velocity variation with depth follows different trends for the sand and shale. The sand and shale are slightly separable for the shallow reservoirs on Vp but the separation is indistinguishable for the deeper reservoirs. Vs is slightly better than Vp to separate sand and shale for both the shallow and deep reservoirs.
8. Because of the velocity variation with depth, other parameters, such as the impedance and Lame's parameters, show variation with depth as well and their sensitivity to lithology also varies with depth.
9. Ratios (the Vp/Vs ratio, Poisson's ratio, and lambda/mu ratio) vary with depth, but their sensitivity to lithology is little affected by the depth.
10. Most of the study in rock properties uses real physical measurements, which is an absolute value similar to well log values, while the seismic data are relative positive-negative values due to the missing low frequencies, plus the arbitrary scaling of the data. Therefore, any promising ability of physical parameters to identify facies and fluids is compromised when these parameters are derived from

the seismic data. The background trend (low frequency) added into the seismic inversion dominates the centers of facies clusters in any cross-plots of the seismically derived attributes, such as lambda*rho versus mu*rho, which are combined to detect gas saturation effectively (Goodway et al, 1997). If a sand background trend is assigned to a shale formation (this happens often), the shale would be classified as sand if the rock property cross-plot templates or knowledge based methods are used. It is necessary to study the bandlimited physical parameters for facies/fluids classifications. The bandlimited rock physical parameters are studied in this thesis. The study shows the bandlimited lithology sensitive parameter (density) still has a strong correlation with lithology, and this conclusion encourages the use of the seismic bandwidth attributes in the prediction of reservoir lithology heterogeneity.

11. Water and bitumen (cold) show differences on some seismically derivable parameters (such as Vp/Vs and Poisson's ratios). But the separation of water and bitumen by using seismic data in practice is difficult if not impossible.

6.2 AVO INVERSION

The AVO inversion for the PP data is applied on the prediction of the lithology heterogeneity of heavy oil reservoirs in the WCSB. With the better understanding of ill-posedness in the AVO inversion, the implementations in this thesis make the AVO inversion more robust and more applicable in the oil sands reservoir characterization. The commonly used Bayesian AVO inversion is evaluated and initial models from the data-driven rock physical interpretation are introduced for a more reliable and theoretically reasonable solution.

The estimator of the Bayesian AVO inversion used by many industrial peers is $(\mathbf{G}^{\mathbf{T}}\mathbf{G} + \sigma_{\mathbf{N}}^{2}\Sigma_{\mathbf{m}}^{-1})^{-1}\mathbf{G}^{\mathbf{T}}\mathbf{d}$ under an assumption of zero mean of the model parameters. This solution is stabilized by the signal/noise ratio and covariance and it is actually the data term in a complete Bayesian estimator. This study shows the zero prior term is not a correct assumption and the prior term in the Bayesian estimator is an important element

in the solution. Therefore, the solution of the Bayesian AVO inversion in this thesis is the complete Bayesian estimator including both the data term and prior term, and it is $\hat{\mathbf{m}} = (\mathbf{G}^{\mathbf{T}}\mathbf{G} + \sigma^2\Sigma_{\mathbf{m}}^{-1})^{-1}\mathbf{G}^{\mathbf{T}}\mathbf{d} + (\mathbf{G}^{\mathbf{T}}\mathbf{G} + \sigma^2\Sigma_{\mathbf{m}}^{-1})^{-1}\sigma^2\Sigma_{\mathbf{m}}{}^{-1}\overline{\mathbf{m}}$. Some modifications make it more reliable for oil sands reservoirs. In addition, the Bayesian AVO inversion is realized in the frequency domain for a more robust solution and better dealing with the offset-dependent tuning. Spatial correlations based on stacked data are used to constrain the inversion. Doing this is as effective as using supergathers (increasing the signal-to-noise ratio or sample number) in the inversion but it considers more local geology.

Two case studies verify the effectiveness of the reliable AVO inversion in the characterization of oil sands reservoir lithology heterogeneity. The case studies show that the AVO inversion derives density attributes from the PP data with a relatively good reliability besides the typical P and S wave attributes. In the second case study, the prediction of lithology in the McMurray Formation in Athabasca is confirmed by blind well tests. The case studies also show that the bandlimited density from the AVO inversion is able to provide key information to the lithology prediction.

The joint PP and PS AVO inversion is briefly discussed in this thesis. The frequency domain implementation of the joint PP and PS inversion is suggested, which is advantageous to deal with the frequency bandwidth difference on both components. A synthetic example demonstrates this advantage.

6.3 IMPEDANCE INVERSION

The analytical Gaussian mean and covariance define a complete model space. The analytical mean stands for the MAP solution of the inversion while the covariance describes the uncertainty of the solution. Elastic properties and errors in the seismic data are often observed as following mono-modal Gaussian distributions, but the reservoir properties follow multi-modal distributions. Simulating the reservoir properties conditional to the seismic data is costly and it is possibly a cost-efficient and robust

process to transform the seismic data to elastic properties by an analytical estimator and subsequently simulate the reservoir properties from the elastic properties.

The implementation of the Bayesian impedance inversion includes the following major features:

1. The impedance instead of logarithmic impedance is the unknown in the inversion so that the Gaussian assumption can be used.
2. The inversion is volume-based -- multiple lateral locations are inverted simultaneously. The local geological characters constrain the inversion of every mini-cube of data.
3. The inversion is designed as a joint post stack P and S impedance and density inversion. Bandlimited P and S impedance and density reflectivities are generated by the AVO inversion, in which the ill-posedness is strong and the solution is stabilized by constraints. The output of the AVO inversion becomes the input of the impedance inversion, which mainly deals with the non-uniqueness. Use of the P and S impedance and density reflectivities instead of the prestack data costs less computation time.
4. Rock property constraints are included. Well logs are studied to derive the statistics of rock properties.
5. Building the initial model is an important first step. Seismic geometrical attributes, AVO attributes and prediction of neural network are used to build an initial model for the inversion. The initial model for the inversion is a mix of the mega layer model and the smoothed prediction of PNN using multiple attributes.

A couple of geometrical attributes are programmed and applied for the initial modeling. The results from new programs of geometrical attributes are better than those from available packages.

A geological model with a point bar system in the McMurray Formation is built based on a comprehensive study of publications on Athabasca oil sands. The geological model

includes point bars, abandoned channels, and fluvial channels in the McMurray Formation. Rock properties of oil sands reservoirs are used to populate the point bar model with the elastic properties for the modeling. Synthetic data with noise added is generated from the elastic property volumes. The two-step inversion (AVO inversion + joint post-stack inversion) is applied on the data, showing the reliability of the method to map the reservoir heterogeneity. The method is able to derive the three elastic parameters with a reasonable stability. The method is worth further improvements to include more realistic low frequency contents and conduct the uncertainty analysis.

6.4 AMPLITUDE PRESERVATION OF SEISMIC DATA FOR RESERVOIR CHARACTERIZATION

Seismic data for reservoir characterization is required to pass through the AVO friendly processing and careful conditioning afterwards. The AVO friendly processing consists of iterations of noise attenuations and surface consistent data balancing. Data examples demonstrate the comparison for the deterministic amplitude recovery and relative amplitude recovery and AVO friendly processing flow. Studies have been made on the data conditioning for reservoir characterization, including the offset dependent tuning and NMO stretching correction, residual NMO correction, AVO QC and fix and the issues with 3D data.

The AVO friendly processing consists of iterations of noise attenuations and surface consistent data balancing. The deterministic amplitude recovery makes theoretical sense but requires reliable velocity and attenuation models. The relative amplitude recovery is robust and at most times results in a similar amplitude restoration as the deterministic inversion. The principles in AVO friendly processing include:

1. Utilizing surface consistent process, e.g. surface-consistent deconvolution, surface-consistent scaling etc.
2. Performing noise attenuation. High signal-noise ratio is important for the AVO analysis.
3. Avoiding trace by trace operations, which may destroy AVO fidelity.

4. Iterative multi-steps of signal and AVO enhancements.
5. Applying the best conventional processing results, such as statics and velocity analysis.

Studies have been made on data conditioning for the reservoir characterization, including the offset dependent tuning and NMO stretching correction, residual NMO correction, and AVO QC and fix. The issues with 3D data are addressed.

A new method is made on correcting the offset-dependent tuning and NMO stretching effect. The NMO stretching can be analytically corrected, but the offset-dependent tuning is inherent in the seismic wave propagation through the field of velocity increasing with depth. Although the tuning effect is usually coupled with NMO stretching, the information loss at the far offset exists before the NMO correction is applied. The frequency bandwidth at the far offset is equivalent to or usually less than that at the near offset. To correct the tuning and stretching, high frequency components at the far offsets need to be compensated, which is done by an inversion implemented in the frequency domain. The inversion is an ill-posed problem, which is constrained by the low frequency or dominant frequency components wherever there is no information loss. The synthetic and real data examples show the method is able to correct the tuning and stretching effect with high fidelity.

Adaptively superbinning 3D data is another development to balance the fold distribution in the irregular geometry of 3D acquisition. The real data example shows the adaptive supergathering improves the reliability of AVO inversion, confirmed by the match of reservoirs at the well controls in a real data example.

AVO preservation needs to be quality controlled before the data is used in the reservoir characterization. Rock property relationships provide general AVO trends for calibration of amplitudes. Improper AVO scaling by processing can be fixed by the offset-dependent scaling with cares, which is demonstrated by a real data example.

In addition, the residual NMO removal using Swan's method and issues with bin spaces in pre-stack time migration of 3D data are discussed in this chapter and demonstrated by examples.

6.5 FUTURE WORK

In the rock property study, more detailed studies on the relationship between the elastic parameters and reservoir properties, such as facies and saturation, will be conducted if the core data and other data sources are available.

Joint PP and PS AVO inversion reduces the ill-posedness of the inversion. The frequency domain inversion is proposed and tested by a synthetic example. It is recommended to test and improve the method on a real dataset.

Geometrical seismic attributes have potential for improving the reservoir heterogeneity predication in the heavy oil areas. But customized coding of algorithms and parameterization are needed to be done in the future.

Much work need to be done on the impedance inversion, deriving the full bandwidth impedance from the seismic data in the future: quantification of the uncertainty of the PNN prediction, the uncertainty analysis of the inversion, the low frequency content from seismic velocity, non-Gaussian probability distributions, and applications of all these on real data.

6.6 SOURCE CODES DEVELOPED

In performing the research for this thesis, source codes for algorithms and displays in Matlab, including

- Crossplotting rock properties for three parameters with statistics displayed.
- Bayesian AVO inversion
- Joint PP and PS AVO inversion

- Wavelet extraction
- Joint post-stack impedance inversion
- Volume-based geometrical attributes – dips and continuity
- NMO stretching and offset-dependent tuning correctioin
- Adaptive supergathering

This page is left blank intentionally.

REFERENCES

Aki, K. and Richards, P. 1980, Quantitative seismology: they and methods: W. H. Freeman and Co.

Alberta Energy and Utility Board (AEUB) and Alberta Geological Survey (AGS), 2000, Historical overview of the Fort McMurray area and oil sands industry in Northeast Alberta: Earth Sciences Report 2000-05.

Alberta Energy and Utility Board (AEUB), 2003, Athabasca Wabiskaw-McMurray regional geological study: AEUB general bulletin 2003-A.

Alemie, W. M., 2010, Stable high-resolution three-term AVO inversion: GeoCanada 2010 Conference technical program.

Alemie, W. and M. Sacchi, 2011, High-resolution three-term AVO inversion by means of a Trivariate Cauchy probability distribution: Geophysics, Vol 76, No. 3, p. R43-R55.

Allen, J. L. and C. Peddy, 1993, Amplitude variation with offset: Gulf Coast case studies: SEG Geophysical Developments Series, Volume 4.

Anderson, P. and F. D. Gray, 2001, Using LMR for dual attribute lithology identification: 71st Annual International Meeting, SEG Expanded Abstracts, 201-202.

Anderson, P., L. Chabot, and F. D. Gray, 2005, A proposed workflow for reservoir characterization using multi-component seismic data: 75th Annual International Meeting, SEG Expanded Abstracts, 991-994.

Avseth, P. A., 2000, Combining rock physics and sedimentary for seismic reservoir characterization of North Sea turbidite systems: Ph.D. thesis, Stanford University.

Backus, G., 1988, Hard and soft prior bounds in geophysical inverse problems: Geophys. J., 94, 249–261.

Bale, R. B. Gratacos, B. Mattocks, S. Roche, K. Poplavskii, and X. Li, 2009, Shear wave splitting applications for fracture analysis and improved imaging: some onshore examples: First Break, 27, 73-83.

Bancroft, J. and S. Sun, 2003, Fresnel zones and the power of stacking used in the preparation of data for AVO analysis: 73rd Annual International Meeting, SEG Expanded Abstracts, 231-234.

Barnes, A. E., 2001, Seismic attributes in your facies: CSEG Recorder, September, 41-47.

Barnola, A., B. Andrieux, T. Tonellot, and O. Voutay, 2003, Pre-stack stratigraphic inversion and attribute analysis for optimal reservoir characterisation: 73rd Annual International Meeting, SEG, Expanded Abstracts.

Barrett, K., 2010, An overview of Saleski: the first SAGD project in Carbonates: GeoCanada 2010 Conference technical program.

Behura, J., N. Kabir, R. Crider, P. Jilek, and E. Lake, 2010, Density extraction from P-wave AVO inversion: Tuscaloosa Trend example: The Leading Edge, vol. 29, 772-777.

Bellman, L., 2008, Oil sands reservoir characterization – an integrated approach: CSEG Recorder, October issue, 7-10.

Bellman, L. and M. Connelly, 2010, 3D reservoir characterization in the Grand Rapids: GeoCanada 2010 technical program abstract.

Bianco, E., S. Kaplan, and D. Schmitt, 2008, Seismic rock physics of steam injection in bituminous oil reservoirs: The Leading Edge, 27, p. 1131-1137.

Bosch, M., C. Luis, J. Rodrigues, A. Navarro, and M. Diaz, 2007, A Monte Carlo approach to the joint estimation of reservoir and elastic parameters from seismic amplitudes: Geophysics, Vol. 72, No. 6, P. O29-O39.

Bosch, M., C. Carvajal, J. Rodrigues, A. Torres, M. Aldana, and J. Sierra, 2009, Petrophysical seismic inversion conditioned to well-log data: Methods and application to a gas reservoir: Geophysics, Vol. 74, No. 2, P. O1-O15.

Brac, J., P. Y. Dequirez, F. Herve, C. Jacuues, P. Lailly, V. Richard, and D. T. van Nieuh, 1988, Inversion with a priori information: an approach to integrated stratigraphic interpretation: SEG int'l annual meeting abstracts, p. 841-844.

Buland, A. and H. Omre, 2003, Bayesian linearized AVO inversion: Geophysics, 68, p. 185-198.

Buland, A., O. Kolbjornsen, and H. Omre, 2003, Rapid spatially coupled AVO inversion in the Fourier domain: Geophysics, 68, p. 824-836.

Buland, A., O. Kolbjornsen, R. Hauge, O. Skjaeveland, and K. Duffaut, 2008, Bayesian lithology and fluid prediction from seismic prestack data: Geophysics, 73, p. C13-C21.

Cambois, G., 2000, Can P-wave AVO be quantitative?: The leading edge, vol. 19, no. 11, p. 1246-1251.

Cambois, G., 2001, AVO and the general inverse theory: CSEG Recorder, 2001, June, p. 74-77.

Cant, D., 2008, The Grand Rapids Formation: An unexploited bitumen reservoir: CSPG-CSEG-CWLS convention abstracts.

Caplan, M., C. Heron, L. Sullivan, E. Herle, J. Keith, A. Bernal, and I. Atkinson, 2008, Evaluation of SAGD performance in a deltaic environment: International Thermal Operations and Heavy Oil Symposium, SPE/PS/CHOA 117821, PS2008-338.

Cary, P., X. Li, G. Popov, and C. Zhang, 2010, Shear-wave splitting in compliant rocks: The Leading Edge, vol. 29, no. 10, 1278-1285.

Cassassuce, F., J. Rector, and M. Hoversten, Study of gas hydrates in the deep-sea Gulf of Mexico from seismic data: The Leading Edge, vol. 23, no. 4, 366-372.

Castagna, J., P., M. L. Batzle, R. L. Eastwood, 1985, Relationships between compressional wave and shear wave velocities in clastic silicate rocks: Geophysics, vol. 50, 571-581.

Castagna, J., P., M. L. Batzle, T. K. Kan, 1993, Rock physics – The link between rock properties and AVO response, in Castagna J. P and M. M. Backus Eds., Offset-dependent reflectivity – theory and practice of AVO analysis: SEG, 135-171.

Castagna, J., 2001, Recent advances in seismic lithologic analysis: Geophysics, 66, p. 42-46.

Castagna, J. P., and Smith, S.W., 1994, Comparison of AVO indicators: A modeling study: Geophysics, 59, 1849–1855.

Castagna, J. P., Swan, H. W., and Foster, D. J., 1998, Framework for AVO gradient and intercept interpretation: Geophysics, 63, 948–956.

Castoro, A., R. E. White, and R. D. Thomas, 2001, Thin-bed AVO: Compensating for effects of NMO on reflectivity sequences: Geophysics, 66, 1714-1720.

Chen, Q. and S. Sidney, 1997, Seismic attribute technology for reservoir forecasting and monitoring: The Leading Edge, vol. 16, 445-448.

Choo, J., J. Downton, and J. Dewar, 2004, LIFT: a new and practical approach to noise and multiple attenuation: CSEG national conventional abstract.

Chopra, S. and K. Marfurt, 2007, Seismic attributes for prospect identification and reservoir characterization: SEG publication.

Claerbout, J., 1985, Imaging the Earth's interior: Blackwell Science.

Cody, J., S. Youn, A. Riddy, and S. Gittins, 2001, Implications of reservoir "compartments" on the design and execution of the Christina Lake thermal recovery project: CSPG convention technical program.

Connelly, M., 2010, West Athabasca Grand Rapids formation, Northeast Alberta, Canada: EAGE presentation.

Connolly, P., 1999, Elastic impedance: The Leading Edge, 18, no. 4, 438-452.

Connolly, P. 2010, Robust reservoir characterization: SEG North America Distinguished Lecture.

Contreras, A., C. Torres-Verdin, W. Chesters, K. Kvien, and M. Globe, 2005, Joint stochastic inversion of petrophysical logs and 3d pre-stack seismic data to assess the spatial continuity of fluid units away from wells: application to a Gulf-Of-Mexico deepwater hydrocarbon reservoir: SPWLA 46th Annual Logging Symposium.

Cooke, D., A. Sena, G. O'Donnell, T. Muryanto, and V. Ball, 1999, What is the best seismic attribute for quantitative seismic reservoir characterization: 69th Annual International Meeting, SEG, Expanded Abstracts,

Das, A. and M. Baztle, 2008, Modeling studies of heavy oil – in between solid and fluid properties: The Leading Edge, 27, 1116 – 1123.

Debeye, H., E. Sabbah, and P. van der Made, 1996, Stochastic inversion: 66th Annual International Meeting, SEG, Expanded Abstracts, p. 1212-1215.

Dembicki, E., 2007, An overview of Alberta oil sands and recovery technologies: 18th Latin American Petroleum Show, Maracaibo, Venezuela.

Dembicki, E., 1994, The Upper Devonian Grosmont Formation: well log evaluation and regional mapping of a heavy oil carbonate reservoir in Northeastern Alberta: Master thesis, University of Alberta.

Demirbag, E., C. Coruh, and J. Costain, 1993, Inversion of P-wave AVO, in Castagna J. P and M. M. Backus Eds., Offset-dependent reflectivity – theory and practice of AVO analysis: SEG, 287-302.

Deutsch, C., 2002, Geostatistical reservoir modeling: Oxford University Press.

Deutsch, C., and A. Journel, 1998, GSLIB: Geostatistical software library: Oxford University Press.

Dong, W., 1999, AVO detectibility against tuning and stretching artefacts: Geophysics, 64, 494-503.

Downton, J., and L. Lines, 2001, Constrained three parameter AVO inversion and uncertainty analysis: 71st Ann Internat. Mtg, SEG, Expanded Abstracts, 238-241.

Downton, J., and L. Lines, 2002, AVO before NMO: 72nd Annual International Meeting, SEG, Expanded Abstracts.

Downton, J., and L. Lines, 2003, High resolution AVO analysis before NMO: 73rd Annual International Meeting, SEG, Expanded Abstracts, 219-222.

Downton, J., 2005, Seismic parameter estimation from AVO inversion: PhD thesis, University of Calgary.

Doyen, P. M., 1988, Porosity from seismic data: A geostatistical approach: Geophysics, **53**, 1263–1275.

Duijndam, A. J. W, 1988a, Bayesian estimation in seismic inversion: Part I, principles: Geophysical prospecting, vol 36, p 878-898.

———, 1988b, Bayesian estimation in seismic inversion: Part II, uncertainty analysis: Geophysical prospecting, vol 36, p 899 – 918.

Dumitrescu, C., L. W. Bellman, and A. Williams, 2005, Delineating productive reservoir in the Canadian Oil Sands using neural networks approach: CSEG convention.

Dumitrescu, C. and L. Lines, 2008, Seismic attributes used for reservoir simulation: application to a heavy oil reservoir in Canada: CSPG-CSEG-CWLS convention abstract.

Dumitrescu, C., L. Lines, D. Vanhooren, and D. Hinks, 2009, Characterization of heavy oil reservoir using Vp/Vs ratio and neural network analysis: CSEG convention.

Dumitrescu, C. and L. Lines, 2009, Case study of a heavy oil reservoir interpretation using Vp/Vs ratio and other seismic attributes: 79th Annual International Meeting, SEG Expanded Abstracts, 1765-1769.

Dusseault, M. B., 2001, Comparing Venuzuelan and Canadian heavy oil and tar sands: Canadian International Petroleum Conference, paper 2001-061.

Earthworks Environment & Resources Ltd, 2003, Technical note: Colored, deterministic & stochastic inversion.

Earthworks Environment & Resources Ltd, 2006, Technical note: Understanding stochastic seismic inversion.

Ellis, D. and J. Singer, 2008, Well logging for Earth Scientists – second edition: Springer.

Evans, J. and Y. Hua, 2008, Early project seismic application at the Ellis River heavy oil project-maximizing the value of VSP and well data: CSEG Expanded abstracts.

Fatti, J., G. Smith, P. Vail, P. Strauss, and P. Levitt, 1994, Detection of gas in sandstone reservoirs using AVO analysis: A 3-D seismic case history using the Geostack technique: Geophysics, 59, no. 9, 1362-1376.

Francis, A., 2005, Limitations of deterministic and advantages of stochastic seismic inversion: CSEG Recorder, February issue, 5-11.

———, 2006a, Understanding stochastic inversion: Part 1: First Break, 24, no. 11, 69–77.

———, 2006b, Understanding stochastic inversion: Part 2: First Break, 24, no. 12, 79–84.

Fustic, M., K. Ahmed, S. Brough, B. Bennett, L. Bloom, M. Asgar-Deen, O. Jokanola, R. Spencer, and S. Larter, 2006, Reservoir and bitumen heterogeneity in Athabasca oil sands: CSPG-CSEG-CWLS joint convention.

Fustic, M., 2007, Stratigraphic dip analysis – A novel application for detailed Geological modeling of point bars, and predicting bitumen grade, McMurray Formation,

Muskeg River Mine, Northeast Alberta: Natural Resources Research, v. 16, no. 1, p. 31-43.

Fustic, M., L. Skulski, W. Hanson, D. Vanhooren, P. Bessette, D. Hinks, L. Bellman, and D. Leckie, 2007, Geological mapping and reservoir characterization of oil sands reservoir by integrating 3D seismic, dipmeter, core descriptions, and analogs in the McMurray Formation, NW Alberta: Extended abstract, AAPG Hedberg Conference, "Heavy oil and bitumen in foreland basins – from processes to products", September 30 – October 3, 2007, Banff, Alberta, Canada.

Gallop, J. 2006, Facies probability from mixture distribution with non-stationary impedance errors: 76th Annual International Meeting, SEG, Expanded Abstracts, 1801-1804.

Gao, D., 2011, Latest developments in seismic texture analysis for subsurface structure, facies, and reservoir characterization: A review: Geophysics, vol. 76, no. 2 p. w1-w13.

Gidlow, M., G. Smith, and P. Vail, 1992, Hydrocarbon detection using fluid factor traces, a case study: How useful is AVO analysis?: Joint SEG/EAEG summer research workshop, Technical program and abstracts, 78-89.

Gingras, M. and D. Rokosh, 2004, A brief overview of the geology of heavy oil, bitumen and oil sand deposits: CSEG National Convention.

Goodway, W., T. Chen, and J. Downton, 1997, Improved AVO fluid detection and lithology discrimination using Lame petrophysical parameters; lambda-rho, mu-rho, lambda/mu fluid stack from P and S inversions: 67th Annual International Meeting, SEG, Expanded Abstracts, 183–186.

Gonzalez, E. H., 2006, Physical and quantitative interpretation of seismic attributes for rocks and fluids identification: PhD thesis, Stanford University.

Gouveia,W., and J. A. Scales, 1998, Bayesian seismic waveform inversion: Parameter estimation and uncertainty analysis: Journal of Geophysical Research, 103, 2759–2779.

Government of Alberta, http://www.energy.gov.ab.ca/OurBuisness/oilsands.asp.

Gray, D., W. Goodway, and T. Chen, 1999, Bridge the gap – using AVO to detect changes in fundamental elastic constants: 61st EAGE meeting.

Gray, D., P. Anderson, and J. Gunderson, 2004, Examination of wide-angle, multi-component, AVO attributes for prediction of shale in heavy oil sands: A case study from the Long Lake Project, Alberta, Canada: 74th Annual International Meeting, SEG, Expanded Abstracts

Gray, D., P. Anderson, and J. Gunderson, 2006, Prediction of shale plugs between wells in heavy oil sands using seismic attributes: Natural Resources Research, vol. 15, no.2 103-109.

Gray, D., 2011, Oil sands: Not your average seismic data: CSPG-CSEG-CWLS convention technical program abstract.

Gulunay, N., M. Magesan, and H. Roende, 2007, Gather flattening: The Leading Edge, vol. 26, 1538-1543.

Gunning, J. and M. E. Glinsky, 2004, Delivery: an open-source model-based Bayesian seismic inversion program: Computer & Geosciences, vol 30, p 619-636.

Haas, A. and O. Dubrule, 1994, Geostatistical inversion - a sequential method of stochastic reservoir modeling constrained by seismic data: First Break, Vol 12, No 11, p561-569.

Hampson, D., J. Schuelke, and J. Quirein, 2001, Use of multi attribute transforms to predict log properties from seismic data: Geophysics, 66, 220-236.

Hampson-Russell Software, Constrained model inversion mathematical theory: Geoview help documentation.

Han D. A. Nur, and D. Morgan, 1986, Effects of porosity and clay content on wave velocities in sandstones: Geophysics, 51, 2093-2107.

Han, D., J. Liu, and M. Baztle, 2008, Seismic properties of heavy oils – measured data: The Leading Edge, 27, 1108-1115.

Hansen, T., A. Journel, A. Tarantola, and K. Mosegaard, 2005, Linear inverse theory and geostatistics: International Association for Mathematical Geology, Toronto.

———, 2006, Linear inverse Gaussian theory and geostatistics: Geophysics, vol 71, no 6, p. R101-R101.

Hansen, T. and K. Mosegaard, 2008, VISIM: Sequential simulation for linear inverse problem: Computer & Geosciences, vol 34, p 53-76.

Hart, B. S., 2002, Validating seismic attribute studies: Beyond statistics: The leading Edge, v. 21, no. 10, 1016-1021

Hart, B. S., 2008, Channel detection in 3-D seismic data using sweetness: AAPG Bulletin, vol. 92, no. 6, 733-742.

Hart, B. S., 2008, Stratigraphically significant attributes: The Leading Edge, 27, 320-324.

Hayes, B.J.R., L.E. Christopher, L. Rosenthal, G. Los, B. McKercher, D. Minken, Y.M. Tremblay, J. Fennell, and D.G. Smith, Cretaceous Mannville Group of the Western Canada Sedimentary Basin: CSPG digital atlas no. 19.

Hein, F., D. Cotterill, and H. Berhane, 2000, An atlas of lithofacies of the McMurray formation Athabasca oil sands deposit, Northeastern Alberta: surface and subsurface: AEUB and AGS Earth Sciences Report 2000-07.

Hernandez, D., S. Lazaratos, and E. Wildermuth, 2009, Benefiting from pre-migration spectral shaping inversion – Comparison between models and real data: 79th Annual International Meeting, SEG Expanded Abstracts, 2388-2392..

Herrmann P., T. Mojesky, M. Magesan, and P. Hugonnet, 2000, De-aliased, high-resolution radon transforms: 70th Annual International Meeting, SEG, Expanded Abstracts, 1953-1956.

Hilterman, F. and Z. Zhou, 2009, Pore-fluid quantification: Unconsolidated vs. consolidated sediments: 79th SEG Annual Meeting Abstracts: 331- 335.

Isaac, H, and G. Margrave, 2011, Hurrah for Hussar! Comparisons of stacked data: CREWES Research Report, vol. 23, no. 55, Univ. of Calgary.

Kan, T. K. and H. Swan, 2001, Geopressure prediction from automatically-derived seismic velocity: Geophysics, vol. 66, p. 1937-1946.

Kim, H., Y. Song, and K. Lee, 1999, Inequality constraint in least-squares inversion of geophysical data: Earth Planets Space, 51, 255-259.

Kato, A., S. Onozuka, and T. Nakayama, 2008, Elastic property changes in a bitumen reservoir during steam injection: The Leading Edge, 27, 1124-1131.

Kelkar, M. and G. Perez, 2002, Applied geostatistics for reservoir characterization: SPE inc.

Kelly and Skidmore, 2001, Non-linear AVO equations and their use in 3-parameter inversion: 71st Annual International Meeting, SEG, Expanded Abstracts, 255-256.

Kjønsberg, H., R. Hauge, O. Kolbjørnsen, and A. Buland, 2010, Bayesian Monte Carlo method for seismic predrill prospect assessment: Geophysics, Vol. 75, No. 2, P. O9-O19.

Krebs, J., J. Anderson, D. Hinkley, R. Neelamani, S. Lee, A. Baumstein, and M. Lacasse, 2009, Fast full-wavefield seismic inversion using encoded sources: Geophysics, vol. 74, no. 6, p. WCC177-188.

Kuhl, H. and M. Sacchi, 2003, Least-squares wave-equation migration for AVP/AVA inversion: Geophysics, vol. 68, no. 1, p. 262-273.

Labrecque, P. A., S. M. Hubbard, J. L., Jensen, 2010, Cyclic sedimentation and three-dimensional stratigraphic architecture in point bar deposits, Cretaceous McMurray formation, Alberta: Implications for reservoir characterization and heterogeneity prediction: GeoCanada 2010 technical program.

Lancaster, S. and D. Whitcombe, 2000, Fast-track 'colored' inversion: 70th Annual International Meeting, SEG Expanded Abstracts,1572-1575.

Larsen, J., 1999, AVO inversion by simultaneous P-P and P-S inversion: M.Sc. thesis, University of Calgary.

Larsen, A., M. Ulvmoen, H. Omre, and A. Buland, 2006, Bayesian lithology/fluid prediction and simulation on the basis of a Markov-chain prior model: Geophysics, 71, no. 5, R69-78.

Lazaratos, S., and C. Finn, 2004, Deterministic spectral balancing for high-fidelity AVO: 74th Annual International Meeting, SEG, Expanded Abstracts, 219-223.

Lazaratos, S., and R. David, 2009, Inversion by pre-migration spectral shaping: 79th Annual International Meeting, SEG Expanded Abstracts, 2383-2387.

Leguijt, J., 2009, Seismically constrained probabilistic reservoir modeling: The Leading Edge, vol., 29, no. 12, p. 1478-1484.

Leuangthong. O., D. Khan, and C. Deutsch, 2008, Solved problems in geostatistics: John Wiley & Sons publication.

Lin, T. L., and R. Phair, 1993, AVO tuning: 63rd Annual International Meeting, SEG Expanded Abstracts, 727-730.

Lin, X., P. Yang, and G. Zhang, 2008, A novel prestack AVO inversion and its application: 78th Annual International Meeting, SEG Expanded Abstracts

Lindseth, R., 1979, Synthetic sonic log – a process of stratigraphic interpretation: Geophysics, 44, 3-26.

Lines, L., H. Agharbarati, P. Daley, J. Embleton, M. Fay, T. Settari, F. Vasheghani, T. Wang, A. Zhang, X. Qi, and D. Schmitt, 2008, Collaborative methods in enhanced cold heavy oil production: The Leading Edge, 27, 1152-1156.

Lines, L. and S. Treitel, 1985, Inversion with a grain of salt: Geophysics, 50, 99-109.

Lines, L., P. Daley, and L. Ibna-hamid, 2010, The accuracy of dipole sonic logs and its implications for seismic interpretation: Journal of Seismic Exploration, 19, 87-102.

Lloyd, H. and G. Margrave, 2011, Comparison of low frequency seismic data to well logs – Hussar example: CREWES Research Report, vol. 23, no. 72, Univ. of Calgary.

Ma, X. Q., 2002, Simultaneous inversion of prestack seismic data for rock properties using simulated annealing: Geophysics, 67, 1877–1885.

Mallick, S., 1995, Model-based inversion of amplitude-variations with offset data using a genetic algorithm: Geophysics, 60, 939–954.

Margrave, G., R. Stewart, and J. Larsen, 2001, Joint PP and PS seismic inversion: The Leading Edge, vol. 20, no. 9, 1048-1052.

Margrave, G., R. Ferguson, and C. Hogan, 2011, Full waveform inversion using wave-equation depth migration with tying to wells: 81st Annual International Meeting, SEG Expanded Abstracts, 2454-2458.

Margrave, G., L. Mewhort, T. Phillips, M. Hall, M. Bertram, D. Lawton, K. Innaen, K. Hall, and K. Bertram, 2011, The Hussar low-frequency experiment: CREWES Research Report, vol. 23, no. 78, Univ. of Calgary.

Mavko, G., Mukerji, T., and Dvorkin, J., 1997, The handbook of rock physics: Cambridge Univ. Press.

McLennan, J. and C. Deutsch, 2004, SAGD reservoir characterization using geostatistics: application to the Athabasca oil sands, Alberta, Canada: Canada Heavy Oil Association, 204.

Menke, W., 1989, Geophysical data analysis: Discrete inverse theory: Academic Press.

Merletti, G. and C. Terres-Verdin, 2006, Accurate detection and spatial delineation of thin-sand sedimentary sequences via joint stochastic inversion of well logs and 3D pre-stack seismic amplitude data: SPE 102444.

Mochinaga, H., S. Onozuka, F, Kono T. Ogawa, A. Takahashi, and T. Torigoe, 2006, Properties of oil sands and bitumen in Athabasca: Abstracts, CSPG-CSEG-CWLS joint convention.

Mukerji, T., G. Mavko, and C. Gomez, 2009, Cross-property physics relations for estimating low-frequency seismic impedance trends from electromagnetic resistivity data: The Leading Edge, vol. 28, no. 1, 94-97.

Nakayama, T., Takahashi, A., L. Skinner, and A Kato, 2008, Monitoring an oil-sands reservoir in northwest Alberta using time-lapse 3D seismic and 3D P-SV converted-wave data: The Leading Edge, 27, 1158-1175.

Nardin, T., J. Carter, B. Falls, J. Irish, S. Stancliffe, B. Varban, N. Wilson, L. Zabcic, and L. Pratt, 2007, Sequence Stratigraphic and Depositional Facies Framework of the Lower Cretaceous McMurray Formation, Kearl Oil Sands Project, Alberta: CSPG-CSEG convention.

Oldenburg, D. W., T. Scheuer, and S. Levy, 1983, Recovery of the acoustic impedance from reflection seismograms: Geophysics, 48, 1318–1337.

Operto, S., J. Vireux, P. Amerstoy, and L. Giraud, 2006, 3D frequency-domain finite-difference modeling of acoustic wave propagation using a massively parallel direct solver: A feasibility study: 76th Annual International Meeting, SEG Expanded Abstracts, 2265–2269.

Ostrander, W. J., 1984, Plane-wave reflection coefficients for gas sands at non-normal angles of incidence: Geophysics, vol. 49, 1637-1648.

Patruyo, D., H. Huang, S. Hubbard, and R. Spencer, 2009, Point bar modeling, middle McMurray formation, Alberta: CSPG-CSEG-CWLS convention, abstracts, p 806-809.

Perez, G., and K. Marfurt, 2006, Correction for wavelet stretch in common-angle migration improves vertical and lateral resolution: 76th Annual International Meeting, SEG, Expanded Abstracts, 254-257.

Petro-Canada, 2001, Commercial application for the approval of the Meadow Creek project: submitted to Alberta EUB, ftp://ftp.gov.ab.ca/env/fs/EIA/2002-07-PetroCanadaMeadowCreekProjectSupplemental/Program%20Files/Meadow/volume1/Volume%201.pdf.

Quakenbush, M., B. Shang, and C. Tuttle, 2006, Poisson impedance: The Leading Edge, Vol. 25, No. 2, 128-138.

Rider, M., 2002, The Geological Interpretation of Well Logs: 2nd edition, revised, Rider-French Consulting Ltd.

Roberts, G., 2000, Wide-angle AVO: 70th Annual International Meeting, SEG, Expanded Abstracts, 134-137.

Robinson A. and T. Davis, 2010, Acoustic impedance inversion for static and dynamic characterization of a CO2 EOR project, Postle Field, Oklahoma: SEG 80th Annual Meeting Expanded Abstracts, 2810-2814.

Rowbotham, P., P. Lamy, P. Swaby, O. Dubrule, and T. Cadoret, 1998, Geostatistical inversion for reservoir characterization: SEG 68th Annual Meeting Expanded Abstracts.

Roy, B., P. Anno, and M. Gurch, 2008, Imaging oil-sand reservoir heterogeneity using wide-angle prestack seismic inversion: The Leading Edge, 27, 1192-1201.

Roy, B., P., Anno, R. Baumel., and J. Durrani, 2005, Analytic correction for wavelet stretch due to imaging: 75th Annual International Meeting, SEG, Expanded Abstracts, 234-237.

Ruger, A., 2002, Reflection coefficients and azimuthal AVO analysis in anisotropic media: SEG geophysical monograph series, No. 10: SEG publication.

Russell, B., 1988, Introduction to seismic inversion methods: SEG publication.

Russell, B. and D. Hampson, 1991, A comparison of post-stack seismic inversion: SEG 61st Annual Meeting Expanded Abstracts, p876-878.

Rutherford, S. R., 1993, Noise discriminating, statistical-amplitude compensation for AVO analysis: Geophysics, 58, 1831–1839.

Rutherford, S. R. and R. H. Williams, 1989, Amplitude versus offset variations in gas sands: Geophysics, 54, 680-688.

Sacchi, M. and T. Ulrych, 1996, Bayesian inversion of acoustic impedance: Research report, CDSST, Univ. of British Columbia.

Sams, M. and D. Saussus, 2010a, Comparison of lithology and net pay uncertainty between deterministic and geostatistical inversion workflows: First break, vol. 28, February, 35-44.

———, 2010b, Low frequency modeling and uncertainty in geostatistical inversion: 72nd EAGE conference & exhibition incorporating SPE EUROPEC 2010, Barcelona, Spain.

Sarzalejo, S. and B. S. Hart, 2006, Stratigraphy and lithologic heterogeneity in the Mannville Group (southeast Saskatchewan) defined by integrating 3-D seismic and log data: Bulletin of Canadian Petroleum Geology, vol. 54, no. 2 138-151.

Scales, J. and L. Tenorio, 2001, Prior information and uncertainty in inverse problems: Geophysics, 66, 389-397.

Schlumberger, 2002, Heavy-Oil Reservoirs: Oilfield Review, autumn issue, 30-51.

Sen, M. and P. Stoffa, 1991, Nonlinear one-dimensional seismic waveform inversion using simulated annealing: Geophysics, 56, 1624-1638.

Simm, R., R. White, and R. Uden, 2000, The anatomy of AVO crossplots: The Leading Edge, vol. 19, p.10-155.

Singleton, S., 2008, The effects of seismic data conditioning on pre-stack simultaneous impedance inversion: 78th Annual International Meeting, SEG Expanded Abstracts, 1506-1510.

Skelt, C., D. Glenn, S. Smith, C. Vu, S. Walden, P. Anderson, and B. Bacon, 2006, Incorporating rock property constraints and geological insights into seismic

inversion for reservoir porosity and net to gross volumes: 76th Annual International Meeting, SEG Expanded Abstracts, 1655-1659.

Smith,G., and Gidlow, P. M., 1987,Weighted stacking for rock property estimation and detection of gas: Geophys. Prosp., 35, 993–1014.

Soni, S., W. Littmann, D. Timko, H, Karkooti, S. Karimi, and S. Kazemshiroodi, 2008, An integrated case study from seismic to simulation through geostatistical inversion: SPE 118178.

Spikes, K. T., 2008, Probabilistic seismic inversion based on rock-physics models for reservoir characterization: Ph.D. thesis, Stanford University.

Stewart, R., 1990, Joint P and P-S seismic inversion: University of Calgary, CREWES Research Report, Vol. 2.

Strobl, R., D. Wightman and S. Youn, 2004, A predictive model for identifying high quality SAGD oil sands reservoirs – observations fro the Encana Foster Creek and Christina Lake projects: CSPG convention technical program.

Strobl, R., 2011, Impact of reservoir quality on SAGD production – Observations from the UTF Phase B oil sands pilot: 2011 CSPG-CSEG-CWLS convention technical program.

Sun, S. and J. Bancroft, 2003, The effect of the Fresnel zone size on AVO analysis for stack data: 73rd Annual International Meeting, SEG Expanded Abstracts, 223-226.

Swan H., 1993, Properties of direct AVO hydrocarbon indicators, in Castagna J. P and M. M. Backus Eds., Offset-dependent reflectivity – theory and practice of AVO analysis: SEG, 78-92.

Swan, H, 1997, Removal of offset-dependent tuning in AVO analysis: 67th Annual International Meeting, SEG, Expanded Abstracts, 175-178.

Swan, H., 2001, Velocities from amplitude variation with offset: Geophysics, vol. 66, 1735-1743.

Swan, H., 2007, Automatic compensation of AVO background drift: The leading edge, no. 12, p. 1528-1536.

Terres-Verdin, C., M. Victoria, G. Merletti, and J. Pendrel, 1999, Trace-based and geostatistical inversion of 3-D seismic data for thin-sand delineation: An application in San Jorge Basin, Argentina: The leading edge, no 9, 1070-1077.

Theune, U., I. O. Jensas, and J. Eidsvik, 2010, Analysis of prior models for a blocky inversion of seismic AVA data: Geophysics, vol. 75, No. 3, p. C25-C35.

Thomas, M., B., P. McGillivray, R. Wong, and S. Hubbard, 2002, Bluesky/Ostracod rock properties – Peace River tar sands: "Not a simple 'sand-tank' model": 75th CSPG convention, Canadian Society of Petroleum Geologists.

Tonellot, T., D. Mace, V. Richard, and M. Cuer, 1999, Prestack elastic waveform inversion using a priori information: 69th Annual International Meeting, SEG, Expanded Abstracts.

Tonellot, T., D. Mace, and V. Richard, 2001, Joint stratigraphic inversion of angle-limited stacks: 71st Annual International Meeting, SEG, Expanded Abstracts.

Tonn, R., 2002, Neural network seismic reservoir characterization in a heavy oil reservoir: The Leading Edge, 21, no. 3, 309-312.

Tonn, R., 2010, Seismic characterization of Statoil's Leimsmer heavy oil reservoir: GeoCanada2010 Conference Presentation.

Ulrych, T., M. Sacchi, and A. Woodbury, 2001, A Bayes tour of inversion: a tutorial: Geophysics, 66, 55-69.

Ulvmoen, M. and H. Omre, 2010, Improved resolution in Bayesian lithology/fluid inversion from prestack seismic data and well observations: Part 1 – Methodology: Geophysics, Vol 75, No 2, p R21-R35.

Ulvmoen, M., H. Omre, and A. Buland, 2010, Improved resolution in Bayesian lithology/fluid inversion from prestack seismic data and well observations: Part 2 – Real case study: Geophysics, Vol 75, No 2, p B73-B82.

Ursenbach, C., A. Hasse, and J. Downton, 2007, Efficient spherical-wave AVO modeling: The Leading Edge, vol. 26, 1584-1589.

Ursin, B., 1990, Offset-dependent geometrical spreading in a layered medium: Geophysics, vol. 55, 492-496.

Van Koughnet, R. W., C. Skidmore, M. Kelly, and R. Lindsay, 2003, Prospecting with the density cube: The Leading Edge, vol. 22, no. 10, 1038-1045.

Varela, O., C. Torres-Verdin, and M. Sen, 2003, Joint stochastic inversion of pre-stack seismic data and well logs for high-resolution reservoir delineation and improved production forecast: 73rd Annual International Meeting, SEG, Expanded Abstracts.

Vasheghani, F. L. Lines, and J. Embleton, 2010, Q and quest for heavy oil viscosity: GeoCanada 2010 technical program.

Walden, A. T., 1991, Making AVO sections more robust: Geophysical Prospecting, vol 41, p 313-321.

Walls, J. D., M. T. Taner, T. Guidish, G. Taylor, D. Dumas, and N. Derzhi, 1999, North Sea reservoir characterization using rock physics, seismic attributes, and neural networks, a case history: 69th Annual International Meeting, SEG, Expanded Abstracts.

Wang, Z. 2001, Fundamentals of seismic rock physics: Geophysics, 66, 398-412.

Watson, I., 2004, Integrated geological and geophysical analysis of a heavy oil reservoir at Pike Peak, Saskatchewan: M.Sc. thesis, University of Calgary.

Walsh, D. 2008, SAGD 101, CSPG-CSEG-CWLS joint convention short course, May 2008.

Webb, M. W., 2011, Incised Valleys and Wabiskaw-McMurray Stratigraphic Nomenclature in the Mackay Region, Northwestern Part of the Athabasca Oil Sands, Alberta: CSPG 2011 convention technical program.

Whale, R., R. Bale, K. Poplavshi, K. Douglas, X. Li, and C. Slind, 2009, Estimating and compensating for anisotropy observed in PS data for a heavy oil reservoir: 79th Annual International Meeting, SEG, Expanded Abstracts.

Widess, M. B., 1973, How thin is a thin bed?: Geophysics, 38, 1176-1180.

Wightman, D.M., Pemberton, S.G., 1997. The Lower Cretaceous (Aptian) McMurray Formation: an Overview of the McMurray Area, Northeastern Alberta. *In*: Petroleum Geology of the Cretaceous Lower Manville Group, editors: Pemberton,

G.S., and James, D.P., Western Canada, Canadian Society of Petroleum Geologists, Memoir 18, 1997. p. 312-344.

Wikimedia.org, Multivariate normal distribution: http://en.wikipedia.org/wiki/Multivariate_normal_distribution.

Willis, B. J. and H. Tang, 2010, Three-dimensional connectivity of point-bar deposits: Journal of Sedimentary Research, vol. 80, 440-454.

Wynne, D. A., M. Attalla, H. Berhane, M. Brulotte, D.K.,Cotterill, R. Strobl, and D.M. Wightman, 1994, Athabasca oil sands database: McMurray/Wabiskaw Deposit: Alberta Energy and Utilities Board/Alberta Geological Survey, Open File Rep. 1994-14.

Xu, Y. and S. Chopra, 2007a, Benefitting from 3D AVO by using adaptive supergathers: The Leading Edge, Vol. 26, No. 12, 1544-1547.

———, 2007b, Improving AVO fidelity by NMO stretching and offset-dependent tuning corrections: Vol. 26, No. 12, 1548-1551.

Xu, Y. and S. Chopra, 2008, Deterministic mapping of reservoir heterogeneity in Athabasca oil sands using surface seismic data: The Leading Edge, Vol. 27, No. 9, 1186-1191

Yeung, K. C., 2007, An overview of Alberta in situ recovery methods: Petroleum Society of CIM – Lloydminster Section, Heavy Oil Technical Symposium.

Yu, G., 1985, Offset-amplitude variation and controlled-amplitude processing: Geophysics, Vol. 50, 2697-2708.

Zheng, Y., J. Wang, and M. Perz, 2008, Pitfalls and tips for seismic fracture analysis: 78th Annual International Meeting, SEG, Expanded Abstracts, 1167-1171.

Zhou, Z., and F. Hilterman, 2007, Is there a basis for all AVO attributes?: 77th Annual International Meeting, SEG Expanded Abstracts, 244–248.

Zou, Y., 2005, Integration of seismic methods with reservoir simulation, Pikes Peak heavy oil field, Saskatchewan: PhD thesis, University of Calgary.